Structural studies of organic and organometallic compounds using x-ray and neutron techniques

Cole, Jacqueline M.

STRUCTURAL STUDIES OF ORGANIC AND ORGANOMETALLIC COMPOUNDS USING X-RAY AND NEUTRON TECHNIQUES

Jacqueline M. Cole

Thesis submitted in part fulfilment of the requirements for the degree of

Doctor of Philosophy

at the

University of Durham

Department of Chemistry

September 1997

STRUCTURAL STUDIES OF ORGANIC AND ORGANOMETALLIC COMPOUNDS USING X-RAY AND NEUTRON TECHNIQUES

Submitted for the degree of Doctor of Philosophy, September 1997, by
Jacqueline M. Cole, University of Durham.

ABSTRACT

This thesis is sub-divided into two parts. Part (i) is entitled 'Structure / Property Relationships in Non-linear Optical Materials' (chapters 1-8) whilst part (ii) is entitled 'Structural Studies of imido, (bis)imido and aryloxide group VA and VIA transition metal complexes' (chapters 9-10).

Chapters 1, 2 and 3 provide an introduction to non-linear optics, X-ray and neutron experimental techniques used in this thesis and charge density studies respectively. Chapters 4 to 8 describe the investigations of the part (i) topic. These include bond length alternation studies on a series of tetracyanoquinodimethane derivatives and a charge density study of one of these compounds in chapter 4. Several other charge density studies are reported in chapters 5 and 6 which concentrate on methyl- nitropyridine and nitroaniline derivatives and the compound, 3-(1,1-dicyanoethenyl)-1-phenyl-4,5-dihydro-1H-pyrazole (DCNP) respectively. Chapter 5 also deals with the effect of intermolecular interactions on the non-linear optical phenomenon whilst in chapter 6, a detailed analysis of the thermal motion present in DCNP is also given. Investigations on intermolecular interactions are also reported in chapters 7 and 8 which studies the compounds, N-methylurea and zinc(tris)thiourea sulphate respectively. In the former case, the neutron derived structure of N-methylurea is reported at two temperatures and it is revealed that disorder is present at the higher temperature. In the latter case, neutron results from an instrument presently in the testing stages of its development are reported and contrasted with those obtained using a well established instrument.

Chapters 9 and 10 describe the investigations of the part (ii) topic. These concentrate on the structural features of two series of organometallic compounds which have potential use as polymerization catalysts. Relationships between structure and reactivity are reported.

DECLARATION

The work described in this thesis was carried out in the Department of Chemistry at the University of Durham and at the Institut Laue Langevin, Grenoble, France, between October 1994 and September 1997, under the supervision of Professor Judith A. K. Howard (at Durham) and Dr. Garry J. McIntyre (at Grenoble). All the work is my own, unless otherwise stated and it has not been submitted previously for a degree at this, or any other university.

Jacqueline M. Cole

ACKNOWLEDGEMENTS

First and foremost, I would like to thank my two supervisors, Professor Judith Howard and Dr. Garry McIntyre, for their continued help, support and encouragement throughout the course of my studentship. I would also like to thank Garry along with Dr. Chick Wilson for being my local contacts for the neutron experiments performed at the ILL and ISIS respectively.

Of course, no experimental crystallographic project is feasible without crystals and in this respect my thanks go to those who have provided the crystals for my experiments: Dr. Evelyn Shepherd and Professor John Sherwood at the University of Strathclyde, Dr. Marek Szablewski and Dr. Graham Cross from the Physics Department at the University of Durham, Dr. David Zelmon from the Wright-Patterson Laboratory in Ohio, U.S.A. and Dr. Michael Chan, Dr. Gary Walker and Professor Vernon Gibson, all three previously from the Chemistry Department at the University of Durham. On a similar note, I would like to thank Janet Moloney and Dr. Hugh MacBride from the Chemistry Department at the University of Durham for crystallizing several of my samples and also to Hugh for helping me synthesize one of them.

I would also like to thank all of the people that have been part of the crystallography group at Durham during the last three years. A special thanks goes to Dr. Roy Copley and Dr. Andrès Goeta for their extensive help with the X-ray charge density data sets collected on the Fddd cryodiffractometer, to Dr. Christian Lehmann for his help in obtaining the X-ray charge density data set collected on the Siemens SMART-CCD diffractometer, to Dr. Vanessa Hoy for her help with the NIPMAT analysis and the Cambridge Structural Database and to Dr. Jason Cole for providing me with three structures that he had determined which formed part of the bond length alternation study. I must also thank the Durham crystallographers Vanessa Hoy, Mark Roden, Janet Moloney and the ecologist Colin Nicholson for constantly putting me up in their house during my various visits to Durham during my second two years.

Finally, I would like to thank all those I have known in Grenoble. In particular, my thanks go to my two office mates, Rob Wimpory and Pia Iannone: to Rob particularly for his general wit and charm, for keeping me company on many an otherwise lonely evening spent at the ILL and for generally just being Rob; and to Pia, especially for her veined attempts at teaching me Italian. Last, but by no means least, I would like to thank Steven Fayers, Ian Matthews and Trevor Mairs for many entertaining times.

TABLE OF CONTENTS

Chapter 2 - X-ray and Neutron Experimental Techniques

LIST OF FIGURES

PART (I) STRUCTURE / PROPERTY RELATIONSHIPS IN NON-LINEAR OPTICAL MATERIALS

Chapter 1 - Introduction to Non-linear Optics

Chapter 2 - X-ray and Neutron Experimental Techniques

PART (II) STRUCTURAL STUDIES OF IMIDO, (BIS)IMIDO AND ARYLOXIDE GROUP VA AND VIA TRANSITION METAL COMPLEXES

Chapter 9 - Structural Studies of Half-Sandwich Imido, (Bis)Imido and Aryloxide Group VA Transition Metal Complexes

Chapter 10 - Structural Studies of (Bis)Imido Group VIA Transition Metal Complexes

LIST OF TABLES

PART (I) STRUCTURE / PROPERTY RELATIONSHIPS IN NON-LINEAR OPTICAL MATERIALS

Chapter 2 - X-ray and Neutron Experimental Techniques

Chapter 4 - Bond Length Alternation and Charge Density Studies of a Series of Tetracyanoquinodimethane Derivatives

LIST OF ABBREVIATIONS

A	Acceptor
BLA	Bond Length Alternation
CCR	Closed-Cycle Refrigerator
CD	Charge Density
CT	Charge Transfer
D	Donor
DCM	Dichloromethane
DCNP	3-(1,1-Dicyanoethenyl)-1-phenyl-4,5-dihydro-1H-pyrazole
DMF	Dimethylfuran
d-ZTS	deuterated Zinc (tris)Thiourea Sulphate
EDD	Electron Deformation Density
esd	estimated standard deviation
fm	Fermis
ILL	Institut Laue Langevin
LB	Langmuir-Blodgett
MBADNP	Methylbenzylaminodinitropyridine
MBANP	Methylbenzylaminonitropyridine
NIPMAT	Non-bonded Interaction Pattern Matrix
NLO	Non-Linear Optical
PSD	Position Sensitive Detector
SDS	Stewart-Davidson-Simpson
SHG	Second Harmonic Generation
TCNQ	Tetracyanoquinodimethane
ZTS	Zinc (tris)Thiourea Sulphate

PART (I)

STRUCTURE / PROPERTY RELATIONSHIPS IN NON-LINEAR OPTICAL MATERIALS

CHAPTER 1

INTRODUCTION TO NON-LINEAR OPTICS

1.1 OVERVIEW

The science of Non-Linear Optics (NLOs) was born in 1875 when J. Kerr observed a quadratic electric field induced charge in the refractive index of CS_2. This became known as the Kerr effect. Other findings of NLO phenomena soon followed, in particular, with the realization of the Pockel's effect in 1883.

These novel effects remained as a mere gleam in the eyes of the pioneering scientists as the effects were, at the time, of a very limited use. Interest died away, leaving their recordings in firmly closed books and journals on remote shelves to gather dust.

However, the invention of the laser in 1960 caused an explosive revival of NLOs and in 1961 P. Franken and co-workers first reported observations of Second Harmonic Generation (SHG) in quartz (Franken, Hill, Peters & Weinreich, 1961). Many more inorganic materials were subsequently found to possess NLO effects and in the early 1970s a further burst of scientific research emanated from the promising new developments in organic NLO materials.

Today, the study of NLOs is a multidisciplinary subject attracting people from all manner of backgrounds - from world specialists in polymeric thin films to those in crystal growth, right through to the mechanical and electrical engineers who continuously endeavour to build faster and better appliances which utilise these effects for use in the most advanced technological systems to devices employed in the everyday world.

A whole host of applications (Michl, 1994; Keiser, 1991; Keller, 1990; Lyons, 1989; Shen, 1984) exist as a result of the ongoing work in NLOs. An exhaustive list and adequate explanation of these applications would provide a substantial book in itself. Hence, only a selection is given here, to illustrate the vast scope and potential of this area of research. Applications include:

- Better visible light lasers - via use of frequency doubling of NLO chromophores which absorb in the U.V./visible range.
- Electrooptical devices - e.g. switches and waveguides.
- Telecommunications - development of high speed optical communications giving rise, in particular, to faster computation in computers.
- Compact data storage - advances towards the Gb/cm^2 range are being made.
- Image processing
- Holography
- Photorefractivity

- Multiphoton spectroscopy - employing Third Harmonic Generation (THG) to develop Coherent Antistokes Raman Scattering (CARS) and Coherent Stokes Raman Scattering (CSRS) techniques which have resulted in a revival of the range of Raman spectroscopy.
- Advances in fundamental studies of spectra - e.g. enhanced understanding of excitons, inhomogeneous line broadening and narrowing.
- SHG as a surface probe - Surface Enhanced Raman Scattering (SERS) , providing information on interfaces between two centrosymmetric substances (in any combination of states), particularly with reference to membrane studies in biological systems. Also, information can be obtained on adsorption strength and surface coverage, on molecular orientation at surfaces and on interfacial electric fields. SHG surface techniques are superior to many other such techniques because they give nearly instantaneous response times so that pulsed lasers can be used. Hence, time-resolved studies can be studied with ease thereby providing many opportunities for reaction kinetics, epitaxial layer crystal growth and surface diffusion.

The importance of the research into NLOs is ever increasing and the need for better understanding of materials exhibiting these effects cannot be over emphasized.

1.2 BASIC THEORY OF NONLINEAR OPTICS

The discussion which follows has been written in as simple a form as possible. For more comprehensive discussions of the theory, one is referred to Oudar & Zyss, 1982, Kleinman, 1962, Wooster, 1938 and Franken & Ward, 1963.

Application of an external electrical field* to any compound invokes a polarization, the extent of which is dependent upon each atom's polarizability within the molecule. These atomic polarizabilities can be summed to give an overall molecular polarizability which in many cases sums to zero, as polarization is a vector quantity and thus, cancelling effects ensue if the intrinsic symmetry of the molecule is high enough.

In simple studies, the polarization, **P**, is given by the linear equation:

$$\mathbf{P} = \varepsilon_0 \chi^{(1)} \mathbf{E} \qquad [1]$$

where ε_0 = permittivity of free space,
$\chi^{(1)}$ = linear susceptibility to polarization,
E = applied electric field.

However, this relation is correct only to a first approximation; indeed, the values calculated from it often deviate strongly from those obtained experimentally, especially when the medium is subjected to a very intense electric field, e.g. a laser pulse.
Therefore, the latter equation must be extended in order to account for higher order effects:

$$\mathbf{P_{TOT}} = \mathbf{P_o} + \varepsilon_0[\chi^{(1)}\mathbf{E} + \chi^{(2)}\mathbf{EE} + \chi^{(3)}\mathbf{EEE} + ...] \qquad [2]$$

where $\mathbf{P_{TOT}}$ = total polarization,
$\mathbf{P_o}$ = any permanent polarization in the medium,
$\chi^{(1)}, \chi^{(2)}, ...\chi^{(n)}$ = the nth order susceptibility to polarization.

This relation relates to polarization on a macroscopic scale. By converting the relevant macroscopic parameters to analogous microscopic ones, we obtain a relation for polarizability on the microscopic scale:

$$\mathbf{P_{TOT}} = \mu + \alpha\,\mathbf{E} + \beta\,\mathbf{EE} + \gamma\,\mathbf{EEE} + ... \qquad [3]$$

---

* The external electric field takes the form of a high power laser as very intense light is required in order to obtain an adequate electronic oscillation of photons.

where μ = the permanent dipole moment,
α = linear polarizability,
β, γ, ... = first, second, ... hyperpolarizability coefficients.

Hence, the induced polarization, $\mathbf{P_i}$, is given by:

$$\mathbf{P_i} = \alpha\mathbf{E} + \beta\,\mathbf{EE} + \gamma\mathbf{EEE} + \ldots \qquad [4]$$

In electronic terms, the hyperpolarizability coefficients relate to the successive higher order harmonics, 2ω, 3ω, ... (polarizability, α, relates to the fundamental frequency, ω). Thus, SHG corresponds to β , THG corresponds to γ and so on.

All harmonics are a result of electron-photon combination. For higher order harmonics to be observed, the *simultaneous* combination of 2, 3, ... electrons and 2, 3, ... photons must occur. For SHG, the following electronic transitions must occur:

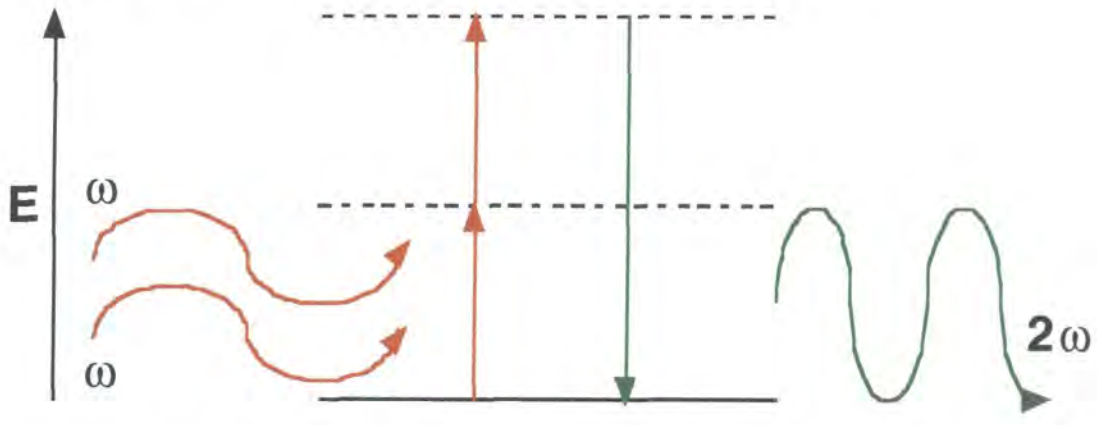

Figure 1.2.1 *- A schematic diagram which illustrates the process of frequency doubling.*

The probability of this simultaneous contribution becomes increasingly unlikely for the higher orders. Indeed, this explains the observation that successive higher order (non-linear) hyperpolarizability coefficients become increasingly lower in magnitude. Moreover, there exists an absolute limit for high-order harmonic generation (Moreno, Plaja & Roso, 1994).

1.2.1 The inherent link to crystallographic symmetry

So far it has been assumed that the NLO effect is isotropic, which would mean that the induced polarization would have to be parallel to the applied field. However, this is not true - molecules have distinct orientations within the unit cell (in the solid state) and hence, the intrinsic electronic structures of molecules are commonly highly anisotropic.

Therefore, the NLO effect can be more appropriately described by the use of tensor notation:

$$\mathbf{P_i} = \alpha_{ij}\mathbf{E_j} + \beta_{ijk}\mathbf{E_j}\mathbf{E_k} + \gamma_{ijkl}\mathbf{E_j}\mathbf{E_k}\mathbf{E_l} + \ldots \qquad [5]$$

where $\mathbf{P_i}$ is a first rank tensor
α_{ij} is a second rank tensor,
β_{ijk} is a third rank tensor,
γ_{ijkl} is a fourth rank tensor.

β_{ijk} can be related to the crystalline first-order non-linearity by the equation:

$$\mathbf{d_{IJK}}(-2\omega;\ \omega,\ \omega) = \eta f_I^{2w} f_J^{w} f_K^{w} \sum_{s=1}^{n} \cos(I,i(s))\cos(J,j(s))\cos(K,k(s))\beta_{ijk}(s) \qquad [6]$$

where $\mathbf{d_{IJK}}$ represents the macroscopic tensorial NLO coefficient in Voigt notation (Cady, 1946);
$(-2\omega;\omega,\omega)$ denotes the type of input and output frequencies*;
η is the number of molecules in the crystal unit volume;
f are the Lorentz local-field factors#;
I,J,K are crystallographic reference frame indices;
i,j,k are molecular frame indices;
n is the number of molecules;
the cosine product terms describe the relationship between the molecular and crystal reference frame.

This Voigt notation (Cady, 1946) was formerly used for piezoelectric calculations, but all the tensorial arguments for SHG are identical. Hence, the restriction of piezoelectricity to non-centrosymmetric crystals also applies to the SHG phenomenon.$

Equation [6] can be simplified to the following:

---

* The frequency arguments in the parentheses to the right of the semicolon relate to the input frequency and those to the left relate to the output frequency. The negative sign is simply a conventional depiction of output frequency as opposed to 'positive' input frequency. Thus, the total sum of the frequencies within the parentheses should equal zero.

The Lorentz local-field factor denotes an inter-relationship between the magnitude of the applied field and that 'felt' by the molecule. It corresponds to the relation, $f(\omega)=(n2 + 2)/3$ where n = refractive index. Indeed, it transpires that the actual field 'felt' by the molecule is *greater* than that of the applied field.

$ However, one must note that the *magnitudes* of all piezoelectric and SHG coefficients are completely uncorrelated because the piezoelectric effect originates from ionic displacements whereas the NLO phenomenon originates from electronic transitions.

$$\mathbf{d_{IJK}}(-2\omega;\ \omega,\ \omega) = f_I^{2w} f_J^{w} f_K^{w} \sum_{t=1}^{P} \mathbf{b^t_{ijk}} \qquad [7]$$

$$\text{where } \mathbf{b^t_{IJK}} = \frac{1}{n(g)} \sum_{s=1}^{n(g)} \cos(I, i(s)) \cos(J, j(s)) \cos(K, k(s)) \beta_{ijk} \qquad [8]$$

and g = the order of the point group;
n(g) = number of equivalent positions in the unit cell.

Hence, β_{ijk} (and $\mathbf{d_{IJK}}$) are inversely proportional to the order of the point group - i.e. the less symmetry present in a material, the higher its potential SHG effect. Indeed, many of the different $\mathbf{d_{IJK}}$ coefficients cancel each other out in the higher symmetry point groups (Wooster, 1938). The extreme example is any molecule belonging to point group 432 where the few non-zero coefficients remaining, after the summation of direction cosines, undergo a further symmetry restriction* such that all remaining components sum to zero. Hence, no SHG effect is observed despite the fact that class 432 is a non-centrosymmetric point group.

In contrast to piezoelectricity, further symmetry restrictions are imposed on the SHG phenomenon, via Kleinman perturbation theory (Kleinman, 1962). This states that:

$$\mathbf{d_{zxx} = d_{xxz} = d_{xzx}} \qquad [9]$$

However, it has been found that this restriction is only valid at low frequencies (Lalama & Garito, 1979) because here absorption and more particularly dispersion, have an important effect - for only 2% dispersion in quartz, β_{ijk} varies by 15% (Franken & Ward, 1963).

It should be noted that all of these symmetry restrictions apply to all even order hyperpolarizability coefficients, not just to β_{ijk}. However, all odd order (hyper)polarizability coefficients, i.e. α_{ij}, γ_{ijkl}, ... have no such symmetry constraints imposed upon them. This differential imposition of constraints is explained mathematically by Wooster, 1938.

It also transpires that, for most compounds, the β_{zzz} hyperpolarizability is by far the most significant (z = the direction along the dipole axis) since μ is inherently related to β_{ijk} (Marder, Bertran & Cheng, 1991) and the first hyperpolarizability is often approximated as a one dimensional effect. This is adequate in simple cases but in order

* The symmetry requires that a cyclical interchange of the axes is possible without affecting the magnitude of the physical constants.

to encompass more complicated systems into this approximation validly, the hyperpolarizability is often modelled in a two dimensional manner (Davydov et al, 1970).

The search for NLO crystals of the even order is thus formally limited to a minor subset of all existing compounds since the ratio of non-centrosymmetric to centrosymmetric molecules is 3:7, as determined using the Cambridge Structural Database (Allen et al, 1991). However, one can induce non-centrosymmetry into formally centrosymmetric materials by various methods as is described in the following section.

1.3 INDUCING NON-CENTROSYMMETRY INTO MATERIALS

1.3.1 Incorporating chirality into molecules

One can quite easily introduce a chiral centre into a formally centrosymmetric molecule, particularly if the molecule is organic. Less easy is the necessary synthesis of the optically pure enantiomer (Menig & Pierce, 1989). By definition, a chiral compound must be non-centrosymmetric due to the non-superimposable characteristics of chirality.

However, it should be noted that the resulting NLO effect is often weak because the departure from centrosymmetry is small due to the molecule's inherent tendency to affect the highest symmetry possible (Zyss, 1982). In order to optimize the NLO effect as far as possible, the chiral centre should not be placed within the area of maximum charge transfer.

It is also worth pointing out that many amino acids exhibit NLO effects due to the innate non-centrosymmetric tendency in nature. Indeed, work on NLO effects of these materials has become increasingly popular (Lecomte, 1995) due to the advances in crystal growth of amino acids (Ducruix & Giege, 1992).

1.3.2 Inclusion complexes

A detailed discussion of inclusion compounds is given by Farina, 1984 and Atwood, Davies & MacNicol, 1984. Studied guest-host systems have included both organic (König, Hoss & Hulliger, 1995) and organometallic (Tam et al, 1989; Anderson, Calabrese, Tam & Williams, 1987) gusets, all of which by themselves do not exhibit significant SHG effects. However, the channels of the host molecules into which the guests form, restrict the guest's packing to a head-to-tail arrangement (as opposed to a head-to-head or tail-to-tail arrangement). This specific arrangement is optimized by electrical poling during the addition of the guest.

Most studies, to date, have used thiourea as a host because it is well known to form channel inclusion complexes (Atwood, Davies & MacNicol, 1984). However, recent studies have shown that perhydrotriphenylene (PHTP) is a promising alternative host candidate (Hoss, Hulliger & König, 1995).

Crystals of inclusion compounds are relatively easy to grow. This facilitates crystallographic studies of these compounds. Such studies clearly illustrate the extent of desired head-to-tail (poled) arrangement of the guest molecule.

1.3.3 Zeolites

As with inclusion complexes, zeolites possess channels in which guest molecules can reside. Therefore, zeolites induce non-centrosymmetry in an analogous way to inclusion compounds. However, the methods differ in a few respects.

The incorporation of hosts into zeolites rather than in inclusion complexes has two advantages, the first being that of zeolite versatility: the size and shape of the necessary cavity is very easy to engineer in zeolites (Finger, Richter-Mendau, Bülow & Kornatowski, 1991) whereas it can prove exceedingly difficult to find an inclusion guest molecule of a suitable topology and one that will crystallize relatively easily for a given host molecule.

The second advantage of zeolites is the relative ease of designing a suitable overall surface charge within the channels of the zeolite such that it will optimize the SHG effect (Marlow, 1991),

$$\text{c.f.} \quad (\text{SHG})^{1/2} \quad \alpha \quad \text{negative surface charge.}$$

The use of zeolites, however, presents one notable disadvantage: they are notoriously difficult to crystallize to an adequate size for structural studies to be performed in order to ascertain the extent of polar arrangement. However, novel crystal growth methods for zeolites have recently received quite a bit of attention (Girnus, Jancke, Vetter, Richter-Mendau & Caro, 1995). Moreover, technology in the structural characterization field has recently shown prolific advances in two respects: first, the dramatic developments in Rietveld refinement (Young, 1991) for powder diffraction, in conjunction with the use of microcrystalline diffraction, magic angle spinning NMR and electron microscopy have been shown to be successful in the determination of zeolite structures and their contents (McCusker, 1991). Secondly, synchotron technology is becoming more and more powerful (Coppens, 1992) such that single-crystal diffraction studies can be performed using crystals of the order of micrometres in each dimension (Garter, Halliday & Singer, 1991).

At present, the development of zeolites as 'vehicles' for inducing SHG in molecules is still at a relatively early stage. Indeed, only a few host molecules have so far been incorporated into zeolites to give the desired effect (Marlow, Caro, Werner, Kornatowski & Dähne, 1993; Werner, Caro, Finger & Kornatowski 1992) e.g. *p*-NA in ZSM-5 (Caro, Finger, Kornatowski & Werner, 1992). However, the potential of the technique holds for a promising future.

1.3.4 Polymeric systems

The simplest example of this type of system involves a guest-host combination whereby the host is a polymer, most commonly polymethylmethacrylate (PMMA) because of its desirable properties+ and the guest is a polar molecule.

The host can be poled into the polymer film by various methods, the most common one being corona poling (Mortazavi, Knoesen, Kowel, Higgins & Dienes, 1987; Singer et al, 1988). In this technique, the guest is incorporated into the polymer when the polymer's glass transition temperature, T_g, is exceeded. A d.c. electric field is then applied which induces polarization such that the dopant orients its molecular dipole axis along the direction of the external electric field. This field is sustained until the system has been allowed to cool to ambient conditions. This induces a 'freezing' effect of the poled orientation of the host and hence overcomes any symmetry restrictions. The poled system will then exhibit SHG effects.

However, various problems exist with this technique:

- The maximum wavelength of absorption, λ_{max}, increases with electric field poling (Haringa & van Pelt, 1979; Charney & Yamaoka, 1972) the extent of which is directly related to the orientation of the chromophore within the film. This hypsochromatic effect is undesirable due to the importance of the development of appliances such as blue/green lasers, whereby the frequency doubling precursor wavelength must remain firmly within the U.V. range.
- The frequent lack of thermal stability - the decay time being related to the value of T_g (Michl, 1994). Although, cross-linking has been found to result in increased stability (Chengzeng et al, 1992a & 1992b).
- Corona poling often gives rise to undesirable surface charges which can inhibit SHG. However, Barry and Soane (1991) have developed a new way of using high pressure CO_2 and heating to a value *below* T_g, which invokes plasticization of the polymer.
- The size of the different domains in polymers often perturbs the NLO effect. This is because, for the maximum SHG effect to be obtained, the particle size should be greater than the coherence length of the material (Kurtz & Perry, 1968).

+ These include slow poled-order decay times due to the fact that PMMA has a low glass transition temperature, T_g (Michl, 1994).A low T_g is also desirable in order to avoid any decomposition during poling (as for many polymers with high T_g values, the decomposition temperature is less than T_g). Also, PMMA has a sufficiently large free volume to encompass most hosts and it can be easily cross-linked (Torkelson & Victor, 1992; Royal, Torkelson & Victor, 1992; Royal & Torkelson, 1992).

More exotic SHG active polymeric films have also been developed. In particular, those involving nematic liquid crystalline thermoplastics (Collings, 1990) as hosts (Bruce & Thornton, 1993). Corona poling is applied to a liquid crystalline polymer and at T_g, a transition to the nematic mesophase follows which, in turn, gives rise to the alignment of mesogens throughout the polymer thereby increasing polar alignment.

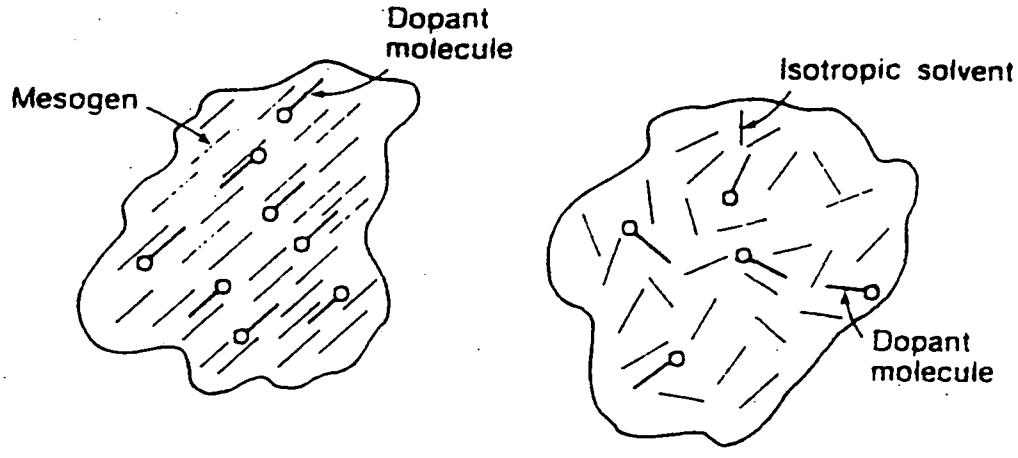

Figure 1.3.1 *- A schematic diagram showing a thermally randomized nematic medium with dopant molecules versus an isotropic medium (Chemela & Zyss, 1987).*

1.3.5 Langmuir-Blodgett Films

Langmuir-Blodgett (LB) films are made up of a hydrophobic and a hydrophilic part of a molecule. These molecules form a film over the surface of water, just as a surfactant does. The process of LB deposition is clearly described by Chemela & Zyss (1987) and is illustrated in ***Figure 1.3.2***. This process results in the formation of a monolayer film over a solid support. Further layers can be implanted on this support, above the already existing films.

These successive layers do not have to be the same material as those films already present on the solid surface. Hence, the system can be molecularly engineered so that the final film consists of alternately donor and acceptor layers, i.e. -D-A-D-A-D-, and organized in a head-to-tail fashion (Girling & Milverton, 1984). Thus, a non-centrosymmetric arrangement results, giving rise to a SHG active material.

These alternately layered films are *stable* solids as determined by Barraud et al. (1986). This is because in LB films, the high interchain van der Waals cohesion effects dominate over the competing polar effects, which tend towards centrosymmetric alignment by nature of the presence of high dipole moments.

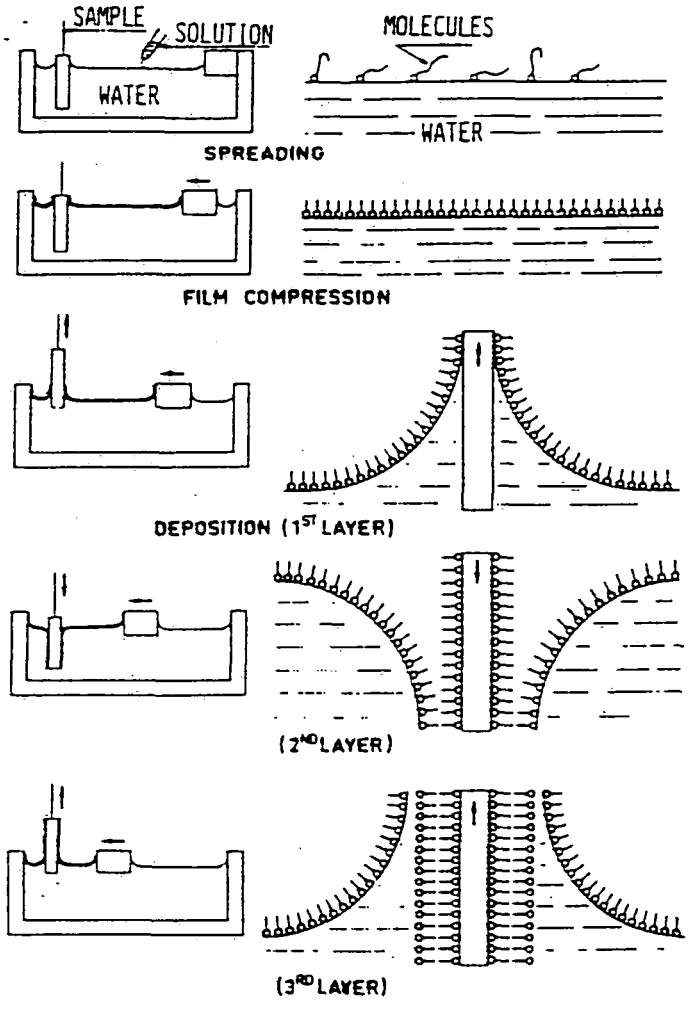

Figure 1.3.2 - A step by step schematic diagram of the LB deposition process (Chemela & Zyss, 1987).

Moreover, the resulting films need not be very thick which means that sharp phase tuning is not required, contrary to the bulk crystal and therefore, handling of the material is easier.

The field of SHG active LB films has yet to be fully exploited. However, results so far obtained (Aktsipetrov, Akhmediev, Mishina & Novak, 1983; Aktsipetrov, Akhmediev, Baranova, Mishina & Novak, 1985; Cade et al, 1985; Ashwell et al, 1990) indicate that a promising future may lie ahead in this area.

1.3.6 Organic salts

Following Meredith's initial findings (Meredith, 1983), Marder and co-workers (Marder, Perry & Schaefer, 1989 and 1992; Marder, Marsh, Perry, Schaefer & Tiemann, 1990; Groves et al, 1989; Marder, Perry, Schaefer & Tiemann, 1991; Boden et al, 1991a & 1991b) and Nakanishki and co-workers (Kato et al, 1990a and 1990b;

Koike et al, 1990; Hamazaki et al, 1989; Kato, Matsuda, Maramatsu, Nakanishi & Okada, 1988) have recently developed this area of potential SHG active compounds. They have shown that formally centrosymmetric cationic chromophores can exhibit a large β value when co-crystallized with various anions (Marder & Perry, 1993). One such material is 4-N,N-dimethylamino-4'-N'-methylstilbazolium toluene-*p*-sulphonate (DAST) which gave an SHG powder efficiency 1000 times that of the standard reference, urea (Marder, Perry & Schaefer, 1989). This finding provided the impetus for the renewed interest in this method.

A rationale for the exceptional β values of these types of compounds has been proposed by Marder, Perry & Schaefer, 1992. Their hypothesis states that the donor-acceptor electrostatic attraction incurred by the formation of alternating cationic and anionic sheets favours the formation of macroscopically polar structures. The two most favourable orientations of these sheets with respect to each other are the parallel and anti-parallel arrangements. From detailed considerations of the combined steric and Coulombic effects, the predominant arrangement appears to be of the parallel nature, i.e. the non-centrosymmetric form.

1.3.7 Reducing symmetry by occlusion

Meredith and co-workers (Weissbuch, Lahav, Leiserowitz, Meredith & Vanherzeele, 1989) have shown that non-centrosymmetry may be achieved via the preferential occlusion of a guest molecule into a formally centrosymmetric molecule, leading to significant NLO effects. Examples include the occlusion of various α-amino acids into α-glycine and *p,p'*-dinitrobenzylideneaniline into *p*-(N-dimethylamino)benzlidene-*p'*-nitroaniline.

It has been shown (Addadi, Berkovitch-Yellin, Lahav, Leiserwitz & Weissbuch, 1986; Frolow et al, 1988) that the dopant may be adsorbed and preferentially occluded through different subsets of the surface sites on the different crystal face, resulting in the formation of a mixed crystal of reduced symmetry to the pure chromophore. The poling of the guest molecule within the host is then a trivial matter.

Note that the method only requires a very minimal dopant concentration in order that a substantial SHG signal is observed (Lahav, Leiserowitz, Meredith, Weissbuch & Wanherzeele, 1989).

1.3.8 Hydrogen bonding effects

Etter and and co-workers (Etter, 1991; Etter & Frankenbach, 1989) have performed detailed studies of the design of non-centrosymmetric molecules via hydrogen bond directed co-crystallization. By applying simple acid / base arguments to hydrogen bonds, the following three basic rules were formulated:

Rule 1: *'All acidic hydrogens available in a molecule will be used in hydrogen bonding in the crystal structure of that compound.'* (Donohue, 1952).

Rule 2: *'All good acceptors will be used in hydrogen bonding when there are available hydrogen bond donors.'* (Etter, 1982).

Rule 3: *'The best hydrogen bond donor and the best hydrogen bond acceptor will preferentially form hydrogen bonds to one another.'* (Etter, 1990).

The latter rule is effectively the result of the first two rules and applies directly to acentric co-crystal design, as is illustrated by the example given in ***Figure 1.3.3***:

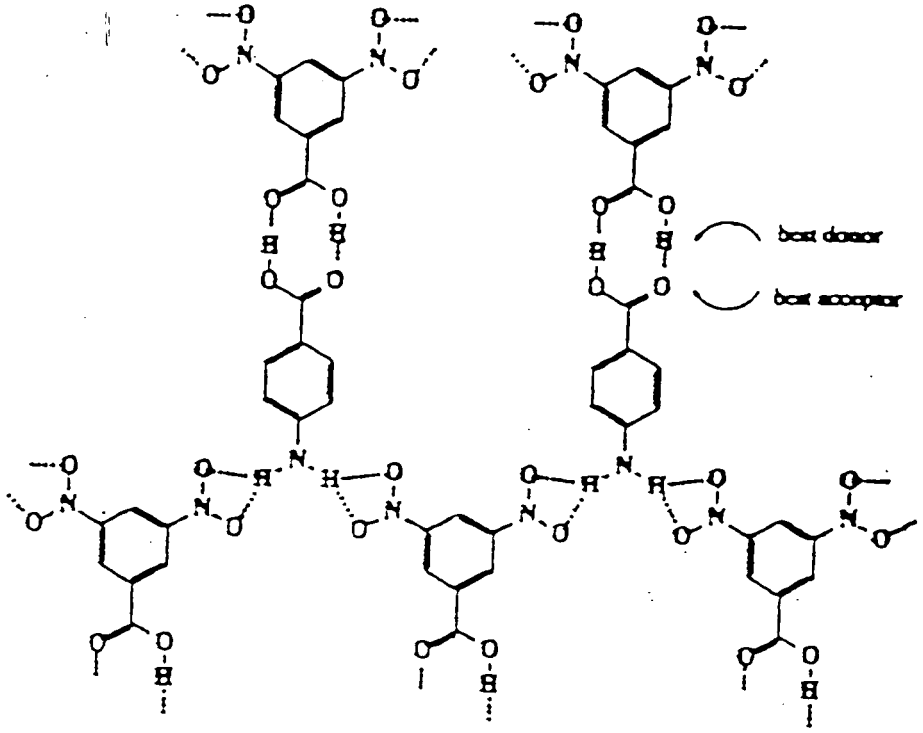

Figure 1.3.3 *- An example of successful co-crystal design: 4-aminobenzoic acid. and 3,5-dinitrobenzoic acid. (Etter, 1991).*

In non-hydrogen-bonded compounds, close packing of bulky and irregular steric substituents is the overriding factor which determines the crystal symmetry. However, in hydrogen-bonded compounds, hydrogen bond directed acentricity occurs despite the presence of steric effects. This is assumed to result from the bond formation prior to crystallization which provides a bias on the packing and which is retained through the nucleation stage.

Therefore, hydrogen bonding can act as a formidable 'tool' for invoking not only the desired crystal non-centrosymmetry, but also certain head-to-tail packing configurations.

1.4 OPTIMIZATION OF THE SHG EFFECT MICROSCOPICALLY AND MACROSCOPICALLY

Once non-centrosymmetry has been established and in the most favourable circumstances, the compound also has very low symmetry, one must next determine the optimal molecular make up of the crystal and the best way to achieve good propagation of SHG throughout the material.

1.4.1 Optimizing SHG microscopically

One can optimize the SHG of a material microscopically by maximizing the value of the molecular hyperpolarizability, β_{ijk}.* Thus, all factors affecting β must be considered.

It has been shown that the predominant factor affecting the β value is the extent of charge transfer (CT) within a molecule (Davydov et al, 1970; Oudar & Zyss, 1982; Oudar, 1977; Lalama & Garito, 1979; Albrecht & Morell, 1979). Moreover, orbital calculations have shown that the transition relating to this effect is that of a π_D-π_A^* type, thus suggesting the need for both the highest occupied molecular orbitals (HOMOs) and lowest unoccupied molecular orbitals (LUMOs) of the molecules to be of a π-type, the energy gap between them being small (so as to facilitate the ease of CT), and the HOMO to contain electron donating atoms.+

In turn, the extent of CT can be related back to the nature of the π-conjugation due to the fact that the CT is taking place through a π-π^* transition. Pioneering studies of π-conjugation of organic molecules were made by Hermann and co-workers (Ducuing & Hermann, 1974; Ducuing, Hermann, & Ricard, 1973; Baughman et al, 1976). Since then, much work has been undertaken in order to gain a deeper understanding into the nature of π -conjugation and its effect on β.

1.4.1.1 Bond Length Alternation Theory

Marder and co-workers (Cheng, Gorman, Marder & Tiemann, 1993; Gorman & Marder, 1993) have used semi-empirical calculations to show that there exists a correlation between β and a molecular parameter, termed bond length alternation, (BLA). BLA corresponds to the average difference, Δr, in bond length between two

* In the following section, the tensor notation of β_{ijk} is dropped because the discussion involves optimizing β overall rather than in an orientational sense.

+ Note, these calculations are based on a two energy level state model. This model is usually accurate enough; however, the model breaks down in some circumstances (Cheng et al, 1991b). Even so, for our purposes, any extraneous effects are negligible as the general features which optimize the effect do not change.

adjacent carbon-carbon bonds in a polyene chain. For example, in a completely delocalized system there will be no BLA, hence, $\Delta r = 0$. This instance is actually very rare because Peierel's distortion effects usually ensue. However, Kuhn found an example where $\Delta r = 0$ in a cyanine dye (Kuhn, 1958) and since then, other symmetrical cyanines have been found possessing this property (Ortiz et al, 1994). Consequently, $\Delta r = 0$ is now called the cyanine limit.

Note that BLA corresponds to the *average* difference in carbon-carbon bond lengths. Thus, BLA is also inherently a measure of the extent of mixing of the different resonance structures which lie in the thermally accessible range. Indeed, this is partly the reason why symmetric cyanines exhibit no Peierel's distortion - they have two degenerate resonant states which when combined, completely cancel out opposing effects.

The exact dependence of β on BLA is illustrated in ***Figure 1.4.1*** :

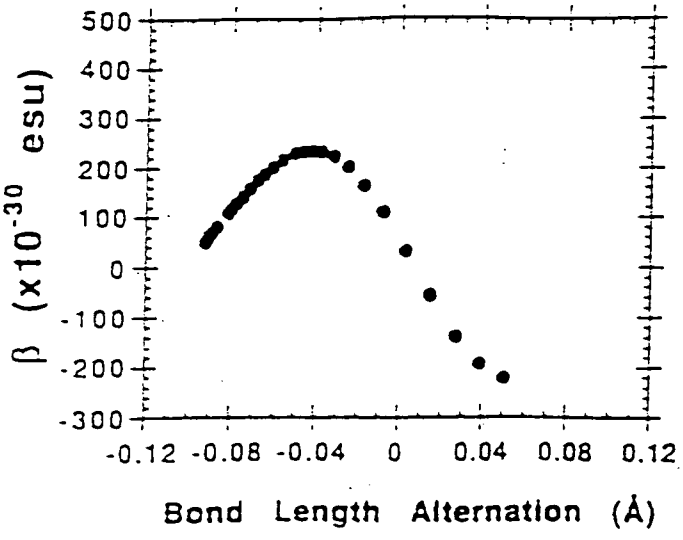

Figure 1.4.1 *- A graph of the first hyperpolarizability, β, versus BLA for $(CH_3)_2N$-$(CH{=}CH)_4CHO$ (Marder & Perry, 1993).*

and experimental evidence exists (Marder et al, 1993) to confirm the validity of these calculations.

The general profile of the graph of β versus BLA does not alter from compound to compound. However, there is a slight change in the value of Δr which gives the maximum β coefficient for each molecule, although it does not deviate much from $\Delta r = 0$. This is expected as complete delocalization will give rise to optimal CT. Therefore, in designing SHG active molecules, one should aim for all π-conjugation to be such that Δr tends to zero.

1.4.1.2 Conjugation Planarity (Cheng et al, 1991a).

A high extent of conjugation planarity leads to a large π-orbital overlap. This, in turn, leads to a greater ease in CT and an increase in donor to acceptor (D-A) interactions.

The torsional angle, θ, between two π-systems would be equal to zero for optimal conditions. The smaller θ is, the lower the transition energy and extinction coefficient, ε, of the π-π* transition and hence, the greater the CT. For the ideal case, in the sense of planarity, the molecular constituents involved in the π-conjugation would be one dimensional, i.e. all the relevant atoms would lie in a line. Obviously, this will only occur if the conjugated parts of the molecules contain exculsively acetelyne links. However, complete or even partial triple bond character is not desirable (see next section) and a compromise must be made so that little or no triple bond character exists but the value of θ remains as low as possible.

1.4.1.3 Effect of Triple Bond Character (Cheng et al, 1991a).

Whilst the presence of triple bonds enhances planarity, they also give rise to extreme BLA, thus invoking a diminution of β. Moreover, the presence of just one triple bond within a predominantly double bonded π-conjugation system will cause a sharp decrease in β. Aside from the effects of BLA, the orbital mismatch between an sp-hybridized triple bond and any adjacent carbon atom of sp^2-hybridization will result in a decrease in the effectiveness of π-delocalization and thence, CT. Additionally, the structural and electronic inhomogeneity in the conjugation path incurs additional diffusion of the electronic wavefunction which reduces β even more (Barzoukas, Blanchard-desce, Josse, Lehn & Zyss, 1989).

In short, if triple bonding is not essential, then it is best to avoid it completely.

1.4.1.4 Delocalization Length (Cheng et al, 1991a).

A correlation has been found between the value of β and delocalization length, L. This correlation appears in the form of a power law dependence:

$$\beta \quad \alpha \quad L^{\eta}$$

where η is an exponent dependent upon several factors:

- The extent of participation of ground-state orbitals to π-conjugation - an increase in L gives rise to a rapid increase in the number of orbitals involved and thus, a large value of η results.

- The extent of dispersive enhancement for structures with low energy CT transitions - the dispersive enhancement increases with an increase in L, again because of the increase in the number of π-orbitals involved.
- Deformational contributions dominated by the *second* order hyperpolarizability, γ_{ijkl}, which perturb η and since γ_{ijkl} is very dependent on L, much more so than β, the perturbation of η due to this effect increases rapidly with an increase in L.

When one or more of the above effects are present in a compound the reliability of the absolute value of η is reduced. However, the general trend of these values with respect to each other in a series of related compounds can prove useful.

1.4.1.5 Extent of Aromaticity

Aromatic substituents are necessary features of an SHG active compound (Barzoukas, Blanchard-desce, Josse, Lehn & Zyss, 1989) as they provide the delocalization required to promote extended π-conjugation through the molecule. They are also important in the sense that the relevant π-π* SHG transition often corresponds to orbitals from the aromatic ring. This is the case for *p*-nitroaniline (*p*-NA), the 'prototype' organic NLO compound, where the π-π* transition is due to the aromatic-to-quinoidal resonance.

However, the ease of CT for an aromatic type ring is less than that of a quinoidal type ring. This is because the quinoidal structure possesses a lower ionization potential and a larger electron affinity than the aromatic system (Brédas & Street, 1985). In other words, polarization of a phenyl unit into a quinoidal form is energetically costly. Hence, aromaticity tends to be retained in most cases. This leads to a localization of D-A interactions at the end groups and a hampering of extended CT which in turn decreases β. Moreover, Morley's calculations (Docherty, Morley & Pugh, 1987) indicate that phenyl groups are much less effective at CT than olefinic groups per unit of physical length.

This undesirable feature of aromaticity has encouraged work to be carried out on thiophene analogues of benzene containing NLOs (Drost, Jen, Rao & Wong, 1993) in order to test the effects of reducing the aromaticity. Results showed much larger NLO susceptibilities. Further still, thiophenes have the advantage of much better solubility than benzene, and a greater potential holds for more extended structures with thiophene derivatives than for benzenoid derivatives. Work is now also extending to pyridine (Bailey et al, 1993) and 2-pyrazoline (Bailey, Cruickshank, Pugh & Sherwood, 1991) systems.

However, aromatic-to-quinoidal resonant interchange is possible in favourable cases, eg. for tetracyanoquinodimethane (Long, Sparks & Trueblood, 1965). In view of this, a comparison of quinoidal versus aromatic nature has been carried out (Brédas, 1987) using BLA theory. Using Valence Effective Hamiltonian (VEH) calculations, a link between the band gap and BLA in aromatic polymers has been elucidated (***Figure 1.4.2***):

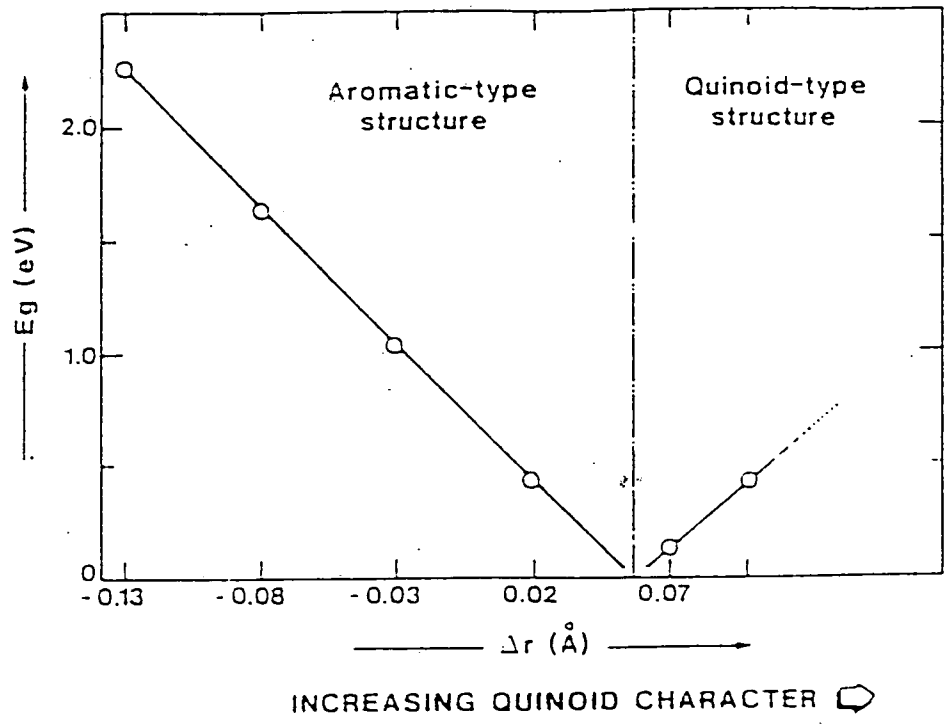

Figure 1.4.2 *- A graph of the bandgap, E_g, versus the extent of BLA for a polythiophene chain (Brédas, 1987).*

The emphasis on the link with the band gap and not directly with the value of β, is due to the fact that this comparison was made initially to understand the nature of conducting polymers, not of SHG molecules. However, the results are just as relevant to SHG studies because the lower the band gap, the greater the ease of charge transfer and hence, the larger the first hyperpolarizability coefficient, β .

The results illustrate clearly that an exact balance of quinoidal and aromatic structure will give rise to the optimum value of β. Indeed, the minimum in the given graph represents the energy cross-over between HOMO and LUMO states. This trend can be rationalized by considering that when we increase the quinoidal nature of a formally aromatic type ring, we destabilize the HOMO and stabilize the LUMO. Hence, a point of cross-over is reached whereby the molecule is termed predominantly quinoidal.

One other point to note is that the VEH calculations in this example (for polythiophene) do not show the band vanishing completely at the cross-over point. This is due to the inherent limitations of VEH calculations: the HOMO and LUMO bands in the given system belong to the same irreducible representation and therefore, a HOMO/LUMO degenerate system may result (i.e. $E_g = 0$). However, VEH calculations do not account for these group theoretical effects and hence, ignores degeneracy.

To summarize, the preservation of π-electron degeneracy by obtaining an equal balance of quinoidal and aromatic nature within a structure will give the optimum value of β. This equal balance is difficult to achieve precisely. However, the following cyanine chromophore possesses two such degenerate CT configurations which exist in a 50:50% probability and the loss of aromatic nature and gain in quinoidal nature in going from one form to the other is the same:

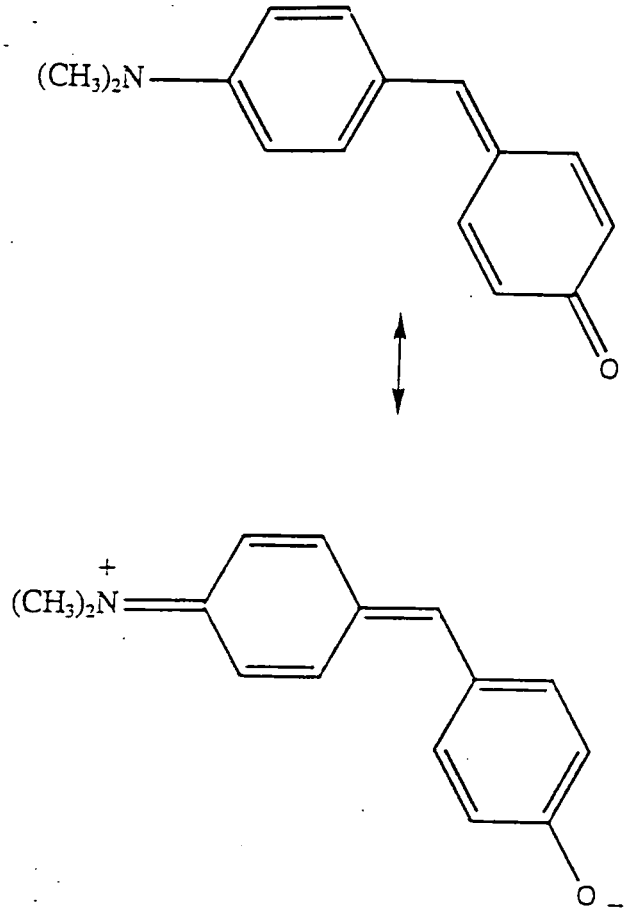

Figure 1.4.3 *- A molecule which exists in two resonant states which interconvert in a balanced energy exchange manner (Beratan, Cheng & Marder, 1991).*

1.4.1.6 Donor-Acceptor Interactions

Without relatively strong donors and acceptors in a molecule, the molecular polarizability, α, will be very low and the extent of charge transfer will be minimal. This will, in turn, lead to a small value of β. However, despite the desirability of strong D-A interactions, they can become too strong as exemplified by results obtained from theoretical calculations (Marder & Perry, 1993):

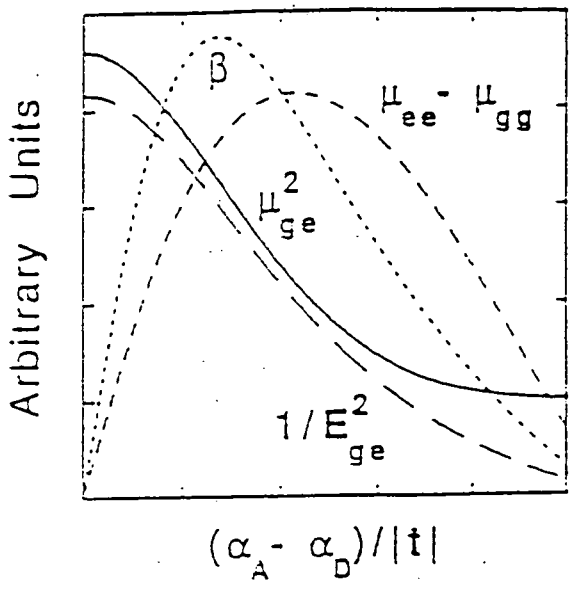

Figure 1.4.4 *- A graph which illustrates the dependence of the strength of D-A interactions on the first hyperpolarizability, β (Marder & Perry, 1993).*

where $(\alpha_A - \alpha_D) / |t|$ is effectively a measure of the extent of D-A interactions. (α_D, α_A = donor and acceptor Coulomb energies respectively; $|t|$ = the coupling matrix element between bridge orbitals for a general four-orbital π-system).

Experimental results have confirmed these calculations (Cheng et al, 1991; Barzoukas, Blanchard-desce, Josse, Lehn & Zyss, 1989; Hesselink & Huijts, 1989). It is particularly important to obtain the correct strength of interactions for small molecules since the correct strength becomes less important as the length of the molecule increases (Barzoukas, Blanchard-desce, Josse, Lehn & Zyss, 1989).

1.4.1.7 Intermolecular Effects

The relevant electronic excitation invoking the SHG effect corresponds to a wavelength of the order of micrometres. However, molecular lengths are of the order of Ångströms. Hence, one cannot consider the origins of the SHG effect purely on the molecular scale.

Intermolecular effects must therefore play an important role linking the molecular SHG origins to the micrometre effect. In particular, hydrogen bonding must be considered as it is the strongest form of intermolecular interaction. Desiraju and co-workers (Sarma et al., 1997) clearly illustrate the importance of hydrogen-bonding in the example material, 4-Iodo-4'-Nitrobiphenyl, where the molecular hyperpolarizability, β, is only 4.3×10^{-36} esu whereas the macroscopic $\chi^{(2)}$ is a moderate 6 x urea. This discrepancy can only be rationalized in terms of the role of hydrogen-bonding and other intermolecular effects since β does not take these effects into account whereas $\chi^{(2)}$ does.

1.4.1.8 The Transition Dipole, $\Delta\mu_{eg}$

The transition dipole, $\Delta\mu_{eg}$, is the change in dipole moment between the ground and excited states of a molecule during the relevant NLO transition,

$$\text{i.e. } \Delta\mu_{eg} = \mu_e - \mu_g. \qquad [10]$$

$\Delta\mu_{eg}$ is dependent upon the strength of D-A interactions (see ***Figure 1.4.4***) and therefore has an inherent link to the first hyperpolarizability, β. As the dominant contribution to β is usually along the charge transfer axis, then the optimum orientation of μ_g respect to μ_e will be along this axis too (Oudar & Zyss, 1982). If, however, a single charge transfer axis cannot be defined, then β must be defined in a plane, i.e. have two-dimensional character, as must $\Delta\mu_{eg}$.

1.4.1.9 Practical Considerations

By considering all of the above factors which affect the value of β, one may synthesise an optimally engineered SHG active molecule. Some such molecularly engineered crystals have already been synthesized (Masse & Pécaut, 1994) and the pathway for more lies wide open. However, one must also appreciate various practical requirements which apply to NLO materials such as thermal stability, adequate solubility, molecular rigidity and an appropriate value of λ_{max} for frequency doubling purposes (there is an upper limit to β due to the increase in λ_{max} with β (Zyss, 1982)).

1.4.2. Optimizing SHG macroscopically

Imagine a laser beam of frequency, ω, passing through an SHG active crystal:

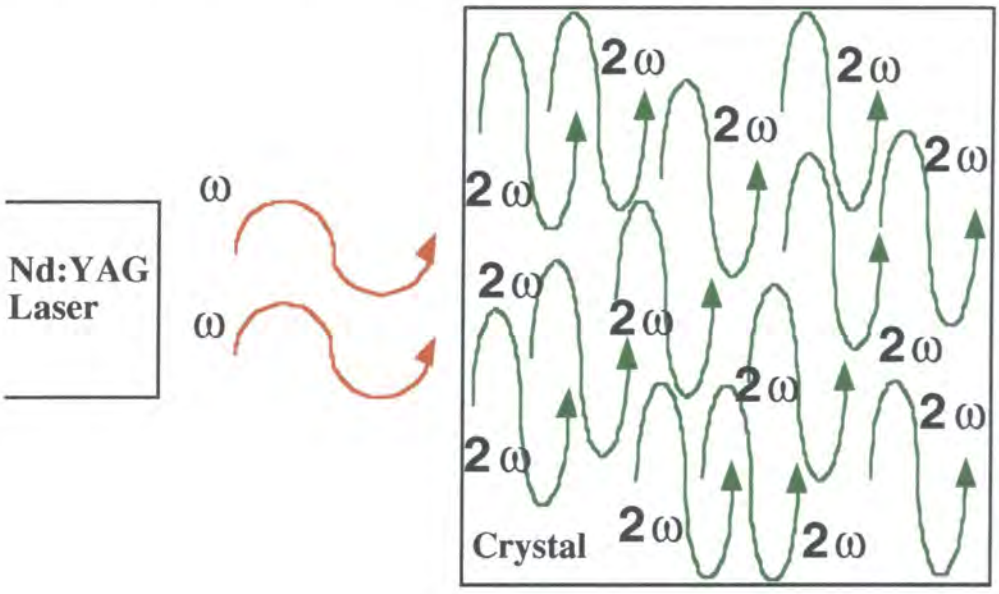

Figure 1.4.5 *- An illustration of a laser beam passing through an SHG active crystal.*

2ω is created at different points in the crystal. For the effect to propagate throughout the crystal, the 2ω waves must be in phase. If so, then the sample is said to be 'phase-matched'.

For all these waves to be in phase with each other, one desires a large coherence length, l_c, - i.e. the distance over which waves remain, at least to some degree, constructive with each other. The coherence length is related to the frequency and the refractive index by the following equation:

$$l_c = (\lambda/4)/(|\, n_\omega - n_{2\omega}|) \; ^* \qquad [11]$$

Hence, if $n^{2\omega} = n^{\omega}$, then l_c becomes infinite. Any material with such a refractive equality would always therefore be phase-matched. However, because of optical dispersion and, in some cases, absorption, $n^{2\omega}$ never equals n^{ω}. Fortunately, there are two ways to circumvent this problem:

---

* For derivation, see Franken & Ward, 1963.

(i) Birefringent Phase-Matching

This method, founded by Giordmaine (1962) and Maker & co-workers (Maker, Terhune, Nisenoff & Savage, 1962), uses birefringence to offset dispersion so that the coherence length tends to infinity. Depending on the 'axial' nature of a given crystal, the components of the refractive index, n_x, n_y and n_z, may differ+. Taking the case of an uniaxial crystal, as an example, one can construct two different ellipsoids which illustrate the variation of refractive index with orientation (***Figure 1.4.6***). The first ellipsoid illustrates the anisotropy of the ordinary refractive index, n_o, (independent of θ) at a frequency, ω; the second corresponds to the extraordinary refractive index, n_e, (a function of θ) at the frequency, 2ω:

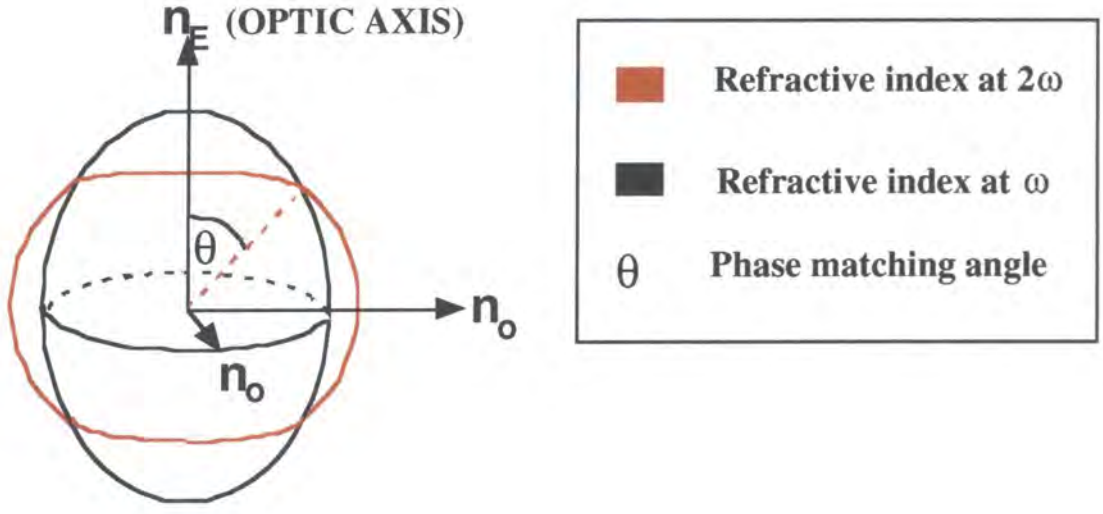

Figure 1.4.6 - *A diagram representing the anisotropy of the refractive index for two different frequencies, ω and 2ω, in an uniaxial crystal.*

If the birefringence is greater than the dispersion (as in this example) the two ellipsoids will intersect. A line can be drawn which joins the origin to the point of interception. The angle between this line and the crystal optic axis, n_z, is known as the phase-matching angle. This is because at the interception point, the values of n will be the same for both frequencies and so light will propagate at the same speed in any given direction, the result being that maximum constructive interference between waves of frequency ω and 2ω ensue.

Therefore, one can adjust the propagation of light through the crystal such that $n_o^{\omega} = n_e^{2\omega}$, giving rise to an infinite coherence length, i.e. the material becomes phase-matched. Note, however, that if overlap of these two constructions does not occur, for

+ There are three different 'axial' natures of a crystal: anaxial ($n_x=n_y=n_z$), uniaxial ($n_x=n_y\neq n_z$) and biaxial ($n_x\neq n_y\neq n_z$).

example if the dispersion is greater than the birefringence (eg. in quartz) or if the crystal is cubic+, then phase-matching is impossible by conventional techniques.

A few points to note on phasematching are:

- It is usually very difficult to orient the crystal *exactly* along the line of light propagation. However, since refractive indices change with temperature, one can 'temperature tune' the crystal. Here, the orientation of the optic axis changes with temperature, until the maximum SHG value is obtained.
- The SHG intensity builds up as the square of the crystal length (Michl, 1994). Thus, the larger the crystal, the better.
- Phasematching is often used to give an indication of the SHG quality and performance.

(ii) Periodic Domain Inversion (PDI).

This technique was founded by Armstrong and co-workers (Armstrong, Bloembergen, Ducuing & Pershan, 1962) and is particularly applicative to crystals which are not phase-matchable. The method requires an SHG active crystal which is made up of a periodic array of domains (each typically 20μm thick) of alternating structural polarity. Such crystal may be successfully engineered by using a combination of conventional photolithographic and electric-field poling techniques (Hu, Thomas & Webjörn, 1996). The presence of the domains causes a periodic 180° phase reversal between the waves involved in the energy transfer throughout the crystal. The thickness of the domains is chosen to be close to the material's inherent coherent length, l_c. Hence, the 180° phase reversal of the waves occurs just as the waves are almost out of phase with each other, the result being that the waves become in phase with each other once again and so the SHG propagates throughout the crystal. This is known as quasi-phase-matching (QPM).

+ This is because all orthogonal components of the refractive index are identical in a cubic crystal and so the indicatrix is completely spherical. This means that the change in refractive index with frequency will be isotropic and thus, the two spheres, one of frequency, ω, and the other of frequency, 2ω, will not coincide: the sphere relating to frequency, 2ω, will simply be larger than that relating to the frequency, ω.

1.5 METHODS USED FOR MEASURING β

1.5.1 Experimental methods

Historically, one used the d.c. Kerr effect[§] (-ω; 0, 0, ω) in order to obtain an estimate for the hyperpolarizability values. Its continued use, especially for gas phase measurements is probably due to the fact that it is still one of the few methods from which an *absolute* value of β can be derived (Michl, 1994; Prasad & Williams, 1991).

Various other techniques which have come into widespread use include the Kurtz powder technique (Prasad & Williams, 1991). This solid state method has been found most useful for identifying non-centrosymmetric materials and can also be used for phase matching.

The most common technique used nowadays is that of Electric Field-Induced Second Harmonic generation (EFISH) measurements (Barzoukas, Blanchard-desce, Josse, Lehm & Zyss, 1989; Prasad & Williams, 1991; Long, 1995; Derhaeg, Persoons & Samyn, 1990). Detailed descriptions of the method are given by Levine and Bethea (1975), Oudar (1977) and Meredith, van Dusen & Williams (1982) whilst a brief summary is given here. ***Figure 1.5.1*** shows the operational set-up for an EFISH experiment:

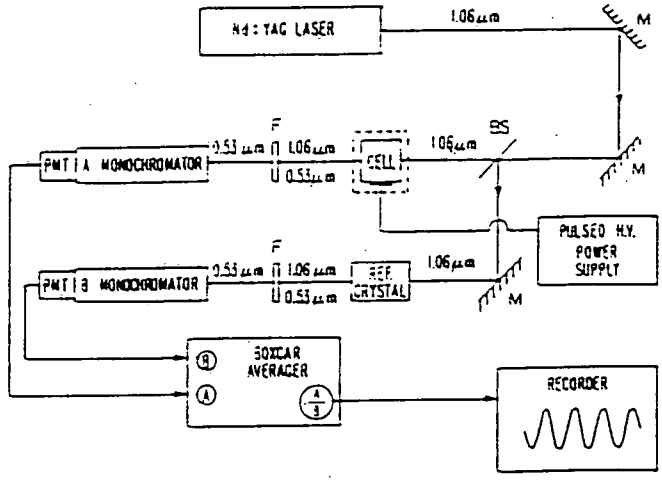

Figure 1.5.1 - A schematic diagram of the operational set up of an EFISH experiment (Prasad & Williams, 1991).

The reference crystal is typically quartz or urea. The fundamental wavelength generally ranges between λ = 1 - 2mm, the exact value being dependent upon the type of laser used (usually either a Nd^{3+}:YAG laser or a dye laser) and whether or not mode-locked Q-switching or stimulated Raman shifts are employed. The sample is in solution form

[§] Also known as the Optical Kerr Effect (OKE).

(typically using chloroform ($CHCl_3$) or dioxane as a solvent) and is contained in a glass cell as depicted in ***Figure 1.5.2(a)***:

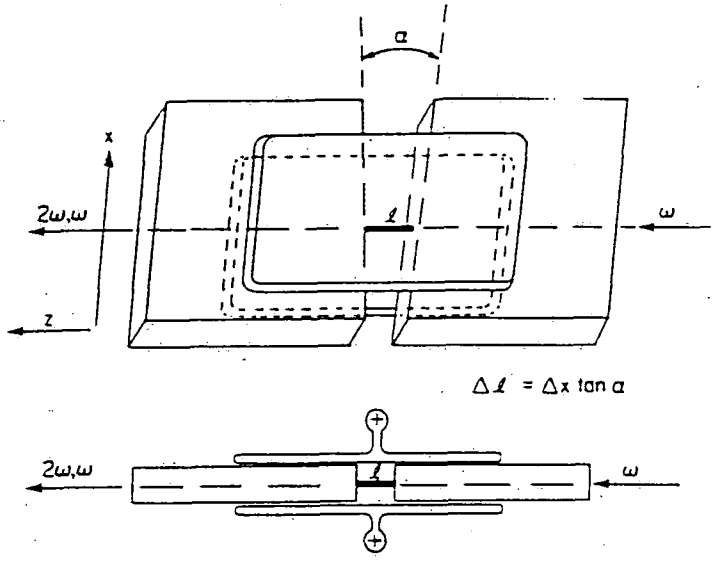

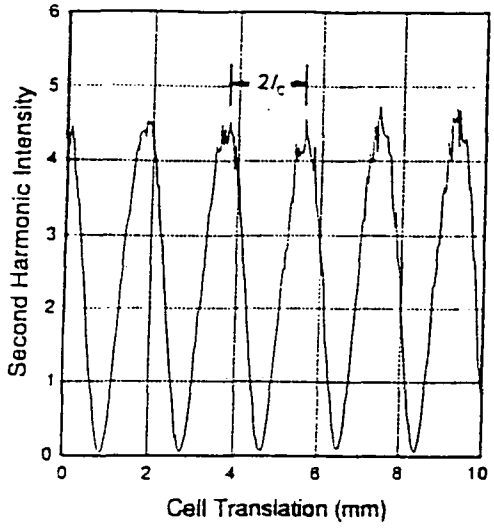

Figure 1.5.2(a) - *An illustration of the glass cell used for EFISH measurementa (Prasad & Williams, 1991).*

Figure 1.5.2(b) - *An example of a wedge fringe pattern (obtained for chloroform) (Prasad & Williams, 1991).*

Note that the electrodes extend a fair way each side of the wedge gap in order to avoid any detrimental effects from fringe fields. A d.c. electric field is imposed by these electrodes.

During the experiment, the cell is translated in the x direction. This provides us with a wedge fringe pattern (see ***Figure 1.5.2(b)***), which illustrates the intensity of SHG (for a given λ) as a function of cell translation and along the molecular dipole direction (Beratan, Cheng & Marder, 1991). The intensity is related to the first hyperpolarizability coefficient, β, by the proportionality equation:

$$I^{SHG}_{(2\omega)} \quad \propto \quad (\mu.\beta)^2$$

The proportionality scale factor is deduced from the reference compound and μ and $I^{SHG}_{(2\omega)}$ are known. Hence, $\beta(-2\omega; \omega, \omega)$, or $\beta(2\omega)$ for short, can be derived.

The resulting dynamic hyperpolarizability coefficient (i.e. dependent upon frequency, ω) possesses dispersion effects (Barzoukas, Blanchard-desce, Josse, Lehn & Zyss, 1989) which are unique to each compound. Therefore, in order to compare different hyperpolarizability coefficients, $\beta(2\omega)$ is divided by the relevant dispersion factor to

give the static result, $\beta(0)$ (i.e. not dependent upon frequency, ω) (Barzoukas, Blanchard-desce, Josse, Lehn & Zyss, 1989). Indeed, the conversion from dynamic to static hyperpolarizability is effectively a normalization process.

Note that when discussing materials which are guests in poled-polymer systems, it is the scalar product, $\mu.\beta(2\omega)$, which is divided by the dispersion effects, leading to $\mu.\beta(0)$ which acts as the relevant figure-of-merit for SHG, instead of $\beta(0)$. This is because $\mu.\beta(0)$ combines both the nonlinearity of the molecule and its ability to couple with a macroscopic poling field (Barzoukas, Blanchard-desce, Josse, Lehn & Zyss, 1989).

The EFISH technique, like any method, has its pitfalls (Marder & Perry, 1993). Firstly, it cannot be used to measure SHG efficiencies of octopolar compounds, e.g. 1,3,5-triamino-2,4,6-trinitrobenzene (TATB) (Brédas, Meyers, Pierce & Zyss, 1992) because the method relies on the specific orientation of the molecular dipole along the direction of the external electric field. Secondly, it is not really a suitable method for ionic species because of the high conductivity of ionic solutions.

At present, the only sufficiently accurate method of determining the first hyperpolarizability coefficient for the two situations above is the Hyper-Rayleigh Scattering (HRS)[+] method (Maker, Savage & Terhune, 1965; Noordman & Hulst, 1996; Clays & Persoons, 1991). This method relies on the direct proportionality between the intensity of the second harmonic scattered light, $I_{2\omega}$ and the average of the macroscopic first order hyperpolarizability, B_{ikl}, for two different volumes, $\langle B_{ikl,1} B_{jmn,2}\rangle_{av}dv$ (correlation of $B_{ikl,1}$ and $B_{jmn,2}$ is assumed to exist only over distances much less than the wavelength). One can extend this proportionality relation to consider β_{ijk} if one makes the approximation that the scattering centres are randomly oriented individual molecules; then $I_{2\omega}$ is proportional to the number density, η, and to $\langle\beta_{uvw} \beta_{xyz}\rangle_{av}dv$, where uvw represent the molecular axes and xyz represent the crystallographic axes. One transforms these axes into each other by averaging the products of the direction cosines over all directions (Cyvin, Rauch & Decius, 1965). The following equation therefore results:

$$I_{2\omega} = gB^2I_o^2 = g \sum_s \eta_s^2\beta_s^2I_o^2 \qquad [12]$$

where g is a factor depending on scattering geometry and containing the averages of the products of the direction cosines and local-field corrections; β_s is the molecular hyperpolarizability of species, s; I_o is the incident light intensity.

[+] Sometimes it is also referred to as Harmonic Light Scattering (HLS).

By adjusting the orientation of the analyser at 2ω to a given direction in xyz, one can analyse any desired tensor of β_S. Hence, all 27 tensorial components of β_{ijk} can be obtained for this technique. Moreover, the resulting six-rank tensor from $<\beta \otimes \beta>$ guarantees a non-zero value for *all* molecules irrespective of symmetry requirements (whereas the EFISH technique always requires electrical poling to induce the non-centrosymmetry).

Note also that the hyper-Raleigh signal, $S_{2\omega}$, is proportional to the square of the incident light intensity. Hence,

$$S_{2\omega} = GB^2I_o^2 \qquad [13]$$

where G is a constant containing geometrical and electronic factors. For a binary system:

$$B^2 = \eta_{solvent}\beta^2_{solvent} + \eta_{solvate}\beta^2_{solvate} \qquad [14]$$

where η_{solute} exhibits a linear dependence of GB^2. Hence, if the solute exists in a low concentration (such that $\eta_{solvent}$ can be assumed constant and any slight change is too minor to alter the refractive index of the solution and thus change $\beta_{solvent}$) then β^2_{solute} can be evaluated from the gradient of a graph showing $\eta_{solvent}$ versus GB^2. Hence, one can separate $\beta_{solvent}$ from β_{solute}, thus providing one with an absolute* value of β of a material in a given medium.

1.5.2 Theoretical methods

The theory of NLOs (Bishop, 1990; Chemela & Zyss, 1987) has developed hand in hand with the progressively more advanced experimental studies. Various models containing all manner of detail and approximations have been designed, both of the *ab initio* type and the semi-empirical. Most calculations have concentrated on the isolated molecule; however, a few have included intermolecular effects (Michl, 1994).

Models for the calculation of both the static and dynamic hyperpolarizabilities have been formulated and, in general, all methods have proved most useful, each type of calculation having its own merits and failures as one might expect.

* Only *absolute* values of β can ever be deduced from this method because $I_{2\omega}$ is proportional to the *square* of β.

1.5.2.1 *ab initio* methods

There are two main *ab initio* methods for determining β. The first is called the *sum-of-states* (SOS) method (Brieger, Hese, Renn & Sodeik, 1983; Brieger, 1984; Andre et al, 1990). The method uses perturbation theory in order to compute the single perturbation of the molecule as a whole by the applied electric field.

The second technique has been termed the *clamped- nucleus* method (Michl, 1994) and involves two steps: the first is the consideration of the extent of electronic motion perturbed by an electric field. Hence, we obtain a perturbed potential energy curve. The second step relates to the solution of the rovibrational Schrödinger equation. Hence, we also obtain information about the rotational and vibrational effect in a material. Using the Born-Oppenheimer approximation, we can simply sum the electronic, rotational and vibrational effects together as each effect is assumed to be in a factorized state.

Several variations on this second method are known. One such variation is the *finite-field* method (Cohen & Roothaan, 1965). This differs from the clamped-nucleus method in that a variety of field strengths are chosen and calculations are computed for each strength. The final total energies are then differentiated numerically, giving the total α,β,... values. The other main variation on the clamped-nucleus method uses the Derivative Numerov-Cooley (DNC) technique which provides a semi-analytical alternative second step to the calculation (Dykstra & Malik, 1987). This method computes directly the derivatives of the vibronic energies which in actual fact correspond to the polarizabilities.

Note the importance of vibrational averaging in all these methods: standard quantum-mechanical calculations usually average the vibrational motion. Hence, the expectation value, $\langle \upsilon(J) \mid P(\mathbf{R}) \mid \upsilon(J) \rangle$ is obtained (where $P(\mathbf{R})$ = a property as a function of internuclear distance). Rotational effects will make only a small contribution to the electronic state. Hence, they can be 'frozen' out of the calculations such that the expectation value $\langle \upsilon(0) \mid P(\mathbf{R}) \mid \upsilon(0) \rangle$ results. The corresponding integral is then easy to calculate and the hyperpolarizability can be obtained accurately.

However, rotational effects are not negligible when determining the vibrational contributions to the hyperpolarizability and a potential energy curve must be derived in order to determine $|\upsilon(J)\rangle$ and thence, integrate. Numerov-Cooley calculations provide a particularly simple method to do this. Indeed, DNC is becoming more and more popular as is the finite field method and both have potential, particularly in the area of pure vibrational spectroscopy where rotational effects are ignored. Further, the study of larger molecules is becoming more of a reality due to the increasing availability of

reliable unperturbed potential surfaces. However, these two clamped-nucleus type methods have one major limitation in that they cannot be applied to *dynamic* hyperpolarizability calculations whereas the SOS method can. The latter method ostensibly seems more useful but, in actual fact, the SOS method is restricted to very simple systems. However, it remains an important method for investigating the influence of rotation on vibrational hyperpolarizability since the rotational effects *are* included.

Developments, so far, in the *ab initio* field have not yet rivaled the success of semi-empirical calculations for polyatomic molecules. However, such good continuing progress in *ab initio* calculations may entice a move towards the use of *ab initio* calculations for not only simple compounds but also fairly large polyatomic molecules.

1.5.2.2 Semi-Empirical Methods

Charge Density Analysis - Various models used to determine β directly from charge density experiments by use of very accurate and low temperature X-ray and neutron (X-N) diffraction techniques have been known for quite a few years, e.g. the bond charge model (Korolkova, Ozerov, Rez & Tsirelson, 1984a and 1984b). These models have proved quite primitive due to the large assumptions made.

However, it has been observed recently that very accurate measurements of μ, α (Hamzaoui, 1995) and β (Fykerat et al., 1995) have been determined from charge density studies. This study uses the theory of Robinson (1967) who showed that β can be determined from the octopolar moment of the charge distribution of a molecule. This is because it is the asymmetry in the distribution of π-electrons that is responsible for μ, α and β. The relationship for β is given in equation [15]:

$$\beta_{ijk} = (3\alpha/a_0 e)(\Omega_{ijk}/n) \qquad [15]$$

where $a_0 = h/me^2 = 0.53\text{Å}$.

α = atomic polarizability.

n = number of valence electrons.

Ω_{ijk} = octopolar moment of the charge distribution = $\iiint \hat{r}_i\hat{r}_j\hat{r}_k\rho(r)\,d^3r$

This technique is still under development and it is hoped that soon the second hyperpolarizablility coefficient, γ, can also be derived (Hamzaoui, 1996).

The potential of this new method cannot be over emphasized since it is the only existing accurate method to determine β in the *solid* state. Moreover, it should, in

theory, give more accurate results than any theoretical calculation, as no assumptions are made. The values obtained from this method may also be compared with β values obtained from solution methods (e.g. EFISH or HRS) in order to gain *unique* information regarding the influence on SHG of the crystal field and solvent effects.

1.6 REFERENCES

Addadi, L., Berkovitch-Yellin, Z., Lahav, M., Leiserwitz, L. & Weissbuch, I. (1986). Top. Stereochem., **16**, 1.

Aktsipetrov, O. A., Akhmediev, N. N., Baranova, I. M., Mishina, E. D. & Novak, V. R. (1985). Zh. Ekps. Teor. Fiz. Pis'ma, **89**, 911.

Aktsipetrov, O. A., Akhmediev, N. N., Mishina, E. D. & Novak, V. R. (1983). Zh. Ekps. Teor. Fiz. Pis'ma, **37**, 175. [JETP Lett, **37**, (1983), 207.

Albrecht, A. C. & Morell, A. (1979). Chem. Phys. Lett., **64**, 46.

Allen, F. H., Davies, J. E., Galloy, J. J., Johnson, O., Kennard, O., Macrae, C. F., Mitchell, E. M., Mitchell, G. F., Smith, J. M. & Watson, D. G. (1991). J. Chem. Inf. Comput. Sci., **31**, 187-204.

Anderson, A. G., Calabrese, J. C., Tam, W. & Williams, I.D. (1987). Chem. Phys. Lett., **134**, 392.

Andre, J. M., Brédas, J. L., Delhalle, J., Fripiat, J. G., Vandervahen, D. J. & Vercuteres, D. P. (1990) in *Modern Techniques in Computational Chemistry: MOTECC-90* (Ed. Clemments E.), ESCOM, Leiden, pp745-783.

Armstrong, J. A., Bloembergen, N., Ducuing, J. & Pershan, P. S. (1962). Phys. Rev., **127**, 1918-1939.

Ashwell, G. J., Dawney, E. J. C., Kuczynski, A. P., Szablewski, M., Sandy, I. M., Bryce, M. R., Grainger, A. M. & Hasan, M. (1990). J. Chem. Soc., Faraday Trans., **86**, 1117.

Atwood, J. L., Davies, J. E. D. & MacNicol, D. D., (Eds.), (1984). *Inclusion Compounds, Volume 2,* Academic Press, New York, ch. 2.

Bailey, R. T., Cruickshank, F. R., Pugh, D., Sherwood, J. N. (1991). Acta. Crystallogr, **A47**, 145.

Bailey, R. T., Bourhill, G., Cruickshank, F. R., Pugh, D., Sherwood, J. N., Simpson, G. S. & Wilkie, S. (1993). Mol. Cryst. Liq. Cryst., **231**, 223.

Barraud, A., Gouzeh, A., Leloup, J. & Palacin, S. (1986). Thin Solid Films, **133**, 117.

Barry, S. & Soane, D. (1991). Appl. Phys. Lett., **58**, 1134.

Barzoukas, M., Blanchard-desce, M., Josse, D., Lehn, J. -M. & Zyss, J. (1989). Chem. Phys., **133** 323.

Baughman, R. H., Chance, R. R., Ducuing, J., Frey, R., Hermann, J. P., Pradere, F. & Sauteret, C. (1976). Phys. Rev. Lett., **36**, 956.

Bishop, D. M. (1990). Rev. Mod. Phys., **62**, 343.

Boden, E. P., Marder, S. R., Perry, J. W., Perry, K. J., Sleva, E. T., Stewart, K. R. & Yakymyshyn, C. P. (1991a). Proc. SPIE, **1560**, 302.

Boden, E. P., Marder, S. R., Perry, J. W., Schaefer, W. P., Stewart K. R. & Yakymyshyn, C. P. (1991b) in *Organic Materials for Nonlinear Optics II*, Royal Society of Chemistry Special Publications, No. 91, (Eds. Hann R.A., Bloor D.), Royal Society of Chemistry, London, p108.

Brédas, J. L. (1987). Synthetic Metals, **17**, 115.

Brédas, J. L., Meyers, F., Pierce, B. M. & Zyss J. (1992). J. Am. Chem. Soc., **114**, 4928.

Brédas, J. L. & Street, G. B. (1985). Acc. Chem. Res., **18**, 309.

Brieger, M. A., Hese, A., Renn, A. & Sodeik, A. (1983). Chem. Phys., **75**, 1.

Brieger, M. A. (1984). Chem. Phys., **89**, 275.

Bruce, D. W. & Thornton, A. (1993). Mol. Cryst. Liq. Cryst., **231**, 253.

Cade, N. A., Cross, G. H., Earls, J. D., Girling, I. R., Kolinsky, P. V. & Peterson, I. R. (1985). Thin Solid Films, **132**, 101.

Cady, W. G. (1946). *Piezoelectricity*, McGraw-Hill, New York.

Charney, E. & Yamaoka K. (1972). J. Am. Chem. Soc., **94**, 8983.

Chemela, D. S. & Zyss, J. (1987). *Nonlinear Optical Properties of Organic Molecules and Crystals, Volume 1*, Academic Press, Inc., Orlando.

Cheng, L., Gorman, C. B., Marder, S. R. & Tiemann, B.G., Proc. SPIE, **1775**, (1993), 19.

Cheng, L. -T., Marder, S. R., Rikken, G., Spangler, C. W., Stiegman, A. E. & Tam, W. (1991a). J. Phys. Chem., **95**, 10643.

Cheng, L. -T., Tam, W., Stevenson, S. H., Meredith, G. R., Rikken, G. & Marder, S. R. (1991b). J. Phys. Chem., **95**, 10631.

Chengzeng, X., Dalton, L. R., Ranon, P. M., Steier, W. H., Wu, B. & Yongqiang, S. (1992a). Macromolecules, **25**, (1992), 6716.

Chengzeng, X., Dalton, L. R., Ranon, P. M., Steier, W. H., Wu, B. & Yongqiang, S. (1992b). Macromolecules, **25**, 6714.

Clays, K. & Persoons, A. (1991). Phys. Rev. Lett., **66**, 2980-2983.

Cohen, H. D. & Roothaan, C. C. J. (1965). J. Chem. Phys., **43**, 534.

Collings, P. J. (1990). *Liquid Crystals, Nature's Delicate Phase of Matter*, Adam Hilger, Bristol.

Coppens, P. (1992). *Synchotron Radiation Crystallography*, Academic Press, Inc., London.

Cyvin, S. J., Rauch, J. E. & Decius, J. C. (1965). J. Chem. Phys., **43**, 4083-4095.

Davydov, B. L., Derkacheva, L. D., Dunina, V. V., Koreneva, L. G., Samokhina, M. A., Zhabotinskii, M. E. & Zolin, V. F. (1970). Zh. Eksp. Teor. Fiz. Pis'ma Red, **12**, 24. [JETP Lett., **12**, (1970), 16.]

Derhaeg, L., Persoons, A. & Samyn, C. (1990) in *Organic Molecules for Nonlinear Optics and Photonics*, (Ed. Messier J., Kajzar R., Prasad P.) NATO ASI Series E: Applied Sciences, **194**, 177.

Docherty, J., Morley, J. O. & Pugh, D. (1987). J. Chem. Soc. Perkin Trans., **2**, 1351.

Donohue, J. (1952). J. Phys. Chem., **56**, 502.

Drost, K. J., Jen, A. K-Y., Rao, V. P. & Wong, K. Y. (1993). J. Chem. Soc. Chem. Commun., 90.

Ducuing, J. & Hermann, J. P. (1974). J. Appl. Phys., **45**, 5100.

Ducuing, J., Hermann, J. P. & Ricard, D. (1973). Appl. Phys. Lett., **23**, 178.

Ducruix, A. & Giege, R. (1992). *Crystallization of Nucleic Acids and Proteins: A Practical Approach*, IRL Press.

Dykstra, C. E. & Malik, D. J. (1987). J. Chem. Phys., **87**, 2806.

Etter, M. C. (1991). J. Phys. Chem., **95**, 4600.

Etter, M. C. & Frankenbach, G. M. (1989). Chem. Mater., **1**, 10.

Etter, M. C. (1982). J. Am. Chem. Soc., **104**, 1095.

Etter, M. C. (1990). Acc. Chem. Res., **23**, 120.

Farina, M. (1984) in *Inclusion Compounds, 2*, Academic Press, London, pp. 69-95.

Finger, G., Richter-Mendau, J., Bülow, M. & Kornatowski, J. (1991). Zeolites, **11**, 443.

Franken, P. A., Hill, A. E., Peters, C. W. & Weinreich, G. (1961). Phys. Rev. Lett, **7**, (1961), 118.

Franken, P. A. & Ward, J. F. (1963). Rev. Mod. Phys., **35**, 23-39.

Frolow, F., Lahav, M., Leiserowitz, L., McMullan, R., Shimon, L. J. W. & Vaida, M. (1988). Science, **241**, 1475.

Fkyerat, A., Guelzim, A., Baert, F., Paulus, W., Heger, G., Zyss, J. & Périgaud, A. (1995). Acta. Crystallogr, **B51**, 197.

Garter, J., Halliday, R. & Singer, L. K. (1991). Zeolites, **20**, 10.

Giordmaine, J. A. (1962). Phys. Rev. Lett., **8**, 19-22.

Girling, I. R. & Milverton, D. R. J. (1984). Thin Solid Films, **115**, 85.

Girnus I., Jancke K., Vetter R., Richter-Mendau J., Caro J. (1995). Zeolites, **15**, 33.

Gorman, C. B. & Marder, S. R. (1993). Proc. Natl. Acad. Sci., USA.

Groves, P. C., Marder, S. R., Perry, J. W., Perry, K. J., Schaefer, W. P. & Tiemann, B. G. (1989). Proc. SPIE, **1147**, 108.

Hamazaki, N., Kagami, M., Mayata, S., Nakanishi, H., Sato, H. & Watanbe, T. (1989). Proc. SPIE, **1147**, 84.

Hamzaoui, F., personnal communication.

Hamzaoui, F. (1995). PhD Thesis, Universite des Sciences et Technologies de Lille, France.

Haringa, E. & van Pelt P. (1979). Ber. Bunsen-Ges., Phys. Chem., **83**, 816.

Hesselink, G. L. J. & Huijts, R. A. (1989). Chem. Phys. Lett., **156**, 209.

Hu, Z. W., Thomas, P. A. & Webjörn, J. (1996). J. Appl. Cryst., **29**, 279-284.

Kato, M., Masaki, A., Matsuda, H., Muramatsu, R., Nakanishi, H., Okada, S. & Otsuka, M. (1990). Jpn. J. Appl. Phys., **29**, 1112.

Kato, M., Matsuda, H., Maramatsu, R., Nakanishi, H. & Okada, S. (1988). Japenese Patent 63-348265.

Keiser, G. (1991). *Optical Fiber Communications*, McGraw Hill Int. Eds., 2nd Ed., New York.

Keller, O. (Ed.), (1990). *Nonlinear Optics in Solids*, Springer-Verlag, Berlin.

Kleinman, D. A. (1962). Phys. Rev., **126**, 1977.

Koike, T., Masaki, A., Matsuda, H., Nakanishi, H., Ohmi, T., Okada, S. & Umegaku, S. (1990). CLEO Technical Digest, **7**, 402.

König, O., Hoss, R. & Hulliger J (1995). Poster abstract, ERICE.

Korolkova, O. V., Ozerov, R. P., Rez, I. S. & Tsirelson, V. G. (1984a). Phys Stat. Sol.,(b), **122**, 599.

Korolkova, O. V., Ozerov, R. P., Rez, I. S. & Tsirelson, V. G. (1984b). Kristallografia, **29**, 5.

Kuhn, H. (1958). Forsch. Chem. Org. Mat., **16**, 169.

Kurtz, S. K. & Perry, T. T. (1968). J. Appl. Phys., **89**, 8798.

Lalama, S. J. & Garito, A. F. (1979). Phys. Rev. A, **20**, 1179.

Lecomte, C. (1995). L-argenine phosphate, British Crystallographic Association Plenary Lecture, Cardiff.

Levine B.F. & Berthea C.G. (1975). J. Chem. Phys., **63**, 2666.

Long, N. J. (1995). Angew. Chem. Int. Ed., Engl., **34**, 21.

Long, R. E., Sparks, R. A. & Trueblood, K. N. (1965). Acta Crystallogr., **18**, 932-939.

Lyons, M. H. (1989). *Materials for Non-linear and Electro-optics, 1989*, J.W.Arrowsmith, Bristol.

Marder, S. R., Beratan, D.N. & Cheng, L.-T. (1991). Science, **252**, 103.

Marder, S. R., Marsh, R. E., Perry, J. W., Schaefer, W. P. & Tiemann, B. G. (1990). Chem. Mater., **2**, 685.

Marder, S. R. & Perry, J.W. (1993). Adv. Mater., **5**, 804.

Marder, S. R., Perry, J. W., Bourhill, G., Gorman, C. B., Tiemann, B. G. & Mansour, K. (1993). Science, **261**, 186.

Marder, S. R., Perry, J. W. & Schaefer, W. P. (1989). Science, **245**, 626.

Marder, S. R., Perry, J. W. & Schaefer, W. P. (1992). J. Mater. Chem., **2**, 985.

Marder, S. R., Perry, J. W., Schaefer, W. P. & Tiemann, B. G. (1991). Organometallics, **10**, 1896.

Marlow F. (1991). Surface Science Letters, **254**, L493.

Marlow F., Caro J., Werner L., Kornatowski J. & Dähne S. (1993). J. Phys. Chem., **97**, 11286.

Maker, P. D., Savage, C. M. & Terhune, R. W. (1965). Phys. Rev. Lett., **14**, 681.

Maker, P. D., Terhune, R. W., Nisenoff, M. & Savage, C. M. (1962). Phys. Rev. Lett., **8**, 21-22.

Masse, R. & Pécaut, J. (1994). J. Mater. Chem., **4**, 1851.

McCusker, L. B. (1991). Acta. Crystallogr., **A47**, 297.

Menig, T. & Pierce, B. P. (1989). J. Org. Chem., **56**, 1584.

Meredith, G. R. (1983) in *Nonlinear Optical Properties of Organic and Polymeric Materials,* ACS Symp. Ser., Volume 233, (Ed. Williams D.J.), American Chemical Society, Washington D.C., p. 27.

Meredith, G. R., van Dusen, J. G. & Williams, D. J. (1982). Macromolecules, **15**, 1385.

Michl, J. (Ed.), (1994). Chem. Rev., **1**.

Moreno, P., Plaja, L. & Roso, L. (1994). Europhys. Lett., **28**, 629.

Mortazavi, M. A., Knoesen, A., Kowel, S. T., Higgins, B. G. & Dienes, A. (1987). J. Opt. Soc. Am. B., **6**, 733.

Noordman, O. F. J. & van Hulst, N. F. (1996). Chem. Phys. Lett., **253**, 145-150.

Ortiz, R., Marder, S. R., Cheng, L. -T., Tiemann, B. G., Caragnero, S. & Ziller, J. W. (1994). J. Chem. Soc., Chem. Commun., 2263.

Oudar, J. L. & Zyss, J. (1982). Phys. Rev. A, **26**, 2016.

Oudar, J. L. (1977). J. Chem. Phys., **67**, 446.

Prasad, P. N. & Williams, D. J. (1991). *Introduction to Nonlinear Optical Effects in Molecules and Polymers*, John Wiley and Sons, Inc, New York, ch. 6.

Robinson, F. N. H. (1967). Bell Syst. Tech. J., pp. 913-956.

Royal, J. & Torkelson, J. (1992). Macromolecules, **25**, 4792.

Royal, J., Torkelson, J. & Victor, J. (1992). Macromolecules, **25**, 729.

Sarma, J. A. R. P., Allen, F. H., Hoy, V. J., Howard, J. A. K., Thaimattam, R., Biradha, K. & Desiraju, G. R. (1997). J. Chem. Soc., Chem. Commun., 101-102.

Shen, Y. R. (1984). *The Principles of Nonlinear Optics*, John Wiley and Sons, New York.

Singer, K. D., Kuzyk, M. G., Holland, W. R., Sohn, J. E., Lalama, S. J., Comizzoli, R. B., Katz, H. E. & Schilling, M. L. (1988). Appl. Phys. Lett., **53**, 1800.

Tam, W., Eaton, D. F., Calabrese, J. C., Williams, I. D., Wang, Y. & Anderson, A. G. (1989). Chem. Mater., **1**, 128.

Torkelson, J. & Victor, J. (1992). Macromolecules, **25**, 2241.

Weissbuch, I., Lahav, M., Leiserowitz, L., Meredith, G. R. & Vanherzeele, H. (1989). Chem. Mater., **1**, 114.

Werner, L., Caro, J., Finger, G. & Kornatowski, J. (1992). Zeolites, **12**, 658.

Wooster, W. A. (1938). *Crystal Physics*, University Press, Cambridge, pp. 1-4.

Young, R. A. (Ed.), (1993). *The Rietveld Method*, International Union Of Crystallography, Oxford University Press, New York.

Zyss, J. (1982). Non-Cryst. Solids, **47**(2), 211.

Zyss, J. & Oudar J. L. (1982). Phys. Rev. A, **26**, 2028.

CHAPTER 2

X-RAY AND NEUTRON EXPERIMENTAL TECHNIQUES

2.1 NEUTRONS AT THE INSTITUT LAUE LANGEVIN, (ILL), GRENOBLE, FRANCE

Eight of the ten neutron experiments described in this thesis were carried out at the ILL. Seven of these were performed on the single-crystal four-circle diffractometer, D9 and one on the single-crystal four-circle diffractometer, D10. Unlike most X-ray facilities, each neutron instrument is unique. Therefore, an outline of the specifications, layout and attributes for each aforementioned instrument are detailed in the following sections.

2.1.1 The ILL Reactor Source

The nuclear reactor at the ILL feeds neutrons to a total of 49 instruments. Neutrons are produced in the core by fission of enriched (to 93%) ^{235}Uranium with thermal neutrons:

$n_{thermal} + {}^{235}U \rightarrow$ 2 fission fragments + 2.5 n + 200meV...

The fission reaction becomes self-sustaining (critical) when an average of 2.5 fast neutrons are produced per fission such that one neutron is available to trigger further fission, 0.5 neutrons are absorbed into other material and the remaining one neutron leaves the core for experimental use.

An illustration of the reactor core is given in ***Figure 2.1.1***. The uranium source is situated in a number of fuel rods, each containing about 9kg of enriched uranium. Control rods (loaded with boron which absorbs neutrons) are interleaved between the fuel rods so that fission can be either accelerated (by moving the control rods up) or deccelerated (by moving the control rods down). Due to the large amount of heat generated during the process (200meV/neutron) the rods are completely immersed in a D_2O coolant which, in turn, is encased in a sealed borated concrete and steel enclosure. This enclosure acts as a biological shield and must remain sealed so as to prevent any release of tritium formed by nuclear reactions with D_2O. D_2O is used rather than H_2O because of its much lower neutron absorption cross-section.

Some of the heat emanating from the reactor core is used to heat a hot source (graphite) which provides neutrons of a high energy (shorter wavelength) at given points in the reactor core. The excess heat from the reactor is also used as an energy source to keep the cold source (liquid D_2) cool so as to provide for low energy (cold) neutrons. All other neutrons released are either thermal or epithermal. The overall flux distribution (total power = 58MW) of the reactor is a Maxwellian function of distance from the core. In view of this, the reactor core is purposely slightly 'under-moderated' so that the thermal flux peaks at ~15cm from the edge of the reactor core, thereby providing the maximum

possible thermal flux for all instruments using thermal neutrons.

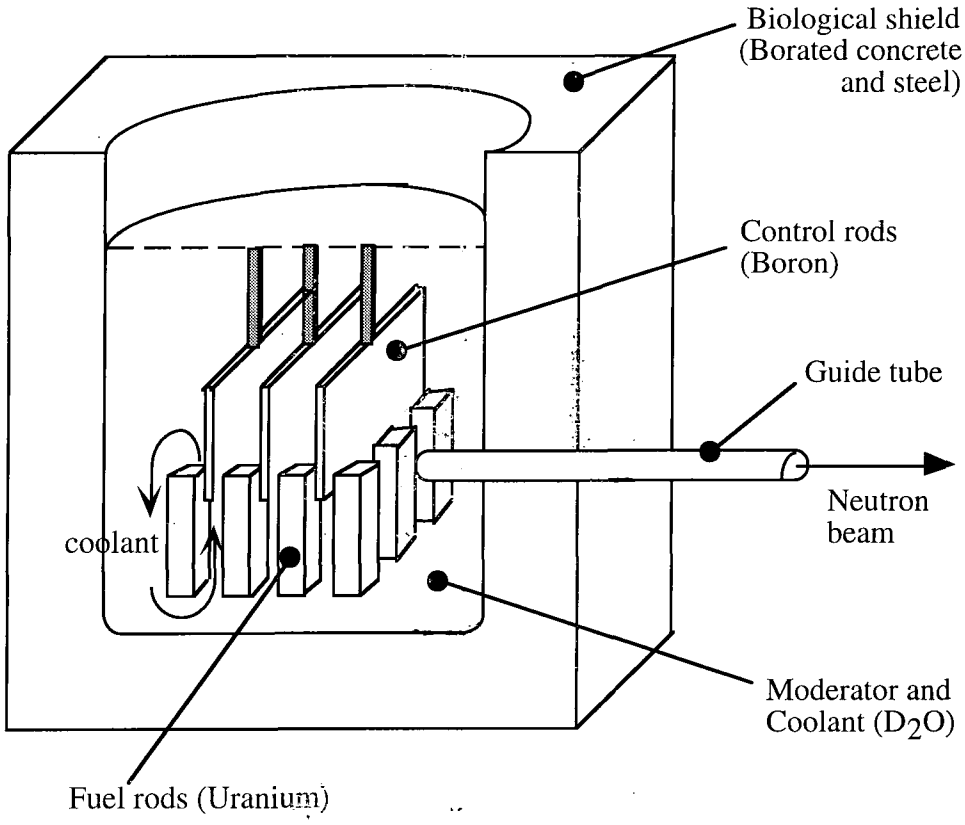

Figure 2.1.1 *- An illustration of the ILL reactor core.*

The neutron beam then passes through a moderator which slows down the neutrons to the required velocity for the respective instruments concerned via many rapid collisions with small hydrogenous molecules such as H_2O or CH_4.

The neutrons leave the reactor core as a continuous beam via guide tubes which are vacuum-sealed rectangular 'pipes' containing a very smooth ^{58}Ni lining on its interior. The vacuum is imposed to prevent absorption of the neutrons by air and the nickel lining allows total internal reflection of the neutron beam by nature of nickel's low refractive index, such that a negligible amount of neutron flux is lost through the tubes. Guide tubes are manufactured to a standard length of one metre so that they can be pieced together to make a guide of any unimetric length and often of some curvature, as this precludes any contamination of other radiation, e.g. γ-rays. The neutrons exit the guide tube at the instrument, at a flux and velocity dependent on the distance travelled from the core and type of source the beam emanated from respectively.

2.1.2 The Single-Crystal Four-Circle Diffractometer, D9

A view of D9 is shown in ***Figure 2.1.2***. The instrument (Kuhs, 1988) is situated very close to the reactor core with the incoming neutrons originating from the graphite hot source, thereby providing a high-flux at short wavelength. The neutron beam is monochomated by reflecting the beam off the exposed (220) face of a Cu crystal (B) at the required angle and resonance filters, which absorb at wavelengths 0.48/2, 0.55/2, 0.70/2 or 0.85/2Å, are used to suppress λ harmonics. All D9 experiments described in this thesis used the Erbium (0.85/2Å) filter. The collimator, made of the highly neutron absorbing polystyrene and B_4C, restricts the diameter of the beam to that of the collimator aperture. The aperture of the collimator is selected based on the size of the crystal used in a given experiment: the collimator aperture should be just larger than the crystal so as to completely bathe the crystal in the beam but at the same time keeping the background to a minimum. The collimator is very efficient such that all data are collected under very low background conditions considering the instrument is located so close to the reactor core. The sample is placed at the centre of four circles, χ, ϕ, ω and θ. Concentric orientation of χ and ω turn the sample vertically and horizontally respectively and orientation of ϕ turns the crystal horizontally about its axis. The detector which is a ^{3}He 32 x 32 pixel 2D Position Sensitive Detector (PSD) is mounted on the 2θ arm which, in the usual bisecting geometry ($\varphi = 0$), always lies at the angle half that of ω. Under normal circumstances, φ is set to only deviate from zero when one is investigating the absorption of the crystal or when one is trying to avoid multiple (double Bragg) reflections. Due to physical barriers, all four circles are limited to the angular ranges: $+80° \leq \chi \leq +200°$, $-180° \leq \phi \leq +180°$, $-24° \leq \omega \leq +45°$ and $+4° \leq 2\theta \leq +120°$.

Figure 2.1.2 *- The single-crystal four-circle diffractometer, D9, at the ILL.*

Additional equipment may be placed around the sample. For example, an APD201 Displex Helium Closed Cycle Refrigerator (CCR) (Archer & Lehmann, 1986) [which can be seen mounted on D9 in ***Figure 2.1.2***] may be used which allows one to cool the sample to any temperature within the range 15-298K. Such an accessory is used in all neutron experiments described in this thesis.

The apparatus comprises two parts: a Displex unit and a compressor. The Displex is mounted vertically above the sample and contains a piston which is used to expand the He and thus, cause a cooling effect. The He is then repressurized by the compressor which is situated at the side of the instrument. This causes a heating effect which is dissipated by a water cooling system in the compressor. The net result is that the crystal cools due to the chilling effect at the crystal end of the Displex unit. The metal pin onto which the crystal is mounted, is attached to a copper block which connects directly to the Displex. The heat from the crystal is withdrawn through the pin and the copper block, through the Displex unit. There obviously exists a large thermal gradient between the temperature of the crystal and the external temperature, i.e. room temperature. Hence, in order to prevent any significant heat loss, the crystal must be sealed off from the external surroundings by a vacuum. Furthermore, below the boiling point of nitrogen (77K) the air condenses and then freezes onto the side of the inner can which encloses the vacuum. This, in turn,

causes a cryopumping effect, i.e. the vacuum increases by several orders of magnitude due to the gas molecules 'freezing out'. Hence, the conduction from the pin is better and so lower temperatures can be reached.

Three different cans are used to effect this vacuum; the first is made out of vanadium (as only incoherent scattering occurs) and encases the sample in a very small quantity of air or an alternate inert gas. The second and third cans are made out of aluminium and a vacuum is sustained between both of these cans and between the aluminium and vanadium can. The inner aluminium can is necessary for heat shielding purposes.

For safety requirements, the whole instrument is confined to a physical enclosure into which one can enter only when the beam is withheld by a shutter. Surroundings of bulk shielding such as 'crispy mix' (B_4C in resin), borated polyethene or lead is not necessary since the neutron beam is monochromated (within substantial shielding) and any stray monochomatic neutrons will be readily absorbed by the air. Moreover, a beam stop comprising a lead block is suitably positioned to absorb all of the direct beam which does not diffract and other radiation, eg. γ-rays, etc. The instrument is controlled using a Microvax II and CAMAC electronics.

All the features described above make D9 a very versatile instrument: its high Q range allowing one to study structural disorder or thermal motion and anharmonicity; its very short λ allowing accurate structural and magnetic studies especially when needing to accurately determine hydrogen positions (a typical λ corresponds to that of a X-H bond length) or when studying compounds containing high thermally absorbing elements (e.g. Gd, Tb); its high flux allowing small crystals (down to sub-mm^3 in some cases) or its PSD and good angular reciprocal space resolution useful for studying twins, satellites and diffuse scattering.

2.1.3 The Single-Crystal Four-Circle Diffractometer, D10

On D10 (***Figure 2.1.3***), neutrons emanate from a thermal guide tube, giving rise to longer wavelengths than those available on D9 and offering good reciprocal space resolution with a reasonable direct space resolution. The required wavelength is obtained by reflection from either a vertically focussing Cu(220) or pyrolitic graphite (PG) monochromator. The Cu monochromator was used for the experiment detailed in this thesis since, despite the fact that the PG monochromator provides a flux five times larger than the Cu monochromator, the minimum possible wavelength is ~ 2.2Å which is too long for a reasonably high resolution structure to be determined.

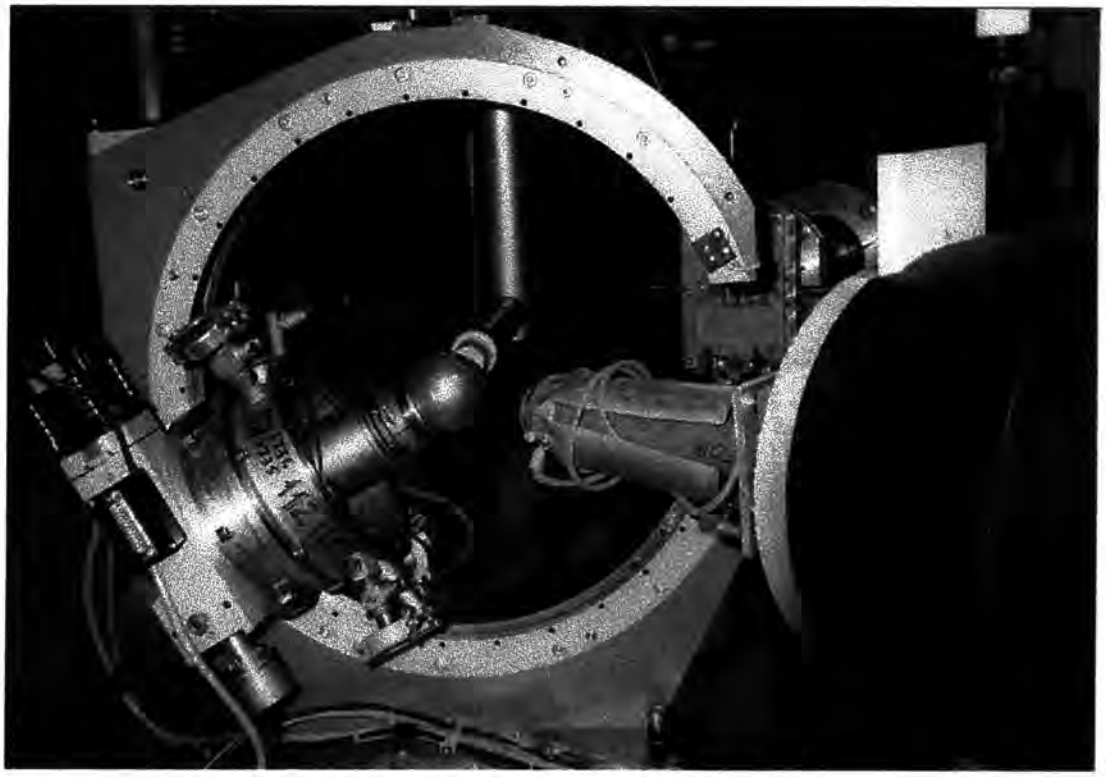

Figure 2.1.3 *- The Single-Crystal Four-Circle Diffractometer, D10, at the ILL.*

No collimation is used since one tries to obtain as much intensity as possible. Hence, in order to remove background effects, two background apertures are placed before the beam. These apertures are larger in the vertical plane than the horizontal, since the monochromator is vertically focussing. The diffracted neutrons also pass through two selected background apertures, one circular aperture about 100mm from the crystal and one rectangular aperture at the entrance to the detector. Unlike D9, D10 possesses a choice of two detectors both of which are single-point counters. Hence, whilst more accurate than a 2-D PSD like on D9, a larger crystal sample must be used if data collection is to proceed at the same rate as D9. Since detector B is coupled with a crystal analyser, detector A is generally used unless one is carrying out inelastic neutron scattering measurements.

As with D9, the sample is situated at the centre of the four circles, χ, ϕ, ω and 2θ (ranges: 0° - 120°, -180° - 180°, 10° - 90° and 0° - 150° respectively) and each circle orients the crystal concentrically and pneumatically using a Tanzboden floor. The cooling system is a He-flow cryostat (***Figure 2.1.4***) which gives access to sample temperatures in the range $1.6K < T < 300K$ whilst retaining full four-circle flexibility during its operation. The He-flow cryostat (Zeyen, Chagnon, Disdier and Morin, 1984) was used in the experiment described in this thesis. He passes from the source reservoir to the cryostat via a siphon which has two cooled Johnston joints which allow rotation through 360° in both ω and χ (the ϕ-shaft rotates inside the cryostat and thus is unaffected). The only

blind region created by use of the system is in the range $-10 < \omega < 10°$ where the siphon passes through the incident beam. However, most reflections with $\theta < 10°$ can be accessed by moving away from the bisecting setting. On entering the cryostat, the He flow splits into two flows, a main He flow and a sample He flow. The main He flow passes through the middle aluminium can around the sample (there are three aluminium cans - an outer, middle and inner can) and then exits the cryostat via a heat exchanger. The sample He flow passes through the inner aluminium can which contains the sample and then exits the cryostat via another heat exchanger. The outer can is necessary for retaining a vacuum. The temperature is controlled by a resistive 290W Compensated Linear Temperature Sensor (CLTS) and a 25W RhFe sample thermometer. The CLTS lies on the main heat exchanger and is linked to a thermo-coax heater. When the sensor detects an increase in temperature, its resistance increases, thus reducing the heating power, and vice versa, thereby regulating the temperature. The RhFe thermometer is used to constantly rescale the CLTS setting since the latter's reproducibility is poor. However, the thermal response of the CLTS is very fast (ΔT of 10K in a few mins) and the overall accuracy of the temperature regulation is < 0.05K and its stability is 0.1K below 10K.

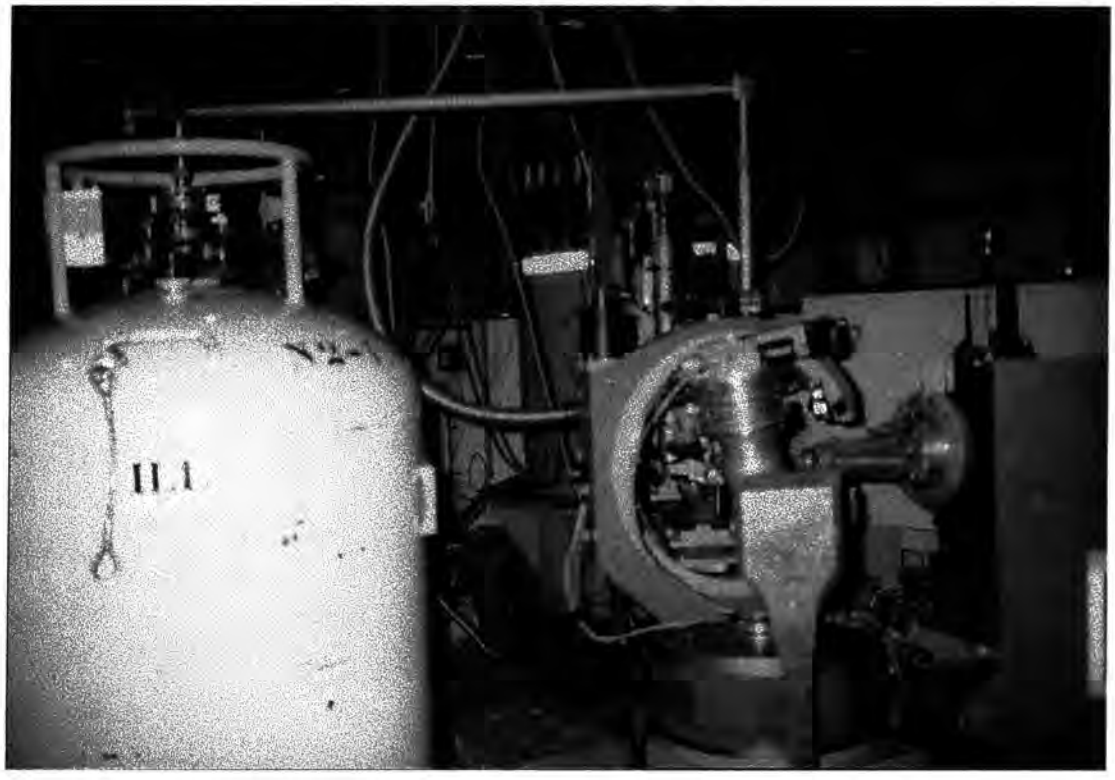

Figure 2.1.4 *- The He flow cryostat on D10.*

In common with D9, the whole instrument is contained within a physical enclosure into which one can only enter when the beam is withheld by the shutter. The non-diffracted beam is stopped by a lead beam stop. The instrument is fully controlled and data collected using a Silicon Graphics workstation and CAMAC electronics.

2.2 NEUTRONS AT THE ISIS PROTON SPALLATION SOURCE, U.K.

The two remaining experiments described in this thesis were carried out on the single crystal diffractometer, SXD at the ISIS Proton Spallation Source, U.K. Unlike the diffraction experiments described in preceeding sections of this chapter, this diffractometer can use the time-of-flight (TOF) technique since its neutrons derive from a pulsed source rather than a continuous steady-state source.

2.2.1 The ISIS Proton Spallation Source, Chilton, U.K.

There are several possible ways to generate a pulsed neutron source: by Bremsstrahlung (breaking radiation) from electron accelerators (e.g. Harwell, LINAC, U.K.), by fission (e.g. SINQ at PSI, Switzerland), or via spallation by protons (e.g. ISIS, U.K.). The spallation technique is much more efficient than the Bremsstrahlung technique and is much more 'politically sound' than a fission process and so was suitably chosen in the design of ISIS.

A schematic of ISIS is given in ***Figure 2.2.1***. The process begins with a H^- ion source created by passing hydrogen gas over a heated nickel tube which produces monatomic hydrogen which, in turn, converts H_2 into H^- via a caesium vapour discharge. The H^- ions are then driven towards a linear accelerator (LINAC) by a 665kV pre-injected potential. The H^- ions are accelerated to 70MeV and are then injected into the synchrotron via a 0.25μm thick Al_2O_3 electron stripper foil which, as the name suggests, strips all of the electrons off the H^- ions, leaving protons to circulate around the synchrotron. The synchrotron is a ten-sided polygon and has one high power magnet at the corner of each side of the synchrotron in order to focus the beam and turn it by the required 36° in order for it to circulate. Along six of the straight parts of the synchrotron lie radiofrequency (RF) cavities which constructively interfere with the proton beam in order to accelerate it cumulatively. Obviously, the frequency of the RF cavity must increase continuously as the beam cycles round the ring so as to keep accelerating it. Two other sides of the polygon are used for vacuum pumping purposes as the ring must be kept at ~5×10^{-8} mbar to avoid unnecessary absorption of the beam. The H^+ ions promptly split into two superperiod modes which are two different phases of standing waves. One mode moves faster than the other such that at the end of their orbit they leave the ring 400 ns apart. A set of fast-acting 'kicker' magnets is used to extract these 'bunches' from the ring, resulting in a pulse of frequency 50Hz and typically consisting of 2.5×10^{13} protons giving an average current of ~200μAmps. The 400 ns time difference between the two bunches is negligible compared to this frequency and therefore one can consider the beam as one single pulse. The extracted pulse is aimed at either a uranium or tantalum target via a set of quadrupolar magnets. On hitting the target, the high energy protons become

deeply embedded in the target nuclei. This causes an 'internal nucleon cascade', followed by an 'internuclear cascade' during which high energy neutrons are ejected and then an 'evaporation' stage whereby all target nuclei de-exite by emission of low energy neutrons and a variety of other nuclear particles and rays. On average, about 30 neutrons are produced per incident particle. A beryllium reflector directs the resultant neutrons through one of four different moderators (two consisting of ambient water, one of liquid methane (90K) and the other of supercritical hydrogen vapour (25K)) and then onto the neutron instruments via guide tubes. The whole process then begins again and repeats continuously every 20 ms (50Hz). Hence, in actual fact, for the bulk of the time there are no neutrons produced. The exact time of the process is very accurately recorded and t = 0 is set at the point where a pulse hits the U / Ta target. The time that each neutron takes from this point until reaching the detector is recorded so as to determine each neutron's wavelength (via the equation λ = ht/ml, where h = Planck's constant, t = time, m = neutron mass, l = distance travelled). This is known as the time-of-flight (TOF) technique. Within the 20 ms time window, all neutrons must be produced, diffracted, moderated and detected in order to avoid frame overlap.

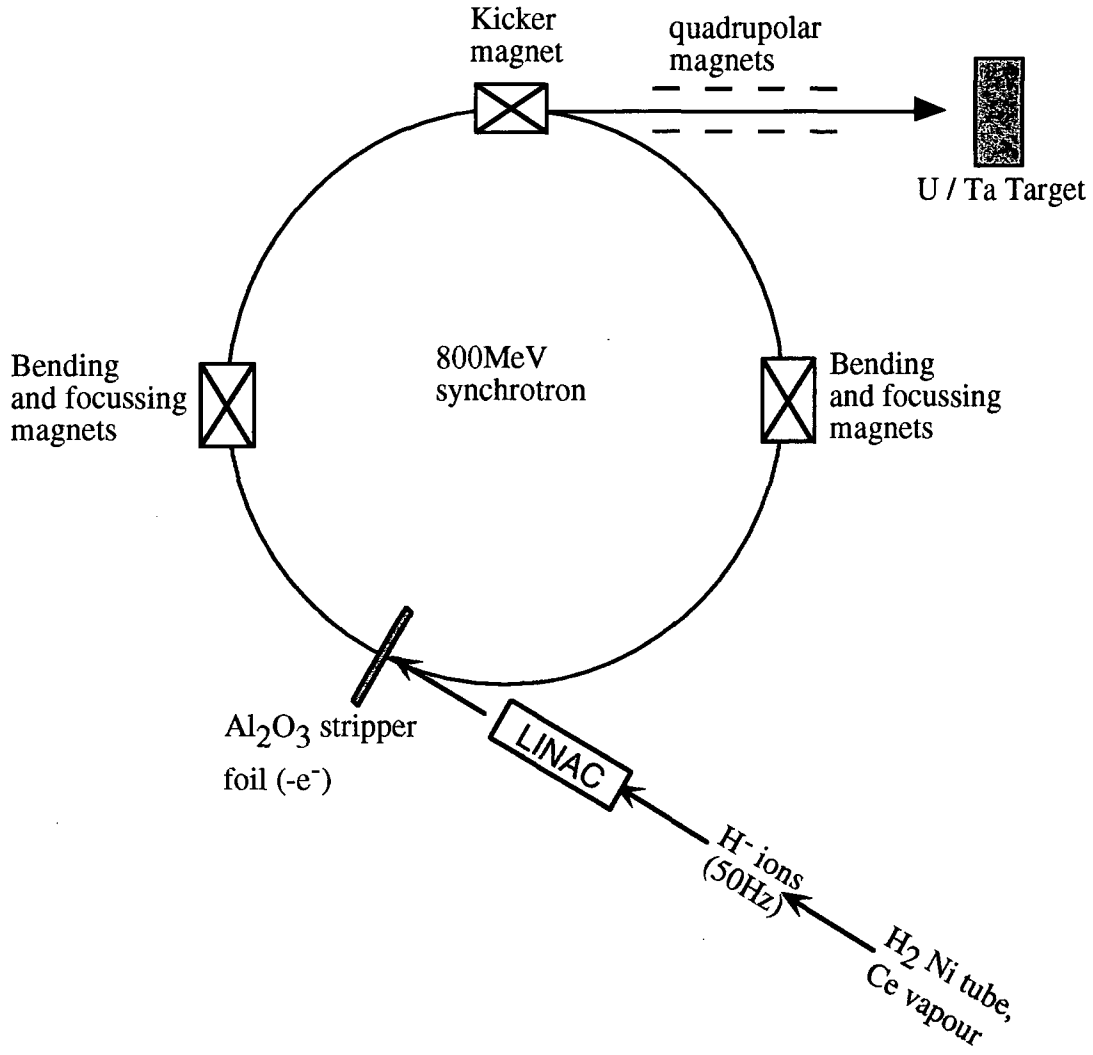

Figure 2.2.1 *- A schematic representation of a proton spallation neutron source.*

2.2.2 The Single Crystal Diffractometer, SXD

Since the neutron source is pulsed, one does not need to monochromate the beam as TOF techniques allow the determination of the wavelength for each peak recorded. Moreover, if one chose to monochromate, one would lose far too much intensity to make any data collection 'worthwhile'. Therefore, instead of keeping the wavelength constant and moving the sample as in D9 and D10 experiments at the ILL, here one allows a white beam of neutrons to penetrate the stationary sample resulting in diffraction at many different wavelengths. This is known as Laue diffraction. Bragg's law is satisfied many times simultaneously and with the instrument's two 2-D detectors, very fast data collections are possible. Moreover, after just a few minutes one can assess the nature and quality of a given crystal (e.g. check for twinning). The sample is exposed to the radiation for a time sufficient enough to obtain a good neutron count for the majority of all peaks present and a graph such as the one shown in ***Figure 2.2.2*** is obtained (the abscissa can be readily converted into d-spacing, wavelength, or Q-resolution). The sample is then tilted progressively first in ϕ and then in χ with a frame of data collected at each χ,ϕ setting.

The layout of SXD is shown in ***Figure 2.2.3***. SXD is situated on a thermal guide and the incoming white beam is moderated by ambient water since this provides a maximum flux at 1.14Å, thereby making the instrument ideal for structural determinations of organic compounds with small unit cells (at ~2.4Å, the flux becomes very low thereby presenting difficulties if one tries to carry out measurements on a stucture of a sizeable unit cell). One of a series of collimators (8-15mm in diameter) is selected to restrict the beam to the required aperture. The sample is placed in the centre of the crystal orienter which comprises a χ and ϕ circle. The sample enclosure is dependent on the type of experiment to be performed. In both of the experiments described in this thesis, a temperature of 100K was required. Hence, the sample enclosure was an Air Products He Displex CCR system as previously described in section 2.1.2. The centres of the instrument's two 64 x 64 pixel ZnS Anger-type scintillation counters, detector 1 and detector 2, lie at 2θ = 125°, ~190mm from the sample and 2θ = 55°, ~150mm from the sample respectively, leaving a gap of only 5 cm (~2°) between the two detectors. A very broad area of reciprocal space is therefore covered. It follows that, although SXD is inferior to D9 and D10 in terms of accuracy, SXD is superior in terms of speed and is therefore very suitable for variable temperature, disorder and hydrogen-bonded studies. The whole instrument is enclosed in a small blockhouse made of steel-reinforced concrete and borated wax and internally lined with 5cm thick borated polyethene, so as to keep background levels to a minimum. The instrument is fully controlled using a VAX Workstation 3600. For a more detailed description of SXD one is referred to Wilson, 1990, 1997a and 1997b.

Figure 2.2.2 *- A typical frame of data obtained from SXD.*

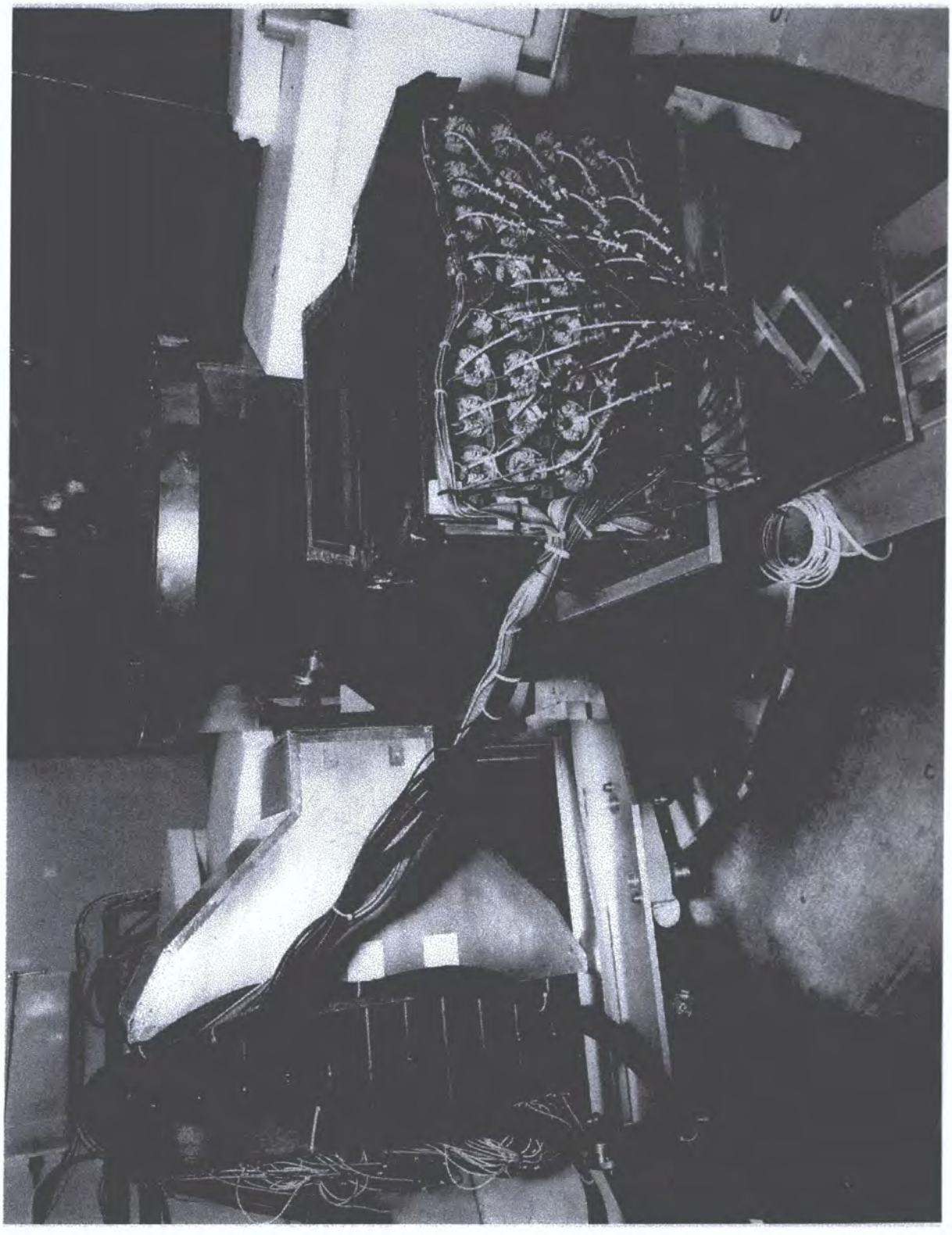

Figure 2.2.3 *- The Single Crystal Diffractometer, SXD, at ISIS.*

2.3 PROCEDURES FOR NEUTRON EXPERIMENTS

2.3.1 Crystal Preparation / Testing for Neutron Experiments

Before every neutron experiment, each batch of crystals has to undergo preliminary tests. The first test is of crystal size which should ideally be in the range 1 mm^3 - 4 mm^3. Next, the crystal quality is investigated. This is assessed by studying the crystals under an optical microscope in order to check that they have a regular and/or well formed crystal habit and do not possess any visible striations or other such faults. Polarizing light is also used to check that the crystals extinguish sharply and completely. If not, they are presumed to be twinned and removed from the batch.

In many cases in this thesis, the source crystals were initially too *large* for neutron diffraction purposes and so had to be cut. Obviously, one had to cut these crystals carefully so as to avoid undue stress and/or cracks in the resulting crystal. Just like wood, most crystals tend to possess a 'grain' in one direction due to the manner in which they grow. Therefore, along this direction it was sufficient to cut the crystal with a sharp scalpel blade. Along other directions, either solvent cutting and/or cutting with a scalpel was employed, depending on how brittle the crystals were. One also tried to cut the crystals so as to leave several natural faces if possible.

Once crystals are of the correct size and optical quality, they are assessed for further qualities by X-ray diffraction techniques. Naturally, the crystals are too big for a conventional X-ray diffraction study. However, by operating the machine at low power (so as to avoid saturating the detector) one can still index a material satisfactorily and gain some insight into the internal crystal quality and mosaicity by examination of the peak profiles. If the crystal indexes successfully, gives satisfactory peak profiles and has any natural crystal faces, then these faces are indexed so as to aid the search procedure in the neutron experiment (see section 2.3.3). Subsequently, the sample is slowly cooled to 100K using an Oxford Cryosystems Cryostream (Cosier & Glazer, 1986) whilst continuously monitoring three reflections, which have only one large value in h, k or l respectively. This enables one to check for the occurrence of any phase transitions or thermal instability / distortion of the material. During cooling, the reflections peaks have to be re-centred several times since the peak moves as the cell contracts. This ends the X-ray tests and the crystal is warmed up at least as slowly as it was originally cooled down. Several crystals from a given batch are tested in this way since one crystal may be different to another. If a crystal passes all of these tests it is ready for neutron diffraction.

One must note that in the case of the one neutron experiment on an air sensitive crystal described in this thesis (chapter 10) no X-ray tests were carried out at all. This was

because only one crystal existed of the compound and we did not want to extract the crystal from the Schlenk tube for testing purposes and risk jeopardizing the neutron experiment.

As a final preparatory step, neutron structure factors are calculated for the compound in question using SHELX-76 (Sheldrick, 1976). This information is useful when starting a neutron experiment since one may want to look at some strong and / or weak reflections prior to data collection, eg. for selecting suitable standard reflections or for testing the indexing of the crystal.

2.3.2 Crystal Mounting onto Neutron Devices

Different neutron instruments employ different crystal mounting techniques. ***Figure 2.3.1*** shows the different types of mounts used for each instrument:

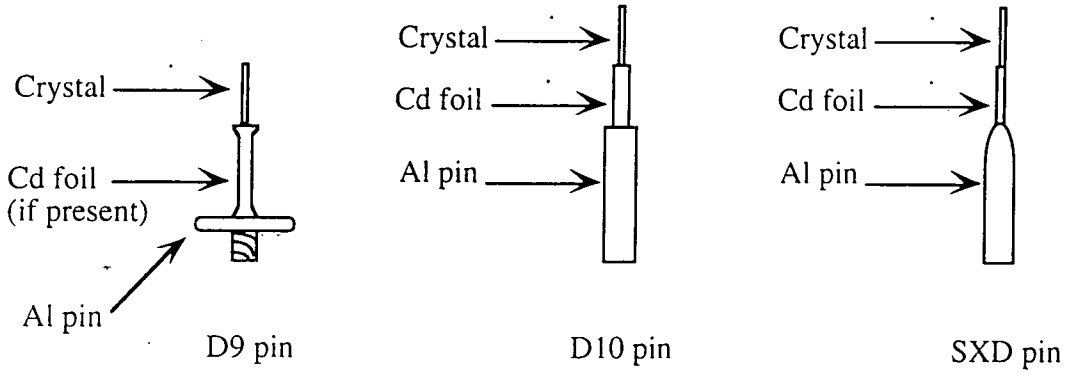

Figure 2.3.1 - Crystal mounts for the instruments D9, D10 and SXD.

The majority of crystals used on D9 were wrapped in very thin aluminium foil prior to mounting so as to protect the sample from the adhesive. For the air-sensitive crystal (chapter 10) silica gel was smeared over the crystal and then the crystal was wrapped in aluminium foil, all whilst in an argon-filled glove box. All ILL experiments used Kwikfill fast-setting epoxy body filler to glue the crystal to the mounting pin whereas the fast-setting epoxy resin, araldite, was used on SXD. The 'stem' of the pin onto which the sample was mounted in all cases but those on D9 is either made of cadmium (D10) or made of aluminium and surrounded in cadmium foil. The stem of D9 pins were chosen to be vanadium or aluminium, depending on whether the sample, in question, exhibits a large amount of incoherent scattering or not.

The mount is attached to the end of the Displex (D9, SXD) or cryostat (D10) which is made up of a copper block (gold-plated in the case of SXD) or a brass block respectively and is screwed in (or in the case of SXD, held in by a 1.5mm hex-head grub screw). The distance from the Displex / cryostat head to the centre of the beam is known in all cases

and so all pins are made to be a specific length so that the crystal should be automatically centred in the beam once mounted onto the instrument. D9 possesses a telescope and adjustment rings on the Displex holder which allows fine centring of the crystal. The pin on SXD is slightly adjustable within the limits of still being held in by the grub screw and the distance from the cold-head of the Displex to the centre of the crystal is simply measured with a ruler and adjusted accordingly so that this length coincides with the known distance to the centre of the beam. Once satisfactorily centred, one may proceed with the neutron experiment.

2.3.3 Searching and Indexing

Most ILL instruments use the common Multidetector Aquisition and Development^ (MAD) software (Barthelemy, 1984) to control the instrument and data collection. First, all known parameters (e.g. cell parameters, wavelength, etc) are entered via the program 'parame' in which one can also specify a number of other measureable parameters (e.g. scan width / resolution in given θ ranges). For D9 and D10, the next stage is searching for reflections. With the cell parameters known, one can calculate 2θ for a given reflection from Bragg's law. These values are set to be low and bisecting (so that there will be less possible hkl combinations for indexing any reflections found), χ is fixed at a given value (e.g. $\chi = 0$) and then ϕ is rotated through 360° in the search for reflections. Once a reflection has been detected by a marked increase in detector counts, the peak must be centred. Since D9 possesses an area detector, this is simply done by centring the peak in the detector (using the visual electronic detector display) by making small adjustments in χ and 2θ. D10 has only a single-point counter and so the peak must be centred by iteratively scanning in ω, 2θ and χ across the peak in order to find its midpoint. A smaller aperture than normal is used for this procedure. The search procedure is repeated until a sufficient number of reflections have been found (usually between 2 and 4) to index the cell. One should note that if the indices of the crystal faces are already known, this facilitates the searching procedure as one can simply find reflections corresponding to these faces.

The searching procedure is unnecessary for experiments on SXD because a multitude of peaks are instantly found when one measures a frame of data on SXD due to the detectors' enormous coverage of reciprocal space.

Since the unit cell parameters are already known for all D9, D10 and SXD experiments, (through prior laboratory X-ray experiments) the crystal does not need to be indexed as such. Only the crystal orientation needs to be determined (Busing & Levy, 1967). This requires a knowledge of the angular values of two observed reflections from non-parallel

^ So-called because the software was originally intended for just D19 at the ILL.

planes. These are used to relate the crystal lattice to the known unit cell axes, thus yielding a 3 x 3 matrix, named B. The unit cell axes are then related to the laboratory frame via a second 3 x 3 matrix, named U. The scattering vector in the laboratory frame is given by the product of these two matrices and Ω, X and Φ:

$$h_\theta = \Omega X \Phi U B h$$

where Ω, X and Φ are the 3 x 3 rotation matrices corresponding to the angular settings, ω, χ and ϕ respectively (for SXD the Ω parameter will not exist). The U matrix is called the orientation matrix and the product UB, which is more commonly discussed, is called the UB-matrix.

Once the crystal orientation has been successfully obtained, the crystal is cooled to the desired temperature, whereby the required experimental measurements may begin. The orientation matrix is continuously updated during data collection, since the more data coverage over reciprocal space one has, the more accurate the UB matrix becomes.

2.3.4 Data Collection Strategies

2.3.4.1 Data collection on D9 / D10

Data collection on D9 / D10 is very straightforward. One simply executes a command file which is set to measure batches of reflections ordered sequentially in h, k and l. ω-xθ scans are performed, with x chosen to keep the reflection in the middle of the detector aperture, were used in conjunction with a scan width, Δω, which was roughly twice the full width of the peak to background. Both x and Δω were defined by a specified resolution curve. Each batch of reflections consists of all of the unique reflections present within a specified θ range. For each subsequent batch, the θ range is set to begin at the previous θ maximum limit and have its upper limit fixed to an angle 10-15° larger. The rationale for the preferred use of this sequence rather than simply measuring reflections in just one large θ range is that if something goes wrong during the experiment and / or one runs out of beam-time, at least a full coverage of unique data will be obtained albeit all within a small θ range; whereas only a fraction of the data will have been measured in the latter method with limited angular coverage of reciprocal space. A certain number of symmetry equivalent reflections (the exact number depending on how much time is available) are also included in the command file betwixt the earlier batches. Furthermore, psi-scans (where typically φ = 0 - 180° or 360°) of a few selected reflections (usually one weak and one strong one) are inserted into the command file during the experiment in order to assess the verity of any subsequent absorption correction performed. Assuming that there no major crystal or mechanical related problems encountered during an

experiment, data collection continues until either beam-time runs out or the intensity of reflections at increasingly high θ angles becomes negligible compared to the background level. If the latter circumstance prevails before the former, then a collection of further symmetry equivalents is often carried out to enhance the counting statistics.

2.3.4.2 Data Collection Strategies on SXD.

One begins by setting both ϕ and χ equal to zero and performing a 'run' which counts neutrons cumulatively over a period of typically 1-5 hours (assuming 180/200μAmp/h) depending on the nature of the material and size of unit cell. The progressive build up of intensity of reflection peaks is recorded in a frame such as the one previously depicted in ***Figure 2.2.2***. Once satisfactory intensities have been obtained, one moves ϕ by a given incremental step (typically between 30-45° depending on how much time is available / how much data one has to collect) and proceeds with the next acquisition. Once ϕ = 180° (the ϕ software limit), χ is tilted by a given increment (typically 30-45°) and frames are measured sequentially moving ϕ again (but back towards ϕ=0) after each run. Once ϕ=0 again, χ is tilted further and the process repeats until all scans are performed at the χ=90° tilt (the χ software limit). Assuming that all is still well by this point, one begins the process of 'tiling' which is where one positions χ and ϕ at their previous values minus half of their original incremental step and then measures runs whilst sequentially moving ϕ / χ by the original incremental values. This 'tiling' process provides a significant amount of reciprocal space overlap thereby improving the statistics of the experiment. Moreover, although one measures equivalent reflections during 'tiling', they are usually measured at different wavelengths and 2θ values to when first measured.

2.3.5 Data Reduction

2.3.5.1 Data Reduction on D10.

Integrated intensities are derived by the program, 'coll5n' (Lehmann & Wilson, 1987). This program integrates peaks using the Lehmann-Larsen method (Lehmann & Larsen, 1974) which determines, across a one-dimensional scan, the minimum stationary points of $d\sigma I/dI$, which represent the points at which a peak starts or finishes relative to the background. This procedure is very reliable although it is negatively biased in the sense that the background it calculates will often be slightly higher than it is in reality. In order to compensate for this, stationary values can be measured at additional points. Alternatively, one can use the widths of neighbouring strong peaks to derive the peak widths of weak peaks (Wilkinson, Khamis, Stansfield & McIntyre, 1988), as is the default option now in 'racer'.

Following peak integration, coll5n (Lehmann & Wilson, 1987) performs a Lorentz correction which accounts for the fact that the diffraction from some indices is measured for a longer time than for others as a result of the way in which 2θ sweeps through reciprocal space. The geometrical correction takes the form of $L=1/\sin 2\theta$ for all ω:xθ scans in equatorial-plane geometry. A polarization correction is not required [in contrast to X-rays] since for neutrons the polarization is equal to 1. The intensities are then converted into structure factor amplitudes.

2.3.5.2 Data Reduction on D9.

Integration is carried out using the program 'racer' (Wilkinson, Khamis, Stansfield & McIntyre, 1988). The program is based on the Lehmann-Larsen method (Lehmann & Larsen, 1974) of peak integration described in the preceding section. However, since the Lehmann-Larsen method applies to a one-dimensional profile and an area detector produces a three-dimensional peak profile, the Lehmann-Larsen method must be adapted to compensate for this. It is not immediately obvious which points should be tested for the $d\sigma I/dI$ minimum when one considers a three-dimensional peak profile and it would be far too time consuming to compute $d\sigma I/dI$ for every observed point! Hence a few assumptions are made: in the input file of the integration program, one states the number of pixels across the detector, the standard volume, stvol (which is an estimated volume which will encompass at least 90% of each peak without including too much background at the same time) and the volume factor, volfac (which defines the multple of stvol to be used as an integration limit for all strong reflections). The centre of the detector is calculated from the number of pixels given and is approximated to be the centre of a reflection (the UB matrix should be sufficiently accurate to validate this approximation). The stvol and volfac parameters are then taken into account and an ellipsoid corresponding to the stvol x volfac volume is modelled around the calculated centre. If the reflection is considered strong (in the input file to the program, a threshold value, sigbr (sigma to background) decides this) then the adapted Lehmann-Larsen method (Lehmann & Larsen, 1974) is applied in the area between the stvol and volfac volume.

The profile is thus determined, recorded in an output file and entered into a 'library of strong reflections' which is 'binned' into reflections of different 2θ values, since profiles often slightly change over 2θ. Any profile with an ellipsoid filling fraction, (fill), of less than a specified percentage, typically 80% or more, is removed from this library. For weak reflections, the profiles of strong reflections at a similar 2θ value are taken as reference and applied within the stvol volume only, taking the background value as that outside of the volume, stvol x volfac. During the integration process, the strong reflections are also used to update the UB matrix and x, y and z offsets.

Following integration, a Lorentz correction is applied before converting the resulting intensities to structure factor amplitudes.

One should note that this program will only work if an 'alphas.dat' file is present in the working directory since this file describes the 'reference zero' of each pixel of the detector. Since no detector has completely homogenous pixels, this file will not describe a completely flat area. However, under normal working conditions, the file should describe a fairly level area.

2.3.5.3 Data Reduction on SXD.

Unlike data reduction procedures for D9 and D10, no variant on the Lehmann-Larsen method of profile fitting is used. This is because the resolution of each pixel for each SXD detector is low (~3mm which corresponds to about one degree) and so each peak will occupy only a few pixels of the detector. This means that if the variant of the Lehmann-Larsen method described for D9 procedures was used, the accuracy of each ellipsoid determined, based on these few pixels would be very poor, thereby resulting in very ill-described peak profiles. Therefore, an in-house program (peakfit) is used instead which collapses each two-dimensional spectrum onto one axis before applying a Gaussian function to each normalized[#] peak on this axis, which also contains an exponential term to account for the exponential change in the neutron beam before and after moderation. The height and width of the Gaussian function are TOF variable parameters as is the time constant of the exponential. The method has been found to give both sensible and reliable integrated reflection data. Although, it should be noted that reflections are excluded from the data set for which this profile fitting procedure fails after four attempts on different integration windows, thus resulting in a somewhat reduced occurrence of very weak or 'unobserved' peaks in the final data set.

A Lorentz correction is then applied before conversion of the intensities into structure factor magnitudes.

2.3.6 Decay, Absorption, Cryostat Shield and Extinction Corrections

2.3.6.1 Decay Corrections.

No decay was observed during any of the neutron experiments and therefore, no such corrections were applied.

[#] Each peak is normalized to the wavelength-dependent incident beam profile using the incoherent scattering from a polycrystalline vanadium sample.

2.3.6.2 Absorption Corrections for D9 and D10 Data.

The program, DATAP (Coppens, 1970) was used to correct for sample absorption in all structures performed on these two instruments. The program is based on Busing and Levy's Gaussian grid integration method (Busing & Levy, 1957) which corrects for absorption by first subdividing the crystal into a grid of a given size (10 x 10 x 10 points was used in all cases described in this thesis) and then calculating the neutron path length from the beam source to each grid point and out along the diffraction direction. The program then sums over all grid points to approximate the integral:

$$A = 1/V \int e^{-\mu t} dV$$

This gives a weighted absorption correction of the whole crystal for a given reflection. The calculation must be repeated for each reflection. Obviously, one can increase the accuracy of such an absorption correction by reducing the grid size although, in general, significant improvements in an absorption correction are only observed if the crystal is of an irregular morphology. Two vital *a priori* pieces of information are required for DATAP (Coppens, 1970). The first piece of information is the indices and dimensions of each face of the crystal measured. This information should be ascertained before the experiment commences in case the crystal fractures or moves during the data collection. The other necessary piece of information is the value of the absorption coefficient of the compound, μ. The method to calculate μ is best illustrated by example:

Calculation of μ for $MoC_{26}H_{40}N_2$ (see chapter 10):

Table 2.3.1 *- Calculation of the total absorption cross-section of* $MoC_{26}H_{40}N_2$.

Element	Number of atoms in the unit cell	σ_{abs} x (λ/constant) x $\sigma_{incoherent}$	$\sigma_{a/molecule}$	$\sigma_{a/unit\ cell}$
Mo	4	2.55 x (0.8405/1.798) x 0.28	1.472	5.888
C	104	0.0035 x (0.8405/1.798) x 0.001	0.0026	0.2704
N	8	1.90 x (0.8405/1.798) x 0.49	0.1378	1.1024
H	160	0.3326 x (0.8405/1.798) x 37	37.156	5944.96
			$\sigma_{a/total}$	5962.06

$V = a.b.c.\sin\beta = 20.240 \times 6.550 \times 19.910 \times \sin(103.99) = 2561.2 Å^3$

$\mu = \sigma_{a/total} / V = 5962.06 / 2561.2 = 2.33\ cm^{-1}$

The respective program is then executed thereby providing a set of absorption corrected intensities. The intensities of the reflections corresponding to the psi-scans that have been measured during data collection (usually of one strong and one weak reflection) before and after the correction are then inspected to test the validity of the correction. ***Figure 2.3.2*** shows typical graphs of intensities from two reflections before and after correction (taken from the compound $MoC_{26}H_{40}N_2$ (chapter 10)). Ideally, all intensities of a given reflection at different φ values should be identical. However, no matter how perfect it is, no absorption correction can ever completely match this ideal because of the omnipresence of other anisotropic effects, e.g. extinction.

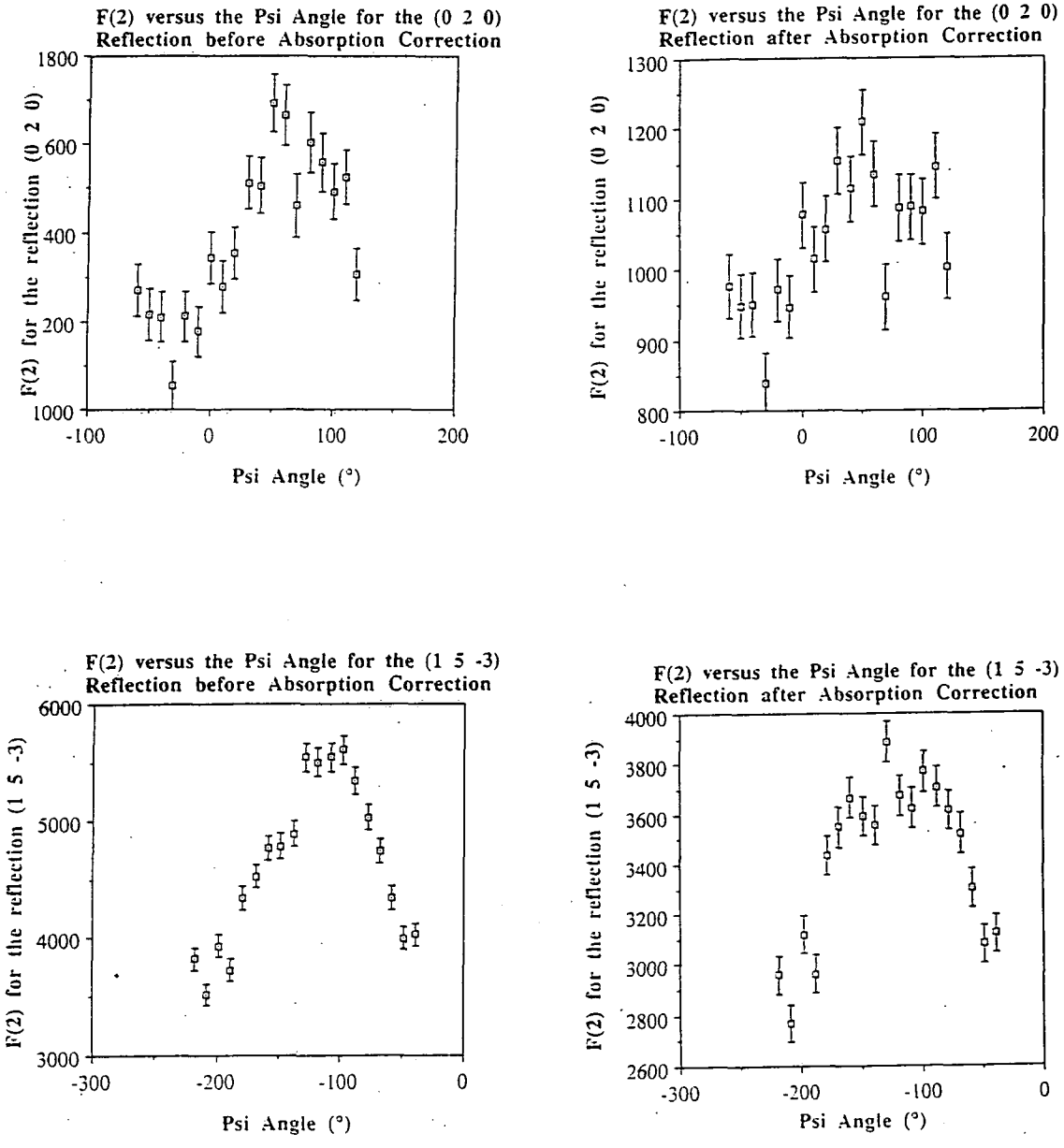

Figure 2.3.2 *- Plots of intensity versus psi angle for two reflections of* $MoC_{26}H_{40}N_2$ *before and after absorption correction.*

2.3.6.3 Absorption Corrections for SXD Data.

In this case, the nature of the absorption effect is more complicated since it is λ-dependent. However, an in-house semi-empirical correction has been formulated to account for the absorption which involves a comparison between the extent of scattering at different parts of reciprocal space of the sample and of the isotropic vanadium standard.

2.3.6.4 Cryostat Shield Corrections.

Where any cryostat shields are not spherical, an additional absorption correction is required in order to account for the effect of the shields. All three cryostat shields on D10 are spherical so no correction is necessary there. Likewise, no such correction is necessary for SXD data since, although the crystal on this instrument is enclosed in a cylindrical casing, the aluminium windows through which the beam passes are too thin to cause any absorption effect.

However, for all D9 data a cryostat shield correction is necessary since, although the outer shield is spherical and the middle shield is made of aluminium and is too thin to cause any absorption effect, the inner shield is cylindrical and made of vanadium and it of significant thickness. The correction is essentially the same as an absorption correction for a crystal, i.e.

$$I = I_0[1/V \int e^{-\mu t} dV]$$

where μ is calculated for vanadium in the same manner as that described for a crystal.

2.3.6.5 Extinction Corrections.

Extinction is caused by the rescattering of a diffracted beam within the crystal. There are two possible types of extinction present when a beam is diffracted through a crystal: (i) primary extinction, which occurs *within* a crystal domain if the domain is sufficiently misorientated relative to others and (ii) secondary extinction which occurs *between* domains if the domains are well oriented with respect to each other.

Extinction corrections take the general form:

$$y_x = (1 + 2x + \text{higher order terms in } x)^{-1/2}$$

where $2x = 2(H\lambda^3/V^2 SIN2\theta)g^*F(\mathbf{h})^2$

where for a primary extinction correction, H = the average mosaic domain radius, t.
for a secondary extinction correction, H = the absorption weighted mean path length for a given reflection, T.

g^* = the extinction parameter which is related to the average mosaic domain radius t and the average domain misorientation g.

$y_x = y_{(primary)} \cdot y_{(secondary)}$ and is the multiplicative term in the otherwise kinematic relation, $I = yF(\mathbf{h})^2$.

All such corrections for D9 and D10 data were applied within the refinement program SHELXL-93 (Sheldrick, 1993). Here the correction takes the form of a refinement parameter, EXTI, in the equation:

$$y = k[1 + 0.001 \times EXTI \times F_c^2 \times \lambda^3/\sin(2\theta)]^{-1/4}$$

where k is the overall scale factor. This correction attempts to correct for both primary and secondary extinction simultaneously.

For SXD data, an isotropic variable wavelength dependent extinction correction is applied within the CCSL (Brown & Matthewman, 1993) least-squares refinement program SFLSQ. This correction is based on the Gaussian Becker-Coppens formalism (Becker & Coppens, 1974) which is given by the equation:

$$y_i = (1 + c_i x_i + a_i x_i^2/(1 + b_i x_i))^{-1/2}$$

where i is a primary or secondary extinction parameter and a_i, b_i and c_i are least-squares refinement parameters as derived by Becker & Coppens, 1974.

2.3.7 Structural Solution and Refinement Procedures

No neutron structure, described in this thesis, needed to be solved since, in all cases, an X-ray model already existed which could be taken as the starting model for the refinement.

All neutron refinements described in this thesis used the full-matrix least-squares refinement program, SHELXL-93 (Sheldrick, 1993). Refinements in SHELXL-93 (Sheldrick, 1993) are based on F^2 and the state of each cycle of least-squares refinement is assessed by the following statistics:

The goodness-of-fit, goof:

$$\text{Goof} = S = [\sum [w(F_o^2 - F_c^2)^2]/(n - p)]^{1/2}$$

where n = number of reflections refined.
p = number of parameters refined.
w = weighting parameter.

The residual 'R'-factor, R1:

$$R1 = \sum | |F_o| - |F_c| | / \sum |F_o|$$

The weighted residual 'R'-factor, wR2:

$$wR2 = [\sum [w(F_o^2-F_c^2)^2]/\sum [w(F_o^2)^2]]^{1/2}$$

where for all neutron refinements, a $1/\sigma^2$ weighting scheme is adopted throughout[&] .

Obviously, one should not judge the state of refinement solely on these parameters since although statistics may show promising results, they do not take into account physical discrepancies such as atomic thermal displacement parameters being non-positive definite, high correlations between atoms and so forth. In other words, one should be prepared to sacrifice apparent optimal statistics for a sensible scientific result.

[&] The use of w should be constrained to conventional X-ray refinements since this refineable parameter is intended to correct for systematic effects which should not be present in a fully corrected neutron data set.

2.4 SINGLE-CRYSTAL DIFFRACTION STUDIES USING LABORATORY SOURCE X-RAYS

All laboratory source X-ray diffraction studies were performed at the University of Durham, U.K. During the three years of this PhD study, the laboratory has housed four different diffractometers, a Rigaku AFC6S diffractometer, a Siemens P4 diffractometer, a Siemens SMART-CCD diffractometer and an in-house Fddd cryodiffractometer (Copley et al, 1997) which is used primarily for experiments performed below liquid nitrogen temperatures. All of these instruments have been used for work reported in this thesis.

The three conventional diffractometers are all equipped with an Oxford Cryosystems Cryostream unit (Cosier & Glazer, 1986) which allows experiments to be carried out at any temperature in the range 85-300K. It uses liquid nitrogen which is pumped from a Dewar through the cryostream and set and maintained at the required temperature by a heating coil and thermal sensor. The thermal sensor is situated very close to the cryostream outlet nozzle so as to monitor the temperature at a position as close to the crystal as possible. Two gas streams emerge from the nozzle. The outer stream consists of warm dry air, provided by a compressor. This air stream surrounds the inner cold nitrogen flow, thus minimising ice formation on the nozzle due to the presence of a large thermal gradient.

2.4.1 Crystal Preparation and Sample Mounting

All crystals are first tested optically in the same manner as described for neutron experiments (section 2.3.1), except that since the X-ray beam is small and X-ray absorption and extinction are much larger than neutron absorption and extinction, all X-ray samples must be much smaller (typically 0.05-0.5mm in each dimension) than those used for neutron experiments (typically greater than $1mm^3$ on edge). A selected crystal is glued onto the end of a glass fibre using a fast-setting epoxy resin or, if the sample is air-sensitive (as for all compounds discussed in chapters 9 and 10), the oil-drop method (Stalke & Kottke, 1993) is employed in which the crystal is encapsulated in a viscous perfluoroether oil which acts as a protective film and which solidifies when placed onto the diffractometer under a 150K liquid nitrogen flow. The glass fibre protrudes from a brass pin and is held in the pin by either plastocene or bees' wax. In turn, the brass pin is fixed into the top of a goniometer head by a grub screw. The goniometer head allows one to translate the crystal in three perpendicular directions so that once the goniometer head is secured to the diffractometer, the position of the crystal can be adjusted such that it lies in the centre of the path of the incoming beam. Once the crystal is centred, the translators are locked by grub screws.

2.5 THE INSTRUMENTS AND THEIR PROCEDURES

2.5.1 The Rigaku AFC6S and Siemens P4 diffractometer

These two diffractometers have practically identical physical features and thus will be described together. The X-ray source is a Molybdenum Kα X-radiation tube (λ = 0.71073Å) which is sometimes changed to a Copper Kα X-radiation tube (λ = 1.5418Å) on the Rigaku AFC6S diffactometer (***Figure 2.5.1***) in order to measure weakly diffracting samples and to determine absolute configurations in light atom structures by anomalous dispersion studies. A (111) graphite crystal plane is used to monochromate the beam and its cross-section is defined using either a 0.2mm, 0.5mm or 0.8mm lead collimator. Each instrument employs Eulerian four-circle equatorial-plane geometry with the crystal oriented by an Eulerian cradle as on the instruments D9 and D10. The goniometer head, onto which the sample is mounted, is screwed onto the ϕ-shaft and the crystal is centered using the instrument's in-built microscope. The crystal is then ready to be investigated using X-rays.

Figure 2.5.1 *- The Rigaku AFC6S diffractometer at Durham, U.K.*

A 'glass-panelled' interlock disables user access to the instrument and opens the shutter of the X-ray beam. Computer controlled software is then used to move the circles in order to search for diffraction from the sample which is detected using the KBr scintillation counter. A lead beam-stop is situated in the direct-line of the incident beam in order to

absorb all non-diffracted X-rays. The Oxford Cryosystems Cryostream cooling device (Cosier & Glazer, 1986) is positioned diagonally above the sample such that collision with the χ circle of the Eulerian cradle is avoided.

The computer controlled software comes from the company that supplies the diffractometers and so is machine model specific. As a result, the experimental routines on each machine differ slightly. The Rigaku AFC6S diffractometer uses *MSC/AFC Diffractometer Control Software* (Molecular Structure Corporation, 1991) whereas the Siemens P4 diffractometer employs the XSCANS software package (Siemens Analytical X-ray Instruments, 1994).

2.5.1.1 Searching and Indexing

In order to obtain a reliable preliminary orientation matrix for a given crystal in an X-ray experiment, one usually requires between 10 and 20 suitable reflections. The Rigaku AFC6S diffractometer is set to search for 20 suitable reflections by systematically 'zig-zagging' through reciprocal space. Once obtained, these 20 reflections are indexed together or if initial indexing fails, in smaller groups. If the indexing procedure fails, one can select the peaks to be indexed manually using given criteria (e.g. good profiles or high intensity).

The Siemens P4 diffractometer performs a hemispherical search through reciprocal space which is centred around the first reflection found and which has a radius equal to the minimum anticipated cell length. An orientation matrix is determined from the first four reflections found and it is then used to try and index subsequent reflections. If this indexing fails, the orientation matrix is redetermined using the updated reflection list and the process repeats until ten reflections have been successfully indexed using the same orientation matrix.

Both instruments use the 'auto-indexing' or 'real space method' strategy (Clegg, 1984, Sparks, 1976 and 1982) to determine the cell parameters and orientation matrix of a given crystal. As its name suggests, this method works in real-space. The three shortest non-coplanar n vectors are arbitrarily assigned the indices 100, 010 and 001 such that a preliminary orientation matrix and unit cell can be generated. Although this unit cell (a', b', c') will probably not be the 'true' cell, it must be a sub-cell of it since all vectors in the true lattice are also vectors in a lattice described by a sub-cell. The program then tests the cell by generating vectors, $t = ua' + vb' + wc'$ (u,v,w = integral value), up to a specified maximum length and calculating the dot product, t.n for each of the 3 n vectors. If t.x is integral (within a small tolerance) for all reflections in the given list, then this x vector is a true lattice vector. Otherwise, a new x vector must be chosen and the whole procedure

repeats until 3 x vectors satisfy this condition.

Following successful indexing, the deduced cell parameters are refined and checks are performed to ensure that the given cell is not actually a sub-cell of the true cell and to ascertain which Bravais lattice type and Laue class the crystal structure may belong to. If the crystal symmetry has been satisfactorily ascertained then one can set up a data collection accordingly.

If one is in *any* doubt whatsoever of the symmetry, one should perform a data collection suitable for a triclinic crystal since this will measure all quadrants of reciprocal space, thereby ensuring collection of all unique data (within a given 2θ range and machine limits) regardless of its symmetry. Moreover, even if the symmetry is ultimately much higher than triclinic, collecting symmetry equivalents is advantageous since it will improve statistics on merging, reduce systematic errors, improve precision and give an indication of internal consistency of data and the absolute configuration if Friedel equivalents are measured. It is always good practice to collect at least some symmetry equivalents (usually Friedel equivalents) although one is inherently limited in angular range by collision limits.

2.5.1.2 Data Collection Strategies

The level of precision of measurement is also regulated internally within each control software package. Precision is proportional to the square root of the measurement time and can therefore be increased by either collecting scans slower or repeatedly. Weak reflections tend to have particularly poor precision, thereby causing the level of precision to be often very disparate. Each control software package therefore attempts to scan reflections to at least a given minimum level of precision and to make the overall precision more uniform. The Rigaku AFC6S diffratometer tries to ensure this by first scanning a given reflection and in the process determining the measurement's precision. If this precision falls below the minimum precision threshold then the reflection is rescanned until either when this threshold has been reached or when the maximum number of rescans permitted, as specified by the user, is reached. Throughout the experiment, the actual time per scan remains constant. The Siemens P4 diffractometer takes an alternative approach to this problem. Each reflection is first prescanned in order to ascertain a rough value of its expected precision. From this, the scan time required to meet the minimum precision threshold (specified by the user) for this reflection is calculated and subsequently, the reflection is scanned at the calculated rate. Therefore, the whole data collection proceeds at a variable scan speed.

The type and width of scan to be used during data collection must also be addressed. Two

types of scan are available, $2\theta/\omega$ scans and ω-scans. The former type of scan involves the concurrent rotation of both the detector and sample whereas in the latter type of scan only the sample is rotated. In general, $2\theta/\omega$ scans are used in preference to ω-scans unless the scans are very broad or one or more of the cell axes is large since in such cases peaks are close in θ and so may overlap the next reflection. The scan width can be either fixed or varied on both diffractometers. In cases where it is fixed, the width is determined on the basis of the widths of the reflections used in the indexing procedure. The desired width should encompass all of the peak intensity of each reflection and as small an amount of background as possible whilst avoiding any chance of clipping the peaks. In cases where the variable width is used, two constant parameters, A and B, from the function $(°\omega) = A + B\tan\theta$ must be evaluated. Parameter A is determined experimentally from high angle data and parameter B is fixed at a value based on the difference between $K\alpha_1$ and $K\alpha_2$ wavelengths. The function itself allows one to account for peak broadening at increasingly higher 2θ values due to increased wavelength dispersion.

The value of 2θ should also be deduced. In most experiments reported in this thesis, this limit was set to be 50° with Molybdenum radiation since above this value most of the data are generally fairly weak (since the X-ray scattering power decreases sharply with increasing $\sin\theta/\lambda$) and improves the refinement very little.

One final matter that needs to be assessed is the nature, quantity and frequency of standard reflections to be measured. In order to be able to detect any problem occurring during data collection, one should periodically survey as large an area of reciprocal space as possible. Bearing this in mind, three reflections of intermediary strength were chosen, each with one alternately large Miller index and were measured every 150 or 100 reflections on the Rigaku AFC6S or the Siemens P4 diffractometer respectively.

2.5.1.3 Data Reduction

Data obtained from the Rigaku AFC6S diffractometer were reduced using the package TEXSAN (Molecular Structure Corporation, 1989) whilst the XSCANS software (Siemens Analytical X-ray Instruments, 1994) used throughout the experiment on the Siemens P4 diffractometer also reduces the data. The intensities are converted into structure factors after a Lorentz and polarization (Lp) correction has been performed. The Lorentz correction is the same as that described previously, where $L = (\sin 2\theta)^{-1}$, whilst the polarization correction, which is also a geometric one, accounts for the partial polarization of both the incident X-ray beam by the graphite monochromator and that invoked during diffraction within the sample. In the latter case, the amount of polarization is dependent on the value of 2θ and is given by $P=(1 + \cos^2 2\theta) / 2$, whereas in the former case, the extent of polarization depends specifically on the orientation of the

monochromator relative to the equatorial plane of the diffractometer and the physical nature of the crystal.

2.5.2 The Siemens SMART-CCD Diffractometer

A view of the Siemens SMART-CCD diffractometer is given in ***Figure 2.5.2***. The instrument employs (111) graphite monochromated molybdenum Kα X-radiation which is collimated using either a 0.2mm, 0.5mm or 0.8mm lead aperture. It possesses only three Eulerian circles since the value of χ is fixed at 54.74°. The goniometer head, onto which the sample is mounted, is mounted onto the ϕ-shaft. The sample is positioned at the centre of these circles and once centred using the in-built microscope diffraction is measured using a 512 x 512 pixel scintillation area detector which employs a charged-coupled-device (CCD) instead of photomultiplier tubes to amplify the output. A lead beam-stop is fixed in the direct line of the incident X-ray beam and a 'glass-panelled' interlock prevents user intervention when the X-ray shutter is open. The Oxford Cryosystems Cryostream cooling device (Cosier & Glazer, 1986) is positioned diagonally above the sample in a similar manner to the other two diffractometers previously described.

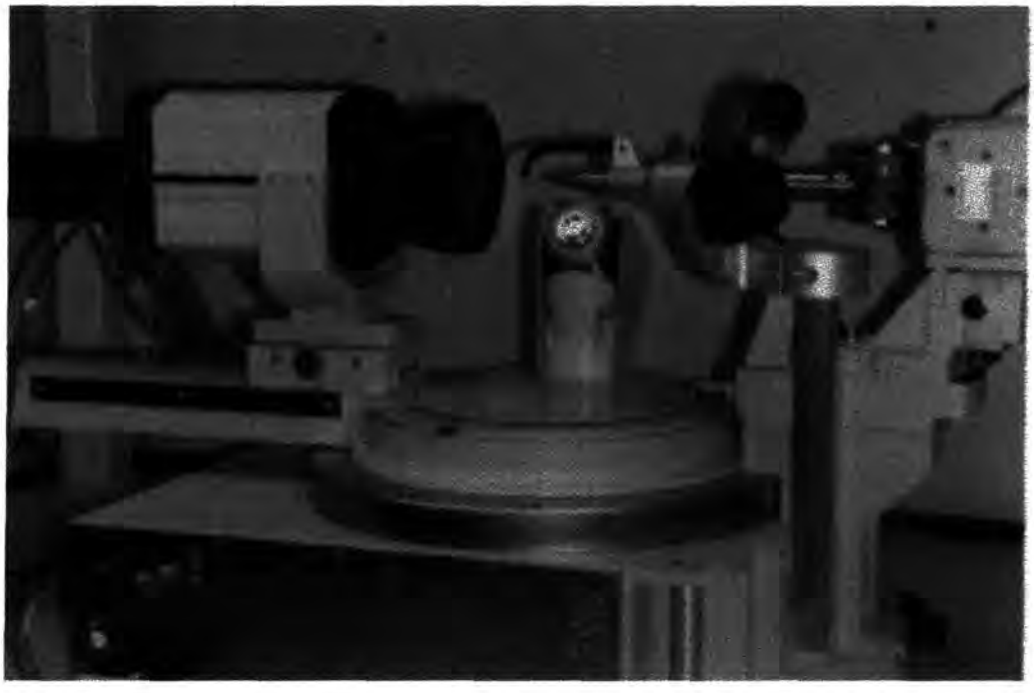

Figure 2.5.2 *- The Siemens SMART-CCD diffractometer at Durham, U.K.*

2.5.2.1 Searching, Indexing and Data Collection Procedures

These three procedures are carried out using the computer control software, SMART (Siemens Analytical X-ray Instruments, 1995c). Since the instrument possesses a two-dimensional PSD, it covers a large area of reciprocal space in the measurement of just one frame of data. This feature allows one to determine very quickly the X-ray quality of the crystal via an 'electronic' rotation photograph. If the X-ray quality looks satisfactory, one continues by searching for reflections. A certain number of frames of data (typically 10-20) are measured at a given X-ray exposure time (typically 5-20 seconds) over three different regions of reciprocal space two of which are mutually orthogonal. Reflections appearing in these frames are then selected by a 'thresholding' procedure which puts into a list all reflections which exceed a minimum I/σ value, which is specified by the user. An attempt is then made to index these reflections. Usually, a minimum of about 20 reflections are necessary for successful indexing. The algorithm used for this procedure (Kabsch, 1993) is similar to that described previously (Sparks, 1976 and 1982). If initial indexing fails, one can try sorting this list of reflections with respect to a given parameter, e.g. mean intensity, 2θ range, etc and then selecting reflections at one end of this scale e.g. of the highest intensity, smallest 2θ range, etc, for re-indexing. Alternatively, one can either simply collect more frames of data and index on a greater number of reflections or remove all of the existing reflections in the list and select reflections manually from the frames, on the basis of good sharp peak profiles and moderate intensities and try to index this subset.

Once a sample has been indexed successfully, the orientation matrix is refined by a least-squares procedure, thereby updating the cell parameters and crystal offsets. One can also check for higher symmetry at this point using the 'Bravais' option. It is then necessary to set up a data collection routine. Due to the virtues of the area detector, data collection strategies on the Siemens SMART-CCD diffractometer are much simpler than those required for the Rigaku AFC6S or Siemens P4 diffractometer. An ω-scan is sufficient and a scan width need not be employed since one is scanning such a large area of reciprocal space per frame. However, a scan step size must be selected. For routine data collections (with Mo Kα X-radiation) this value is typically set to -0.3 in ω. Occasionally, one reduces this value to -0.15 if the reflections are obviously sharper than normal or if a greater accuracy is required for some reason. In such cases, the number of scans should obviously be doubled. Standard reflections, like those collected on the Rigaku AFC6S or the Siemens P4, cannot be collected on an area detector system. However, since data collection on the Siemens SMART-CCD is so fast (typically 8-12 hours) crystal decay is usually negligible[@]. A full hemisphere of reciprocal space is

[@] It is possible to assess the extent of any crystal decay with the Siemens SMART-CCD by repeating a small number of the frames from the beginning of the experiment at the end.

surveyed by collecting frames of data, in batches at predetermined angular settings, to a maximum value of 2θ . This value is usually 50° for the reasons described previously although, here, the value will also depend upon the distance between the crystal and the detector (which is typically 6 cm). The level of precision is selected by the user's decision on the length of time for which each frames is exposed to the X-ray irradiation. For a standard data collection, this time is typically set to 10-40 seconds depending on the apparent diffracting strength of the sample.

At the end of the data collection, one selects the reflections which were used initially to index the cell and enough others from frames collected over all areas of reciprocal space in oder to make up 512 reflections (the maximum permitted number of reflections in a least-squares input) which are used to refine more accurately the cell.

2.5.2.2 Data Reduction

All of the frames are then integrated using the program SAINT (Siemens Analytical X-ray Instruments, 1995b), the procedure of which is described by Kabsch (1988). Each three-dimensional peak profile is placed a three-dimensional box of a given size, as specified by the user, where the box comprises a grid of 9 x 9 x 9 points. The size of the box is constant for each data set and is chosen by analysing a variety of reflections, prior to the data reduction, in terms of their width in the x and y directions and the full-width-half-maximum of the ω-rocking curve width (the z-direction). The largest widths in each direction are taken as the dimensions of the box. The integration proceeds in two stages. In the first stage, only the strong reflections (as determined by a specified $I/\sigma(I)$ threshold) are considered. For each profile, the most intense point in the three-dimensional box is determined in order to calculate the background which is assumed to be lower than 2% of this maximum intensity. All points above this 2% threshold are considered as a signal and are normalized. The profiles of all of the strong reflections are stored in a temporary file. The second stage of integration is then performed, in which, all weak reflections are considered. The profile of each of these reflections is approximated to that of the nearest strong reflection profile stored. The weak reflection is then normalized according to this profile. Following integration, an Lp correction is applied before conversion of the resulting intensities to structure factor amplitudes. Here, the Lorentz factor takes the form:

$$|\mathbf{S}.(\mathbf{u} \times \mathbf{So})| / (|\mathbf{S}|.|\mathbf{So}|)$$

where **So** and **S** are incident and diffracted beam wavevectors of the reflection respectively and **u** is the unit vector along the direction of the rotation axis. The polarization factor is slightly more complicated and takes the form, $P = \langle \sin 2\varphi \rangle$, where:

$$<\sin 2\varphi> = (1-2p)[1-(\mathbf{n}.\mathbf{S} / |\mathbf{S}|)2] + p\{1 + [\mathbf{S}.\mathbf{So} / (|\mathbf{S}||\mathbf{So}|)]2\}$$

where p is the probability that the electric-field vector is in the polarization plane and 1-p is the probability that the electic-field vector is parallel to the normal of this plane, **n**.

The level of decay is then analysed by comparing reflection intensities with the same hkl indices and the same φ-values from the beginning and the end of the data collection. A linear correction is applied where necessary.

2.5.3 Decay, Absorption and Extinction Corrections

2.5.3.1 Decay Correction

For all Rigaku AFC6S, Siemens P4 and Siemens SMART-CCD data, the level of decay is assessed during data reduction in TEXSAN (Molecular Structure Corporation, 1989), SAINT (Siemens Analytical X-ray Instruments, 1995b) and XSCANS (Siemens Analytical X-ray Instruments, 1994) respectively. Since no decay was detected in any X-ray experiment, no such correction was applied.

2.5.3.2 Absorption Correction

The TEXSAN software (Molecular Structure Corporation, 1989) incorporates an absorption correction program (North, Phillips & Mathews, 1968) for Rigaku AFC6S data whereas all Siemens P4 and Siemens SMART-CCD data must be absorption corrected using a separate program, e.g. XPREP (Sheldrick, 1995). Each program corrects for absorption using the same basic correction factor as used in neutrons: $A = 1/V \int e^{-\mu t} dV$. However, whereas a numerical type of correction is applied to all neutron data using a knowledge of the face indices, in routine X-ray experiments face indices are not generally measured. Instead, an empirical absorption correction is performed which uses φ-scans which are, by default, measured at the end of a data collection on each instrument and are read into a separate file from the bulk data. This file is read into the absorption correction program and used to apply the correction which analyses the different intensities of a given reflection at different ϕ-values due to differing path lengths through the crystal. For one experiment on the Siemens SMART-CCD reported in this thesis, the empirical abosrption correction program, DIFABS (Walker & Stuart, 1983) was used instead.

2.5.3.3 Extinction Correction

In all Rigaku AFC6S, Siemens P4 and Siemens SMART-CCD X-ray experiments where

an extinction correction was necessary, the parameter EXTI was refined isotropically as described in section 2.3.6.5.

2.5.4 Space Group Determination

The reduced data of a sample are analysed in XPREP (Sheldrick, 1995) in order to determine the space group of the crystal in question. The program must take into account the crystal parameters, the Bravais lattice type (P, A, B, C, I, F), the Laue symmetry, all systematic absences and a form of the mean value of the normalised structure, $<|E^2|-1>$ in order to deduce the space group. The value of the latter factor can alone suggest whether the crystal structure possesses a centre of inversion or not. For a centrosymmetric and non-centrosymmetric structure, $<|E^2|-1>$ will tend towards 0.97 and 0.74 respectively in the majority of cases. However, in some cases, particularly where a heavy metal is present in the structure, the $<|E^2|-1>$ value will provide misleading information since it will distort the statistics of intensity distributions.

2.5.5 Structure Solution and Refinement

Once the correct space group of a crystal has been determined, its full structural solution is sought. This is not a simple task since one measures the *intensity* of data rather than the *amplitude* and so although one can easily deduce structure factor amplitudes from the observed data ($I = F^2$), because of the squaring function, one has no idea of the relative phases of these amplitudes. With no knowledge of the phases, the data is rendered useless since the structure factors can only be converted into an electron density distribution via a Fourier transform which can only be solved if one knows the phases. This is the so-called 'phase-problem'.

Fortunately, two methods have been developed which overcome this problem. Both, direct methods (Harker & Kasper, 1947 and 1948; Gillis, 1948a and 1948b; Karle & Hauptman, 1950; Sayre, 1952) and Patterson methods (Patterson, 1944), are commonly used to solve single-crystal structures from X-ray data.

2.5.5.1 Direct Methods

This method (Harker & Kasper, 1947 and 1948; Gillis, 1948a and 1948b; Karle & Hauptman, 1950; Sayre, 1952) relies on the fact that structure factor magnitudes and phases are correlated through an *a priori* partial knowledge of the nature of the electron density distribution.

The convolution of the structure factor magnitudes and phases give the complete structure

factor, the Fourier transform of which is the electron density contribution, $\rho(x)$. We inherently possess some information about the electron density, e.g. $\rho(x) \geq 0$, $\int \rho^3(x)dV$ must equal a maximum, many of the atoms in a given structure may be very similar (this especially applies to organic compounds). Such information is expressed as mathematical constraints on the function, $\rho(x)$ and since $\rho(x)$ is related to the structure factor, F(h), corresponding structure factor constraints are formulated. Since the structure factor magnitudes are already known, these constraints apply mainly to the phases.

A given number of strong reflections are arbitrarily assigned phases and the constraints are applied such that, in favourable cases, all phases may then be determined. Obviously, the more constraints available, the easier the determination of the un-assigned phases. Since the initial partial assignment of phases is completely arbitrary, the procedure will seldom give the correct solution. Moreover, it is not instinctively obvious which is the correct solution. Hence, this procedure is repeated, typically 30-200 times and for each solution a combined figure of merit (CFOM) is calculated in order to identify the best solution.

The phases of the best solution are then used to generate an electron density map from which one can pick out atoms at given positions and use them as a starting model for structural refinement. This starting model is usually incomplete since one can only very seldomly pick out *all* of the atoms directly from such an electron density map.

The remaining 'missing' atoms are found by difference Fourier synthesis which is performed in conjunction with the least-squares refinement. The phases that are known are used to approximate the unknown phases. The electron density distribution of the incomplete model is then calculated and subtracted from the observed electron density distribution. A map of the difference density is then plotted in which the 'missing' atoms show up as positive peaks.

2.5.5.2 Patterson Methods

Although direct methods (Harker & Kasper, 1947 and 1948; Gillis, 1948a and 1948b; Karle & Hauptman, 1950; Sayre, 1952) are now generally considered to be the most powerful techniques, Patterson methods (Patterson, 1944) are still commonly employed when solving a structure containing one or more heavy-atoms. This is because, in such cases, the constraint involving Sayre's equation (Sayre, 1952) in direct methods cannot be applied so readily since all atoms are *not* of very equal scattering power and by limiting the constraints in direct methods, one reduces its effectiveness.

In contrast, Patterson methods (Patterson, 1944) only tend to succeed if the atomic

weights of selected atoms are very disparate since this factor forms the basis of the method. The Patterson method (Patterson, 1944) simply ignores the phase-problem and so whilst the electron density is described by:

$$\rho_{xyz} = (k/V) \sum_h \sum_k \sum_l \{F_{hkl} \cos[2\pi(hx + ky + lz) - \phi_{hkl}]\}$$

(where k = scaling factor, V = unit cell volume and the summation is carried out over all data, F_{hkl}, ϕ_{hkl})

the Patterson function is described by:

$$P_{uvw} = (k^2/V) \sum_h \sum_k \sum_l \{F^2_{hkl} \cos[2\pi(hu + kv + lw)]\}$$

Just as an electron density map can be generated, once the phases are known, a Patterson map can be generated in the same way but without a knowledge of the phases. Such a map describes 'vector-space' rather than 'real-space' as shown in an electron density map. Hence, whilst the peaks in an electron density map relate to atomic positions, the peaks in a Patterson map correspond to interatomic vectors. Each atom is mapped to all possible atoms in the unit cell. The intensity of each peak in the Patterson map corresponds to the product of the atomic weights of each pair of atoms linked by a vector. Interatomic vectors of symmetry equivalent pairs of atoms are superimposed on the Patterson map giving rise to peaks of apparently double, quadupole,... weighted magnitudes. By the nature of the mapping, all vectors are able to map onto themselves. Hence, the most intense peak will inevitably lie at (0 0 0). After this, the most intense peak will relate to the joining of the heaviest atom in the molecule with itself in the neighbouring molecule not related by symmetry. Its position in real-space can be deduced by the simple vector calculation: OA - OB = 2x, 2y, 2z. Once the atomic position of one atom has been deduced, the determination of other slightly less heavy atoms becomes easier. Obviously, the more heavy atoms of similar atomic weights present, the more difficult it is to interpret the Patterson map.

Once atomic positions of the principal heavy atom(s) have been identified, they form the starting model for the structural refinement. Difference Fourier synthesis is then used to calculate the 'heavy-atom' phases for all structure factor magnitudes. Since the heavy atoms will dominate the total scattering, this will give fairly reliable phases. The resulting structure factors are used to generate an electron density distribution map. From this map, the atomic positions of further atoms present in the molecule can be located. The increasingly complete model is successively refined, locating further 'missing' atoms in each successive electron density distribution map, until all non-hydrogen (and sometimes even hydrogen) atoms have been found.

Both, direct (Harker & Kasper, 1947 and 1948; Gillis, 1948a and 1948b; Karle & Hauptman, 1950; Sayre, 1952) and Patterson (Patterson, 1944) methods, were employed to solve structures throughout this thesis using the program, SHELXS-86 (Sheldrick, 1990).

All X-ray derived structures, given in this thesis, were refined using the SHELXL-93 (Sheldrick, 1993) package, as described in section 2.3.7.

2.5.6 The Fddd Four-Circle Cryodiffractometer

The Fddd four-circle diffractometer (Copley et al., 1997) is shown in ***Figure 2.5.3***. The instrument has been developed in order to perform X-ray diffraction experiments at temperatures as low as 9K. The diffractometer comprises: a Siemens rotating anode generator, a Huber goniometer with offset χ-circle, a Siemens Fast Scintillation single-point Detector (FSD) and an APD512 Displex He closed-cycle refridgerator (CCR) (Archer & Lehmann, 1986). The belt-driven rotating anode gives an X-ray flux that is far in excess of that obtained from a sealed X-ray tube. This leads to faster data collections and the opportunity to study smaller samples. The 18kW rotating anode generator employs a rotating (6000rpm) molybdenum target in conjunction with a high brilliance 0.3 x 3 mm filament, typically with generator settings of 52kV and 76mA (4.0kW). A Leybold 'Turbovac 361' Turbo Molecular Pump (TMP) is used to maintain an anode chamber vacuum of 3 x 10^7 mbar. The X-rays are monochromated by a Huber '151' graphite crystal which operates in the parallel mode. A lead collimator (3 mm in diameter) is used to restrict the incoming beam aperture. The X-rays pass through two concentric cylindrical Beryllium heat shrouds (6.5 and 4.5 cm in diameter) before reaching the sample. Both of these shrouds are evacuated (to about 10^5 mbar) for thermal insulation and the inner shroud also shields against radiative heat losses. A second lead collimator (3 mm in diameter) is placed at the entrance to the detector for diffracted beam collimation. This collimator also prevents the detection of background due to these Beryllium shrouds. The instrument is controlled and data collected remotely using a DEC MicroVax 3300 workstation operating VMS5.1 and CAMAC electronics§ .

§ The remote control was modified to the given system during the course of my studentship. Hence, the Fddd cryodiffractometer experiment given in chapter 4 utilised the old system: a VAX/VMS 3000 workstation and Superior Electric electronics.

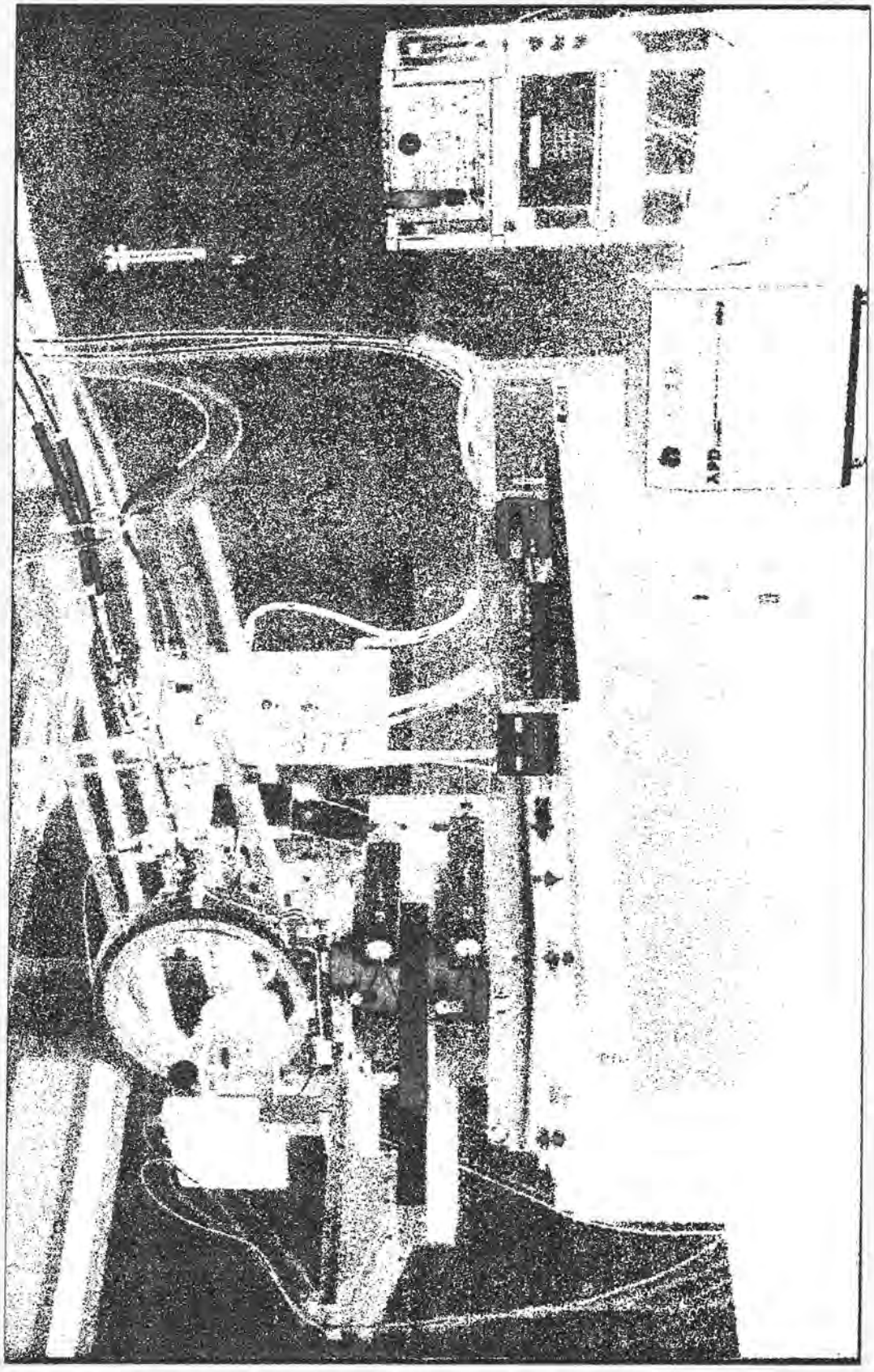

Figure 2.5.3 - The Fddd Cryo-Diffractometer at Durham, U.K.

2.5.6.1 Crystal Preparation and Mounting.

A good quality crystal of a size 0.05 - 0.3 mm on edge is mounted on a sharpened 0.3 mm graphite pencil 'lead' using a low temperature (4K) epoxy glue (Oxford Instruments, TRZ0004). In turn, the graphite leads are held in a Cu sample mount which screws directly onto the Displex head.

2.5.6.2 Experimental Procedures.

During the course of my studentship, the control software has also been modified. The Fddd cryodiffractometer experiment described in chapter 4 utilised the old software which originated from Crystal Logic Inc.. All other Fddd cryodiffractometer experiments detailed in this thesis used the previously described MAD (Barthelemy, 1984) control software and coll5n (Lehmann & Wilson, 1987) for data reduction (see section 2.3.5.1).

2.6 REFERENCES

Alcock, N. W. (1974). Acta Crystallogr., **A30**, 332-335.

Archer, J. M. & Lehmann, M. S. (1986). J. Appl. Cryst., **19**, 456-458.

Barthelemy, A. (1984). MAD. Institut Laue Langevin Technical Report, 84BA15T.

Becker, P. & Coppens, P. (1974). Acta Crystallogr., **A30**, 129-148.

Blank, H. & Maier, B. (Ed.), (1988). "The Yellow Book, Guide to Neutron Research Facilities at the ILL", (Institut von Laue - paul Langevin, Grenoble, France).

Brown, P. J. & Matthewman, J. C. (1993). CCSL. The Cambridge Crystallographic Subroutine Library, Report RAL-93-009. Rutherford Appleton Laboratory, Oxon, U.K.

Busing, W. R. & Levy, H. A. (1957). Acta Crystallogr., **10**, 180-182.

Busing, W. R. & Levy, H. A. (1967). Acta Crystallogr., **22**, 457-464.

Clegg, W. (1984). J. Appl. Cryst., **17**, 334.

Copley, R. C. B., Goeta, A. E., Lehmann, C. W., Cole, J. C., Yufit, D. S., Howard, J. A. K. & Archer, J. M. (1997). J. Appl. Cryst., **30**, 413-417.

Coppens, P. (1970). DATAP. *The Evaluation of Absorption and Extinction in Single-Crystal Structure Analysis* in "Crystallographic Computing", Ed. Ahmed, F. R., (Munksgaard, Copenhagen).

Cosier, J. & Glazer, A. M. (1986). J. Appl. Cryst., **19**, 105.

Gillis, J. (1948a). Acta Crystallogr., **1**, 76-80.

Gillis, J. (1948b). Acta Crystallogr., **1**, 174-179.

Hall, S. R., Flack, H. D. & Stewart, J. M. (Ed.), (1992). Xtal3.2 Reference Manual. Universities of Western Australia, Geneva and Maryland, (Lamb, Perth).

Harker, D. & Kasper, J. S. (1947). J. Chem. Phys., **15**, 882.

Harker, D. & Kasper, J. S. (1948). Acta Crystallogr., **1**, 70-75.

Kabsch, W. (1988). J. Appl. Cryst., **21**, 916-924.

Kabsch, W. (1993). J. Appl. Cryst., **26**, 795-800.

Karle, J. & Hauptman, H. (1950). Acta Crystallogr., **3**, 181-187.

Kuhs, W. F. (1988). Materials Science Forum, **27/28**, 25-34.

Lehmann, M. S. & Larsen, F. K., (1974). Acta Crystallogr. **A30**, 580-584.

Lehmann, M. S. & Wilson, S. (1987). COLL5N. College V, Data reduction system: Treatment of reflection profiles.

Molecular Structure Corporation (1989). TEXSAN. Version 5.0, TEXRAY Structure Analysis Package. MSC, 3200 Research Drive, The Woodlands, TX77381, U.S.A.

Molecular Structure Corporation (1991). *MSC/AFC Diffractometer Control Software.* MSC. 3200 Research Forest Drive, The Woodlands, TX77381, U.S.A.

North, A. C. T., Phillips, D. C. & Mathews, F. S. (1968). Acta Crystallogr. **A24**, 351-359.

Patterson, A. L. (1944). Phys. Rev., **65**, 195.

Sayre, D. (1952). Acta Crystallogr. **5**, 60-65.

Sheldrick, G. M. (1976). *Program for crystal structure determination.* University of Cambridge, England.

Sheldrick, G. M. (1990). Acta Crystallogr. **A46**, 467-473.

Sheldrick, G. M. (1993). SHELXL-93. *Program for the Refinement of Crystal Structures using Single Crystal Diffraction Data*, University of Göttingen, Germany.

Sheldrick, G. M. (1995). XPREP in SHELXTL. Version 5.03/VMS. Siemens Analytical X-ray Instruments, Inc., Madison, Wisconsin, U.S.A.

Siemens Analytical X-ray Instruments, (1994). XSCANS. *X-ray Single Crystals Analysis System*, Version 2.1, Siemens Analytical X-ray Instruments, Inc., Madison, Wisconsin, U.S.A.

Siemens Analytical X-ray Instruments, (1995a). ASTRO. Version 4.050. Siemens Analytical X-ray Instruments, Inc., Madison, Wisconsin, U.S.A.

Siemens Analytical X-ray Instruments, (1995b). SAINT. Version 4.050. Siemens Analytical X-ray Instruments, Inc., Madison, Wisconsin, U.S.A.

Siemens Analytical X-ray Instruments, (1995c). SMART. Version 4.050. Siemens Analytical X-ray Instruments, Inc., Madison, Wisconsin, U.S.A.

Sparks, R. A. (1976). "Crystallographic Computing Techniques", Ed. Ahmed, F. R., (Munksgaard, Copenhagen) pp 452-467.

Sparks, R. A. (1982). "Crystallographic Computing", Ed. Sayre, D., (Clarendon Press, Oxford) pp 1-18.

Stalke, D. S. & Kottke, T. (1993). J. Appl. Cryst., **26**, 615-619.

Walker, N. & Stuart, D. (1983). Acta Crystallogr., **A39**, 158-166.

Wilkinson, C., Khamis, H. W., Stansfield, R. F. D. & McIntyre, G. J. (1988). J. Appl. Cryst., **21**, 471-478.

Wilson, C. C., (1990). *Data analysis of reciprocal space volumes,* in Neutron Scattering Data Analysis, Ed. Johnson, M. W., IoP Conference Series Vol. **107**. Adam Hilger, Bristol.

Wilson, C. C., (1997a). J. Appl. Cryst., **30**, 184-189.

Wilson, C. C., (1997b). J. Mol. Struct., in press.

Zeyen, C. M. E., Chagnon, R., Disdier, F. & Morin, H., (1984). Revue Phys. Appl., **19**, 789-791.

CHAPTER 3

INTRODUCTION TO CHARGE DENSITY STUDIES

3.1 INTRODUCTION

The standard X-ray diffraction techniques described in Chapter 2 are adequate if one simply requires a three-dimensional representation of a molecule with knowledge of its bond lengths and angles to the precision of several decimal places. However, if one requires a more in-depth analysis of the bonding or any charge, polarization or electrostatic determinations, then conventional modelling is unsuitable.

Conventional diffraction techniques use the Independent Atom Model (IAM) which defines atomic positions to be at the centre of electron density contours in regions where atoms are suspected. It is assumed that the surrounding electron density will be spherical and of a radius equal to the van der Waals distance of the atom type. Moreover, each atom is assumed to carry no charge.

In heavier elements where the electron core is well defined by X-rays, the true atomic centre will be determined with reasonable accuracy by the IAM. However, the sphericity assumption made on such an atom type may not be so accurate because of the diffuse d and f orbital electrons and crystal field effects, unaccounted for by the model. Furthermore, it is difficult to distinguish the valence electron density of such atoms from the dominating core electrons by conventional Fourier techniques and so the exact nature of bonding around this heavy atom may be difficult to ascertain.

In lighter elements where the major part of the total electron density is made up of valence electrons, the electron core is ill-defined and so therefore is the atomic centre in the IAM approximation. The hydrogen atom is the most extreme example of this as it consists solely of one valence electron - by nature of the IAM, the centre of electron density from this one electron will erroneously be taken to be the atomic centre as well. This will lead to X-H bond distances which are too short.

One can reduce the valence / core electron density bias by performing a normal refinement as well as a separate high-angle refinement since low angle scattering is predominantly due to valence electron density whereas above about 0.6Å^{-1} almost all scattering derives from the core electrons (Coppens & Hall, 1982). It is of course preferable to have an extensive data set when carrying out such separated refinements.

Furthermore, one can better distinguish between valence and core electrons by lowering the temperature of data collection since this reduces the dampening of intensity, caused by thermal smearing, *c.f.* the Debye-Waller factor:

$$F(\mathbf{h}) = \sum_{\kappa=1}^{n} \sum_{\kappa=1}^{n} f_\kappa T_\kappa \exp(2\pi i \mathbf{H}.\mathbf{r}(\kappa))$$

where f_κ = the scattering factor.
$F(\mathbf{h})$ = the structure factor.
$T_\kappa = \exp(-16\pi^2 u_{ij}^2 \sin^2\theta/\lambda^2)$ = Debye-Waller factor

Experiments carried out at 100K have shown up to an 150 fold increase in intensity at $\sin\theta/\lambda = 1.0 Å^{-1}$ compared to experiments performed at 298K and at 10K the data / parameter ratio may be as much as doubled when compared to the 100K experiment (Mallinson, 1995). However, the presence of hydrogen / deuterium zero-point motion will often reduce such gains.

A much better way to determine accurately the atomic positions in molecules is to use neutron diffraction. This technique determines the nuclear structure rather than the electronic structure as with X-rays. If one therefore uses the atomic positions from the refined neutron data as a rigid model for the X-ray refinement, one should obtain more accurate results, assuming that both the neutron and X-ray experiments have been carried out under similar conditions, e.g. same temperature.

However, despite all improvements resulting from a careful undertaking of low-temperature extensive data collections and combining them with neutron experiments where possible, the IAM still remains inadequate for detailed bonding analysis, as a result of its atomic-neutrality assumption. No atomic charge leads to no polarizability or electrostatic effects. Hence, the model will take no account of acid/base tendencies, ionic tendencies, charge transfer or crystal field effects and will assume all molecules have no dipole moment, let alone a moment of any higher order.

As these effects can so drastically effect the valence electron distribution in a molecule, one must find another model to study bonding.

3.2 LINEAR COMBINATION OF ATOMIC ORBITALS

Whereas the IAM assumes electrons around an atom to be spherical as in the isolated atom, this method takes into account molecular orbital (MO) representations. An MO is described by the summation:

$$\chi_i = \sum \sum c_{i\mu}\phi_\mu$$

where χ_i = the MO function;
$c_{i\mu}$ = the MO contribution from the atomic orbital, μ;
ϕ_μ = the atomic basis function.

Different atomic basis functions can be used. The most popular is the Hartree-Fock (HF) minimal basis set. Here, the basis orbitals are single-Slater functions and one exists for each inner and valence shell for each atom. The Slater determinant can be written as:

$$\phi = \sum_i \sum_{j \geq i} \mathbf{P_{ij}}[\chi_1(1)\chi_2(2)...\chi_n(n)]$$

where ϕ is the wavefunction and $\mathbf{P_{ij}}$ is the electron permutation operator (with eigenvalues equal to +1 or -1 for even and odd permutations respectively). Electron density is related to the wavefunction such that:

$$\rho(r) = \int |\psi|^2 dr$$

$$\Rightarrow \quad \rho(r) = \sum n_i \chi_i^2$$

$$\Rightarrow \quad \rho(r) = \sum_\mu \sum_\nu P_{\mu\nu}\phi_\mu(r)\phi_\nu(r)$$

where $P_{\mu\nu}$ is the density matrix which describes the population of orbital product density functions, $\phi_\mu(r)\phi_\nu(r)$. This representation of s, p, d and f orbitals provides a directional constraint on the atoms and in particular, allows for the orthogonality relationships between px, py and pz, which in turn introduces radial modes into the model. Moreover, electron overlap and lone pairs are considered and the resulting positive and negative lobes of the product function allow one to account for migration of electron density from orbital to orbital.

This model is therefore superior to the IAM by its accountability of electron density overlap, orbital and lone-pair representation and charge transfer between atoms.

3.3 THE SPHERICAL-ATOM KAPPA FORMALISM

This model splits the core and valence electron density distinctly into two parts as exemplified by the equation:

$$\rho_{atom} = \rho_{core} + P_v\kappa'^3\rho_{valence}(\kappa' r) \quad \#$$

where P_v is the population of the valence shell and κ' is a parameter which denotes the degree of expansion or contraction of the valence shell around a given atom. If $\kappa' > 1$ then the shell is contracted; if $\kappa' < 1$ then the valence shell is expanded. The exact value of κ' is derived from the normalization of the valence electron density and its accuracy may be assessed by its level of agreement with the linear relationship $\kappa' \alpha q$, where q is the charge of a particular atom type (Coppens, 1995). Alternatively, one can perform theoretical studies in order to determine the value of κ' (Brown & Spackman, 1991) and compare these with the experimental result.

The κ' parameter is related to the scattering factor by the inverse relationship:

$$f_{valence}(S) = \text{fourier transform of } f_{valence}\,(S/\kappa')$$

Hence, a κ'-modified scattering factor may be obtained directly from the unperturbed IAM scattering factors in the literature. A classic example of this is the Stewart-Davidson-Simpson (SDS) form factor for hydrogen which models hydrogen with a kappa parameter, $\kappa' \approx 1.16$, as derived from theoretical studies on H_2 (Stewart, Davidson & Simpson, 1965). Indeed, the SDS form factor has become the standard for hydrogen in X-ray structure analysis. When available, neutron data can be used to obtain even more accurate values of κ' for X-H bonds (Coppens, 1995).

In practice, the κ'-formalism leads to net charges which are in good agreement with accepted electronegativity concepts, and molecular dipole moments which are close to those ascertained by other experimental and theoretical methods.

ρ_{core} is sometimes referred to as the promolecule density, ρ_{pro}.

3.4 MULTIPOLAR REFINEMENT USING ASPHERICAL ATOM-CENTRED DENSITY FUNCTIONS

Atomic density functions are usually expressed in polar co-ordinates, r, θ and ϕ, where r represents the radial component of the density function and the angular components, θ and ϕ emanate from Real Spherical Harmonic functions, $Y_{lm\pm}(\theta,\phi)$. The total electron density is represented by the equation:

$$\rho_{atom}(\mathbf{r}) = P_c\rho_{core}(r) + P_v\kappa^3\rho_{valence}(\kappa' r) + \sum_{l=0}^{l_{max}} \kappa''^3 R_l(\kappa' r) \sum_{m=0}^{l} P_{lm\pm} d_{lm\pm}(\mathbf{r}/r)$$

where P_c and P_v are the populations of the core and valence shells respectively;
κ' is the expansion / contraction factor for the valence shell as hitherto discussed;
l corresponds to the monopolar (l=0), dipolar (l=1), quadupolar (l=2), octopolar (l=3) and hexadecapolar (l=4) terms;
m corresponds to the orientation of l terms;
P_{lm} is a population constant for a given l and m;
$d_{lm\pm}$ is the normalized associated Legendre function;
R_{lm} represents the radial function;
and κ'' is the expansion / contraction parameter for the multipoles (κ'' may be split into monopolar, dipolar, quadrupolar, octopolar or hexadecapolar kappa values; however, this is not usually done because they are usually strongly correlated with each other).

The latter equation is often simplified to:

$$\rho_{total}(r) = \rho_c P_c(r) + \rho_v P_v(\kappa' r) + \sum_{l=1}^{l_{max}} Y_{lm} R_{lm}(\theta,\phi,r,\kappa'')$$

where the summation in the equation above begins at l = 1 rather than at l = 0, i.e. at the dipolar rather than the monopolar level. The reason for this is simply that HF calculations much better describe monopoles than do the Slater determinants in the spherical harmonic summation. Therefore, the HF monopolar description resides in the $\rho_v P_v(r,\kappa')$ term whereas all higher order terms remain in the given Slater determining summation. Conversely, HF calculations describe all aspherical multipoles much worse than do Slater functions and so are never used for anything other than monopoles.

The Slater-type radial function used is defined by:

$$R_l(r) = \kappa^3[(\xi^{n_l+3})/(n_l + 2)!](\kappa r)^{n(l)}\exp(-\kappa\xi\pi)$$

where ξ is the energy-optimized single Slater orbital exponent for the electron subshells of isolated atoms (Slater, 1930): $\xi = (Z-\sigma)/n$, (Z = charge, σ = screening constant, n = principal quantum number) and for each element it is taken from tabulated values (Clementi & Raimondi, 1963).

The value of n must be greater than 1 due to Poisson's electrostatic requirements (Stewart, 1977) and ones choice depends upon the elemental nature of the atom in question (Hansen & Coppens, 1978).

The radial and angular functions described above are used in all cases reported in this thesis. However, it is not the only formalism available: Gaussian type (Stewart, 1980) and harmonic oscillator (Kurki-Suonio, 1977) radial functions also exist and Hirshfeld has developed a formalism (Hirshfeld, 1971) which uses cosine functions instead of spherical harmonics. However, such formalisms are less commonly employed.

At present, the multipolar formalism gives the best described representation of bonding orbitals and also has the flexibility to incorporate HF models into it for the spherical components of each atom. Moreover, the populations of each multipoles (and therefore all orbitals) are obtainable which provide us with a wealth of information, e.g. the extent of crystal field effects, charge transfer between atoms, acid / base tendencies, etc, and allows the calculation of electrostatic effects, multipolar moments and (hyper)polarizability coefficients. The multipolar formalism was therefore employed in all charge density studies reported in this thesis.

3.5 PERFORMING THE EXPERIMENTS AND REFINING THE RESULTS

First, one must consider what type of data to collect. In the ideal case one would carry out two experiments: one neutron and one X-ray diffraction experiment and both would be performed at the same temperature which would be as low as possible for reasons hitherto discussed. Moreover, one would collect data up to the highest resolution possible ($\sin\theta/\lambda \approx 0.8\text{-}0.9 Å^{-1}$ is considered minimum) with as many symmetry equivalents as are obtainable and with as full a coverage of reciprocal space as is permitted by machine contraints. One would also wish to carry out the data collection as slowly as possible to ensure the best statistics possible. However, one must usually compensate the speed of data collection with the amount of data collected due to feasible time restraints of data collection and even if one had unlimited machine time for an experiment, one should beware of using the maximum time possible because of the danger of crystal decay due to extended exposure to radiation or machine problems which may affect the experiment. However, the increasing use of two-dimensional X-ray detectors instead of single-point counters/detectors and charge-coupled-devices (CCDs) rather than less sensitive photomultiplier tubes allow much faster data collection such that the overall time restraint is less important.

Data reduction, merging and relevant corrections (such as absorption and / or extinction) proceed separately for each diffraction technique. The neutron data is then refined using full-matrix least-squares techniques, using a conventional crystal structure refinement package. All resulting atomic positions and the temperature factors for hydrogen are then used as fixed parameters in the X-ray refinement. Note that the neutron determined temperature factors for hydrogen must be first scaled with respect to the X-ray determined non-hydrogen temperature factors in order to account for the use of different machines and so forth. There are several proposed methods for the manner in which to carry out this scaling but the two recommended methods, based on tests on the standard α-oxalic acid dihydrate IUCr project (Coppens et al, 1984), are anisotropic additive corrections (Blessing, 1995). It is one of these which is used throughout this thesis. Once a suitable starting model has been obtained, X-ray refinement of the non-hydrogen temperature factors and all monopoles ensues and once stable, κ'-refinement is introduced. A different κ'-parameter is introduced for each element type and all are refined (except perhaps for the hydrogen atoms where κ' is sometimes fixed at the SDS value of 1.16). Once converged, dipolar terms for all atoms are introduced to the refinement (usually only bond directed ones are placed on the hydrogen atoms) and then quadupolar, octopolar and/or hexadecapolar terms (depending on the element type*) are

* For first-row elements, hexadecapolar terms are never used as they correspond to f-orbitals which will have an electron population tending to zero. Octopolar terms are not always necessary, though they are often used as electron population is not always insignificant. For second-row elements, octopolar terms

successively introduced in the refinement for all non-hydrogen atoms. The κ' parameters are then 'tweaked' by splitting them further into different κ' parameters for different chemical environments, e.g. different sp^x-hybridizations. Finally, κ'' is then allowed to refine in order to take into account the extent of expansion / contraction of these multipoles.

However, sometimes neutron data is not available through crystal growth problems, lack of neutron time available or other barriers. In such cases, one can just use X-ray data to refine all positions and thermal parameters, although one must concentrate much more on obtaining intense and accurate high angle data and various constraints must be applied, such as the fixing of X-H bond lengths and angles to idealized values and setting κ' to the SDS value for hydrogen. Otherwise, the procedure is essentially the same as the method hitherto discussed.

---

are essential and hexadecapolar terms are often necessary. For all other elements, all multipolar terms up to and including hexadecapolar terms must be included.

3.6 TESTING THE REFINEMENT

As the refinement proceeds, one can test the model by several means. First, the 'rigid-bond' test devised by Hirshfeld (1976) should be performed, which allows one to evaluate the degree of accuracy to which the anisotropic displacement parameters are modelled. This test is based on the assumption that all bonds will vibrate homogeneously and so mutually bonded atoms should possess anisotropic displacement parameters which are displaced along the bond by the same amount as the other atom is, on average. This theory invokes the following condition:

$$\Delta_{A,B} = z^2_{A,B} - z^2_{B,A} = 0$$

where $z^2_{A,B}$ is the mean square displacement of atom A towards atom B and vice versa for $z^2_{B,A}$. Hirshfeld's recommended tolerance of this condition is $\Delta_{A,B} \leq 0.001$Å for all atoms at least as heavy as carbon and deviations above this tolerance level indicate inadequately derived vibrational parameters. However, one should be aware that any systematic error will not cause any extra deviation on $\Delta_{A,B}$ as its effect will be uniform over all atoms and will therefore cancel itself out. For all hydrogen atoms, the rigid-bond test may be performed once one has taken into account the mass difference between hydrogen atom and the atom to which it is bonded (Eriksson & Hermansson, 1983).

Secondly, one can examine the amount of electron density which is unaccounted for by the model via contour mapping of $F_{obs} - F_{multipole}$ for all positions across the molecule in direct space. If this 'residual density map' is flat and featureless, then a well-fitted model has been obtained. On the other hand, if contours greater than about $\pm 0.6 e Å^{-3}$ exist in the map or specific atomic or bonding features are apparent, the inadequacies of the model in terms of these features must be addressed and corrected for.

Thirdly, the accuracy of the refined κ' value can be investigated by its extent of agreement with the linear relationship $\kappa' \alpha q$ as hitherto discussed.

3.7 ANALYSIS OF RESULTS

Once a satisfactory multipolar model has been obtained, it can be used in various fashions to yield useful information about the bonding and various properties of the molecule in question.

3.7.1 Bonding and polarizability of electrons

In a similar fashion to the formation of a residual density map, a contour plot which maps out ρ-ρ_{IAM} across the molecule in direct space will yield a two-dimensional representation which illustrates where the valence density is situated in relation to the atomic positions. By examining the relative concentrations and levels of the contours between bonds in this 'Electron Deformation Density (EDD) map' one can immediately ascertain, by eye, their relative strengths. Moreover, by consideration of the contour shapes one can identify the extent and sense of polarization of atoms and the direction of the charge transfer pervading through the molecule. One can also directly observe any lone pair density present and gain some insight into the relative roles that different orbitals play in the bonding, particularly if one also examines the relevant multipolar populations in conjunction with this.

One should note that an EDD is a static map, i.e. one that has had all of the thermal motion removed by Fourier deconvolution. It is opposed to a dynamic map which retains all thermal information. A static map has advantages over a dynamic one in that the lack of thermal motion in a static map means that sharp bonding features of a map will not be blurred and there should be no confusion between thermal and bonding effects. However, one must be aware that deconvolution is never always perfect because of the loss of information during the initial Fourier transformation which gives the electron density and so residual thermal effects may be retained.

3.7.2 Laplacians, critical Points and ellipticities

One can pinpoint areas of maximum and minimum bonding strength and of saddlepoints, by evaluating the stationary points of the electron density over three-dimensional space via the first order differentiation condition:

$$\nabla\rho(\mathbf{r_c}) = \mathbf{i}\delta\rho/\delta x + \mathbf{j}\delta\rho/\delta y + \mathbf{k}\delta\rho/\delta z = 0$$

where r_c is the position vector of the corresponding critical point.

Critical points exist wherever the above condition is satisfied. In order to ascertain

whether these critical points are maxima, minima or saddle points, one must calculate the *second* derivative of the electron density over three-dimensional space so that one can determine the sense of curvature. This yields nine derivatives which make up the Hessian matrix:

$$\begin{matrix} \delta^2\rho/\delta x^2 & \delta^2\rho/\delta x\delta y & \delta^2\rho/\delta x\delta z \\ \delta^2\rho/\delta y\delta x & \delta^2\rho/\delta y^2 & \delta^2\rho/\delta y\delta z \\ \delta^2\rho/\delta z\delta x & \delta^2\rho/\delta z\delta y & \delta^2\rho/\delta z^2 \end{matrix} = \begin{matrix} \lambda_{11} & \lambda_{12} & \lambda_{13} \\ \lambda_{21} & \lambda_{22} & \lambda_{23} \\ \lambda_{31} & \lambda_{32} & \lambda_{33} \end{matrix}$$

where λ_{mn} correspond to the second derivatives obtained by the combination of first-order differentials.

All off-diagonal elements of the array will sum to zero as a result of the orthogonality relationships between x, y and z, c.f. the Kronecker delta, $\delta ij = i.j = 0$. The non-zero diagonal elements (eigenvalues) are therefore the only determining parameters of the second differential. Hence,

$$\nabla^2\rho(\mathbf{r}) = \delta^2\rho/\delta x^2 + \delta^2\rho/\delta y^2 + \delta^2\rho/\delta z^2$$

where $\nabla^2\rho(r)$ is called the Laplacian and $\delta^2\rho/\delta x^2$, $\delta^2\rho/\delta y^2$ and $\delta^2\rho/\delta z^2$ correspond to the eigenvalues λ_{11}, λ_{22} and λ_{33}. By convention, λ_{11}, λ_{22} and λ_{33} are simplified to λ_1, λ_2 and λ_3.

The type of critical point is then determined by a consideration of the *senses* of these eigenvalues. All critical points are characterized by two parameters: a rank, ω and a signature, σ, which are ordered in parentheses as (ω,σ). The rank represents the number of non-zero eigenvalues at a given critical point whereas the value of the signature derives from the sum of all three senses of diagonal elements.

There are four principal types of stable critical points, all of which have a rank equal to three since critical points with any other rank do not represent a true local minimum or maximum:

(3,-3) points - these occur at *nuclear positions* as all λ values, which relate to the sense of curvature, are negative (i.e. maximum stationary values).

(3,-1) points - these represent *bond* critical points. In the two orthogonal directions perpendicular to the bond vector lie local maxima, and along the bond vector there is a local minumum which is the point of minimum overlap between the atoms. By the nature of bonding, there must always exist one of these points between any bond. However,

one should always bear in mind that bond critical points will not always lie directly along the bond vector between the two atoms, e.g. if bonds are strained.

(3, +1) points - these possess two local minima and one local maxima. These type of points usually relate to the centre of rings where the two local minima correspond to the plane of the *ring* (as all around it is a ring of greater electron density) and the local maxima is perpendicular to the ring (since on moving out of the plane, the electron density decreases).

(3, +3) points - which relate to a point of local minima in all three-dimensions. The centre of a *cage* is such an example.

Hence, critical point determination is useful in analysing exact nuclear positions, centroids of rings and cages and determining whether bent bonds and / or polarization effects are present or not.

Once can also use the *magnitudes* of these eigenvalues to yield information about the amount of π-bonding present in bonds via the equation:

$$\varepsilon = (\lambda_1 - \lambda_2)/\lambda_2$$

where λ_1 and λ_2 are the eigenvalues perpendicular to bond vector (by convention, the z-axis is perpendicular to a bond) and ε is the bond ellipticity which gives a measure of the amount of π-bonding ensuing in a bond.

Consider the following:

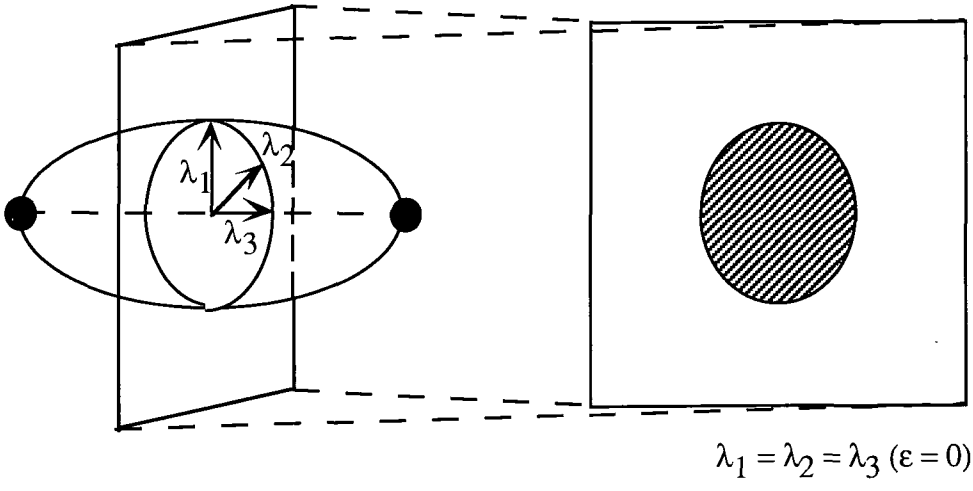

Figure 3.7.1 *- An illustration of zero ellipticity in a bond.*

If two atoms are purely σ-bonded, then the cross-section of a bond will be spherical, as depicted above. In turn, λ_1 and λ_2 will represent the radius of this sphere at orthogonal orientations and will be equal to each other. By nature of the above equation, the ellipticity, i.e. the deviation from a sphere will be $\varepsilon = 0$. However, if π-bonding is present, electron density will be present above and below the σ-bond and so λ_1 will be larger than λ_2. The stronger the π-bonding the greater the disparity between λ_1 and λ_2 and therefore the larger the value of ε.

However, one should wary of the presence of any triple-bonding character in a bond since this will increase λ_2 which will result in a deceivingly lower value of ε. Hence, where triple bonding is present, ellipticity values become too complicated to be interpretable. Moreover, ellipticity values will be rendered invalid where ionic tendencies prevail, for example, in a hydrogen-bond where there is no π-bonding present.

A topological analysis of the Laplacian itself can also yield some very useful information. Laplacian values illustrate the extent of the curvature of the electron density at a point, **r**. The greater the curvature, the larger the value of $\nabla^2(\mathbf{r})$. Moreover, $\nabla^2(\mathbf{r})$ values may be positive or negative. The value is positive where there exists a local depletion of charge and negative where there is a local excess. This feature thus provides the Laplacian with a distinct advantage over the electron density itself because the former can distinguish between charge due to atomic sites (local depletion and hence positive values resulting) and charge due to bonding between atoms (local charge excess and hence negative values resulting) whereas there is no such distinction possible for electron density data.

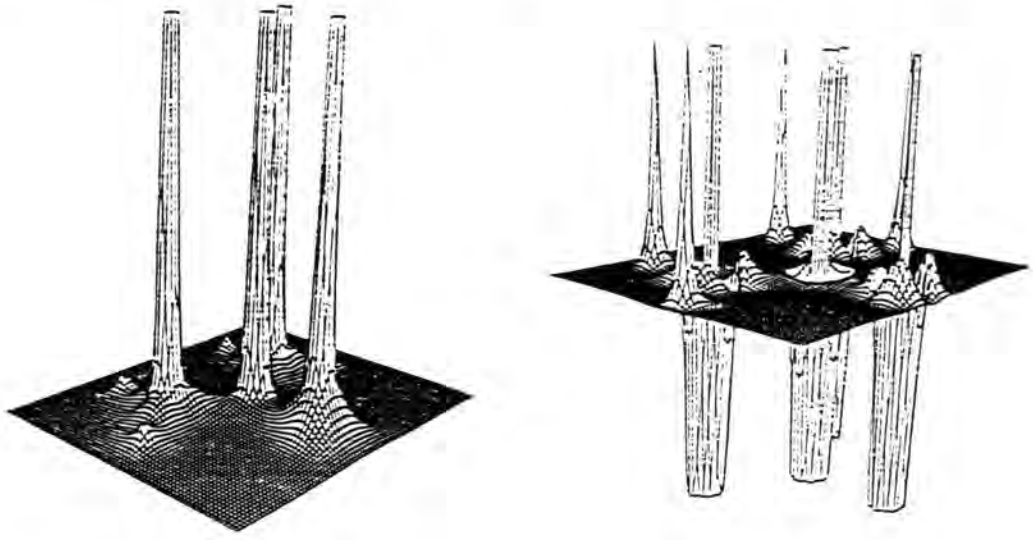

a **b**

Figure 3.7.2 *- Topological views of the (a) total electron density and (b) negative Laplacian of the urea molecule (Craven & Stewart, 1990).*

Moreover, one can analyse the charge depletion / excess areas within a molecule such that one can obtain an indication of the acidic nature of the molecule. For example, if there are large regions of local charge depletion in the valence shell charge contribution of central atoms in a particular molecule, then the molecule is a strong Lewis acid, as these depleted regions serve as good reactive sites for nucleophiles (and vice versa for strong Lewis bases/ideal electrophilic behaviour). However, when studying nucleophilic/electrophilic behaviour in this way, one must remember not to ignore other effects such as sterics (e.g. if a Bu^t ligand is present) and the stability of the molecule.

Laplacians can also be useful in determining the nature of ligands in various systems, especially in organometallics, where there is, in general, transfer to vicinal ligands. Chromium hexacarbonyl, $Cr(CO)_6$, is a good example of this (Rees & Mitschler, 1976) as the CO ligand is a particularly electron-withdrawing ligand.

Laplacians can also be used to determine the structure stability of a molecule which is useful because it gives information about the mechanics of a system, especially with respect to potential and kinetic energy densities (Bader & Essén, 1984).

In order to assign electron density / populations to specific atoms, one must find a way of separating the continuous electron density into packages belonging to each atom. One can either impose a rigid partitioning model whereby an atoms's electron density is surrounded by a distinct fixed border between other atoms (discrete boundary partitioning) or one can make an allowance for 'shared' electron density overlapping between atoms around the boundary between atoms (fuzzy boundary partitioning). Several of each type of partitioning methods exist. The two most common discrete partitioning methods are van der Waals ratio partitioning and partitioning based on surface zero flux. The former method considers each point in space, i, locates all nearest atoms within a given range from i and then, taking two atoms at a time, A and B, the ratios of the van der Waal's radii with respect to i are determined:

$$[(r_i - r_A).r_{AB}]/R_A \qquad \text{and} \qquad [(r_i - r_B).r_{BA}]/R_B$$

The point, i, is assigned to the smallest of the two ratios and the method repeats with the atom possessing the smallest ratio and the next atom in the range, until all atoms within the range have been compared. The atom which retains the lowest ratio is deemed to possess all electron density at the point, i. In the latter discrete boundary partitioning method, bond critical paths make up the boundaries between atoms as these represent paths of minimum bonding density between atoms.

The most common fuzzy boundary space partitioning method was proposed by Hirshfeld

and is called the stockholder's concept (Hirshfeld, 1977). It is based on the idea that at a point, r, the contribution of electron density, $w_i(r)$, to a given atom of density, $\rho^{at}(r)$, out of the total electron density at this point, $\rho_{total}(r)$ will be in proportion to the 'investment' of the given atom's promolecule density, $\rho_{spherical}(r)$,

$$\text{i.e. } w_i(r) = \rho_i^{at}(r) / \rho_{total}(r)$$

where $w_i(r) = \rho_{spherical,\,i}(r) / [\text{sum of } (j=1 \text{ - atom}) \rho_{spherical,\,j}(r)$

3.7.3 Multipolar moments, molecular dipoles and (hyper)polarizabilities

Whilst charge density methods will never override the more standard techniques used for calculating the dipole and quadrupolar moments of a molecule, it sould be remembered that charge density analyses provide tensorial values of the multipolar moments whereas most standard techniques provide just one overall value of the moment concerned. Moreover, charge density analyses are derived from solid state results whereas all other techniques are based on liquid or gaseous phases. Thus, one can compare values of the moments from both multipolar and standard techniques in order to provide information on intermolecular and / or solvent effects.

The values obtained from charge density analyses will very strongly depend on the method of space partitioning used. All such calculations reported in this thesis use the pseudoatom model. Hence, only this method is given. For a more comprehensive review on molecular electrostatic moments from X-ray diffraction, one is referred to Spackman, 1992.

The nth moment is given by the integral:

$$\text{nth moment},a_1,a_2,a_3,\ldots,a_{n-1} = \int \rho_j^{total}(\mathbf{r}) r_{a1},r_{a2},r_{a3},\ldots r_{a1}\, \mathbf{dr}$$

Hence, the dipolar (p_a), quadupolar (Θ_{ab}) and octopolar (Ω_{abc}) tensorial moments are given by the following equations, where a, b and c denote any combination of cartesian coordinates, x, y and z:

$$p_a = \sum_{j=1}^{n} a_j(Z_j - P_c - P_v) + q_{ja}$$

$$\Theta_{ab} = \sum_{j=1}^{n} a_j b_j(Z_j - P_c - P_v) + b_j p_{ja} + a_j p_{jb} + q_{jab}$$

$$\Omega_{abc} = \sum_{j=1}^{n} a_j b_j c_j (Z_j - P_c - P_v) + a_j b_j p_{jc} + a_j c_j p_{jb} + b_j c_j p_{ja} + a_j Q_{jbc} + b_j Q_{jac} + c_j Q_{jab} + q_{jabc}$$

where Z_j = atomic charge of atom, j,
P_c = core population of atom, j,
P_v = valence population of atom, j,
q_j = the relevant moment's contribution to the charge distribution.

Obviously, one can obtain each total moment by summing the various tensorial contributions.

For each multipolar moment, q_j must be derived from the integral of the Slater-type radial function (assuming these are used to describe the multipoles in the refinement) multiplied by the relevant associated Legendre function and the population coefficient.

For the dipolar term,

$$q_{ja} = 4P_{jlm} (n_l + 3)! / 3\kappa'_j\xi(n_l + 2)!$$

For the quadrupolar term,

$$q_{jab} = -3\pi P_{jlm}(n_l + 3)(n_l + 2) / 15(\kappa'_j\xi)^2$$

To date, we have been unsuccessful in deriving the corresponding octopolar term. This is unfortunate since it is this charge distribution term which relates to the first hyperpolarizability coefficient, β_{ijk}, as we saw in chapter 1. However, the above calculations at least allow us to calculate the linear polarizability tensorial coefficients since these are related to the quadrupolar terms by the equations (Hamzaoui, 1995):

$$|\alpha_{ii}| = 16\pi^2 m |Q_{ii}|^2 / h^2$$

$$\alpha_{ij} = 8\pi^2 m Q_{ij} [Q_{ii} + Q_{jj} + 2Q_{ij}] / h^2$$

where α_{ij} = the linear polarizability,
m = the mass of an electron,
h = Planck's constant,

Of course, each moment (and therefore all tensors derived from them) is origin dependent and so we must specify an origin. By convention, we take the centre of mass to be the

origin. Such a convention was considered most apt since other methods which are used to derive such moments usually relate to the molecular centre of mass in some manner (Stogryn & Stogryn, 1966).

3.7.4 The electrostatic potential and its derivatives

Electrostatic forces are relatively long range and therefore often play an important role in intermolecular effects and in determining the best points of nucleophilic / electrophilic attack in a reaction.

One can evaluate the electrostatic potential and its derivatives (electric field and electric field gradient) by using the multipolar formalism either in direct or reciprocal space. In direct space, the calculations are based on the point charge model and values at a point, p, are obtained directly from the multipolar population coefficients:

$$\Phi(R_p) = \sum_{m \neq p} [Z_m / |R_{mp}|] - \sum_m \int [\rho_{lm}(\mathbf{r}_m)/|r_p|]dr_m$$

$$E(R_p) = \sum_{m \neq p} [Z_m R_{mp}/|R_{mp}|^3] - \sum_m \int [r_p \rho_{lm}(r_m)/|r_p|^3]dr_m$$

$$\nabla E_{\alpha\beta}(R_p) = - \sum_{m \neq p} [Z_m(3R_\alpha R_\beta - \delta_{\alpha\beta}|R_{mp}|^2) / |R_{mp}|^5] + \sum_m \int [\rho_{lm}(r_m)(3r_\alpha r_\beta -$$

$$\delta_{\alpha\beta}|r_p|^2 / |r_p|^5]dr_m$$

By nature of the method, the potential and its derivatives are determined as if the molecule has been 'lifted' from the crystal. Therefore, this method focuses on the electrostatic quantities of the periphery of the molecule, i.e. the region of interest for intermolecular interactions.

In reciprocal space, the electrostatic potential and its derivatives are determined by Fourier summation of the structure factors in a similar fashion to that described for the discrete partitioning method of multipolar moment determination. The relevant equations are:

$$\Phi(r) = (1/\pi V) \sum F(\mathbf{H})/H^2 \exp(-2\pi i \mathbf{H}.r)$$

$$E(r) = (-2\pi i/V) (\sum F(\mathbf{H})/H^2)\mathbf{H}\exp(-2\pi i \mathbf{H}.r)$$

$$(\nabla:E)(r) = 4\pi \sum H:HF(\mathbf{H}) / H^2 \exp (-2\pi i \mathbf{H}.r)$$

Note that as the order of the derivative of the potential increases, the summation in reciprocal space becomes increasingly dependent on higher order structure factors. Hence, the accuracy of the higher order derivatives of the potential may be hampered by Fourier series termination effects. It is therefore usually better to use ΔF in the summations (assuming that the predominant potential comes from the valence electronic contribution as core electron density should be sufficiently shielded by the valence electrons to invoke a negligible effect). The equation for the potential then becomes:

$$\Phi(r) = \Phi_{\text{promolecule crystal}}(r) - \langle \Phi_{\text{promolecule crystal}}(r) \rangle + \Delta\Phi(r)$$

where $\Delta\Phi(r) = (-1/\pi V) \sum_{H \neq 0} \Delta F(H) / H^2 \exp(-2\pi i \mathbf{H}.r)$

and similar for the electric field and electric field gradient.

One can also improve accuracy by using a shorter wavelength of radiation (hence, $\sin\theta/\lambda_{max}$ = higher) and a lower temperature (more intensity to higher angle).

Note that whilst the calculations of the multipolar moments tend to parallel those to determine the electrostatic potential and its derivatives, there is one important difference in that while atomic moments are local, the electrostatic properties depend on both the local and peripheral electron distribution of the *whole* molecule.

3.8 'MULTIPOLAR' PROGRAMS

Over the years, various programs have been written for kappa and multipolar refinements. Such programs include VALRAY (Stewart, 1976; Stewart & Spackman, 1976), MOLLY (Hansen & Coppens, 1978) and POP (Craven, Weber & He, 1987; Epstein, Ruble & Craven, 1982). Each of these programs have their particular advantages and limitations and so, depending on the molecule and the type of data collected, a different program may have to be chosen each time. As a result, in the early 1990s, a multi-national project was established in order to produce one program which would combine all advantages of the separate programs and iron out all limitations. This resulted in the birth of the program, XD (Koritsanszky et al, 1994) and is the program which is used throughout this thesis.

XD (Koritsanszky et al, 1994) was written in a very modular manner in the sense that each part is independent of another such that one can use as comprehensive a model as one wishes and then the results can be viewed by a separate graphical interface.

It contains a least-squares refinement program and includes possible IAM and / or κ' and / or κ'' and / or multipolar refinement. The multipolar formalism is taken from the Hansen and Coppens model (1978). The radial functions of the valence deformation density are of single Slater-type and the parameters for these functions, n(l) and ξ(l) are obtained from the single-zeta wavefunctions (Clementi & Raimondi, (1963). Scattering factors were calculated from the ground state Slater-type orbital HF atomic wavefunctions of Clementi and Roetti (1974).

The program also allows one to correct for isotropic extinction and anomalous dispersion and a weighting parameter may also be assigned to the refinement. However, for an accurately determined data set, one should not need these options.

Either harmonic or anharmonic anisotropic displacement parameters can be refined, although in all cases in this thesis we restricted our refinements to the harmonic model. All atoms are related to each other by a local co-ordinate system and where necessary dummy atoms may be included. XD (Koritsanszky et al, 1994) also incorporates Hirshfeld's rigid bond test (Hirshfeld, 1976) which can be determined after carrying out each batch of cycles of least squares refinement.

The analysis features of XD (Koritsanszky et al, 1994) include maps of core density, valence density, total density, deformation density ($\Delta\rho$), Laplacian density ($\nabla^2\rho$), electrostatic potential, V(r), using either a crude approximation or using the method of Su and Coppens (1992), nuclear potential and errors in ρ and $\nabla^2\rho$. Residual density maps

may also be calculated by Fourier calculations and dipolar and quadrupolar moments, based on a pseudoatom model, critical points and ellipticities can be determined by use of particular modules in the program.

3.9 THE CHOICE OF COMPOUND TO STUDY

As extensive time, resources and effort are employed in a charge density study, one must very carefully consider which type of compound should be best suited for it. If one had a completely free choice of a substance to study, the compound would:

- form crystals of a good quality and size.
- have a small unit cell.
- contain as few atoms as possible.
- contain no heavy atoms.
- be air stable.
- be centrosymmetric.
- crystallize in a high symmetry crystal system.
- not possess any libration or disorder of any type.

However, one must remember that our scientific interest in compounds for charge density analysis, radically confines our choice to a small range of compounds. We therefore have to attempt to find a material in this limited range which will satisfy as many of the above criteria as possible. Obviously, in the case of NLO materials, the centrosymmetric criteria cannot be formally met. However, as we saw in chapter 1, one can avoid the non-centrosymmetric constraint if one studies compounds which are formally centrosymmetric but which can be poled to effect the non-centrosymmetric requirement. In this thesis, the charge density study of one such compound is reported. Non-centrosymmetric compounds are the subject of the two other charge density studies reported.

3.10 REFERENCES

Bader, R. F. W. & Essén, H. (1984). J. Chem. Phys., **80**, 1943-1960.

Blessing, R. H. (1995). Acta Crystallogr., **B51**, 816-823.

Brown, A. S. & Spackman, M. A. (1991). Acta Crystallogr., **A47**, 21-29.

Clementi, E. & Raimondi, D. L. (1963). J. Chem. Phys., **63**, 2686-2689.

Coppens, P., Dam, J., Harkema, S., Feil, D., Feld, R., Lehmann, M. S., Goddard, R., Krüger, C., Helner, E., Johansen, H., Larsen, F. K., Koetzle, T. F., McMullan, R. K., Maslen, E. N. & Stevens, E. D. (1984). Acta Crystallogr., **A40**, 184-195.

Coppens, P. & Hall, M. B. (Eds) (1982). *'Electron Distributions and the Chemical Bond'*, Plenum Press, New York, p. 63.

Coppens, P. (1995). *'Chemical Bonding and the X-ray Scattering Formalism'* in course notes from *'The International School and Workshop in Charge Density Analysis'* (La Plata, Argentina).

Craven, B. M. & Stewart, R. F. (1990). Trans. Am. Cryst. Assoc., **26**, 47.

Craven, B. M., Weber, H. P. & He, X. (1987). Tech. Report TR-87-2, Department of Crystallography, University of Pittsburgh, PA 15260.

Epstein, J., Ruble, J. R. & Craven, B. M. (1982). Acta Crystallogr., **B38**, 140-149.

Eriksson, A. & Hermansson, K. (1983). Acta Crystallogr., **B39**, 703-711.

Hamzaoui, F. (1995). PhD Thesis, Universite des Sciences et Technologies de Lille, France.

Hansen, N. K. & Coppens, P. (1978). Acta Crystallogr., **A34**, 909-921.

Hirshfeld, F. L. (1971). Acta Crystallogr., **B27**, 769-781.

Hirshfeld, F. L., (1976). Acta Crystallogr., **A32**, 239-244.

Hirshfeld, F. L. (1977). Theoret. Chim. Acta, **44**, 129.

Koritsanszky, T., Howard, S., Richter, T., Mallinson, P., Su, Z. & Hansen, N. (1994). XD. *A Computer Program Package for Multipole Refinement and Analysis of Charge Densities from Diffraction Data.* Berlin, Cardiff, Glasgow, Buffalo, Nancy.

Kurki-Suonio, K. (1977). Isr. J. Chem., **16**, 132-136.

Mallinson, P. R. (1995). *'Multipole Analysis of Experimental Charge Densities'*, in course notes from *'The International School and Workshop in Charge Density Analysis'* (La Plata, Argentina), p. 9.

Rees, B. & Mitschler, A. (1976). J. Am. Chem. Soc., **98**, 7918.

Slater, J. C. (1930). Phys. Rev., **36**, 57.

Spackman, M. A. (1992). Chem Rev., **92**, 1769.

Stewart, R. F. (1976). Acta Crystallogr., **A32**, 565-574.

Stewart, R. F. (1977). Isr. J. Chem., **16**, 124.

Stewart, R. F. (1980) in 'Electron and Magnetization Densities of Molecules and Solids', Ed. Becker, P., Plenum Press, New York, pp. 439-441.

Stewart, R. F., Davidson, E. R. & Simpson, W. T. (1965). J. Chem. Phys., **42**, 3175-3187.

Stewart, R. F. & Spackman, M. A. (1976). VALRAY System, Department of Chemistry, Carnegie-Mellon University, Pittsburgh, PA 15213.

Stogryn, D. E. & Stogryn, A. P. (1966). Mol. Phys., **11**, 371-393.

Su, Z. W. & Coppens, P. (1992). Acta Crystallogr., **A48**, 188.

CHAPTER 4

BOND LENGTH ALTERNATION AND CHARGE DENSITY STUDIES OF A SERIES OF TETRACYANOQUINODIMETHANE DERIVATIVES

4.1 INTRODUCTION

Several tetracyanoquinodimethane (TCNQ) derivatives (Cole, Howard, Cross & Szablewski, 1995) have shown great promise in terms of NLO potential, as a result of their molecular planarity, high extent of conjugation and large dipolar moments. The high dipolar moments result from the tendency of such compounds to fluctuate between a formally quinoidal state and a zwitterionic one in the manner shown in ***Figure 4.1.1***:

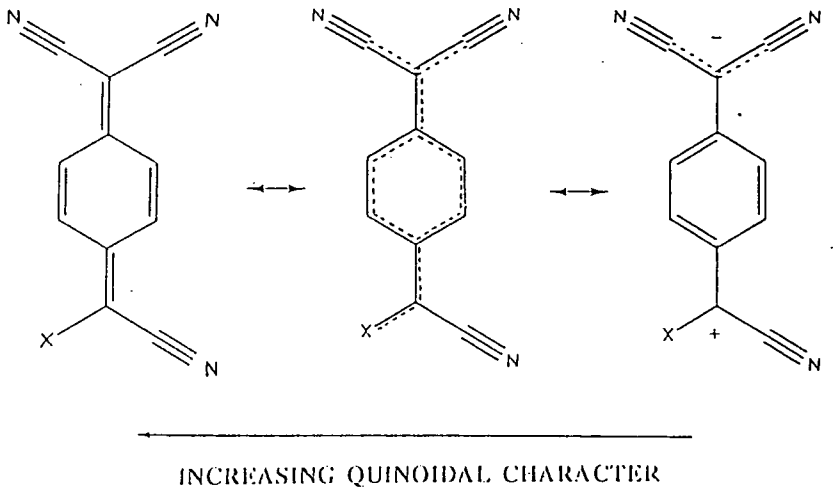

Figure 4.1.1 *- TCNQ derivatives undergoing interconversion between quinoidal and zwitterionic states.*

However, high dipole moments often inherently cause molecules to align with each other in an opposing head-to-tail fashion in the solid state such that the moments cancel and the compound packs in a centrosymmetric manner. As discussed in chapter 1, the presence of centrosymmetry precludes any compound from being NLO active. This former constraint is avoided in these predominantly centrosymmetric compounds by electrically poling them into a thin polymer film (polymethylmethacrylate, PMMA) such that they align closely in a head-to-tail fashion (i.e. become effectively non-centrosymmetric) and therefore exhibit a positive NLO response via EFISH measurements (see chapter 1). The electrically poled alignment has a typical lifetime of 18-36 hours.

Therefore, in terms of assessing the structure / property relationships in these materials, the nature of their solid state packing is unimportant since the NLO active state concerns only the molecular geometry.

The molecular geometry of these materials was studied using conventional laboratory source X-ray diffraction techniques in order to obtain structures of all seven compounds and use them to study the extent of bond length alternation (BLA) in these compounds and so help to optimize the molecular hyperpolarizability, β. X-ray structures of compounds **I**, **II**, **VI** and **VII**, as shown in ***Figure 4.1.2***, were solved by the author whilst X-ray structures of compounds **III**-**V** (also shown in ***Figure 4.1.2***) were determined by Jason C. Cole, from the same laboratory. All compounds were synthesized by Dr. Marek Szablewski and co-workers.

A second molecular geometry study was made, which used a combination of X-ray and neutron techniques in order to perform a charge density study on compound **I**. The aim of the study was to (a) gain some insight into the exact nature of electronic polarization in the compound and (b) to try to measure the solid state dipole moment and linear polarizability coefficients of the compound. Compound **I** was selected for this study simply because of the greater success we had had in growing neutron-sized crystals of this compound compared to the others. An analogous study on compound **III** was also attempted since crystallization experiments produced the next best results. However, despite several attempts at obtaining a neutron structure of **III**, measuring different batches of crystals, at different temperatures and at different neutron sources, no useful results prevailed. For reference, the attempts are reported but due the lack of success with the neutron measurements, the study on compound **III** was concluded at this point.

4.2 BOND LENGTH ALTERNATION ANALYSIS OF COMPOUNDS I-VII

From the discussion in chapter 1, section 1.4.1.1, we saw that there is a relationship between the molecular hyperpolarizability, β, and the bond length alternation (BLA) such that where the BLA ~ 0, β is at a maximum. Therefore, for these TCNQ derivatives, the completely delocalized valence model, as depicted in the centre of ***Figure 4.1.1*** and which corresponds to a 50:50 zwitterionic:quinoidal ratio, will give the most optimal value of β.

In view of this, for the seven compounds structurally characterized by X-ray diffraction, the percentage of quinoidal character relative to the zwitterionic form was determined from calculations based on the experimental bond length parameters. Results from solvatochromatism experiments performed by the Physics Department at the University of Durham were used to confirm the prevailing trends.

4.2.1 Experimental

4.2.1.1 Synthesis

Compounds **I** and **II** were prepared by the reaction of TCNQ with 4-methylpiperidine and N,N-diethylamine respectively in THF, by methods analogous to those described by Hertler, Hartzler, Acker & Benson (1962). Compounds **III**, **V**, **VI** and **VII** were prepared by the action of tertiary amines on TCNQ (Szablewski, 1994) while **IV** was the unexpected result of the reaction of TCNQ with 1-pyrrolidino-1-cyclopentene in 1,4-dioxane.

4.2.1.2 X-ray Crystallography

Data for **I-II** and **III-VI** were collected using a Siemens P4 and Rigaku AFC6S four-circle diffractometer respectively. Data for compound **VII** was collected using a Siemens SMART-CCD diffractometer. Mo Kα X-radiation was used for all experiments except that for compound **VI**. In this case, Cu Kα X-radiation was used since the crystal diffracted weakly. All experiments were performed at 150K and employed the standard instrumental and experimental procedures as described in chapter 2.

All structures were solved by direct methods using SHELXS-86 (Sheldrick, 1990) and refined by full-matrix least-squares methods on F^2 using SHELXL-93 (Sheldrick, 1993). Atomic scattering factors were taken from International Tables for Crystallography, Volume C, Mathematical, Physical and Chemical Tables (1992).

All data were corrected for Lorentz and polarization effects. An isotropic extinction correction was applied to the data for compounds **V** and **VI** [extinction parameter, EXTI = 0.026(4) and 0.0028(3) respectively] and an absorption correction (using integrated ψ-scans) was applied to compound **VII**.

Positional and anisotropic atomic displacement parameters were refined for all non-hydrogen atoms, except for carbon atoms C(13)-C(14) in structure **IV** and C(19)-C(22) in structure **VII** (see below). Positional parameters for all hydrogen atoms in structures **I, II, III** and **V** were freely refined. For compounds **IV** and **VI**, the hydrogen positional parameters were calculated such that the C-H distances were fixed to 0.96Å. Idealized geometry was employed for all hydrogen positional parameters in structures **VII** except for the hydrogen atoms ligated to carbon atoms C(20) and C(22), which were located in the difference map but not refined. Isotropic atomic displacement parameters were refined for all hydrogen atoms in structures **I, III** and **V**. In compounds **II, IV** and **VI**, all hydrogen thermal parameters were fixed at $1.2U_{eq}(C)$ as were the thermal parameters of all hydrogen atoms in structure **VII** except for those corresponding to terminal hydrogen atoms. These thermal parameters were fixed at $1.5U_{eq}(C)$.

In compound **IV**, part of the cyclopentyl ring, C(13)-C(14), is disordered in a 3:1 ratio and so the corresponding thermal parameters are only refined isotropically. In compound **VII**, disorder is present (in an 11:9 ratio) in the two terminal ethyl groups. As a result, the thermal parameters of the carbon atoms C(19)-C(22) were fixed at $0.08Å^2$. Dichloromethane solvent is also present in the lattice of **VII** in a molecule:solvent ratio of 1:1.

A summary of all crystal, data collection and refinement parameters is given in ***Table 4.2.1***. Bond lengths and angles are given for all seven compounds in ***Tables 4.2.2*** and ***4.2.3*** respectively and a 50% probability thermal ellipsoid plot of each compound is shown in ***Figure 4.2.1.*** Fractional co-ordinates and thermal displacement parameters for all seven compounds are given in ***Appendix A.4.1-A.4.14***.

Compound	I	II	III	IV	V	VI	VII
Molecular Formula	$C_{18}H_{24}N_4$	$C_{17}H_{16}N_4$	$C_{17}H_{16}N_4$	$C_{15}H_{12}N_4$	$C_{18}H_{15}N_5$	$C_{25}H_{28}N_4$	$C_{22.5}H_{25}ClN_4O_2$
Formula weight	296.41	276.34	276.34	248.29	301.35	384.51	418.92
a(Å)	11.262(2)	6.970(1)	7.221(2)	6.837(1)	7.615(4)	6.620(1)	44.424(1)
b(Å)	12.867(3)	14.233(3)	7.262(1)	25.080(5)	7.962(4)	22.050(4)	7.5523(2)
c(Å)	12.510(3)	7.633(2)	14.670(2)	7.386(1)	14.740(4)	14.845(3)	13.3590(1)
α(deg)	90.00	90.00	76.97(1)	90.00	91.45(4)	90.00	90.00
β(deg)	112.11(3)	107.91(3)	82.28(1)	92.70(3)	96.93(4)	99.36(3)	106.386(1)
γ(deg)	90.00	90.00	79.40(1)	90.00	118.03(4)	90.00	90.00
Cell Volume(Å^3)	1679.5(6)	720.5(3)	733.2(2)	1265.1(4)	779.7(6)	2138.1(7)	4299.9(2)
Crystal System	monoclinic	monoclinic	triclinic	monoclinic	triclinic	monoclinic	monoclinic
Space Group	$P2_1/c$	Pn	P-1	$P2_1/n$	P-1	$P2_1/n$	C2/c
Z	4	2	2	4	2	4	8
Calculated Density (gcm^{-1})	1.17	1.27	1.25	1.30	1.28	1.195	1.294
Absorption Coefficient (mm^{-1})	0.072	0.079	0.077	0.082	0.081	0.553	0.204
Crystal Morphology	Block	Needle	Needle	Plate	Plate	Needle	Plate
Crystal Colour	Brown	Purple	Emerald green	Dark purple	Metallic green	Emerald green	Turquoise
Crystal Size (mm)	0.3 x 0.2 x 0.2	0.6 x 0.4 x 0.1	0.5 x 0.2 x 0.1	0.3 x 0.2 x 0.05	0.5 x 0.5 x 0.2	0.55 x 0.1 x 0.08	0.3 x 0.3 x 0.03
2θ range (°)	2.37-25.00	2.86-27.41	2.86-25.89	2.88-25.03	2.80-27.50	3.62-74.80	2.74-23.24
Total number of reflections	3758	1654	2816	2233	3847	4118	7187
Unique reflections	2949	1526	2592	2057	3590	3798	2894
Observed Reflections [I>2σ(I)]	1550	1331	1712	542	2641	2143	1409
R_{int}	0.0370	0.0252	0.0301	0.0945	0.0090	0.0350	0.1554
Data / Parameters	2949/295	1525/238	2591/255	2056/173	3589/269	3790/263	2890/250
R1 [I > 2σ(I)]	0.0374	0.0352	0.0417	0.0586	0.0381	0.0473	0.0945
wR2 [I > 2σ(I)]	0.0607	0.0788	0.0729	0.1137	0.1009	0.1114	0.2225
Goodness of fit on F^2	0.764	1.037	1.280	0.920	1.034	1.010	1.090
Weighting Scheme Parameters Used	a=0.025 b=0.00	a=0.05 b=0.015	a=0.00 b=0.02	a=0.046 b=0.00	a=0.055 b=0.00	a=0.048 b=2.412	a=0.122 b=10.73
$\Delta\rho_{(max, min)}$ (eÅ^3)	0.129/-0.208	0.148/-0.159	0.202/-0.160	0.232/-0.216	0.280/-0.183	0.269/-0.280	0.369/-0.398

Table 4.2.1 *- A summary of crystal, data collection and refinement parameters for compounds* ***I-VII****.*

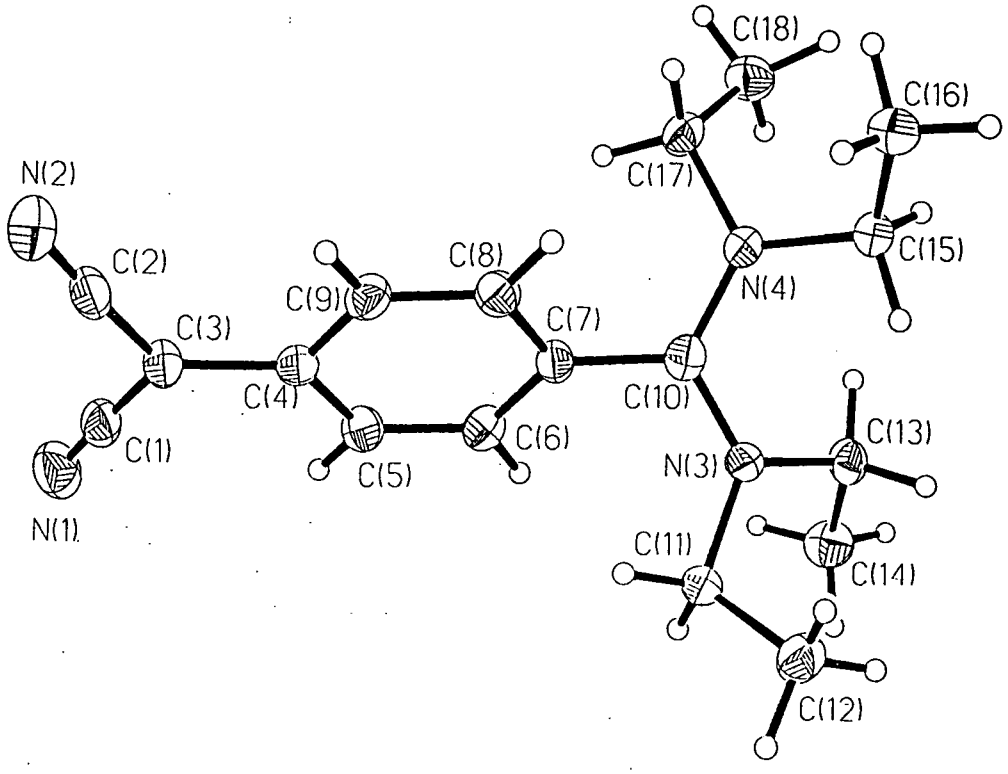
C(18)
C(16)
C(17)
N(2)
C(2)
C(8)
C(15)
C(9)
N(4)
C(3)
C(7)
C(4)
C(10)
C(1)
C(6)
C(13)
C(5)
N(3)
N(1)
C(11)
C(14)
C(12)

(a)

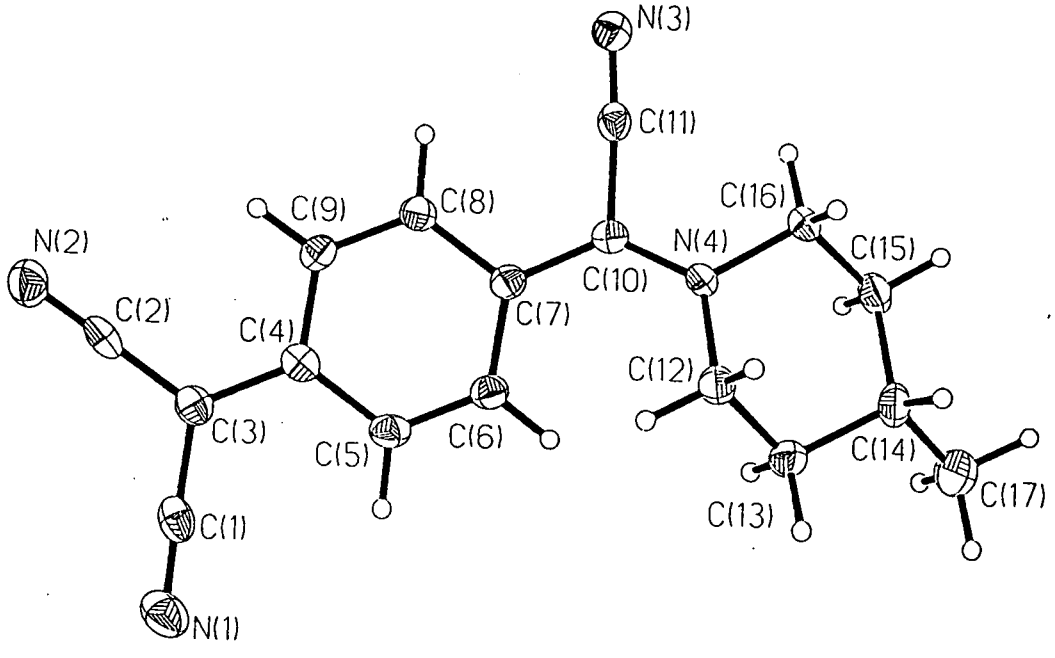
N(3)
C(11)
C(9)
C(8)
C(16)
N(2)
N(4)
C(15)
C(10)
C(2)
C(7)
C(4)
C(12)
C(3)
C(5)
C(6)
C(14)
C(1)
C(13)
C(17)
N(1)

(b)

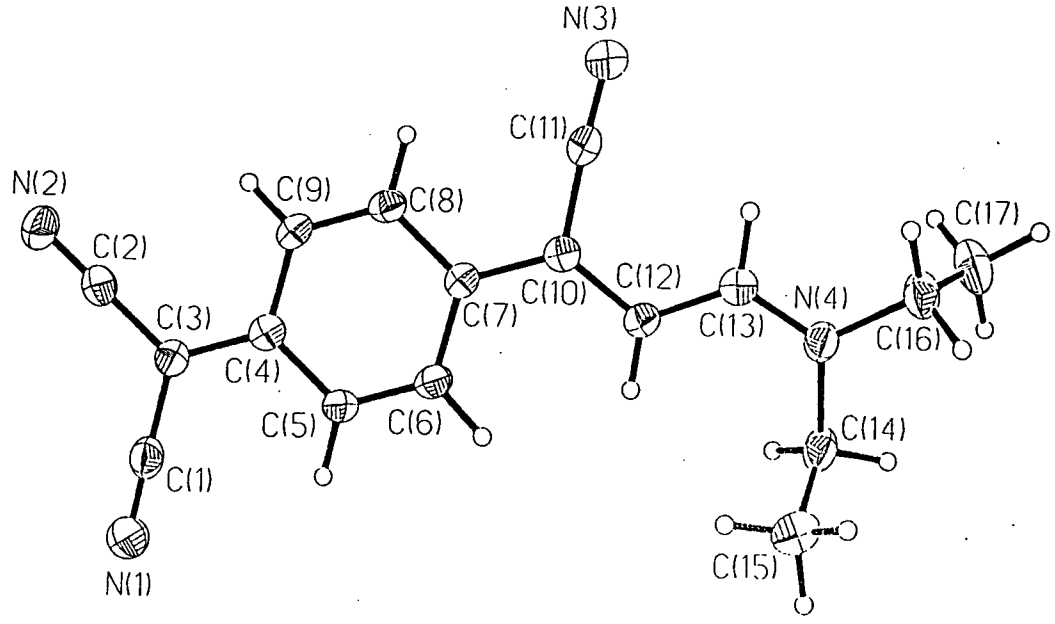
N(3)
C(11)
N(2)
C(9)
C(8)
C(17)
C(2)
C(10)
C(12)
C(7)
N(4)
C(3)
C(13)
C(16)
C(4)
C(5)
C(6)
C(14)
C(1)
C(15)
N(1)

(c)

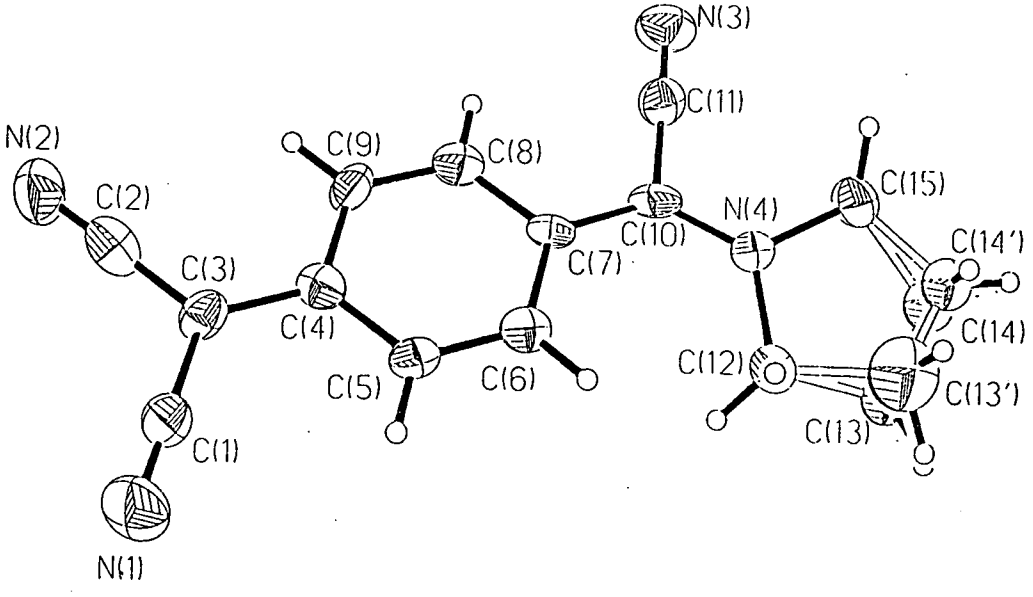
N(3)
C(11)
N(2)
C(9)
C(8)
C(15)
C(2)
C(10)
N(4)
C(14')
C(7)
C(3)
C(4)
C(14)
C(12)
C(5)
C(6)
C(13')
C(1)
C(13)
N(1)

(d)

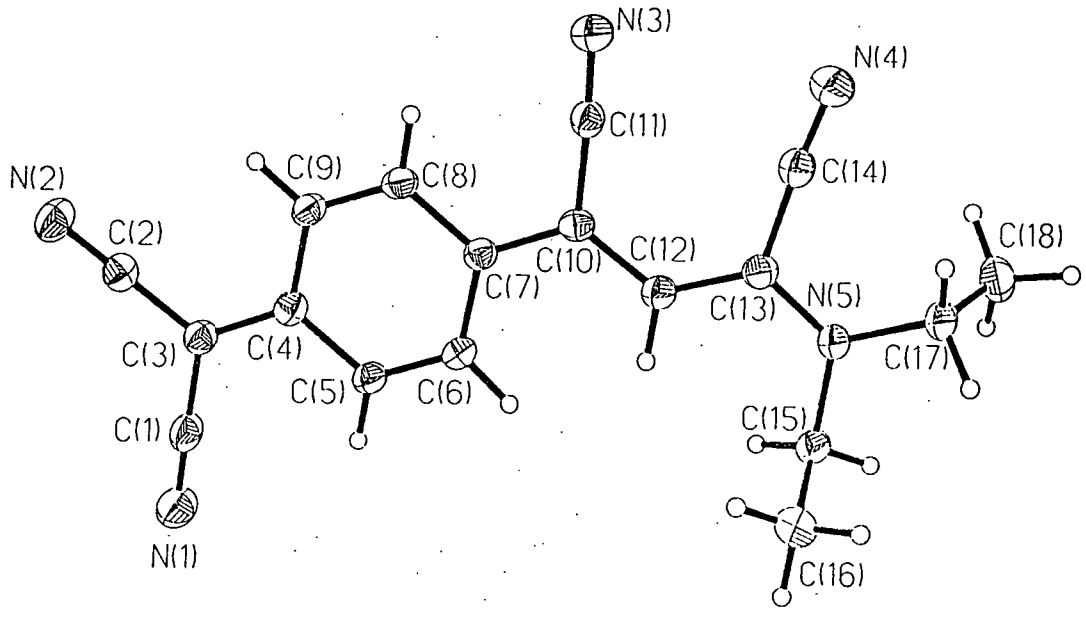
N(3)
N(4)
C(11)
C(14)
C(9)
C(8)
N(2)
C(2)
C(10)
C(12)
C(18)
C(7)
C(13)
N(5)
C(3)
C(4)
C(17)
C(5)
C(6)
C(1)
C(15)
N(1)
C(16)

(e)

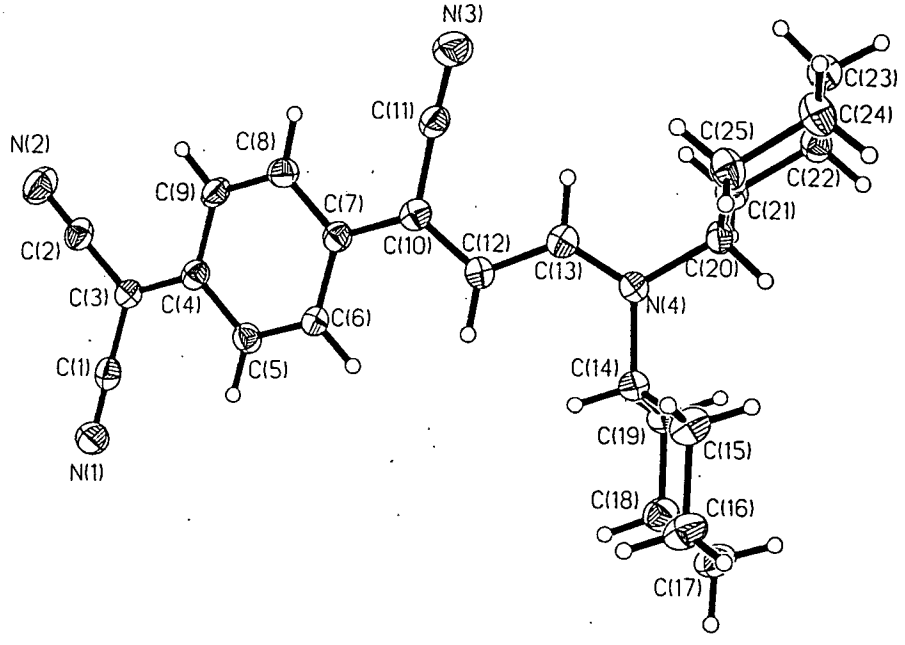
N(3)
C(11)
C(23)
C(24)
C(25)
N(2)
C(8)
C(22)
C(9)
C(7)
C(21)
C(2)
C(10)
C(12)
C(13)
C(20)
C(3)
C(4)
N(4)
C(6)
C(1)
C(5)
C(14)
C(19)
C(15)
N(1)
C(18)
C(16)
C(17)

(f)

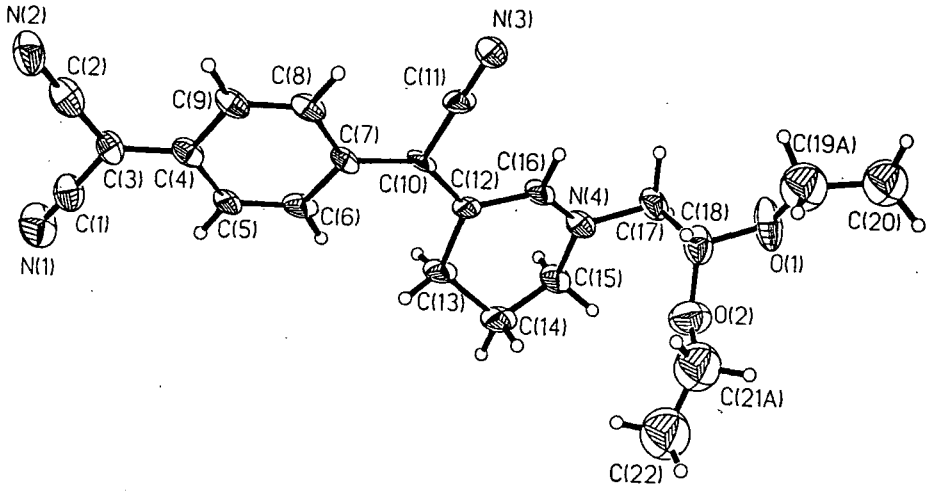

(g)

Figure 4.2.1 *- 50% probability thermal ellipsoid plots of (a)* ***I****, (b)* ***II****, (c)* ***III****, (d)* ***IV****, (e)* ***V****, (f)* ***VI*** *and (g)* ***VII****.*

Table 4.2.2 *- Bond lengths (Å) for all seven compounds (excluding those bonds involving hydrogens).*

BOND	BOND LENGTHS (Å)						
	I	**II**	**III**	**IV**	**V**	**VI**	**VII**
O(1)-C(18)	---	---	---	---	---	---	1.406(9)
O(1)-C(19A)	---	---	---	---	---	---	1.34(2)
O(1)-C(19B)	---	---	---	---	---	---	1.39(2)
N(1)-C(1)	1.159(3)	1.153(5)	1.155(3)	1.146(8)	1.152(2)	1.165(4)	1.137(8)
N(2)-C(2)	1.162(3)	1.154(4)	1.157(2)	1.159(9)	1.148(2)	1.153(4)	1.15(1)
N(3)-C(10)	1.339(2)	---	---	---	---	---	---
N(3)-C(11)	1.487(2)	1.145(4)	1.150(2)	1.153(8)	1.148(2)	1.149(4)	1.149(7)
N(3)-C(13)	1.486(2)	---	---	---	---	---	---
N(4)-C(10)	1.343(2)	1.321(4)	---	1.333(9)	---	---	---
N(4)-C(12)	---	1.479(4)	---	1.474(7)	---	---	---
N(4)-C(13)	---	---	1.316(2)	---	---	---	---
N(4)-C(14)	---	---	1.478(2)	---	1.150(2)	1.491(4)	---
N(4)-C(15)	1.483(2)	---	---	1.491(7)	---	---	1.489(6)
N(4)-C(16)	---	1.479(4)	1.476(3)	---	---	---	1.296(8)
N(4)-C(17)	1.484(2)	---	---	---	---	---	1.479(9)
N(4)-C(20)	---	---	---	---	---	1.497(4)	---
N(5)-C(13)	---	---	---	---	1.347(2)	---	---
N(5)-C(15)	---	---	---	---	1.471(2)	---	---
N(5)-C(17)	---	---	---	---	1.481(2)	---	---
C(1)-C(3)	1.407(3)	1.417(4)	1.418(3)	1.43(1)	1.423(2)	1.409(4)	1.45(1)
C(2)-C(3)	1.415(3)	1.423(5)	1.421(3)	1.40(1)	1.427(2)	1.419(4)	1.42(1)
C(3)-C(4)	1.450(2)	1.427(4)	1.420(3)	1.405(9)	1.404(2)	1.423(4)	1.40(1)
C(4)-C(5)	1.412(3)	1.419(4)	1.425(3)	1.421(8)	1.438(2)	1.429(4)	1.41(1)
C(4)-C(9)	1.408(3)	1.415(4)	1.417(3)	1.426(8)	1.428(2)	1.410(4)	1.434(9)
C(5)-C(6)	1.382(3)	1.361(4)	1.363(3)	1.363(8)	1.356(2)	1.369(4)	1.36(1)
C(6)-C(7)	1.396(3)	1.418(4)	1.417(3)	1.424(8)	1.431(2)	1.417(4)	1.437(9)
C(7)-C(8)	1.398(3)	1.430(4)	1.421(3)	1.435(9)	1.435(2)	1.418(4)	1.41(1)
C(7)-C(10)	1.464(2)	1.428(4)	1.427(2)	1.397(9)	1.418(2)	1.435(4)	1.42(1)
C(8)-C(9)	1.379(3)	1.363(4)	1.367(3)	1.351(8)	1.361(2)	1.372(4)	1.36(1)
C(10)-C(11)	---	1.463(4)	1.453(3)	1.46(1)	1.448(2)	1.454(4)	1.450(9)
C(10)-C(12)	---	---	1.388(3)	---	1.411(2)	1.393(4)	1.40(1)
C(11)-C(12)	1.516(3)	---	---	---	---	---	---
C(12)-C(13)	---	1.522(5)	1.399(3)	1.551(7)	1.393(2)	1.412(4)	1.521(8)

C(12)-C(13')	---	---	---	1.551(9)	---	---	---
C(12)-C(16)	---	---	---	---	---	---	1.416(9)
C(13)-C(14)	1.521(3)	1.533(4)	---	1.550(9)	1.454(2)	---	1.51(1)
C(13')-C(14')	---	---	---	1.55(1)	---	---	---
C(14)-C(15)	---	1.534(4)	1.523(3)	1.559(9)	---	1.528(4)	1.522(9)
C(14)-C(17)	---	1.523(5)	---	---	---	---	---
C(14)-C(19)	---	---	---	---	---	1.536(4)	---
C(14')-C(15)	---	---	---	1.56(1)	---	---	---
C(15)-C(16)	1.519(3)	1.515(4)	---	---	1.518(2)	1.529(4)	---
C(16)-C(17)	---	---	1.516(3)	---	---	1.534(5)	---
C(17)-C(18)	1.521(3)	---	---	---	1.517(2)	1.527(5)	1.49(1)
C(18)-C(19)	---	---	---	---	---	1.530(4)	---
C(19A)-C(20)	---	---	---	---	---	---	1.55(2)
C(19B)-C(20)	---	---	---	---	---	---	1.47(3)
C(20)-C(21)	---	---	---	---	---	1.526(4)	---
C(20)-C(25)	---	---	---	---	---	1.526(4)	---
C(21)-C(22)	---	---	---	---	---	1.531(4)	---
C(21A)-C(22)	---	---	---	---	---	---	1.35(2)
C(21B)-C(22)	---	---	---	---	---	---	1.51(3)
C(22)-C(23)	---	---	---	---	---	1.529(4)	---
C(23)-C(24)	---	---	---	---	---	1.523(5)	---
C(24)-C(25)	---	---	---	---	---	1.535(4)	---

Table 4.2.3 *- Bond angles (°) for all seven compounds (excluding those bonds involving hydrogens).*

ANGLE	BOND ANGLE (°)						
	I	**II**	**III**	**IV**	**V**	**VI**	**VII**
C(19A)-O(1)-C(18)	---	---	---	---	---	---	115(1)
C(19B)-O(1)-C(18)	---	---	---	---	---	---	119(1)
C(18)-O(2)-C(21A)	---	---	---	---	---	---	111(1)
C(18)-O(2)-C(21B)	---	---	---	---	---	---	121(1)
C(10)-N(3)-C(11)	121.1(2)	---	---	---	---	---	---
C(10)-N(3)-C(13)	122.4(2)	---	---	---	---	---	---
C(11)-N(3)-C(13)	116.4(2)	---	---	---	---	---	---
C(10)-N(4)-C(12)	---	125.3(2)	---	125.4(6)	---	---	---
C(10)-N(4)-C(15)	122.3(2)	---	---	123.8(6)	---	---	---
C(10)-N(4)-C(16)	---	123.4(2)	---	---	---	---	---

C(10)-N(4)-C(17)	121.3(2)	---	---	---	---	---	---
C(12)-N(4)-C(15)	---	---	---	110.6(5)	---	---	---
C(12)-N(4)-C(16)	---	110.6(2)	---	---	---	---	---
C(13)-N(4)-C(14)	---	---	122.6(2)	---	---	122.2(2)	---
C(13)-N(4)-C(16)	---	---	119.9(2)	---	---	---	---
C(13)-N(4)-C(20)	---	---	---	---	---	118.3(2)	---
C(14)-N(4)-C(16)	---	---	117.4(2)	---	---	---	---
C(14)-N(4)-C(20)	---	---	---	---	---	119.3(2)	---
C(15)-N(4)-C(16)	---	---	---	---	---	---	122.1(6)
C(15)-N(4)-C(17)	116.4(2)	---	---	---	---	---	117.0(6)
C(16)-N(4)-C(17)	---	---	---	---	---	---	120.9(5)
C(13)-N(5)-C(15)	---	---	---	---	122.3(1)	---	---
C(13)-N(5)-C(17)	---	---	---	---	122.1(1)	---	---
C(15)-N(5)-C(17)	---	---	---	---	115.2(1)	---	---
N(1)-C(1)-C(3)	177.5(2)	177.3(4)	178.8(2)	178.9(9)	178.5(2)	178.8(4)	179(1)
N(2)-C(2)-C(3)	176.7(2)	179.2(3)	179.0(2)	178.8(9)	179.5(1)	179.4(3)	178.6(9)
C(1)-C(3)-C(2)	119.1(2)	117.6(3)	116.7(2)	116.1(7)	117.2(1)	117.2(3)	115.6(7)
C(1)-C(3)-C(4)	120.9(2)	120.8(3)	121.6(2)	121.5(7)	121.1(1)	120.8(3)	122.1(7)
C(2)-C(3)-C(4)	120.0(2)	121.6(3)	121.7(2)	122.4(7)	121.6(1)	121.9(3)	122.3(6)
C(3)-C(4)-C(5)	122.0(2)	121.0(3)	121.2(2)	121.6(6)	120.3(1)	121.4(3)	122.5(6)
C(3)-C(4)-C(9)	121.0(2)	121.2(3)	121.6(2)	121.6(7)	122.1(1)	121.9(3)	121.9(7)
C(5)-C(4)-C(9)	117.0(2)	117.8(3)	117.2(2)	116.8(6)	117.6(1)	116.7(3)	115.6(7)
C(4)-C(5)-C(6)	121.1(6)	121.7(3)	121.6(2)	121.6(7)	121.2(1)	121.8(3)	123.3(6)
C(5)-C(6)-C(7)	121.0(2)	120.8(3)	121.2(2)	122.1(7)	121.6(1)	121.1(3)	120.4(7)
C(6)-C(7)-C(8)	118.6(2)	117.2(3)	117.2(2)	115.5(7)	116.9(1)	117.2(3)	116.5(7)
C(6)-C(7)-C(10)	121.2(2)	124.0(3)	121.5(2)	124.8(7)	122.3(1)	121.9(3)	122.6(7)
C(8)-C(7)-C(10)	120.3(2)	118.8(3)	121.4(2)	119.7(6)	120.8(1)	120.9(3)	120.8(6)
C(7)-C(8)-C(9)	120.5(2)	121.6(3)	121.7(2)	122.6(7)	121.9(1)	121.7(3)	122.7(6)
C(4)-C(9)-C(8)	121.7(2)	120.6(3)	121.0(2)	121.3(7)	120.8(1)	121.5(3)	121.4(7)
N(3)-C(10)-N(4)	120.7(2)	---	---	---	---	---	---
N(3)-C(10)-C(7)	120.3(2)	---	---	---	---	---	---
N(4)-C(10)-C(7)	119.1(2)	129.9(2)	---	130.7(6)	---	---	---
N(4)-C(10)-C(11)	---	115.2(3)	---	112.2(7)	---	---	---
C(7)-C(10)-C(11)	---	114.8(2)	117.2(2)	117.1(7)	115.6(1)	116.6(3)	114.2(7)
C(7)-C(10)-C(12)	---	---	126.3(2)	---	124.0(1)	126.7(3)	131.8(6)
C(11)-C(10)-C(12)	---	---	116.4(2)	---	120.3(1)	116.6(3)	114.0(2)
N(3)-C(11)-C(10)	---	175.6(3)	176.9(2)	178.9(9)	176.9(1)	176.7(3)	178.5(9)
N(3)-C(11)-C(12)	111.2(2)	---	---	---	---	---	---

N(4)-C(12)-C(13)	---	110.3(3)	---	103.3(6)	---	---	---
N(4)-C(12)-C(13')	---	---	---	102(1)	---	---	---
C(10)-C(12)-C(13)	---	---	121.5(2)	---	128.8(1)	120.0(3)	123.5(7)
C(10)-C(12)-C(16)	---	---	---	---	---	---	119.6(5)
C(13)-C(12)-C(16)	---	---	---	---	---	---	116.9(7)
N(3)-C(13)-C(14)	110.9(2)	---	---	---	---	---	---
N(4)-C(13)-C(12)	---	---	126.4(2)	---	---	128.6(3)	---
N(5)-C(13)-C(12)	---	---	---	---	124.0(1)	---	---
N(5)-C(13)-C(14)	---	---	---	---	113.8(1)	---	---
C(12)-C(13)-C(14)	---	110.7(3)	---	99.6(6)	122.2(1)	---	111.2(6)
C(12)-C(13')-C(14')	---	---	---	103(2)	---	---	---
N(4)-C(14)-C(13)	---	---	---	---	176.0(2)	---	---
N(4)-C(14)-C(15)	---	---	112.0(4)	---	---	112.1(3)	---
N(4)-C(14)-C(19)	---	---	---	---	---	110.1(2)	---
C(13)-C(14)-C(15)	---	109.7(2)	---	100.8(7)	---	---	111.9(5)
C(13)-C(14)-C(17)	---	111.2(3)	---	---	---	---	---
C(15)-C(14)-C(17)	---	111.8(3)	---	---	---	---	---
C(15)-C(14)-C(19)	---	---	---	---	---	111.6(2)	---
C(13')-C(14')-C(15)	---	---	---	97(2)	---	---	---
N(4)-C(15)-C(14)	---	---	---	102.2(5)	---	---	107.0(5)
N(4)-C(15)-C(14')	---	---	---	104(1)	---	---	---
N(4)-C(15)-C(16)	111.3(2)	---	---	---	---	---	---
N(5)-C(15)-C(16)	---	---	---	---	111.9(1)	---	---
C(14)-C(15)-C(16)	---	112.6(3)	---	---	---	109.5(3)	---
N(4)-C(16)-C(12)	---	---	---	---	---	---	124.7(5)
N(4)-C(16)-C(15)	---	109.9(3)	---	---	---	---	---
N(4)-C(16)-C(17)	---	---	112.1(2)	---	---	---	---
C(15)-C(16)-C(17)	---	---	---	---	---	111.2(3)	---
N(4)-C(17)-C(18)	111.2(2)	---	---	---	---	---	110.9(6)
N(5)-C(17)-C(18)	---	---	---	---	112.3(1)	---	---
C(16)-C(17)-C(18)	---	---	---	---	---	111.0(3)	---
O(1)-C(18)-O(2)	---	---	---	---	---	---	109.3(7)
O(1)-C(18)-C(17)	---	---	---	---	---	---	107.0(6)
O(2)-C(18)-C(17)	---	---	---	---	---	---	108.8(6)
C(17)-C(18)-C(19)	---	---	---	---	---	111.0(3)	---
C(14)-C(19)-C(18)	---	---	---	---	---	110.3(3)	---
O(1)-C(19A)-C(20)	---	---	---	---	---	---	110(2)

O(1)-C(19B)-C(20)	---	---	---	---	---	---	112(2)
N(4)-C(20)-C(21)	---	---	---	---	---	111.2(2)	---
N(4)-C(20)-C(25)	---	---	---	---	---	110.5(2)	---
C(21)-C(20)-C(25)	---	---	---	---	---	112.3(2)	---
O(2)-C(21A)-C(22)	---	---	---	---	---	---	113(2)
O(2)-C(21B)-C(22)	---	---	---	---	---	---	110(2)
C(20)-C(21)-C(22)	---	---	---	---	---	110.1(2)	---
C(21)-C(22)-C(23)	---	---	---	---	---	110.6(3)	---
C(22)-C(23)-C(24)	---	---	---	---	---	110.4(3)	---
C(23)-C(24)-C(25)	---	---	---	---	---	111.1(3)	---
C(20)-C(25)-C(24)	---	---	---	---	---	110.9(3)	---

4.2.1.3 Solvatochromatism

The spectra in solution of the compounds exhibit a solvatochromic absorption band which is ascribed to the main intra-molecular charge-transfer band. As an index of solvent polarity we prefer to use simply the solvent dielectric constant. In the description of the reaction field evolution of the gas-phase dipole moment (Bottcher, 1972) the only non-solute variable is the solvent dielectric constant. Thus, for molecules of similar type, i.e. similar gas-phase dipole moments and polarizabilities, the solvatochromatism in the absence of bonding interactions should be similar. In this spirit we present the data in ***Table 4.2.4*** as an aid to classifying the molecules of the present study. Spectral data were unavailable for compounds **VI** and **VII**.

Table 4.2.4 - *Solvatochromatism (Wavelength in units of nm) of the lowest energy excitation band of compounds* ***I-V***.

Solvent	ε	**I**	**II**	**III**	**IV**	**V**
$CHCl_3$	4.8	481	636	717	---	721
PhCl	5.6	---	636	722	617	727
DCM	8.9	459	639	720	611	723
C_6H_{10}=O	16.1	---	636	715	613	785
DMF	36.7	433	629	693	607	802
MeCN	37.5	---	628	698	604	785

Notable trends emerge for compounds **I** and **III** wherein over the studied range of solvents, the solvatochromism is negative. This implies that the ground state dipole moment of the solute in these solutions contains more zwitterionic than quinoidal

character (*vide infra*). There is no clear trend in the solvatochromism for compounds **II** and **IV** whose solvatochromism is similar. These compounds are structurally similar in any case but in the higher polarity solvents one might assign a negative solvatochromism. The solvatochromism of **V** is clearly positive, contrasting with **I** and **III** and demonstrating that the ground state structure is predominantly quinoidal.

4.2.2 Discussion

The nature of time-averaged BLA (Marder & Perry, 1993; Marder et al., 1994) of all seven molecules was analysed. A ratio of the TCNQ-like quinoidal bonding over that of the zwitterionic form was determined for each bond in the common framework of the molecule. The common framework was taken to be the connectivities from carbon atoms C(3) to C(10). The cyano groups were excluded from this framework despite being common to all the structures. This is because there is no evidence for any participation of the cyano groups in any quinoidal / zwitterionic interchange, since the valence models of both the completely quinoidal and zwitterionic form show no cyano group involvement and besides, each cyano bond shows very clear typical triple bond character as determined by analysis of the corresponding C≡N bond distances (1.137(8)Å-1.165(4)Å). Any deviation from the expected value of each C≡N bond is more likely to be a result of hydrogen-bonding influences than anything else.

The reference bond length values for each of the two extreme types of bonding were obtained from the unweighted sample mean values in Allen et al., 1987. The unweighted rather than the weighted mean values were used in common with previous work (Taylor & Kennard, 1983, 1985 & 1986) and in preference to the results from the single photographic study reported on TCNQ itself (Long, Sparks & Trueblood, 1965).

The bond length ratios, X_S, were obtained from the following analysis. First, the average bond deviation in the backbone of each structure was calculated from the ideal form of the TCNQ backbone, derived using the published means (Allen et al, 1987).

$$D^{S}_{TCNQ} = \frac{\sum_{i=1}^{N_b} \left| b_i^S - b_i^{TCNQ} \right|}{N_b}$$

where b_i^S is the i'th bond in structure S and b_i^{TCNQ} is the i'th bond in the ideal TCNQ form. N_b is the number of bonds over which the average was derived.

Using the same equation, a value for D_{TCNQ}^{ZWIT} was then derived, by calculating the deviation of the ideal zwitterionic form from the TCNQ form. A structure with this value of deviation from the quinoidal form can be regarded as representing "0% TCNQ character" whereas a structure with a deviation, D_{TCNQ}^{S} = 0.0 can be regarded as having "100% TCNQ character". Thus we can define the ratio for structure S, X_S as

$$X_S = \frac{D_{TCNQ}^{ZWIT} - D_{TCNQ}^{S}}{D_{TCNQ}^{ZWIT}} \times 100\%$$

These calculations were deemed valid by the fact that the errors on the given experimental bond distance values and the corresponding R factors obtained [for $I \geq 2\sigma(I)$] were, on average, significantly less than those used in determining the reference values [C-C bond of esd ≤ 0.010Å and R≤0.07]. Ratios X_s are given in ***Table 4.2.5***.

From ***Table 4.2.5***, it can be seen that the molecules in order of increasing quinoidal nature are **I**, **II**, **VI**, **III**, **VII**, **IV** and **V**, the latter two exhibiting a particularly high quinoidal nature and **I** showing anomalously low quinoidal tendencies.

The proposed rationale for this ordering is twofold. First, the presence of the C(11)≡N(3) bond is important for retaining the extended conjugation needed to promote the quinoidal character in the molecule. **I** is the only molecule in this series not to have this extra C≡N group, and therein the extent of conjugation supports only low quinoidal characteristics. On the other hand, **V** contains an extra C≡N group compared to **II**, **III**, **IV**, **VI** and **VII** and this is sited such as to increase the conjugation further. The dramatic effect of this extra C≡N group can be seen by comparing **V** and **III**, which are essentially isostructural except for this extra C≡N group and yet the quinoidal nature of **III** is much lower than for **V**.

The second factor affecting the quinoidal extent of the molecules is the presence of the heteroatom N vicinal to a C atom involved in conjugation. In all seven molecules where a skeletal heteroatom N is present and vicinal to a C=C bond, the length of C-N bond is more characteristic of a double bond than a single bond, the latter being expected from considerations of the overall bond order at the adjacent C site. This extra bonding electron density is due to donation from the amino lone pair, which reduces the formal positive charge on the adjacent carbon atom, and in turn increases the formal positive charge on the amino nitrogen. The greater the localization of this positive charge

	Bond Distance								
	Quinoidal	Zwitterionic	Structure **I**	Structure **II**	Structure **III**	Structure **IV**	Structure **V**	Structure **VI**	Structure **VII**
C(3)-C(4)	1.392	1.470	1.450(2)	1.427(4)	1.420(3)	1.405(9)	1.404(2)	1.423(4)	1.40(1)
C(4)-C(5)	1.432	1.380	1.412(3)	1.419(4)	1.425(3)	1.421(8)	1.438(2)	1.429(4)	1.41(1)
C(5)-C(6)	1.352	1.380	1.382(3)	1.361(4)	1.363(4)	1.363(8)	1.356(2)	1.369(4)	1.36(1)
C(6)-C(7)	1.432	1.380	1.396(3)	1.418(4)	1.417(3)	1.424(8)	1.431(2)	1.417(4)	1.437(9)
C(7)-C(8)	1.432	1.380	1.398(3)	1.430(4)	1.421(3)	1.435(9)	1.435(2)	1.418(4)	1.41(1)
C(8)-C(9)	1.352	1.380	1.379(3)	1.363(4)	1.367(3)	1.351(8)	1.361(2)	1.372(4)	1.36(1)
C(4)-C(9)	1.432	1.380	1.408(3)	1.415(4)	1.417(3)	1.426(8)	1.428(2)	1.410(4)	1.434(9)
C(7)-C(10)	1.392	1.470	1.464(2)	1.428(4)	1.427(3)	1.397(9)	1.417(2)	1.435(4)	1.42(1)
D^{S}_{TCNQ}	0.0	0.053	0.038(1)	0.017(2)	0.016(1)	0.007(3)	0.008(1)	0.021(2)	0.012(5)
X_S	100%	0%	27(2)%	67(4)%	70(2)%	87(6)%	85(2)%	61(4)%	75(10)%

Table 4.2.5 *- A comparison of quinoidal versus aromatic character for compounds* ***I-VII****.*

around the nitrogen atom, the shorter the C-N bond. This counteracts the quinoidal nature of the system, which in the limit, would cause the former C=C bond to have no π character.

VII exhibits the shortest such C-N bond [1.296(8)Å] due to the high degree of localization of the positive charge. Thus, the quinoidal nature of the molecule is reduced markedly. **III** possesses the next shortest such C-N bond [1.316(2)Å]. Both of these molecules and compound **VI** show similar extents of quinoidal character. This stands to reason since all three compounds are skeletally identical up to the point where the conjugation ends (except that the saturated side of the ring in **VII** replaces the C-H bond in **III**, but this difference is not expected to affect the quinoidal / zwitterionic inclinations of the compound). **VII** appears marginally more quinoidal than **III** despite its greater localization of positive charge and it is notably more quinoidal than **VI**. This is presumably because the lone pairs on the oxygen atoms in **VII** can donate electron density to the C(18)-O bond, thereby inducing some π-density into this bond whilst the lone pair on the N(4) atom can donate electron density to the N(4)-C(17) bond, thereby inducing π-density into the C-N bond. The result being that the quinoidal type conjugation is extended at the expense of the alternative zwitterionic type conjugation (***Figure 4.2.2***). The lower than average relevant bond lengths, C(18)-O(1), C(18)-O(2) and C(17)-N(4) (1.406(9)Å, 1.399(9)Å and 1.479(9)Å respectively compared to relevant C-O and C-N literature values of 1.426Å and 1.479Å respectively (Allen et al, 1987) support this hypothesis.

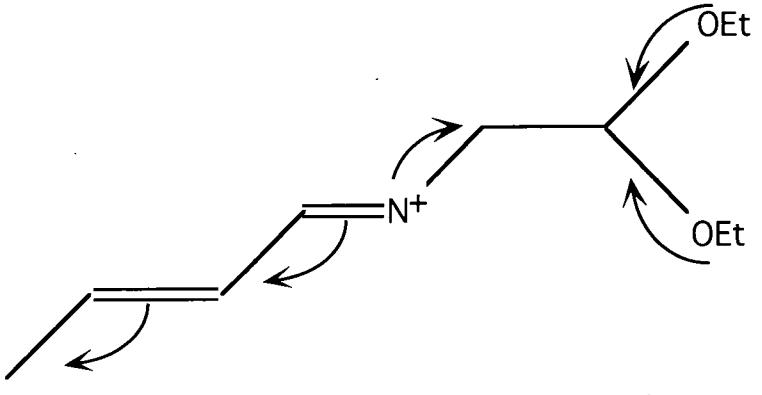

Figure 4.2.2 *- The mechanism for lone pair donation in compound **VII**.*

With regard to the negatively charged component of the zwitterion, a perturbation of bonding characteristics also exists. The effect is spread essentially in a symmetrical manner between the two cyano groups C(1)≡N(1) and C(2)≡N(2), seen by the general lengthening of these bonds compared to the corresponding C≡N distance of 1.144Å in TCNQ; also, the consistent shortening of the C(1)-C(3) and C(2)-C(3) formally σ-bonds in **I-VII** compared to the corresponding distance in TCNQ (1.427Å). A more

extended, though smaller, effect is observed by noting the consistently shorter separations for C(3)-C(4) compared with C(7)-C(10) for each molecule.

4.2.2.1 Packing Effects

All seven molecules pack in primitive space groups and all but **II** are centrosymmetric. The preponderance of centrosymmetry arises firstly from the compounds' inclination to be planar, which encourages plane-to-plane van der Waals contacts, and secondly from the compounds' dipolar character which further favours anti-parallel alignment.

II is interesting because it is non-centrosymmetric. **II** adopts a head-to-tail arrangement in layers in the space group Pn, the non-centrosymmetric analogue of **IV**'s space group. Powder SHG studies of **II**, measured using 1.907μm radiation, show a powder efficiency 13 times that of the urea standard sample thereby confirming the non-centrosymmetry and nonlinearity simultaneously. Otherwise **II** is very similar to **IV** except for the nature of the hetero-atomic ring. Returning to the ordering in the quinoidal / zwitterionic tendency of our series, at the molecular level we might expect **II** and **IV** to exhibit rather similar bond-length alternation. Indeed in solution, **II** and **IV** behave rather similarly in their solvatochromism (***Table 4.2.4***) and their calculated gas phase dipole moments [using the COSMIC force field within 'NEMESIS' (Oxford Molecular, 1994)] are also very similar [approx. 8.4 and 9.4 respectively]. The observed marked differences in BLA are therefore presumably due to the differences in crystal packing. Molecules of compound **II** are arranged to give a polar crystal in which the local fields may act to promote zwitterionic character. Molecules in the crystal of compound **IV**, by contrast, experience the reverse field of neighbouring dipoles acting to reduce the condensed phase-equilibrium moments.

Molecules **III** and **V** each possess a noticeably longer chain linked to the common framework of this series of compounds. This reduces their ability to comply with high symmetry operations, consequent upon their non-planarity and the large number of similar low-energy conformations possible.

Secondary interactions exist in **III**-**VII** in the form of hydrogen bonds. A summary of these interactions is given in ***Table 4.2.6***. The precision of the hydrogen positions in structures **III** and **V** is high enough for confidence in the lengths of the C≡N...H contacts that are noted in ***Table 4.2.6***. However the exact lengths of the contacts noted for structures **IV, VI** and **VII** must be judged with care since all hydrogen atoms were added at idealized positions and, for structures **IV** and **VII**, disorder is present.

*Table 4.2.6 - A summary of intermolecular contacts present in compounds **III-VII**.*

Compound	Contact	Distance (Å)
III	N(1)...H(14B)	2.51(2)
	N(2)...H(14A)	2.56(2)
	N(3)...H(6)	2.59(2)
IV	N(2)...H(13A)	2.61(1)
	N(3)...H(12A)	2.542(9)
V	N(2)...H(17A)	2.53(2)
	N(3)...H(5)	2.59(2)
VI	N(1)...H(6A)	2.62(1)
	N(1)...H(12A)	2.42(1)
	N(1)...H(14A)	2.56(1)
VII	O(1)...H(23A)	2.35(3)
	N(2)...H(18)	2.49(2)
	N(3)...H(6)	2.50(1)
	Cl(1)...H(19C)	2.77(2)

The distances given in ***Table 4.2.6*** are all considerably shorter than the sum of the associated van der Waals radii [1.2Å for hydrogen, 1.55Å for nitrogen (Bondi, 1964)]. Structures **III-VII** all pack in layers, as in seen in ***Figure 4.2.7***, maximizing these interactions. The third interaction given for structure **III** [between N(1) and H(14B)] and the fourth given for structure **VII** [between H(19C) and part of the CH_2Cl_2 solvent, Cl(1)] are not shown in ***Figure 4.2.7***. These act between the layers of molecules rather than within the layer.

The intermolecular interactions noted for structures **III-VI** are classical examples of C≡N···H hydrogen bonds. The O...H-C and C-H...Cl hydrogen-bonding interactions present in **VII** are slightly more unusual, although many such interactions have been previously determined (Taylor & Kennard, 1982). All given contacts could be considered to be structure determining.

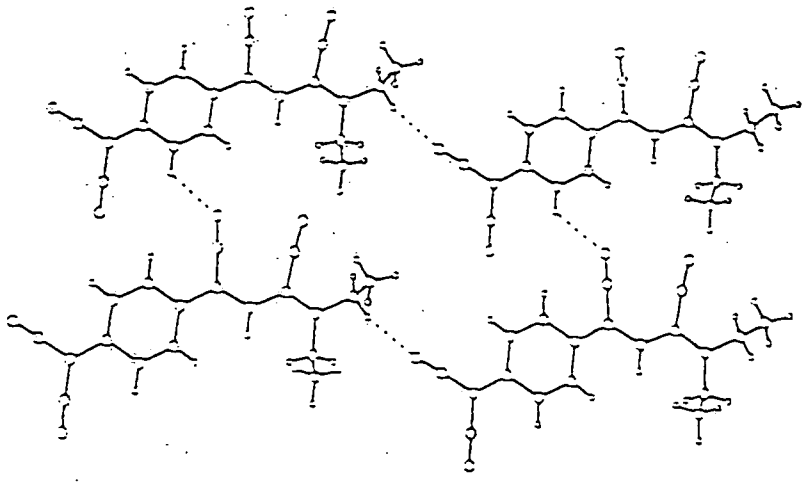

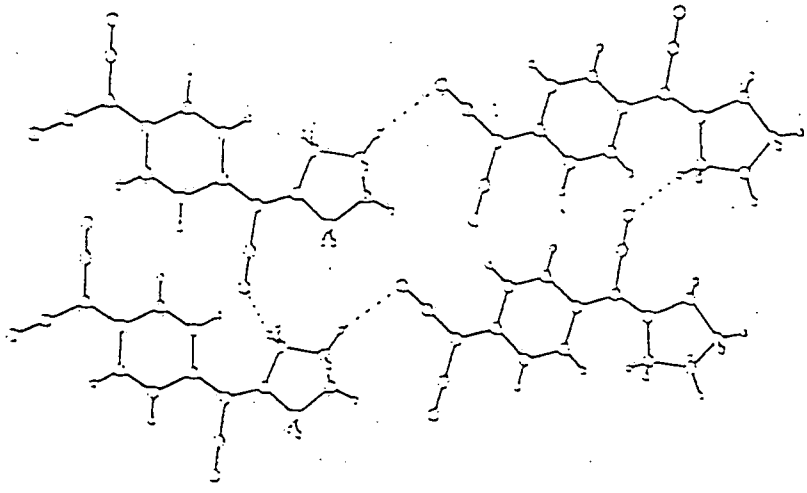

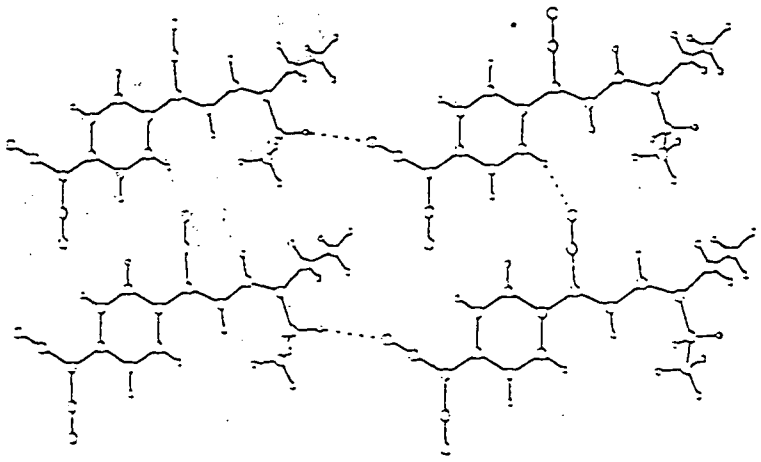

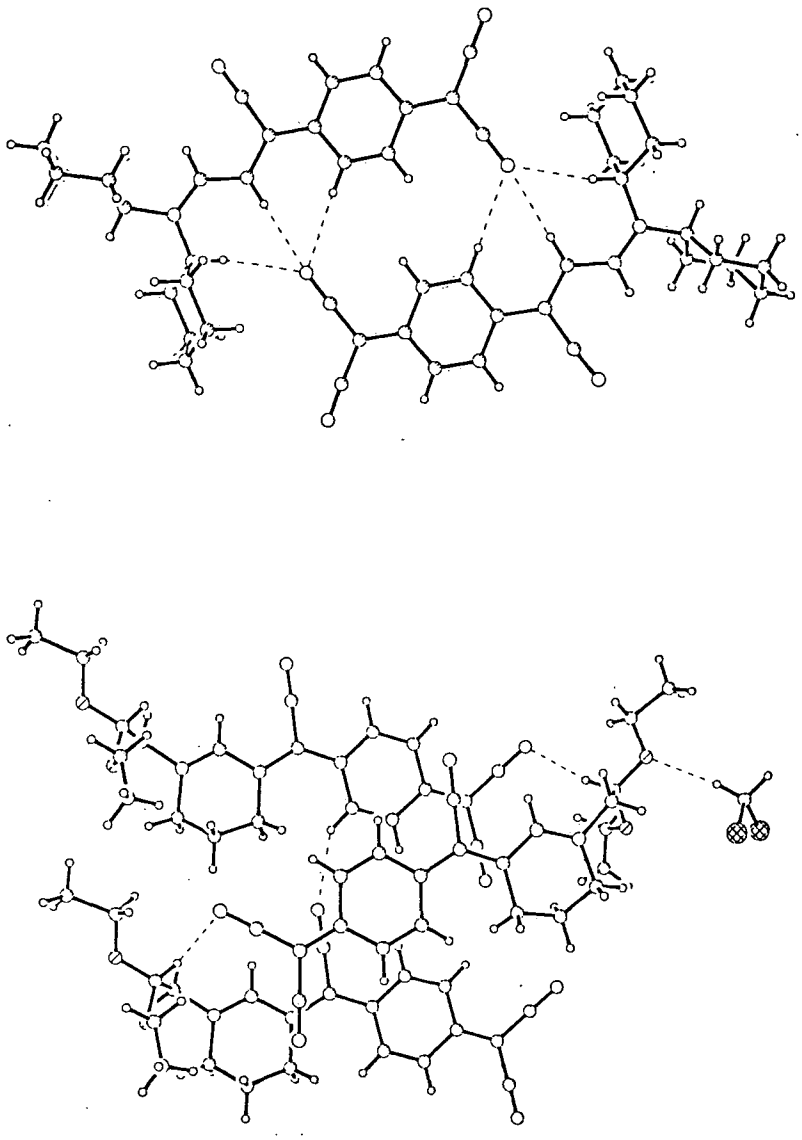

*Figure 4.2.7 - The molecular packing of structures **III-VII** respectively.*

4.2.3 Concluding remarks

The presence of the C(10)-C≡N nitrile group in the common framework of these molecules has been found to be vital if a significant quinoidal character is to be retained in these compounds. Moreover, the presence of extra nitile groups in the substituted part of the molecule further increases the quinoidal character. The chain length and degree of planarity of these substituted components also seem important as does the relative localization of the positive charge around the nitrogen atoms, resulting from the lone-pair donation. The crystal field effect can override these molecular constraints, providing the polarizing field required to evolve the ground-state structure towards the zwitterionic form. In two crystal structures comprising molecules of nearly identical

molecular structure, but where one is non-centrosymmetric, the consequent macroscopic polarity polarizes the molecules and produces quite distinct differences in the bond-length alternation compared with its non-polar homologue. Second harmonic generation from powder samples of the non-centrosymmetric material confirms the macroscopic optical non-linearity. This study suggests that further work correlating crystal-state molecular polarization with free-state or solution-state polarization could provide valuable evidence to confirm the theoretical predictions that non-linear optical susceptibilities can be optimized by tuning the local field effects.

4.3 A CHARGE DENSITY STUDY OF COMPOUND I

In order to obtain the most accurate results, it was decided to use a combination of X-ray and neutron diffraction experimental techniques for this study. Moreover, each experiment was carried out at the lowest common stable temperature possible by the two techniques in order to avoid any disruptive temperature effects.

4.3.1 The 20K X-ray structure of compound I

4.3.1.1 Experimental

A crystal of dimensions 0.24 x 0.24 x 0.14 mm was mounted on a sharpened 0.3mm graphite pencil lead using epoxy glue (Oxford Instruments, TRZ0004). After allowing the glue to dry for 24h, a copper mount was used to attach the graphite fibre to the lower stage of the Fddd cryodiffractometer's Air Products '512' Displex. The crystal was optically centred before the two beryllium shrouds were put into place. The sample chamber was then evacuated. Once the pressure in the sample chamber had reached 1 x 10^{-5} mbar, the He compressor supplying the cryostat was turned on. The crystal was cooled at 0.75Kmin^{-1} to 150K and then at 0.14Kmin^{-1} to 20K.

The following monoclinic cell was obtained for the crystal at 20K, using 24 centred reflections with 2θ between 22.15° and 23.92°:

a=11.174(2)Å, b=12.859(2)Å, c=12.486(2)Å, β=112.00(1)°, volume=1663.5(5)Å^3.

Seven shells of data (see ***Table 4.3.1***) were collected in bisecting mode using 2θ/ω scans. The scan width was set from 1.3° (in 2θ) below K-α_1 to 1.6° (in 2θ) above K-α_2. A constant scan speed of 6° (in 2θ) a minute was used. Seven standard reflections were measured every 193 reflections except for in shell 6, when only five could be reached due to the χ restriction.

The data was collected over a one month period. During this time, there were several technical difficulties, which included the diffractometer occasionally losing its ϕ position. This was a particular problem during shell 3. This shell was eventually abandonned in favour of shell 4, where the problem was less prevalent. During shell 2 the X-ray filament burnt out and had to be replaced. Also during this shell there was a general power failure and the crystal temperature fell to 10K. The temperature was brought back to 20K and the crystal recentred. The X-ray generator tripped off on at least four other occasions. Between shells 8 and 9 the Displex had to be turned off and the sample chamber re-evacuated before cooling back to 20K, recentring and

continuing. All data affected by the above problems were deleted from the dataset and recollected.

Table 4.3.1 *- A summary of the range of data collection in the seven shells.*

Shell number	2θ range (°)	Data collected		
1	6-40	-h to h	-k to k	-l to l
2	40-50	-h to h	-k to k	-l to l
3	50-60	0 to 10	-k to k	-l to l
4	50-60	-h to -5	-k to k	-l to l
5	60-80	-h to 0	0 to k	-l to l
6	80-95%	-h to h	-k to k	-l to l
7	60-80	-h to 0	-k to 0	-l to l

A total of 41407 reflections were collected, with 1441 of these being standards. φ-scan measurements were taken on several reflections but these were eventually not exploited: no absorption correction was necessary due to the small size of the crystal and the small value of the absorption coefficent.

After data collection had finished, the data was initially reduced using the Crystal Logics software provided with the Fddd cryodiffractometer (Copley et al., 1997). The output was analysed to assess the effect of graphite powder lines on the data. The in-house program GRAPHITE was used to do this. It uses reflection profiles to identify those reflections with unusually high backgrounds. Analysis of these in terms of damaged left and right backgrounds exposes clear trends that match the positions of the known graphite lines. Clearly at 2θ positions between the damaged left and right backgrounds, the peaks themselves contain a contribution from the graphite fibre. The GRAPHITE program allows the user to specify regions of data to be removed, both in terms of 2θ and χ positions to try to counter this. The areas removed for this data collection are detailed in ***Table 4.3.2***:

% Owing to physical restrictions, χ was limited to values less than 55°.

Table 4.3.2 *- A summary of the areas of data removed in order to counter graphite effects.*

2θ	χ	data lost
10.0 to 14.0	-20.0 to 20.0	62
18.0 to 22.0	-80.0 to -60.0	29
18.0 to 22.0	60.0 to 80.0	29
22.5 to 26.5	-10.0 to 10.0	132

After removal of this data, a further 79 data at other angular positions were rejected by GRAPHITE because of high backgrounds. In total, 331 reflections were removed from the dataset. This represents under 1% of the reflections collected.

After identifying the graphite damaged data, the raw data was processed with the in-house program DREAMIN to convert the output into a format acceptable for the DREAM suite of programs (Blessing, 1989). To achieve this, DREAMIN had to truncate each scan to make it symmetric about $K\overline{\alpha}$ and had to manipulate the observed scan to give 96 equally spaced profile points.

The DREAM package (Blessing, 1989) was then used to reduce, scale and merge the reflection output from DREAMIN, with the exception of the 313 removed reflections. An R_{int} of 0.0272 was obtained.

Before proceeding with a multipolar refinement, a preliminary assessment of the quality of the data was made by using the data to refine the structure in SHELXL-93 (Sheldrick, 1993). Positional and anisotropic displacement parameters were refined for all non-hydrogen atoms and isotropic displacement parameters were refined for all hydrogen atoms. All relevant crystal, data collection and refinement parameters are given in ***Table 4.3.3***:

Table 4.3.3 *- A summary of crystal, data collection and refinement parameters for the 20K X-ray structure of compound* ***I****.*

Compound	**I**	Compound	**I**
Molecular Formula	$C_{18}H_{24}N_4$	Absorption coefficient (mm^{-1})	0.072
Formula weight	296.41	Crystal Morphology	rectangular
a(Å)	11.174(2)	Crystal Colour	yellowy-brown
b(Å)	12.859(2)	Crystal Size (mm)	0.24 x 0.24 x 0.14
c(Å)	12.486(2)	Total number of reflections	41407
α(°)	90	Unique reflections	14919
β(°)	112.00(1)	Observed Reflections [I>2σ(I)]	8562
γ(°)	90	R_{int}	0.0272
Cell Volume($Å^3$)	1663.4(5)	$(\sin\theta / \lambda)_{max}$	0.920
Crystal System	monoclinic	Data / Parameters	14907 / 295
Space Group	P2(1)/c	R1 [I > 2σ(I)]	0.0604
Z	4	wR2 [I > 2σ(I)]	0.1018
Calculated Density (gcm^{-1})	1.184	Goodness of fit on F^2	1.123
Temperature (K)	20.0(1)	Weighting Scheme	$1/\sigma^2$
Wavelength (Å)	0.71073	$\Delta\rho_{(max, min)}$ ($eÅ^3$)	0.720 / -0.447

4.3.1.2 Structural Details

A 50% probability thermal ellipsoid plot of the 20K X-ray derived structure is given in ***Figure 4.3.1***. Bond lengths and selected bond angles are given in ***Tables 4.3.4*** and ***4.3.5***. Fractional coordinates and anisotropic displacement parameters are given in ***Appendix A.4.15*** and ***A.4.16***.

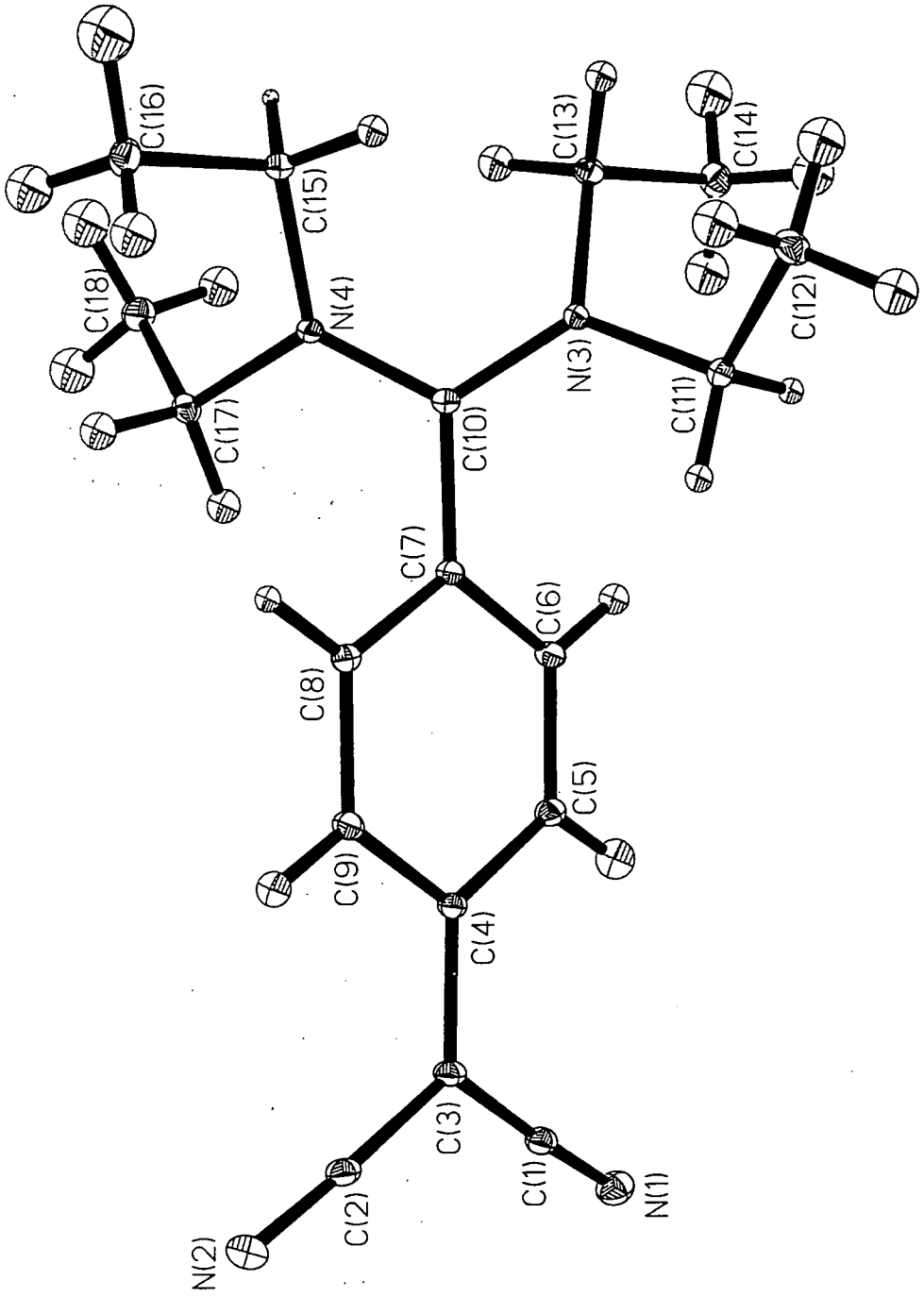

Figure 4.3.1 *- A 50% probability thermal ellipsoid plot of the 20K X-ray structure of compound* ***I****.*

Table 4.3.4 *- Bond distances for the 20K X-ray structure of compound* ***I****.*

Bond	Distance (Å)	Bond	Distance (Å)
N(1)-C(1)	1.166(1)	C(11)-H(11A)	0.98(1)
N(2)-C(2)	1.164(1)	C(11)-H(11B)	0.97(1)
N(3)-C(10)	1.3425(9)	C(12)-H(12A)	0.99(1)
N(3)-C(11)	1.479(1)	C(12)-H(12B)	0.97(1)
N(3)-C(13)	1.4827(9)	C(12)-H(12C)	0.98(1)
N(4)-C(10)	1.3454(9)	C(13)-C(14)	1.528(1)
N(4)-C(15)	1.481(1)	C(13)-H(13A)	0.10(1)
N(4)-C(17)	1.4833(9)	C(13)-H(13B)	1.00(1)
C(1)-C(3)	1.413(1)	C(14)-H(14A)	0.98(1)
C(2)-C(3)	1.413(1)	C(14)-H(14B)	1.00(1)
C(3)-C(4)	1.444(1)	C(14)-H(14C)	1.02(1)
C(4)-C(9)	1.418(1)	C(15)-C(16)	1.527(1)
C(4)-C(5)	1.420(1)	C(15)-H(15A)	0.98(1)
C(5)-C(6)	1.386(1)	C(15)-H(15B)	0.98(1)
C(5)-H(5)	0.98(1)	C(16)-H(16A)	1.02(1)
C(6)-C(7)	1.407(1)	C(16)-H(16B)	0.99(1)
C(6)-H(6)	0.97(1)	C(16)-H(16C)	0.10(1)
C(7)-C(8)	1.407(1)	C(17)-C(18)	1.524(1)
C(7)-C(10)	1.467(1)	C(17)-H(17A)	0.10(1)
C(8)-C(9)	1.384(1)	C(17)-H(17B)	0.99(1)
C(8)-H(8)	0.99(1)	C(18)-H(18A)	0.98(1)
C(9)-H(9)	0.96(1)	C(18)-H(18B)	0.99(1)
C(11)-C(12)	1.524(1)	C(18)-H(18C)	0.98(1)

Table 4.3.5 - Selected bond angles for the 20K X-ray structure of compound I.

Bond	Distance (Å)	Bond	Distance (Å)
C(10)-N(3)-C(11)	121.26(6)	C(6)-C(5)-C(4)	121.15(7)
C(10)-N(3)-C(13)	122.19(6)	C(5)-C(6)-C(7)	120.83(7)
C(11)-N(3)-C(13)	116.52(6)	C(8)-C(7)-C(6)	118.47(6)
C(10)-N(4)-C(15)	121.90(6)	C(8)-C(7)-C(10)	119.85(6)
C(10)-N(4)-C(17)	121.26(6)	C(6)-C(7)-C(10)	121.69(6)
C(15)-N(4)-C(17)	116.84(6)	C(9)-C(8)-C(7)	120.94(7)
N(1)-C(1)-C(3)	177.37(8)	C(8)-C(9)-C(4)	121.22(7)
N(2)-C(2)-C(3)	176.45(8)	N(3)-C(10)-N(4)	121.03(6)
C(2)-C(3)-C(1)	118.95(7)	N(3)-C(10)-C(7)	119.96(6)
C(2)-C(3)-C(4)	119.97(7)	N(4)-C(10)-C(7)	119.01(6)
C(1)-C(3)-C(4)	120.99(7)	N(3)-C(11)-C(12)	111.47(6)
C(9)-C(4)-C(5)	117.34(6)	N(3)-C(13)-C(14)	111.00(6)
C(9)-C(4)-C(3)	120.84(6)	N(4)-C(15)-C(16)	111.13(6)
C(5)-C(4)-C(3)	121.82(7)	N(4)-C(17)-C(18)	110.93(6)

The R_{int} of the data is very low, thus suggesting that the accuracy of the data measured is adequate for a charge density study. Moreover, the data seems to give a good fit to the model as reflected in the consistently low esds of the geometry, the low goodness-of-fit and the small amount of residual electron density present. Despite this, however, the R1 does seem a little high.

The thermal parameters of all atoms are expectedly much smaller than those derived from the 150K X-ray experiment (see section 4.2.1.2).

4.3.2 The 20K neutron structure of compound I

4.3.2.1 Experimental

The neutron structure of **I** was determined using D9 at the ILL. A cubic-shaped crystal of dimensions, 1.0 x 1.0 x 1.0 mm was glued onto a vanadium mount using Kwikfill epoxy resin. The base of the mount was screwed into the head of the Displex and the crystal was centred optically using the telescope. The height of the crystal was purposely left slightly too low in order to allow for the contraction of the Displex when cooled to 20K. A 5mm aperture was used in order to include all of the crystal and to suppress as much background as possible. The calibrated wavelength of the beam was 0.8417(2)Å. Half-wavelength contamination was removed with an erbium filter.

Reflections were then sought by driving to each face and manually altering ω and / or ϕ until enough reflections were obtained to uniquely index the crystal. RAFD9 (Filhol, 1987) was used to refine the unit cell and obtain a UB matrix. The three cryostat shields were then placed around the sample and the outer two were evacuated. The sample was cooled to 20K during which time the (-1 2 3) reflection was repeatedly measured in order to check that the crystal was not thermally damaged. This reflection profile remained similar down to 20K and so a variety of other reflections were scanned in order to improve the UB matrix. A unique set of data was then collected in the 2θ shells, $2\theta \leq 20°$, $20 \leq 2\theta \leq 30°$, $30° \leq 2\theta \leq 40°$, $40° \leq 2\theta \leq 60°$ and $60° \leq 2\theta \leq 70°$. Some symmetry equivalent reflections were also collected within these shells. ω-xθ scans, with x chosen to keep the reflection in the middle of the detector aperture, were used in conjunction with a scan width, $\Delta\omega$, which was roughly twice the full width of the peak to background. Both x and $\Delta\omega$ varied with the Bragg angle, θ:

θ	1.00	15.00	30.00	45.00	60.00
x	1.00	1.00	1.20	2.00	2.00
$\Delta\omega$	2.10	1.50	0.90	2.50	4.20

A default scan time of 50000 monitor counts was employed. One standard relection [the (130)] was measured every 50 reflections in order to monitor any problems. A marked variation in the intensity of the standard reflection was observed throughout the data collection. This variation was due to detector instability which is thought to have decreased the accuracy of the experimental results to a minor degree. The temperature remained static throughout the experiment.

A total number of 3773 reflections were measured at 20K over nine days of data collection. The data were reduced using RACER (Wilkinson, Khamis, Stansfield, & McIntyre, 1988) in the manner detailed in chapter 2, section 2.3.5.2. The resulting structure factor magnitudes were then corrected for absorption through the crystal and the cryostat shield using DATAP (Coppens, 1970) and a local program, ABSCAN respectively.

The corrected data were used to refine the starting model derived from the previously described 150K X-ray experiment, using SHELXL-93 (Sheldrick, 1993). Positional and anisotropic displacement parameters were refined for all atoms. All relevant crystal, data collection and refinement parameters are given in ***Table 4.3.6:***

Table 4.3.6 *- A summary of crystal, data collection and refinement parameters for the 20K neutron structure of compound* ***I****.*

Compound	I	Compound	I
Molecular Formula	$C_{18}H_{24}N_4$	Absorption coefficient (mm^{-1})	0.2137
Formula weight	296.41	Crystal Morphology	cubic
a(Å)	11.178(1)*	Crystal Colour	yellowy-brown
b(Å)	12.859(1)*	Crystal Size (mm)	1.0 x 1.0 x 1.0
c(Å)	12.476(1)*	Total number of reflections	3773
α(°)	90	Unique reflections	3443
β(°)	112.044(5)*	Observed Reflections [I>2σ(I)]	2184
γ(°)	90	R_{int}	0.0583
Cell Volume($Å^3$)	1184.00	$(\sin\theta / \lambda)_{max}$	0.978
Crystal System	monoclinic	Data / Parameters	3417 / 415
Space Group	P2(1)/c	R1 [I > 2σ(I)]	0.0532
Z	4	wR2 [I > 2σ(I)]	0.0890
Calculated Density (gcm^{-1})	1.182	Goodness of fit on F^2	1.330
Temperature (K)	20.0(2)	Weighting Scheme	$1/\sigma^2$
Wavelength (Å)	0.8417(2)	$\Delta\rho_{(max, min)}$ ($fmÅ^{-3}$)	1.108 / -1.096

4.3.2.2 Structural Details

A 50% probability thermal ellipsoid plot of the 20K neutron derived structure is given in ***Figure 4.3.2***. Bond lengths and selected bond angles are given in ***Tables 4.3.7***and ***4.3.8*** Fractional coordinates and anisotropic displacement parameters are given in ***Appendix A.4.17*** and ***A.4.18***

* Although these cell parameters are neutron derived, the 20K X-ray determined cell parameters, a = 11.174(2)Å, b = 12.859(2)Å, c = 12.486(2)Å, β = 112.00(1)° were used in all correction and refinement procedures since they are deemed more accurate than neutron derived values. Moreover, the neutron wavelength's esd was not used in the calculation of the neutron derived cell parameters.

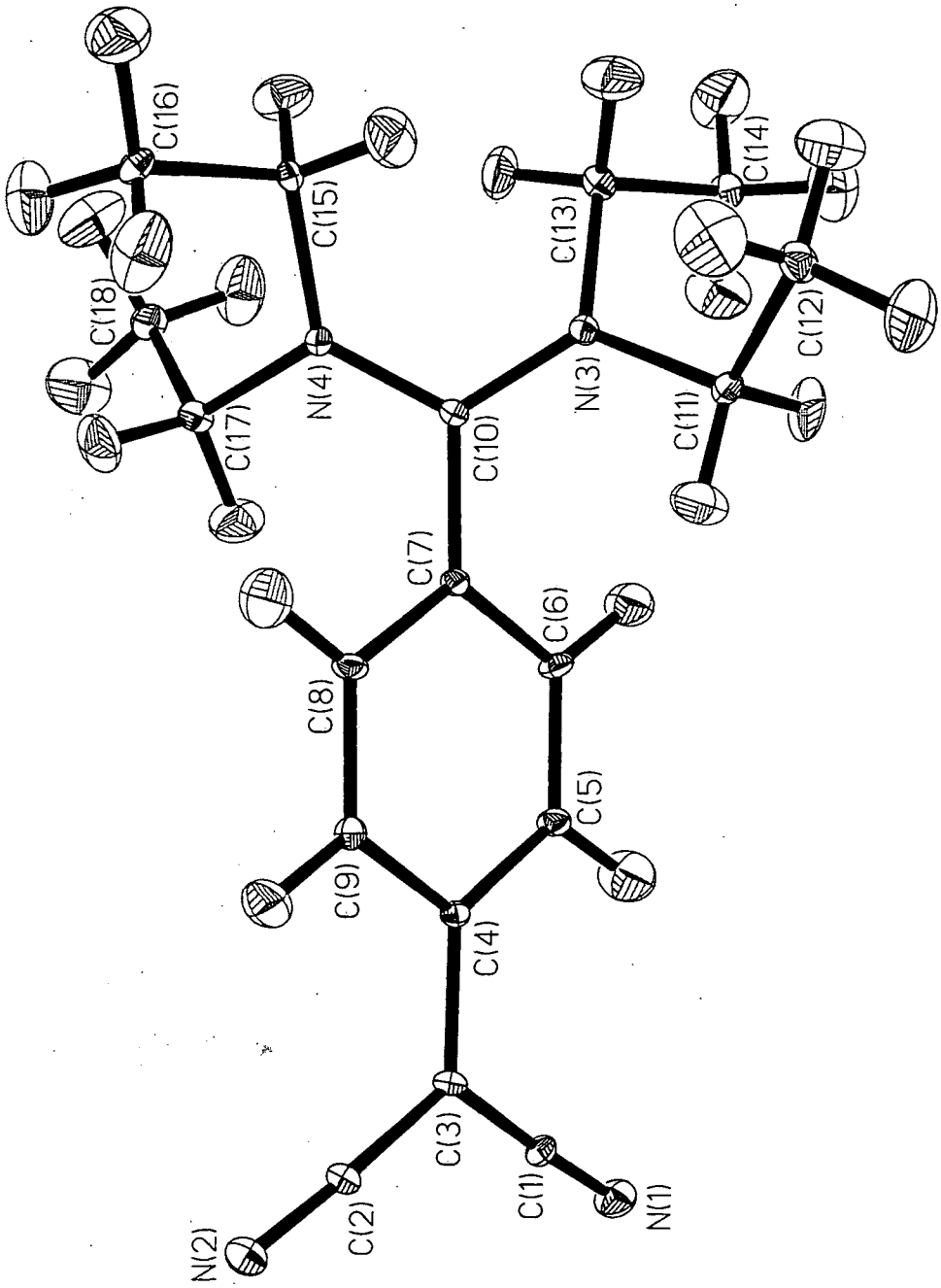

Figure 4.3.2 *- A 50% probability thermal ellipsoid plot of the 20K neutron structure of compound* ***I****.*

Table 4.3.7 *- Bond lengths for the 20K neutron structure of compound* ***I****.*

Bond	Distance (Å)	Bond	Distance (Å)
N(1)-C(1)	1.167(4)	C(6)-H(6)	1.091(6)
N(2)-C(2)	1.173(4)	C(8)-H(8)	1.089(7)
N(3)-C(10)	1.340(3)	C(9)-H(9)	1.084(6)
N(3)-C(11)	1.480(4)	C(11)-H(11A)	1.085(6)
N(3)-C(13)	1.482(3)	C(11)-H(11B)	1.076(7)
N(4)-C(10)	1.349(4)	C(12)-H(12A)	1.097(7)
N(4)-C(17)	1.480(3)	C(12)-H(12B)	1.077(7)
N(4)-C(15)	1.481(3)	C(12)-H(12C)	1.090(8)
C(1)-C(3)	1.416(4)	C(13)-H(13A)	1.101(7)
C(2)-C(3)	1.403(4)	C(13)-H(13B)	1.087(7)
C(3)-C(4)	1.439(4)	C(14)-H(14A)	1.079(8)
C(4)-C(5)	1.419(4)	C(14)-H(14B)	1.080(7)
C(4)-C(9)	1.424(4)	C(14)-H(14C)	1.098(7)
C(5)-C(6)	1.390(4)	C(15)-H(15A)	1.079(7)
C(6)-C(7)	1.418(4)	C(15)-H(15B)	1.097(6)
C(7)-C(8)	1.404(4)	C(16)-H(16A)	1.097(7)
C(7)-C(10)	1.464(4)	C(16)-H(16B)	1.092(7)
C(8)-C(9)	1.389(4)	C(16)-H(16C)	1.090(7)
C(11)-C(12)	1.527(4)	C(17)-H(17A)	1.086(7)
C(13)-C(14)	1.529(4)	C(17)-H(17B)	1.084(7)
C(15)-C(16)	1.525(4)	C(18)-H(18A)	1.085(8)
C(17)-C(18)	1.527(4)	C(18)-H(18B)	1.092(7)
C(5)-H(5)	1.080(7)	C(18)-H(18C)	1.085(7)

*Table 4.3.8 - Selected bond angles for the 20K neutron structure of compound **I**.*

Angle	Angle(°)	Angle	Angle(°)
C(10)-N(3)-C(11)	121.1(2)	C(6)-C(5)-C(4)	121.3(3)
C(10)-N(3)-C(13)	122.4(2)	C(5)-C(6)-C(7)	120.5(3)
C(11)-N(3)-C(13)	116.5(2)	C(8)-C(7)-C(6)	118.7(2)
C(10)-N(4)-C(17)	121.4(2)	C(8)-C(7)-C(10)	120.2(3)
C(10)-N(4)-C(15)	121.8(2)	C(6)-C(7)-C(10)	121.2(2)
C(17)-N(4)-C(15)	116.8(2)	C(9)-C(8)-C(7)	121.0(3)
N(1)-C(1)-C(3)	177.5(3)	C(8)-C(9)-C(4)	121.1(3)
N(2)-C(2)-C(3)	176.6(3)	N(3)-C(10)-N(4)	120.9(2)
C(2)-C(3)-C(1)	119.1(2)	N(3)-C(10)-C(7)	120.4(2)
C(2)-C(3)-C(4)	120.3(3)	N(4)-C(10)-C(7)	118.6(2)
C(1)-C(3)-C(4)	120.6(2)	N(3)-C(11)-C(12)	111.5(2)
C(5)-C(4)-C(9)	117.5(2)	N(3)-C(13)-C(14)	111.0(2)
C(5)-C(4)-C(3)	122.1(3)	N(4)-C(15)-C(16)	111.4(2)
C(9)-C(4)-C(3)	120.5(2)	N(4)-C(17)-C(18)	111.2(2)

Despite the detector instabilities present during the experiment, the refinement gives promising results. All statistics imply a good fit of the data to the model. Moreover, although the esds in the geometry are slightly higher than one would normally expect from such a neutron experiment, they still appear to be accurate enough for a charge density study. In particular, the hydrogen atoms are well defined.

The anisotropic displacement parameters are consistently larger than those obtained from the 20K X-ray experiment. This is expected since the neutron experiment used a PSD whereas a single-point counter was used for the 20K X-ray experiment.

All structural features are very similar to the X-ray derived features.

4.3.3 The Multipolar refinement

The corrected data were scaled and merged using the DREAM package (Blessing, 1989) in preparation for the XD (Koritsanszky et al., 1994) refinement. The X-ray derived coordinates and thermal parameters of all atoms were then refined in XD. Once the refinement had converged, a κ' parameter for each atom was introduced. All κ' values relating to non-hydrogen atoms were initially set at 1.0 and refined whereas the κ' value for hydrogen atoms was fixed to the SDS value of 1.16. The results were then combined with the neutron parameters.

The neutron derived coordinates and thermal parameters had been refined using SHELXL-93 (Sheldrick, 1993). The hydrogen coordinates and anisotropic displacement parameters in the XD refinement were replaced by the neutron derived ones. Whilst the coordinates directly substituted the X-ray derived ones, the neutron derived hydrogen thermal parameters had to be scaled with respect to the X-ray ones before substitution. The scaling parameter was derived from the difference between the X-ray and neutron derived non-hydrogen anisotropic displacement parameters according to the formula derived by Blessing (1995):

$$U_X^{ij} = U_N^{ij} + \Delta U^{ij}$$

where $\Delta U^{ij} = \sum_a \left[\sum_a wU_X^{ij} - \sum_a wU_N^{ij} \right] / \sum_a w$

and $w = 1 / \sigma^2$

where $\sigma = \sigma(U_X^{ij} - U_N^{ij}) = [\sigma^2(U_X^{ij} + \sigma^2(U_N^{ij})]^{1/2}$

The scaling parameter was small [-5.40×10^{-4}], thus indicating that there is good agreement between the thermal parameters from the two techniques. The scaling parameter was simply added to all of the hydrogen thermal parameters to give the substituted values. The hydrogen positions and thermal parameters were then fixed in the XD refinement and the remainder were refined. Multipolar terms were then introduced starting with the refinement of Hartree-Fock derived monopoles and dipoles (bond-directed ones for hydrogen atoms) on all atoms. Once converged, quadrupolar and octopolar terms were refined for all non-hydrogen atoms. Refinement at the hexadecapolar level for all non-hydrogen atoms was also tried. However, the population of these functions was negligible [maximum hexadecapolar function population was less than twice its esd] and so were not included in latter refinements.

The κ' parameters were then sub-divided into six values which reflected the different chemical environments in which atoms of a given element resided. The six κ' values represented the six following groups of atoms:

Group 1: All *sp* hybridized nitrogen atoms [N(1) and N(2)].
Group 2: All sp^2 hybridized nitrogen atoms [N(3) and N(4)].
Group 3: All *sp* hybridized carbon atoms [C(1) and C(2)].
Group 4: All sp^2 hybridized carbon atoms [C(3) to C(10)].
Group 5: All sp^3 hybridized carbon atoms [C(11) to C(18)].
Group 6: All hydrogen atoms.

κ' values for the first five groups were refined. The κ' value for group six was constrained to 1.16. κ'' parameters were then refined for each group of atoms except group 6 (here κ'' was fixed at the SDS value of 1.16) such that, for all of the multipoles (l = 0-3), the value of κ'' in each κ group was constrained to have the same value. Final κ' and κ'' values are given in ***Table 4.3.9***

Table 4.3.9 - *Kappa values for each of the six groups of atoms in* ***I***

Group number	κ' value	κ'' value
1	0.985(6)	0.98(5)
2	0.983(7)	0.81(3)
3	1.01(1)	0.92(4)
4	1.010(5)	0.90(1)
5	1.007(6)	0.88(1)
6	1.16	1.16

4.3.4 Results and discussion

A summary of refinement details are given in ***Table 4.3.10*** . Bond distances and selected bond angles are given in ***Tables 4.3.11*** and ***4.3.12***. Fractional coordinates and anisotropic displacement parameters for all non-hydrogen atoms are given in ***Appendix A.4.19*** and ***A.4.20*** respectively. ***Figure 4.3.3*** shows dynamic model maps, $F_{multipole}$-$F_{spherical}$ for the principal molecular fragments, which represent the contribution of the multipolar terms to the model. The corresponding static maps are not given here because they show very little difference since the thermal vibration in the molecule is so small. Residual density maps of the molecule also given in ***Figure 4.3.3***, show featureless regions of only a little residual electron density, thus indicating that the electron distribution is well described by the multipole model. The rigid-bond test, which was applied to all bonds not involving hydrogen during the refinement, was satisfied throughout.

Table 4.3.10 *- A summary of refinement parameters for the charge density study of* ***I****.*

Parameter	Value	Parameter	Value
Scale Factor	0.2484(6)	Weighting Scheme	$1/\sigma^2$
Criterion for observed data	$F = 3\sigma(F)$	$R_w(F)$	0.0334
R(F)	0.0361	$R_w(F^2)$	0.0626
$R(F^2)$	0.0447	GOF_w	1.1089
$R_{all}(F)$	0.1567	Data / Parameter	5143 / 609
$R_{all}(F^2)$	0.0816	$\Delta/\sigma_{(min/max)}$	$0.5x10^{-7}$ / $0.2x10^{-2}$
GOF	1.0647	$\Delta\rho_{(min/max)}$	-0.190 / 0.124

Table 4.3.11 *- Bond distances for* ***I*** *as derived from the charge density study.*

Bond	Distance (Å)	Bond	Distance (Å)
N(1)-C(1)	1.173(2)	C(11)-H(11A)	1.0836(9)
N(2)-C(2)	1.172(2)	C(11)-H(11B)	1.071(1)
N(3)-C(10)	1.343(1)	C(12)-H(12A)	1.098(1)
N(3)-C(11)	1.477(1)	C(12)-H(12B)	1.081(1)
N(3)-C(13)	1.481(1)	C(12)-H(12C)	1.087(1)
N(4)-C(10)	1.346(1)	C(13)-C(14)	1.527(1)
N(4)-C(15)	1.478(1)	C(13)-H(13A)	1.099(1)
N(4)-C(17)	1.481(1)	C(13)-H(13B)	1.087(1)
C(1)-C(3)	1.409(2)	C(14)-H(14A)	1.080(1)
C(2)-C(3)	1.408(2)	C(14)-H(14B)	1.080(1)
C(3)-C(4)	1.443(1)	C(14)-H(14C)	1.101(1)
C(4)-C(5)	1.421(1)	C(15)-C(16)	1.528(1)
C(4)-C(9)	1.421(1)	C(15)-H(15A)	1.081(1)
C(5)-C(6)	1.389(1)	C(15)-H(15B)	1.093(1)
C(5)-H(5)	1.0824(9)	C(16)-H(16A)	1.097(1)
C(6)-C(7)	1.410(1)	C(16)-H(16B)	1.092(1)
C(6)-H(6)	1.092(1)	C(16)-H(16C)	1.089(1)
C(7)-C(8)	1.407(1)	C(17)-C(18)	1.526(1)
C(7)-C(10)	1.467(1)	C(17)-H(17A)	1.087(1)
C(8)-C(9)	1.387(1)	C(17)-H(17B)	1.082(1)
C(8)-H(8)	1.091(1)	C(18)-H(18A)	1.087(1)
C(9)-H(9)	1.087(1)	C(18)-H(18B)	1.089(1)
C(11)-C(12)	1.525(1)	C(18)-H(18C)	1.087(1)

*Table 4.3.12 - Selected bond angles for **I** as derived from the charge density study.*

Angle	Angle(°)	Angle	Angle(°)
C(10)-N(3)-C(11)	121.0(1)	C(6)-C(5)-C(4)	121.2(1)
C(10)-N(3)-C(13)	122.4(1)	C(5)-C(6)-C(7)	120.7(1)
C(11)-N(3)-C(13)	116.4(1)	C(8)-C(7)-C(6)	118.6(1)
C(10)-N(4)-C(17)	121.4(1)	C(8)-C(7)-C(10)	119.8(1)
C(10)-N(4)-C(15)	121.8(1)	C(6)-C(7)-C(10)	121.6(1)
C(17)-N(4)-C(15)	116.8(1)	C(9)-C(8)-C(7)	120.9(1)
N(1)-C(1)-C(3)	177.2(2)	C(8)-C(9)-C(4)	121.1(1)
N(2)-C(2)-C(3)	176.4(2)	N(3)-C(10)-N(4)	121.1(1)
C(2)-C(3)-C(1)	118.8(1)	N(3)-C(10)-C(7)	120.0(1)
C(2)-C(3)-C(4)	120.0(1)	N(4)-C(10)-C(7)	119.0(1)
C(1)-C(3)-C(4)	121.0(1)	N(3)-C(11)-C(12)	111.5(1)
C(5)-C(4)-C(9)	117.4(1)	N(3)-C(13)-C(14)	111.2(1)
C(5)-C(4)-C(3)	122.8(1)	N(4)-C(15)-C(16)	111.4(1)
C(9)-C(4)-C(3)	120.8(1)	N(4)-C(17)-C(18)	111.1(1)

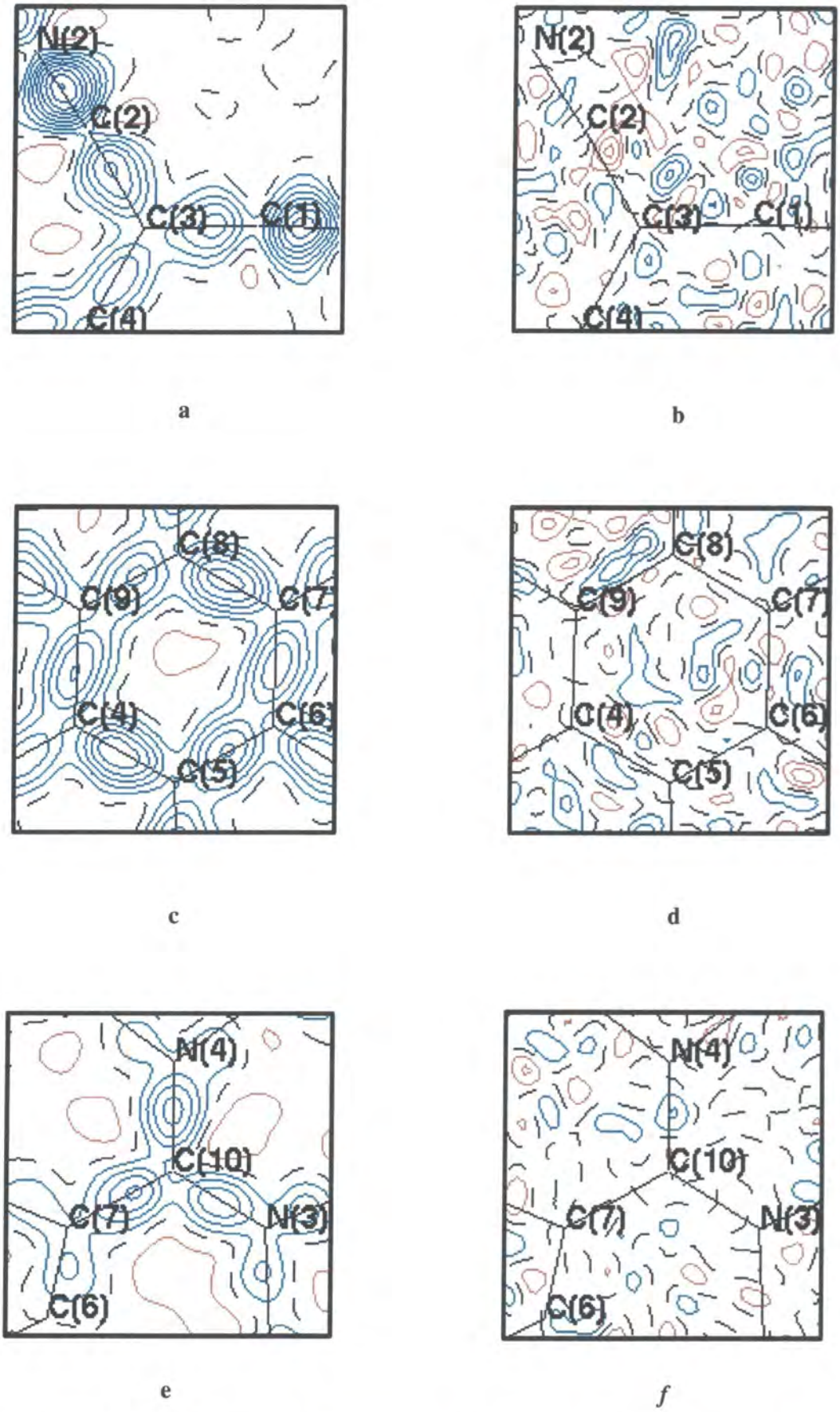

Figure 4.3.3 *– Dynamic and residual maps for the (a / b) nitrile, (c / d) phenyl, (e / f) formally positively charged group in* ***I*** *out to sinθ/λ=0.7A−1 and with contour levels of 0.1 e/A (blue lines are positive, red lines are negative, black lines are zero).*

Since an electroneutrality constraint is applied over the whole asymmetric unit, the extent of charge transfer ensuing in the molecule can be derived wholly from the monopole populations. The charge on a given atom is the difference between the monopole population for this atom, as observed from the charge density study and the number of valence electrons classically present in the atom, e.g. for a carbon atom, the expected monopole population would be four. The charges present on each atom in **I** are given in ***Table 4.3.13.***

Table 4.3.13 *- Pseudoatomic charges for each atom in* ***I****.*

Atom	Charge	Atom	Charge	Atom	Charge
N(1)	-0.2080	C(13)	0.0528	H(13B)	0.0255
N(2)	-0.2357	C(14)	-0.1203	H(14A)	0.0161
N(3)	-0.3249	C(15)	0.0480	H(14B)	0.0002
N(4)	-0.3618	C(16)	-0.0282	H(14C)	0.2013
C(1)	-0.0919	C(17)	0.0775	H(15A)	0.0611
C(2)	-0.1129	C(18)	-0.0320	H(15B)	0.0804
C(3)	-0.0598	H(5)	0.0573	H(16A)	0.0409
C(4)	0.0556	H(6)	0.0781	H(16B)	0.0234
C(5)	0.0355	H(8)	-0.0158	H(16C)	0.0807
C(6)	-0.0402	H(9)	-0.0190	H(17A)	0.0636
C(7)	0.0482	H(11A)	-0.0066	H(17B)	0.0368
C(8)	-0.0130	H(11B)	0.0772	H(18A)	0.0734
C(9)	-0.0183	H(12A)	-0.0475	H(18B)	0.1180
C(10)	0.1390	H(12B)	-0.0142	H(18C)	-0.0104
C(11)	0.0330	H(12C)	0.1718		
C(12)	-0.0007	H(13A)	0.0654		

All values of the derived charges conform to simple electronegativity expectations. The nitrogen atoms appear to dominate the charge transfer through the molecule. The charge transfer is concentrated in two areas: the nitrile group and the area surrounding the formal zwitterionic positive charge. The respective pseudoatom charges of the phenyl ring atoms are small, thus indicating that the delocalized ring charge is fairly localized within the ring.

EDD maps for the planar parts of the molecule are given in ***Figure 4.3.4***. These maps illustrate the nature and extent of the polarization ensuing in the molecule. All critical points and ellipticity values found within the molecule are given in ***Tables 4.3.14*** and ***4.3.15***.

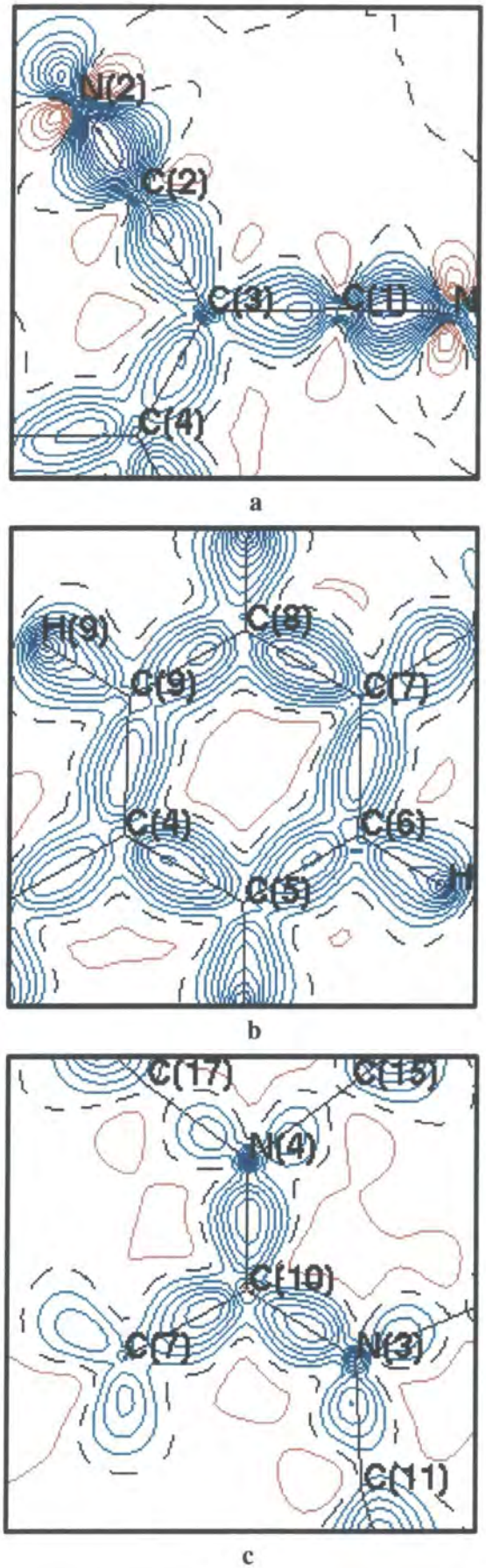

Figure 4.3.4 *– Deformation density maps for the (a) nitrile, (b) phenyl, (c) formally positively charged group in* ***I*** *out to sinθ/λ=2.0A−1 and with contour levels of 0.1 e./A (blue lines are positive, red lines are negative, black lines are zero).*

Table 4.3.14 *- Information regarding all (3, -1) bond critical points located within the molecule of* ***I***

Bond	λ_1	λ_2	λ_3	ρ	$\nabla^2\rho$	ε	R_{ij}	d1	d2
N(1)-C(1)	-27.61	-26.44	32.24	3.279	-21.805	0.04	1.17	0.757	0.416
N(2)-C(2)	-29.03	-28.34	33.53	3.420	-23.851	0.02	1.17	0.758	0.414
N(3)-C(10)	-18.98	-15.52	10.15	2.310	-24.353	0.22	1.34	0.811	0.532
N(3)-C(11)	-11.18	-10.03	11.83	1.645	-9.381	0.11	1.48	0.881	0.596
N(3)-C(13)	-11.65	-10.27	11.69	1.651	-10.231	0.13	1.48	0.877	0.604
N(4)-C(10)	-19.49	-15.17	11.06	2.313	-23.603	0.28	1.35	0.803	0.544
N(4)-C(15)	-10.80	-9.85	12.12	1.592	-8.530	0.10	1.48	0.866	0.612
N(4)-C(17)	-10.15	-9.43	12.07	1.567	-7.516	0.08	1.48	0.876	0.605
C(1)-C(3)	-14.01	-11.32	11.84	1.946	-13.487	0.24	1.41	0.750	0.659
C(2)-C(3)	-14.66	-12.58	11.86	2.012	-15.383	0.17	1.41	0.744	0.663
C(3)-C(4)	-13.48	-11.42	11.26	1.870	-13.636	0.18	1.44	0.729	0.713
C(4)-C(5)	-15.96	-13.71	11.27	2.113	-18.404	0.16	1.42	0.730	0.691
C(4)-C(9)	-14.28	-12.19	11.81	1.994	-14.666	0.17	1.42	0.716	0.705
C(5)-C(6)	-15.60	-13.18	10.57	2.099	-18.208	0.18	1.39	0.674	0.715
C(5)-H(5)	-17.24	-16.08	16.01	1.861	-17.317	0.07	1.08	0.702	0.381
C(6)-C(7)	-15.18	-12.57	11.32	2.034	-16.431	0.21	1.41	0.701	0.709
C(6)-H(6)	-17.33	-15.99	16.94	1.836	-16.371	0.08	1.09	0.723	0.369
C(7)-C(8)	-16.92	-13.86	11.32	2.186	-19.462	0.22	1.41	0.690	0.718
C(7)-C(10)	-12.65	-11.14	10.92	1.791	-12.877	0.14	1.47	0.681	0.787
C(8)-C(9)	-15.15	-12.64	10.91	2.101	-16.874	0.20	1.39	0.726	0.661
C(8)-H(8)	-16.71	-15.29	14.65	1.872	-17.357	0.09	1.09	0.671	0.420
C(9)-H(9)	-16.82	-15.96	16.26	1.883	-16.517	0.05	1.09	0.689	0.398
C(11)-C(12)	-9.95	-9.18	10.89	1.538	-8.244	0.08	1.53	0.792	0.733
C(11)-H(11)	-16.73	-15.94	15.45	1.893	-17.211	0.05	1.08	0.684	0.400
C(11)-H(11)	-16.81	-16.32	16.62	1.853	-16.511	0.03	1.08	0.714	0.367
C(12)-H(12)	-14.85	-13.78	14.45	1.783	-14.170	0.08	1.10	0.667	0.431
C(12)-H(12)	-15.08	-14.32	14.80	1.783	-14.601	0.05	1.08	0.667	0.413
C(12)-H(12)	-15.95	-15.38	16.96	1.728	-14.368	0.04	1.09	0.742	0.345
C(13)-C(14)	-10.59	-10.42	11.31	1.648	-9.698	0.02	1.53	0.792	0.736
C(13)-H(13)	-15.60	-14.64	15.33	1.752	-14.909	0.07	1.10	0.708	0.391
C(13)-H(13)	-16.96	-15.89	15.83	1.866	-17.022	0.07	1.09	0.701	0.387
C(14)-H(14)	-15.35	-14.86	15.47	1.789	-14.736	0.03	1.08	0.683	0.397
C(14)-H(14)	-15.75	-15.54	15.46	1.849	-15.825	0.01	1.08	0.679	0.401
C(14)-H(14)	-14.74	-14.23	16.53	1.610	-12.445	0.04	1.10	0.754	0.347

C(15)-C(16)	-10.72	-10.13	11.20	1.631	-9.648	0.06	1.53	0.792	0.737
C(15)-H(15)	-16.63	-15.28	15.31	1.820	-16.606	0.09	1.08	0.695	0.387
C(15)-H(15)	-16.94	-15.88	16.25	1.837	-16.562	0.07	1.09	0.722	0.372
C(16)-H(16)	-13.51	-12.72	14.17	1.641	-12.057	0.06	1.10	0.675	0.422
C(16)-H(16)	-15.58	-15.39	16.00	1.812	-14.972	0.01	1.09	0.701	0.391
C(16)-H(16)	-15.94	-15.55	15.89	1.805	-15.606	0.02	1.09	0.709	0.380
C(17)-C(18)	-11.02	-9.97	11.09	1.640	-9.898	0.11	1.53	0.765	0.761
C(17)-H(17)	-16.36	-15.70	16.96	1.813	-15.092	0.04	1.09	0.719	0.369
C(17)-H(17)	-15.56	-14.50	15.37	1.766	-14.681	0.07	1.08	0.687	0.395
C(18)-H(18)	-16.28	-16.03	15.26	1.845	-17.046	0.02	1.09	0.700	0.387
C(18)-H(18)	-15.92	-15.44	15.88	1.771	-15.467	0.03	1.09	0.720	0.369
C(18)-H(18)	-15.46	-14.65	13.55	1.835	-16.563	0.05	1.09	0.656	0.432

[R_{ij} is the length of the bond path between the atoms; d1 and d2 represent the distance between the first and second atoms specified in the bond column and the critical point respectively].

Table 4.3.15 - *Information regarding the (3,+1) ring critical point located within the molecule of* ***I***.

Distance (Å) between critical point and atom X						λ_1	λ_2	λ_3	ρ	$\nabla^2\rho$
C(4)	C(5)	C(6)	C(7)	C(8)	C(9)					
1.439	1.399	1.391	1.407	1.395	1.405	-0.28	1.71	2.23	0.1292	3.7

The EDD map in ***Figure 4.3.4a*** illustrates the high level of triple-bonded character in each nitrile group. Corresponding critical points lie noticeably closer to the carbon atom than the nitrogen atom as expected and ellipticity values are small. The nitrogen lone pairs on both N(1) and N(2) can be clearly seen. Electron density in the adjoining C(1)-C(3) and C(2)-C(3) bonds appears to be polarized towards each nitrile group as expected from electronegativity arguments. Corresponding ellipticity values for these bonds are typical for a delocalized π-bonded system, thus indicating that these bonds are strongly conjugated to each nitrile group. Moreover, the C(3)-C(4) bond [$\varepsilon = 0.18$] is conjugated to the phenyl ring, thereby extending the conjugation from the nitrile groups right across the phenyl ring. Given that the structure represents an average of two electronic states, the even spread of delocalized electron density centred around C(3) shows that the time-averaged molecule at 20K is a fairly even mixture of the two states. On observing this, we performed the same BLA calculations as those described in section 4.2, using the geometry derived from this charge-density study. The resulting value of the percentage of quinoidal character, X_S, was 37(1)%, i.e. 10% more quinoidal than that observed for the molecule at 150K and corresponding to a fairly

even mix of the two states. It also shows that the quinoidal form is slightly more energetically favourable that the zwitterionic state.

The EDD map of the phenyl ring shows that the zwitterionic (aromatic) form is more favoured over the quinoidal form. All bonds have very similar concentrations of electron density. Relevant ellipticity values are typical for phenyl ring bonds. However, the ellipticity values corresponding to the bonds, C(4)-C(5) and C(4)-C(9), are slightly lower than those of other bonds in the phenyl ring. Presumably, this slight diminution in π-bonding is a simply a consequence of the conjugation with the C(3) atom. All C-C bond critical points lie at the centres of each respective bond. A (3,+1) critical point was located at the centre of the ring. The corresponding local depletion of charge at this centre is typical for such an environment.

In common with the C(3) site, there is quite a lot of π electron density surrounding the C(10) atom, judging by the ellipticity values. The ellipticity value for the bond, C(7)-C(10), implies that C(10) is conjugated with the phenyl ring. This conjugation represents the fair degree of the quinoidal state present in the time-averaged molecule. The slightly higher ellipticity values for the N(3)-C(10) and N(4)-C(10) bonds and the very high level of local charge concentration in these bonds, as deduced from the $-\nabla^2\rho$ values, indicate that N(3) and N(4) are involved in stabilising the formal postive charge in the zwitterionic form.

In summary, conjugation is seen to exist throughout all of the planar component of the molecule. This shows that there is a fair mixture of the quinoidal and zwitterionic states in the time-averaged molecule at 20K. BLA calculations indicate that the ratio is about 4:6 in favour of the zwitterionic form at this temperature. This fairly even mixture must enhance the SHG output microscopically since it corresponds to a BLA value close to the optimum value of zero.

4.3.5 Calculations of the dipole moment and the linear polarizability coefficients from the charge density results.

The methods for calculating the dipole moment and the linear polarizability coefficients are given in chapter 3. The determined values are given in ***Table 4.3.16*** along with the calculated values of the respective quadrupolar moments. Literature values of these quantities are commonly given in a variety of units so we chose to use the recommended SI units.

Table 4.3.16 *- Values of the dipolar and quadrupolar moments and the linear polarizability tensorial coefficients of* ***I****.*

Dipolar moment (x 10^{-30} Cm)		Quadrupolar moments (x 10^{-39} Cm^2)		Polarizability coefficients (x 10^{-39} C)	
p_x	-24.02	Θ_{xx}	-61.10	$\lvert\alpha_{xx}\rvert$	1222.95
p_y	-36.69	Θ_{yy}	-150.94	$\lvert\alpha_{yy}\rvert$	7464.23
p_z	76.39	Θ_{zz}	15.20	$\lvert\alpha_{zz}\rvert$	75.70
		Θ_{xy}	-108.37	α_{xy}	7611.73
$\lvert p_{total}\rvert$	88.06	Θ_{xz}	126.60	α_{xz}	4299.17
		Θ_{yz}	187.81	α_{yz}	7380.33

The overall value for the dipole moment is very large compared to the series of such values determined from various molecules by Spackman (1992). This is expected because of the highly charged nitrogen atoms and the extensive level of conjugation throughout the plane of the molecule. The value compares well to those detemined for **I** in the gas phase (33.36 x 10^{-30} Cm) and the liquid phase (66.71 x 10^{-30} Cm) by Philip Thomas from the Physics Department at the University of Durham. The value increases from the gas phase through to the solid state presumably because of the increasing effect of intermolecular interactions. ***Figure 4.3.5*** shows that the dipole moment projects from the molecular centre of mass along the vector which bisects the two amino groups. This directionality is very interesting since it corresponds to that which one would associate with the quinoidal state of the molecule, even though we have seen previously that the zwitterionic form (where the direction of the dipole would be reversed by 180°) is the slightly more common time-averaged state. The noticeably higher charge on the amino nitrogen atoms compared to that on the nitrogen atoms in the nitrile group (see ***Table 4.3.13***) is thought to tip the directional balance in favour of the quinoidal form since the charge of the molecule is principally dominated by the nitrogen atoms. The directionality of the dipole moment could not be determined from the gas-phase and liquid state calculations.

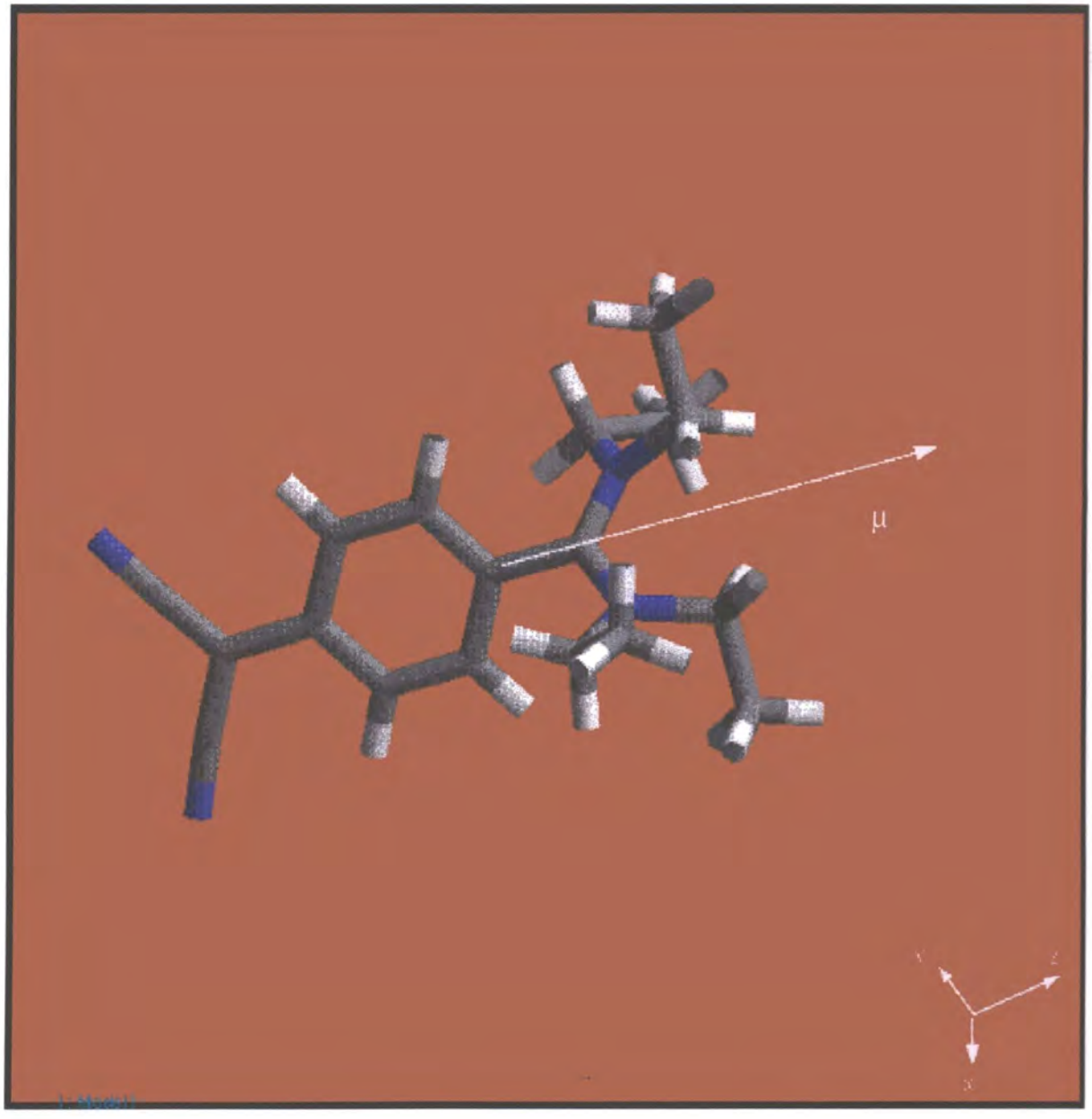

Figure 4.3.5 *– The direction of the dipole moment in* ***I****.*

The quadrupolar moments are on average three orders of magnitude greater than the series of quadrupolar values determined from various molecules by Spackman (1992). Given that the calculation of the polarizability coefficient simply involves constants and the squaring of the relevant quadrupolar moment(s), the corresponding linear polarizability coefficients must also be several orders of magnitude larger than one might usually find. Since so few reports of the polarizability coefficients, as derived from charge density studies, have been made, we cannot yet make a detailed comparison between our results and those obtained for compounds from other multipolar refinements. A large anisotropy of the linear polarizability is evident from the results. The $|\alpha_{xx}|$ and $|\alpha_{zz}|$ values are much smaller than the other polarizability coefficients and all three coefficients involving a y-component are by far the largest. This directionality is slightly surprising since, although we would instinctively think that the α_{yz} coefficient would be very large since this coefficient most closely corresponds to the direction of the molecular axis, the xy and yy planes approximately 45° to this axis. As a result, we wish to evaluate the linear polarizability coefficients by another means so that we can fully understand this anisotropy.

Further calculations are presently underway to try and determine the octopolar moments and therefore be able to evaluate values for the first hyperpolarizability coefficients in a similar manner to that used in determining the polarizability coefficients.

4.4 THE ATTEMPTED NEUTRON STRUCTURAL DETERMINATION OF COMPOUND III

Several attempts were made to obtain a neutron structure of **III**. However, despite measuring different batches of crystals, at different temperatures[#] and at different neutron sources, no useful results prevailed. Details of the attempts are summarized below:

(1) The first attempt used the instrument D9 at the ILL. One seeded and one unseeded crystal batch were available. A crystal (dimensions 5.5 x 0.8 x 0.25 mm) was chosen from the unseeded batch and placed on the instrument. A UB matrix was obtained and the sample was set to cool to 20K. However, at about 120K, the crystal split. A second crystal (dimensions 0.7 x 0.3 x 0.25 mm) was selected, this time from the seeded batch, and was similarly investigated. Again, the crystal indexed and the sample was set to cool to 20K. This crystal also broke up on cooling, this time at 250K. A third crystal (0.6 x 3.3 x 0.2 mm) was selected (from the unseeded batch). Here, however, we could not obtain a UB matrix and the reflection profiles were already poor at room temperature. This investigation was therefore concluded.

(2) The second attempt was made on SXD at ISIS. A new batch of crystals had been grown for the experiment. However, although these were of good quality, they were small. The chosen crystal (3.0 x 0.5 x 0.1 mm) was mounted and placed on the instrument. On cooling, the peaks became broader but no more than one distinct peak was observed. We initially supposed that the increase in the peak width was simply due to the effect of the peak shifting in position with temperature whilst continuously accumulating neutron counts. Therefore, once the sample was at 20K, two runs (at χ = 0; ϕ = 0° and 120° and at a rate of 1500μAmphrs) were performed. Whilst the first run gave reasonable peak profiles, the second run showed that the peaks were in fact split. Hence, the sample was warmed up and the investigation concluded.

(3) The third attempt was made again on D9 at the ILL. A further new batch of crystals had been grown and because of the previous problems of crystals splitting during cooling, we proposed to carry out this experiment at room temperature. Although this is not generally desirable for a charge density study (Angermund, Claus, Goddard & Krüger, 1985), the presence of hydrogen-bonding within the lattice made the study potentially feasible for a successful charge density analysis (Toriumi & Saito, 1983). A crystal (4.0 x 0.75 x 0.2 mm) was selected, mounted onto a vanadium pin and placed upon the instrument. Once centred, peaks were sought and then indexed. The intensity

[#] The complementary charge density X-ray experiment had not been collected prior to any of these attempts to obtain a neutron structure. Hence, one could quite freely choose a temperature.

of the peaks was low due to the prominent thermal effects present at 297K. However, it was decided to proceed with a data collection. A total of 1974 reflections were measured over four days. The resulting data were processed and duly corrected. However, the overall intensity of the data was too low to yield any sensibly refined model.

4.5 CONCLUSIONS

A bond-length alternation study on a series of tetracyanoquinodimethane derivatives has been made. Results show that the time-averaged level of quinoidal / zwitterionic character present varies between each compound. From the analysis of this variation, several molecular features which strongly affect this variation are pin-pointed.

The charge density study on one of these compounds, **I**, shows a well-fitted model. The results show that there is a fair mix of the two electronic states. Moreover, BLA calculations, using the charge density derived bond geometry, show that the ratio of quinoidal : zwitterionic character at 20K is about 10% greater than that at 150K. This indicates that the quinoidal state is slightly more energetically favourable than the zwitterionic form. The dipole moment compares very well with the previously determined gas-phase and liquid state calculations and was found to lie along the molecular axis projecting from the centre of mass towards the amino groups. The values for the quadrupolar moments and the related linear polarizability coefficients are very large compared to results previously reported in the literature (Spackman, 1992). The anisotropy of these coefficients is not completely understood. Therefore, the determination of quadrupolar moments by other means is the subject of future work.

4.6 REFERENCES

Allen, F. H., Brammer, L., Kennard, O., Orpen, A. G., Taylor, R. & Watson, D. G. (1987). *J. Chem. Soc., Perkin Trans. II*, S1-S19.

Angermund, K., Claus, K. H., Goddard, R. & Krüger, C. (1985). *Angew. Chem. Int. Ed. Engl.*, **24**, 237-247.

Blessing, R. H. (1989). J. Appl. Cryst., **22**, 396-397.

Bondi, A. (1964). *J. Phys. Chem.*, **64**, 441-451.

Cole, J. C., Howard, J. A. K., Cross, G. H. & Szablewski, M. (1995). *Acta Crystallogr.* **C51**, 715.

Copley, R. C. B., Goeta, A. E., Lehmann, C. W., Cole, J. C., Yufit, D. S., Howard, J. A. K. & Archer, J. M. (1997). J. Appl. Cryst., **30**, 413-417.

Coppens, P. (1970). DATAP. *The Evaluation of Absorption and Extinction in Single-Crystal Structure Analysis* in "Crystallographic Computing", Ed. Ahmed, F. R., (Munksgaard, Copenhagen).

Filhol, A. (1987). Institut Laue Langevin Technical Report, 87FT19T.

Hertler, W., R., Hartzler, H. D., Acker, D. S. & Benson, R. E. (1962). *J. Am. Chem. Soc.*, **84**, 3387.

International Tables for Crystallography, Volume C, Mathematical, Physical and Chemical Tables (1992). Ed. Wilson, A. J. C., Dordrecht, Boston, London. Tables 4.2.6.8 & 6.1.1.4. 219-222, 500-503.

Long, R. E., Sparks, R. A. & Trueblood, K. N. (1965). *Acta Crystallogr.* **18**, 932-939.

Marder, S. R., Cheng, L-T., Tiemann, B. G., Friedli, A. C., Blanchard-Desce, M., Perry, J. W. & Skindhøj, J. (1994). *Science*, **263**, 511-514.

Marder, S. R. & Perry, J. W. (1993). *Adv. Mater.*, **5**, 804-815.

Oxford Molecular (1994). NEMESIS Version 2.0. Oxford Molecular Ltd. The Magdalen Centre, Oxford Science Park, Oxford, OX4 4GA.

Sheldrick, G. M. (1990). *Acta Crystallogr.* **A46**, 467-473.

Sheldrick, G. M. (1993). SHELXL-93. *Program for the Refinement of Crystal Structures using Single Crystal Diffraction Data*, University of Göttingen, Germany.

Siemens Analytical X-ray Instruments, (1995a). ASTRO. Version 4.050. Siemens Analytical X-ray Instruments, Inc., Madison, Wisconsin, U.S.A.

Siemens Analytical X-ray Instruments, (1995b). SAINT. Version 4.050. Siemens Analytical X-ray Instruments, Inc., Madison, Wisconsin, U.S.A.

Szablewski, M. (1994). *J. Org. Chem.*, **59**, 954.

Taylor, R. & Kennard, O. (1982). J. Am. Chem. Soc., **104**, 5061-5070.

Taylor, R. & Kennard, O. (1983). *Acta Crystallogr.* **B39**, 517-525.

Taylor, R. & Kennard, O. (1985). *Acta Crystallogr.* **A41**, 85-89.

Taylor, R. & Kennard, O. (1986). *J. Chem. Inf. Comp. Sci.*, **26**, 28.

Toriumi, K. & Saito, Y. (1983). Adv. Inorg. Chem. Radiochem., **27**, 27.

Wilkinson, C., Khamis, H. W., Stansfield, R. F. D. & McIntyre, G. J. (1988). J. Appl. Cryst., **21**, 471-478.

CHAPTER 5

METHYL- NITROPYRIDINES AND NITROANILINES

5.1 INTRODUCTION

In chapter 1, we saw that certain structural features of a compound must be present if a good SHG output is to be obtained. On a *molecular* scale, the extent of charge transfer is assumed to dominate the SHG output. Charge transfer is maximised when there are significant:

- Donor-Acceptor (D-A) interactions
- Conjugation (and hence, planarity)
- Aromaticity
- Transition Dipoles

On a *macroscopic* scale, a high SHG output requires:

- Non-centrosymmetry
- Strong intermolecular interactions
- Good phase-matching ability

As stated previously, β and $\chi^{(2)}$ are the parameters which quantify the SHG effect on the molecular and macroscopic scale respectively. Hence, optimizing the charge transfer in a compound will optimize β and $\chi^{(2)}$ will be at a maximum when the three macroscopic features given above are optimal.

In an attempt to find the best organic SHG materials, molecules have been engineered which contain as many of these important features as possible. The classical combination of donor-acceptor groups (where D = Me and A = NO_2) placed at either end of a conjugated organic system and including an aromatic moiety, has shown particular success in methyl- nitropyridine (Twieg, Azema, Jain & Cheng, 1982) and methyl-nitroaniline derivatives (Tsunekawa, Gotoh & Iwamoto, 1990). One methyl-nitropyridine derivative, 5-nitro-2-{[1-phenylethyl]-amino}pyridine (more commonly known as methylbenzylamino-nitropyridine, hereafter MBANP) was found to exhibit an SHG output of 25 times that of urea (Twieg, Azema, Jain & Cheng, 1982) and one methyl- nitroaniline, 4-nitro-4'-methylbenzylidene aniline (hereafter NMBA) was shown to exhibit a similar SHG output, although its exact value is in dispute (Bailey et al, 1993).

The 295K X-ray derived structure of MBANP was reported, first in 1986 (Twieg & Dirk, 1986) and then again in 1988 (Kondo et al, 1988). The molecule crystallizes in the non-centrosymmetric space group, $P2_1$ and its three-dimensional packing is dictated by hydrogen-bonding. Both of these features are largely responsible for the high value of $\chi^{(2)}$. However, the third principal factor affecting the value of $\chi^{(2)}$, the phase-matching

ability, is not so optimal. The phase-matching angle, θ_{PM}, i.e. the angle between the charge transfer axis[+] of the molecule and the screw axis that generates the herringbone structure is 34° (Bailey, Cruickshank, Pavlides, Pugh & Sherwood, 1991). This does not compare very well with the optimum value of 54.74°, as derived by Oudar & Zyss (1982).

In view of this poor phase-matching ability, a similar derivative, 3,5-dinitro-2-{[1-phenylethyl]-amino}pyridine (more commonly known as methylbenzylamino-dinitropyridine, hereafter MBADNP) was synthesized and characterized in an attempt to retain all of the attributes of MBANP whilst improving on its phase-matching ability. This work is described in this chapter together with the determination of the room temperature and low temperature X-ray structures of MBANP. The neutron structures of MBANP and MBADNP were also determined in order to investigate the nature of the hydrogen-bonding and to relate the structural effects with the surprising NLO results. The neutron results were then used in combination with accurate low temperature X-ray data for charge density studies.

The X-ray derived structure of NMBA was first reported in 1977 (Ponomarev et al, 1977). Two forms of NMBA were found to exist: a triclinic form and a monoclinic form. Whilst both polymorphs can be crystallized from different solvents, the monoclinic form can be converted into the triclinic form via a reversible phase transition at 338 ± 5°K. It is the monoclinic form of NMBA which is responsible for the compound's SHG activity since it is non-centrosymmetric (Pc) whereas the triclinic polymorph is centrosymmetric (P-1).

Despite the large SHG value of NMBA, no details of the hydrogen-bonding have been reported in either form and the phase-matching angle of the monoclinic form is a far from optimal 72.88°. We were therefore keen to establish whether there really were any hydrogen-bond contacts present within the lattice which simply had not been reported or whether an unexpected 'third party' was responsible for the large macroscopic $\chi^{(2)}$ value.

A 20K neutron study of NMBA was therefore carried out in order to ascertain whether or not any hydrogen-bonding was present within the lattice. The low temperature was chosen for this study so that the data could also be used in combination with a complementary 20K X-ray data set for charge density analysis.

[+] This is defined as the resultant polarization vector caused by charge transfer.

5.2 THE 20K, 100K AND 295K X-RAY STRUCTURES OF MBANP

Although the 295K X-ray structure of MBANP had already been reported (Twieg & Dirk, 1986; Kondo et al, 1988) no low temperature studies had been performed. Hence, the 100K and 20K X-ray structures were determined in order to (a) determine the hydrogen-bonding more accurately; (b) to assess how strongly thermal factors affected the non-bonded interactions; (c) check for any anomalous thermal effects and (c) check for the existence of any phase-transition. The 295K X-ray structure of MBANP was also redetermined using the same crystal and instrument as that used for the 100K study, so that we could make a more direct comparison of the structure at different temperatures than would be possible from the literature sources.

5.2.1 Experimental

The 100K and 295K X-ray structures were determined using the Rigaku AFC6S diffractometer. The same crystal was used for the structural determination at both temperatures. Cu Kα X-radiation was employed since the crystal diffracted weakly. Conventional experimental and data reduction procedures, as described in chapter 2, were followed throughout.

The 20K X-ray structure of MBANP was determined using the Fddd cryodiffractometer (Copley et al, 1997). A different crystal to the one used for the 100K and 295K structural determinations had to be used for this experiment since the focusing limit cross-section of the cryodiffractometer beam is 0.3 mm in diameter. Mo Kα X-radiation, obtained using an 18kW rotating anode generator, was employed. Conventional experimental and data reduction procedures (see chapter 2), using MAD (Barthelemy, 1984) and COLL5N (Lehmann & Wilson, 1987) software respectively and CAMAC electronics, were followed throughout.

A φ-scan absorption correction (North, Phillips, Mathews, 1968) was applied to the 100K and 295K data [Tmin/max = 0.612 / 1.000 (100K); 0.5992 / 1.0000 (295K)]. The structure was solved by direct methods using SHELXS-86 (Sheldrick, 1990) and refined by full-matrix least-squares methods on F^2 using SHELXL-93 (Sheldrick, 1993). Atomic scattering factors were taken from International Tables for Crystallography, Volume C, Mathematical, Physical and Chemical Tables (1992). An isotropic extinction correction was applied during the refinement of the 100K and 295K structures [the parameter, EXTI = 0.31(4) (100K); 0.28(4) (295K)].

Positional and anisotropic displacement parameters were refined for all non-hydrogen atoms. In the 100K and 295K structural refinements, idealized geometry was employed

for all hydrogen positional parameters whilst these parameters were fully refined in the 20K structural refinement. In all cases, hydrogen thermal parameters were fixed at $1.2U_{eq}$ of the ligated carbon atoms. A summary of crystal, data collection and refinement parameters for each structure is given in ***Table 5.2.1***.

Table 5.2.1 *- A summary of crystal, data collection and refinement parameters for the 20K, 100K and 295K X-ray structures of MBANP.*

Compound	MBANP(20K)	MBANP(100K)	MBANP(295K)
Molecular Formula	$C_{13}H_{13}N_3O_2$	$C_{13}H_{13}N_3O_2$	$C_{13}H_{13}N_3O_2$
Formula weight	243.26	243.26	243.26
a(Å)	5.321(1)	5.324(1)	5.394(1)
b(Å)	6.293(1)	6.317(1)	6.380(1)
c(Å)	17.650(4)	17.726(4)	17.953(4)
α(°)	90	90	90
β(°)	93.65(3)	93.59(3)	94.72(3)
γ(°)	90	90	90
Cell Volume(Å^3)	589.8(2)	595.0(2)	615.7(2)
Crystal System	monoclinic	monoclinic	monoclinic
Space Group	P2(1)	P2(1)	P2(1)
Z	2	2	2
Calculated Density (gcm^{-1})	1.370	1.358	1.312
Temperature (K)	20.0(1)	100(2)	295(2)
Wavelength (Å)	0.71073	1.54178	1.54178
Absorption coefficient (mm^{-1})	0.095	0.775	0.748
Crystal Morphology	plate	plate	plate
Crystal Colour	yellow	yellow	yellow
Crystal Size (mm)	0.36 x 0.32 x 0.08	5.0 x 2.5 x 0.1	5.0 x 2.5 x 0.1
Total number of reflections	3221	1251	1283
Unique reflections	2532	1128	1163
Observed Reflections [I>2σ(I)]	2102	1112	1110
R_{int}	0.0286	0.1705	0.1447
θ range (°)	3.44 - 32.06	5.00 - 75.10	4.94 - 74.97
Data / Parameters	2509 / 202	1127 / 164	1163 / 164
R1 [I > 2σ(I)]	0.0610	0.0893	0.0836
wR2 [I > 2σ(I)]	0.1376	0.2269	0.2327
Goodness of fit on F^2	1.062	1.061	1.082
Weighting Scheme	a = 0.0482; b = 1.2660	a = 0.2147; b = 0.1034	a = 0.2037; b = 0.0662
Absolute structure parameter	1(2)	0.7(6)	1.0(8)
$\Delta\rho_{(max, min)}$ (eÅ^{-3})	0.565 / -0.495	0.498 / -0.621	0.320 / -0.372

5.2.2 Structural Details

50% probability thermal ellipsoid plots of the 20K, 100K and 295K X-ray structures of MBANP are shown in ***Figures 5.2.1***, ***5.2.2*** and ***5.2.3*** respectively. Bond distances and selected bond angles are given in ***Tables 5.2.2*** and ***5.2.3***. Fractional coordinates and anisotropic displacement parameters are given in ***Appendix A.5.1 - A.5.6***.

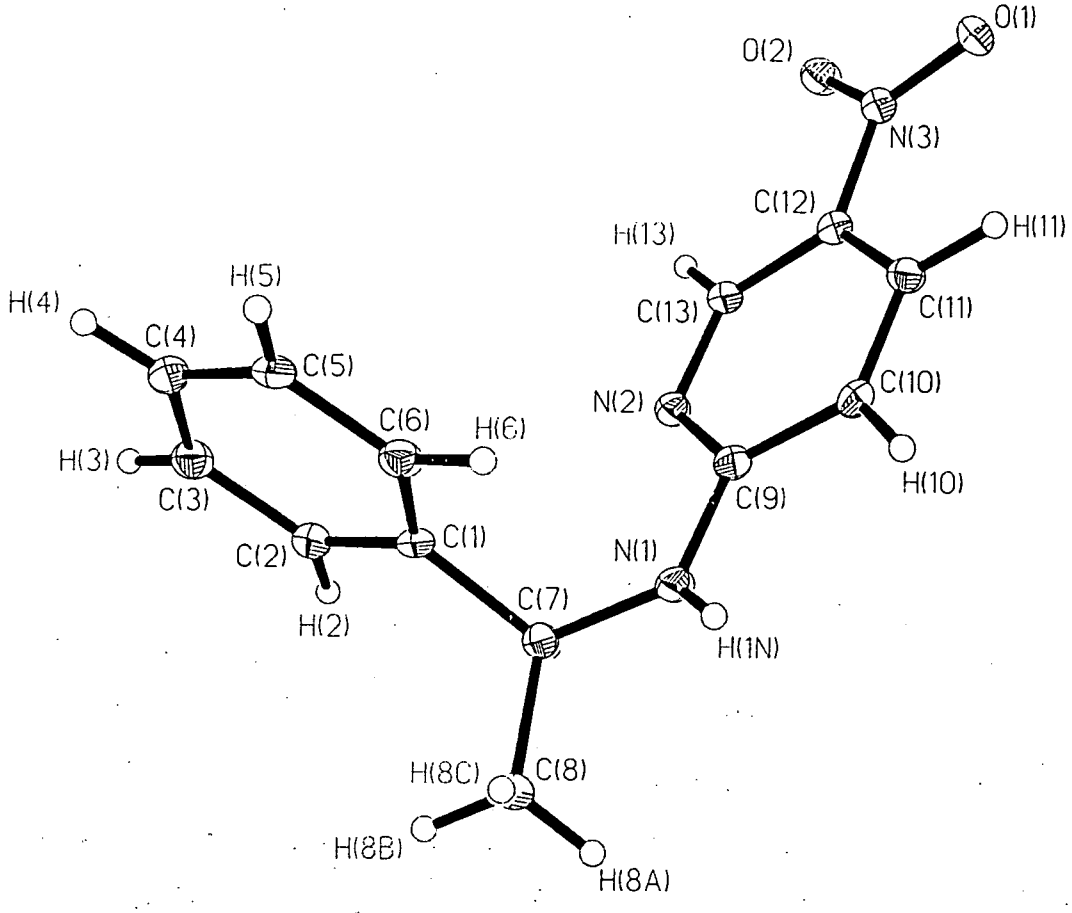

Figure 5.2.1 *- A 50% probability thermal ellipsoid plot of the 20K X-ray structure of MBANP.*

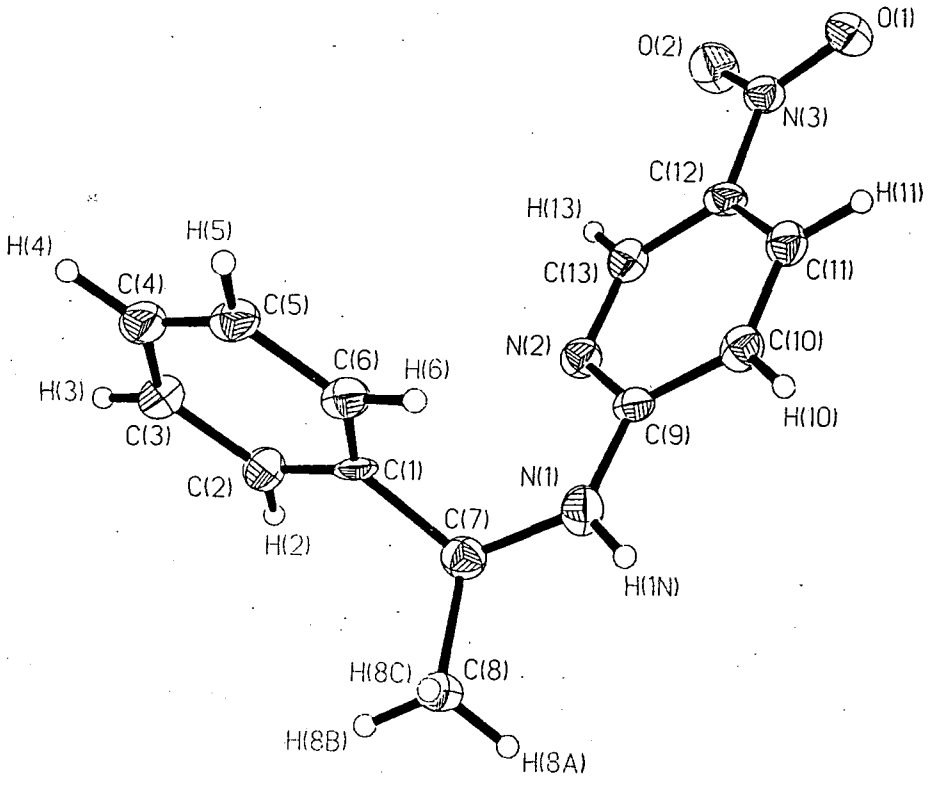

Figure 5.2.2 *- A 50% probability thermal ellipsoid plot of the 100K X-ray structure of MBANP.*

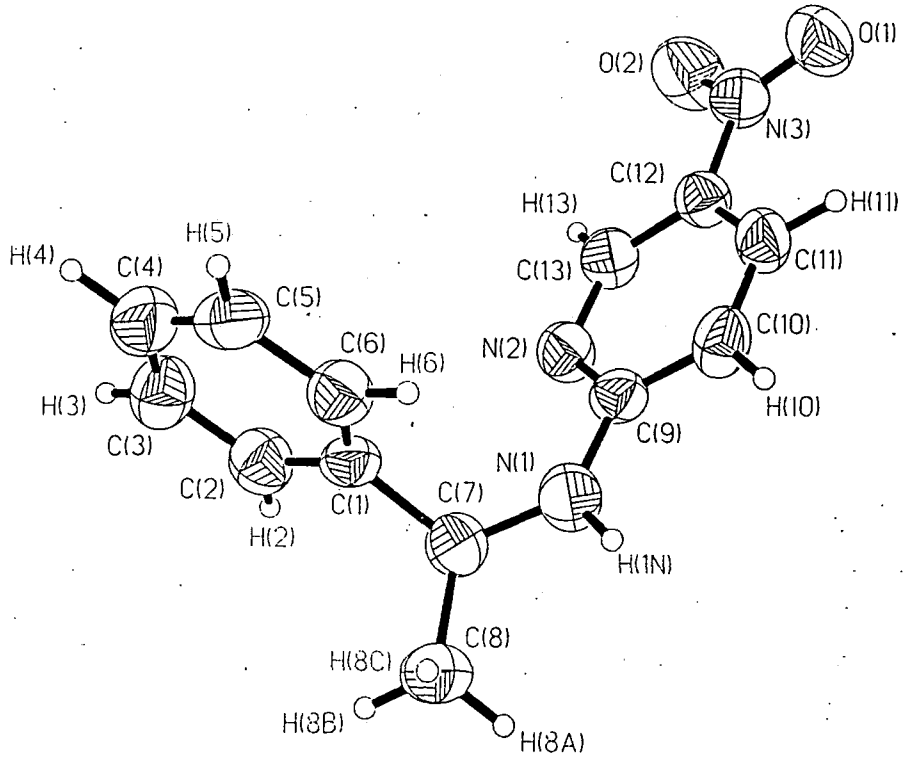

Figure 5.2.3 *- A 50% probability thermal ellipsoid plot of the 295K X-ray structure of MBANP.*

Table 5.2.2 *- Bond lengths of the 20K, 100K and 295K X-ray structures of MBANP.*

Bond	Distance (Å) at 20K	Distance (Å) at 100K	Distance (Å) at 295K
O(1)-N(3)	1.235(4)	1.227(5)	1.212(5)
O(2)-N(3)	1.246(4)	1.230(4)	1.227(5)
N(1)-C(9)	1.350(5)	1.353(7)	1.354(6)
N(1)-C(7)	1.453(4)	1.459(5)	1.445(5)
N(1)-H(1N)	0.74(5)	0.90	0.90
N(2)-C(13)	1.337(5)	1.330(7)	1.336(7)
N(2)-C(9)	1.357(4)	1.359(5)	1.354(5)
N(3)-C(12)	1.443(5)	1.440(7)	1.439(6)
C(1)-C(2)	1.393(5)	1.399(5)	1.388(6)
C(1)-C(6)	1.395(5)	1.368(6)	1.369(7)
C(1)-C(7)	1.523(5)	1.539(6)	1.536(6)
C(2)-C(3)	1.397(5)	1.403(6)	1.387(7)
C(2)-H(2)	1.05(5)	0.96	0.96
C(3)-C(4)	1.374(5)	1.392(7)	1.373(9)
C(3)-H(3)	1.00(4)	0.96	0.96
C(4)-C(5)	1.395(5)	1.387(5)	1.376(7)
C(4)-H(4)	0.92(5)	0.96	0.96
C(5)-C(6)	1.390(5)	1.401(6)	1.403(6)
C(5)-H(5)	0.95(5)	0.96	0.96
C(6)-H(6)	0.99(4)	0.96	0.96
C(7)-C(8)	1.526(5)	1.524(8)	1.531(8)
C(7)-H(7)	1.10(4)	0.96	0.96
C(8)-H(8A)	0.95(5)	0.96	0.96
C(8)-H(8B)	1.02(5)	0.96	0.96
C(8)-H(8C)	1.00(4)	0.96	0.96
C(9)-C(10)	1.419(4)	1.429(5)	1.411(6)
C(10)-C(11)	1.371(5)	1.350(8)	1.358(7)
C(10)-H(10)	1.01(5)	0.96	0.96
C(11)-C(12)	1.403(5)	1.400(6)	1.388(6)
C(11)-H(11)	1.03(4)	0.96	0.96
C(12)-C(13)	1.378(4)	1.397(6)	1.390(6)
C(13)-H(13)	0.95(4)	0.96	0.96

Table 5.2.3 *- Selected bond angles of the 20K, 100K and 295K X-ray structures of MBANP.*

Angle	Angle (°) at 20K	Angle (°) at 100K	Angle (°) at 295K
C(9)-N(1)-C(7)	124.0(3)	123.7(3)	124.1(4)
C(9)-N(1)-H(1N)	114(4)	118.3(2)	118.0(2)
C(7)-N(1)-H(1N)	122(4)	118.0(3)	117.9(2)
C(13)-N(2)-C(9)	117.0(3)	117.1(3)	116.8(4)
O(1)-N(3)-O(2)	123.0(3)	121.5(4)	122.0(5)
O(1)-N(3)-C(12)	118.5(3)	119.3(3)	119.6(4)
O(2)-N(3)-C(12)	118.5(3)	119.1(4)	118.4(4)
C(2)-C(1)-C(7)	118.7(3)	117.4(4)	118.6(4)
C(6)-C(1)-C(7)	122.0(3)	121.1(3)	121.2(4)
N(1)-C(7)-C(1)	112.6(3)	112.7(4)	113.3(4)
N(1)-C(7)-C(8)	108.8(3)	108.6(3)	108.6(4)
C(1)-C(7)-C(8)	109.5(3)	110.2(3)	109.9(3)
N(1)-C(9)-N(2)	117.7(3)	117.3(4)	117.2(4)
N(1)-C(9)-C(10)	119.6(3)	120.0(3)	120.2(4)
C(13)-C(12)-N(3)	119.7(3)	119.7(4)	120.7(4)
C(11)-C(12)-N(3)	120.0(3)	120.6(4)	120.0(4)

The absolute structure parameters (Flack, 1983) given in ***Table 5.2.1*** show that the absolute configuration of MBANP could not be determined reliably using the X-ray data. Fortunately, however, the absolute configuration of the chiral centre in the starting material, (S)-1-phenylethylamine (which is carried through in the synthesis) was known *a priori* (Cruickshank, 1997). The X-ray structures were therefore refined according to this configuration.

All bond lengths and angles are very similar to the literature source values (Twieg & Dirk, 1986; Kondo et al, 1988) and the geometrical uncertainties reported here are smaller than those reported by Kondo et al, 1988 and are similar to those reported by Twieg & Dirk, 1986. The bond lengths and angles are slightly effected by temperature.

The vibrational parameters increase linearly with temperature as expected. However, the rate of linear increase in thermal motion with temperature is not entirely uniform as one would expect if the molecule vibrated in a purely concerted fashion. Plots of each principal anisotropic displacement parameter against temperature for each atom (***Figures 5.2.4-5.2.6***) show that O(1), O(2), C(3), C(4), C(5) and C(8) are librating slightly. This is not so surprising since O(1), O(2) and C(8) are terminal atoms and C(3), C(4)

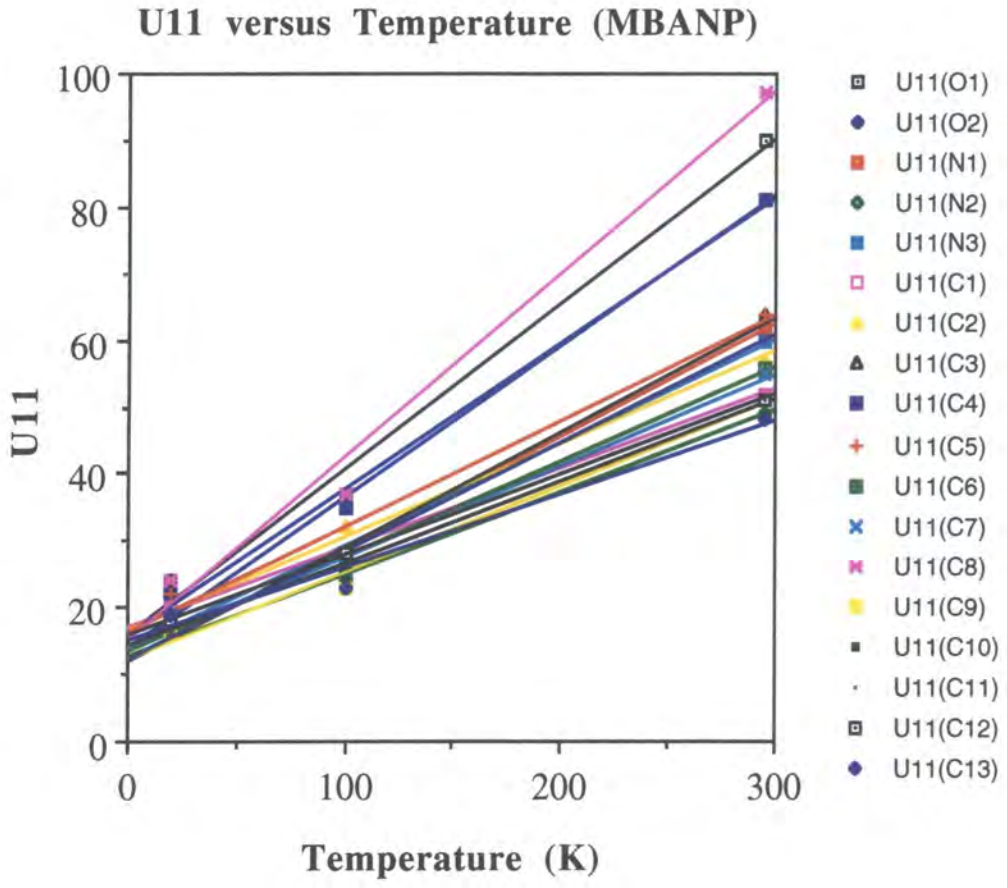

Figure 5.2.4 *- Plots of the anisotropic displacement parameter, U11, versus temperature for each non-hydrogen atom in MBANP.*

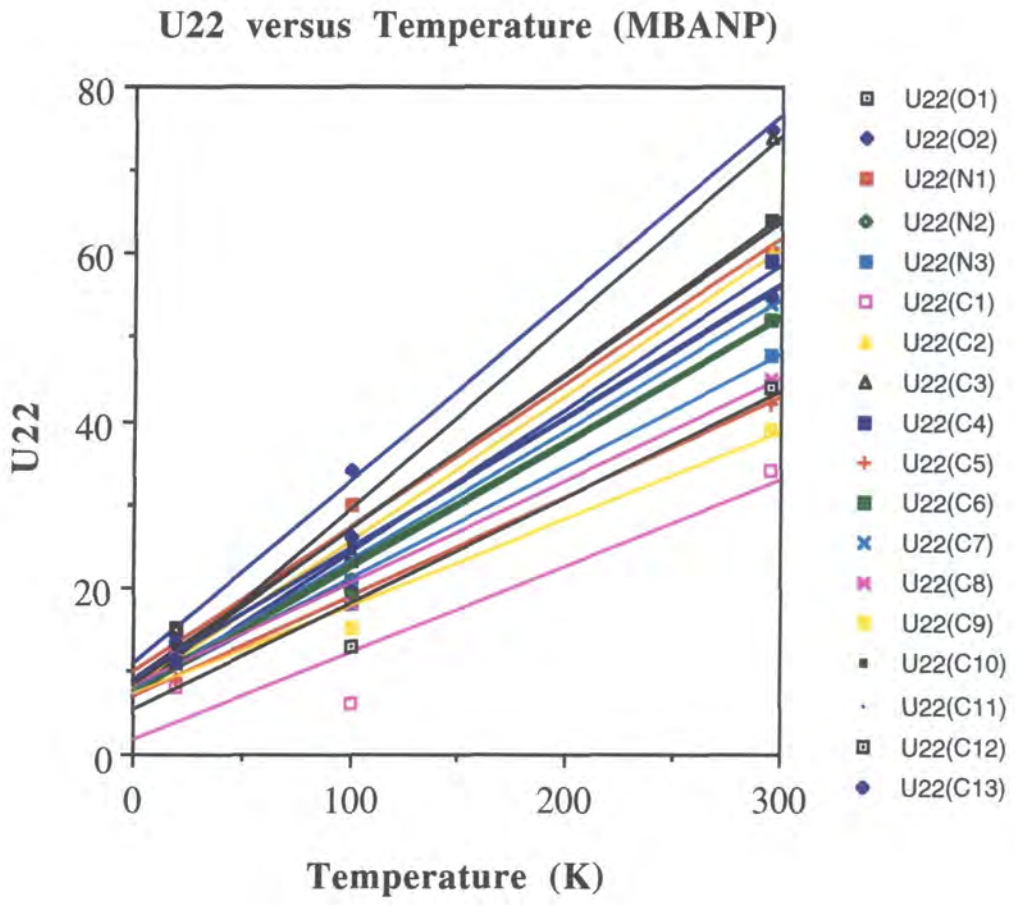

Figure 5.2.5 *- Plots of the anisotropic displacement parameter, U22, versus temperature for each non-hydrogen atom in MBANP.*

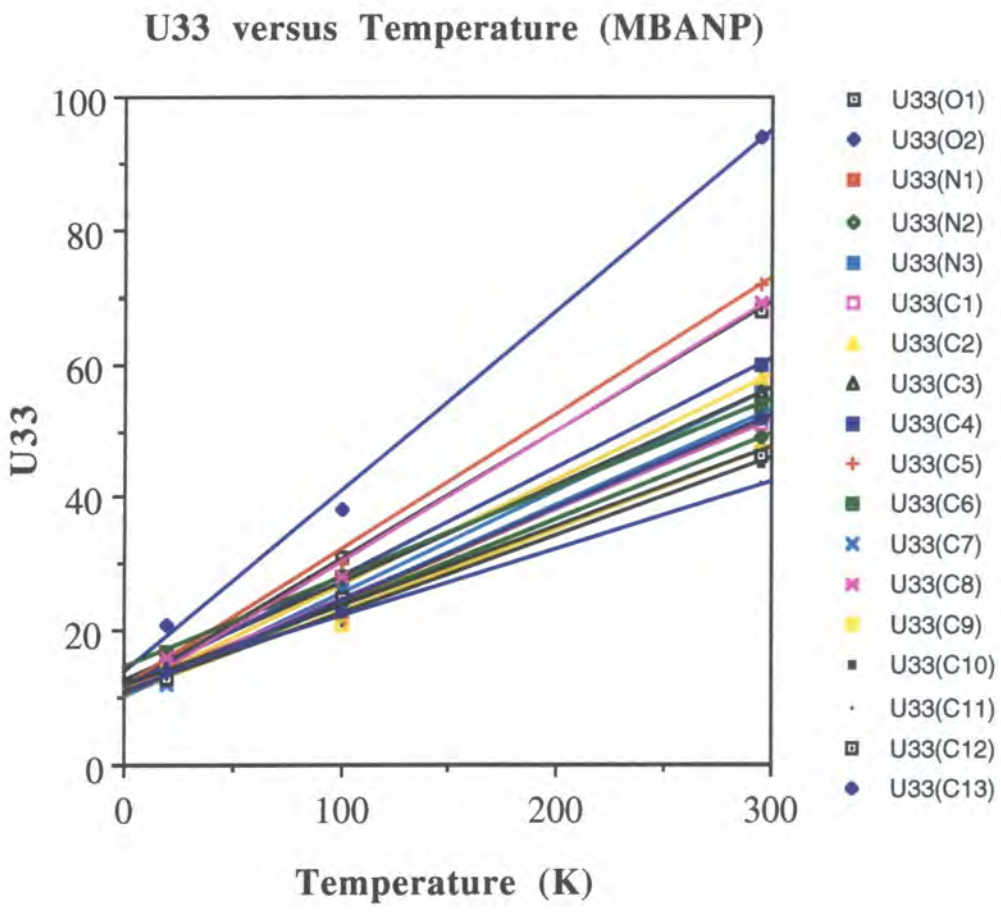

Figure 5.2.6 *- Plots of the anisotropic displacement parameter, U33, versus temperature for each non-hydrogen atom in MBANP.*

and C(5) are situated at the non-substituted side of the phenyl group. Given the last statement, we presume that there is a small amount of internal motion present about the out-of-plane vector perpendicular to the C(1)-C(7) bond. The libration was considered too small to merit any extensive thermal motion analysis.

The three-dimensional molecular packing arrangement of MBANP is given in ***Figure 5.2.7***. As reported previously (Twieg & Dirk, 1986; Kondo et al, 1988) intermolecular contacts are present within the lattice. This study shows that two *intra*molecular interactions are also present. A summary of the inter- and intramolecular contacts derived from this study is given in ***Table 5.2.4***:

Table 5.2.4 *- A summary of the inter- and intramolecular contacts in MBANP at 20K, 100K and 295K.*

Non-bonded contacts	Distance (Å) at 20K	Distance (Å) at 100K	Distance (Å) at 295K
Intramolecular			
O(1)...H(11)-C(11)	2.53(5)	2.50(6)	2.49(7)
O(2)...H(13)-C(13)	2.42(5)	2.43(7)	2.41(7)
Intermolecular			
O(1)...H(10)-C(10)[a]	2.55(5)	2.56(6)	2.59(7)
O(2)...H(1N)-N(1)[b]	2.27(5)	2.11(6)	2.16(6)

symmetry codes: a = 2-x, y-1/2, 2-z; b = x-1, y-1, z.

As expected, the O(2)...H(1N)-N(1) contact [B] is the strongest one. This interaction propagates along the (110) direction. The other, much weaker, intermolecular interaction, O(1)...H(10)-C(10) [A], propagates along a similar direction. The two intramolecular interactions, O(1)...H(11)-C(11) and O(2)...H(13)-C(13) are situated at either side of the nitro group, thus linking it more firmly with the more rigid phenyl group. We presume that, in the absence of these contacts, the libration of O(1) and O(2) would be greater than it is. Within error, there seems to be no variation in the strength of the hydrogen-bonding with temperature.

The variation of the value of each cell parameter with temperature was also investigated. Results show (***Figure 5.2.8***) that all cell parameters increase with temperature. However, whilst the cell parameters, b and c, increase *linearly* with temperature, cell parameters, a and β, vary in a distinctly *non-linear* fashion with temperature. The cause

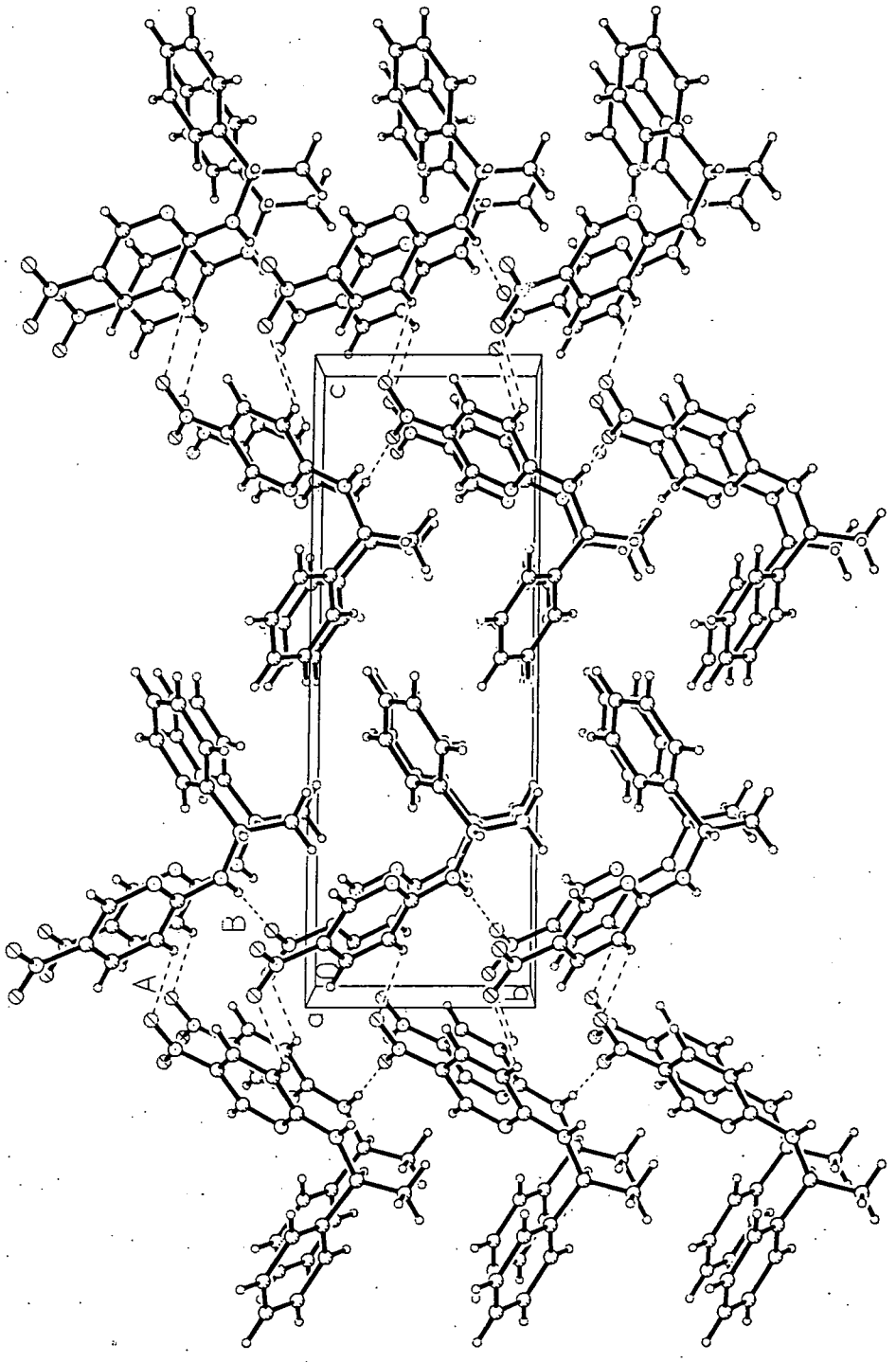

Figure 5.2.7 *- The molecular packing arrangement of MBANP.*

Cell parameter, a versus Temperature (MBANP)

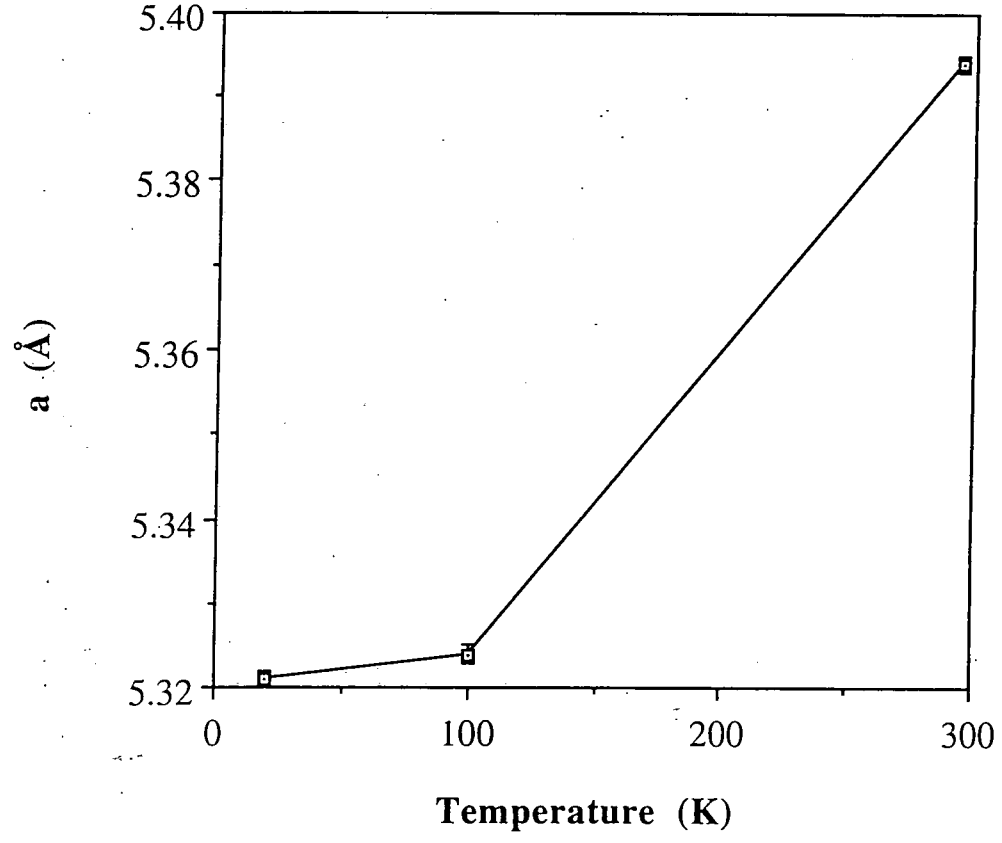

Cell parameter, b versus Temperature (MBANP)

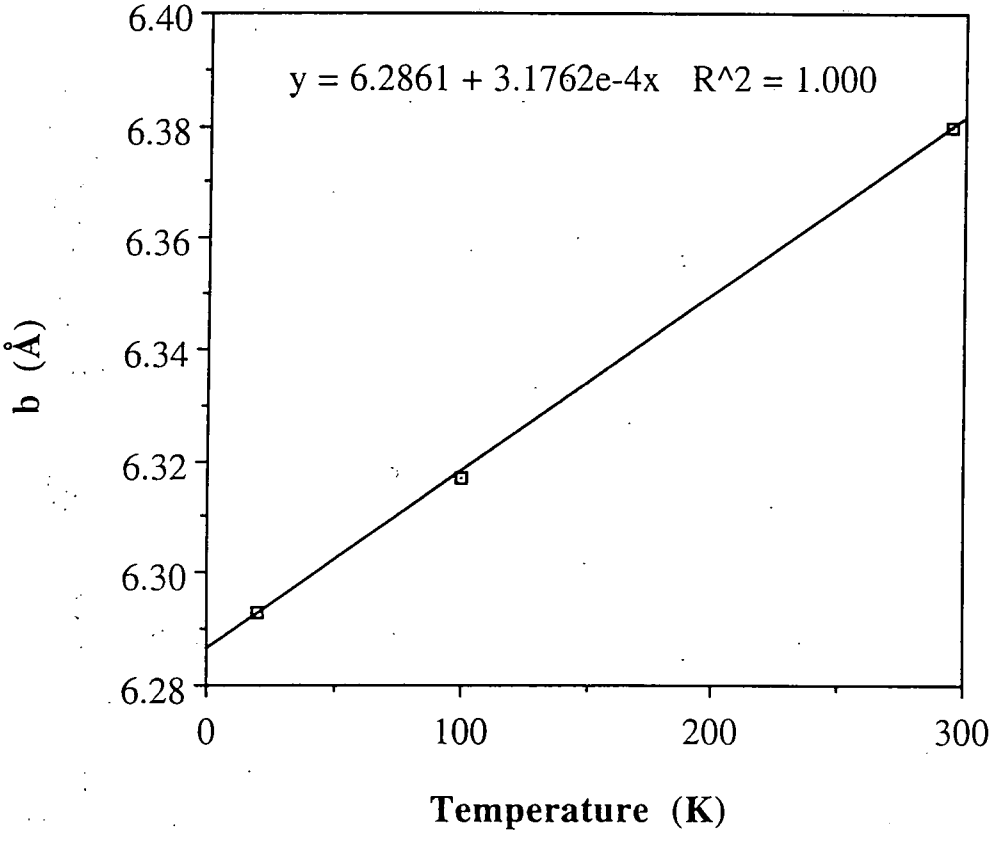

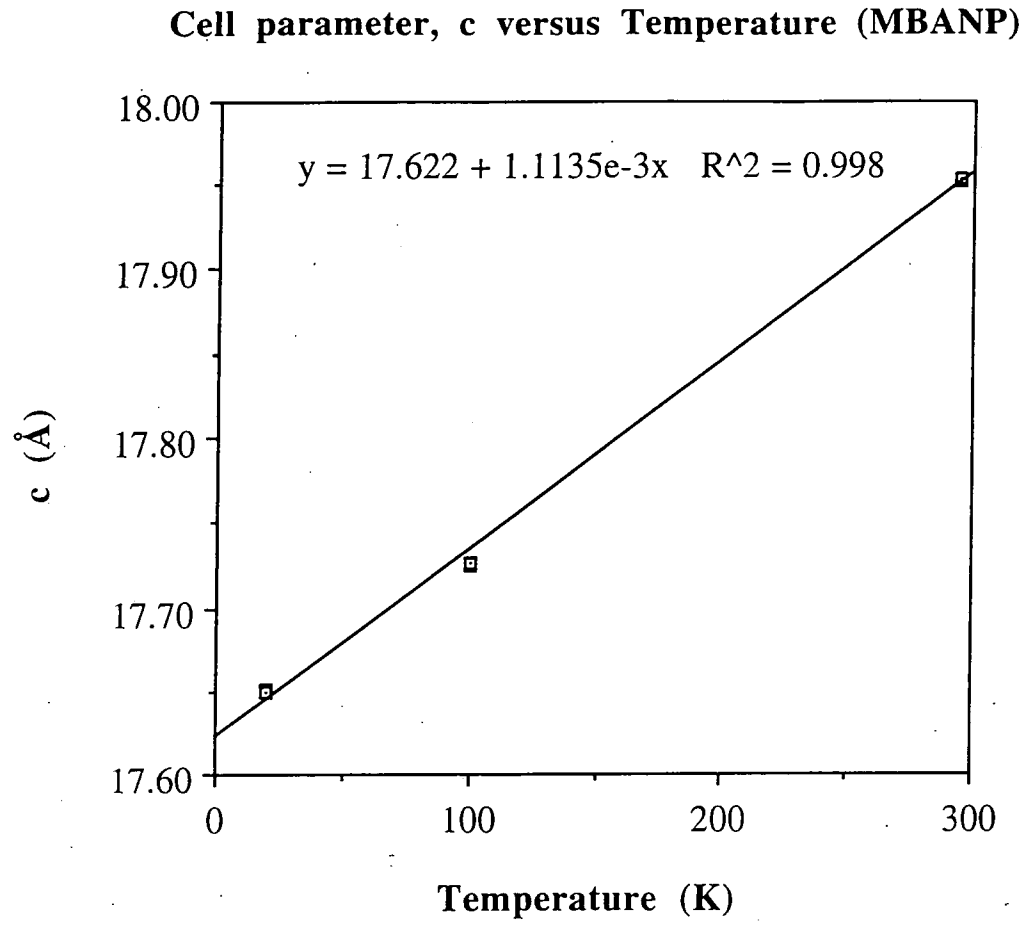

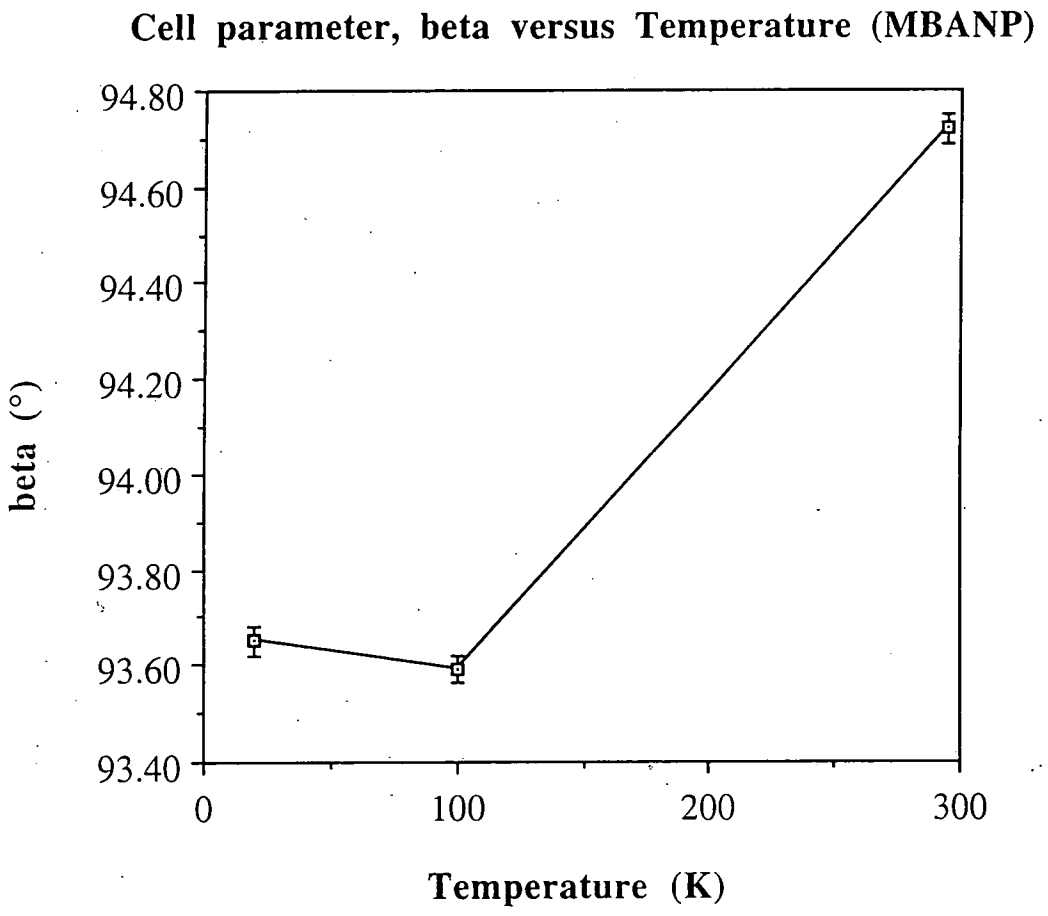

Figure 5.2.8 - Plots of the unit cell parameters, a, b, c and β versus temperature for MBANP.

of this non-linearity is unknown since we observed no phase transition or any structural disorder. One could argue that a plot based on only three points should be assessed with caution, especially when one of these points was measured using a different instrument and crystal. However, since the cell parameters, b and c, show such a good agreement with the linear fit against temperature, we believe that our comparison is valid. Admittedly, in order to classify this non-linearity in more detail, further measurements are necessary.

5.3 SYNTHESIS AND CHARACTERIZATION OF MBADNP

By adding an extra nitro group at the *ortho* position in the pyridine ring of MBANP, the D-A interactions would be enhanced and three more possible classical hydrogen-bond acceptors would become available. Furthermore, the charge-transfer axis would be shifted from the N(1)---N(3) to N(1)---C(11) vectorial direction. Presumably, the orientation of the molecule with respect to the screw-axis would also change after this substitution and so a new phase-matching angle is not predictable.

In an attempt to produce a compound with more optimal SHG properties than MBANP, the dinitro analogue, MBADNP, was therefore synthesized and characterized and the phase matching angle measured. The synthesis, chemical analysis and crystallization was performed with the help of Dr. J. A. Hugh MacBride in the Department of Chemistry at the University of Durham, U.K.

5.3.1 Synthesis

The starting materials, 2-chloro-3,5-dinitropyridine, R-(+)-1-phenylethylamine, triethylamine and all solvents were commercial materials used without further purification. The following synthetic conditions are milder than those used previously to prepare the mono-nitro analogue (Twieg, Jain, Cheng, Crowley & Azema, 1982). R-(+)-1-phenylethylamine (0.60 g, 5 mmol) and 2-chloro-3,5-dinitropyridine (1.0 g, 5 mmol) in ethanol (30 cm^3) were warmed to about 60 °C for 10 minutes and allowed to cool for 5 minutes before addition of triethylamine (0.7 cm^3, 5 mmol). After 20 hours at room temperature, yellow irregular plates of MBADNP (1.21 g, 84%) formed. These were separated and washed with ethanol, raised to 96-96.5 °C (m.p. 94-95 °C) and recrystallized from propan-1-ol.

5.3.2 Chemical analysis

Elemental analysis for $C_{13}H_{12}N_4O_4$ (288) found (required): %C = 54.25 (54.15), %H = 4.16 (4.19), %N = 19.74 (19.44).

Infra-red data, principal bands (KBr, cm^{-1}): 3374 (NH str.), 1608(s, NH bend); 1587 (Py skel.); 1538, 1522 (asym. NO_2 str.); 1317 (sym. NO_2 str.); 1269, 1201 (C-NH-C str.).

Optical activity: $[\alpha]^{22}_D$ ($CHCl_3$): -134°.

^1H NMR data (400 MHz, $CDCl_3$, 298 K): 1.70 (d, J_{CH} = 6.8 Hz,), 5.65 (dq, J_{CH} ca. 7,

6 Hz), 7.30-7.40 (m, C_6H_5), 9.02 (br. d, J_{NH} ca. 6 Hz), 9.21 and 9.22 (overlapping d, J = 2.4 Hz, Py H_γ and Py $H_{\alpha'}$).

^{13}C NMR data (100.58 MHz, $CDCl_3$, 298 K): 22.39 (CH_3), 51.62 (alk. CH), 126.05, 127.85, 128.91 (C_6H_5, o, p, m), 131.35 (Py C_γ), 134.04 (C_6H_5, ipso), 142.04 (Py C_α), 150.83 and 152.84 (Py C_β and $C_{\beta'}$), 151.19 (Py $C_{\alpha'}$).

^1H-^{13}C HETCOR showed coupling between the following resonances (^1H-^{13}C): 1.70-22.39 (CH_3), 5.65-51.62 (alk. CH), ca. 7.3-127.85 (C_6H_5, p), ca. 7.4-126.05 and 128.91 (C_6H_5, o and m), 9.21-142.04 (Py C_γ), 9.22-151.19 (Py C_α).

Ultra-Violet data: λ_{max} (MeOH, nm, log ε): 330 (4.24), 380 (inflexion, 3.84).

5.3.3 The X-ray structure of MBADNP

5.3.3.1 Experimental

The X-ray derived structure of MBADNP was determined at 100K using a Siemens SMART-CCD diffractometer. Conventional experimental and data reduction procedures, as described in chapter 2, were followed throughout. The data collection nominally covered over a hemisphere of reciprocal space, by a combination of three sets of exposures; each set had a different ϕ angle for the crystal and each exposure covered 0.3° in ω. The crystal-to-detector distance was 6.004 cm. Coverage of the unique set is more than 97% complete to at least 25° in θ. Crystal decay was monitored by repeating the initial frames at the end of data collection and analysing the duplicate reflections. No absorption correction was applied. The structure was solved by direct methods using SHELXS-86 (Sheldrick, 1990) and refined by full-matrix least-squares methods on F^2 using SHELXL-93 (Sheldrick, 1993). Atomic scattering factors were taken from International Tables for Crystallography, Volume C, Mathematical, Physical and Chemical Tables (1992).

Positional and anisotropic displacement parameters for all non-H atoms and positional parameters of all H atoms were refined. Methyl H isotropic displacement parameters were constrained to be $1.5U_{eq}$ of the ligated carbon atoms whilst all other H isotropic displacement parameters were fixed at $1.2U_{eq}$(C).

A summary of crystal, data collection and refinement parameters is given in ***Table 5.3.1***.

Table 5.3.1 *- A summary of crystal, data collection and refinement parameters for the 100K X-ray structure of MBADNP.*

Compound	MBADNP	Compound	MBADNP
Molecular Formula	$C_{13}H_{12}N_4O_4$	Absorption coefficient (mm^{-1})	0.114
Formula weight	288.27	Crystal Morphology	plate
a(Å)	8.389(1)	Crystal Colour	yellow
b(Å)	8.580(1)	Crystal Size (mm)	0.45 x 0.35 x 0.10
c(Å)	8.934(1)	Total number of reflections	2576
α(°)	90	Unique reflections	1723
β(°)	93.689(2)	Observed Reflections [I>2σ(I)]	1566
γ(°)	90	R_{int}	0.0548
Cell Volume($Å^3$)	641.7(2)	θ range	2.28 - 25.10
Crystal System	monoclinic	Data / Parameters	1713 / 226
Space Group	P2(1)	R1 [I > 2σ(I)]	0.0449
Z	2	wR2 [I > 2σ(I)]	0.0971
Calculated Density (gcm^{-1})	1.492	Goodness of fit on F^2	1.169
Temperature (K)	100(2)	Weighting Scheme	a = 0.0334; b = 0.5637
Wavelength (Å)	0.71073	$\Delta\rho_{(max, min)}$ ($eÅ^{-3}$)	0.224 / -0.228

5.3.3.1 Structural Details

A 50% probability thermal ellipsoid plot of the 100K X-ray structure of MBADNP is shown in ***Figure 5.3.1***. Bond distances and selected bond angles are given in ***Tables 5.3.2*** and ***5.3.3***. Fractional coordinates and anisotropic displacement parameters are given in ***Appendix A.5.7*** and ***A.5.8***.

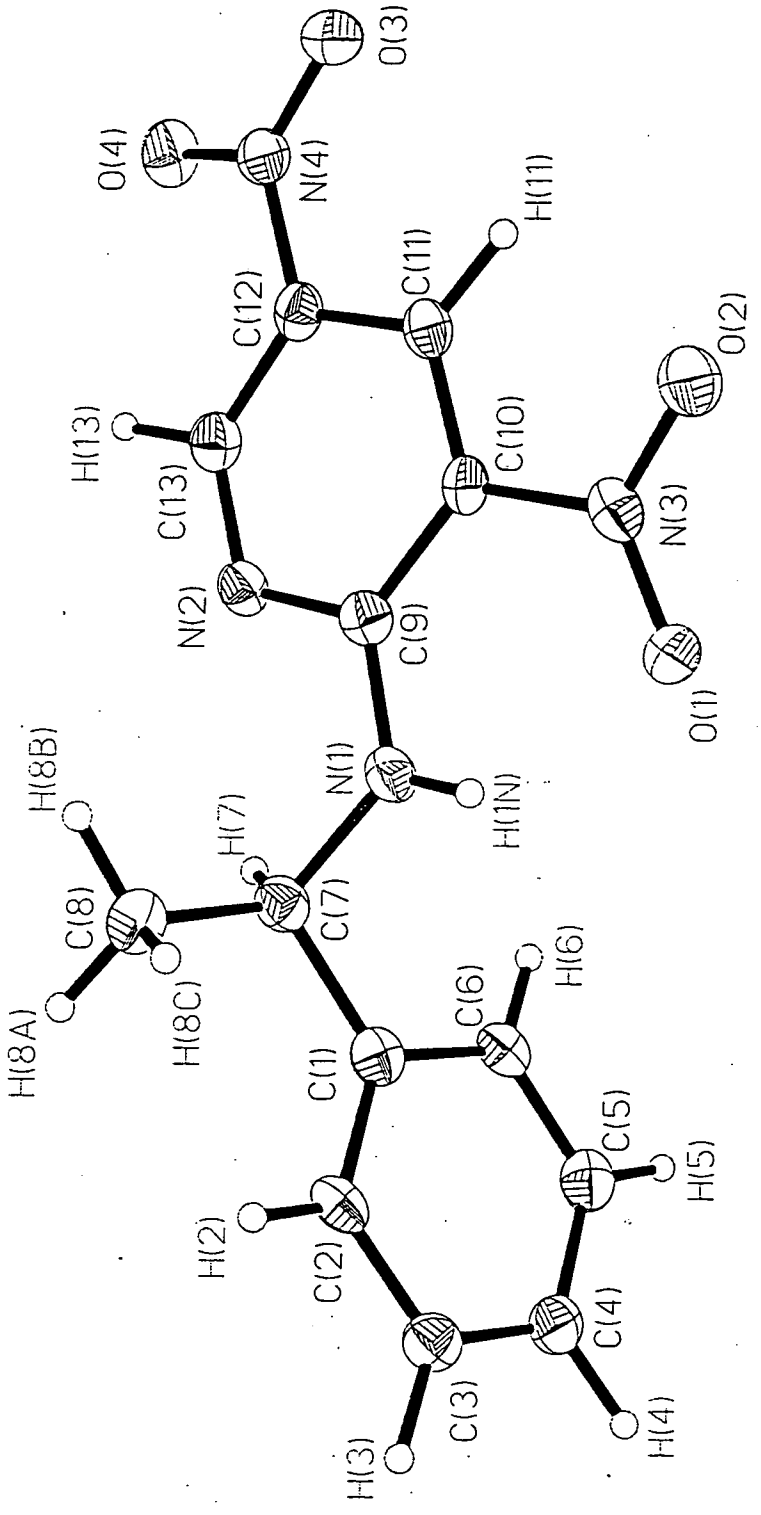

Figure 5.3.1 *- A 50% probability thermal ellipsoid plot of the 100K X-ray structure of MBADNP.*

Table 5.3.2 *- Bond lengths of the 100K X-ray structure of MBADNP.*

Bond	Distance (Å)	Bond	Distance (Å)
O(1)-N(3)	1.238(4)	C(5)-H(5)	1.00(5)
O(1)-H(1N)	2.06(5)	C(6)-H(6)	0.94(5)
O(2)-N(3)	1.234(4)	C(7)-C(8)	1.525(6)
O(3)-N(4)	1.229(4)	C(7)-H(7)	0.98(4)
O(4)-N(4)	1.240(4)	C(8)-H(8A)	1.06(5)
N(1)-C(9)	1.345(5)	C(8)-H(8B)	0.99(5)
N(1)-C(7)	1.476(5)	C(8)-H(8C)	1.01(5)
N(1)-H(1N)	0.81(5)	C(9)-C(10)	1.436(5)
N(2)-C(13)	1.327(5)	C(10)-C(11)	1.363(5)
N(2)-C(9)	1.359(5)	C(11)-C(12)	1.388(5)
N(3)-C(10)	1.452(5)	C(11)-H(11)	1.00(5)
N(4)-C(12)	1.452(5)	C(12)-C(13)	1.382(6)
C(1)-C(2)	1.379(5)	C(13)-H(13)	1.06(4)
C(1)-C(6)	1.400(6)	Inter/Intra-molecular contacts	
C(1)-C(7)	1.532(5)		
C(2)-C(3)	1.400(6)		
C(2)-H(2)	0.89(5)	O(1)···H(1N)-N(1)	2.06(5)
C(3)-C(4)	1.385(6)	O(1)···H(3)-C(3)	2.63(5)
C(3)-H(3)	1.05(4)	O(2)···H(11)-C(11)	2.35(4)
C(4)-C(5)	1.394(6)	O(3)···H(5)-C(5)	2.55(6)
C(4)-H(4)	1.06(4)	O(4)···H(1N)-N(1)	2.51(6)
C(5)-C(6)	1.390(6)	O(4)···H(13)-C(13)	2.45(4)

Table 5.3.3 - Selected bond angles of the 100K X-ray structure of MBADNP.

Angle	Angle(°)	Angle	Angle(°)
C(9)-N(1)-C(7)	123.9(3)	N(1)-C(7)-C(1)	107.5(3)
C(13)-N(2)-C(9)	118.5(3)	C(8)-C(7)-C(1)	114.1(3)
O(2)-N(3)-O(1)	122.3(3)	N(1)-C(9)-N(2)	116.1(4)
O(2)-N(3)-C(10)	118.1(3)	N(1)-C(9)-C(10)	123.8(3)
O(1)-N(3)-C(10)	119.5(3)	N(2)-C(9)-C(10)	120.1(3)
O(3)-N(4)-O(4)	123.3(3)	C(11)-C(10)-N(3)	117.5(3)
O(3)-N(4)-C(12)	118.6(3)	C(9)-C(10)-N(3)	122.1(3)
O(4)-N(4)-C(12)	118.0(3)	C(13)-C(12)-N(4)	120.5(3)
C(2)-C(1)-C(7)	122.7(4)	C(11)-C(12)-N(4)	119.3(3)
C(6)-C(1)-C(7)	118.9(4)	N(2)-C(13)-C(12)	123.2(4)
N(1)-C(7)-C(8)	110.3(3)		

The two planar six membered rings in the molecule are linked via a twisted -CH(CH_3)-NH- unit, showing a twist angle between the two rings of 106.5(1)°. The maximum deviations from planarity for the benzyl and pyridyl rings are 0.013(4) Å [C(6)] and 0.018(4) Å [C(10)] respectively. However, the two -NO_2 pyridyl substituents deviate from the pyridyl mean plane by 9.1(2)° (*p*-NO_2) and 13.2(2)° (*o*-NO_2) which, in turn, leads to a nitro-nitro dihedral angle of 16.6(4)°. The twist of the *o*-NO_2 group results from the intra-molecular hydrogen-bonds, O(1)···H(1N)-N(1) [2.06(5) Å] and O(2)···H(11)-C(11) [2.35(4)Å], and the weak intermolecular hydrogen-bond, C(3)-H(3)···O(1) [2.63(5) Å] (symmetry code: -x-1, y-1/2, 2-z) [A] may also play a marginal role in the extent of the twist. Hydrogen-bonding also seems to be responsible for the twist of the *p*-NO_2 group, although here there are one intramolecular and two intermolecular interactions. The C(13)-H(13)···O(4) [2.45(4)Å] and O(4)···H(1N)-N(1) [2.51(6) Å] (symmetry code: x-1, y, z) [B] contacts force the NO_2 group out of the pyridyl mean plane whilst the slightly weaker hydrogen-bond, C(5)-H(5)···O(3) [2.55(6) Å] (symmetry code: x-1, y, z+1) [C] counteracts this and turns the substituent back into the plane. The slight difference in deviation of the two NO_2 groups from the pyridyl mean plane is assumed to be a result of the balancing of different hydrogen-bonds.

The molecule packs in a head-to-tail herringbone semi-layer-like fashion (***Figure 5.3.2***), linked by the hydrogen-bonding hitherto described. The compound crystallizes in the non-centrosymmetric space group $P2_1$ and, by definition, (Franken & Ward, 1963) the compound must therefore exhibit a second harmonic response. Hence, the powder SHG efficiency was tested (using a Nd:YAG laser, reflection mode, fundamental 8 ns pulses, 3 Hz, < 1 mJ, λ = 1.064 μm) and gave a response of approximately 4 times that

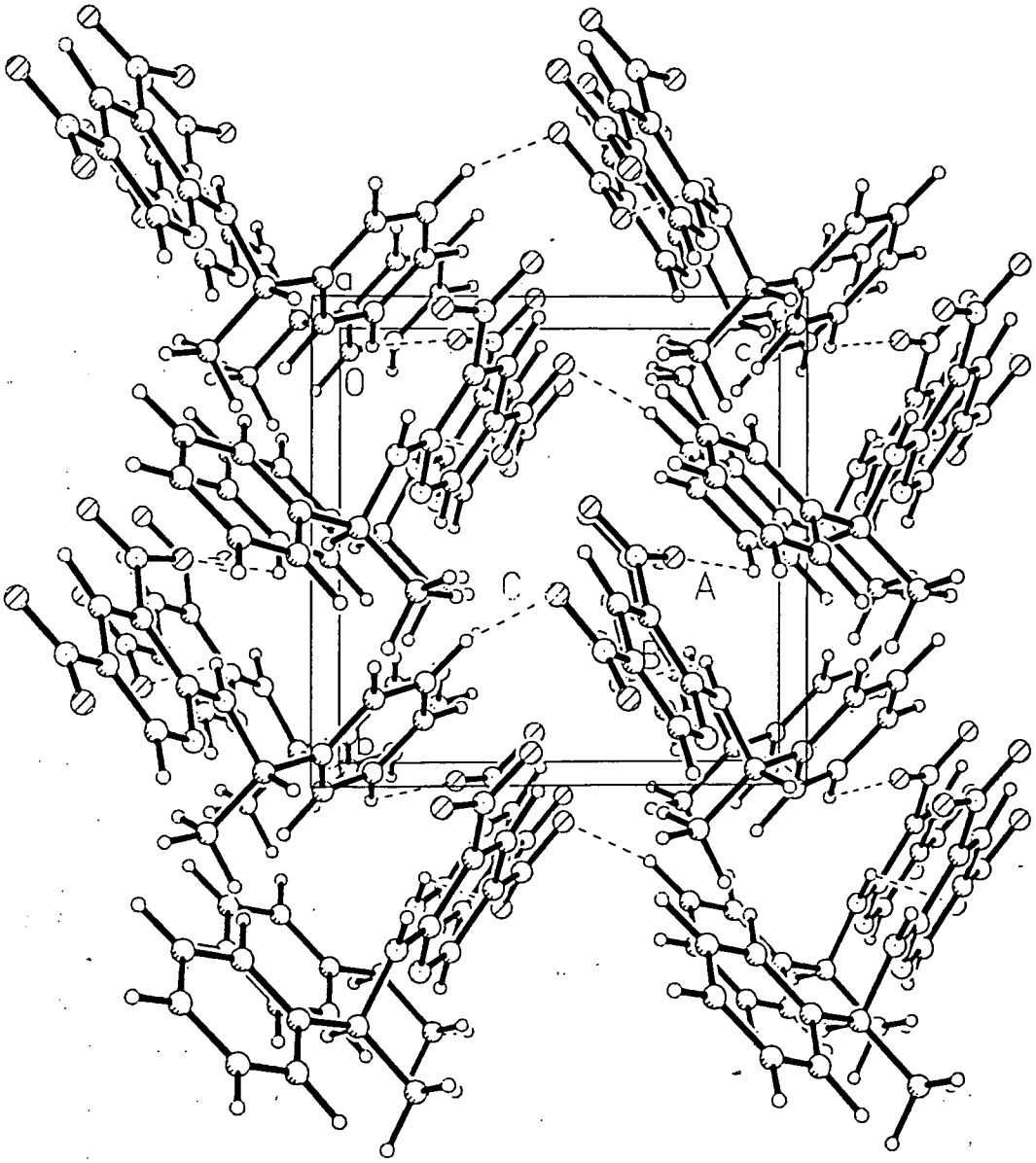

Figure 5.3.2 *- The molecular packing arrangement of the 100K X-ray structure of MBADNP.*

of urea. We are grateful to Dr. Graham H. Cross (Physics Department, University of Durham) for performing this measurement.

The phase-matching ability of the compound was also investigated. Since the molecule crystallizes in the space group, $P2_1$, optimal phase matching is achieved when the angle between the 2_1 screw-axis and the charge-transfer axis is $\theta = 54.7°$ (Oudar & Zyss, 1982). The charge transfer axis in this molecule is not obvious since the lack of π-bonding in the branch between the two rings precludes any possible π-conjugation across the whole molecule. The π-conjugation is therefore localized in two distinct parts, one at either end of the molecule. Given this and the fact that the principal electron donating and withdrawing substituents are concentrated around the pyridine ring, one can assume that the benzyl group plays a neutral role in the charge transfer process. Such an assumption was also made previously for the mono-nitro analogue (Bailey, Cruickshank, Pavlides, Pugh & Sherwood, 1991).Using this approximation, along with the assumption that β_{zzz} (where z is along the molecular axis) is by far the most dominant tensorial component of the molecular hyperpolarizability, β, (Lalama & Garito, 1979) the charge transfer axis can be approximated to the molecular axis of the $-NH-C_5N(NO_2)_2(H)_2$ moiety. The corresponding phase-matching angle was then determined to be $\theta = 63°$. This is only $+8.3°$ from the optimal angle and therefore suggests that the compound has high phase-matching potential.

When we compare these results to those of MBANP, whilst appreciating the principal factors affecting the SHG activity of an organic compound, a discrepancy becomes apparent: the macroscopic value of $\chi^{(2)}$ is much larger for MBANP than for MBADNP even though:

- The molecular charge transfer is better in MBADNP than in MBANP;
- The phase-matching angle is more optimal in MBADNP than in MBANP;
- Both compounds crystallize in the same space group
- Both compounds pack in a similar manner with hydrogen-bonding dictating the three-dimensional lattice arrangement

We aimed to resolve this apparent discrepancy using neutron diffraction.

5.4 NEUTRON DIFFRACTION STUDIES OF MBANP AND MBADNP

A closer inspection of the 100K X-ray structures of MBANP and MBADNP revealed that MBADNP packs less efficiently than MBANP. We proposed a link between the decrease in efficiency of the packing and the decrease in the magnitude of the macroscopic SHG, $\chi^{(2)}$. Moreover, since hydrogen-bonding appears to dominate the three-dimensional arrangement of each compound, we wished to evaluate the hydrogen-bonding more accurately than was determined using X-ray diffraction.

5.4.1 Experimental

The neutron structures of both MBANP and MBADNP were determined at 20K using D9 at the ILL. The calibrated wavelength of the beam was 0.8372(1)Å. Half-wavelength contamination was removed with an erbium filter.

Three crystals of MBANP were tested before successful results were obtained from a fourth (of dimensions 4.3 x 2.0 x 1.0 mm). All four crystals had been cut from the same parent crystal of dimensions 45 x 25 x 10 mm. The first crystal was solvent-cut using dimethylfuran whereas the others were cut using a sharp scalpel-blade. The successful crystal was mounted on an aluminium pin and a beam collimator of diameter 6mm was used. An orientation matrix was obtained and the sample was cooled to 20K using an Air Products 201 (Archer & Lehmann, 1986) He Displex CCR. On cooling, the intensity of the reflections increased, although their profiles remained broad. Despite this, it was decided to proceed with data collection. Data were collected in batches of $0° \leq 2\theta \leq 25°$, $25° \leq 2\theta \leq 30°$, $30° \leq 2\theta \leq 35°$, $35° \leq 2\theta \leq 40°$ and $40° \leq 2\theta \leq 45°$. ω-xθ scans, with x chosen to keep the reflection in the middle of the detector aperture, were used in conjunction with a scan width, $\Delta\omega$, which was roughly twice the full width of the peak at background. Both x and $\Delta\omega$ varied with the Bragg angle, θ:

θ	1.00	15.00	30.00	45.00	60.00
x	1.20	1.20	1.50	2.00	2.00
$\Delta\omega$	8.00	7.50	8.50	9.50	10.00

A default scan time of 40000 monitor counts was employed. One standard reflection (0 -1 4) was measured every 50 reflections in order to monitor the constancy of the intensity. Data collection proceeded with no problems.

The first tested crystal of MBADNP gave successful results. The crystal (dimensions 3.0 x 2.5 x 1.0 mm) was mounted onto a vanadium pin and placed upon the instrument. An orientation matrix was obtained and the sample was cooled to 20K using an Air Products

201 (Archer & Lehmann, 1986) He Displex CCR. The peak profiles remained sharp and intense throughout cooling. Data collection was then initiated, proceeding in shells of $0° \leq 2\theta \leq 30°$, $30° \leq 2\theta \leq 35°$, $35° \leq 2\theta \leq 40°$, $40° \leq 2\theta \leq 45°$. ω-xθ scans, with x chosen to keep the reflection in the middle of the detector aperture, were used in conjunction with a scan width, $\Delta\omega$, which was roughly twice the full width of the peak to background. Both x and $\Delta\omega$ varied with the Bragg angle, θ:

θ	1.00	15.00	30.00	45.00	60.00
x	1.20	1.20	1.50	2.00	2.00
$\Delta\omega$	2.50	1.60	1.60	2.80	4.20

A default scan time of 30000 monitor counts was employed. One standard reflection (0 0 5) was measured every 50 reflections in order to monitor the constancy of the intensity. During the collection of the $35° \leq 2\theta \leq 40°$ batch, the temperature rose to 112K and so the data collection had to be interrupted briefly whilst the sample was recooled to 20K. This caused no subsequent problems and the data collection proceeded without further interruption.

Both sets of data were reduced in the manner described in chapter 2. The chosen values of the integration parameters, STVOL, VOLFAC, SIGBR and FILL were 800, 3.0, 0.7, 0.8 and 800, 5.0, 0.05, 0.1 for the MBANP and MBADNP data reductions respectively. Cryostat shield and crystal absorption corrections were then applied using the local program ABSCAN and the DATAP program (Coppens, 1970) respectively [transmission ranges: 0.7263 - 0.8574 (MBANP) and 0.7569 - 0.8802 (MBADNP)].

Each structure was refined by full-matrix least-squares refinement using SHELXL-93 (Sheldrick, 1993). Positional and anisotropic displacement parameters were refined for all atoms in both cases.

A summary of crystal, data collection and refinement parameters for each structure is given in ***Table 5.4.1***.

Table 5.4.1 *- A summary of crystal, data collection and refinement parameters for the 20K neutron structures of MBANP and MBADNP.*

Compound	MBANP	MBADNP
Molecular Formula	$C_{13}H_{13}N_3O_2$	$C_{13}H_{12}N_4O_4$
Formula weight	243.00	288.00
a(Å)	5.3260(6)*	8.3467(8)*
b(Å)	6.301(1)*	8.5673(8)*
c(Å)	17.673(4)*	8.8999(8)*
α(°)	90	90
β(°)	93.42(1)*	93.954(8)*
γ(°)	90	90
Cell Volume(Å^3)	589.8(2)	636.1(4)
Crystal System	monoclinic	monoclinic
Space Group	P2(1)	P2(1)
Z	2	2
Calculated Density (gcm^{-1})	1.368	1.504
Temperature (K)	20.0(1)	20.0(1)
Wavelength (Å)	0.8372(1)	0.8372(1)
Absorption coefficient (mm^{-1})	0.1582	0.1407
Crystal Morphology	rectangular block	hexagonal prism
Crystal Colour	yellow	yellow
Crystal Size (mm)	4.3 x 2.0 x 1.0	3.0 x 2.5 x 1.0
Total number of reflections	4116	3755
Unique reflections	2805	3401
Observed Reflections [I>2σ(I)]	2619	3267
R_{int}	0.0384	0.0283
$(\sin\theta/\lambda)_{max}$	0.816	0.825
Data / Parameters	2799 / 280	3397 / 298
R1 [I > 2σ(I)]	0.0732	0.0291
wR2 [I > 2σ(I)]	0.1051	0.0464
Goodness of fit on F^2	2.557	1.471
Weighting Scheme	$1/\sigma^2$	$1/\sigma^2$
$\Delta\rho_{(max, min)}$ (fmÅ^{-3})	1.719 / -1.789	0.815 / -0.909

* Although these cell parameters are neutron derived, the 20K X-ray determined cell parameters, a = 5.321(1)Å, b = 6.293(1)Å, c = 17.650(4)Å, β = 93.65(3)° [MBANP] and a = 8.352(3)Å, b = 8.570(3)Å, c = 8.909(4)Å, β = 93.98(2)° [MBADNP] were used in all calculation, correction and refinement procedures since they are deemed more accurate than neutron derived values. Moreover, the neutron wavelength's esd was not used in the calculation of the neutron derived cell parameters.

5.4.2 Structural Details

A 50% probability thermal ellipsoid plot of each structure is given in ***Figures 5.4.1*** and ***5.4.2***. Bond lengths and selected bond angles for each structure are given in ***Tables 5.4.2*** and ***5.4.3*** respectively. Fractional coordinates and anisotropic displacement parameters are given in ***Appendix A.5.9 - A.5.12***.

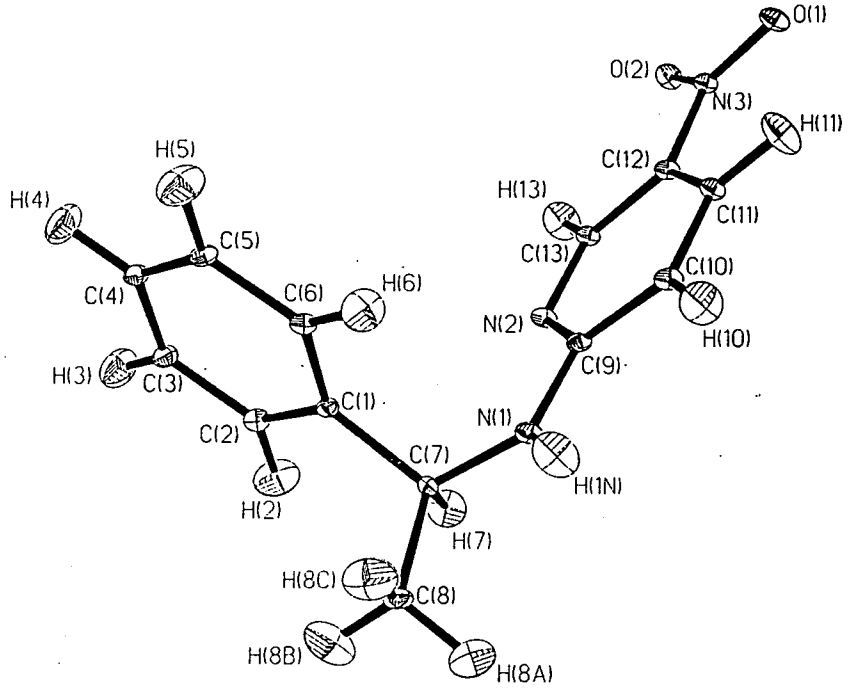

Figure 5.4.1 - A 50% probability thermal ellipsoid plot of the 20K neutron structure of MBANP.

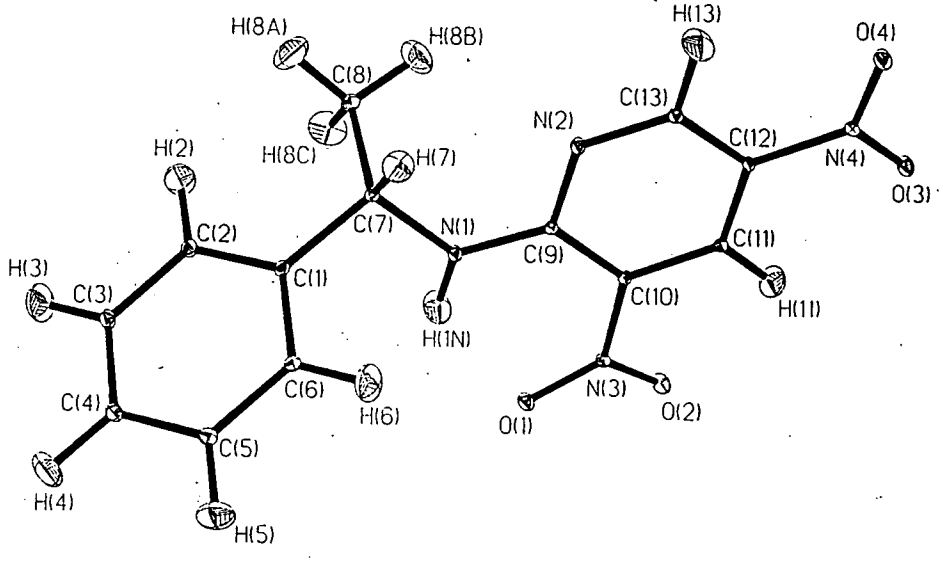

Figure 5.4.2 - A 50% probability thermal ellipsoid plot of the 20K neutron structure of MBADNP.

Table 5.4.2 *- Bond lengths for the 20K neutron structures of MBANP and MBADNP.*

Bond	MBANP distance (Å)	MBADNP distance (Å)	Bond	MBANP distance (Å)	MBADNP distance (Å)
O(1)-N(3)	1.226(4)	1.239(1)	C(3)-H(3)	1.072(8)	1.089(2)
O(2)-N(3)	1.237(3)	1.223(1)	C(4)-C(5)	1.385(4)	1.400(1)
O(3)-N(4)	---	1.229(1)	C(4)-H(4)	1.080(7)	1.090(2)
O(4)-N(4)	---	1.234(1)	C(5)-C(6)	1.399(4)	1.395(1)
N(1)-C(9)	1.354(3)	1.338(1)	C(5)-H(5)	1.084(6)	1.084(2)
N(1)-C(7)	1.455(3)	1.473(1)	C(6)-H(6)	1.087(6)	1.086(2)
N(1)-H(1N)	1.019(5)	1.013(2)	C(7)-C(8)	1.532(4)	1.532(1)
N(2)-C(13)	1.337(3)	1.321(1)	C(7)-H(7)	1.106(6)	1.101(2)
N(2)-C(9)	1.354(3)	1.361(1)	C(8)-H(8A)	1.085(8)	1.094(3)
N(3)-C(10)	---	1.454(1)	C(8)-H(8B)	1.076(8)	1.098(2)
N(3)-C(12)	1.443(3)	---	C(8)-H(8C)	1.080(7)	1.093(2)
N(4)-C(12)	---	1.447(1)	C(9)-C(10)	1.418(4)	1.437(1)
C(1)-C(2)	1.394(4)	1.397(1)	C(10)-C(11)	1.369(4)	1.381(1)
C(1)-C(6)	1.404(3)	1.403(1)	C(10)-H(10)	1.073(7)	---
C(1)-C(7)	1.522(4)	1.521(1)	C(11)-C(12)	1.409(3)	1.387(1)
C(2)-C(3)	1.388(4)	1.401(1)	C(11)-H(11)	1.082(7)	1.084(2)
C(2)-H(2)	1.089(6)	1.089(2)	C(12)-C(13)	1.386(4)	1.398(1)
C(3)-C(4)	1.396(4)	1.395(1)	C(13)-H(13)	1.088(7)	1.090(2)

Table 5.4.3 *- Selected bond angles for the 20K neutron structures of MBANP and MBADNP.*

Angle	MBANP angle (°)	MBADNP angle (°)	Angle	MBANP angle (°)	MBADNP angle (°)
C(7)-N(1)-C(9)	123.4(2)	123.85(6)	C(6)-C(1)-C(7)	121.4(2)	118.93(8)
C(9)-N(1)-H(1N)	117.2(4)	117.0(1)	N(1)-C(7)-C(1)	112.9(2)	107.46(7)
C(7)-N(1)-H(1N)	118.3(4)	118.2(1)	N(1)-C(7)-C(8)	108.3(2)	110.40(7)
C(9)-N(2)-C(13)	117.6(2)	119.59(7)	C(1)-C(7)-C(8)	109.2(2)	114.39(7)
O(1)-N(3)-O(2)	123.1(3)	123.21(9)	N(1)-C(9)-N(2)	117.8(2)	116.87(7)
O(1)-N(3)-C(10)	---	118.30(8)	N(1)-C(9)-C(10)	119.5(2)	123.57(7)
O(1)-N(3)-C(12)	119.0(2)	---	C(9)-C(10)-N(3)	---	122.87(7)
O(2)-N(3)-C(10)	---	118.47(8)	C(11)-C(10)-N(3)	---	116.60(7)
O(2)-N(3)-C(12)	117.9(2)	---	C(11)-C(12)-N(3)	120.0(2)	---
O(3)-N(4)-O(4)	---	123.82(8)	C(11)-C(12)-N(4)	---	119.70(7)
O(3)-N(4)-C(12)	---	117.98(7)	C(13)-C(12)-N(3)	120.0(2)	---
O(4)-N(4)-C(12)	---	118.20(7)	C(13)-C(12)-N(4)	---	120.22(7)
C(2)-C(1)-C(7)	119.1(2)	122.47(8)			

A comparative study of the nature of the three-dimensional packing and the extent of hydrogen-bonding present in MBANP and MBADNP was made. For views of the three-dimensional packing of MBANP and MBADNP, one is referred back to ***Figures 5.2.7*** and ***5.3.2*** respectively. A summary of all non-bonded contacts for each compound is given in ***Table 5.4.4***. In both structures, all non-bonded contacts determined previously by X-ray diffraction are also present here and are stronger than those determined using X-ray diffraction. Moreover, in MBADNP, five further interactions were found using neutron diffraction. This is expected since H-X distances, obtained using X-ray diffraction, appear artificially shorter than their values and thus, X-ray derived H...X distances appear longer than those derived from neutron diffraction studies.

Table 5.4.4 *- A summary of all non-bonded contacts present in MBANP and MBADNP.*

Intramolecular contact	Distance (Å)	Intermolecular contact	Distance (Å)
MBANP		MBANP	
C(11)-H(11)...O(1)	2.464(8)	N(1)-H(1N)...O(2)[a]	2.009(7)
C(13)-H(13)...O(2)	2.398(8)	C(10)-H(10)...O(1)[b]	2.488(7)
MBADNP		MBADNP	
O(1)...N(1)	2.684(2)	N(1)-H(1N)...O(4)[c]	2.316(3)
N(1)-H(1N)...O(1)	1.971(3)	C(2)-H(2)...C(4)[d]	2.627(3)
C(2)-H(2)...C(8)	2.528(3)	C(3)-H(3)...O(1)[e]	2.562(3)
C(7)-H(7)...N(2)	2.447(2)	C(5)-H(5)...O(3)[f]	2.438(4)
C(11)-H(11)...O(2)	2.359(3)	C(6)-H(6)...C(8)[g]	2.666(3)

symmetry codes: a = x-1,y-1,z; b = 2-x, y-1/2, 1-z; c = x-1, y, z; d = 3-x, y-1/2, -z; e = 3-x, y-1/2, -z; f = x-1, y, z+1; g = 2-x, 1/2+y, -z.

These results show that MBANP possesses one very strong intermolecular hydrogen bond, N(1)-H(1N)...O(2) [2.009(7)Å], one secondary intermolecular hydrogen-bond, C(10)-H(10)...O(1) [2.488(7)Å] and two intramolecular contacts, C(11)-H(11)...O(1) [2.464(8)Å] and C(13)-H(13)...O(2) [2.398(8)Å] of intermediate strength. This arrangement uses all possible classical hydrogen-bond donors and acceptors. Furthermore, the planes stack almost on top of each other (see ***Figure 5.2.7***) with an interplanar spacing of 6.29(2)Å along the b direction and only 5.32(2)Å along the a direction. This very efficient and close packing is ideal for effective propagation of the SHG phenomenon throughout the solid.

On the other hand, MBADNP contains five intramolecular interactions and five intermolecular ones. Four of the intramolecular hydrogen-bonds are intermediate-weak in strength. The other intramolecular hydrogen-bond, N(1)-H(1N)...O(1) [1.971(3)Å], however, is strong and as the molecule adjusts to try to accommodate it, a twist in the chain between the two rings is invoked. This twist precludes ideal herringbone formation in the three-dimensional lattice and disrupts what would otherwise be layer-like close packing (see ***Figure 5.3.2***). An interplanar spacing of 8.6(2)Å along the b direction results, which is noticeably larger than that in MBANP. Moreover, although the interplanar spacing along the a direction in MBADNP [4.1(2)Å] is shorter than the

corresponding spacing in MBANP, the molecules in MBADNP do not lie directly side by side as in MBANP but are significantly displaced away from each other.

The intermolecular hydrogen-bonding is thus effected. The twist deterring the molecules from slotting over each other efficiently (in contrast to MBANP) causes fewer close contacts to ensue. Not all hydrogen-bond donors and acceptors are utilized and all of the intermolecular hydrogen-bonds are of weak-intermediate strength.

The formation of the one strong intramolecular hydrogen-bond is therefore at the expense of the efficiency of intermolecular packing. We believe that this, in turn, is the cause of the much lower efficiency of SHG propagation through the three-dimensional solid of MBADNP compared to MBANP.

5.5 CHARGE DENSITY STUDIES OF MBANP AND MBADNP

Charge density studies were performed on both of these compounds in order that (a) the solid-state molecular polarizability coefficients could be calculated for each compound; (b) we could ascertain the exact nature of the charge-transfer occurring across the molecule and (c) we could establish the polarization effects of both the inter- and intra-molecular hydrogen-bonding contacts.

5.5.1 A charge density study of MBANP

Since we already possessed a 20K neutron derived structure of MBANP, a complementary 20K X-ray data set was sought. We used the Fddd cryodiffractometer (Copley et al, 1997) at Durham in order to obtain this. However, in the preparative stages of the experiment we became skeptical about the feasibility of such a study since tests on the Siemens SMART-CCD showed that all of the Bragg reflections of the crystal had extremely broad peak profiles (in common with the corresponding neutron experiment). Given this, we were not surprised to find that none of the crystals diffracted very far out in reciprocal space. The broad peak profiles seemed to be an inherent feature of the *compound* rather than an inherent feature of the *crystals* used, since the same result was obtained however the crystals had been grown.

The largest possible crystal (within the limits of the X-ray beam aperture) was chosen in order to provide the most intense reflections possible at high angles. The crystal (dimensions 0.36 x 0.32 x 0.08 mm) was mounted on a graphite lead, placed upon the instrument, indexed and cooled to 20K. Once the crystal had reached this temperature, we began data collection. Just over a quadrant of data[#] satisfying the range $0° \leq 2\theta \leq 54°$ was first collected. Sufficient intensity was present throughout and on reducing the data, an R_{int} of 2.47% was obtained. We therefore decided to go on collecting data to a higher 2θ value (64°). However, in this range, the intensity was very low, verging on negligible for many reflections. Hence, the data collection was terminated, the existing data were reduced and the structure refined as a conventional X-ray study. One is referred back to the earlier section 5.2, for the structural results and discussion.

5.5.2 A charge density study of MBADNP

5.5.2.1 Experimental

A crystal of dimensions 0.30 x 0.26 x 0.20 mm was mounted on a sharpened 0.3mm graphite pencil lead using epoxy glue (Oxford Instruments, TRZ0004). After allowing

[#] where $-1 \leq h \leq 6$, $-1 \leq k \leq 8$, $-22 \leq l \leq 22$.

the glue to dry for 24h, a copper mount was used to attach the graphite fibre to the lower stage of the Fddd cryodiffractometer's Air Products '512' Displex. The crystal was optically centred before the two beryllium shrouds were put into place. The sample chamber was then evacuated. Once the pressure in the sample chamber had reached 1 x 10^{-5} mbar, the He compressor supplying the cryostat was turned on. The crystal was cooled at $2Kmin^{-1}$ to 20K.

The following monoclinic cell was obtained for the crystal at 20K, using 24 centred reflections with 2θ between 19.97° and 36.11°:

a=8.352(3)Å, b=8.570(3)Å, c=8.909(4)Å, β=93.98(2)°, volume=636.1(4)Å^3.

Eleven shells of data (see ***Table 5.5.1***) were collected in bisecting mode using ω scans. The scan width was constant (1.4°) throughout the experiment. Four standard reflections were measured every 146 reflections.

Data were collected over a one month period. During this time, there were several technical difficulties, which included the diffractometer occasionally losing its ϕ or χ position. Also, there were several general power failures during this month and so the crystal temperature consequently fell to 10K a few times. Each time that this happened, the temperature was brought back to 20K and the crystal recentred. All data effected by the above problems were deleted from the dataset and recollected.

Table 5.5.1 *- A summary of the range of data collection in the eleven shells.*

Shell number	2θ range (°)	Data collected		
1	4-60	-h to 0	-k to 0	-l to l
2	4-60	0 to h	0 to k	-l to l
3	4-60	-h to 0	0 to k	-l to l
4	60-70	-h to 0	-k to 0	-l to l
5	60-70	0 to h	0 to k	-l to l
6	60-70	0 to h	-k to 0	-l to l
7	70-80	-h to 0	-k to 0	-l to l
8	70-80	0 to h	0 to k	-l to l
9	4-60	0 to h	-k to 0	-l to l
10	60-70	-h to 0	0 to k	-l to l
11	4-50	-h to 0	-k to 0	-l to l

16462 reflections were collected in total. The resulting data were reduced using COLL5N

(Lehmann & Wilson, 1987) and corrected for absorption effects using the DATAP (Coppens, 1970) program. Some φ-scan measurements, which had been performed for several reflections during the experiment, were used to check that the model used for the absorption correction was satisfactory. A graphite correction was unnecessary since the graphite lead affected so few reflections and those that it did affect were obvious by the reflections' 2θ values of 14-15° and so could be removed manually.

Before going on to merge the data in preparation of the multipolar refinement, a preliminary assessment of the quality of the data was made by using the data to refine the structure using SHELXL-93 (Sheldrick, 1993).

Positional and anisotropic displacement parameters were refined for all non-hydrogen atoms and positional and isotropic displacement parameters were refined for all hydrogen atoms. All relevant crystal, data collection and refinement parameters are given in ***Table 5.5.2***

Table 5.5.2 *- A summary of crystal, data collection and refinement parameters for the 20K X-ray structure of MBADNP.*

Compound	MBADNP	Compound	MBADNP
Molecular Formula	$C_{13}H_{12}N_4O_4$	Absorption coefficient (mm^{-1})	0.115
Formula weight	288.27	Crystal Morphology	block
a(Å)	8.352(3)	Crystal Colour	yellow
b(Å)	8.570(3)	Crystal Size (mm)	0.30 x 0.26 x 0.20
c(Å)	8.909(4)	Total number of reflections	16427
α(°)	90	Unique reflections	7873
β(°)	93.98(2)	Observed Reflections [I>2σ(I)]	7614
γ(°)	90	R_{int}	0.0203
Cell Volume($Å^3$)	636.1(4)	$(\sin\theta/\lambda)_{max}$	0.831
Crystal System	monoclinic	Data / Parameters	7873 / 238
Space Group	P2(1)	R1 [I > 2σ(I)]	0.0379
Z	2	wR2 [I > 2σ(I)]	0.0679
Calculated Density (gcm^{-1})	1.505	Goodness of fit on F^2	3.825
Temperature (K)	20.0(1)	Weighting Scheme	$1/\sigma^2$
Wavelength (Å)	0.71073	$\Delta\rho_{(max, min)}$ ($eÅ^{-3}$)	0.656 / -0.417

5.5.2.2 Structural Details

A 50% probability thermal ellipsoid plot of the 20K X-ray derived structure of MBADNP is given in ***Figure 5.5.1***. Bond lengths and selected bond angles are given in ***Tables 5.5.3*** and ***5.5.4*** respectively. Fractional coordinates and anisotropic displacement parameters are given in ***Appendix A.5.13*** and ***A.5.14.***

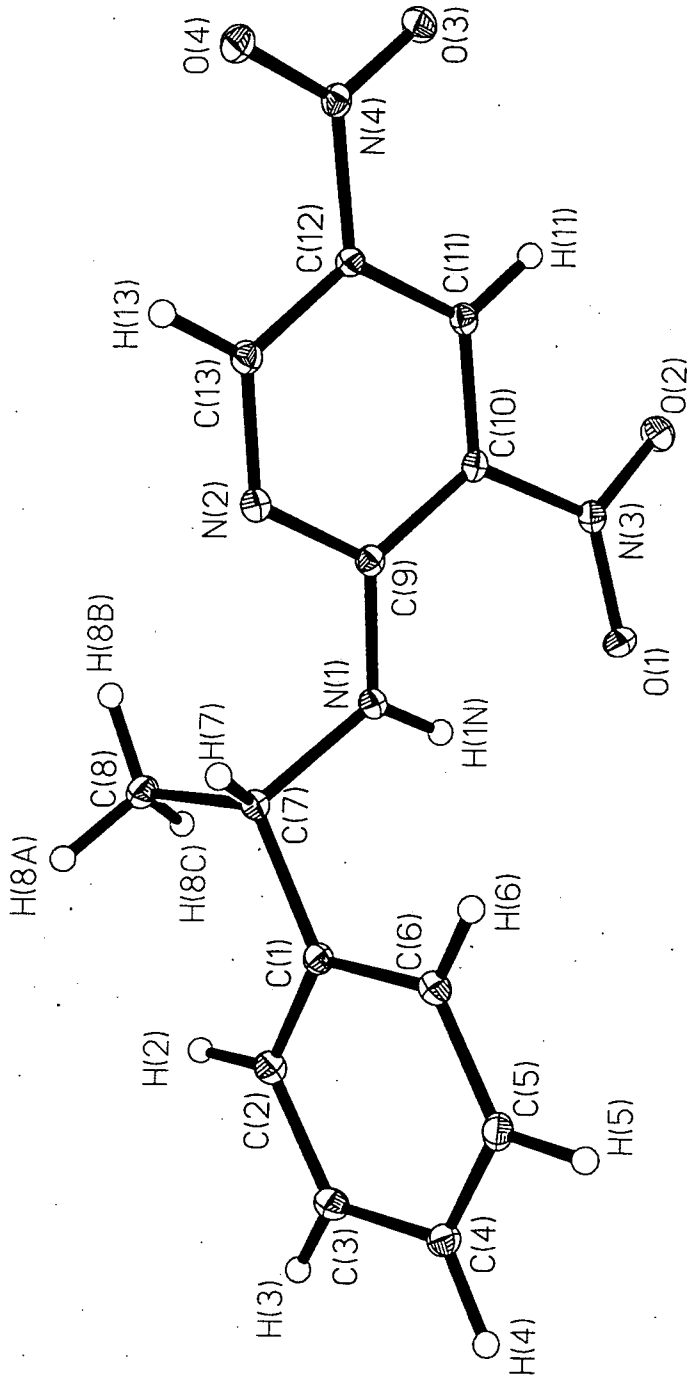

Figure 5.5.1 *- A 50% probability thermal ellipsoid plot of the 20K X-ray structure of MBADNP.*

Table 5.5.3 *- Bond lengths for the 20K X-ray structure of MBADNP.*

Bond	Distance (Å)	Bond	Distance (Å)
O(1)-N(3)	1.2437(9)	C(3)-H(3)	0.96(1)
O(2)-N(3)	1.2321(9)	C(4)-C(5)	1.393(1)
O(3)-N(4)	1.2339(9)	C(4)-H(4)	0.991(9)
O(4)-N(4)	1.2372(9)	C(5)-C(6)	1.391(1)
N(1)-C(9)	1.341(1)	C(5)-H(5)	0.10(1)
N(1)-C(7)	1.473(1)	C(6)-H(6)	0.93(1)
N(1)-H(1N)	0.87(1)	C(7)-C(8)	1.526(1)
N(2)-C(13)	1.329(1)	C(7)-H(7)	0.958(9)
N(2)-C(9)	1.358(1)	C(8)-H(8A)	0.10(1)
N(3)-C(10)	1.451(1)	C(8)-H(8B)	0.97(1)
N(4)-C(12)	1.447(1)	C(8)-H(8C)	0.99(1)
C(1)-C(2)	1.388(1)	C(9)-C(10)	1.437(1)
C(1)-C(6)	1.405(1)	C(10)-C(11)	1.379(1)
C(1)-C(7)	1.529(1)	C(11)-C(12)	1.379(1)
C(2)-C(3)	1.401(1)	C(11)-H(11)	0.94(1)
C(2)-H(2)	0.96(1)	C(12)-C(13)	1.399(1)
C(3)-C(4)	1.393(1)	C(13)-H(13)	0.97(1)

Table 5.5.4 *- Selected bond angles for the 20K X-ray structure of MBADNP.*

Angle	Angle (°)	Angle	Angle (°)
C(7)-N(1)-C(9)	123.59(7)	C(6)-C(1)-C(7)	118.80(7)
C(9)-N(1)-H(1N)	115.2(7)	N(1)-C(7)-C(1)	107.43(7)
C(7)-N(1)-H(1N)	120.4(7)	N(1)-C(7)-C(8)	110.64(7)
C(9)-N(2)-C(13)	119.35(7)	C(1)-C(7)-C(8)	114.23(7)
O(1)-N(3)-O(2)	122.71(7)	N(1)-C(9)-N(2)	116.74(7)
O(1)-N(3)-C(10)	118.68(7)	N(1)-C(9)-C(10)	123.41(8)
O(2)-N(3)-C(10)	118.60(7)	C(9)-C(10)-N(3)	122.80(7)
O(3)-N(4)-O(4)	123.54(7)	C(11)-C(10)-N(3)	116.88(7)
O(3)-N(4)-C(12)	118.07(7)	C(11)-C(12)-N(4)	119.85(7)
O(4)-N(4)-C(12)	118.39(7)	C(13)-C(12)-N(4)	119.74(7)
C(2)-C(1)-C(7)	122.57(7)		

The bond geometry is very similar but more accurate than that derived from the 100K X-ray study, as expected. The R_{int} of the data is low, thus suggesting that the accuracy

of the data measured is adequate for a charge density study. Moreover, the data seems to give a good fit to the model as reflected in the consistently low esds of the geometry, the low statistical R-factors and the small amount of residual electron density present. The thermal parameters of all atoms are significantly smaller than those derived from the 100K X-ray experiment, as expected.

On the basis of this level of accuracy and consistency, the data were deemed fit for a full charge density analysis.

5.5.2.3 The Multipolar Refinement

The corrected data were scaled and merged using the DREAM package (Blessing, 1989) in preparation for the XD (Koritsanszky et al., 1994) refinement. The X-ray derived coordinates and thermal parameters of all atoms were then refined in XD. Once the refinement had converged, a κ' parameter for each atom was introduced. All κ' values relating to non-hydrogen atoms were initially set at 1.0 and refined whereas the κ' value for hydrogen atoms was fixed to the SDS value of 1.16. The results were then combined with the neutron parameters.

The neutron derived coordinates and thermal parameters had been refined using SHELXL-93 (Sheldrick, 1993). The hydrogen coordinates and anisotropic displacement parameters in the XD refinement were replaced by the neutron derived ones. Whilst the coordinates directly substituted the X-ray derived ones, the neutron derived hydrogen thermal parameters had to be scaled with respect to the X-ray thermal parameters before substitution. The scaling parameter was derived from the difference between the X-ray and neutron derived non-hydrogen anisotropic displacement parameters according to the formula derived by Blessing (1995):

$$U_X^{ij} = U_N^{ij} + \Delta U^{ij}$$

where $\Delta U^{ij} = \sum_a \left[\sum_a wU_X^{ij} - \sum_a wU_N^{ij} \right] / \sum_a w$

and $w = 1 / \sigma^2$

where $\sigma = \sigma(U_X^{ij} - U_N^{ij}) = [\sigma^2(U_X^{ij} + \sigma^2(U_N^{ij})]^{1/2}$

The scaling parameter, ΔU^{ij}, was small [4.99×10^{-4}], thus indicating that there is good agreement between the thermal parameters. The scaling parameter was simply added to all of the hydrogen thermal parameters to give the substituted values.

The hydrogen positions and thermal parameters were then fixed in the XD refinement and the remainder was refined. Multipolar terms were then introduced starting with the refinement of Hartree-Fock derived monopoles and dipoles (bond directed ones for hydrogen atoms) on all atoms. Once converged, quadrupolar and octopolar terms were refined for all non-hydrogen atoms. Refinement at the hexadecapolar level for all non-hydrogen atoms was also tried. However, the population of these functions was negligible [maximum hexadecapolar function population was about twice its esd] and so were not included in the successive refinements.

An attempt was then made to sub-divide the κ' parameters into six values which reflected the different chemical environments in which atoms of a given element resided. The atoms were grouped in the following way:

Group 1: All oxygen atoms.
Group 2: N(1), N(3), N(4).
Group 3: N(2).
Group 4: All sp^2 hybridized carbon atoms.
Group 5: All sp^3 hybridized carbon atoms [C(7) and C(8)].
Group 6: All hydrogen atoms.

κ' parameters of all but the last group were refined. However, the κ' parameters did not converge very well, the statistics became poorer and the results gave unrealistic values of atomic charges. Hence, the previous refinement was taken to be the final one.

5.5.2.4 Results and Discussion

A summary of refinement details are given in ***Table 5.5.5***. Bond distances and selected bond angles are given in ***Tables 5.5.6*** and ***5.5.7***. From which, one can see that the geometry is very similar to that derived from the neutron study. Fractional coordinates and anisotropic displacement parameters for all non-hydrogen atoms are given in ***Appendix A.5.15*** and ***A.5.16*** respectively. ***Figure 5.5.2*** shows dynamic model maps, $F_{multipole}$-$F_{spherical}$ for each molecular fragment, which represent the contribution of the multipolar terms to the model. The corresponding static maps are not given here because they show very little difference since the thermal vibration in the molecule is so small. Residual density maps of the molecule, given in ***Figure 5.5.3***, show featureless regions of only a little residual electron density, thus indicating that the electron distribution is well described by the multipole model. The rigid-bond test, which was applied to all bonds not involving hydrogen during the refinement, showed that only one bond [N(1)-C(7)] has a difference in mean square displacement amplitudes along the bond direction [0.0013Å^2] which slightly exceeds 0.001Å^2, thus failing to satisfy the test

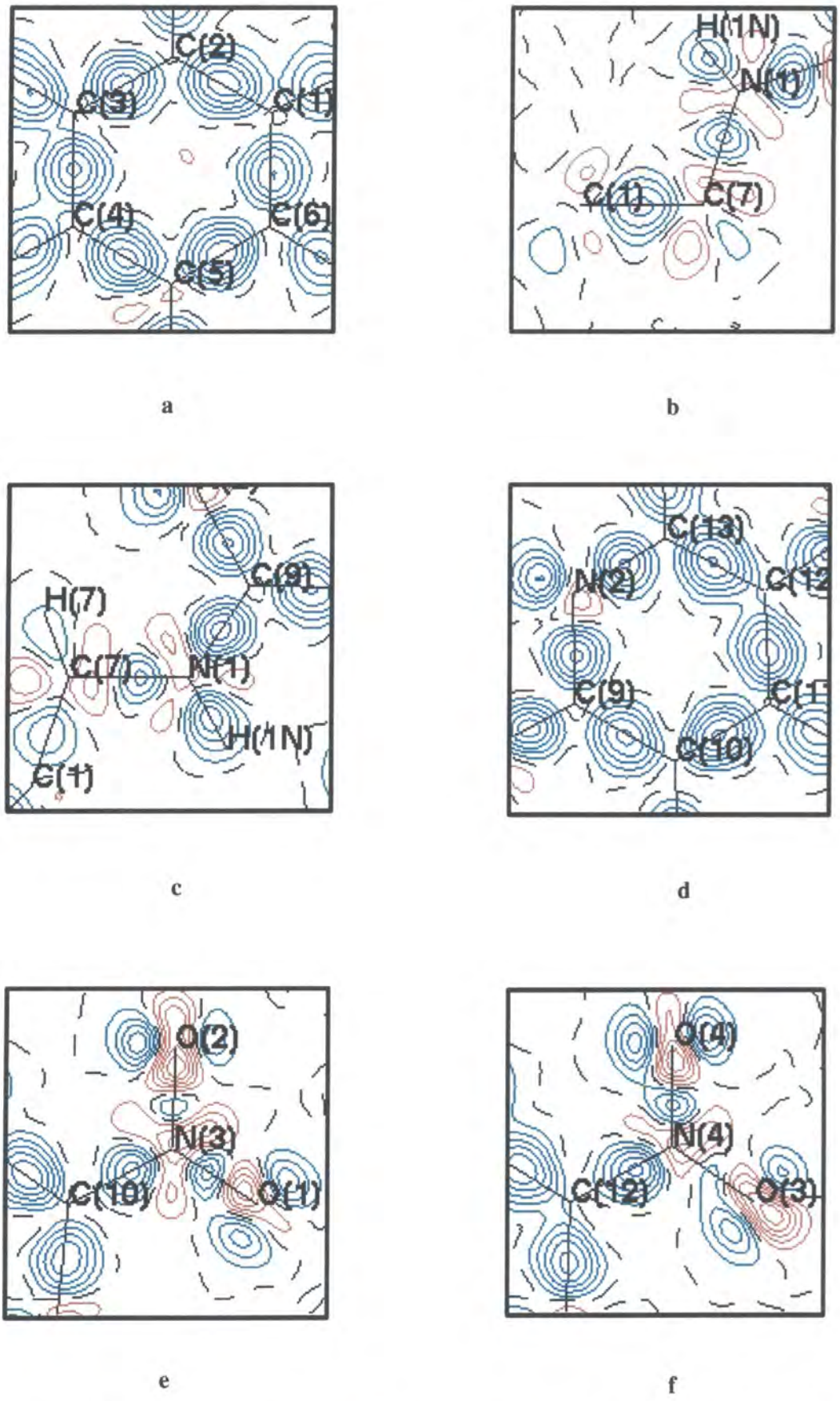

Figure 5.5.2 *– Dynamic model maps of the (a) phenyl, (b) C(1) to N(1), (c) C(7) to C(9), (d) pyridine, (e) meta–nitro, (f) para–nitro groups in MBADNP out to sinθ/λ=0.7A–1 and with contour levels of 0.1 e/A (blue lines are positive, red lines are negative, black lines are zero).*

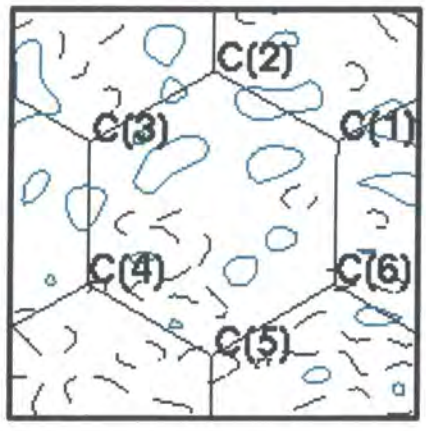

a

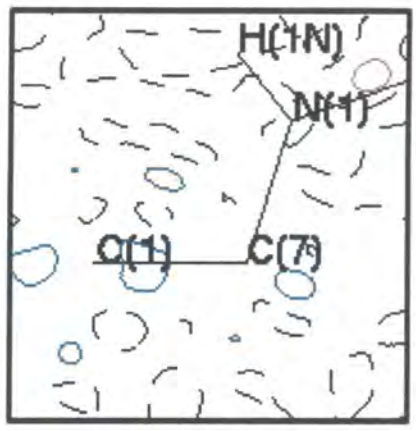

b

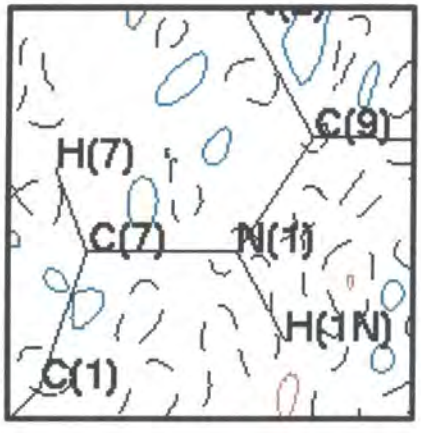

c

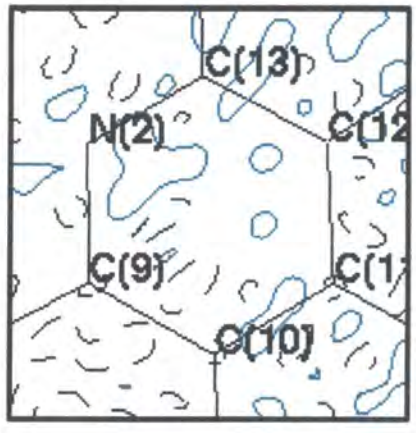

d

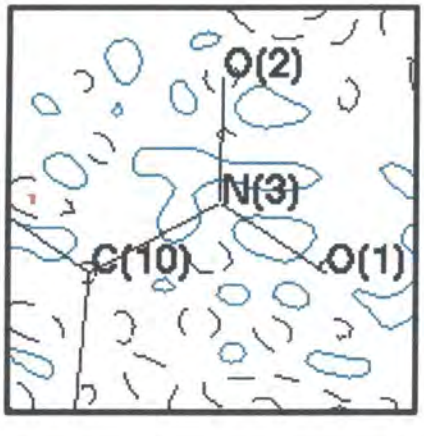

e

f

Figure 5.5.3 *– Residual density maps of the (a) phenyl, (b) C(1) to N(1), (c) C(7) to C(9), (d) pyridine, (e) meta–nitro, (f) para–nitro groups in MBADNP out to sinθ/λ=0.7A–1 and with contour levels of 0.1 e/A (blue lines are positive, red lines are negative, black lines are zero).*

criterion. The cause for this is unknown but it is probably not significant since the value is only about a tenth of the actual values for the corresponding thermal parameters.

Table 5.5.5 *- A summary of refinement parameters for the charge density study of MBADNP.*

Parameter	Value	Parameter	Value
Scale Factor	0.595(1)	Weighting Scheme	$1/\sigma^2$
Criterion for observed data	$F = 2\sigma(F)$	$R_w(F)$	0.0176
R(F)	0.0171	$R_w(F^2)$	0.0357
$R(F^2)$	0.0300	GOF_w	1.0591
$R_{all}(F)$	0.0171	Data / Parameter	3890 / 552
$R_{all}(F^2)$	0.0300	$\Delta/\sigma_{(min/max)}$	$0.9x10^{-9}$ / $0.2x10^{-5}$
GOF	1.0419	$\Delta\rho_{(min/max)}$	-0.112 / 0.173

Table 5.5.6 *- Bond lengths for MBADNP as derived from the charge density study.*

Bond	Distance (Å)	Bond	Distance (Å)
O(1)-N(3)	1.239(1)	C(3)-H(3)	1.088(1)
O(2)-N(3)	1.228(1)	C(4)-C(5)	1.401(1)
O(3)-N(4)	1.234(1)	C(4)-H(4)	1.0927(8)
O(4)-N(4)	1.235(1)	C(5)-C(6)	1.393(1)
N(1)-C(7)	1.472(1)	C(5)-H(5)	1.085(1)
N(1)-C(9)	1.338(1)	C(6)-H(6)	1.087(1)
N(1)-H(1N)	1.015(1)	C(7)-C(8)	1.529(1)
N(2)-C(9)	1.361(1)	C(7)-H(7)	1.1013(8)
N(2)-C(13)	1.322(1)	C(8)-H(8A)	1.093(1)
N(3)-C(10)	1.453(1)	C(8)-H(8B)	1.0968(8)
N(4)-C(12)	1.446(1)	C(8)-H(8C)	1.0946(8)
C(1)-C(2)	1.3992(9)	C(9)-C(10)	1.436(1)
C(1)-C(6)	1.403(1)	C(10)-C(11)	1.381(1)
C(1)-C(7)	1.5238(9)	C(11)-C(12)	1.386(1)
C(2)-C(3)	1.399(1)	C(11)-H(11)	1.088(1)
C(2)-H(2)	1.087(1)	C(12)-C(13)	1.401(1)
C(3)-C(4)	1.394(1)	C(13)-H(13)	1.087(1)

Table 5.5.7 *- Selected bond angles for MBADNP as derived from the charge density study.*

Angle	Angle (°)	Angle	Angle (°)
C(7)-N(1)-C(9)	123.9(1)	C(6)-C(1)-C(7)	119.0(1)
C(7)-N(1)-H(1N)	118.2(1)	N(1)-C(7)-C(1)	107.4(1)
C(9)-N(1)-H(1N)	116.9(1)	N(1)-C(7)-C(8)	110.5(1)
C(9)-N(2)-C(13)	119.6(1)	C(1)-C(7)-C(8)	114.5(1)
O(1)-N(3)-O(2)	123.0(1)	N(1)-C(9)-N(2)	116.8(1)
O(1)-N(3)-C(10)	118.4(1)	N(1)-C(9)-C(10)	123.6(1)
O(2)-N(3)-C(10)	118.6(1)	N(3)-C(10)-C(9)	122.9(1)
O(3)-N(4)-O(4)	123.8(1)	N(3)-C(10)-C(11)	116.7(1)
O(3)-N(4)-C(12)	118.1(1)	N(4)-C(12)-C(11)	119.8(1)
O(4)-N(4)-C(12)	118.1(1)	N(4)-C(12)-C(13)	120.2(1)
C(2)-C(1)-C(7)	122.3(1)		

Since an electroneutrality constraint is applied over the whole asymmetric unit, the extent of charge-transfer ensuing in the molecule can be derived wholly from the monopole populations. The charge on a given atom is the difference between the monopole population for this atom, as observed from the charge density study and the number of valence electrons classically present in the atom, e.g. for a carbon atom, the expected monopole population would be four. The charges present on each atom in MBADNP are given in ***Table 5.5.8***.

Table 5.5.8 *- Pseudoatomic charges for each atom in MBADNP.*

Atom	Charge	Atom	Charge	Atom	Charge
O(1)	-0.1634	C(4)	-0.1617	H(2)	0.1737
O(2)	-0.0090	C(5)	0.0711	H(3)	0.0861
O(3)	-0.0049	C(6)	-0.0460	H(4)	0.1233
O(4)	-0.0950	C(7)	-0.0095	H(5)	0.1183
N(1)	-0.0437	C(8)	-0.1644	H(6)	0.1813
N(2)	0.0386	C(9)	-0.1003	H(7)	0.1211
N(3)	0.1706	C(10)	-0.1531	H(8A)	-0.0561
N(4)	0.0841	C(11)	-0.0495	H(8B)	0.0990
C(1)	-0.0443	C(12)	-0.2363	H(8C)	0.1128
C(2)	-0.0829	C(13)	-0.2380	H(11)	0.1644
C(3)	-0.2381	H(1N)	0.1908	H(13)	0.1613

All values of the derived charges conform to simple electronegativity expectations. The charge is concentrated in two areas: the phenyl ring and the pyridine ring. The respective pseudoatom charges of the branch atoms C(7) and N(1) are very small compared with those for atoms in each ring. Therefore, the two areas of charge-transfer are localized in each ring. This helps validate our assumption made previously about the charge transfer axis when calculating the phase-matching angle of MBADNP (see section 5.3.3.2).

Electron deformation density maps of the molecule, ρ-ρ_{IAM}, which effectively represent the valence density, are given in ***Figure 5.5.4***. These maps illustrate the nature and extent of the polarization ensuing in the molecule. Also, all critical points and ellipticity values found within the molecule are given in ***Tables 5.5.9*** and ***5.5.10***.

Table 5.5.9 - *Information regarding all (3, -1) bond critical points located within the molecule of MBADNP.*

Bond	λ_1	λ_2	λ_3	ρ	$\nabla^2\rho$	ε	R_{ij}	d1	d2
O(1)-N(3)	-29.49	-25.94	48.17	3.182	-7.258	0.14	1.24	0.630	0.609
O(1)-H(1N)	-0.83	-0.69	4.31	0.191	2.786	0.21	2.00	1.209	0.787
O(2)-N(3)	-28.01	-25.86	45.26	3.106	-8.605	0.08	1.23	0.628	0.600
O(3)-N(4)	-26.75	-24.98	43.69	3.064	-8.042	0.07	1.23	0.666	0.568
O(4)-N(4)	-28.19	-27.20	48.35	3.200	-7.036	0.04	1.24	0.633	0.603
N(1)-C(7)	-9.92	-9.21	7.28	1.570	-11.855	0.08	1.47	0.908	0.564
N(1)-C(9)	-20.31	-18.04	9.54	2.407	-28.814	0.13	1.34	0.788	0.550
N(1)-H(1N)	-27.00	-25.74	30.52	2.047	-22.221	0.05	1.02	0.769	0.246
N(2)-C(9)	-18.39	-16.53	14.40	2.309	-20.518	0.11	1.36	0.750	0.610
N(2)-C(13)	-19.65	-18.36	10.88	2.438	-27.139	0.07	1.32	0.760	0.562
N(3)-C(10)	-13.10	-10.35	10.20	1.777	-13.257	0.27	1.45	0.873	0.581
N(4)-C(12)	-14.01	-10.91	11.53	1.870	-13.391	0.28	1.45	0.858	0.588
C(1)-C(2)	-15.59	-13.12	10.13	2.119	-18.581	0.19	1.40	0.697	0.702
C(1)-C(6)	-14.90	-12.64	9.21	2.027	-18.331	0.18	1.40	0.660	0.744
C(1)-C(7)	-11.11	-11.00	10.45	1.675	-11.664	0.01	1.52	0.770	0.754
C(2)-C(3)	-16.13	-13.64	9.43	2.109	-20.334	0.18	1.40	0.694	0.705
C(2)-H(2)	-16.25	-15.29	14.19	1.749	-17.348	0.06	1.09	0.715	0.372
C(3)-C(4)	-15.37	-13.21	9.10	2.078	-19.483	0.16	1.39	0.699	0.695
C(3)-H(3)	-16.94	-15.70	19.26	1.753	-13.385	0.08	1.09	0.748	0.340
C(4)-C(5)	-15.84	-13.06	9.37	2.079	-19.522	0.21	1.40	0.668	0.733
C(4)-H(4)	-15.86	-15.35	18.85	1.670	-12.364	0.03	1.09	0.755	0.338
C(5)-C(6)	-16.69	-14.23	9.28	2.156	-21.636	0.17	1.39	0.684	0.709
C(5)-H(5)	-15.82	-14.61	12.98	1.722	-17.451	0.08	1.08	0.688	0.397

C(6)-H(6)	-16.10	-15.58	14.49	1.721	-17.190	0.03	1.09	0.722	0.365
C(7)-C(8)	-10.18	-9.78	9.95	1.586	-10.019	0.04	1.53	0.801	0.728
C(7)-H(7)	-15.51	-15.14	15.85	1.720	-14.805	0.02	1.10	0.734	0.367
C(8)-H(8A)	-13.58	-12.89	13.89	1.668	-12.586	0.05	1.09	0.672	0.421
C(8)-H(8B)	-15.43	-15.01	15.49	1.727	-14.948	0.03	1.10	0.721	0.376
C(8)-H(8C)	-15.04	-14.57	15.54	1.695	-14.073	0.03	1.09	0.722	0.373
C(9)-C(10)	-14.47	-12.23	9.98	1.953	-16.731	0.18	1.44	0.703	0.734
C(10)-C(11)	-16.91	-14.23	9.40	2.205	-21.745	0.19	1.38	0.707	0.675
C(11)-C(12)	-15.85	-13.22	9.18	2.130	-19.885	0.20	1.39	0.723	0.663
C(11)-H(11)	-16.89	-16.24	15.94	1.768	-17.191	0.04	1.09	0.735	0.353
C(12)-C(13)	-15.61	-13.20	9.85	2.133	-18.953	0.18	1.40	0.681	0.720
C(13)-H(13)	-16.81	-15.88	16.01	1.769	-16.672	0.06	1.09	0.733	0.353

[R_{ij} is the length of the bond path between the atoms; d1 and d2 represent the distance between the first and second atoms specified in the bond column and the critical point respectively].

Table 5.5.10 *- Information regarding all (3,+1) ring critical points located within the molecule of MBADNP.*

Distance (Å) between critical point and atom X						λ_1	λ_2	λ_3	ρ	$\nabla^2\rho$
C(1)	C(2)	C(3)	C(4)	C(5)	C(6)					
1.404	1.392	1.399	1.411	1.398	1.384	-0.46	1.76	1.88	0.2193	3.2
C(9)	C(10)	C(11)	C(12)	C(13)	N(2)					
1.361	1.343	1.402	1.393	1.382	1.408	-0.60	1.95	2.08	0.2441	3.4
C(9)	C(10)	N(3)	O(1)	H(1N)	N(1)					
1.521	1.555	1.550	1.365	1.139	1.446	-0.39	0.70	1.78	0.1435	2.1

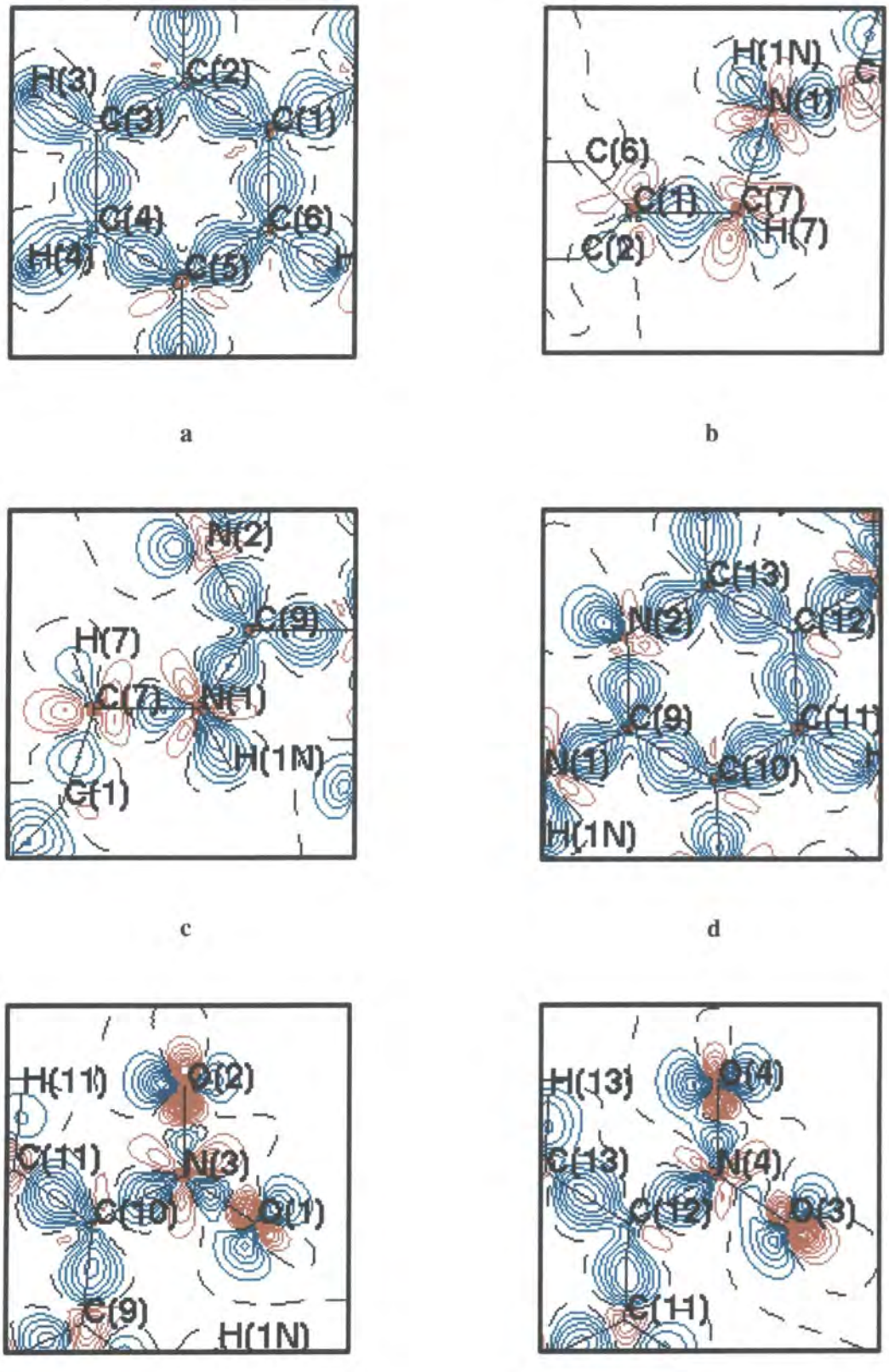

Figure 5.5.4 *– Deformation density maps of the (a) phenyl, (b) C(1) to N(1), (c) C(7) to C(9), (d) pyridine, (e) meta–nitro, (f) para–nitro groups in MBADNP to sinθ/λ=2.0A–1 and with contour levels of 0.1 eA (blue lines are positive, red lines are negative, black lines are zero).*

The electron density in each bond of the pyridine ring is essentially symmetrically distributed between the respective atoms, thus indicating that there is no polarization within the ring. The critical points existing almost at the mid-points between the bonds C(9)-C(10), C(10)-C(11), C(11)-C(12) and C(12)-C(13) confirm this. The critical points between the bonds N(2)-C(9) and N(2)-C(13), are displaced from the bond distance mid-point towards the carbon atom in both cases. However, this simply reflects the greater contribution of electron density to the bond from the more electronegative nitrogen atom. The ring is delocalized with the nitrogen atom contributing electron density (in a p-orbital perpendicular to the plane shown) to the ring in order to satisfy the 4n+2 Huckel's rule for aromaticity. The ellipticity values of the N(2)-C(9) and N(2)-C(13) bonds are slightly lower than the more typical values for other atoms in the ring, which reflects the slightly poorer orbital overlap between the two different elemental types. The nitrogen's lone pair can be clearly seen in the plane pointing away from the ring in ***Figure 5.5.4.*** A local depletion of charge is present at the centre of the ring as expected. A corresponding (3,+1) critical point was located.

The *meta-* and *para-*nitro groups show a similar valence electron distribution to each other. In both groups, there is a larger amount of electron density present between the C-N bond than one would expect from a σ-bond. An examination of the relevant C-N ellipticity values reveals that there is a significant amount of π-bonding present in this bond. Thus, the nitrogen out-of-plane p-orbital must be involved in conjugation with the ring. The concentration of charge in this bond causes a corresponding depletion in charge of the N-O bonds which would normally be delocalized. Therefore, the ellipticity values for the N-O bonds are more typical of a single-bond than a double-bond. There is slightly more charge-transfer from the O-N bonds to the N-C bond in the *para-* group than the *meta-* group, judging by the ellipticity values. The less well-developed positive lobes on the nitrogen atom in the *para-* group compared to those in the *meta-* group in the EDD maps also reflect this. As a result of this conjugation, the C-N bond is slightly polarized towards the carbon atom as is evident from the relevant EDD maps and the relevant pseudoatomic charges (see ***Table 5.5.8***). The two lone pairs on each oxygen atom can be clearly seen in the EDD maps.

The ellipticity value for the N(1)-C(9) bond suggests that the N(1) atom may be slightly conjugated to the pyridine ring. Other than this, only σ-bonding is present in the branch between the two rings, judging by the relevant ellipticity values. Hence, in principle, the branch is free to rotate. However, as we saw in section 5.4, an intramolecular hydrogen-bond, N(1)-H(1N)...O(1), severely restricts such freedom. A bond critical point relating to this hydrogen-bond was located (see ***Table 5.5.9***), therefore proving that the bond exists. The EDD map, given in ***Figure 5.5.5***, illustrates the oxygen lone pair directionality towards the hydrogen atom and the Laplacian map in ***Figure 5.5.5*** shows

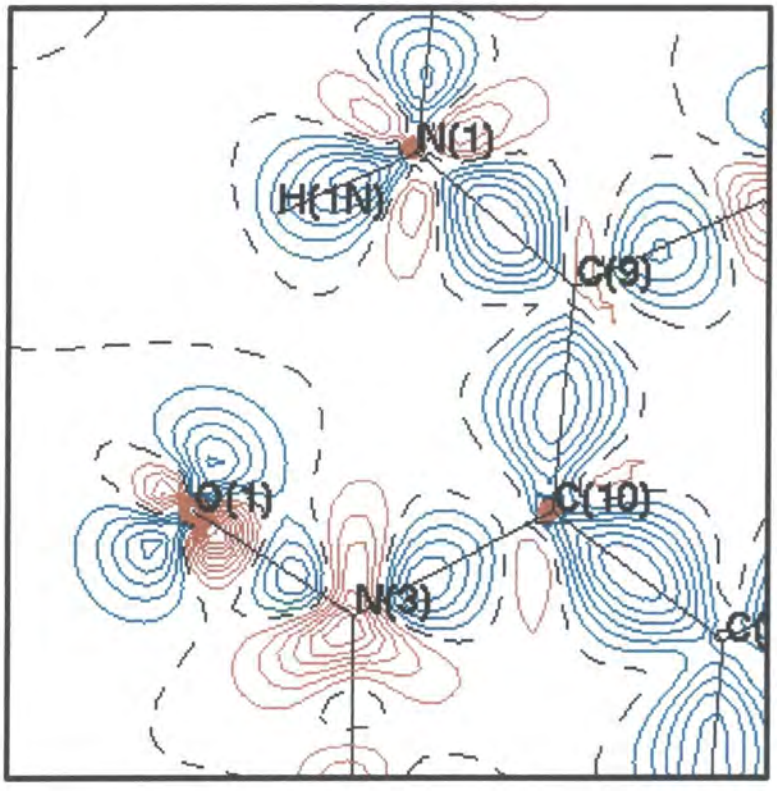

a

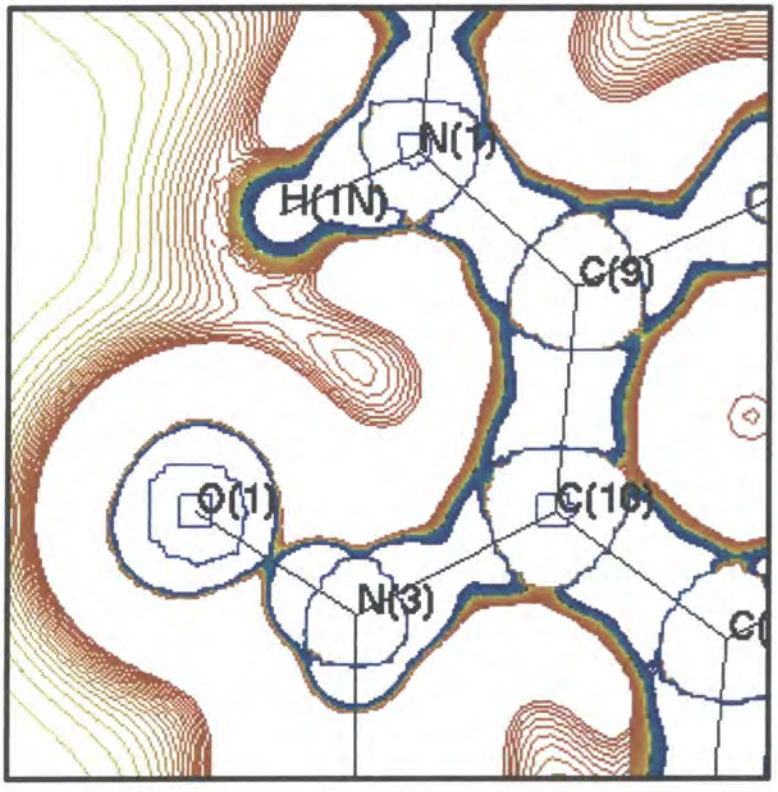

b

Figure 5.5.5 *– (a) deformation density and (b) Laplacian maps showing the hydrogen–bond, N(1)–H(1N)...O(1) in MBADNP out to sinθ/λ=2.0A–1 and with contour levels of 0.1 e/A and O.2 e/A respectively (blue lines are positive, red lines are negative, black lines are zero).*

the local depletion of charge, near to the hydrogen atom and along the H(1N)...O(1) bond vector, that one would expect for a hydrogen-bond since such a hydrogen atom would be very acidic. The latter map also shows local charge depletion near the centre of the ring which is made by the formation of this hydrogen-bond. A critical point of the type (3,+1), relating to this depletion in charge was located (see ***Table 5.5.10***). No evidence was found for any of the other four possible intra-molecular hydrogen-bonds implied by the X-ray and neutron structural results. Therefore, we presume that these contacts result simply from the physical geometrical restrictions imposed within the molecule rather than from electrostatic interactions. The methyl group, which is bonded to the C(7) atom in the branch and lies out of the overall plane of the molecule, shows no special features.

All bond critical points in the phenyl ring lie close to the bond mid-point, thus indicating that there is no electronic polarization present here. Ellipticity values all lie between 0.11 and 0.22 [mean value = 0.16] which show that the ring is fairly uniformly delocalized. All adjoining hydrogen atoms are polarized towards the carbon atoms to which they are bonded, as expected. A local depletion of charge is present at the centre of the ring and a corresponding (3,+1) critical point was located. The level of charge depletion is approximately the same as that determined at the centre of the pyridine ring.

In summary, the polarization is primarily present within close proximity of the pyridine group. Therefore, we believe that this part of the molecule is the most important with respect to the NLO effect. The intra-molecular hydrogen-bond determined in this study and the pseudo-ring which it makes on its formation, may well enhance the effect.

5.5.2.5 Calculations of the Dipole Moment and the Linear Polarizability Coefficients from the Charge Density Results.

The methods for calculating the dipole moment and the linear polarizability coefficients are given in chapter 3. The determined values are given in ***Table 5.5.11*** along with the calculated values of the respective quadrupolar moments. As mentioned in chapter 4, literature values of these quantities are given in various units and so we chose to use the recommended SI units.

Table 5.5.11 *- Values of the dipolar and quadrupolar moments and the linear polarizability tensorial coefficients of MBADNP.*

Dipolar moment (x 10^{-30} Cm)		Quadrupolar moments (x 10^{-39} Cm^2)		Polarizability coefficients (x 10^{-39} C)	
p_x	9.01	Θ_{xx}	23.12	$\lvert\alpha_{xx}\rvert$	175.07
p_y	-11.34	Θ_{yy}	1.57	$\lvert\alpha_{yy}\rvert$	0.81
p_z	-13.01	Θ_{zz}	13.18	$\lvert\alpha_{zz}\rvert$	56.93
		Θ_{xy}	-14.19	α_{xy}	8.58
$\lvert p_{total}\rvert$	19.35	Θ_{xz}	-14.99	α_{xz}	-15.50
		Θ_{yz}	-5.21	α_{yz}	-3.70

The overall value for the dipole moment is moderately large compared to the series of such values determined from various molecules by Spackman (1992). This is expected since the molecule possesses several strong donor and acceptor groups. ***Figure 5.5.6*** shows that the dipole moment projects from the molecular centre of mass along the vector which bisects the two nitro groups. This directionality is identical to that assumed for the charge-transfer axis reported in section 5.3.3.2, thus indicating that the monopolar contribution to the dipole moment is the determining one.

The quadrupolar moments range from moderate to extremely large compared to values from a series of such values determined from various molecules by Spackman (1992). Given that the calculation of the polarizability coefficient simply involves constants and the squaring of the relevant quadrupolar moment(s), the corresponding linear polarizability coefficients must also vary from moderate to extremely large in size. Since so few reports of the polarizability coefficients, as derived from charge density studies, have been made, we cannot yet make a good comparison between our results and those obtained for compounds from other multipolar refinements. A large anisotropy of the linear polarizability is evident from the results. The α_{xx} value is by far the largest component of the linear polarizability and α_{zz} is the second largest. The resultant direction of the polarizability, if we consider just these two coefficients, is roughly along the molecular axis.

At present, no other values for the dipole or quadrupolar moments have been determined using other means. This is the subject of further work as is the determination of values for the linear polarizability since no other reported values of these exist at present either. Further calculations are also underway to try and determine the octopolar moments and therefore be able to evaluate values for the first hyperpolarizability coefficients in the solid state.

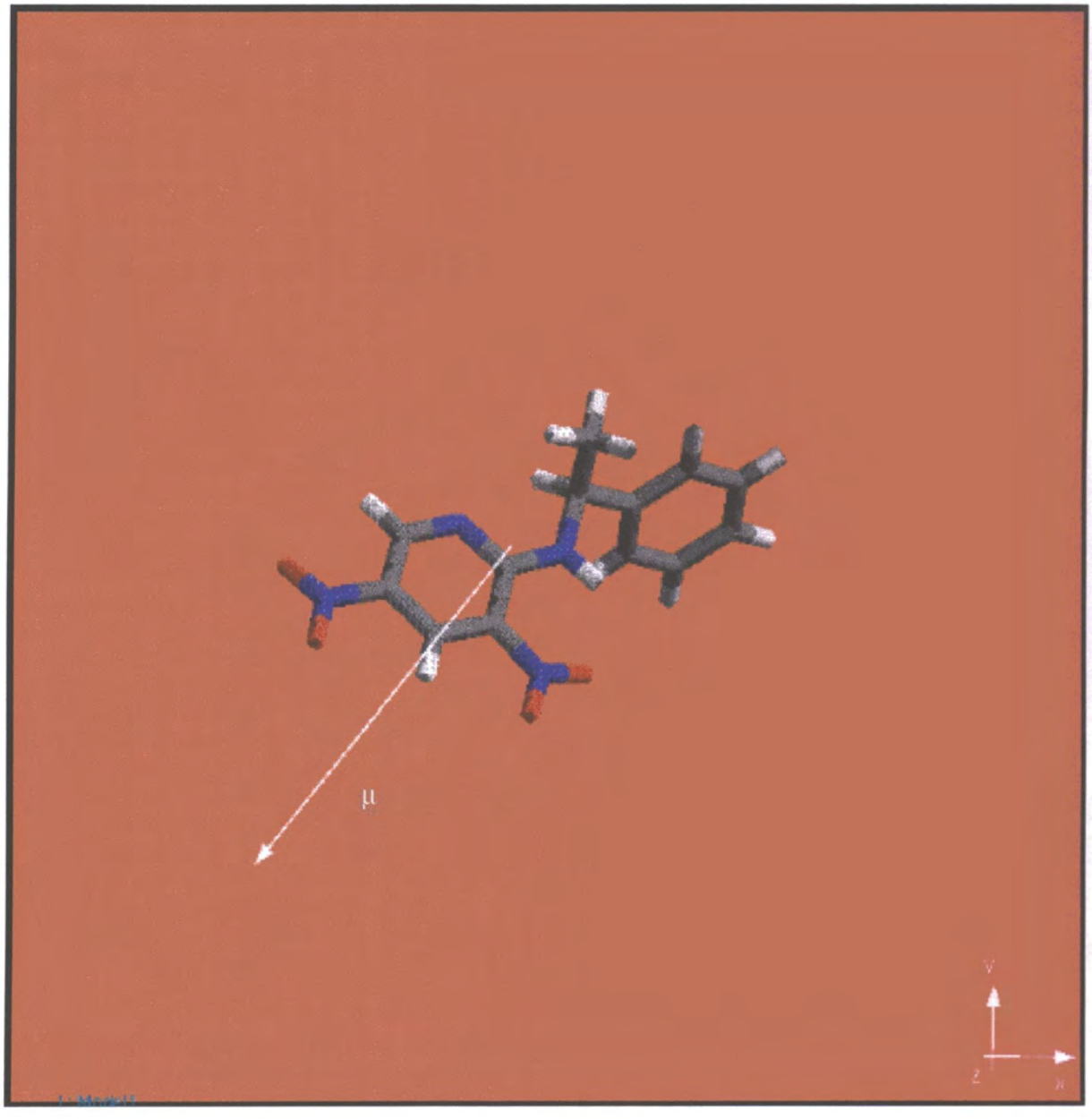

Figure 5.5.6 *– The direction of the dipole moment in MBADNP.*

5.6 THE NEUTRON STRUCTURE OF NMBA

The neutron structure of NMBA was determined in order to ascertain whether or not any hydrogen-bonding is present in the three-dimensional lattice and is the cause of the large macroscopic $\chi^{(2)}$ value.

5.6.1 Experimental

D10 at the ILL was used for this experiment. A Cu (200) monochromator was employed. This provided a wavelength of 1.2617(3)Å, calibrated using a standard ruby crystal.

A crystal of dimensions 5.3 x 2.1 x 1.2 mm was cut from a parent crystal (dimensions: mm) using a sharp scalpel blade. The crystal was wrapped in aluminium foil, mounted onto a cadmium pin and then placed onto the cryostat. Reflections were found and centred using a detector aperture size of 10 x 8 mm. The centred reflections were used in order to obtain a suitable UB matrix. The sample was then cooled to 20K during which time the peak profiles remained sharp and intense. Data collection was subsequently initiated with a modified detector aperture of 16-20 mm. Batches in the range $0° \leq 2\theta \leq 40°$, $40° \leq 2\theta \leq 70°$ were collected. ω-xθ scans, with x chosen to keep the reflection in the middle of the detector aperture, were used in conjunction with a scan width, $\Delta\omega$, which was roughly twice the full width of the peak to background. Both x and $\Delta\omega$ varied with the Bragg angle, θ:

θ	0.00	15.00	30.00	45.00	65.00
x	0.00	0.75	1.30	1.90	2.00
$\Delta\omega$	0.00	1.80	1.70	2.00	3.00

A default scan time of 10000 monitor counts was employed. A standard reflection (1 -2 -2) was measured every 50 reflections in order to monitor the constancy of the intensity. During the collection of the first batch of data we noticed that there were shoulders present on several of the peaks. However, we decided to continue the collection since (a) the majority of the reflections had very sharp and intense peak profiles and (b) since the only crystal available to us was the parent crystal from which this one was cut.

Data collection proceeded smoothly and the data were reduced using COLL5N (Lehmann & Wilson, 1987). The peak profiles given in the output to the data reduction program were analysed. It was noticed that all reflections with a low value of l had peak profiles which either possessed a shoulder or were very broad. In other words, a second Bragg peak nearly superimposed the principal one. This contamination is unlikely to be due to twinning or the presence of a satellite crystal since only the c direction is effected. We do

not know of any suitable explanation. However, we removed all 1217 reflections corresponding to |l| = 0, 1 or 2 from the data file in order to prevent this contamination from affecting the structural refinement. An absorption correction was then applied using the DATAP program (Coppens, 1970) [transmission range: 0.6175-0.8055].

The structure was refined by full-matrix least-squares refinement using SHELXL-93 (Sheldrick, 1993) against 1349 reflections. During the refinement, an isotropic extinction correction was applied [extinction parameter, EXTI = 0.0071(6)]. Positional and anisotropic displacement parameters were refined for all atoms.

A summary of crystal, data collection and refinement parameters is given in ***Table 5.6.1***.

Table 5.6.1 *- A summary of crystal, data collection and refinement parameters for the 20K neutron structure of NMBA.*

Compound	NMBA	Compound	NMBA
Molecular Formula	$C_{14}H_{12}N_2O_2$	Absorption coefficient (mm^{-1})	0.18
Formula weight	240.00	Crystal Morphology	block
a(Å)	7.305(4)	Crystal Colour	yellow
b(Å)	11.495(5)	Crystal Size (mm)	5.3 x 2.1 x 1.2
c(Å)	7.240(3)	Total number of reflections	1877
α(°)	90	Unique reflections	1349
β(°)	109.71(5)	Observed Reflections [I>2σ(I)]	1304
γ(°)	90	R_{int}	0.0169
Cell Volume(Å^3)	572.3(5)	$(\sin\theta/\lambda)_{max}$	0.827
Crystal System	monoclinic	Data / Parameters	1349 / 272
Space Group	Pc	R1 [I > 2σ(I)]	0.0306
Z	2	wR2 [I > 2σ(I)]	0.0469
Calculated Density (gcm^{-1})	1.393	Goodness of fit on F^2	1.960
Temperature (K)	20.0(1)	Weighting Scheme	$1/\sigma^2$
Wavelength (Å)	1.2617(3)	$\Delta\rho_{(max, min)}$ ($fmÅ^{-3}$)	0.516 / -0.503

5.6.2 Structural details

A 50% probability thermal ellipsoid plot of the 20K neutron derived structure of NMBA is given in ***Figure 5.6.1***. Bond lengths and selected bond angles are given in ***Tables 5.6.2*** and ***5.6.3*** respectively. Fractional coordinates and anisotropic displacement parameters are given in ***Appendix A.5.17***and ***A.5.18***

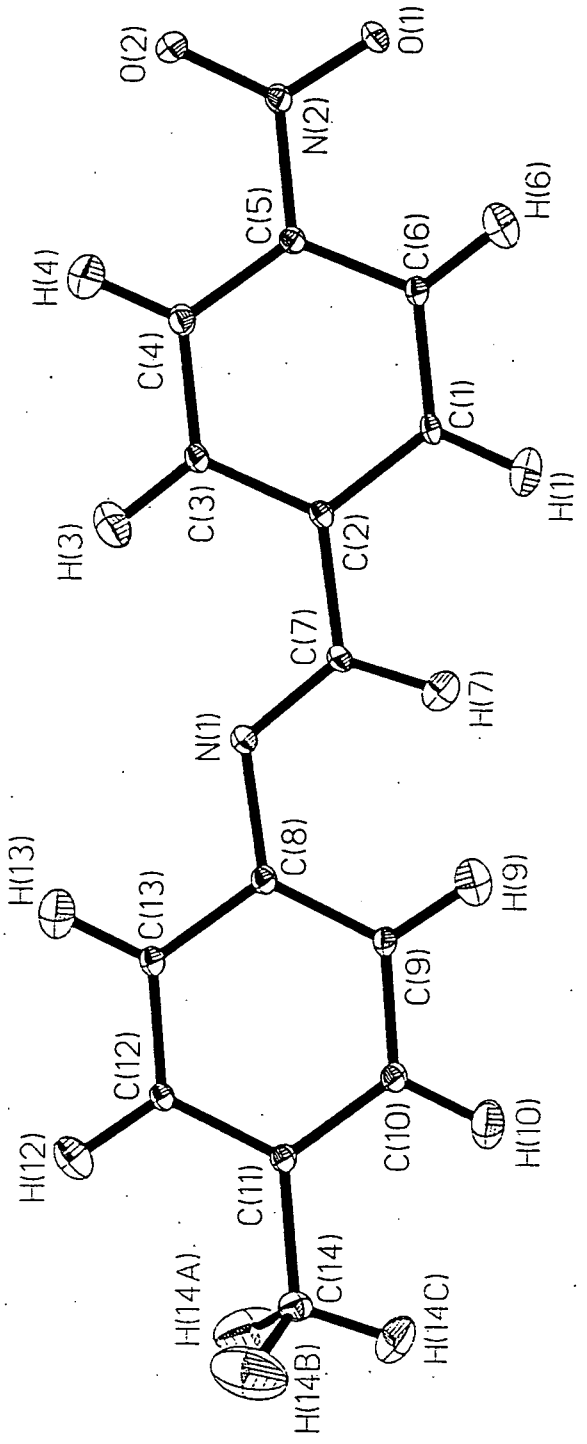

Figure 5.6.1 *- A 50% probability thermal ellipsoid plot of the 20K neutron structure of NMBA.*

Table 5.6.2 *- Bond lengths for the 20K neutron structure of NMBA.*

Atom	Distance (Å)	Bond	Distance (Å)
O(1)-N(2)	1.233(2)	C(7)-H(7)	1.093(6)
O(2)-N(2)	1.216(3)	C(8)-C(9)	1.397(3)
N(1)-C(7)	1.278(2)	C(8)-C(13)	1.405(3)
N(1)-C(8)	1.420(3)	C(9)-C(10)	1.394(3)
N(2)-C(5)	1.464(3)	C(9)-H(9)	1.091(5)
C(1)-C(6)	1.396(3)	C(10)-C(11)	1.402(3)
C(1)-C(2)	1.401(3)	C(10)-H(10)	1.093(6)
C(1)-H(1)	1.078(6)	C(11)-C(12)	1.402(3)
C(2)-C(3)	1.402(3)	C(11)-C(14)	1.502(4)
C(2)-C(7)	1.471(3)	C(12)-C(13)	1.390(3)
C(3)-C(4)	1.387(4)	C(12)-H(12)	1.089(5)
C(3)-H(3)	1.083(4)	C(13)-H(13)	1.091(6)
C(4)-C(5)	1.390(3)	C(14)-H(14A)	1.081(6)
C(4)-H(4)	1.088(6)	C(14)-H(14B)	1.093(4)
C(5)-C(6)	1.389(3)	C(14)-H(14C)	1.084(7)
C(6)-H(6)	1.095(5)		

Table 5.6.3 *- Selected bond angles for the 20K neutron structure of NMBA.*

Angle	Angle (°)	Angle	Angle (°)
C(7)-N(1)-C(8)	120.9(1)	C(4)-C(5)-N(2)	118.8(2)
O(2)-N(2)-O(1)	123.5(2)	N(1)-C(7)-C(2)	121.6(2)
O(2)-N(2)-C(5)	118.8(2)	N(1)-C(7)-H(7)	123.0(3)
O(1)-N(2)-C(5)	117.7(2)	C(2)-C(7)-H(7)	115.3(3)
C(2)-C(1)-H(1)	120.0(4)	C(9)-C(8)-N(1)	125.3(2)
C(6)-C(1)-H(1)	119.8(3)	C(13)-C(8)-N(1)	116.4(2)
C(1)-C(2)-C(7)	118.7(2)	C(10)-C(11)-C(14)	120.9(2)
C(3)-C(2)-C(7)	121.6(2)	C(12)-C(11)-C(14)	121.3(2)
C(6)-C(5)-N(2)	118.5(2)		

In contrast to all other neutron structures reported in this thesis so far, the neutron derived cell parameters of NMBA were used for the structural refinement. This was simply because no 20K X-ray derived cell parameters were available to us.

The two aromatic rings in the molecule are linked via a -CH=N- moiety and each ring is

twisted relative to the other by 3.9(1)°. The twist angle of each phenyl ring relative to the mean plane of the molecule is 2.6(1)° [C(1)-C(6)] and 1.3(1)° [C(8)-C(13)]. The nitro group deviates from the mean plane of the molecule by 12.2(1)°. The molecule is therefore almost completely planar, as reported previously (Bailey et al, 1993).

The high degree of planarity is obviously due to the omnipresent π-conjugation throughout the molecule. This, in turn, promotes the methyl-nitro D-A interactions across the molecule thereby enhancing the molecular charge-transfer and giving rise to the high value of β.

All of the molecular geometry is as one would expect, except for the slight deviation from conventional sp^2 geometry around C(7) and C(8) (see ***Table 5.6.3***). We believe that these deviations result from the influence of the intramolecular non-bonded contact, H(7)...H(9) [1.97(1)Å]. This contact is repulsive and so will have forced the H(7)-C(7)-N(1)-C(8)-C(9)-H(9) moiety to open out as much as possible in order to minimize its strength.

All non-bonded contacts present in NMBA are summarized in ***Table 5.6.4***. The intramolecular interactions, O(1)...H(6)-C(6) [2.413(8)Å] and O(2)...H(4)-C(4) [2.439(7)Å] link the oxygen of the nitro group to the more rigid adjacent phenyl group. This presumably restricts the movement of the nitro group and may cause it to be slightly more planar than it would be otherwise. The other two intramolecular non-bonded contacts are weak and have no obvious effect on the geometry.

Table 5.6.4 *- A summary of all intramolecular and intermolecular non-bonded contacts present in NMBA.*

Intramolecular non-bonded contacts in NMBA		Intermolecular non-bonded contacts in NMBA	
Contact	Distance (Å)	Contact	Distance (Å)
C(3)-H(3)...N(1)	2.569(8)	C(1)-H(1)...O(1)[a]	2.344(9)
C(4)-H(4)...O(2)	2.439(7)	C(7)-H(7)...O(1)[b]	2.380(8)
C(6)-H(6)...O(1)	2.413(8)	C(12)-H(12)...π[c]	2.583(1)
C(7)-H(7)...C(9)	2.583(9)	C(14)-H(14A)...N(1)[d]	2.588(9)
H(7)...H(9)	1.97(1)		

symmetry codes: a = 1+x, 2-y, 1/2+z; b = x-1, 2-y, 1/2-z; c = x, 1-y, 1/2-z; d = x-1, 1-y, 1/2-z.

All intermolecular interactions are of the type C-H...X (where X = N, O or π). C-H...X interactions were first classified as hydrogen-bonds by Taylor & Kennard (1982). Whilst more commonly present in structures where no strong donors or acceptors exist (Hoy

1996), these types of interactions clearly dictate the three-dimensional arrangement of the molecule, despite the presence of several oxygen and nitrogen atoms per molecule.

Both of the principal intermolecular interactions link O(1) of one molecule to the H(1)-C(1)-C(2)-C(7)-H(7) moiety of another, thereby invoking the formation of a six-membered ring. The O(1)...H(7)-C(7) interaction [2.380(8)Å] (B) may also play a role in the aforementioned slight deviation of C(7) from regular sp^2 geometry. However, since the slightly stronger O(1)...H(1)-C(1) interaction [2.344(9)Å] (A) does not cause any such geometrical distortion at C(1) due to the formation of this 'ring', we expect that any effect of the O(1)...H(7)-C(7) interaction on C(7) will be very small.

The two weaker intermolecular interactions, N(1)...H(14A)-C(14) [2.588(9)Å] (D) and π(aromatic)...H(12)-C(12) [2.58(1)Å] (C), involve either a N or π hydrogen-bond acceptor. Whilst the former type of acceptor is very common, π...H-C interactions are rare (Viswamitra, Radhakrishnan & Desiraju, 1993). Moreover, although π...H-C interactions are generally fairly weak, they can be structurally significant (Steiner, 1995a & 1995b). In this compound, the π acceptor originates from the centre of the C(8)-C(13) phenyl ring and the corresponding hydrogen-bond lies in a direction almost completely perpendicular to the ring. The H(12) atom, to which the π acceptor is linked, therefore lies almost directly below the centre of the ring. The molecule to which the H(12) atom is attached lies perpendicular to the molecule containing the π acceptor. This interaction and the N(1)...H(14A)-C(14) contact hold the molecules together along the b direction (see ***Figure 5.6.2b***).

A view of the three-dimensional molecular packing arrangement of NMBA, looking down the a axis, is given in ***Figure 5.6.2a***, from which one can see that molecules translated along the c direction pack parallel to each other as do the molecules translated along the a direction. However, the two parallel sets of molecules are perpendicular to each other. The mean interplanar spacings between molecules along the a and c directions are 2.6(1)Å and 5.9(1)Å respectively. The former distance is very short. Moreover, some intermolecular atomic distances lie very close to these values since the parallel molecules pack almost directly on top of each other.

Such parallel and close layer-like stacking of molecules is very favourable for the promotion of charge transfer through a lattice. Therefore, the packing arrangement is also very favourable for SHG activity and must be responsible, in part, for the large value of $\chi^{(2)}$.

In conclusion, the study shows that hydrogen-bonding does indeed seem to dictate the three-dimensional packing of NMBA. The intermolecular hydrogen-bonds present do not

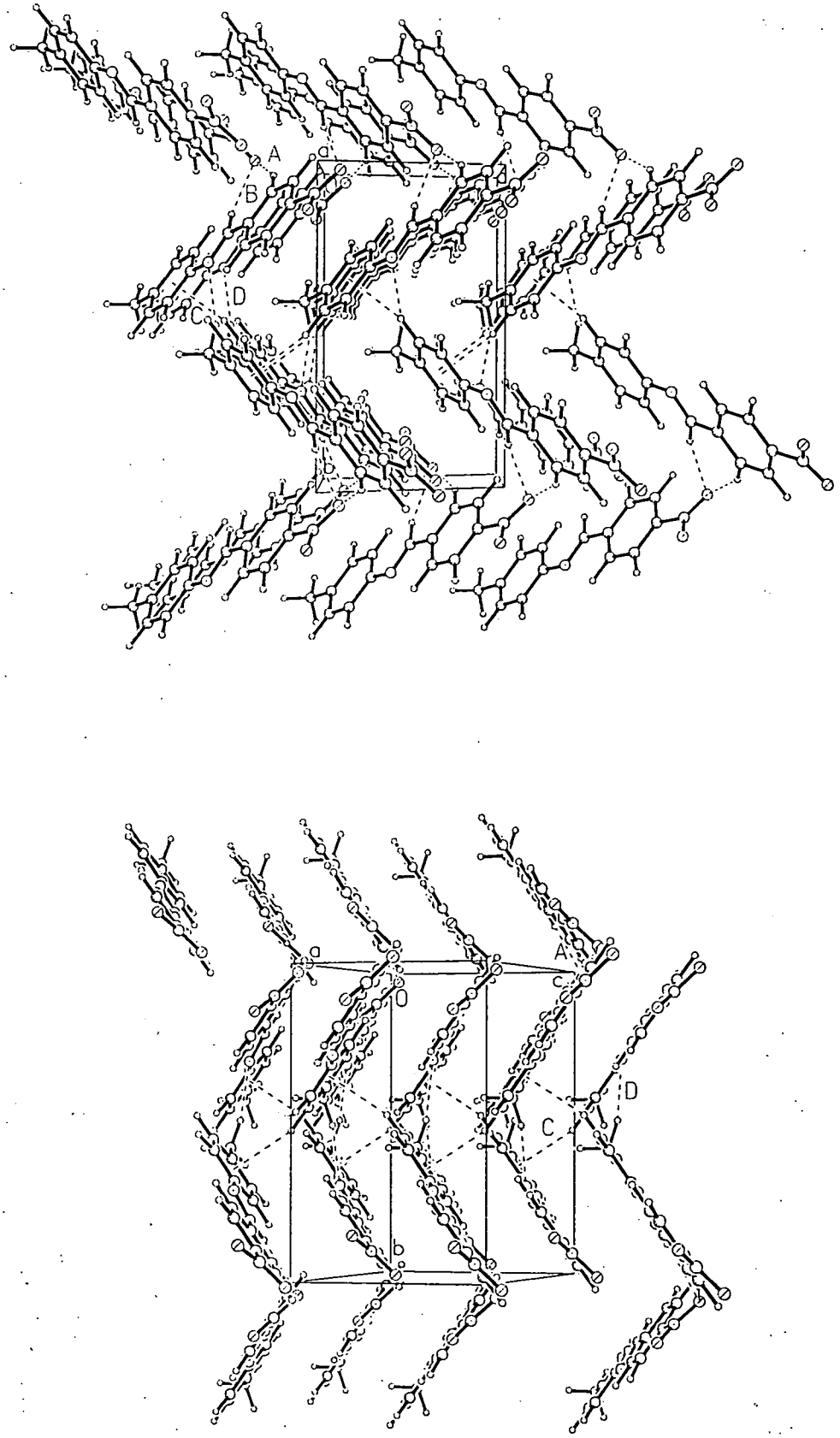

Figure 5.6.2 *- The molecular packing arrangement of the 20K neutron structure of NMBA as viewed (a) down the a axis and (b) along the b and c axes.*

involve the classical F, O or N hydrogen-bond donors. Instead, only C-H...X (X = N, O or π) intermolecular interactions are present. These interactions presumably enhance the value of $\chi(2)$. Moreover, as a result of both the hydrogen-bonding and the extreme planarity of the molecule (aided by intramolecular interactions), the molecules stack in a very close, parallel and layer-like manner with short interplanar spacings. This enhances charge-transfer between molecules and therefore further improves the value of $\chi(2)$.

5.7 A CHARGE DENSITY STUDY OF NMBA

Several X-ray size crystals were cut off the parent crystal (20 x 7 x 3 mm) using a sharp scalpel blade. Preliminary tests were carried out using the SMART-CCD diffractometer. These tests, however, gave very unpromising results since none of the crystals tested diffracted far enough out in reciprocal space to make a charge density study viable. The study was therefore concluded at this point. We believe that the poor diffracting ability may have been caused by the contamination of extra Bragg peaks in reflections of low l value, as observed in the neutron study. By growing new NMBA crystals, we may be able to circumvent this problem. However, attempts at crystallization have so far been unsuccessful.

5.8 CONCLUSIONS

The synthesis and characterization of a new SHG active compound, MBADNP and further characterization of the known compounds MBANP and NMBA has been made. The studies show that hydrogen-bonding has a large effect on the value of the macroscopic value of $\chi^{(2)}$ in all three compounds detailed. The importance of high planarity and efficient close packing is also illustrated.

The charge density study on MBADNP shows a well-fitted model. The results show various features including the location of the strong intramolecular hydrogen-bond, N(1)-H(1N)...O(1), the charge-transfer axis which corresponds to that assumed previously when the phase-matching angle was calculated. The dipole moment lies along the charge-transfer axis and is moderately large. The linear polarizability coefficients vary in size from moderate to extremely large and high anisotropy is apparent.

Further work needs to be done on several accounts. Firstly, the anomalous variation of the cell parameters with temperature in MBANP needs to be clarified by further measurements and subsequently understood. Secondly, it may prove useful to determine why reflections in all MBANP crystals seem to be inherently so broad. Thirdly, we wish to determine values for dipole moments and linear polarizabilities for MBADNP using methods other than charge density analysis and compare these with the results reported here. Finally, it would be instructive to ascertain the exact nature of the extra Bragg peaks present in the low l values of the NMBA structure since we may then be able to reintroduce the presently excluded data and model the existing structure in conjunction with 'structure' present in the Bragg peaks. New crystals of NMBA, grown by different techniques from those at present, would also allow us to ascertain whether these extra Bragg peaks are inherent in the crystal or the compound.

5.9 REFERENCES

Archer, J. M. & Lehmann, M. S. (1986). J. Appl. Cryst., **19**, 456-458.

Barthelemy, A. (1984). MAD. Institut Laue Langevin Technical Report, 84BA15T.

Bailey, R. T., Bourhill, G., Cruickshank, F. R., Pugh, D., Sherwood, J. N. & Simpson, G. S. (1993). J. Appl. Phys., **73**, 1591-1597.

Bailey, R. T., Cruickshank, F. R., Pavlides, P., Pugh, D. & Sherwood, J. N. (1991). J. Phys. D: Appl. Phys., **24**, 135-145.

Blessing, R. H. (1989). J. Appl. Cryst., **22**, 396-397.

Copley, R. C. B., Goeta, A. E., Lehmann, C. W., Cole, J. C., Yufit, D. S., Howard, J. A. K. & Archer, J. M. (1997). J. Appl. Cryst., **30**, 413-417.

Coppens, P. (1970). DATAP. *The Evaluation of Absorption and Extinction in Single-Crystal Structure Analysis* in "Crystallographic Computing", Ed. Ahmed, F. R., (Munksgaard, Copenhagen).

Cruickshank, F. R. (1997). Personal communication.

Flack, H. D. (1983). Acta Crystallogr., **A39**, 876-881.

Franken, P. A. & Ward, J. F. (1963). Rev. Mod. Phys., **35**, 23-39.

Hoy, V. J. (1996). PhD Thesis, University of Durham, p186.

International Tables for Crystallography, Volume C, Mathematical, Physical and Chemical Tables (1992). Ed. Wilson, A. J. C., Dordrecht, Boston, London. Tables 4.2.6.8 & 6.1.1.4. 219-222, 500-503.

Kondo, T., Ogasawara, N., Ito, R., Ishida, K., Tanase, T., Murata, T. & Hidai, M. (1988). Acta Crystallogr., **C44**, 102-104.

Koritsanszky, T., Howard, S., Richter, T., Mallinson, P., Su, Z. & Hansen, N. (1994). XD. *A Computer Program Package for Multipole Refinement and Analysis of Charge Densities from Diffraction Data.* Berlin, Cardiff, Glasgow, Buffalo, Nancy.

Lalama, S. J. & Garito, A. F. (1979). Phys. Rev. A, **20**, 1179-1194.

Lehmann, M. S. & Wilson, S. (1987). COLL5N. College V, Data reduction system: Treatment of reflection profiles.

North, A. C. T., Phillips, D. C. & Mathews, F. S. (1968). Acta Crystallogr. **A24**, 351-359.

Oudar, J. L. & Zyss, J. (1982). Phys. Rev. A, **26**, 2016-2027.

Ponomarev, V. I., Filipenko, O. S., Atovmyan, L. O., Grazhulene, S. S., Lempert, S. A. & Shigorin, V. D. (1977). Sov. Phys. Crystallogr., **22**, 223-225.

Sheldrick, G. M. (1990). Acta Crystallogr. **A46**, 467-473.

Sheldrick, G. M. (1993). SHELXL-93. *Program for the Refinement of Crystal Structures using Single Crystal Diffraction Data*, University of Göttingen, Germany.

Steiner, T. (1995a). J. Chem. Soc., Chem. Commun., 95-97.

Steiner, T. (1995b). J. Chem. Soc., Perkin Trans. 2, 1321-1326.

Taylor, R. & Kennard, O. (1982). J. Am. Chem. Soc., **104**, 5061-5070.

Tsunekawa, T., Gotoh, T. & Iwamoto, M. (1990). Chem. Phys. Lett., **166**, 353-357.

Twieg, R. J., Azema, A., Jain, K. & Cheng, Y. Y. (1982). Chem. Phys. Lett., **92**, 208-211.

Twieg, R. J. & Dirk, C. W. (1986). IBM report, RJ 5237(54077).

Twieg, R. J., Jain, K., Cheng, Y., Crowley, J. & Azema, A. (1982). Polymer Prepr. Am. Chem. Soc. Div. Polym. Chem., **23**, 147-148.

Viswamitra, M., Radhakrishnan, R., Bandekar, J. & Desiraju, G. R. (1993). J. Am. Chem. Soc., **115**, 4868-4869.

CHAPTER 6

3-(1,1-DICYANOETHENYL)-1-PHENYL-4,5-DIHYDRO-1H-PYRAZOLE

6.1 INTRODUCTION

The room temperature X-ray derived crystal structure of 3-(1,1-dicyanoethenyl)-1-phenyl-4,5-dihydro-1H-pyrazole (hereafter DCNP) was first reported in 1988 (Allen et al., 1988). In this study, DCNP was one in a series of 1,3-disubstituted 4,5-dihydro-1H-pyrazoles being assessed for linear optical, linear electro-optical, and NLO potential. The basic heteroatomic ring alone had already shown good potential and promising results were obtained from calculations (Docherty, Pugh & Morley, 1985) of dipole moments and molecular hyperpolarizabilities (both static and dynamic) for six 1,3-disubstituents. Of these six, only DCNP was further studied (Miniewicz, Palewska, Lipinski, Kowal & Swedek, 1994; Allen et al., 1988; Black et al., 1993) since (a) it was the only compound deemed to crystallize in a non-centrosymmetric space group (based on powder SHG tests) and so the only compound to give experimental confirmation of the SHG potential; (b) despite the lack of choice, DCNP showed exceptional NLO potential, giving powder SHG signals of approximately 100 times that of urea when using a fundamental wavelength, λ_f, of 1.9μm. At the more common λ_f of 1.06μm, a signal of only 1.6 times that of urea resulted but this is simply because of the reabsorption of the 532nm harmonic radiation.

From these further studies (Miniewicz, Palewska, Lipinski, Kowal & Swedek, 1994; Allen et al., 1988; Black et al., 1993) it was shown that:

- the NLO effect results principally from a very intense electronic transition which involves a charge redistribution from the sp^2 nitrogen atom in the five-membered ring to the vicinal nitrogen atom;
- the very planar and layer-like solid-state packing of the compound is responsible for the very high linear electro-optical effect;
- the high planarity of the compound makes two-state model quantum-mechanical calculations very valid;
- the compound also exhibits photoconductive and pyroelectric properties;
- very large and high quality crystals of DCNP can be grown.

All of these findings enticed us to investigate the structure / property relationships further and to examine, in detail, the nature of the charge-transfer within the five-membered ring. These investigations took the form of accurate and complementary neutron and X-ray structural determinations, carried out in order to perform a multipolar refinement and an in-depth analysis of the thermal motion within the structure using variable temperature X-ray studies.

6.2 THE 100K NEUTRON STRUCTURE OF DCNP

6.2.1 Experimental

The neutron structure of DCNP was determined using data collected on SXD at ISIS. A total of nine days was used to study DCNP, of which only seven days constituted data collection time. The two days spent not collecting data were spent at the preparative stages of the experiment. A triangular crystal (of dimensions 9.0 x 2.5 x 0.75 mm) was mounted and placed on the instrument. Peaks from initial frames were promising and so the crystal was cooled. However, on cooling to 20K, the crystal split (somewhere below 50K). The data collection temperature was not critical and so a second crystal (dimensions 7.0 x 3.0 x 2.0 mm) was cut from the same parent crystal (dimensions 22 x 14 x 7 mm) as the first crystal, mounted (in the manner described in chapter 2, section 2.3.2) and cooled only to 100K, in an attempt to avoid a recurrent crystal splitting problem. The crystal was cooled to 100K successfully, showed intense peaks with good profiles and indexed correctly. Thus, data collection was initiated and based on the following strategy:

Initially, frames were collected for 800μAhrs and ϕ and χ were moved sequentially in 45° and 30° increments respectively, starting at ϕ and χ = 0°. After 300μAhrs of the frame where ϕ=45° and χ=30°, the data collection was briefly halted in order to reduce the frame time to 700μAhrs in view of the amount of beam time remaining (assuming an average of 170μA/hr) and restarted at ϕ=0°, χ=60°. After the ϕ=90°, χ=60° frame, the data collection skipped to the χ=90° runs as a precautionary measure such that if something went wrong, these would still have been collected. Tiling then began and during which the frames which had initially been skipped were collected *en route* as χ continuously decreased. At the start of the frame corresponding to settings, ϕ=45°, χ=30°, the frame time was re-set to 800μAhrs since the reliablility and flux of the source had been very good throughout the experiment (190-200μA/hr with very few and limited stoppages) and data collection continued until tiling was complete.

The only minor problem encountered during the data collection was when the data collection temperature rose to 115K very early on the sixth day of data collection. When discovered, the data collection was interrupted, the crystal was re-cooled to 100K and the experiment was re-started at the last completely isothermal frame. No crystal decay, damage, movement or any other such possible resulting problem occurred due to this temperature variation.

The standard procedures for SXD, as described in chapter 2, were used to process and correct the complete data set. The subsequent structural refinement was carried out using SHELXL-93 (Sheldrick, 1993). Cell parameters, for the refinement, were taken from a

preliminary 100K X-ray experiment [a = 11.571(2)Å, b = 12.258(3)Å, c = 7.868(2)Å and β = 90.11(3)°] since such parameters are considered more reliable than those derived from a neutron source. All relevant crystal, data collection and refinement parameters are summarized in ***Table 6.2.1*** below:

Table 6.2.1 *- A summary of crystal, data collection and refinement parameters for the 100K neutron structure of DCNP.*

Compound	DCNP	Compound	DCNP
Molecular Formula	$C_{13}H_{10}N_4$	Crystal Morphology	pointed needle
Formula weight	220.0	Crystal Colour	red / cyan
a(Å)	11.571(2)@	Crystal Size (mm)	2 x 3 x 7
b(Å)	12.258(3)@	Total number of reflections	7808
c(Å)	7.868(2)@	Unique reflections	1867
α(°)	90	Observed Reflections [I>2σ(I)]	1863
β(°)	90.11(3)@	R_{int}	0.060
γ(°)	90	$(\sin\theta / \lambda)_{max}$	0.7-0.8
Cell Volume(Å^3)	1116.0(4)	Data / Parameters	1863 / 244
Crystal System	monoclinic	R1 [I > 2σ(I)]	0.0731
Space Group	Cc	wR2 [I > 2σ(I)]	0.0831
Z	4	Goodness of fit on F^2	4.016
Calculated Density (gcm^{-1})	1.321	Weighting Scheme	$1/\sigma^2$
Temperature (K)	100.0(2)	$\Delta\rho_{(max, min)}$ (fmÅ^{-3})	2.224/-1.463

6.2.2 Structural Details

A 50% probability thermal ellipsoid plot of the 100K neutron structure is shown in ***Figure 6.2.1***. Tables of fractional coordinates and anisotropic displacement parameters are given in ***Appendix A.6.1*** and ***A.6.2*** respectively.

@ These are the values derived from the preliminary 100K X-ray experiment.

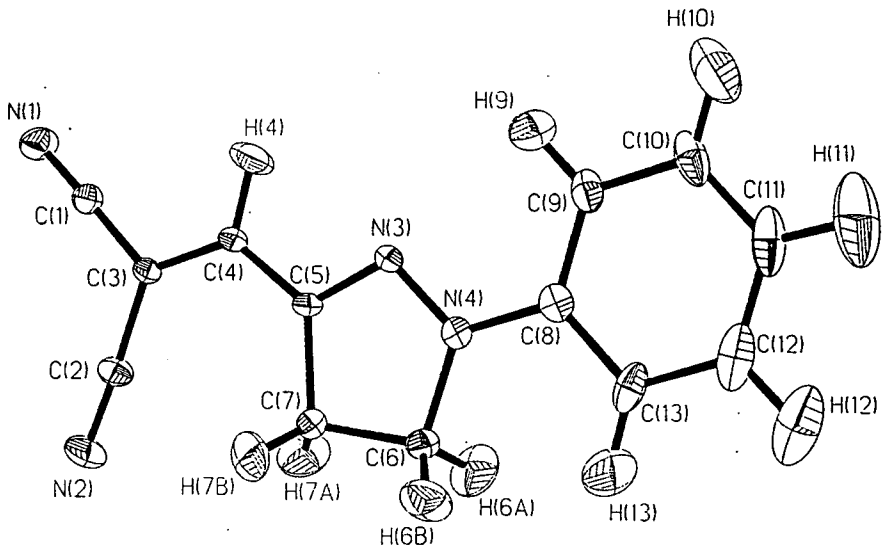

Figure 6.2.1 *- A 50% probability thermal ellipsoid plot of the 100K neutron structure of DCNP.*

Table 6.2.2 *- Bond Lengths for the neutron structure of DCNP.*

Bond	Distance (Å)	Bond	Distance (Å)
N(1)-C(1)	1.161(3)	C(4)-H(4)	1.065(7)
N(2)-C(2)	1.155(3)	C(6)-H(6A)	1.093(9)
N(3)-C(5)	1.306(3)	C(6)-H(6B)	1.100(7)
N(3)-N(4)	1.331(3)	C(7)-H(7A)	1.077(7)
N(4)-C(8)	1.392(3)	C(7)-H(7B)	1.083(9)
N(4)-C(6)	1.481(4)	C(9)-H(9)	1.064(8)
C(1)-C(3)	1.416(4)	C(10)-H(10)	1.071(10)
C(2)-C(3)	1.419(4)	C(11)-H(11)	1.085(8)
C(3)-C(4)	1.377(4)	C(12)-H(12)	1.084(10)
C(4)-C(5)	1.413(4)	C(13)-H(13)	1.035(10)
C(5)-C(7)	1.516(4)	Intermolecular Contacts	
C(6)-C(7)	1.534(4)		
C(8)-C(9)	1.392(5)		
C(8)-C(13)	1.405(4)	Contact	Distance (Å)
C(9)-C(10)	1.388(4)	N(1)...H(4)-C(4)	2.513(8)
C(10)-C(11)	1.396(6)	N(1)...H(12)-C(12)	2.49(1)
C(11)-C(12)	1.396(6)		
C(12)-C(13)	1.387(5)		

Table 6.2.3 *- Selected bond angles for the neutron structure of DCNP.*

Angle	Angle (°)	Angle	Angle (°)
C(5)-N(3)-N(4)	109.7(2)	C(5)-C(7)-C(6)	101.4(2)
N(3)-N(4)-C(8)	120.6(2)	N(4)-C(8)-C(9)	120.9(3)
N(3)-N(4)-C(6)	113.1(2)	N(4)-C(8)-C(13)	119.2(3)
C(8)-N(4)-C(6)	125.9(2)	C(10)-C(9)-H(9)	119.9(5)
N(1)-C(1)-C(3)	178.0(3)	C(8)-C(9)-H(9)	119.6(4)
N(2)-C(2)-C(3)	176.6(3)	C(9)-C(10)-H(10)	120.9(5)
C(4)-C(3)-C(1)	119.6(2)	C(11)-C(10)-H(10)	119.1(5)
C(4)-C(3)-C(2)	124.6(3)	C(10)-C(11)-H(11)	122.4(8)
C(1)-C(3)-C(2)	115.8(2)	C(12)-C(11)-H(11)	118.3(8)
C(3)-C(4)-C(5)	127.0(2)	C(13)-C(12)-H(12)	120.1(7)
N(3)-C(5)-C(4)	117.3(2)	C(11)-C(12)-H(12)	118.6(7)
N(3)-C(5)-C(7)	112.7(2)	C(12)-C(13)-H(13)	119.3(5)
C(4)-C(5)-C(7)	130.0(2)	C(8)-C(13)-H(13)	121.7(5)
N(4)-C(6)-C(7)	102.1(2)		

The bond lengths and angles of the molecule (***Tables 6.2.2 and 6.2.3***) are significantly more accurate than the published room temperature conventional X-ray derived results (Allen et al., 1988), as expected. In particular, the hydrogen atoms are much better defined and all C-H distances are consistently longer than the reported X-ray values. From this greater accuracy, emerged the presence of two C-H...N hydrogen-bonds. No hydrogen-bonding was reported in the published study. The contacts are considered to be fairly weak [C(4)-H(4)...N(1) = 2.513(8)Å, (A); C(12)-H(12)...N(1) = 2.49(1)Å (B)] but even so, they are thought to dictate the three-dimensional packing of the compound. ***Figure 6.2.2*** illustrates how the hydrogen-bonds hold the molecules together in a corrugated layer formation. Hydrogen-bonding thus may be considered to be responsible for the extremely large electro-optic coefficient reported, since the magnitude of the phenomenon is largely dependent upon the parallel alignment of the molecules (Miniewicz, Palewska, Lipinski, Kowal & Swedek, 1994). Moreover, hydrogen-bonding may be considered, in part, responsible for the proliferation of the SHG effect through the layers.

The hydrogen-bonding may also cause the increase in angles, C(2)-C(3)-C(4), C(3)-C(4)-C(5) and C(4)-C(5)-C(6) (see ***Table 6.2.3***) away from the ideal 120° sp^2 geometry.

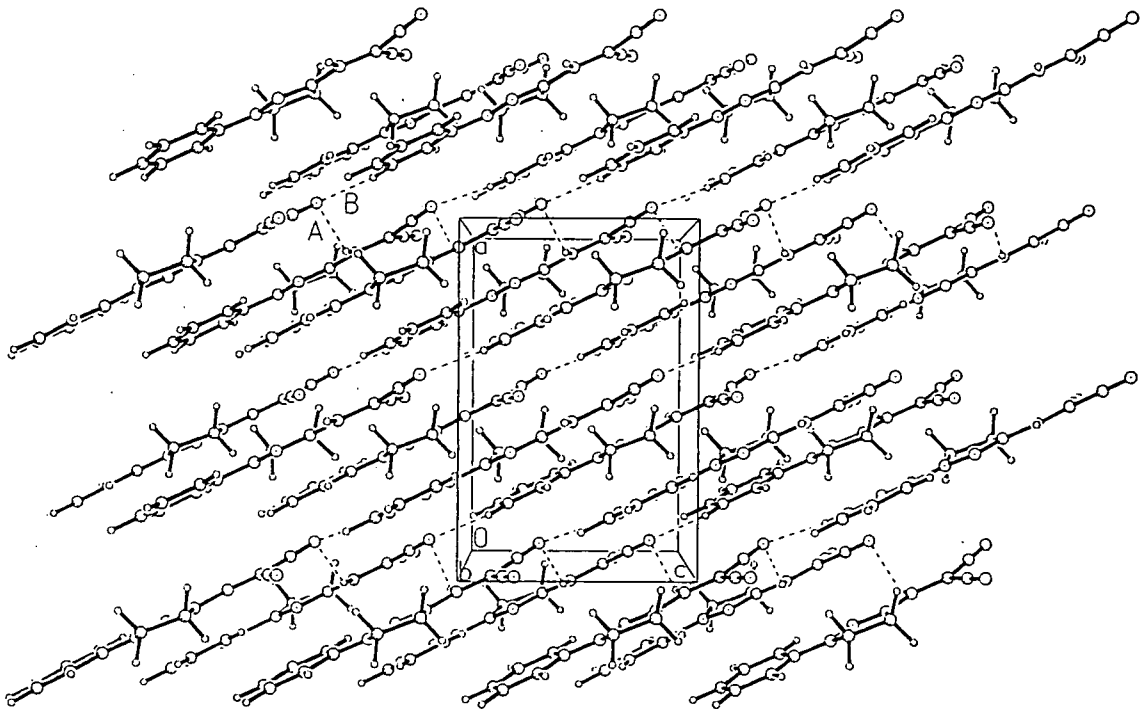

Figure 6.2.2 *- The molecular packing arrangement of the 100K neutron structure of DCNP.*

The uncertainty in the hydrogen-bond contact distance, N(1)...H(12)-C(12) is slightly greater than that for the other hydrogen-bond. This is due to the rather striking peculiar anisotropic thermal behaviour in the phenyl ring (see ***Figure 6.2.1***). This unusual thermal motion was attributed to libration about the vector given by the cross-product of the C(6)-N(4) and N(3)-N(4) bond vectors and passing through the carbon atom, C(8). This motion does not appear to distort the internal phenyl ring geometry [internal ring angles lie between 119.0(3)° and 121.2(3)°]. However, the sequential increase in (a) the uncertainty of the C-C-H (external) phenyl angles and (b) their slight deviation from 120°, as one passes across the phenyl ring from C(8) towards C(11), suggests a slight geometrical distortion due to libration. Consequently, the corresponding phenyl hydrogen fractional coordinate esds, particularly in the b and c directions are noticeably large.

Such deviations also appear in the geometry of the reported X-ray study (Allen et al., 1988) although, here, no thermal ellipsoid plot or any discussion of libration is reported.

6.3 THE 100K X-RAY STRUCTURE OF DCNP

6.3.1 Experimental

In common with the neutron study, the only crystalline sample available to us was the large parent crystal, as described previously. When carrying out the previous experiments, we found that cleaving this crystal along the (001) direction caused the crystal to splay. Presumably, this was a consequence of the extremely planar nature of the molecules. Although this did not present major problems when performing the neutron experiment, cutting a sufficiently good quality crystal to a size, 0.1-0.5mm on edge, was a serious challenge. The conventional use of a sharp scalpel blade alone was rendered unsuitable since all crystals cleaved to the correct size by this method were far too striated or split, even to obtain any vaguely sensible cell dimensions.

In view of this, we turned to the method of solvent cutting. A crystal which had been cut to suitable dimensions by a scalpel blade in the two facile directions was selected and glued to the top of a 0.3mm Lindeman capillary which, in turn, was held into a brass pin by bees wax and which extended from the pin by 12mm. The brass pin was placed into a goniometer head and screwed onto the apparatus shown in ***Figure 6.3.1*** such that the (001) face was in the horizontal plane:

The middle part of the chosen crystal appeared to possess the best quality. Hence, the crystal was translated into the solvent such that one of the undesired ends was dissolved. Once the crystal had been cut to the point of its best quality (as determined by using the microscope) the crystal was removed from the solvent and the goniometer head was unscrewed from the apparatus. The crystal was carefully removed from the capillary, turned over and re-glued such that the solvent-cut end was at the tip of the capillary. (Due to the 'capillary' action of the solvent, the solvent-cut end had a pseudo-triangular profile and so fitted well into the top of the capillary). The goniometer head was re-screwed onto the solvent cutting apparatus and the dissolving procedure was repeated in order to remove the other undesired end of the crystal. The resulting crystal was of a size 0.5 x 0.3 x 0.15 mm and of sufficiently high quality for a charge density study. The crystal, still on the goniometer head, was removed from the solvent-cutting apparatus and placed upon the Siemens SMART-CCD diffractometer for the X-ray study.

Figure 6.3.1 *- The solvent cutting apparatus used to cut the DCNP crystal for the 100K X-ray charge density study.*

The crystal was successfully indexed at room temperature using the standard procedures, as discussed in chapter 2, section 2.5.2.1 and intense diffraction was observed out to high 2θ values in these frames. On this basis, the crystal was deemed suitable for a charge density study. The sample was cooled to 100K and the cell refined. The Siemens program, ASTRO (Siemens Analytical X-ray Instruments, 1995) was then used which allows one to optimize the data collection strategy such that a complete data set out to a given resolution and with a stated level of redundancy is obtained. It was decided to collect two batches of data: first, one low angle full sphere of data up to 60° in 2θ (in -0.3 steps) and second, a high-angle hemisphere of data measuring out to 2θ = 109° (in -0.3 steps). Each frame was collected for 45 seconds and a total of 10 runs were used. The complete data collection strategy is summarized in ***Table 6.3.1***:

Table 6.3.1 *- A summary of the 100K X-ray data collection strategy.*

Run No.	2θ	ω	ϕ	χ	Frames
Low Angle Data					
0	-29	-26	0	54.7	606
1	-29	-21	88	54.7	435
2	-29	-26	0	54.7	50
3	-29	-23	180	54.7	606
4	-29	-26	270	54.7	435
5	+29	-26	0	54.7	200
6	-29	-26	0	54.7	50
High Angle Data					
7	-80	-80	0	54.7	681
8	-80	-62	90	54.7	361
9	-80	-60	180	54.7	381
A	-29	-26	0	54.7	50

The three runs of 50 frames each are repeated scans of the first 50 frames in the first run and were collected in order to act as standards. Data was collected over a period of five days and the collection proceeded without any problems.

Once data collection had finished, a unit cell was refined, using the low angle batch only, with a threshold I/σI value of 50, a coverage of radius 350 pixels and with a minimum and maximum resolution of 0.5Å^{-1} and 2.0Å^{-1} respectively. The data were then reduced using standard procedures as detailed in chapter 2, section 2.5.2.2. A unit cell based on *all* data was produced by this data reduction procedure. However, this cell based, in part, on high angle data (threshold = 10 I/σI) is less accurate and is also effected by the

presence of Mo Kα and Kβ splitting. Therefore, the previously determined low angle cell was used in subsequent data refinement.

Before going on to correct accurately and merge the raw data for multipolar refinement, a psi-scan absorption correction was performed (transmission factors: 0.9419 - 0.9941) and the resulting data refined using SHELXL-93 (Sheldrick, 1993) in order to evaluate the quality of the data.

Positional and anisotropic displacement parameters were refined for all non-hydrogen atoms and positional and isotropic displacement parameters were refined for all hydrogen atoms. All relevant crystal, data collection and refinement parameters are given in ***Table 6.3.2***:

Table 6.3.2 - *A summary of crystal, data collection and conventional refinement parameters for the 100K X-ray structure of DCNP.*

Compound	DCNP	Compound	DCNP
Molecular Formula	$C_{13}H_{10}N_4$	Crystal Morphology	irregular
Formula weight	222.25	Crystal Colour	red / cyan
a(Å)	11.5972(2)	Crystal Size (mm)	0.5 x 0.3 x 0.15
b(Å)	12.2873(2)	Total number of reflections	16798
c(Å)	7.8877(1)	Unique reflections	10048
α(°)	90	Observed Reflections [I>2σ(I)]	6421
β(°)	90.021(1)	R_{int}	0.0288
γ(°)	90	$(\sin\theta / \lambda)_{max}$	0.968
Cell Volume(Å^3)	1123.98(3)	Data / Parameters	9977 / 194
Crystal System	monoclinic	R1 [I > 2σ(I)]	0.0763
Space Group	Cc	wR2 [I > 2σ(I)]	0.0745
Z	4	Goodness of fit on F^2	2.382
Calculated Density (gcm^{-1})	1.313	Weighting Scheme	$1/\sigma^2$
Temperature (K)	100(2)	$\Delta\rho_{(max, min)}$ (eÅ^{-3})	0.765 / -0.441

6.3.2 Structural Details

A 50% probability thermal ellipsoid plot of the 100K X-ray derived structure is given in ***Figure 6.3.2*** :

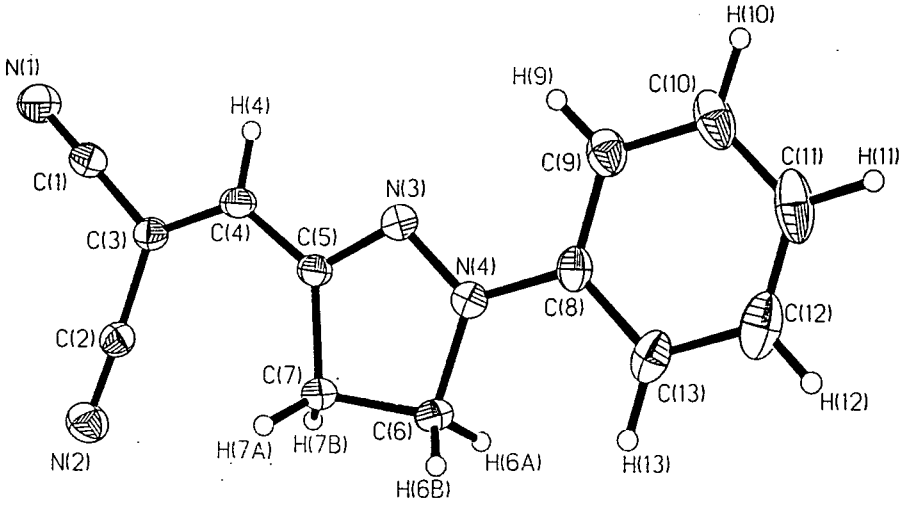

Figure 6.3.2 *- A 50% probability thermal ellipsoid plot of the 100K X-ray structure of DCNP.*

Table 6.3.3 *- Bond lengths of the 100K X-ray structure of DCNP.*

Bond	Distance (Å)	Bond	Distance (Å)
N(1)-C(1)	1.156(1)	C(4)-H(4)	0.920(8)
N(2)-C(2)	1.153(1)	C(6)-H(6A)	0.945(8)
N(3)-C(5)	1.318(1)	C(6)-H(6B)	0.982(9)
N(3)-N(4)	1.3319(9)	C(7)-H(7A)	0.980(9)
N(4)-C(8)	1.3992(9)	C(7)-H(7B)	0.975(9)
N(4)-C(6)	1.496(1)	C(9)-H(9)	0.904(9)
C(1)-C(3)	1.433(1)	C(10)-H(10)	0.97(1)
C(2)-C(3)	1.439(1)	C(11)-H(11)	0.96(1)
C(3)-C(4)	1.370(1)	C(12)-H(12)	0.87(1)
C(4)-C(5)	1.418(1)	C(13)-H(13)	0.991(9)
C(5)-C(7)	1.519(1)	Intermolecular Contacts	
C(6)-C(7)	1.542(1)		
C(8)-C(9)	1.394(1)		
C(8)-C(13)	1.407(1)	Contact	Distance (Å)
C(9)-C(10)	1.386(1)	N(1)...H(4)-C(4)	2.644(9)
C(10)-C(11)	1.405(2)	N(1)...H(12)-C(12)	2.71(1)
C(11)-C(12)	1.382(2)		
C(12)-C(13)	1.392(1)		

Table 6.3.4 *- Selected bond angles of the 100K X-ray structure of DCNP.*

Angle	Angle (°)	Angle	Angle (°)
C(5)-N(3)-N(4)	109.72(6)	C(5)-C(7)-C(6)	101.52(6)
N(3)-N(4)-C(8)	120.86(6)	N(4)-C(8)-C(9)	120.66(7)
N(3)-N(4)-C(6)	113.11(6)	N(4)-C(8)-C(13)	119.34(7)
C(8)-N(4)-C(6)	125.65(6)	C(10)-C(9)-H(9)	120.9(6)
N(1)-C(1)-C(3)	178.24(8)	C(8)-C(9)-H(9)	119.2(6)
N(2)-C(2)-C(3)	177.36(9)	C(9)-C(10)-H(10)	121.0(6)
C(4)-C(3)-C(1)	120.38(7)	C(11)-C(10)-H(10)	118.4(6)
C(4)-C(3)-C(2)	124.88(8)	C(10)-C(11)-H(11)	118.5(7)
C(1)-C(3)-C(2)	114.74(7)	C(12)-C(11)-H(11)	122.4(7)
C(3)-C(4)-C(5)	127.25(7)	C(13)-C(12)-H(12)	118.7(8)
N(3)-C(5)-C(4)	117.26(6)	C(11)-C(12)-H(12)	120.0(8)
N(3)-C(5)-C(7)	112.81(7)	C(12)-C(13)-H(13)	120.3(6)
C(4)-C(5)-C(7)	129.92(7)	C(8)-C(13)-H(13)	120.4(6)
N(4)-C(6)-C(7)	101.98(5)		

Bond lengths and selected bond angles are given in ***Tables 6.3.3 and 6.3.4***. Fractional coordinates and anisotropic atomic displacement parameters are given in ***Appendix A.6.3*** and ***A.6.4***. Although R1 and the goodness-of-fit seem to be rather large, the very low esds of the geometry indicate that the data are adequate for a multipolar refinement. As with the neutron refinement, the most poorly defined atoms are the hydrogens attached to the phenyl ring, which reiterates that libration is present. Moreover, the libration can clearly be seen in ***Figure 6.3.2*** by the nature of the unusual shapes of the phenyl group thermal ellipsoids.

The magnitude of all of the aniotropic displacement parameters are expectedly greater than those derived from the neutron experiment. In general, all structural features are very similar to the neutron derived features.

6.4 THE MULTIPOLAR REFINEMENT

Since a multipolar refinement requires very accurate data, an accurate absorption correction was deemed necessary, despite the very low value of the absorption coefficient, μ = 0.08 mm^{-1}. However, this presented us with a problem since the absorption correction method, considered most accurate, requires the indices of the crystal faces, yet the crystal used had no visible faces. This was because, by the nature of the crystal solvent-cutting technique used, the crystal was rounded and irregular in its morphology. Hence, a different type of absorption correction method had to be used. The program, SADABS (Sheldrick, 1996) was chosen to perform the absorption correction. SADABS (Siemens Area Detector ABSorption correction) takes advantage of the generally high level of data redundancy, resulting from data being collected with an area detector system, and performs an empirical correction by comparing the intensities of equivalent reflections collection at different angle settings. By the nature this method, it also corrects for effects such as the presence of the capillary in the beam at select angles. This results in a deceivingly large transmission range, since it is not only the crystal absorption being taken into account.

The R_{int} of the data decreased from 0.0246 to 0.0193 as a result of the correction and transmission factors ranged from 0.710 to 1.000 (a calculated range for just the crystal absorption: 0.961 to 0.988). In order to check that the absorption correction was appropriate, both the absorption corrected and non-corrected data was merged using the SORTAV program (part of the DREAM (Blessing, 1989) package) and a preliminary[$] XD (Koritsanszky et al., 1994) refinement was performed on each data set. The refinement of the absorption corrected data gave marginally better results than the refinement of the uncorrected data. Hence, the absorption correction was deemed appropriate and used in the more comprehensive XD (Koritsanszky et al., 1994) refinement.

However, this XD (Koritsanszky et al., 1994) study yielded no meaningful results since, despite all attempts to model the data, including refining:

- the X-ray data alone
- the X-ray data substituted with idealized hydrogen positional parameters
- the X-ray data substituted with fixed neutron derived hydrogen anisotropic displacement parameters, scaled with respect to the X-ray thermal parameters in the manner described by Blessing (1995).

[$] Only positional and anisotropic displacement parameters were refined and all multipolar terms/parameters were set to zero.

- the X-ray data substituted with fixed neutron derived hydrogen positional and anisotropic displacement parameters, also scaled with respect to the X-ray thermal parameters
- the X-ray data substituted with fixed neutron derived non-hydrogen and hydrogen anisotropic displacement parameters and positional parameters for the hydrogen atoms
- the X-ray data substituted with all neutron derived fixed parameters

with kappa and/or multipolar terms up to and including the octopolar level.

The conventional R-factor, based on F, never decreased below 10% throughout, the goodness-of-fit always remained greater than 3.5 and the rigid-bond test was never satisfied, even though the refinements always fully converged and the data-to-parameter ratio was always plentiful.

The causes of the failure of this charge density study are still not known. However, we suspect that using the SMART-CCD for data collection, before much was known about optimal area detector data collection strategies and the presence of molecular libration may have been contributary factors.

6.5 AN INVESTIGATION OF THE PECULIAR ANISOTROPIC THERMAL BEHAVIOUR IN DCNP

The unusual thermal motion, preliminary ascribed to libration in section 6.2, was investigated. In order to rule out the possibility of disorder, a looming phase-transition or some subtle form of twinning, all of which could manifest themselves in terms of odd thermal ellipsoids, X-ray studies of the compound were performed at various temperatures (90K, 100K, 200K and 290K) using the Siemens SMART-CCD. The latter three temperatures were chosen such that the resulting anisotropic displacement parameters could be plotted against as large a temperature range as possible, within the limits of the Oxford Cryosystems Cryostream (Cosier & Glazer, 1986), so that a linear, or otherwise, change in thermal motion with temperature could be ascertained. The 90K temperature was chosen predominantly to preclude (or otherwise) the possibility of a phase-transition.

6.5.1 Experimental

The Siemens SMART-CCD diffractometer is ideal for a variable temperature study since, by nature of its large area detector, one can collect a complete hemisphere of data of a compound at several different temperatures in just a few days. Not only does this make the experiment very economical and 'user friendly', given the high demand of such a machine, but also, it significantly reduces the possibility of crystal decay or any instrumental problems, both of which would induce large systematic errors between the data sets due to the forced use of two or more different crystals or different instrumental environments.

Since a very accurate 100K X-ray data set had already been collected on the Siemens SMART-CCD diffractometer for the purposes of multipolar refinement, the aforementioned SHELXL-93 (Sheldrick, 1993) refinement of this data was used as the 100K data set in this investigation. Moreover, the crystal which had been used for this experiment was still mounted on the original capillary and brass pin and showed no signs of having decayed. Hence, this crystal was also used throughout this study.

All three X-ray experiments employed the Siemens SMART-CCD diffractometer and were carried out using conventional procedures, as described in chapter 2. Similarly, the data was reduced using the procedures described in chapter 2. No absorption correction was applied to any data set since the value of the absorption coefficient was so small (μ = 0.08 mm^{-1}).

All three data sets were refined by full-matrix least-squares methods on F^2 using SHELXL-93 (Sheldrick, 1993). Atomic scattering factors were taken from International Tables for Crystallography, Volume C, Mathematical, Physical and Chemical Tables (1992). Isotropic extinction corrections were applied in each structural refinement [extinction parameter, EXTI = 0.004516, 0.019959 and 0.011592 for the 90K, 200K and 290K data sets respectively].

In all three refinements, positional and anisotropic displacement parameters were refined for all non-hydrogen atoms and positional and isotropic displacement parameters were refined for all hydrogen atoms.

A summary of crystal, data collection and refinement parameters for each of the three experiments is given in ***Table 6.5.1***.

Table 6.5.1 *- A summary of crystal, data collection and refinement parameters for the 90K, 200K and 290K X-ray structures of DCNP.*

Compound	DCNP(90K)	DCNP(200K)	DCNP(290K)
Molecular Formula	$C_{13}H_{10}N_4$	$C_{13}H_{10}N_4$	$C_{13}H_{10}N_4$
Formula weight	220.0	220.0	220.0
a(Å)	11.5945(3)	11.7304(4)	11.8751(5)
b(Å)	12.2912(4)	12.3278(2)	12.3735(5)
c(Å)	7.8944(2)	7.8844(2)	7.8876(3)
α(°)	90	90	90
β(°)	90.018(1)	90.173(2)	90.412(2)
γ(°)	90	90	90
Cell Volume(Å^3)	1125.03(5)	1140.16(5)	1158.95(8)
Crystal System	monoclinic	monoclinic	monoclinic
Space Group	Cc	Cc	Cc
Z	4	4	4
Calculated Density (gcm^{-1})	1.312	1.295	1.274
Temperature (K)	90(2)	200(2)	290(2)
Crystal Morphology	irregular	irregular	irregular
Crystal Colour	red / cyan	red / cyan	red / cyan
Crystal Size (mm)	0.5 x 0.3 x 0.15	0.5 x 0.3 x 0.15	0.5 x 0.3 x 0.15
Total number of reflections	3921	4054	4000
Unique reflections	2029	2402	2112
Observed Reflections [I>2σ(I)]	1893	2394	1557
R_{int}	0.0300	0.0377	0.0346
Data / Parameters	2028 / 195	2394 / 195	2098 / 195
R1 [I > 2σ(I)]	0.0348	0.0463	0.0514
wR2 [I > 2σ(I)]	0.0787	0.0678	0.0886
Goodness of fit on F^2	1.158	1.668	1.305
Weighting Scheme	a = 0.0274; b = 0.5936	$1 / \sigma^2$	a = 0.0130; b = 0.3922
$\Delta\rho_{(max, min)}$ (eÅ^{-3})	0.152 / -0.155	0.221/-0.147	0.111 / -0.099

6.5.2. Results and discussion

50% probability thermal ellipsoid plots of the 90K, 200K and 290K DCNP structure are shown in ***Figures 6.5.1a -6.5.1c*** respectively. Bond lengths and selected bond angles for the each structure are given in ***Tables 6.5.2*** and ***6.5.3***. Fractional coordinates and anisotropic displacement parameters are given in ***Appendix A.6.5-A.6.10***.

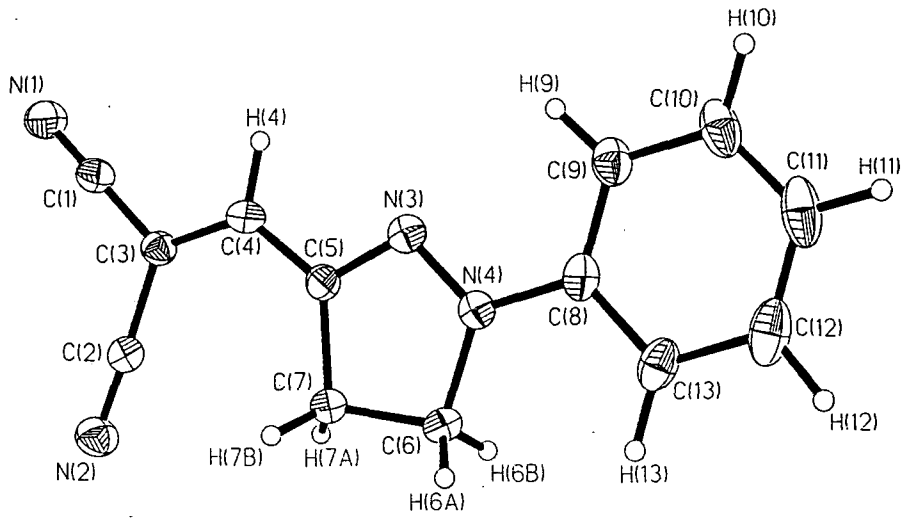

(a)

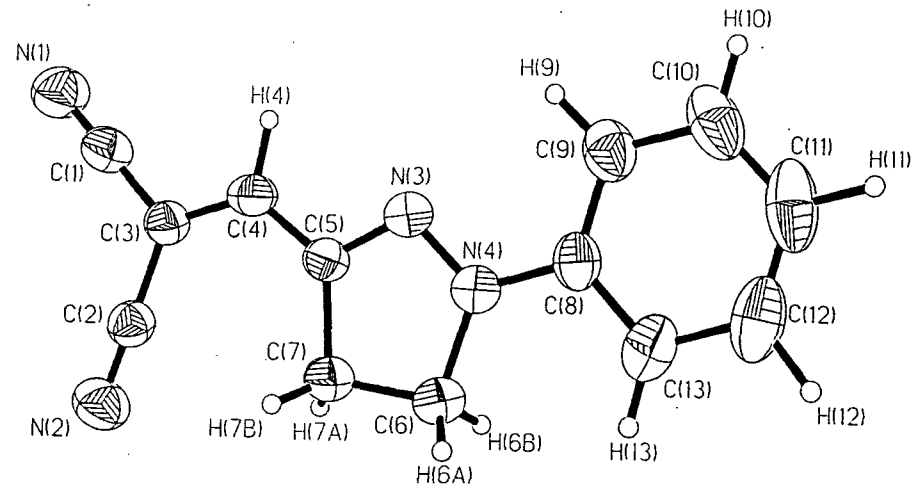

(b)

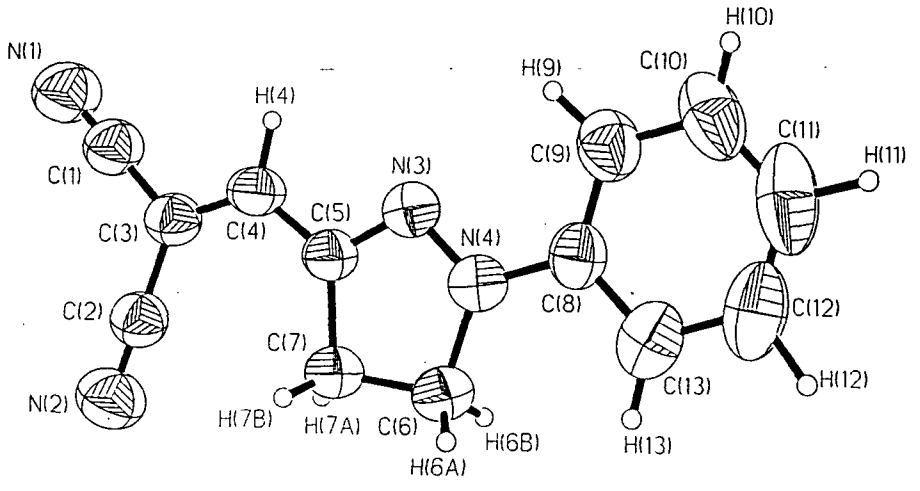

(c)

Figure 6.5.1 *- 50% probability thermal ellipsoid plots of the X-ray structure of DCNP at (a) 90K, (b) 200K, (c) 290K.*

Table 6.5.2 *- Bond lengths of the 90K, 200K and 290K X-ray structures of DCNP.*

Bond	Distance (Å) at 90K	Distance (Å) at 200K	Distance (Å) at 290K
N(1)-C(1)	1.156(3)	1.153(3)	1.151(4)
N(2)-C(2)	1.144(2)	1.147(2)	1.140(4)
N(3)-C(5)	1.317(3)	1.316(3)	1.319(4)
N(3)-N(4)	1.333(2)	1.332(2)	1.324(4)
N(4)-C(8)	1.404(2)	1.399(2)	1.397(4)
N(4)-C(6)	1.493(3)	1.490(3)	1.493(4)
C(1)-C(3)	1.439(3)	1.433(3)	1.433(5)
C(2)-C(3)	1.446(3)	1.435(3)	1.428(5)
C(3)-C(4)	1.364(3)	1.357(3)	1.352(5)
C(4)-C(5)	1.420(3)	1.413(3)	1.411(5)
C(4)-H(4)	0.98(2)	1.00(2)	0.95(3)
C(5)-C(7)	1.522(3)	1.509(3)	1.508(5)
C(6)-C(7)	1.543(3)	1.533(3)	1.534(5)
C(6)-H(6A)	1.00(2)	1.01(2)	1.06(4)
C(6)-H(6B)	0.94(2)	0.95(2)	0.90(3)
C(7)-H(7A)	0.95(3)	1.01(2)	1.00(4)
C(7)-H(7B)	0.98(3)	0.96(2)	0.94(3)
C(8)-C(9)	1.395(3)	1.391(3)	1.390(5)
C(8)-C(13)	1.411(3)	1.405(3)	1.398(5)
C(9)-C(10)	1.391(3)	1.388(3)	1.385(6)
C(9)-H(9)	0.98(3)	1.02(2)	1.02(4)
C(10)-C(11)	1.399(4)	1.387(4)	1.387(8)
C(10)-H(10)	1.00(3)	0.93(2)	0.90(4)
C(11)-C(12)	1.385(4)	1.369(4)	1.357(8)
C(11)-H(11)	0.96(3)	1.02(3)	1.00(5)
C(12)-C(13)	1.408(4)	1.397(4)	1.390(7)
C(12)-H(12)	0.99(3)	1.04(3)	1.07(4)
C(13)-H(13)	1.03(2)	0.97(2)	0.98(4)
Intermolecular Contacts			
Contact	Contact (Å) at 90K	Contact (Å) at 200K	Contact (Å) at 290K
N(1)...H(4)-C(4)	2.59(2)	2.62(2)	2.69(3)
N(1)...H(12)-C(12)	2.61(3)	2.59(3)	2.61(4)

Table 6.5.3 - Bond angles of the 90K, 200K and 290K X-ray structures of DCNP.

Angle	Angle (°) at 90K	Angle (°) at 200K	Angle (°) at 290K
C(5)-N(3)-N(4)	109.8(2)	109.9(2)	109.8(2)
N(3)-N(4)-C(8)	120.8(2)	121.1(2)	121.4(2)
N(3)-N(4)-C(6)	113.2(2)	112.9(2)	113.1(3)
C(8)-N(4)-C(6)	125.6(2)	125.7(2)	125.3(3)
N(1)-C(1)-C(3)	178.3(2)	178.3(2)	178.1(4)
N(2)-C(2)-C(3)	178.0(2)	178.6(2)	178.7(4)
C(4)-C(3)-C(1)	120.5(2)	120.7(2)	120.6(3)
C(4)-C(3)-C(2)	125.2(2)	125.4(2)	125.2(3)
C(1)-C(3)-C(2)	114.4(2)	113.9(2)	114.2(3)
C(3)-C(4)-C(5)	127.3(2)	127.8(2)	128.2(3)
N(3)-C(5)-C(4)	117.4(2)	117.5(2)	117.8(2)
N(3)-C(5)-C(7)	112.7(2)	112.4(2)	112.6(3)
C(4)-C(5)-C(7)	129.9(2)	130.1(2)	129.6(3)
N(4)-C(6)-C(7)	102.0(2)	101.9(2)	102.0(3)
C(5)-C(7)-C(6)	101.5(2)	102.1(2)	101.9(3)
N(4)-C(8)-C(9)	120.5(2)	120.3(2)	120.2(3)
N(4)-C(8)-C(13)	119.0(2)	119.5(2)	119.9(3)
C(10)-C(9)-H(9)	124(2)	123.7(14)	124(2)
C(8)-C(9)-H(9)	117(2)	117.6(14)	117(2)
C(9)-C(10)-H(10)	120(2)	118(2)	118(3)
C(11)-C(10)-H(10)	119(2)	120(2)	121(3)
C(10)-C(11)-H(11)	121(2)	122(2)	122(3)
C(12)-C(11)-H(11)	119(2)	119(2)	119(3)
C(13)-C(12)-H(12)	115(2)	115(2)	113(3)
C(11)-C(12)-H(12)	124(2)	124(2)	126(3)
C(12)-C(13)-H(13)	120(2)	119(2)	118(3)
C(8)-C(13)-H(13)	121(2)	122(2)	123(3)

Simply by viewing ***Figures 6.5.1a***, ***6.5.1b*** and ***6.5.1c***, one can immediately see that the unusual thermal motion observed in the 100K structures is present at all measured temperatures. This precludes the possibility of a phase-transition in the vicinity of 100K. Moreover, this thermal motion is seen to increase steadily with temperature, thus ruling out the possibility of any subtle twinning or static disorder. No evidence of any dynamical disorder was apparent within this temperature range either and so this was also thought to be an unlikely cause to the motion.

Having ruled out these possibilities, we tested for libration by plotting the value of each principal anisotropic displacement parameter for all non-hydrogen atoms against temperature (***Figures 6.5.2-6.5.4***):

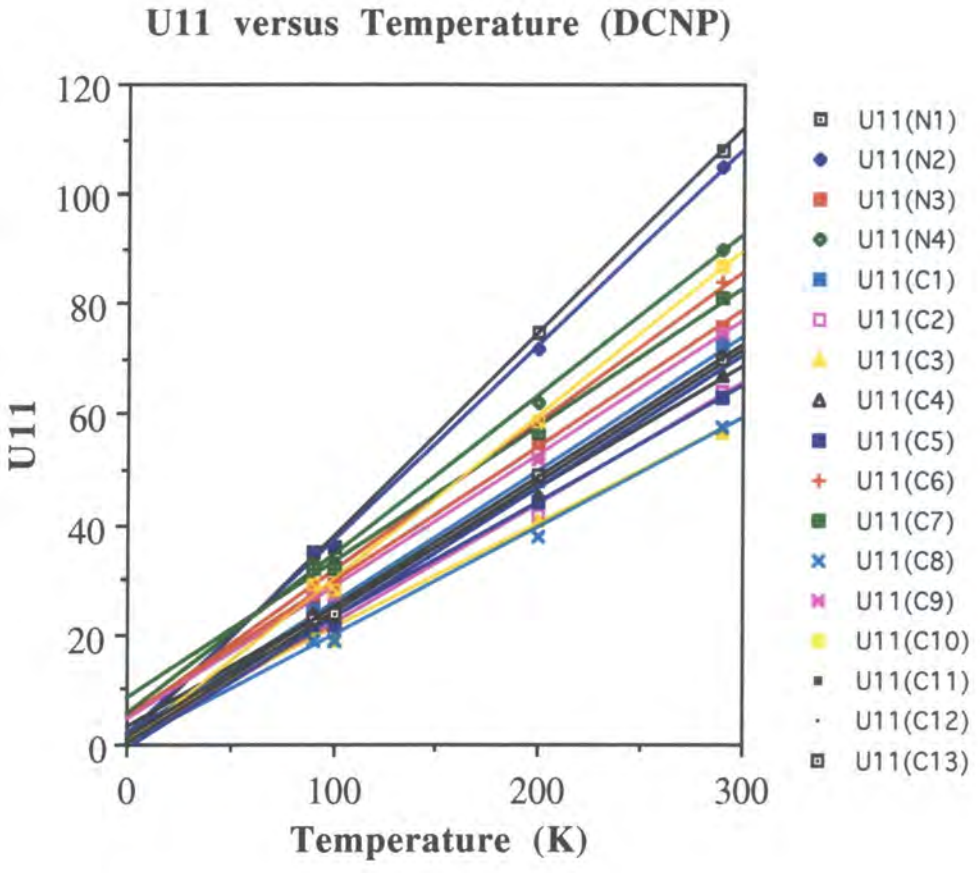

Figure 6.5.2 - *Plots of the anisotropic displacement parameter, U11, versus temperature for each non-hydrogen atom in DCNP.*

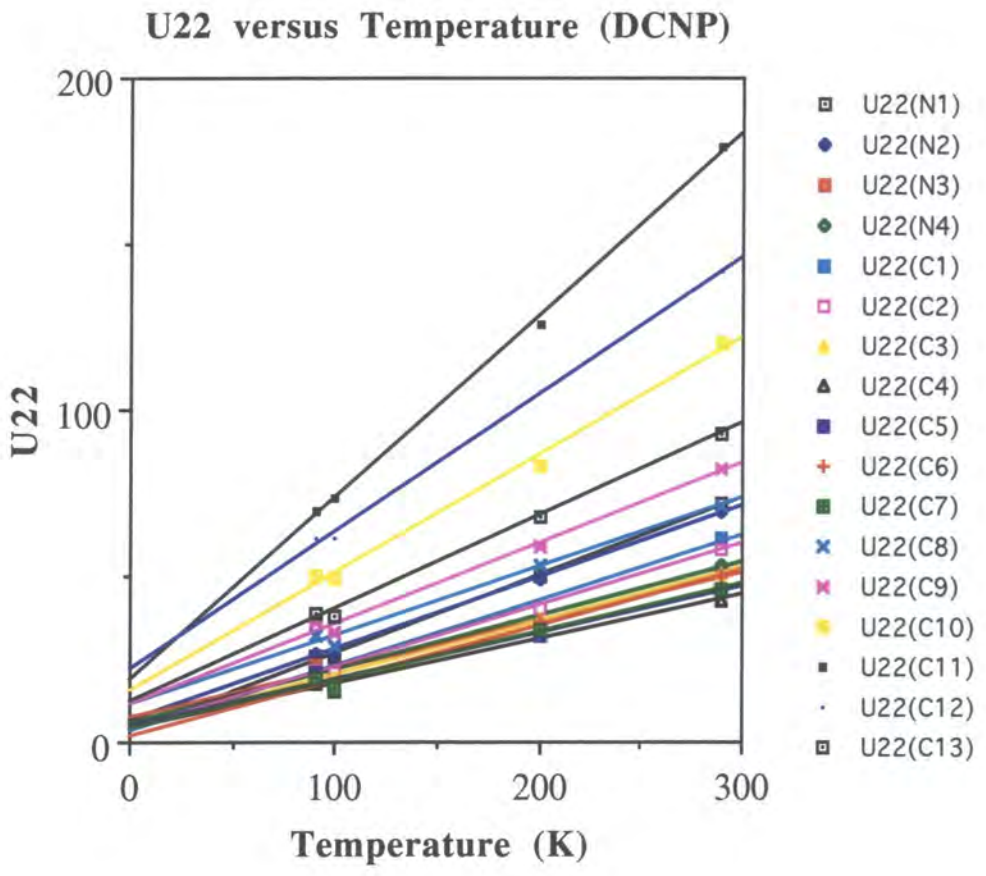

Figure 6.5.3 *- Plots of the anisotropic displacement parameter, U22, versus temperature for each non-hydrogen atom in DCNP.*

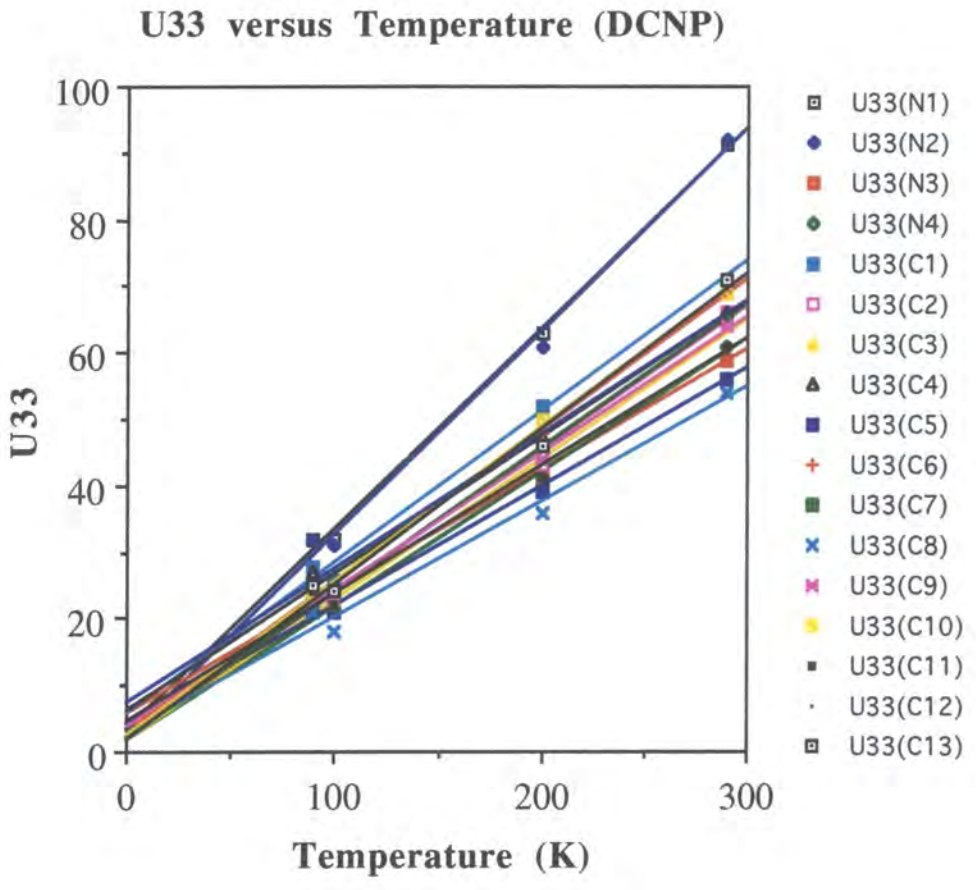

Figure 6.5.4 *- Plots of the anisotropic displacement parameter, U33, versus temperature for each non-hydrogen atom in DCNP.*

All plots are linear, thus, confirming that the unusual motion is probably due to libration. The gradient of each plot (i.e. the rate of increase in U_{ii}) indicates to what extent the translational component of the libration is affecting each atom. Hence, three further graphs were plotted (***Figures 6.5.5-6.5.7***) which show the variation in the rate of increase in each U_{ii} value with temperature across all non-hydrogen atoms:

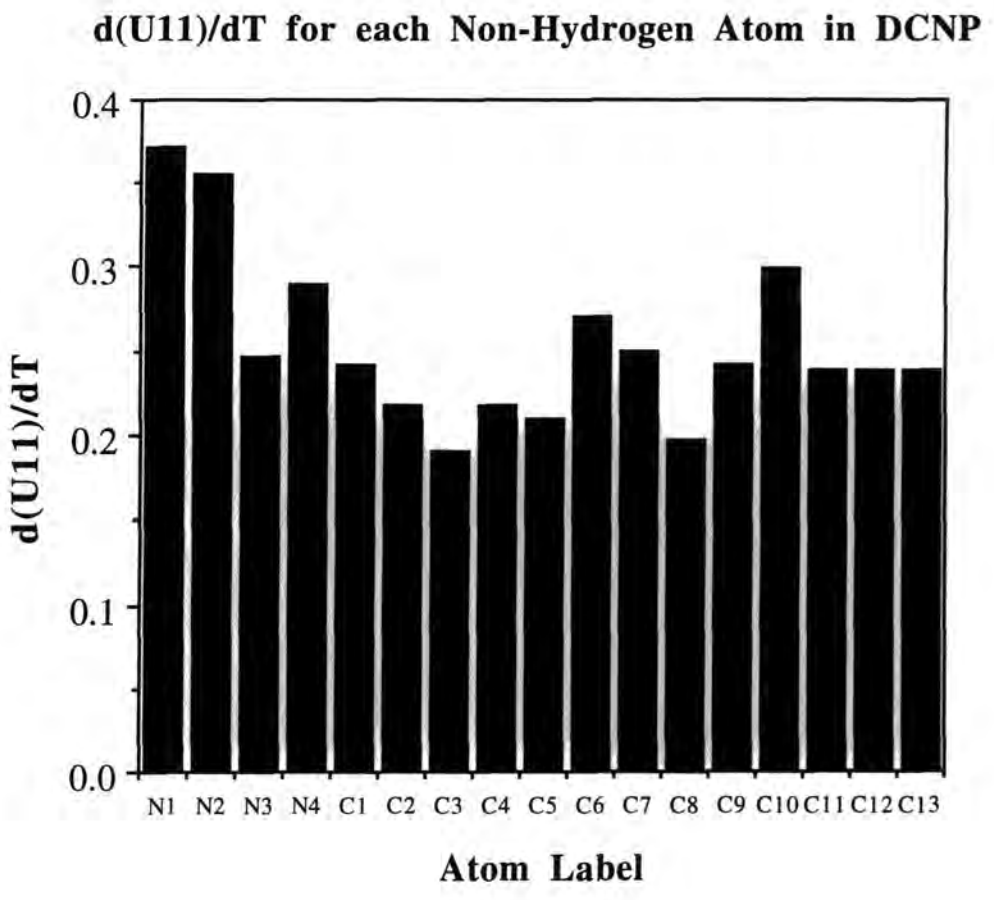

Figure 6.5.5 *- A graph showing the rate of increase in U11 with temperature for each non-hydrogen atom in DCNP.*

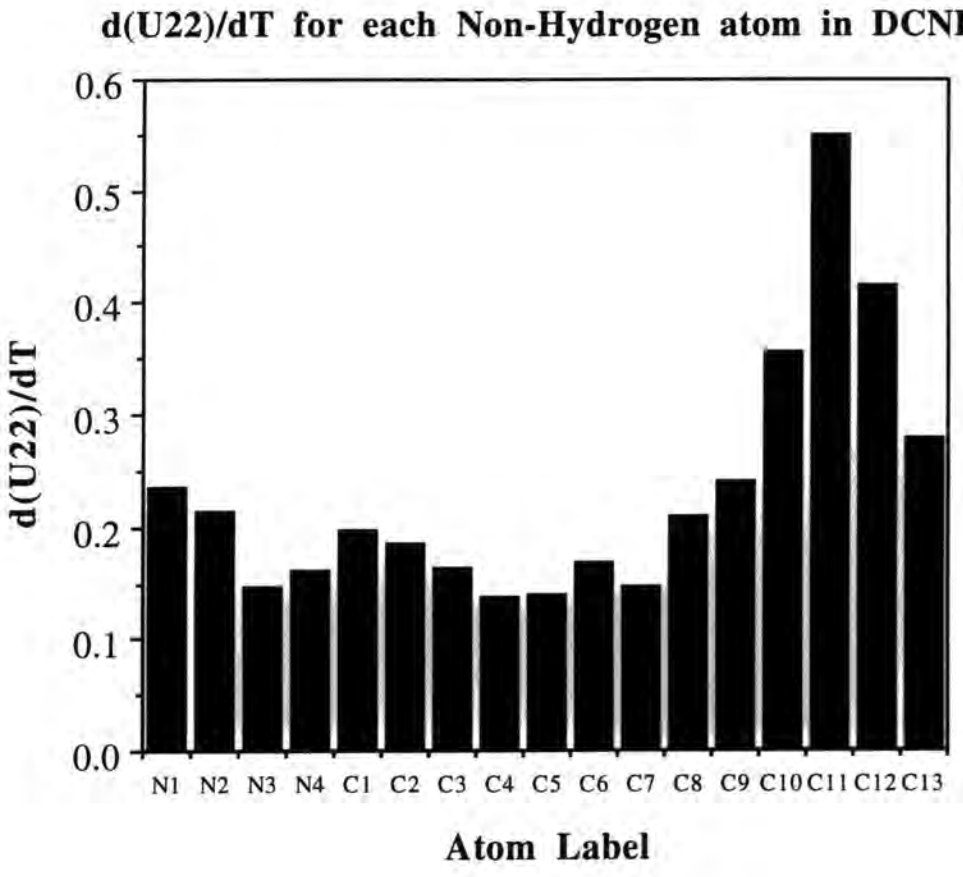

Figure 6.5.6 *- A graph showing the rate of increase in U22 with temperature for each non-hydrogen atom in DCNP.*

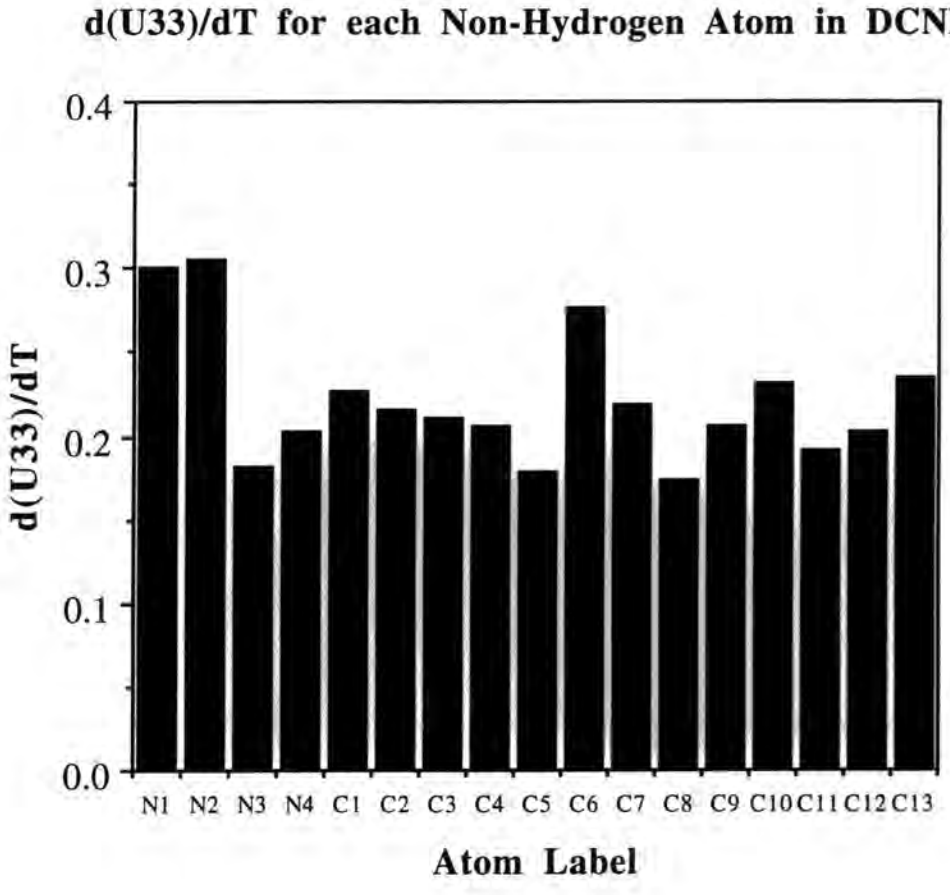

Figure 6.5.7 *- A graph showing the rate of increase in U33 with temperature for each non-hydrogen atom in DCNP.*

These graphs reveal some interesting features: not only is libration present in the phenyl ring [C(8) -> C(13)] but the terminal nitrogen atoms in each nitrile group [N(1) and N(2)] are also librating to almost the same extent as the phenyl ring and the pyrazole ring [C(5) -> C(7)] is librating slightly.

From these results, we initially thought that the whole molecule was a rigid-body, librating about a pivot point, central within the molecule. However, on closer inspection of the graph above, we can see that this cannot be so since if it were the case, the overall libration would gradually decrease on passing across the molecule from the terminal atoms, C(11), N(1) and N(2) towards the centre. Instead, the extent of libration does not vary in a systematic way across the molecule from the terminal atoms towards the centre.

Therefore, we now believe that the three regions of the molecule, identified above, are librating in an independent but concerted way. It has been shown (section 6.2.2) that the molecules pack in a head-to-tail arrangement such that the nitrile groups in one molecule are adjacent to the phenyl groups in the next molecule. There is an aromatic C-H...N

hydrogen-bond [C(12)-H(12)...N(1)] between the two molecular fragments (see section 6.2.2). We suspect that the libration in the phenyl ring is mirrored by the terminal nitrogen atoms in the nitrile groups because of this close proximity. The small amount of libration present in the pyrazole ring is presumably the result of the non-concerted librations of its substituents.

6.6 QUANTIFYING THE LIBRATIONAL EFFECTS IN DCNP

In order to investigate the effects of this libration on the molecular geometry of DCNP, a series of calculations were performed, using the THMA11 program (Trueblood, 1990).

6.6.1 The THMA11 Program

This program performs a TLS correction, where elements T, L and S represent matrices which describe the pure translational motion, the pure librational motion and the correlation between the two, respectively. A libration axis for each non-rigid part* of the molecule must be specified in the input file so that the mean square tortional amplitude, $<\phi^2>$ can be calculated. The rest of the molecule is assumed to be a rigid-body. The components of T, L, S and $<\phi^2>$ are then fitted to the input atomic U_{ij} values by a linear least-squares procedure. Correlations of both, overall and internal motion, are given in the output file along with the corrections to all unique interatomic distances below a specified value. Some approximate harmonic frequencies and force constants for internal motion are also given, as determined from simple quantum-mechanical expressions.

The program also performs a rigid-bond analysis (Hirshfeld, 1976) which evaluates the differences of the observed mean square displacement amplitude (MSDA) between each atom and every other atom. By suitably analysing these MSDA values, one can obtain further information about the nature of the internal motion.

Finally, a comparison of the vibration tensors for each atom is made and printed in the output along with an 'R-factor' for all U_{ij}s based on the following equation:

$$R = \sqrt{(\text{sum of}(w\Delta U)^2/\text{sum of}\ (wU_{obs})^2)}$$

6.6.2 The THMA11 Analyses

TLS and ϕ analyses were carried out for both the neutron and all of the variable temperature X-ray refinements. The analysis of the neutron results used all 27 atoms whereas only 17 atoms (i.e. just the non-hydrogen atoms) were used in the analysis of the X-ray derived results. In each case, the phenyl ring (excluding the phenyl hydrogen atoms) was specified as the one non-rigid body whose libration axis was defined by the vector corresponding to the cross-product of the bond vectors, N(3)-N(4) and C(6)-N(4) and passing through the atom C(8).

---

* It is non-rigid compared to the rest of the molecule but rigid in itself.

The analyses showed that the overall libration of the *rigid* group was fairly small but increased linearly with temperature, as expected (see ***Table 6.6.1*** and ***Figure 6.6.1***).

Table 6.6.1 - *The overall libration in the structural refinements.*

The Type of Analysis	Libration (degrees^2)	Root mean square of libration
90K X-ray	1.806	1.344
100K X-ray	2.257	1.502
200K X-ray	3.781	1.944
290K X-ray	5.534	2.352
100K neutron	3.735[&]	1.933[&]

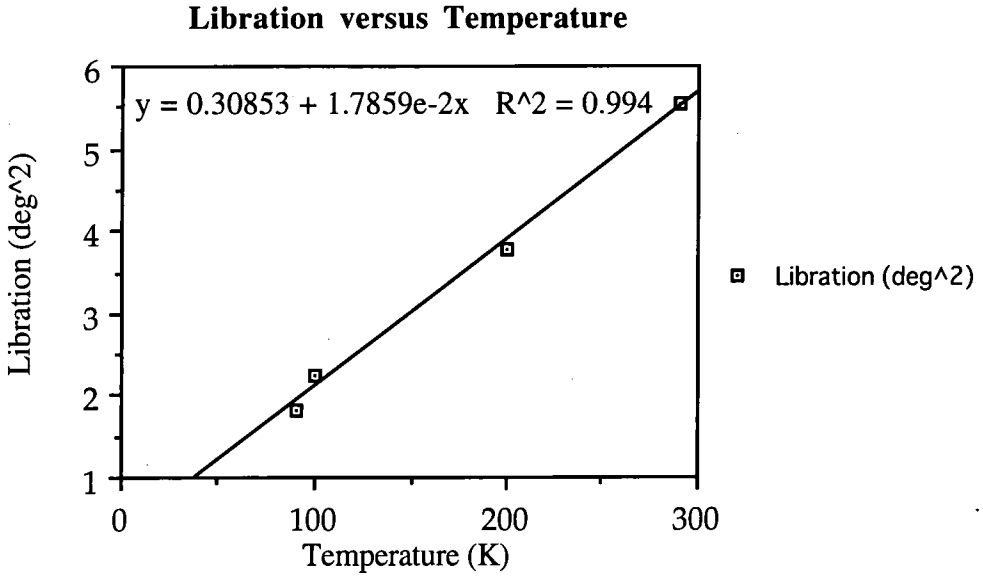

Figure 6.6.1 - *A plot of the overall libration of the rigid group against temperature.*

However, the overall and internal motion correlations showed that the librational effect was rather large along the L33 direction (perpendicular to the libration axis (L11) and the direction of motion of the first atom of the group (L22), in a right-handed system) (see ***Table 6.6.2***).

[&] The values obtained from the 100K neutron analysis differ from those obtained from the 100K X-ray analysis. This is expected since the two different techniques determined anisotropic displacement parameters in a different manner (Blessing, 1995). Suitable scaling methods exist in order to minimise this difference (Blessing, 1995). However, scaling was unsuitable in this case since the original neutron derived parameters were necessary in order to determine a riding correction (see later) for the X-H distances.

Table 6.6.2 *- The librational coefficients calculated in the given analyses.*

Analysis	L11 (deg^2)	L12 (deg^2)	L13 (deg^2)	L22 (deg^2)	L23 (deg^2)	L33 (deg^2)
90K X-ray	3.0(6)	0.1(3)	3.2(8)	-0.1(3)	0.2(3)	9(2)
100K X-ray	3.3(6)	0.2(3)	3.0(8)	-0.1(3)	0.3(3)	10(2)
200K X-ray	7(1)	0.4(5)	7(2)	0.3(5)	0.5(5)	19(3)
290K X-ray	10(1)	0.3(7)	10(2)	0.6(7)	0.8(7)	27(4)
100K neutron	5(7)&	0.6(4)&	5(1)&	-0.2(4)&	0.0(4)&	16(2)&

The translational component of the libration (***Table 6.6.3***) occurs predominantly in the principal directions, T11, T22 and T33 (defined in the same axis as the librational terms). The coefficients of S are all zero within their esds.

Table 6.6.3 *- Translational coefficients for the given analysis*

Analysis	T11 ($Å^2$)	T12 ($Å^2$)	T13 ($Å^2$)	T22 ($Å^2$)	T23 ($Å^2$)	T33 ($Å^2$)
90K X-ray	0.022(1)	-0.001(1)	-0.001(1)	0.021(1)	0.000(1)	0.023(1)
100K X-ray	0.022(1)	-0.001(1)	0.001(1)	0.018(1)	0.000(1)	0.022(1)
200K X-ray	0.042(2)	-0.001(1)	0.002(1)	0.034(2)	-0.001(1)	0.042(1)
290K X-ray	0.062(2)	-0.002(2)	0.002(1)	0.048(2)	0.000(1)	0.061(2)
100K neutron	0.015(2)&	0.000(1)&	0.000(1)&	0.013(1)&	-0.001(1)&	0.018(1)&

The overall amount of ϕ rotation and translation of the *non-rigid* phenyl group appears to be small. However, no actual values can be assigned to this motion since the errors calculated are as large as the values determined.

In each study, a correction was made to all bond distances which involve atoms affected by libration since libration causes an apparent *foreshortening* of a true interatomic distance (Cruickshank, 1956; Cruickshank, 1961; Busing & Levy, 1957; Busing & Levy, 1964). Moreover, in the 100K neutron analysis, a riding (Busing & Levy, 1964) and anharmonic (Ibers, 1959) correction is made for all X-H bond distances. The riding correction (Busing & Levy, 1964) is required since the hydrogen atoms are much lighter than any atom bonded to it (e.g. C or N) and so their anisotropic displacement parameters will predominantly reflect the extent of internal vibrations ensuing rather than any contribution to the molecular libration. The anharmonicity correction (Jeffrey & Ruble, 1984; Craven & Swaminathan, 1984) is required since anharmonicity exists in the X-H stretching vibration (Ibers, 1959) which incurs an apparent *lengthening* of the X-H distance. The anharmonic correction is therefore opposite to the riding correction, often resulting in a net correction of almost zero.

Table 6.6.4 shows the corrected interatomic distances for all libration effected non-hydrogen atoms in each analysis and ***Table 6.6.5*** shows the various corrections made to all hydrogen atoms in the 100K neutron analysis.

Table 6.6.4 - *Corrections to bond distances involving libration effected non-hydrogen atoms.*

Bond	Libration corrected distance (Å)				
	90K X-ray	100K X-ray	200K X-ray#	290K X-ray#	100K neutron
C(8)-C(9)	1.397	1.396	1.400	1.401	1.393
C(8)-C(13)	1.412	1.409	1.411	1.407	1.406
C(9)-C(10)	1.392	1.388	1.392	1.390	1.389
C(10)-C(11)	1.400	1.406	1.393	1.395	1.397
C(11)-C(12)	1.387	1.384	1.377	1.368	1.397
C(12)-C(13)	1.409	1.394	1.401	1.396	1.388
Average correction to libration	+0.0015	+0.0017	+0.0029	+0.0036	+0.0011

Table 6.6.5 - *Corrections to bond distances involving hydrogen atoms from the 100K neutron analysis.*

Bond	Uncorrected distance (Å)	Anharmonic correction (Å)	Riding correction (Å)	Corrected distance (Å)
C(4)-H(4)	1.0650	-0.0114	+0.0248	1.079
C(6)-H(6A)	1.0931	-0.0110	+0.0314	1.113
C(6)-H(6B)	1.0999	-0.0035	+0.0235	1.120
C(7)-H(7A)	1.0769	-0.0062	+0.0318	1.102
C(7)-H(7B)	1.0829	-0.0113	+0.0346	1.129
C(9)-H(9)	1.0642	-0.0173	+0.0189	1.066
C(10)-H(10)	1.0708	-0.0421	+0.0314	1.060
C(11)-H(11)	1.0847	-0.0216	+0.0401	1.103
C(12)-H(12)	1.0842	-0.0152	+0.0309	1.100
C(13)-H(13)	1.0349	-0.0021	+0.0328	1.066

A rigid-body correction was also made on all non-hydrogen atoms for these two data sets (see following page) and the values given include this correction.

In all but the 200K and 290K X-ray analyses, corrections are made only to distances involving hydrogen atoms and atoms within the non-rigid group. In the 200K and 290K X-ray analyses, an additional correction is made to all non-hydrogen atoms. This correction is a rigid body correction (Busing & Levy, 1964) which implies uncorrelated motion. Such motion was suspected in the previous section.

New U_{ij} values were also calculated in order to account for the libration. These values are displayed in ***Appendix A.6.11-A.6.15***. An R-factor was determined for all U_{ij} values and for just the diagonal U_{ii} values in each study. These are given in ***Table 6.6.6***.

Table 6.6.6 *- R-factors for all U_{ij} values and just the diagonal U_{ii} values for each analysis.*

Type of Analysis	R-factor (of all U_{ij} values)	R-factor (of just U_{ii} values)
90K X-ray	0.126(2)	0.097(2)
100K X-ray	0.131(3)	0.103(3)
200K X-ray	0.124(4)	0.100(4)
290K X-ray	0.110(6)	0.091(6)
100K neutron	0.276(5)	0.237(5)

Finally, the rigid-bond test (Hirshfeld, 1976) showed a few interesting features. In particular, ΔMSDA values for N(1) and N(2) were noticeably high in the 290K X-ray analysis and negative trends were observed for ΔMSDA non-hydrogen - non-hydrogen values of N(2) and C(2). This means that the nitrile groups are also librating as previously stated in section 6.5.2. However, they could not be modelled as non-rigid groups in the THMA11 analyses since, when initially modelled as such, the refinement became unstable.

6.7 INVESTIGATING THE THERMAL PROPERTIES OF DCNP

When any NLO material is subjected to laser radiation, thermal gradients are induced within the crystal, through optical absorption. The presence of these gradients alter the phase-matching characteristics of the material since the refractive indices of a crystal vary with temperature. Therefore, a detailed knowledge of the thermal characteristics of such a material are very important for industrial applications.

In particular, specific heat, thermal expansion and thermal conductivity measurements are typically carried out to investigate the thermal behaviour (Kerkoc et al., 1996). Since we were fortunate enough to have variable temperature X-ray derived cell parameters from the previous studies (section 6.3 and 6.5), a thermal expansivity study on DCNP was undertaken. Specific heat and thermal conductivity studies were not carried out since neither differential scanning calorimetry nor any thermal diffusivity determining method was available to us.

6.7.1 Calculations

Initially, graphs of each cell parameter length versus temperature were plotted (see ***Figure 6.7.1***) in order to confirm that the variation is linear. A graph was also plotted (***Figure 6.7.2***) to compare the variation in the normalized cell parameters (cell length / cell length at 100K) with temperature.

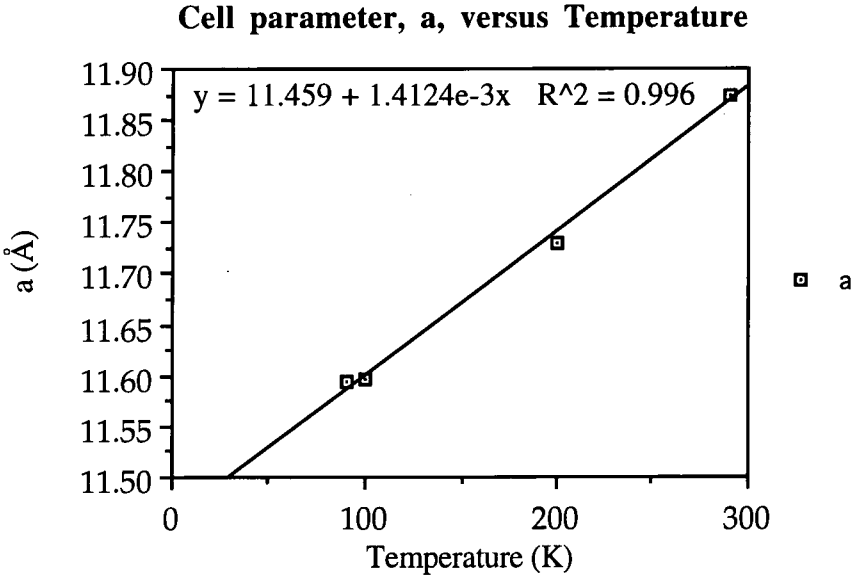

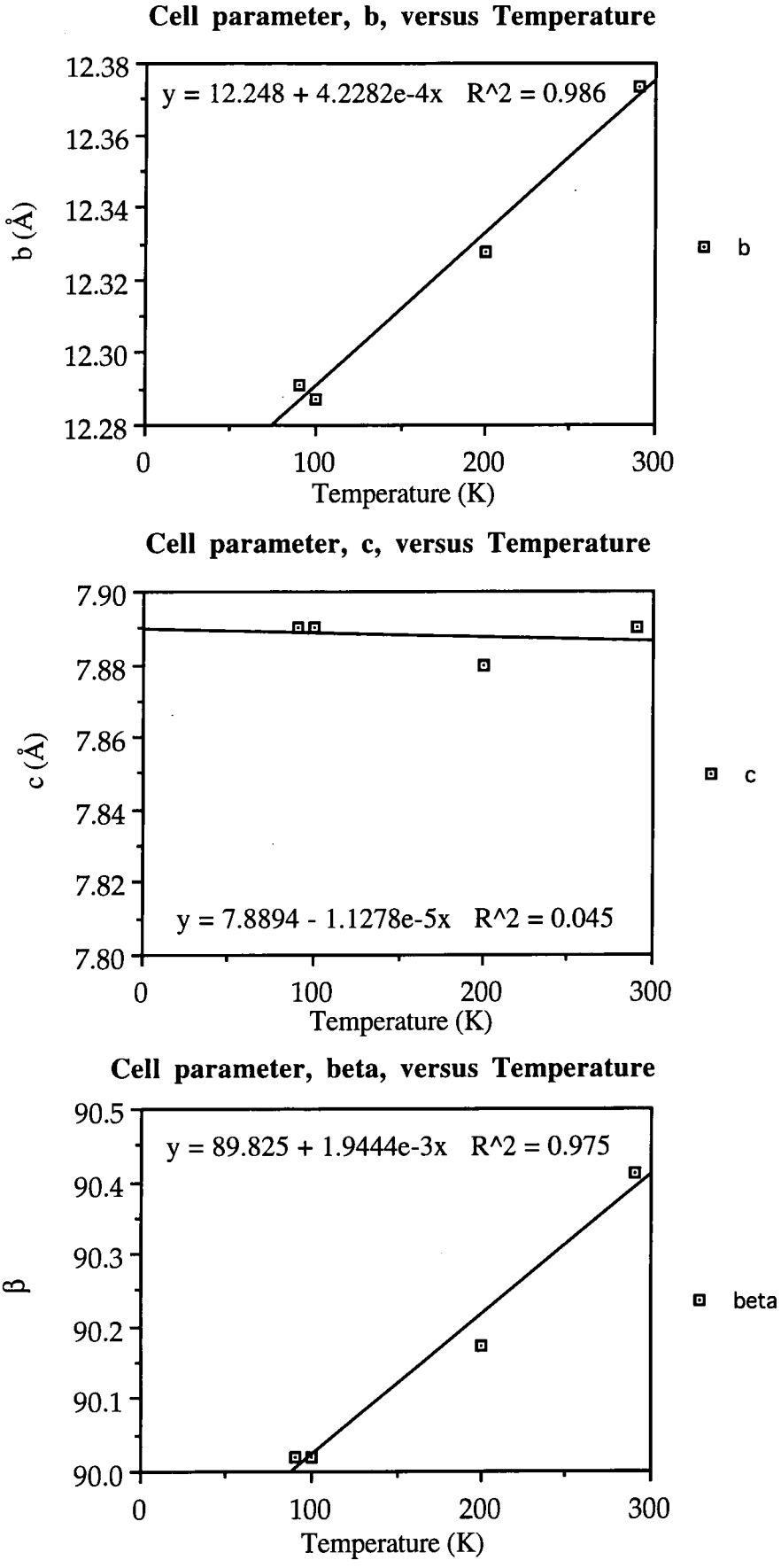

Figure 6.7.1 *- Plots of the unit cell parameters, a, b, c and β versus temperature for DCNP.*

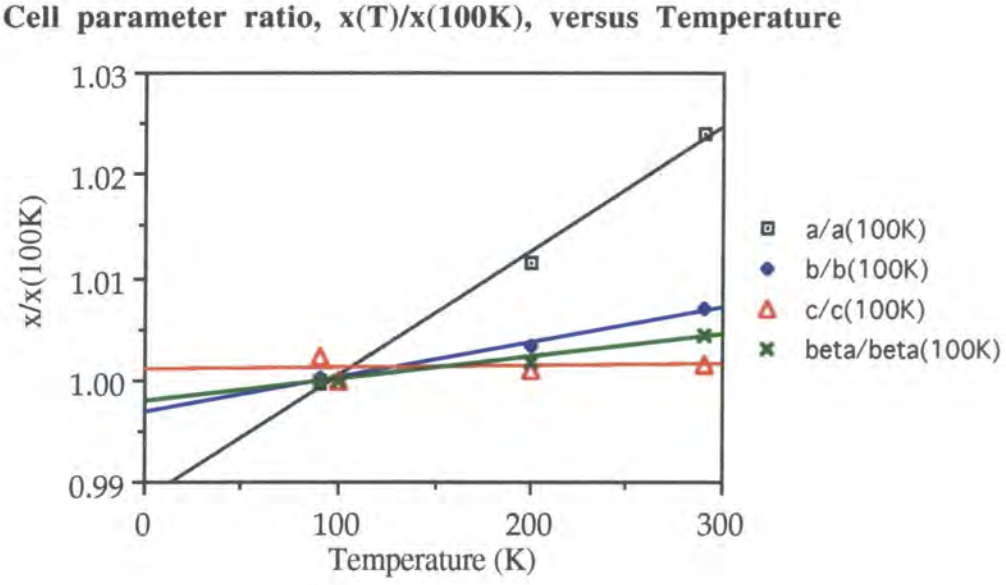

Figure 6.7.2 *- Plots of the normalised unit cell parameters against temperature.*

The thermal expansion tensor of DCNP was then evaluated by the following procedure used for monoclinic systems (Cruickshank, 1997):

The non-zero thermal expansivity coefficients of the tensor are first determined by evaluating the following expressions which describe the lengths of the crystallographic axes, a, b, c and the angle β as a function of temperature:

The elements of the tensor:

$$\begin{matrix} \alpha_{11} & 0 & \alpha_{13} \\ 0 & \alpha_{22} & 0 \\ \alpha_{31} & 0 & \alpha_{33} \end{matrix}$$

from:

$$\alpha_{11} = d(\ln a)/dT + \cot(\beta)d\beta/dT$$

$$\alpha_{22} = d(\ln b)/dT$$

$$\alpha_{33} = d(\ln c)/dT$$

$$\alpha_{13} = \alpha_{31} = 1/2[\cot(\beta)\{d(\ln a)/dT - d(\ln c)/dT\} - d(\beta)/dT$$

Of course, this tensor being described in the monoclinic crystal axes cannot be diagonal but can be made so by using the piezoelectric axis set, i.e. c, b and a* and:

$$\tan 2\phi = 2\alpha_{13}/(\alpha_{33} - \alpha_{11})$$

where ϕ is the angle of anticlockwise rotation about the b crystallographic axes (looking down the b axis of a right handed axis set) of the x principal axis from the a* axis. In this notation we have:

$$S_{11} = \alpha_{11}\cos^2\phi + \alpha_{33}\sin^2\phi - \alpha_{13}\sin 2\phi$$

$$S_{22} = \alpha_{22}$$

$$S_{33} = \alpha_{11}\sin^2\phi + \alpha_{33}\cos^2\phi + \alpha_{13}\sin 2\phi$$

where S_{ii} are the diagonal elements of the thermal expansion tensor in its principal, diagonalized form.

6.7.2 Results

All values of the derivatives were taken from the gradients of relevant graphs and the reference value of β in the cot(β) terms was taken to be that measured at 100K. The calculated values of both the thermal expansivity coefficients, α_{ij} and the principal, diagonalized thermal expansion tensor elements, S_{ii}, are given in ***Table 6.7.1*** below:

Table 6.7.1 *- The thermal expansion coefficients and tensor elements of DCNP.*

Thermal Expansion Coefficients	
α_{11}	0.02202
α_{22}	0.02311
α_{33}	0.00355
α_{13} / α_{31}	-0.04840
Diagonalized Thermal Expansion Tensor Elements	
S_{11}	0.06206
S_{22}	0.02311
S_{33}	-0.06733

These values are fairly large for an organic molecule, suggesting that the expansivity is significant and should be taken into account when considering phase-matching characteristics.

6.8 CONCLUSIONS

This chapter has provided a detailed structural investigation of the compound, DCNP. An accurate 100K neutron derived structure was determined which revealed a hydrogen-bonded three-dimensional network and some rather unusual thermal behaviour. This unusual anisotropic thermal motion was also apparent in the subsequently reported accurate 100K X-ray study and was attributed to libration. Further X-ray structural characterization of the compound were made at three other temperatures in order to confirm that libration was, indeed, the cause of this atypical thermal motion and to investigate the extent of this libration. The libration was modelled, thus allowing a suitable correction to be applied to the molecular geometry. The variable temperature X-ray studies were also used in order to calculate the thermal expansivity of the compound, as part of an analysis of the overall thermal behaviour of the compound.

Further work, including specific heat, thermal conductivity measurements and diffraction studies at lower temperatures needs to be carried out in order to fully elucidate the compound's thermal behaviour.

6.9 REFERENCES

Allen, S., McLean, T. D., Gordon, P. F., Bothwell, B. D., Hursthouse, M. B. & Karaulov, S. A. (1988). J. Appl. Phys., **64**, 2583-2590.

Black, S. N., Davey, R. J., Morley, P. R., Halfpenny, P., Shepherd, E. E. A. & Sherwood, J. N. (1993). J. Mater. Chem., **3**, 129-132.

Blessing, R. H. (1989). J. Appl. Cryst., **22**, 396-397.

Blessing, R. H. (1995). Acta Crystallogr. **B51**, 816-823.

Busing, W. R. & Levy, H. A. (1957). J. Chem. Phys., **26**, 563-568.

Busing, W.R. & Levy, H. A. (1964). Acta Crystallogr. **17**, 142-146.

Cosier, J. & Glazer, A. M. (1986). J. Appl. Cryst., **19**, 105.

Craven, B. M. & Swaminathan, S. (1984). Trans. Am. Crystallogr. Assoc., **20**, 133-135.

Cruickshank, D. W. J. (1956). Acta Crystallogr., **9**, 757-758.

Cruickshank, D. W. J. (1961). Acta Crystallogr., **14**, 896-897.

Cruickshank, F. R. (1997). Private Communication.

Docherty, V. J., Pugh, D. & Morley, J. O. (1985). J. Chem. Soc., Faraday Trans. 2., **81**, 1179-1192.

Hirshfeld, F. L. (1976). Acta Crystallogr. **A34**, 909-921.

Ibers, J. A. (1959). Acta Crystallogr., **12**, 251-252.

International Tables for Crystallography, Volume C, Mathematical, Physical and Chemical Tables (1992). Ed. Wilson, A. J. C., Dordrecht, Boston, London. Tables 4.2.6.8 & 6.1.1.4. 219-222, 500-503.

Jeffrey, G. A. & Ruble, J. R. (1984). Trans. Am. Crystallogr. Assoc., **20**, 129-132.

Kerkoc, P., Venkataramanan, V., Lochran, S., Bailey, R. T., Cruickshank, F. R., Pugh, D., Sherwood, J. N., Moseley, R., Goeta, A. E., Lehmann, C. W. & Howard, J. A. K. (1996). J. Appl. Phys., **80**, 6666-6669.

Koritsanszky, T., Howard, S., Richter, T., Mallinson, P., Su, Z. & Hansen, N. (1994). XD. *A Computer Program Package for Multipole Refinement and Analysis of Charge Densities from Diffraction Data.* Berlin, Cardiff, Glasgow, Buffalo, Nancy.

Miniewicz, A., Palewska, K., Lipinski, J., Kowal, R. & Swedek, B. (1994). Mol. Cryst. Liq. Cryst., **253**, 41-50.

Sheldrick, G. M. (1993). SHELXL-93. *Program for the Refinement of Crystal Structures using Single Crystal Diffraction Data*, University of Göttingen, Germany.

Sheldrick, G. M. (1996). SADABS. *Siemens Area Detector Absorption correction program*, University of Göttingen, Germany.

Siemens Analytical X-ray Instruments (1995). ASTRO Version 4.050. Siemens Analytical X-ray Instruments, Madison, U.S.A.

Trueblood, K. N. (1990). THMA11. *Program for Thermal Motion Analysis.* University of California, Los Angeles, U.S.A.

CHAPTER 7

N-METHYLUREA

7.1 INTRODUCTION

Urea is an important compound within the non-linear optical industry since it is the most commonly used SHG standard reference material. Urea has therefore been studied extensively in terms of its thermal properties [Andersson, Matsuo, Suga & Ferloni, 1992; Andersson & Ross, 1994; Ruehrwein & Huffman, 1946; Sasaski & Yokotake, 1966; Gambino & Bros, 1988] and its non-linear optical properties [Morell, Albrecht, Levin & Tang, 1979; Yoshida, 1975].

Because of its industrial importance and the simplicity of the molecule, the three-dimensional structure of urea has also been studied extensively using X-ray crystallographic methods [Mark & Weissenberg, 1923; Hendriks, 1928; Wyckoff, 1930; Corey & Wyckoff, 1933; Vaughan & Donohue, 1952; Sklar, Senko & Post, 1961; Caron & Donohue, 1964 & 1969; Lebioda, Hodorowicz & Lewinski, 1978; Swaminathan, Craven, Spackman & Stewart, 1984] and neutron diffraction [Worsham, Levy & Peterson, 1957; Swaminathan, Craven & McMullan, 1984]. In particular, these studies have concentrated on hydrogen-bonding patterns [Vaughan & Donohue, 1952; Worsham, Levy & Peterson, 1956], thermal motion analysis [Caron & Donohue, 1964 & 1969; Swaminathan, Craven & McMullen, 1984] and charge density analysis [Vaughan & Donohue, 1952; Swaminathan, Craven, Spackman & Stewart, 1984].

Given all this, it is perhaps surprising to learn that, although thermal and non-linear optical properties of the simplest monoalkyl derivatives of urea, i.e. N-alkylurea (alkyl = Me, Et, Pr, Bu) have also been characterized,* very little structural work has been carried out on these compounds.

In view of this, it was decided to carry out an in-depth structural study on the first of these derivatives, N-methylurea, concentrating on the extent of hydrogen-bonding present in the compound. An attempt to link the structural results with the thermal and non-linear optical properties was also made.

7.1.1 Background information on thermal and non-linear optical properties of N-methylurea.

Non-linear optical investigations have shown (Yoshida, 1975; Morell, Albrecht, Levin & Tang, 1979) that N-methylurea possesses a very similar second-order optical non-linearity and optical damage threshold to urea. More detailed information is unavailable since the work is confined to a patent (Yoshida, 1975). Birefringent studies (Bailey et al, 1995) have also been performed which give values for all of the refractive index

* See section 7.1.1 for details.

coefficients and show that the compound is phase-matchable.

The thermal properties of N-methylurea have been investigated in terms of thermal expansivity (Bailey et al, 1995), thermal conductivity (Bailey et al, 1995), heat capacity (Kozyro et al, 1993; Ferloni & Della Gatta, 1995; Bailey et al, 1995) and thermodynamic behaviour (Kozyro et al, 1993). Thermal expansivity measurements (Bailey et al., 1995) show that two of the three cell parameters (b and c) increase linearly with temperature whilst the cell parameter, a, decreases linearly with increasing temperature up until about 275K where the cell parameter, a, no longer varies with temperature but remains fixed at about 8.475Å (thus resulting in a thermal expansivity of zero). No explanation for this sudden change at 275K was given.

The thermal conductivity of N-methylurea (Bailey et al, 1995) was found to be much larger along the crystallographic a direction than along the b and c directions. This anisotropy was attributed to the strong hydrogen-bonding effects along the a direction.

Three independent studies on the variation of the heat capacity of N-methylurea with temperature have been reported (Kozyro et al, 1993; Ferloni & Della Gatta, 1995; Bailey et al., 1995). One of these reports (Ferloni & Della Gatta, 1995) shows that their measurements only agree with those given in the earlier study (Kozyro et al, 1993) up to about 300K. Above this temperature, the results from Kozyro et al. (1995) show a deviation from the otherwise linear change with temperature, whereas measurements performed by Ferloni & Della Gatta (1995) show that the variation with temperature remains linear throughout. In the other study (Bailey et al., 1995) the graph showing the variation of heat capacity with temperature gives measurements only up to about 305K, so these results cannot be used to confirm (or otherwise) this deviation from linearity.

The thermodynamic studies on N-methylurea (Kozyro et al, 1993) included measurements of the standard enthalpy of combustion, the sublimation enthalpy and the vapour pressure over liquid N-methylurea. Using these and heat capacity measurements, statistical calculations of standard molar thermodynamical functions were also carried out. These calculations provided values for the molar heat capacity, the molar enthalpy increment, the molar entropy increment, the standard molar Gibbs free energy of formation, the standard molar enthalpy of formation (Simirsky, Kabo & Frenkel, 1987), the molar enthalpy of evaporation and the molar entropy. The principal moments of inertia for both external rotation of *cis-* and *trans-* configurations of N-methylurea and internal rotation of the $-CH_3$ group were also determined, as was the potential energy barrier to internal rotation of the $-CH_3$ group [$V_o = 7.1 kJmol^{-1}$] (Saito, Machida, Uno, 1975).

7.1.2 Previous crystallographic work carried out on N-methylurea.

The X-ray derived structure of N-methylurea was first reported in 1933 (Corey & Wyckoff, 1933). However, the authors at the time suggested that the reported structure might be incorrect. In 1976, Huiszoon & Tiemessen confirmed this worrying suspicion and simultaneously reported the correct three-dimensional structure (Huiszoon & Tiemessen, 1976). They also showed that three O...H-N hydrogen-bonds of moderate strength were present in the lattice.

7.2 HYDROGEN-BONDING STUDIES ON N-METHYLUREA

In fashion with previous studies on urea (Vaughan & Donohue, 1952; Worsham, Levy & Peterson, 1956), hydrogen-bonding was also studied in N-methylurea. Moreover, since there is a proposed link between the nature of intermolecular interactions and the macroscopic SHG value, $\chi^{(2)}$ (see chapter 1), it is important to characterize these interactions as fully as possible. Since neutron diffraction is the most accurate technique for determining the positions of hydrogen atoms, a neutron study of N-methylurea was undertaken. The neutron derived structure of N-methylurea was determined at two different temperatures in order to investigate how the hydrogen-bonding was effected by a change in temperature.

7.2.1 Experimental

The neutron structure of N-methylurea was determined using data collected on SXD at ISIS. A total of nine days was allocated to us for the study, during which two sets of data were collected, one at 100K and the other at 250K. A crystal (of dimensions 4.0 x 2.0 x 1.5 mm) was cut from a parent crystal (42 x 8 x 7 mm), mounted on an aluminium pin and fixed onto the cold-head of the Displex cryorefridgerator.

Peaks from initial frames were strong and had good profiles. Consequently, the sample was successfully indexed using a frame of data collected for only a few μAmphrs. The sample was then cooled to 100K, during which time no problems occurred. Following which, data collection was started which used the strategy detailed in chapter 2. Up to the point of tiling, each frame was collected for 500 μAmphrs. When tiling began, this was reduced to 250 μAmphrs. ϕ and χ were moved in increments of 40° and 30° respectively, starting at $\phi = 0°$, $\chi = 0°$ initially and starting at $\phi = 20°$, $\chi = 75°$ when the tiling process began. No problems occurred during the experiment and the beam was fairly stable throughout, albeit low (at about 130 μAmp/hr) due to the presence of some internal damage in the ring during the cycle in which the experiment was carried out.

The temperature was then raised to 250K, at which a second set of data was collected for the remaining 2 days. The data collection procedure was identical to that used for the 100K data collection except that, in the 250K data collection, each frame was collected for only 150 μAmphrs up to the point of tiling, where it was reduced to 100 μAmphrs. Also, in the 250K data collection, a second $\phi = 0$, $\chi = 0$ frame was collected at the end of the experiment in order to improve the statistics. Again, no problems were encountered during data collection and the beam remained steady throughout.

Standard SXD procedures, as detailed in Chapter 2, were used to process and correct

both data sets. Subsequent structural refinements were carried out using SHELXL-93 (Sheldrick, 1993). Cell parameters, for each refinement, were taken from previous single-crystal 100K and 250K X-ray diffraction measurements (Cruickshank, 1997) since such parameters are more reliable than those derived from a neutron source. All relevant crystal, data collection and refinement parameters for each data set are summarized in ***Table 7.2.1***:

Table 7.2.1 *- A summary of crystal, data collection and refinement parameters for the 100K and 250K neutron structures of N-methylurea.*

Compound	N-methylurea (100K)	N-methylurea (250K)
Molecular Formula	$C_2H_6N_2O$	$C_2H_6N_2O$
Formula weight	74.00	74.00
a(Å)	8.555(2)%	8.482(4)%
b(Å)	6.796(1)%	6.923(4)%
c(Å)	6.793(3)%	6.898(3)%
Cell Volume(Å^3)	394.9(2)	405.1(3)
Crystal System	orthorhombic	orthorhombic
Space Group	$P2_12_12_1$	$P2_12_12_1$
Z	4	4
Calculated Density (gcm^{-1})	1.245	1.213
Wavelength	white beam	white beam
Crystal Morphology	block	block
Crystal Colour	transparent	transparent
Crystal Size (mm)	4.0 x 2.0 x 1.5	4.0 x 2.0 x 1.5
Total number of reflections	8734	2675
Unique reflections	1460	437
Observed Reflections [I>2σ(I)]	1459	436
R_{int}	0.0608	0.0763
Data / Parameters	1459 / 100	436 / 94
R1 [I > 2σ(I)]	0.0732	0.0715
wR2 [I > 2σ(I)]	0.0810	0.0921
Goodness of fit on F^2	4.712	4.689
Weighting Scheme	$1 / \sigma^2$	$1 / \sigma^2$
$\Delta\rho_{(max, min)}$ (fmÅ^{-3})	2.663 / -2.329	0.755 / -0.747

% These values are taken from 100K and 250K single-crystal X-ray structural refinements (Cruickshank, 1997) since they are deemed to be more accurate than those determined from neutron measurements.

7.2.2 Structural Details

50% probability thermal ellipsoid plots of the 100K and 250K neutron structure are shown in ***Figure 7.2.1a and 7.2.1b*** respectively. All bond lengths and angles are given in ***Tables*** *7.2.2* and *7.2.3* respectively. Corresponding fractional coordinates and anisotropic displacement parameters reside in ***Appendix*** *A.7.1-4* .

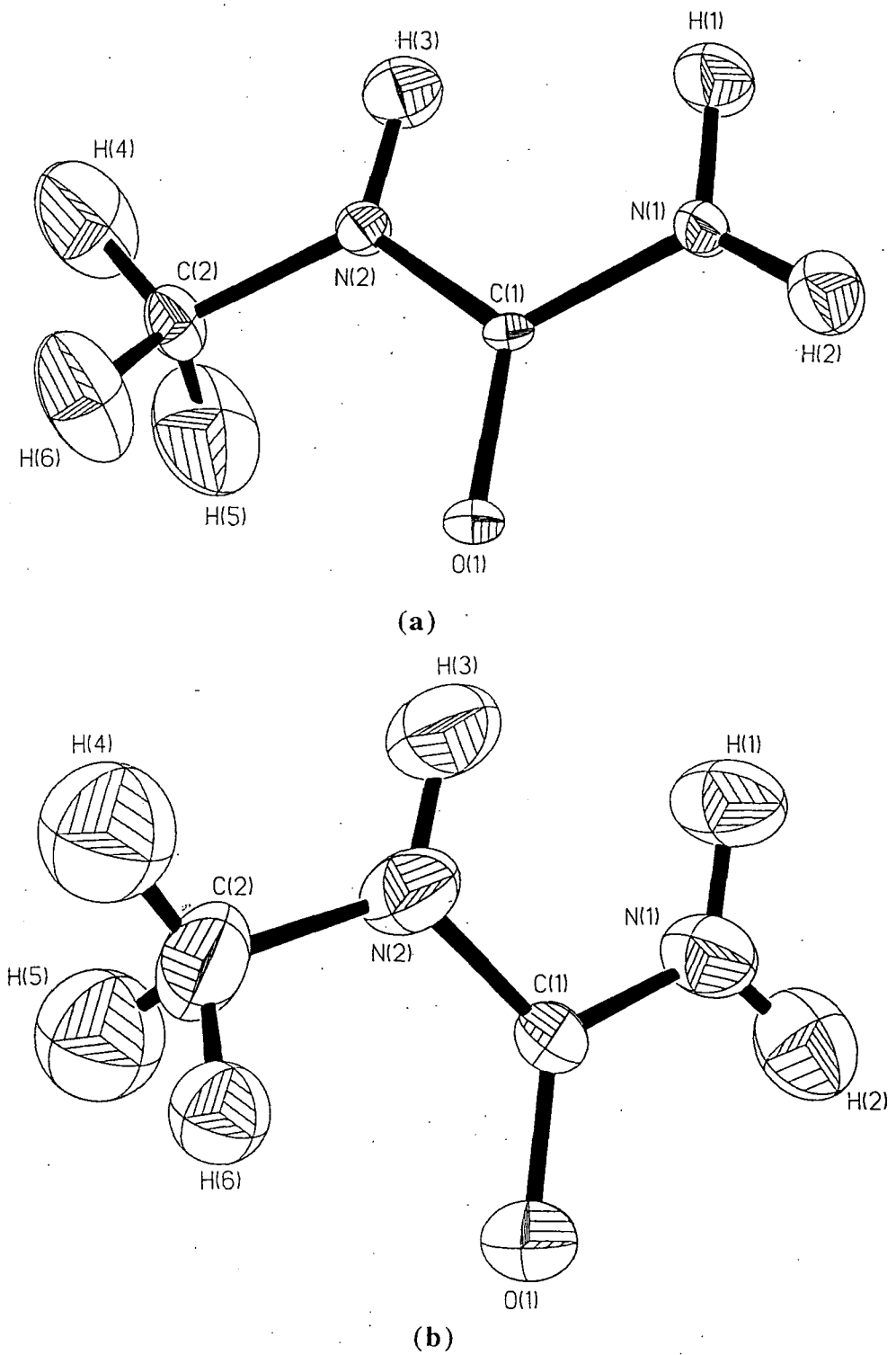

Figure 7.2.1 *- 50% probability thermal ellipsoid plots of (a) the 100K and (b) the 250K neutron structure of N-methylurea.*

Table 7.2.2 *- Bond lengths of the 100K and 250K neutron structures of N-methylurea.*

Bond	Distance (Å) at 100K	Distance (Å) at 250K
O(1)-C(1)	1.249(2)	1.240(5)
N(1)-C(1)	1.349(2)	1.344(5)
N(1)-H(1)	1.003(3)	1.00(1)
N(1)-H(2)	1.004(3)	0.96(2)
N(2)-C(1)	1.347(1)	1.352(4)
N(2)-C(2)	1.444(2)	1.427(6)
N(2)-H(3)	1.006(3)	0.99(1)
C(2)-H(4)	1.052(4)	1.10(3)
C(2)-H(4')	---	0.95(3)
C(2)-H(5)	1.062(5)	1.19(3)
C(2)-H(5')	---	1.04(4)
C(2)-H(6)	1.061(4)	1.10(3)
C(2)-H(6')	---	1.08(3)

Table 7.2.3 - Bond angles of the 100K and 250K neutron structures of N-methylurea.

Angle	Angle(°) at 100K	Angle(°) at 250K
C(1)-N(1)-H(1)	119.2(2)	118.8(6)
C(1)-N(1)-H(2)	118.6(2)	118.3(7)
H(1)-N(1)-H(2)	121.1(2)	121.8(8)
C(1)-N(2)-C(2)	121.07(9)	121.9(4)
C(1)-N(2)-H(3)	117.8(2)	117.7(6)
C(2)-N(2)-H(3)	120.9(2)	120.3(6)
O(1)-C(1)-N(1)	122.0(1)	122.1(4)
O(1)-C(1)-N(2)	122.0(1)	121.8(4)
N(1)-C(1)-N(2)	116.06(8)	116.0(3)
N(2)-C(2)-H(4)	110.3(3)	109.4(14)
N(2)-C(2)-H(4')	---	117.3(14)
N(2)-C(2)-H(5)	111.7(3)	106(2)
N(2)-C(2)-H(5')	---	113(2)
N(2)-C(2)-H(6)	112.2(2)	113.7(13)
N(2)-C(2)-H(6')	---	112.9(13)
H(4)-C(2)-H(5)	106.8(5)	137(2)
H(4')-C(2)-H(5')	---	67(2)
H(4)-C(2)-H(6)	108.9(4)	111(2)
H(5)-C(2)-H(6)	106.7(4)	74(2)
H(4')-C(2)-H(6')	---	113(2)
H(5')-C(2)-H(6')	---	126(2)

The neutron derived molecular geometry is very similar to the X-ray derived geometry (Huiszoon & Tiemessen, 1976). Moreover, within error, there appears to be no variation in the bond geometry with temperature.

The hydrogen positions determined in this study are naturally more accurate than those reported by Huiszoon & Tiemessen (1976). The overall accuracy of the 250K neutron derived structural determination of N-methylurea is necessarily lower than the 100K structural determination, given the much smaller amount of time used to collect the 250K data set. Therefore, our hydrogen-bonding studies concentrated primarily on the 100K structure, although an analysis at both temperatures is reported.

The 250K structural refinement of N-methylurea yielded a striking result: the methyl group is disordered. For simplicity, the 250K thermal ellipsoid plot, given in ***Figure 7.2.1b***, shows an undisordered isotropic representation of the methyl group but it is still

fairly evident that the ellipsoids given are anomalously large as they are. The bond geometry for both, the disordered part labelled H(n), and the disordered part labelled H(n'), is given in ***Tables 7.2.2*** and ***7.2.3***. The hydrogen atoms are disordered in a 50:50 ratio and are angularly separated in the manner shown in ***Figure 7.2.2***. The disorder is thought to be static since the internal barrier for rotation of the CH_3 group is 7.1kJmol^{-1} (Saito, Machida & Uno, 1975) which corresponds to 853K.

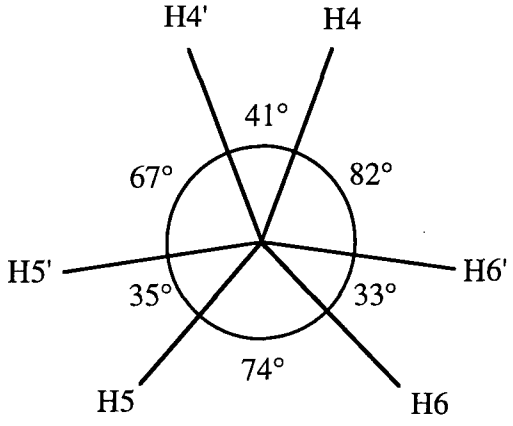

Figure 7.2.2 *- A cross-section of the methyl group showing the relative angular separations of the hydrogen atoms.*

We believe that this disorder could be responsible for the aforementioned (i) sudden lack of variation in cell parameter, a, with temperature at T > 250K (Bailey et al, 1995) and (ii) deviation from linearity of the change in heat capacity with temperature at T > 275-300K, as observed by Kozyro et al, (1993).

At both temperatures, the molecules pack together in a very similar manner. The three-dimensional lattice arrangement is dictated by hydrogen-bonding. ***Figure 7.2.3*** shows how the molecules are held together by an O(1)...H(2)-N(1) [A] interaction [1.949Å; symmetry code: 1/2-x, 2-y, 1/2+z] in a clockwise and anti-clockwise helical arrangement, where each helix runs along the b direction. This contact also constrains the molecules to align in a head-to-tail parallel fashion along the c direction. Five other principal non-bonded contacts involving O(1) (see ***Table 7.2.4***) keep each molecule fixed in the zig-zagged head-to-tail anti-parallel arrangement along the a direction. Presumably, the N...O contacts occur primarily because of the close proximity of the O(1) atom as necessitated by the hydrogen-bonding involving H(1), H(2) and H(3). A comparison of the distances of these interactions at 100K and 250K (see ***Table 7.2.4***) shows that the non-bonded contacts are slightly weaker at the elevated temperature.

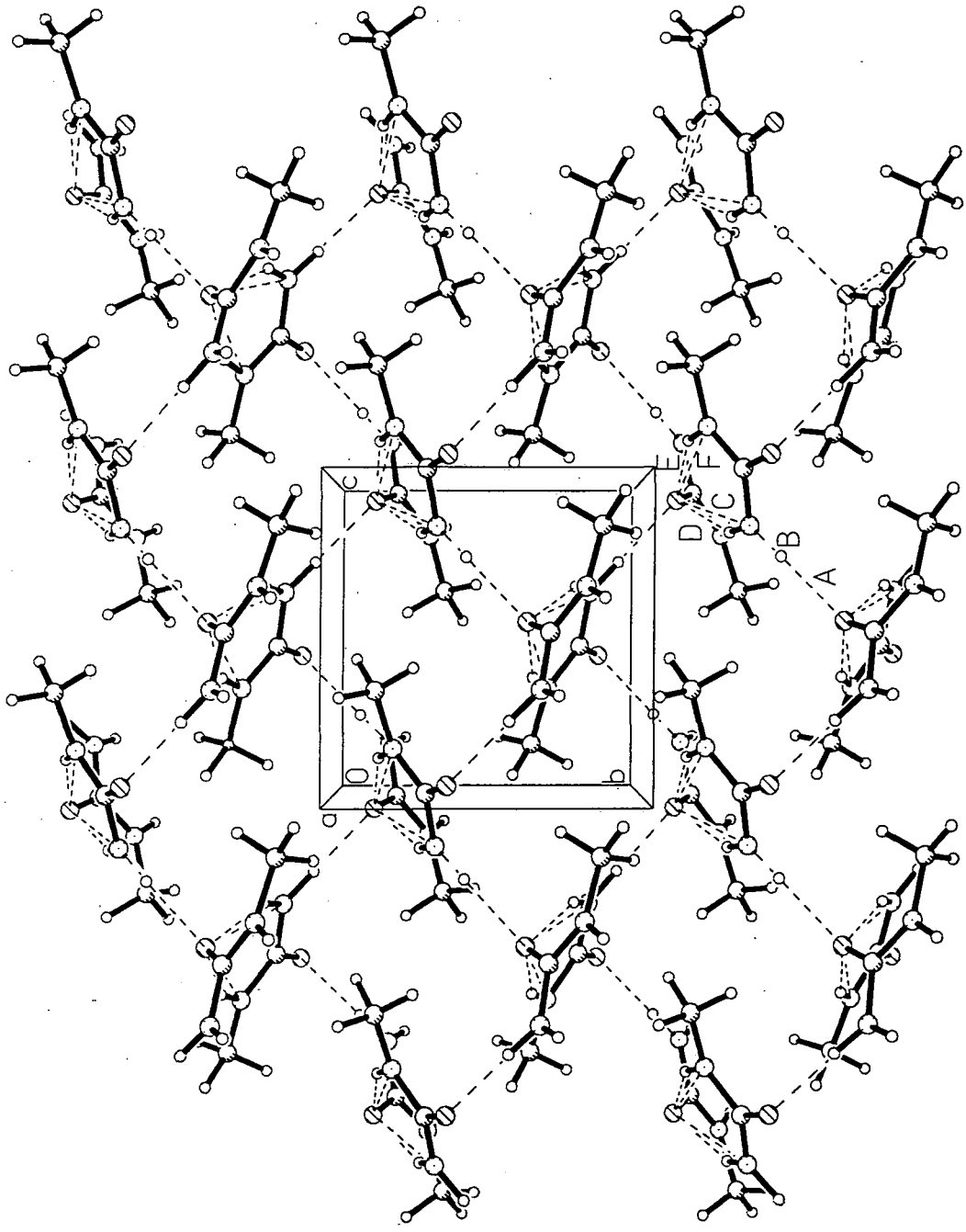

Figure 7.2.3 *- The molecular packing arrangement of the neutron structure of N-methylurea.*

Table 7.2.4 - A summary of the six principal non-bonded contacts present in N-methylurea.

Contact label	Contact	Distance (Å) at 100K	Distance (Å) at 250K
A	O(1)...H(2)-N(1)	1.949(3)	2.00(3)
B	O(1)...N(1)	2.945(2)	2.950(5)
C	O(1)...N(2)	2.910(2)	2.937(5)
D	O(1)...H(3)-N(2)	1.977(3)	2.02(1)
E	O(1)...H(1)-N(1)	2.050(3)	2.08(1)
F	O(1)...N(1)	2.952(2)	2.984(5)

symmetry codes: A: 1/2-x,2-y,1/2+z; B: 1/2-x,2-y,z-1/2; C: x-1/2,3/2-y,1-z; D: x-1/2,3/2-y,1-z; E: x-1/2,3/2-y,1-z; F: x-1/2,3/2-y,1-z.

Whilst these are the primary non-bonded contacts affecting the three-dimensional arrangement of the molecule, we also investigated all secondary non-bonded contacts, using a program called NIPMAT (Rowland, 1995), in order to obtain a more detailed understanding of the intermolecular interactions ensuing in the lattice.

7.2.3 Non-bonded Interaction Pattern MATrix (NIPMAT) analysis

The Non-bonded Interaction Pattern MATrix (NIPMAT) program (Rowland, 1995) was used to analyse all non-bonded contacts within the N-methylurea lattice.

The NIPMAT program (Rowland, 1995) takes the coordinates of each atom in turn and calculates the shortest non-bonded contact between this atom and all of the atoms from neighbouring molecules in the unit cell. The relevant sum of the van der Waals' radii is then subtracted from each contact distance in order to remove the effects of differing atomic sizes. The program then plots these normalized values in a shaded square matrix where the rows and columns are labelled by each atom in the asymmetric unit. The darker matrix elements represent the stronger contacts whilst the lighter elements reflect weak interactions. If a matrix element is unshaded (i.e. is white) then there is no contact[#] between the two atoms depicted by the row and column labelling.

This approach has several advantages over other programs typically used to determine non-bonded contacts, e.g. XP in SHELXTL (Sheldrick, 1995) or Platon (Spek, 1990). Firstly, it allows for the fact that such an interaction is electrostatic in origin and therefore its strength will fall off as a function of 1/r, rather than just disappearing at a given

[#] There is no contact within the tolerance of the sum of the van der Waals' radii of the two atoms concerned plus 1Å or -1.5Å.

threshold value (e.g greater than the sum of the van der Waals' radii)[@]. Secondly, the program uses no *a priori* information about the types of atoms that should interact with each other. It therefore provides a much more systematic and unbiased approach to the problem. Thirdly, the graphical representation of the results allows one very easily and quickly to assess them by eye. Moreover, it makes patterns between very similar molecules a lot easier to pick out. Of course, one must always analyse the angles of the contacts determined with care since the program will take no account of the necessary angular requirements (generally > 90°) for a valid interaction.

7.2.4 Results and discussion

The NIPMATs corresponding to the 100K and 250K neutron structural refinements of N-methylurea are given in ***Figures 7.2.4*** and ***7.2.5*** respectively. From which, one can immediately see that O(1) is, by far, the most involved non-bonded contact acceptor. This is expected since the atom is so electronegative and is so exposed to neighbouring molecules. C(1) appears to be the next best non-bonded contact acceptor. However, given that this atom must be electropositive, these calculated close-contacts cannot represent true non-bonded interactions but must simply reflect the closeness of the atom to O(1).

The two hydrogen atoms most commonly involved in the hydrogen-bonding are H(1) and H(2). This is expected since they are very electropositive by nature of their bonding with N(1). One might instinctively think that H(3) would also be involved in as many contacts. However, whilst it interacts very strongly with O(1) and fairly strongly with C(1), it forms only very weak contacts with other atoms. Its lack of intermolecular contacts compared to H(1) and H(2) presumably results from the fact that H(1) and H(2) lie at one end of the molecule and are therefore in a more accessible position for intermolecular interaction than H(3). H(4), H(5) and H(6) appear to be involved in non-bonded contacts, in a similar degree to each other. The NIPMATs also show that there are several quite short H...H distances. These contacts are repulsive and therefore must result as a consequence of the close-packing.

Several additional non-bonded contacts are present in the 250K structure as a result of the disorder: a weak hydrogen-bond, O(1)...H(6')-C(2) [2.57(3)Å; symmetry code: 1/2-x,2-y,z-1/2] and several H...H repulsive interactions (see ***Figure 7.2.5***).

One should note that whilst the NIPMAT analysis provides detailed and essentially unbiased results, it does not take into account the possible presence of any intra-

[@] Strictly speaking, a 'threshold' value is also used in the NIPMAT calculation but it is very large, compared to those used in other programs, such that it will only 'cut-off' the very trailing edge of a V α 1/r curve.

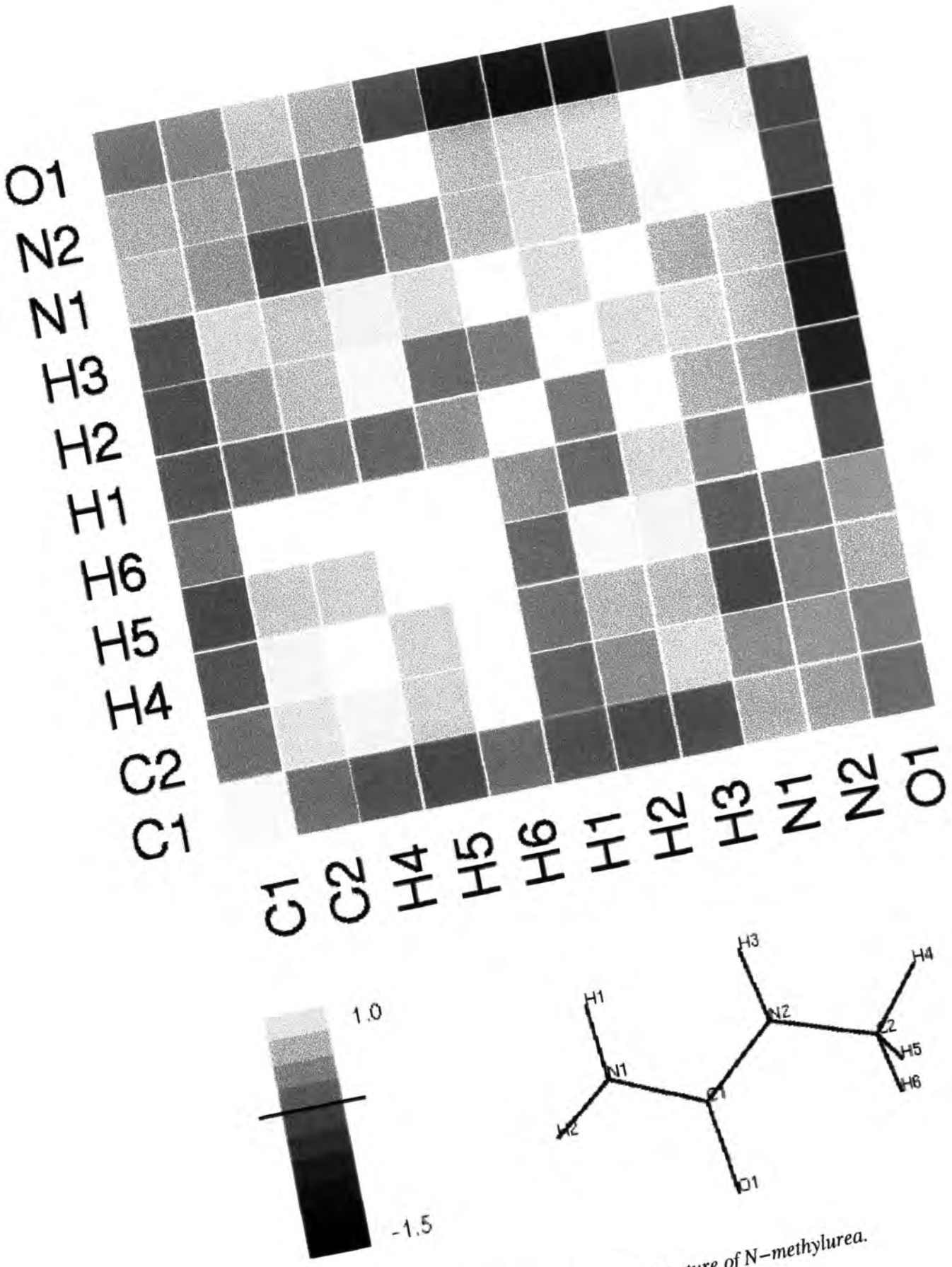

Figure 7.2.4 – A NIPMAT for the 100K neutron structure of N–methylurea.

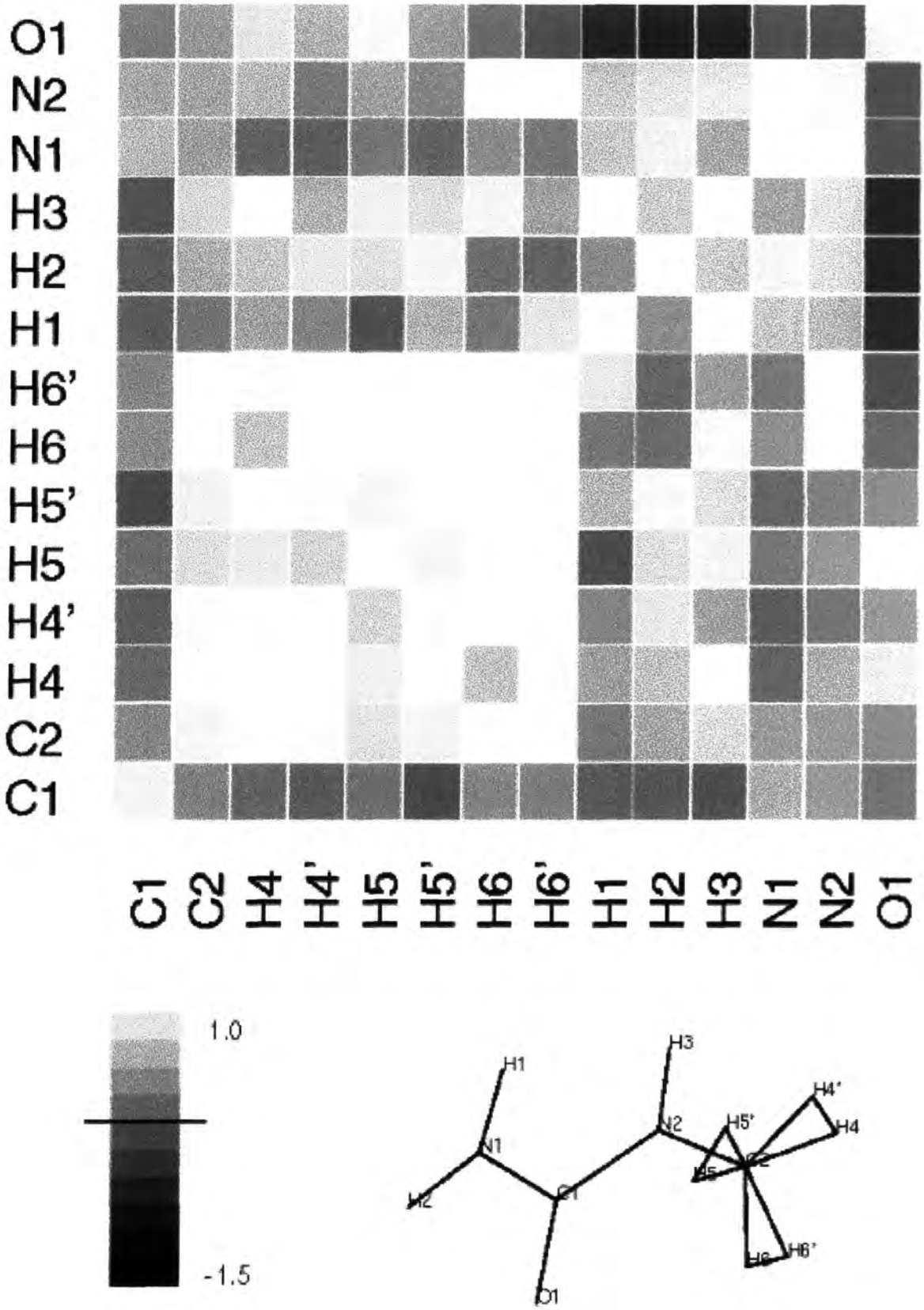

***Figure 7.2.5** – A NIPMAT for the 250K neutron structure of N–methylurea.*

molecular interactions. Therefore, in conjunction with this analysis, SHELXTL (Sheldrick, 1995) was used to ascertain whether or not any intra-molecular contacts existed. Two such contacts were found: a repulsive H(1)...H(3) contact [2.16(2)Å] and a weak hydrogen-bond, O(1)...H(6)-C(2) [2.47(3)Å].

7.3 CONCLUSIONS

The 100K and 250K neutron structures of N-methylurea are reported. The methyl group is shown to be disordered at 250K. We believe that this disorder could be responsible for the previously reported sudden lack of variation in cell parameter, a, with temperature above 250K (Bailey et al., 1995) and the deviation from linearity of the change in heat capacity with temperature at T > 275-300K (Kozyro et al., 1993).

Extensive hydrogen-bonding is found to dictate the three-dimensional packing arrangement. In particular, the O(1)...H(2)-N(1) interaction determines the packing along the b and c directions. Other primary and secondary contacts aid this interaction in maintaining a very close-packed lattice. The strength of these interactions is slightly diminished at the elevated temperature. We believe that the extensive hydrogen-bonding is responsible for the significant observed SHG output.

7.4 REFERENCES

Andersson, O., Matsuo, T., Suga, H. & Ferloni, P. (1993). International Journal of Thermophysics, **14**, 149-158.

Andersson, O. & Ross, R. G. (1994). International Journal of Thermophysics, **15**, 513-524.

Bailey, R. T., Cruickshank, F. R., Kerkoc, P., Lochran, S., Pugh, D., Sherwood, J. N., Blake, A. J. & Parsons, S. (1995). J. Appl. Phys., **78**, 3102-3106.

Bailey, R. T., Cruickshank, F. R., Sherwood, J. N., Simpson, G. S. & Wilkie, S. (1995). J. Appl. Phys., **78**, 1388-1390.

Caron, A. & Donohue, J. (1964). Acta Crystallogr., **17**, 544-546.

Caron, A. & Donohue, J. (1969). Acta Crystallogr., **B25**, 404.

Corey, R. B. & Wycoff, R. W. G. (1933). Z. Kristallogr., **85**, 132-142.

Cruickshank, F. R. (1997). Personal communication.

Ferloni, P. & Della Gatta, G. (1995). Thermochimica Acta, **266**, 203-212.

Gambino, M. & Bros, J. P. (1988). Thermochim.Acta, **127**, 223.

Hendriks, S. B. (1928). J. Am. Chem. Soc., **63**, 2455.

Huiszoon, C. & Tiemessen, G. W. M. (1976). Acta Crystallogr., **B32**, 1604-1606.

Kozyro, A. A., Kabo, G. J., Krasulin, A. P., Sevruk, V. M., Simirsky, V. V., Sheiman, M. S. & Frenkel, M. L. (1993). J. Chem. Thermodynamics, **25**, 1409-1417.

Lebioda, Hodorowicz, S. & Lewinski, K. (1978). Phys. Stat. Sol., **49**, K27-K30.

Mark, H. & Weissenberg, K. (1923). Z. Phys., **16**, 1.

Morell, J. A., Albrecht, A. C., Levin, K. H. & Tang, C. L. (1979). J. Chem. Phys., **71**, 5063-5068.

Rowland, R. S. (1995). Am. Cryst. Assoc. Abstr., **23**, 63 (Abstract 2a.5.B, Montreal Meeting).

Ruehrwein, R. A. & Huffman, H. M. (1946). J. Am. Chem. Soc., **68**, 1759.

Saito, Y., Machida, K. & Uno, T. (1975). Spectrochim. Acta, **31A**, 1237.

Sasaski, K. & Yokotake, T. (1966). Reports Gov. Chem. Ind. Res. Inst. Tokyo, **61**, 309.

Sheldrick, G. M. (1993). SHELXL-93. *Program for the Refinement of Crystal Structures using Single Crystal Diffraction Data*, University of Göttingen, Germany.

Sheldrick, G. M. (1995). SHELXTL. Version 5.03/VMS. Siemens Analytical X-ray Instruments, Inc., Madison, Wisconsin, U.S.A.

Simirsky, V. V., Kabo, G. J. & Frenkel, M. L. (1987). J. Chem. Thermodynamics, **19**, 1121.

Sklar, N., Senko, M. E. & Post, B. (1961). Acta Crystallogr., **14**, 716-720.

Spek, A. L. (1990). Acta Crystallogr., **A46**, C34.

Swaminathan, S., Craven, B. M. & McMullan, R. K. (1984). Acta Crystallogr., **B40**, 300-306.

Swaminathan, S., Craven, B. M., Spackman, M. A. & Stewart, R. F. (1984). Acta Crystallogr., **B40**, 398-404.

Vaughan, P. & Donohue, J. (1952). Acta Crystallogr., **5**, 530-535.

Worsham, J. E., Levy, H. A. & Peterson, S. W. (1957). Acta Crystallogr., **10**, 319-323.

Wyckoff, R. (1930). Z. Kristallogr., **75**, 529.

Yoshida, S. (1975). U.S. Patent No. 3895242 (15th July).

CHAPTER 8

ZINC (TRIS)THIOUREA SULPHATE

8.1 INTRODUCTION

Whilst the previous chapters have concentrated on the study of organic compounds, in this chapter we turn our attention to a novel organometallic NLO material, zinc (tris)thiourea sulphate (hereafter ZTS). The impetus for such a study lies in the fact that organometallic materials possess few of the problems which are associated with organic NLO materials (e.g. low thermal resistance, mechanical and chemical robustness). Moreover, they retain all of the advantages of organic materials over their inorganic counterparts (e.g. high optical thresholds and versatility in molecular design). In other words, organometallic compounds are the optimal compromise between organic and inorganic NLO candidates.

Since urea is the classic SHG reference material, urea and its analogues were amongst the first organic subjects to be stoichiometrically incorporated into inorganic salts. Only inorganic salts which possessed a parent metal with an almost complete electronic *d*-shell were chosen in order to avoid air-sensitive products.

Several promising candidates resulted from these systematic studies (Xing, Jiang, Shao & Xu, 1987; Tao, Jiang, Xu & Shao, 1988; Wang et al, 1989; Marcy et al, 1992). One such candidate was ZTS which has been studied extensively in terms of its electro-optic, piezoelectric, dielectic (Ramabadran, Zelmon & Kennedy, 1992), non-linear optical (Marcy et al, 1992) and thermal properties (Kerkoc et al, 1996). These reports show that ZTS:

- gives a high SHG output,
- has a very low power threshold for observable SHG,
- is critically phase-matchable,
- has respectable electro-optic and piezoelectric coefficient values compared to KDP,
- has a heat capacity and thermal expansivity which varies linearly with temperature,
- and has a large thermal conductivity anisotropy (conductivity along the crystallographic direction, c >> a).

One minor problem with ZTS is that it weakly absorbs in the optical region, 1.04 μm. This absorption is thought to occur as a result of the presence of an overtone of the N-H absorption band (Ramabadran, McPherson & Zelmon, 1994). However, this problem can be circumvented by deuterating the compound, since the absorption peak is then shifted by 0.4 μm away from the 1064 nm region. Optical properties of deuterated ZTS are reported by Ramabadran, McPherson & Zelmon (1994). The results are fairly similar to those of non-deuterated ZTS although deuterated ZTS is not critically phase-matchable.

Spectroscopic (Venkataramanan, Srinivasan & Bhat, 1994) and crystallographic (Andretti, Cavalca & Musatti, 1968) studies have also been carried out on ZTS. The former study reports on the lattice and individual group vibrations of ZTS whilst the latter study describes the X-ray derived structure of ZTS and its three-dimensional packing arrangement which is dictated by hydrogen-bonding. Given that the X-ray study was performed in 1968, photographic methods were used. Moreover, all of the hydrogen atoms were calculated assuming ideal sp^2 geometry. Hence, no hydrogen-bond distances were reported. Instead, N...O distances, where a hydrogen atom is present between these two atoms, are given, thus assuming the hydrogen-bonding. We were therefore keen to determine the exact nature of the hydrogen-bonding and did so by locating the hydrogen atomic positions directly from a neutron diffraction study.

The neutron structure of the deuterated form of ZTS was also determined as a prelude to a coherent inelastic neutron scattering experiment which was performed in order to determine the three-dimensional phonon dispersion within the material. The details of this inelastic neutron experiment are not reported here since analysis is still underway. However, the neutron structure of deuterated ZTS is discussed in this study and an analysis of the effects of deuteration on the hydrogen-bonding is made.

The two elastic neutron experiments mentioned above were carried out using D9 at the ILL. One further neutron derived structure of ZTS is also reported in this chapter. This structure was determined using the instrument, LADI (Wilkinson & Lehmann, 1991) at the ILL, which is in the latter stages of development. The instrument is formally designed for protein crystallography but since it is still in the testing stages of its development it was considered pertinent to ascertain whether or not small molecule crystallography was at least feasible using the instrument. ZTS was one of several compounds selected for this test since it had already been performed on D9 and it had given good results. The results from LADI are compared with the analogous results obtained using D9 in order to help to assess the feasibility of small molecule crystallography on this instrument.

8.2 HYDROGEN-BONDING STUDIES OF ZTS AND D-ZTS.

8.2.1 Experimental

The neutron structures of both ZTS and d-ZTS were determined at 100K using D9 at the ILL. The calibrated wavelength of the beam was 0.8369(2)Å. Half-wavelength contamination was removed with an erbium filter.

Crystals of dimensions 4.1 x 2.8 x 2.1 mm [ZTS] and 5.0 x 5.0 x 5.0 mm [d-ZTS] were used for the experiments. The use of such large crystals is generally discouraged since absorption and/or extinction effects can be very severe in crystals of this size. However, due to external constraints, we were unable to cut either crystal.

In turn, each crystal was covered in aluminium foil, mounted onto an aluminium pin and placed onto the head of the Displex unit. Since the d-ZTS crystal was particularly large, a strip of cadmium foil was placed cylindrically around the aluminium pin in order to enlarge the base of the mount so that the crystal would be more firmly fixed to it.

Beam collimators of diameter 8 mm and 10 mm were used for the ZTS and d-ZTS experiment respectively. Once a UB matrix had been obtained, each sample was cooled to 100K using an Air Products 201 He Displex CCR (Archer & Lehmann, 1986). The peak profiles of reflections from both compounds were very sharp and intense, particularly for the deuterated sample since very little incoherent scattering was present in this case. Thus, data collection was undertaken in both cases.

In the ZTS experiment, all unique data were collected in two batches, the first in the range $0° \leq \theta \leq 30°$ and the second in the range $30° \leq \theta \leq 45°$. Two batches of symmetry equivalents (-h k l) in the ranges $40° \leq \theta \leq 45°$ and $35° \leq \theta \leq 40°$ were then collected sequentially. ω-xθ scans, with x chosen to keep the reflection in the middle of the detector aperture, were used in conjunction with a scan width, $\Delta\omega$, which was roughly twice the full width of the peak to background. Both x and $\Delta\omega$ varied with the Bragg angle, θ:

θ	1.00	15.00	30.00	45.00	60.00
x	1.00	1.00	1.50	2.00	2.00
$\Delta\omega$	2.20	1.40	2.20	3.80	4.70

A default scan time of 40000 monitor counts was employed.

In the d-ZTS experiment, data were collected in three batches: where $0° \leq \theta \leq 30°$ (hkl), $30° \leq \theta \leq 32°$ (h $\pm$k $\pm$l) and $32° \leq \theta \leq 45°$ (hkl). ω-xθ scans, with x chosen to keep the reflection in the middle of the detector aperture, were used in conjunction with a scan width, $\Delta\omega$, which was roughly twice the full width of the peak to background. Both x and $\Delta\omega$ varied with the Bragg angle, θ:

θ	1.00	15.00	30.00	45.00	60.00
x	1.00	1.00	1.50	2.00	2.00
$\Delta\omega$	2.20	1.40	2.25	3.80	4.70

A default scan time of 20000 monitor counts was employed.

In both experiments, a standard reflection (0 3 0) was measured every 50 reflections in order to monitor the constancy of the intensity. In both cases, data collection proceeded with no problems.

Both sets of data were reduced in the manner described in chapter 2, section 2.3.5.2. The chosen values of the integration parameters, STVOL, VOLFAC, SIGBR and FILL were 800, 3.0, 0.5, 0.05 and 800, 3.0, 0.5, 0.1 for the ZTS and d-ZTS data reductions respectively. Cryostat shield and crystal absorption corrections were then applied using the local program ABSCAN and the DATAP program (Coppens, 1970) respectively [transmission ranges: 0.7119 - 0.7847 (ZTS) and 0.9960 - 0.9966 (d-ZTS)].

Each structure was refined by full-matrix least-squares refinement using SHELXL-93 (Sheldrick, 1993). Positional and anisotropic displacement parameters were refined for all atoms in both cases. An isotropic extinction correction was applied during the refinement of both structures [the extinction parameter, EXTI = 0.0290(5) (ZTS); 0.550(8) (d-ZTS)]. Since extinction effects were severe in the d-ZTS data, the worst affected 109 reflections [where $\Delta/\sigma > 10$] were omitted from the refinement.

A summary of crystal, data collection and refinement parameters for each structure is given in ***Table 8.2.1***.

Table 8.2.1 *- A summary of crystal, data collection and refinement parameters for the 100K neutron structures of ZTS and d-ZTS.*

Compound	ZTS	d-ZTS
Molecular Formula	$ZnC_3H_{12}N_6O_4S_4$	$ZnC_3D_{12}N_6O_4S_4$
Formula weight	389.40	389.40
a(Å)	11.0616(9)	11.0608(5)
b(Å)	7.7264(6)	7.7278(4)
c(Å)	15.558(1)	15.542(1)
α(°)	90	90
β(°)	90	90
γ(°)	90	90
Cell Volume(Å^3)	1329.7(2)	1328.4(1)
Crystal System	orthorhombic	orthorhombic
Space Group	Pca2(1)	Pca2(1)
Z	4	4
Calculated Density (gcm^{-1})	1.945	1.947
Temperature (K)	100.0(1)	100.0(1)
Wavelength (Å)	0.8369(2)	0.8369(2)
Absorption coefficient (mm^{-1})	0.1335	0.0008
Crystal Morphology	truncated rectangular prism	cube
Crystal Colour	transparent	transparent
Crystal Size (mm)	4.1 x 2.8 x 2.1	5.0 x 5.0 x 5.0
Total number of reflections	4454	4191
Unique reflections	3503	3460
Observed Reflections [I>2σ(I)]	3217	3342
R_{int}	0.0264	0.0267
$(\sin\theta/\lambda)_{max}$	0.855	0.810
Data / Parameters	3493 / 272	3351 / 273
R1 [I > 2σ(I)]	0.0350	0.0263
wR2 [I > 2σ(I)]	0.0433	0.0563
Goodness of fit on F^2	1.559	4.300
Weighting Scheme	$1/\sigma^2$	$1/\sigma^2$
$\Delta\rho_{(max, min)}$ (fmÅ^{-3})	0.898 / -0.898	0.732 / -1.149

8.2.2 Structural details

A 50% probability thermal ellipsoid plot of the structure of ZTS and d-ZTS is given in ***Figures 8.2.1*** and ***8.2.2*** respectively. Bond lengths and angles for each structure are given in ***Tables 8.2.2*** and ***8.2.3*** respectively. Fractional coordinates and anisotropic displacement parameters are given in ***Appendix A.8.1 - A.8.4***.

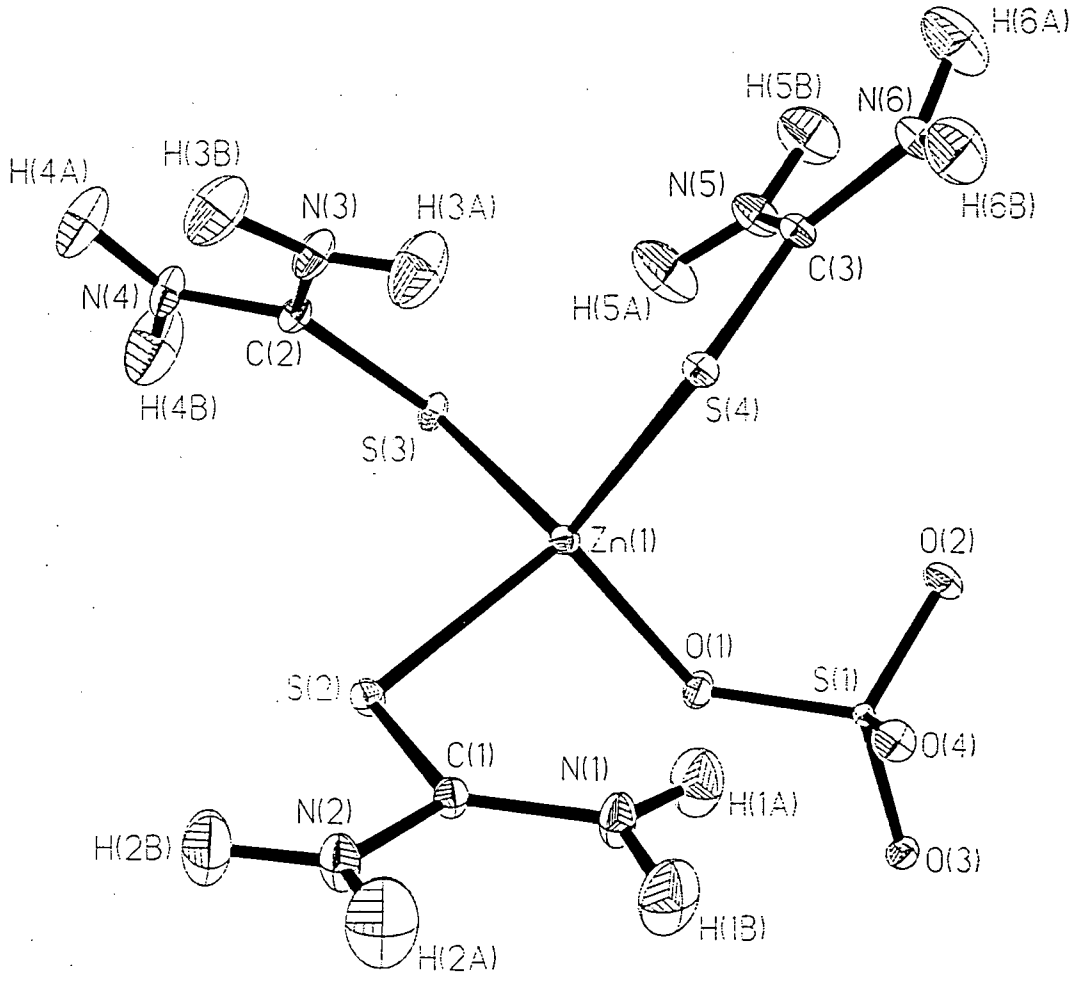

Figure 8.2.1 - A 50% probability thermal ellipsoid plot of the 100K neutron structure of ZTS.

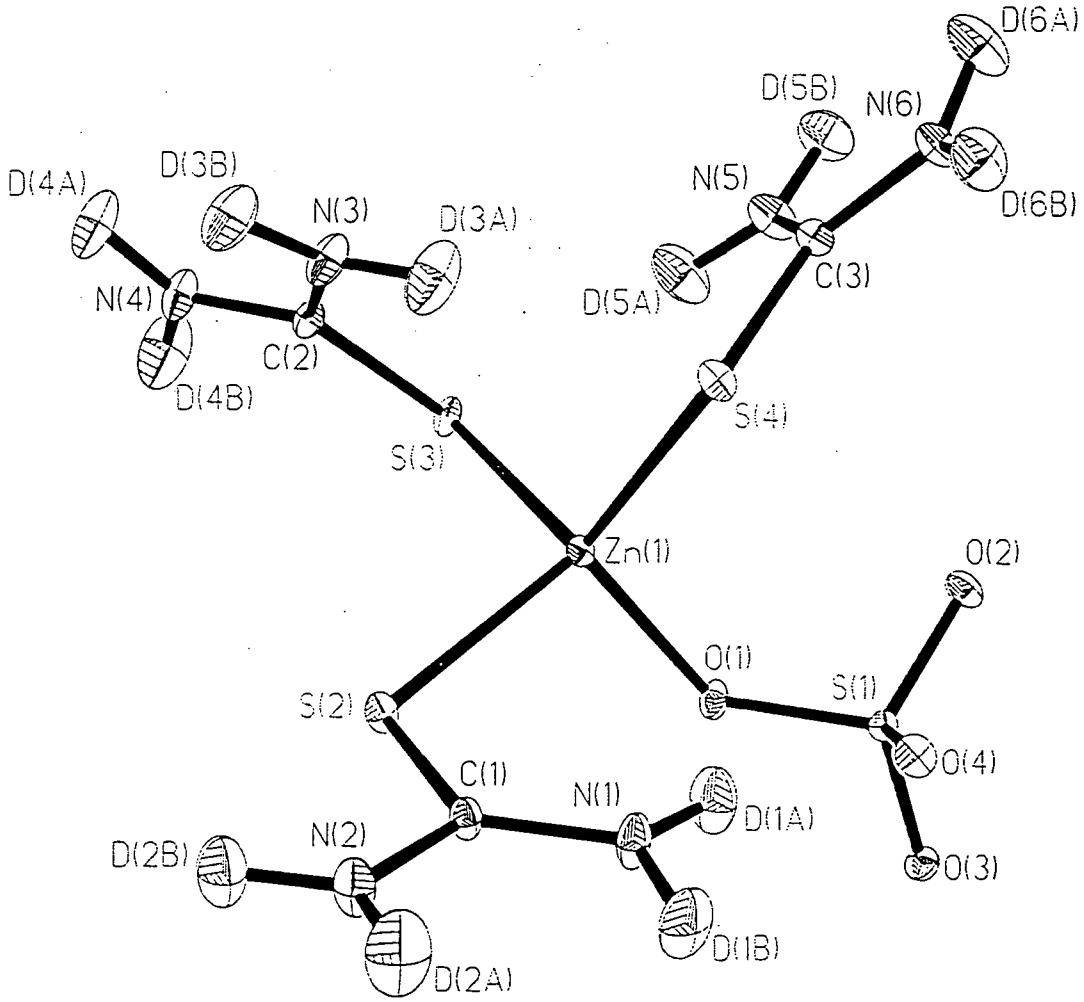

Figure 8.2.2 - A 50% probability thermal ellipsoid plot of the 100K neutron structure of d-ZTS.

Table 8.2.2 - Bond lengths for the 100K neutron structures of ZTS and d-ZTS.

Bond	ZTS distance (Å)	d-ZTS distance (Å)	Bond	ZTS distance (Å)	d-ZTS distance (Å)
Zn(1)-S(2)	2.324(2)	2.327(3)	N(2)-H/D(2A)	1.003(3)	1.014(2)
Zn(1)-S(3)	2.328(2)	2.328(3)	N(2)-H/D(2B)	1.021(2)	1.013(2)
Zn(1)-S(4)	2.317(2)	2.318(2)	N(3)-C(2)	1.323(1)	1.324(1)
Zn(1)-O(1)	1.980(2)	1.978(2)	N(3)-H/D(3A)	1.006(3)	1.008(2)
S(1)-O(1)	1.514(2)	1.515(3)	N(3)-H/D(3B)	1.025(2)	1.024(2)
S(1)-O(2)	1.465(2)	1.462(3)	N(4)-C(2)	1.323(1)	1.323(1)
S(1)-O(3)	1.473(2)	1.472(2)	N(4)-H/D(4A)	1.020(3)	1.017(2)
S(1)-O(4)	1.468(2)	1.472(2)	N(4)-H/D(4B)	1.003(3)	1.006(2)
S(2)-C(1)	1.727(2)	1.729(3)	N(5)-C(3)	1.326(1)	1.327(1)
S(3)-C(2)	1.742(2)	1.740(2)	N(5)-H/D(5A)	1.013(3)	1.009(2)
S(4)-C(3)	1.738(2)	1.734(3)	N(5)-H/D(5B)	1.022(3)	1.022(2)
N(1)-C(1)	1.323(1)	1.323(1)	N(6)-C(3)	1.324(1)	1.321(1)
N(1)-H/D(1A)	1.016(2)	1.012(2)	N(6)-H/D(6A)	1.012(3)	1.010(2)
N(1)-H/D(1B)	1.021(2)	1.021(2)	N(6)-H/D(6B)	1.014(2)	1.019(2)
N(2)-C(1)	1.329(1)	1.328(1)			

Table 8.2.3 - Bond angles for the 100K neutron structures of ZTS and d-ZTS.

Angle	ZTS angle (°)	d-ZTS angle (°)	Angle	ZTS angle (°)	d-ZTS angle (°)
S(2)-Zn(1)-S(3)	103.24(9)	103.1(1)	C(2)-N(3)-H/D(3A)	119.9(2)	119.7(1)
S(2)-Zn(1)-S(4)	110.91(9)	110.98(9)	C(2)-N(3)-H/D(3B)	121.2(2)	121.3(1)
S(2)-Zn(1)-O(1)	105.92(8)	106.03(9)	H/D(3A)-N(3)-H/D(3B)	117.5(2)	117.5(1)
S(3)-Zn(1)-S(4)	114.6(1)	114.4(1)	C(2)-N(4)-H/D(4A)	120.7(2)	120.1(1)
S(3)-Zn(1)-O(1)	108.04(7)	108.02(8)	C(2)-N(4)-H/D(4B)	119.0(2)	118.9(1)
S(4)-Zn(1)-O(1)	113.37(8)	113.49(9)	H/D(4A)-N(4)-H/D(4B)	120.2(2)	120.9(2)
O(1)-S(1)-O(2)	109.1(2)	109.0(2)	C(3)-N(5)-H/D(5A)	119.7(2)	119.5(1)
O(1)-S(1)-O(3)	106.5(1)	106.4(2)	C(3)-N(5)-H/D(5B)	120.3(2)	120.3(1)
O(1)-S(1)-O(4)	108.4(1)	108.2(2)	H/D(5A)-N(5)-H/D(5B)	119.5(2)	119.7(1)
O(2)-S(1)-O(3)	110.6(2)	111.1(2)	C(3)-N(6)-H/D(6A)	120.0(2)	120.5(1)
O(2)-S(1)-O(4)	111.5(1)	111.4(2)	C(3)-N(6)-H/D(6B)	118.9(2)	119.8(1)
O(3)-S(1)-O(4)	110.6(2)	110.7(2)	H/D(6A)-N(6)-H/D(6B)	119.9(2)	118.8(1)
Zn(1)-S(2)-C(1)	107.1(1)	106.9(1)	S(2)-C(1)-N(1)	123.1(1)	123.3(1)
Zn(1)-S(3)-C(2)	100.8(1)	100.8(1)	S(2)-C(1)-N(2)	117.4(1)	117.1(1)
Zn(1)-S(4)-C(3)	106.7(1)	106.8(1)	S(3)-C(2)-N(3)	122.4(1)	122.5(1)
Zn(1)-O(1)-S(1)	124.5(1)	124.6(1)	S(3)-C(2)-N(4)	118.1(1)	118.0(1)
C(1)-N(1)-H/D(1A)	122.3(2)	122.3(1)	S(4)-C(3)-N(5)	123.0(1)	123.0(1)
C(1)-N(1)-H/D(1B)	119.5(2)	119.8(1)	S(4)-C(3)-N(6)	117.2(1)	117.3(1)
H/D(1A)-N(1)-H/D(1B)	117.5(2)	117.2(2)	N(1)-C(1)-N(2)	119.51(8)	119.60(9)
C(1)-N(2)-H/D(2A)	121.3(2)	120.8(1)	N(3)-C(2)-N(4)	119.53(8)	119.47(9)
C(1)-N(2)-H/D(2B)	120.6(2)	120.6(1)	N(5)-C(3)-N(6)	119.77(8)	119.71(9)
H/D(2A)-N(2)-H/D(2B)	118.0(2)	118.5(2)			

The neutron derived cell parameters of both ZTS and d-ZTS were used for each structural refinement since no 100K X-ray laboratory source cell parameters were at our disposal. Cell parameters, a and b, for ZTS and d-ZTS are the same within three esds. However, the cell parameter, c, of d-ZTS is slightly smaller than that for ZTS.

The level of deuteration in d-ZTS was found to be 97%, as determined by the common refinement of the deuterium atom occupancy factors.

The bond geometries of ZTS and d-ZTS are almost identical to each other and are very similar to the previously reported X-ray structure (Andretti, Cavalca & Musatti, 1968). The zinc (II) ion is 4-coordinate and lies in a tetrahedral site, as is typical for such a species. However, this tetrahedral site is slightly distorted due to the need for steric

alleviation between the sulphate group and the S(4)-C(NH/D_2)$_2$ group since the sulphate ion coordinates to the zinc ion at an angle, Zn(1)-O(1)-S(1) of 124.5(1)° in ZTS [124.6(1)° in d-ZTS]. Given this angle, we presume that one of the lone pairs on O(1) is involved in the coordination to the zinc ion. As a result of the close proximity of these groups, the distance S(1)...S(4) [3.861(3)Å in ZTS; 3.867(3)Å in d-ZTS] is just outside the sum of twice the van der Waals radii of sulphur [3.60Å] (Bondi, 1964).

The three thiourea molecules bind to the zinc ion in a symmetric manner such that if the sulphate group was not tilted due to the Zn(1)-O(1)-S(1) interaction, then the molecule would belong to the C_{3v} point group. All Zn-S-C angles are approximately tetrahedral as expected. All three thiourea ligands are very planar as illustrated by least-squares mean plane calculations given in the original structural report (Andretti, Cavalca & Musatti, 1968). Furthermore, the sulphur atom in each thiourea group comes into very close contact with each nitrogen and hydrogen / deuterium atom within the same group. These contacts, listed in ***Table 8.2.4*** are much less than the sum of the van der Waals radius of each respective pair of atoms [$r_{vdw}(S) + r_{vdw}(N) = 1.8 + 1.55 = 3.15$Å; $r_{vdw}(S) + r_{vdw}(H) = 1.8 + 1.2 = 3.0$Å] (Bondi, 1964) and so must, in part, be responsible for the retention of such a high degree of planarity in each thiourea group. Whilst it is not surprising that these short contacts arise, given the nature of the internal bond geometry and the diffuseness of the sulphur atom, it is perhaps intriguing that all S...N(X) and S...H(XA) contacts [where X = odd] are noticeably longer than all S...N(X) and S...H(XB) contacts [where X = even]. We presume that this asymmetry is caused by the corresponding asymmetry in the S-C-N angles where all S-C-N(X) angles [X = odd] are a few degrees greater than the expected ideal sp^2 geometry whilst all S-C-N(X) angles [where X = even] are a few degrees less than the ideal value (all related N-C-N angles are ideal). We believe that these deviations are caused by the effects of steric repulsion between each amine group [where X = odd] and the neighbouring thiourea group since each amine group [where X = odd] necessarily points towards the next thiourea group, as a result of the tetrahedral Zn-S-C angles.

All N-H/D distances are typical for such a compound. There is very little difference between the N-H and N-D values except in the case of the N(2)-H/D(2A) bond where the N(2)-H(2A) distance [1.003(3)Å] is markedly shorter than the N(2)-D(2A) distance [1.014(2)Å]. The cause for this difference may be related to the fact that H(2A) / D(2A) atoms have comparitively large thermal ellipsoids and so the isotope effect is emphasized for this atom.

The molecules pack directly on top of each other in layers down the b axis as shown in ***Figure 8.2.3***. Hydrogen-bonds are present in all three axial directions (***Figures***

8.2.3-8.2.4) and so are responsible for keeping each layer intact and for binding the layers together. All non-bonded contacts are given in ***Table 8.2.4*** .

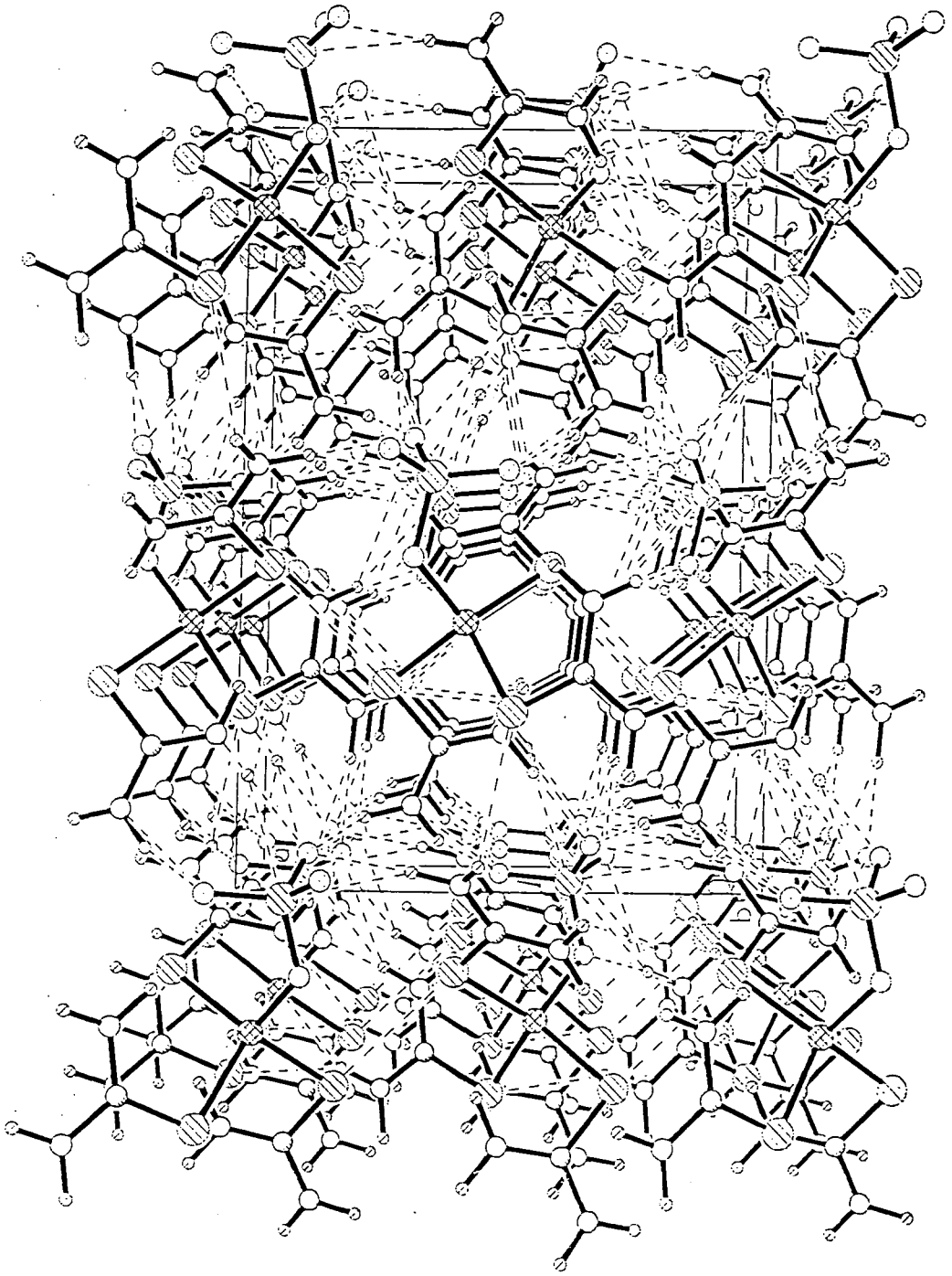

Figure 8.2.3 - The molecular packing arrangement of the 100K neutron structure of ZTS / d-ZTS viewed looking down the b axis.

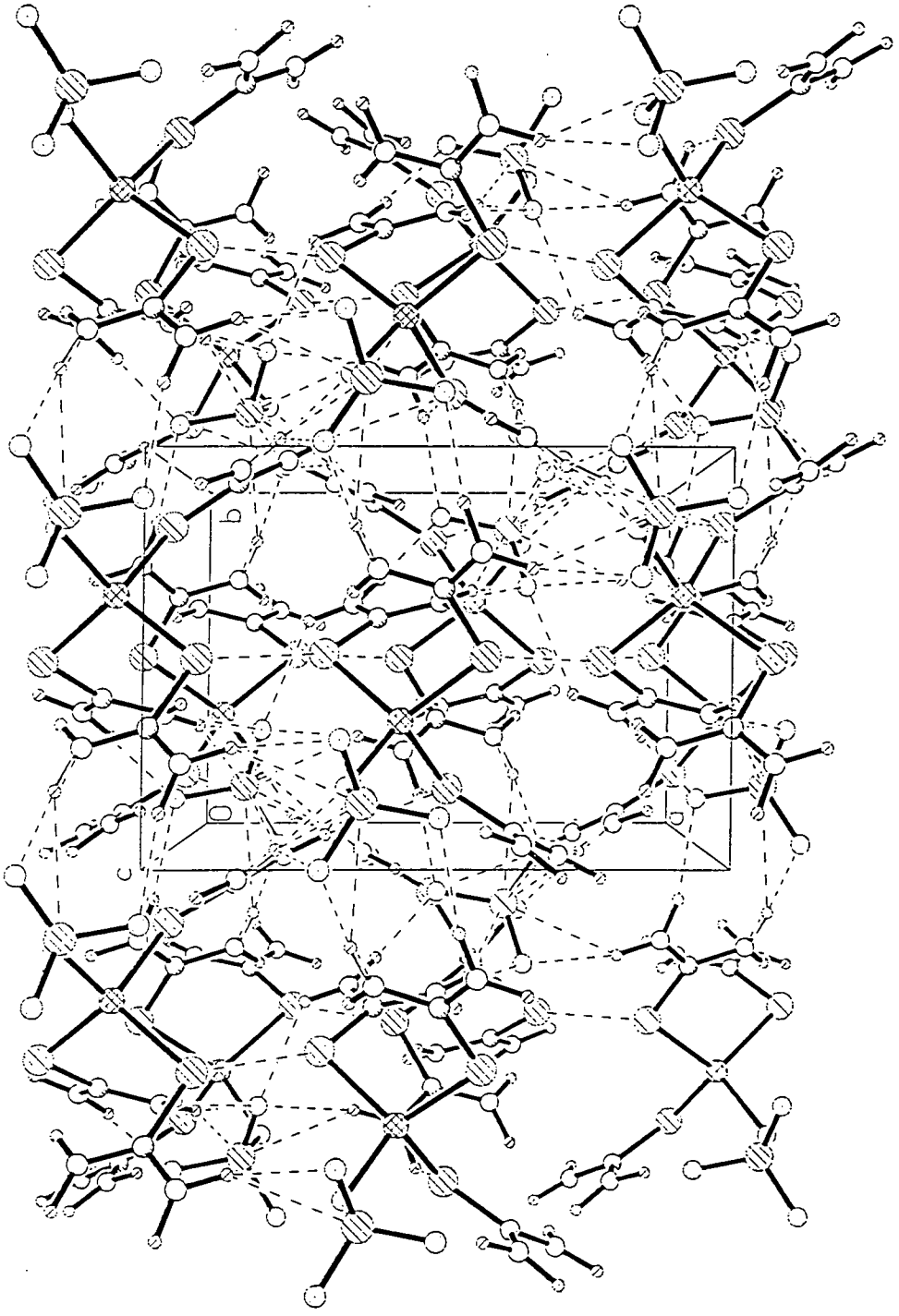

Figure 8.2.4 - The molecular packing arrangement of the 100K neutron structure of ZTS / d-ZTS viewed looking down the c axis.

Table 8.2.4 - A summary of all non-bonded contacts present in ZTS and d-ZTS.

Intramolecular non-bonded contacts			Intermolecular non-bonded contacts		
Contact	Distance in ZTS	Distance in d-ZTS	Contact	Distance in ZTS	Distance in d-ZTS
S(2)...N(1)	2.689(2)	2.693(3)	S(3)...S(4)[a]	3.263(3)	3.264(3)
S(2)...N(2)	2.619(2)	2.617(2)	S(1)...H/D(3B)-N(3)[b]	2.678(3)	2.678(3)
S(3)...N(3)	2.693(2)	2.694(2)	S(1)...H/D(6B)-N(6)[c]	2.652(3)	2.645(3)
S(3)...N(4)	2.637(2)	2.634(3)	S(2)...H/D(2A)-N(2)[d]	2.590(3)	2.585(3)
S(4)...N(5)	2.700(2)	2.697(2)	O(1)...H/D(1B)-N(1)[e]	1.869(2)	1.870(2)
S(4)...N(6)	2.622(2)	2.617(3)	O(2)...H/D(3B)-N(3)[f]	1.861(3)	1.865(2)
S(2)...H/D(1A)-N(1)*	2.871(3)	2.876(3)	O(2)...H/D(6B)-N(6)[g]	2.045(2)	2.044(2)
S(2)...H/D(2B)-N(2)*	2.723(3)	2.715(3)	O(3)...H/D(2B)-N(2)[h]	1.952(3)	1.959(2)
S(3)...H/D(3A)-N(3)*	2.822(3)	2.822(3)	O(3)...H/D(5B)-N(5)[i]	1.815(2)	1.811(2)
S(3)...H/D(4B)-N(4)*	2.718(3)	2.717(3)	O(4)...H/D(4A)-N(4)[j]	1.951(3)	1.945(2)
S(3)...H/D(5A)-N(5)	2.470(3)	2.478(3)	O(4)...H/D(6A)-N(6)[k]	2.135(2)	2.140(2)
S(4)...H/D(3A)-N(3)	2.544(3)	2.529(3)			
S(4)...H/D(5A)-N(5)*	2.836(3)	2.829(3)			
S(4)...H/D(6B)-N(6)*	2.691(3)	2.703(3)			
O(4)...H/D(1A)-N(1)	1.985(2)	1.985(2)			

symmetry codes: a = 1/2+x,1-y,z; b = 2-x,1-y,z-1/2; c = 1/2+x,1-y,z; d = 1/2+x,2-y,z; e = 1/2+x,2-y,z; f = 2-x,1-y,z-1/2; g = x-1/2,1-y,z; h = 2-x,2-y,z-1/2; i = x,1+y,z; j = 2-x,1-y,1/2+z; k = x,y-1,z.

Two very strong hydrogen-bonds [O(3)...H(5B)-N(5) and O(1)...H(1B)-N(1)], one fairly strong hydrogen-bond [O(4)...H(6A)-N(6)] and one weak hydrogen-bond [S(2)...H(2A)-N(2)] take force principally along the b direction and therefore hold the stacked layers together very tightly. Another particularly strong hydrogen-bond [O(2)...H(3B)-N(3)] and two other hydrogen-bonds [O(4)...H(4A)-N(4) and O(3)...H(2B)-N(2)] hold the molecules in layer formation along the c direction. Along the a direction, the layer formation is retained by the fairly strong hydrogen-bond, O(2)...H(6B)-N(6) with perhaps a little help from the much weaker S(1)...H(6B)-N(6) interaction.

The molecules are therefore very tightly contained in all directions within the lattice. This explains why the thermal motion within both the ZTS and d-ZTS molecules (***Figures 8.2.1*** and ***8.2.2***) is so small, even for the hydrogen / deuterium atoms since all such

* Although these are non-bonded contacts, they cannot be considered as hydrogen-bonds since the S...H-N angles (69°-75°) are less than 90°.

atoms, except H/D(4B), are involved in at least one hydrogen-bond. The presence of such close packing and extensive hydrogen-bonding thus largely explains why the material exhibits a high SHG output. Furthermore, given the extremely small thermal motion at 100K, the detrimental effects of the N-H overtone to the SHG output would presumably be reduced considerably at this temperature.

Several intramolecular interactions also exist (see ***Table 8.2.4***) although all of these except the O(4)...H(1A)-N(1) interaction are weak. The fairly strong O(4)...H(1A)-N(1) hydrogen-bond forms as a result of the close proximity of the sulphate group to the cation.

8.3 THE NEUTRON DERIVED STRUCTURE OF ZTS AS DETERMINED USING LADI

As stated previously, LADI (Wilkinson & Lehmann, 1991) is an instrument at the ILL which is currently under development. It was placed on a thermal guide tube at the ILL earlier in 1997 in order to perform tests on a range of small molecules. ZTS was one of the materials tested and a comparative study of the results obtained with those from the D9 experiment was made.

Since LADI (Wilkinson & Lehmann, 1991) is still under development, the instrumental details and experimental procedures are described here rather than in chapter 2, since they may be subject to change.

8.3.1 The LAue DIffractometer, LADI

LADI (Wilkinson & Lehmann, 1991) is a Laue diffractometer and therefore a white beam with limited wavelength spread is required for its successful operation. Such a beam is achieved by continuously 'chopping' the raw beam at a given frequency. Two choppers are necessary to produce the desired effect: the first chopper converts the continuous white beam into a pulsed beam whilst the second chopper acts as a velocity selector, thereby providing a beam of a chosen, limited wavelength band.

The resultant beam enters the instrument enclosure. A schematic diagram of the instrument is shown in ***Figure 8.3.1*** and pictures of the instrument, with and without its casing, are given in ***Figures 8.3.2*** and ***8.3.3*** respectively. The beam enters the detector surface via a small vertical hole, which is situated in a position equidistant from the horizontal edges of the drum. Some of the beam is diffracted by the sample which is positioned at the centre of the drum on a mount which is movable in the phi-direction (rotation about an axis perpendicular to the beam). The undiffracted beam leaves the drum by a further small vertical hole, situated diametrically opposite the entrant hole and is absorbed by a beam stop.

The diffracted beam penetrates the surrounding 4 mm thick cylindrical aluminium drum (at a point dependent upon the angle of diffraction) and passes to its exterior onto which are mounted eight 200 x 200 mm^2 image plates (Cipriani, Dauvergne, Gabriel, Wilkinson & Lehmann, 1994; Cipriani, Castagna, Lehmann & Wilkinson, 1995; Cipriani, Castagna, Wilkinson, Oleinek & Lehmann, 1996). Given that the drum is 400 mm in length and 318.3 mm in diameter, these image plates cover most of the drum's surface area. The image plates therefore continuously absorb all of the diffraction emanating from the sample as long as the beam remains on. The chosen exposure time of the beam to the

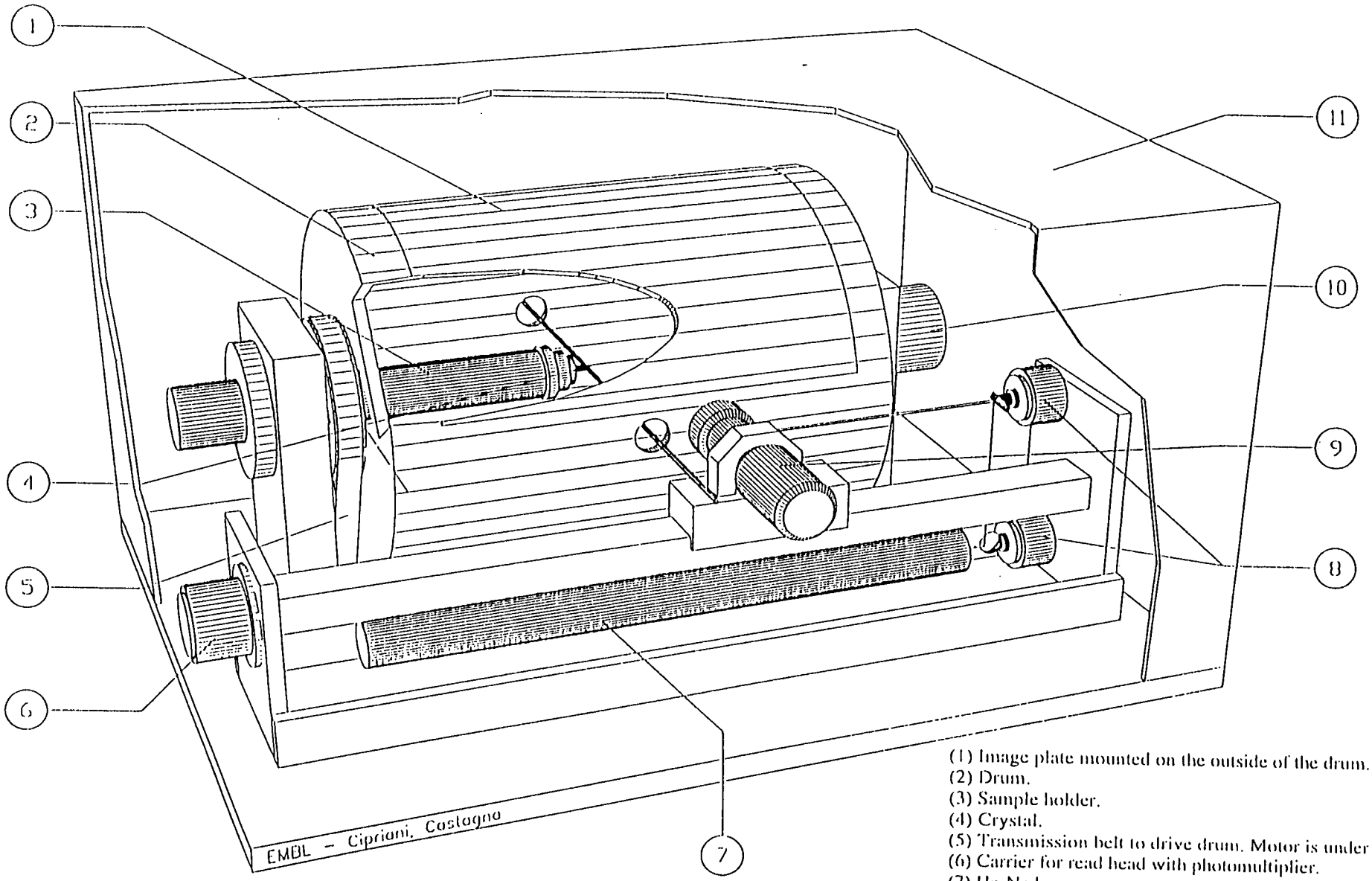

Figure 8.3.1 - A schematic representation of the instrument, LADI.

(1) Image plate mounted on the outside of the drum.
(2) Drum.
(3) Sample holder.
(4) Crystal.
(5) Transmission belt to drive drum. Motor is under table.
(6) Carrier for read head with photomultiplier.
(7) He-Ne laser.
(8) Mirrors for bringing laser light to the read head.
(9) Read head with photomultiplier.
(10) Encoder for drum rotation.
(11) Cover.

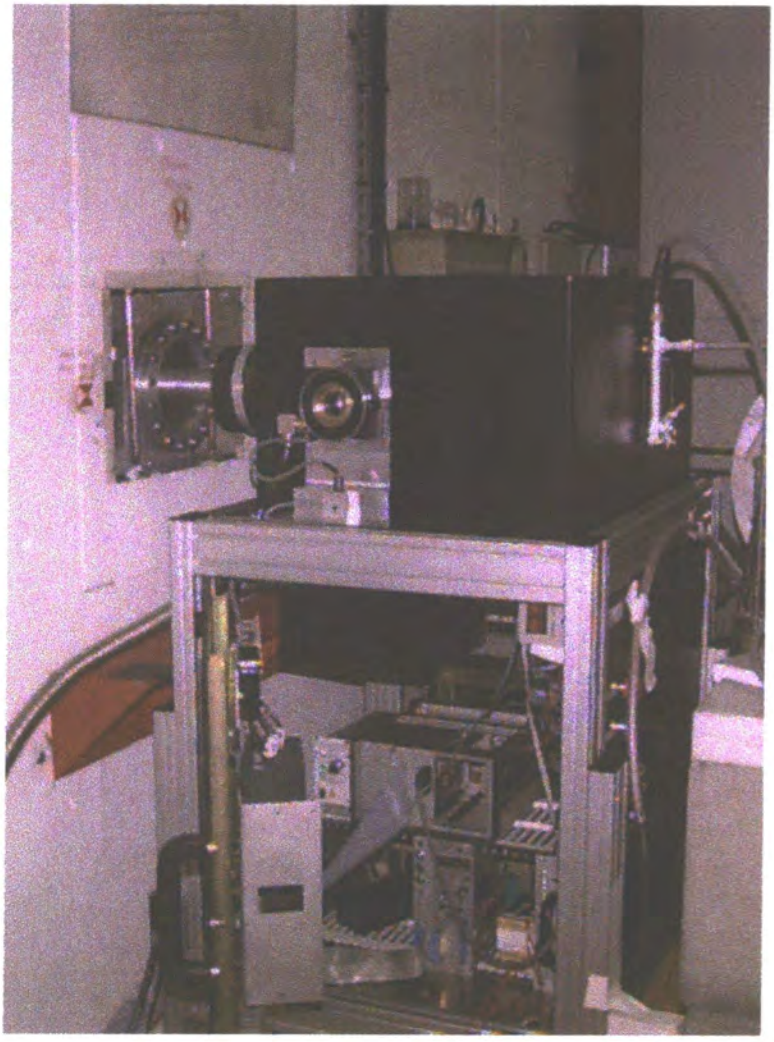

Figure 8.3.2 *- The Laue Diffractometer at the ILL.*

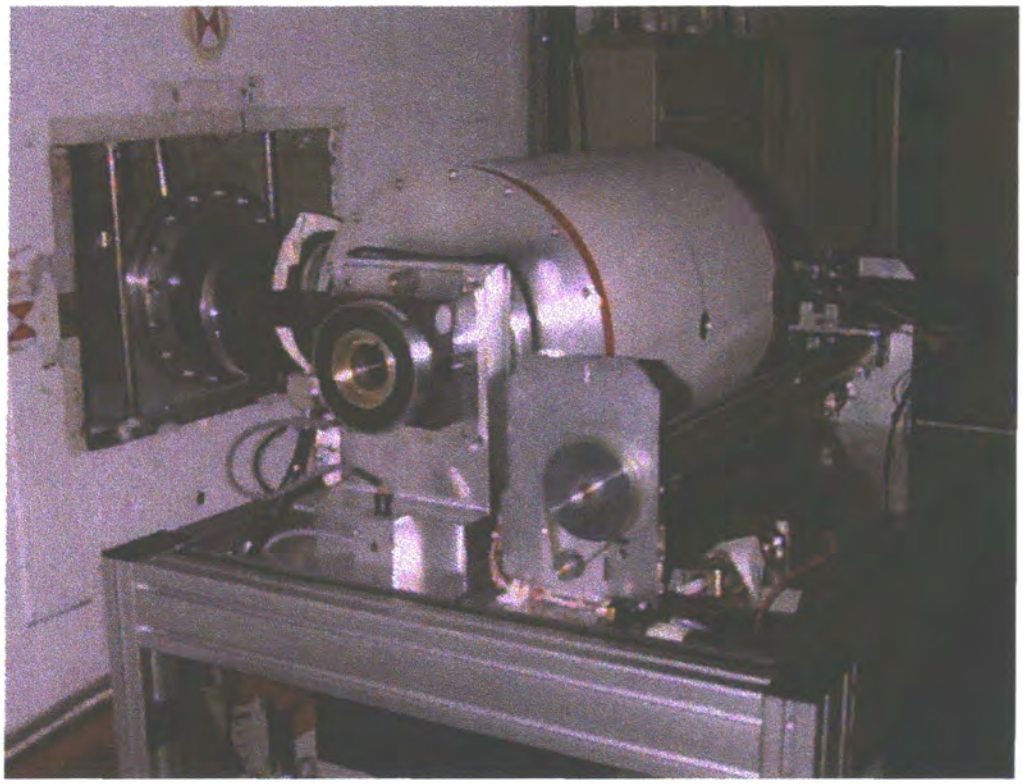

Figure 8.3.3 *- The Laue Diffractometer at the ILL (without casing).*

image plates depends on the scattering strength of the given sample but is typically between 1-5 hours. Obviously, the longer the exposure time, the more intense the spots that are recorded on the image plates.

Once the beam is switched off, the diffraction information needs to be extracted from the image plates. This is accomplished by reflecting a laser light (from a He-Ne laser) off mirrors situated on a movable head, and onto the image plate. The blue light stimulated by the laser is recorded by a photmultiplier tube which scans across the drum from one side to the other whilst the drum rotates at 350 rpm. The information from each pixel (200 x 200 μm^2) is thus collected sequentially in a raster manner along the vertical direction. The readout time is about five minutes, after which the recorded information is displayed on a Macintosh Quadra computer which is also used to manipulate the data and to control the instrment. An example of one such display, taken from our experiment, is shown in ***Figure 8.3.4***. Once this information has been stored in the computer, it must be erased from the image plates in preparation for the next exposure. A lamp, positioned on the side of the drum opposite to the photomultiplier, is used to wipe the image plates clean. The process is then repeated for the next exposure. In order to obtain data over a sufficient range of reciprocal space, one must record such exposures at several different values of phi.

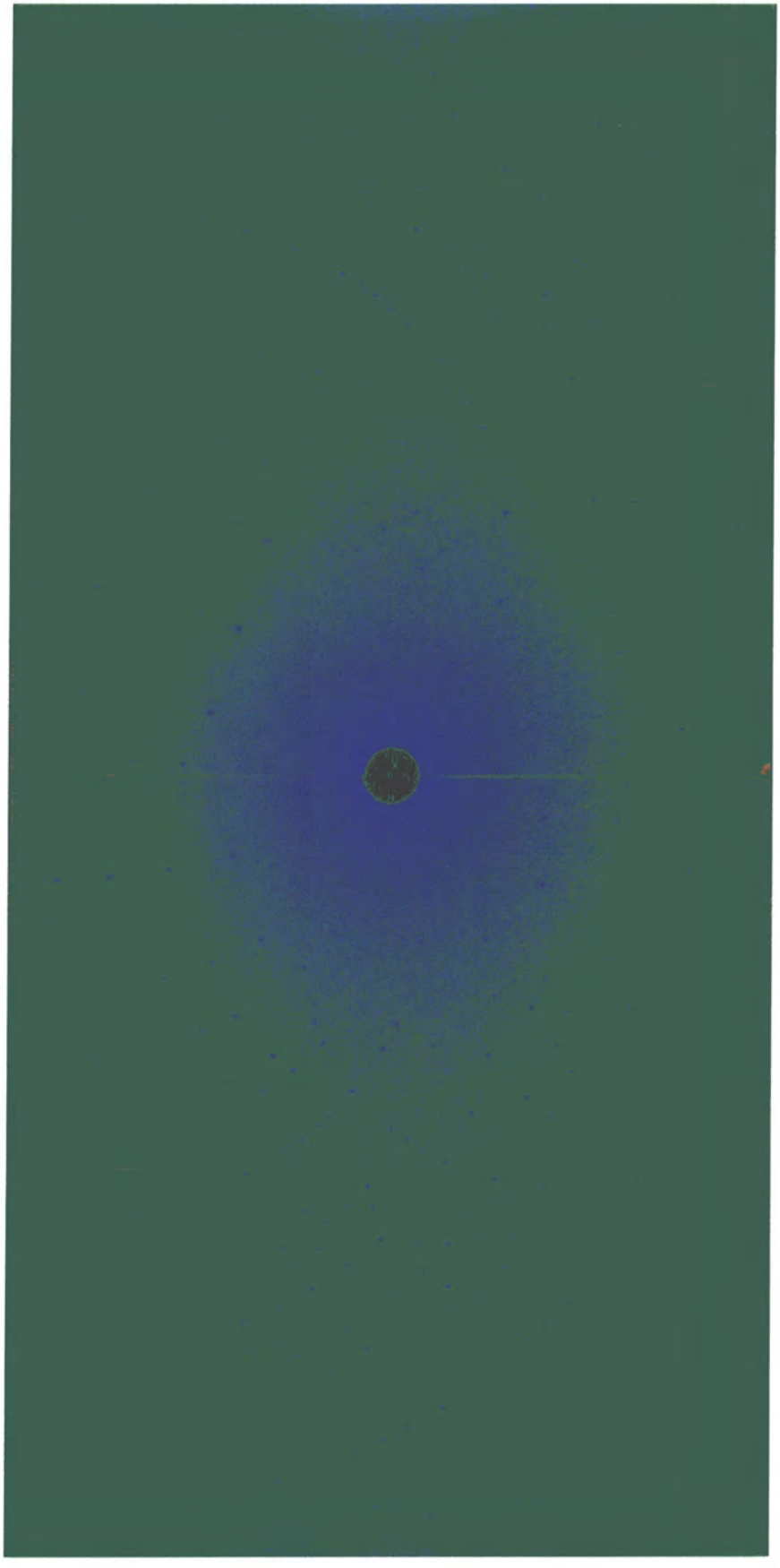

Figure 8.3.4 *- A frame of ZTS data collected on LADI at phi = 0.*

8.3.2 Data analysis

The resulting data must be indexed, reduced and normalized with respect to wavelength distribution.

The program, LAUEGEN (Campbell, 1995; Campbell, Hao, Harding, Nguti & Wilkinson, 1997) uses the diffraction pattern present in the image in conjunction with the known cell parameters to obtain a UB matrix for each orientation of the phi angle. This matrix is used to integrate the data corresponding to this phi orientation. The local reduction program, called 'integrate' follows the same theory as the previously described program, RACER (Wilkinson, Khamis, Stansfield, & McIntyre, 1988).

The reduced data is then normalized with respect to the wavelength distribution using the program, LAUENORM (Campbell, Habash, Helliwell & Moffat, 1986). Here, symmetry equivalents are used to obtain scale factors as a function of wavelength (Fox & Holmes, 1966). These refined scale factors are then fitted by a Chebechev polynomial which is used to represent the wavelength distribution.

Several 'R-factors' are produced in the output to the normalization which give one an indication of the level of quality of the resulting data. These values are calculated from the formula:

$$R = \sum (|I_l - I_{mean}|) / \sum (I_{mean})$$

where I_l is the Laue intensity,
and for R1, I_{mean} is the mean intensity of all measurements and for the reflection (and all symmetry equivalents).
and for R2, I_{mean} is the mean intensity of all measurements of the same sign.
and for R3, I_{mean} is the mean intensity of all measurement of the same sign for all reflections and with λ values with 0.1Å.

A list of reflection intensities is also output in order for a standard structural refinement to be performed. So far, no methods exist to correct the data for absorption or extinction effects.

8.3.3 The experimental procedure used for ZTS

The experimental procedure was very straightforward. A crystal (2.0 x 1.1 x 0.8 mm) of ZTS was glued on an aluminium pin, as used on D9. Given that the compound was orthorhombic, the crystal was mounted in such a way that more than one principal face was exposed along the phi-direction. The pin was screwed onto the sample holder which was then inserted into the instrument such that the crystal lay at the centre of the incident beam. The sample was cooled to 100K using an Oxford Cryosystems Cryostream (Cosier & Glazer, 1986) in order to match the temperature of the previous D9 experiment. Once the crystal was at 100K, the phi angle was set to 0° and the crystal was exposed to the neutron beam for two hours. Following which, the beam was switched off, the data was read and, once stored, it was erased from the image plates using the laser. Phi was then moved by 20° in preparation for the next exposure.

This procedure was repeated five times such that six exposures were taken in total at 20° intervals in the range 0°-100°. During the experiment, the crystal warmed up several times. The affected 'shots' were abandoned and repeated once the crystal had re-cooled to 100K. No problems resulted from this fluctuation in temperature.

The resulting data was analysed in accordance with the procedures described in the previous section. Whilst the full wavelength band was appoximately 0.9 - 2.8 Å (see ***Figure 8.3.5***), only data within the range 1.1-1.9Å was processed. This is because, outside this range, the number of reflections observed was small and if they were included in the processing, they would invoke a bad fit to the Chebechev polynomial on scaling. An R1, R2 and R3 of 0.095, 0.085 and 0.078 (based on 4190, 3684 and 1460 reflections respectively) was obtained on the final processing.

The resulting list of reflection intensities of ZTS were used in the subsequent full-matrix least-squares SHELXL-93 (Sheldrick, 1993) refinement. A summary of the crystal, data collection and refinement parameters is given in ***Table 8.3.1*** below:

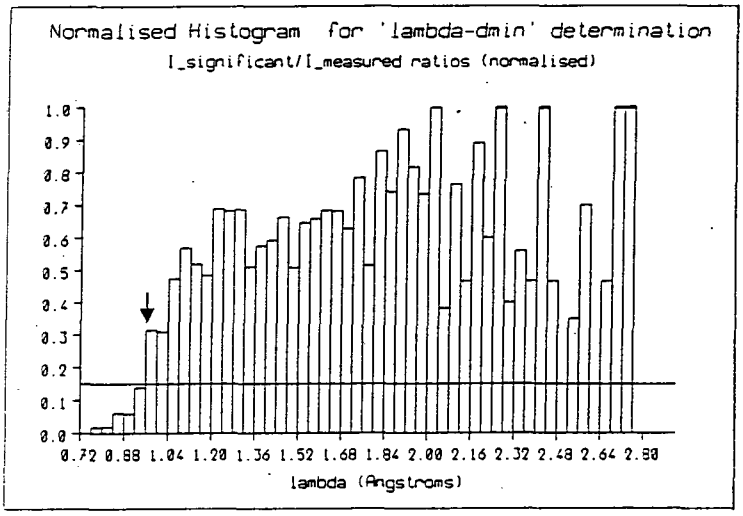

Figure 8.3.5 *- The wavelength distribution on LADI for ZTS at phi = 40°.*

Table 8.3.1 *- A summary of crystal, data collection and refinement parameters for the 100K neutron structure of ZTS as determined using LADI.*

Compound	ZTS	Compound	ZTS
Molecular Formula	$ZnC_3H_{12}N_6O_4S_4$	Absorption coefficient (mm^{-1})	0.1335
Formula weight	389.40	Crystal Morphology	rectangular
a(Å)	11.10#	Crystal Colour	transparent
b(Å)	7.75#	Crystal Size (mm)	2.0 x 1.1 x 0.8
c(Å)	15.56#	Total number of reflections	4190
α(°)	90	Unique reflections	1104
β(°)	90	Observed Reflections [I>2σ(I)]	1032
γ(°)	90	R_{int}	0.078
Cell Volume($Å^3$)	1329.7(2)	θ range	5.34 - 31.64
Crystal System	orthorhombic	Data / Parameters	1087 / 272
Space Group	Pca2(1)	R1 [I > 2σ(I)]	0.0447
Z	4	wR2 [I > 2σ(I)]	0.0952
Calculated Density (gcm^{-1})	1.945	Goodness of fit on F^2	1.228
Temperature (K)	100(2)	Weighting Scheme	a = 0.07
Wavelength (Å)	1.1-1.9	$\Delta\rho_{(max, min)}$ ($fmÅ^{-3}$)	0.748 / -0.855

These parameters were derived from the LADI (Wilkinson & Lehmann, 1991) data analysis but the D9 derived cell parameters were used in all refinement procedures since they are more accurate.

8.3.4 The structural results

A 50% probability thermal ellipsoid plot of the 100K structure of ZTS is shown in ***Figure 8.3.6***. Bond distances and bond angles are given in ***Tables 8.3.2*** and ***8.3.3***. Fractional coordinates and anisotropic displacement parameters are given in ***Appendix A.8.5*** and ***A.8.6*** respectively.

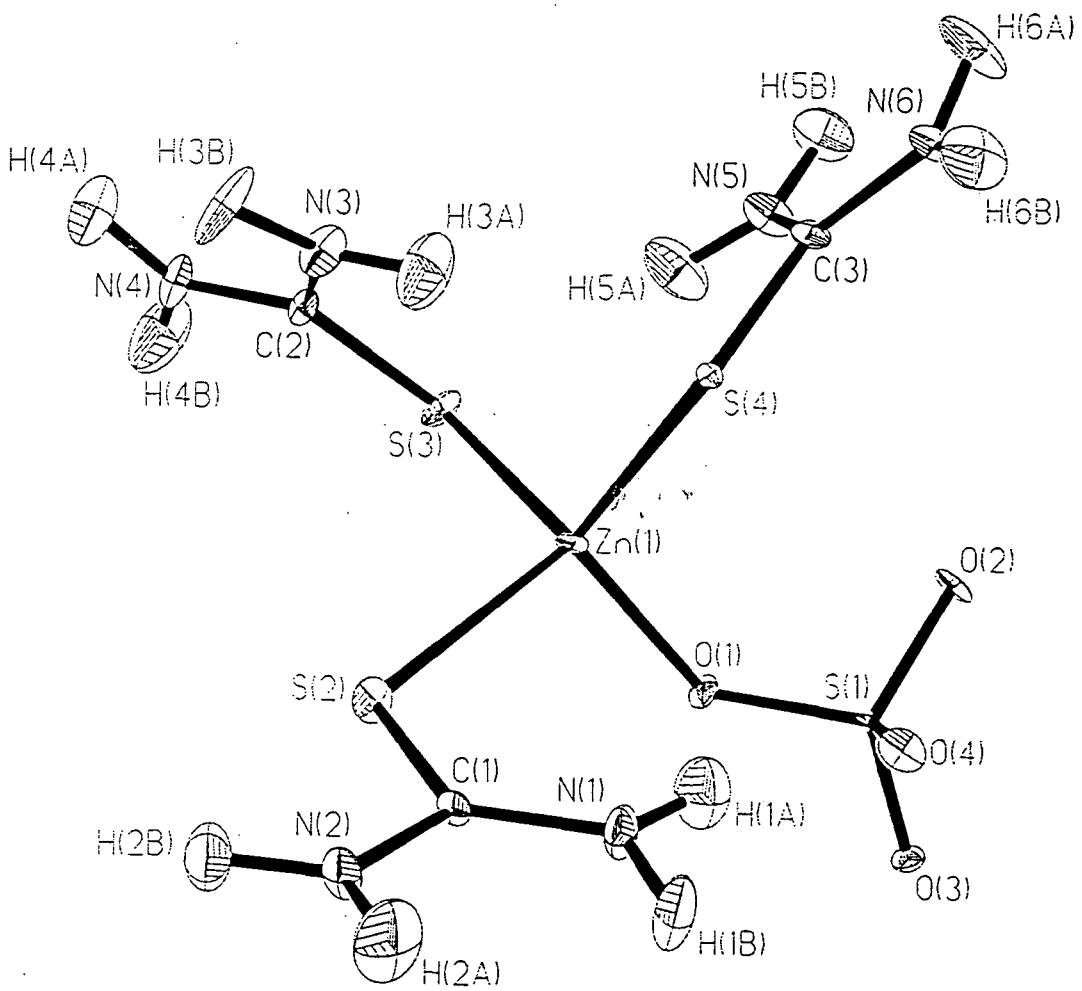

Figure 8.3.6 *- A 50% probability thermal ellipsoid plot of the 100K neutron structure of ZTS as determined on LADI.*

Table 8.3.2 *- Bond lengths for the 100K neutron structure of ZTS as determined using LADI.*

Bond	Distance (Å)	Bond	Distance (Å)
Zn(1)-S(2)	2.328(9)	N(2)-H(2A)	1.006(8)
Zn(1)-S(3)	2.328(9)	N(2)-H(2B)	1.03(1)
Zn(1)-S(4)	2.313(8)	N(3)-C(2)	1.316(4)
Zn(1)-O(1)	1.975(5)	N(3)-H(3A)	0.99(1)
S(1)-O(1)	1.520(9)	N(3)-H(3B)	1.034(7)
S(1)-O(2)	1.476(8)	N(4)-C(2)	1.326(4)
S(1)-O(3)	1.467(7)	N(4)-H(4A)	1.018(9)
S(1)-O(4)	1.466(7)	N(4)-H(4B)	1.007(9)
S(2)-C(1)	1.732(8)	N(5)-C(3)	1.324(4)
S(3)-C(2)	1.742(9)	N(5)-H(5A)	1.008(9)
S(4)-C(3)	1.744(8)	N(5)-H(5B)	1.030(8)
N(1)-C(1)	1.325(5)	N(6)-C(3)	1.323(5)
N(1)-H(1A)	1.007(9)	N(6)-H(6A)	1.010(8)
N(1)-H(1B)	1.019(9)	N(6)-H(6B)	1.003(8)
N(2)-C(1)	1.327(5)		

Table 8.3.3 - Bond angles for the 100K neutron structure of ZTS as determined using LADI.

Angle	Angle (°)	Angle	Angle (°)
S(2)-Zn(1)-S(3)	102.8(4)	C(2)-N(3)-H(3A)	120.4(5)
S(2)-Zn(1)-S(4)	110.7(3)	C(2)-N(3)-H(3B)	120.5(5)
S(2)-Zn(1)-O(1)	106.0(3)	H(3A)-N(3)-H(3B)	117.7(7)
S(3)-Zn(1)-S(4)	114.6(3)	C(2)-N(4)-H(4A)	119.5(5)
S(3)-Zn(1)-O(1)	108.1(3)	C(2)-N(4)-H(4B)	119.8(6)
S(4)-Zn(1)-O(1)	113.7(3)	H(4A)-N(4)-H(4B)	120.6(7)
O(1)-S(1)-O(2)	108.5(5)	C(3)-N(5)-H(5A)	119.6(5)
O(1)-S(1)-O(3)	106.6(5)	C(3)-N(5)-H(5B)	120.0(5)
O(1)-S(1)-O(4)	108.2(5)	H(5A)-N(5)-H(5B)	120.0(6)
O(2)-S(1)-O(3)	110.7(5)	C(3)-N(6)-H(6A)	119.3(6)
O(2)-S(1)-O(4)	111.1(5)	C(3)-N(6)-H(6B)	120.3(5)
O(3)-S(1)-O(4)	111.5(5)	H(6A)-N(6)-H(6B)	119.6(7)
Zn(1)-S(2)-C(1)	107.0(4)	S(2)-C(1)-N(1)	122.9(4)
Zn(1)-S(3)-C(2)	101.1(4)	S(2)-C(1)-N(2)	117.6(4)
Zn(1)-S(4)-C(3)	106.5(4)	S(3)-C(2)-N(3)	122.1(4)
Zn(1)-O(1)-S(1)	124.7(3)	S(3)-C(2)-N(4)	117.6(4)
C(1)-N(1)-H(1A)	123.6(5)	S(4)-C(3)-N(5)	122.7(4)
C(1)-N(1)-H(1B)	121.1(5)	S(4)-C(3)-N(6)	117.4(3)
H(1A)-N(1)-H(1B)	114.7(7)	N(1)-C(1)-N(2)	119.5(3)
C(1)-N(2)-H(2A)	120.0(6)	N(3)-C(2)-N(4)	120.2(3)
C(1)-N(2)-H(2B)	120.5(6)	N(5)-C(3)-N(6)	119.9(3)
H(2A)-N(2)-H(2B)	119.5(7)		

The bond geometry here compares very well with the D9 geometry and all distances and angles are easily the same within three esds. By comparing ***Figure 8.3.6*** with ***Figure 8.2.1***, we can also see that the thermal motion modelled using either D9 or LADI (Wilkinson & Lehmann, 1991) data is practically identical. The D9 derived geometry is noticeably more accurate than the LADI (Wilkinson & Lehmann, 1991) derived geometry but this was expected since we are comparing results from Laue data collected over only 12 hours to that obtained from data collected at a single wavelength and over 135 hours (5 and 3/5 days) on a crystal 12 times the volume. Indeed, the aim of this study was not to try and compete against D9 but was to compare the results and use the D9 data in order to assess the validity of the measurements obtained using LADI (Wilkinson & Lehmann, 1991). Moreover, we wished to ascertain whether or not the LADI (Wilkinson & Lehmann, 1991) data was accurate enough for the required analysis. If so, then LADI

(Wilkinson & Lehmann, 1991) could potentially act as a much faster substitute for measurements, presently performed on D9, where the very high degree of accuracy is not critical for a successful result to be obtained.

With this in mind, all non-bonded contacts, as derived from the LADI (Wilkinson & Lehmann, 1991) geometry, were calculated in order to see whether or not hydrogen-bonding studies were feasible using LADI. All non-bonded contacts are given in ***Table 8.3.4***.

Table 8.3.4 *- A summary of all non-bonded contacts present in ZTS as determined using LADI data.*

Intramolecular non-bonded contacts in ZTS		Intermolecular non-bonded contacts in ZTS	
Contact	Distance (Å)	Contact	Distance (Å)
S(2)...N(1)	2.692(9)	S(3)...S(4)[a]	3.26(1)
S(2)...N(2)	2.624(8)	S(1)...H(3B)-N(3)[b]	2.68(1)
S(3)...N(3)	2.685(9)	S(1)...H(6B)-N(6)[c]	2.66(1)
S(3)...N(4)	2.634(9)	S(2)...H(2A)-N(2)[d]	2.60(1)
S(4)...N(5)	2.700(8)	O(1)...H(1B)-N(1)[e]	1.87(1)
S(4)...N(6)	2.630(8)	O(2)...H(3B)-N(3)[f]	1.86(1)
S(2)...H(1A)-N(1)*	2.89(1)	O(2)...H(6B)-N(6)[g]	2.05(1)
S(2)...H(2B)-N(2)*	2.73(1)	O(3)...H(2B)-N(2)[h]	1.95(1)
S(3)...H(3A)-N(3)*	2.81(1)	O(3)...H(5B)-N(5)[i]	1.81(1)
S(3)...H(4B)-N(4)*	2.73(1)	O(4)...H(4A)-N(4)[j]	1.94(1)
S(3)...H(5A)-N(5)	2.49(1)	O(4)...H(6A)-N(6)[k]	2.15(1)
S(4)...H(3A)-N(3)	2.55(1)		
S(4)...H(5A)-N(5)*	2.83(1)		
S(4)...H(6B)-N(6)*	2.72(1)		
O(4)...H(1A)-N(1)	1.99(1)		

symmetry codes: a = 1/2+x,1-y,z; b = 2-x,1-y,z-1/2; c = 1/2+x,1-y,z; d = 1/2+x,2-y,z; e = 1/2+x,2-y,z; f = 2-x,1-y,z-1/2; g = x-1/2,1-y,z; h = 2-x,2-y,z-1/2; i = x,1+y,z; j = 2-x,1-y,1/2+z; k = x,y-1,z.

Although all hydrogen-bond distances reported here can only be stated up to and including two decimal places, the relative strengths of these contacts are still obvious. Hence, the use of these values would provide the same structural discussions and conclusions to those given using the D9 data. We can therefore confirm that such

* Although these are non-bonded contacts, they cannot be considered as hydrogen-bonds since the S...H-N angles (69°-75°) are less than 90°.

hydrogen-bonding studies are eminently feasible using LADI (Wilkinson & Lehmann, 1991).

8.4 CONCLUSIONS

The neutron studies of ZTS and d-ZTS show that deuteration causes essentially no difference in the structural features of the compound. The molecules are seen to pack very closely together with extensive hydrogen-bonding dictating the exact nature of the packing arrangement. Indeed, the hydrogen-bonding is so extensive that all but one hydrogen / deuterium atom is involved in at least one such non-bonded contact. Moreover, several of the hydrogen-bonds are very strong. As a result, the amount of thermal motion of all atoms in the molecule is very small. S...S interactions are also observed in the crystal lattice. Such close packing and hydrogen-bonding is thought to be the cause of the high SHG output observed.

The comparative study of the structures of ZTS, as determined using D9 and the development instrument LADI, shows promising results. The LADI data does not give as accurate results as the D9 data. However, the results obtained from LADI are accurate enough to describe the hydrogen-bonding patterns present in ZTS and the relative strengths of these interactions, with the same conclusions being drawn as for the D9 results. Therefore, we believe that LADI data is adequate for hydrogen-bonding studies. Other studies should determine the instrument's suitability in other research areas.

8.5 REFERENCES

Andretti, G. D., Cavalca, L. & Musatti, A. (1968). Acta Crystallogr., **B24**, 683-690.

Archer, J. M. & Lehmann, M. S. (1986). J. Appl. Cryst., **19**, 456-458.

Bondi, A. (1964). *J. Phys. Chem.*, **64**, 441-451.

Campbell, J. W. (1995). *'LAUEGEN an X-windows based Program for the Processing of Laue X-ray Diffraction Data'*, J. Appl. Cryst., **28**, 228-236.

Campbell, J. W., Habash, J., Helliwell, J. R. & Moffat, K. (1986). *'Determination of the wavelength normalisation curve in the Laue method'*, Quarterly for Protein Crystallography, **18**.

Campbell, J. W., Hao, Q., Harding, M. M., Nguti, N. D. & Wilkinson, C. (1997). J. Appl. Cryst., (in preparation).

Cipriani, F., Castagna, J.-C., Lehmann, M. S. & Wilkinson, C. (1995). Physica B, **213 & 214**, 975-977.

Cipriani, F., Castagna, J.-C., Wilkinson, C., Oleinek, P. & Lehmann, M. S. (1996). J. Neutron Research, **4**, 79-85.

Cipriani, F., Dauvergne, F., Gabriel, A., Wilkinson, C. & Lehmann, M. S. (1994). Biophysical Chemistry, **53**, 5-14.

Coppens, P. (1970). DATAP. *The Evaluation of Absorption and Extinction in Single-Crystal Structure Analysis* in "Crystallographic Computing", Ed. Ahmed, F. R., (Munksgaard, Copenhagen).

Cosier, J. & Glazer, A. M. (1986). J. Appl. Cryst., **19**, 105.

Fox, G . C. & Holmes, K. C. (1966). Acta Crystallogr., **20**, 886-891.

Kerkoc, P., Venkataramanan, V., Lochran, S., Bailey, R. T., Cruickshank, F. R., Pugh, D., Sherwood, J. N., Moseley, R., Goeta, A. E., Lehmann, C. W., Howard, J. A. K. (1996). J. Appl. Phys., **80**, 6666-6669.

Marcy, H. O., Warren, L. F., Webb, M. S., Ebbers, C. A., Velsko, S. P., Kennedy, G. C. & Catella, G. C. (1992). App. Opt., **31**, 5051-5060.

Ramabadran, U. B., McPherson, A. L., Zelmon, D. E. (1994). J. Appl. Phys., **76**, 1150-1154.

Ramabadran, U. B., Zelmon, D. E. & Kennedy, G. C. (1992). Appl. Phys. Lett., **60**, 2589-2591.

Sheldrick, G. M. (1993). SHELXL-93. *Program for the Refinement of Crystal Structures using Single Crystal Diffraction Data*, University of Göttingen, Germany.

Tao, M., Jiang, M., Xu, D. & Shao, Z. (1988). Kexue Tongbao (foreign lang. ed.), **33**, 651-654.

Venkataramanan, V., Srinivasan, M. R. & Bhat, H. L. (1994). J. Raman Spect., **25**, 805-811.

Wang, W. S., Sutter, K., Bosshard, Ch., Pan, Z., Arend, H., Gunter, P., Chapuis, G. & Nicolo, F. (1988). Jpn. J. Appl. Phys., **27**, 1138-1141.

Wilkinson, C., Khamis, H. W., Stansfield, R. F. D. & McIntyre, G. J. (1988). J. Appl. Cryst., **21**, 471-478.

Wilkinson, C. & Lehmann, M. S. (1991). Nucl. Instr. and Meth., **A310**,411-415.

Xing, G., Jiang, M., Shao, Z. & Xu, D. (1987). Chin. Phys. Lasers, **14**, 357-364.

Zhang, N., Jiang, M., Yuan, D., Xu, D. & Tao, X. (1989). Chin. Phys. Lett., **6**, 283-290.

PART (II)

STRUCTURAL STUDIES OF IMIDO, (BIS)IMIDO AND ARYLOXIDE GROUP VA AND VIA TRANSITION METAL COMPLEXES.

CHAPTER 9

STRUCTURAL STUDIES OF HALF-SANDWICH IMIDO, (BIS)IMIDO AND ARYLOXIDE GROUP VA TRANSITION METAL COMPLEXES.

9.1. INTRODUCTION

High-oxidation transition-metal complexes have found widespread application as reagents in organic synthesis (Negishi, 1991; Buchwald & Nielsen, 1988; Schwartz & Labinger, 1976; Takahashi et al, 1991; Tidwell, Senn & Buchwald, 1991) and as polymerisation catalysts (Coles, Dalby, Gibson, Clegg & Elsegood, 1995; Schoettel, Kress & Osborn, 1989; Jordan, 1991; Kaminsky, 1994; Tilley, 1993). Such compounds containing a transition-metal of a low d^n configuration have shown particular promise since, in these complexes, the metal environment is electron deficient. As a result, there has been much interest in Group IVA complexes (Coles, Dalby, Gibson, Clegg & Elsegood, 1995; Jordan, 1991; Kaminsky, 1994; Tilley, 1993; Brintzinger, Fisher, Mülhaupt, Rieger & Waymouth, 1995) and especially in bent metallocene complexes (Jordan, Bajgur, Willet & Scott, 1986; Hlatky, Turner & Eckman, 1989; Ewen & Elder, 1993; Chien, Tsai & Rausch, 1991; Yang, Stern & Marks, 1991 and 1994; Buchwald, Watson & Huffman, 1986; Buchwald, Watson, Wannamaker & Dewan, 1989).

Work in Durham has concentrated on Group VA complexes which are isolobal to Group IVA bent metallocene complexes. Each cyclopentadienyl (Cp) ligand is isolobal with a ligand of general formula, RN^{2-} and RO^{-} (***Figure 9.1.1***). Moreover, imido and oxo ligands have been found to stabilize high-oxidation transition-metal complexes due to the ligand's ability to participate in extensive ligand-to-metal π donation (Nugent & Mayer, 1988). Hence, a series of half-sandwich imido, (bis)imido and aryloxide Group VA complexes were synthesized and characterized and their reactivity was investigated in order to compare and contrast their chemical behaviour with their isolobal Group IVA counterparts (Williams et al, 1992; Chan, 1995; Chan, Cole, Gibson & Howard, 1997a, 1997b, 1997c and 1997d; Chan et al., 1997). Bulky R groups were chosen throughout since they reduce the tendency for imido / oxo bridging (Gibson & Kee, 1989).

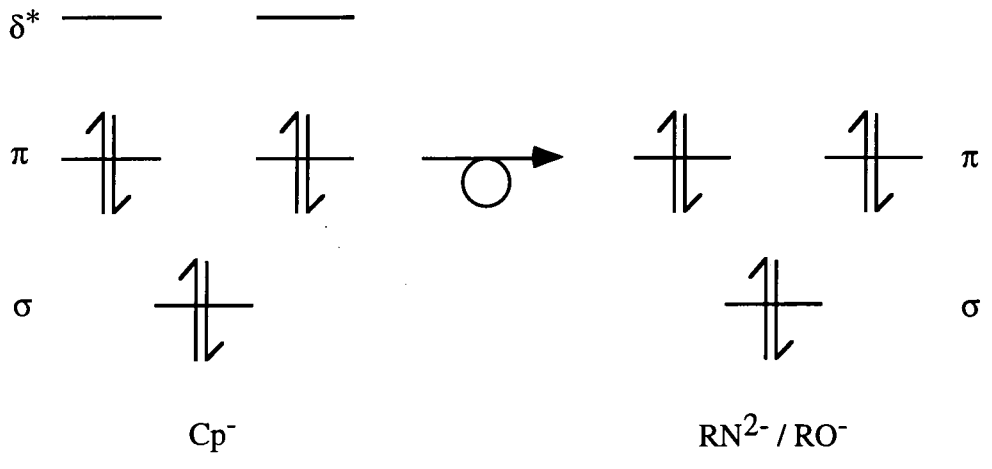

Figure 9.1.1 *- The isolobal relationship between Cp^- and RN^{2-} / RO^- ligands.*

In this chapter, the structural studies of ten half-sandwich imido, (bis)imido and aryloxide Group VA transition-metal complexes are reported, one of which was determined by Dr. Christian W. Lehmann but it is included for comparative purposes. Various novel structural features are highlighted and discussions on the isolobal relationship and the complexes' potential as catalysts and reagents in organic synthesis are given.

9.2 NOVEL μ-METHYL COMPLEXES OF VANADIUM AND THE RELEVANCE TO BIMOLECULAR DEACTIVATION OF HOMOGENEOUS IMIDOVANADIUM POLYMERISATION CATALYSTS

9.2.1 Abstract

Attempted dimethylation of [CpV(N-2,6-$^{i}Pr_2C_6H_3$)]Cl_2 (**1**) using Grignard reagents affords novel μ-methyl complexes arising by reductive dimerization; the structure of one of these products, [CpV(N-2,6-$^{i}Pr_2C_6H_3$)(μ-Me)$_2$)]$_2$(μ-Mg) (**2**), reveals V-(μ-Me)-Mg, V-Mg, N-Mg and C-H...Mg interactions.

9.2.2 Introduction

There is presently much interest in the development of new generation 'non-metallocene' catalysts for the polymerization of α-olefins. These include, for example, alkoxide (van den Linden, Schaverien, Meijboom, Ganter & Orpen, 1995), thiolate (Miyatake, Mizunuma & Kajugo, 1993), amide (Scollard, McConville & Rettig, 1997; Mack & Eisen, 1996), imide (Coles & Gibson, 1994; Coles, Dalby, Gibson, Clegg & Elsegood, 1995), tetradentate Schiff base (Tjaden, Swenson & Jordan, 1995) and macrocyclic procatalysts (Brand, Capriotti & Arnold, 1994; Uhrammer, Black, Gardner, Olsen & Jordan, 1993). Recent work on the isolobal relationship between Group IVA metallocenes and Group VA half-sandwich imido species at Durham (Williams et al, 1992; Cockcroft et al, 1992; Siemeling & Gibson, 1992; Dyer, Gibson, Howard, Whittle & Wilson, 1992) has shown that vanadium complexes of the type CpV(NR)Cl_2 are particularly active amongst these Group VA metal pro-catalysts (Coles & Gibson, 1994). Typically, they give high initial polymerization activities but die over the course of a few minutes, a kinetic profile that is not uncommon in many homogeneous Ziegler-type polymerization systems. In order to gain more insight into the deactivation process and to be able to control this behaviour, we set out to synthesise and characterise well-defined cationic alkyl versions of these catalysts. Methyl derivatives were targeted since such species have proved to be suitable precursors in metallocene systems (Jordan, Bajgur, Willet & Scott, 1986; Hlatky, Turner & Eckman, 1989; Ewen & Elder, 1993; Chien, Tsai & Rausch, 1991; Yang, Stern & Marks, 1991 and 1994). Here, we describe two highly unusual products arising from reactions of **1** with methylmagnesium halides under differing conditions of solvent and Grignard reagent. The products are structurally exceptional and provide insight into the bimolecular deactivation process occurring in [CpV(NR)] polymerization systems.

9.2.3 Experimental

The crystal structure determinations of **2** and **3** were carried out using the Siemens P4 diffractometer and the Siemens SMART-CCD diffractometer respectively. Both crystals were mounted using the oil-drop method (Stalke & Kottke, 1994) and graphite monochromatized Mo-Kα radiation (λ=0.71073Å) was employed. Data collections were carried out at 150K and no decay was observed during any of the experiments. For compound **2**, cell refinement, data collection and data reduction proceeded via Siemens XSCANS (Siemens Analytical X-ray Instruments, 1994) whereas Siemens SMART software (Siemens Analytical X-ray Instruments, 1995a and 1995b) was used for **3**.

Both structures were solved using SHELXS-86 (Sheldrick, 1990) by Patterson [structure (**2**)], direct [structure (**3**)] and difference Fourier methods. Subsequent least-squares refinement used the SHELXL-93 (Sheldrick, 1993) package. Scattering factors were taken from International Tables for Crystallography, Vol. C, 1992.

All non-hydrogen positional parameters were refined as were anisotropic displacement parameters for all non-hydrogen atoms in **3** and for vanadium in **2**. The bridging hydrogen positions in **2** were found in the difference map but not refined. Isotropic displacement parameters of all other hydrogen atoms were modelled in the riding model [$U_{iso}(H) = 1.2\ U_{eq}(C)$]. The solvent hexane was located in the lattice of **3**. Its carbon atoms were modelled in the same manner to all other non-hydrogen atoms. However, it was not possible to model the hydrogen atoms of the solvent at all.

A summary of crystal, data collection and refinement parameters for the structural determinations of **2** and **3** is given in ***Table 9.2.1***. Fractional coordinates of structures (**2**) and (**3**) are given in ***Appendix A.9.1*** and ***A.9.2*** respectively. Anisotropic displacement parameters for structure (**3**) are given in ***Appendix A.9.3***.

Table 9.2.1 *- Crystallographic data for compounds 2 and 3.*

Compound	**2**	**3**
Molecular Formula	$Mg_{0.5}VC_{19}H_{28}N$	$V_2C_{35}H_{47}N_2.1/2C_6H_{12}$
Formula weight	333.52	597.63
a(Å)	10.220(2)	9.924(2)
b(Å)	9.909(2)	21.653(4)
c(Å)	18.658(3)	16.235(3)
α(°)	90	90
β(°)	104.94(1)	98.73(3)
γ(°)	90	90
Cell Volume(Å^3)	1825.6(6)	3448(1)
Crystal System	monoclinic	monoclinic
Space Group	$P2_1/c$	$P2_1/n$
Z	4	4
Calculated Density (gcm^{-1})	1.213	1.151
Temperature (K)	150(2)	150(2)
Wavelength (Å)	0.71073	0.71073
Absorption coefficient (mm^{-1})	0.556	0.565
Crystal Morphology	irregular plate	diamond
Crystal Colour	orange-red	deep red
Crystal Size (mm)	0.40 x 0.36 x 0.15	0.80 x 0.62 x 0.40
Total number of reflections	3272	12933
Unique reflections	2184	4865
Observed Reflections [I>2σ(I)]	818	4560
R_{int}	0.1006	0.0353
θ range (°)	2.06-22.48	1.58-23.25
Data / Parameters	2179 / 91	4857 / 364
R1 [I > 2σ(I)]	0.0602	0.0531
wR2 [I > 2σ(I)]	0.0912	0.1476
Goodness of fit on F^2	0.729	1.208
Weighting Scheme	a = 0.0003	a = 0.0650; b = 5.1588
$\Delta\rho_{(max, min)}$ (eÅ^{-3})	0.415 / -0.269	1.081 / -0.342

9.2.4 Results and discussion

The synthesis of the starting complex (**1**) has been described previously by Teuben and co-workers (Buijink, Meetsma, Teuben, Kooijman & Spek, 1995). The paramagnetic magnesium-containing di-vanadium complex (**2**) was isolated from the reaction of (**1**) with excess MeMgBr in diethyl ether. The molecular structure is shown in ***Figure 9.2.1*** and selected bond distances and angles are given in ***Table 9.2.2***.

Table 9.2.2 - *Selected bond lengths and angles for compound (2).*

Bond	Distance (Å)	Angle	Angle (°)
V(1)-N(1)	1.724(6)	N(1)-V(1)-C(18)	100.5(3)
V(1)-C(18)	2.200(7)	N(1)-V(1)-C(19)	101.3(3)
V(1)-C(19)	2.227(7)	C(18)-V(1)-C(19)	91.0(3)
V(1)-Mg	2.594(1)	N(1)-V(1)-Mg	62.7(2)
Mg-N(1)	2.366(6)	C(18)-V(1)-Mg	59.6(2)
Mg-C(18)	2.408(7)	C(19)-V(1)-Mg	58.6(2)
Mg-C(19)	2.382(7)	C(1)-N(1)-V(1)	160.6(5)
		V(1)-C(18)-Mg	68.4(2)
		V(1)-C(19)-Mg	68.4(2)

(**2**) crystallizes as a dimer in the centrosymmetric space group $P2_1/c$, with the magnesium atom located at the centre of inversion. The structure consists of two methyl groups bridging between the vanadium atom of the [CpV(NAr)] fragment and the magnesium core. The V-Mg distance of 2.594(1)Å is very similar to other proposed metal-Mg bonds (Ni-Mg bond of 2.615Å, see Kaschube, Pörschke, Angermund, Krüger & Wiile, 1988; Co-Mg bonds of 2.565Å and 2.480Å, see Jonas, Koepe & Krüger, 1986; Mo-Mg bonds of 2.853Å and 2.737Å, see Green et al, 1974) and therefore may be viewed as a direct V-Mg interaction. The N-Mg distance of 2.366(6)Å is within the range for a genuine bonding interaction (Viebrock & Weiss, 1994) although the V-N distance of 1.724(6)Å [1.60-1.68Å in terminal imides (Nugent & Mayer, 1988), 1.84-1.85Å in bridging imides (Scollard, McConville & Rettig, 1997; Jordan, Bajgur, Willet & Scott, 1986; Solan, Cozzi, Floriani, Chiesi-Villa & Rizzoli, 1994)] and the V-N-C_{ipso} angle of 160.6(5)° suggests that the interaction is weak and that the imido unit behaves more as a terminal ligand to the vanadium centre than a bridging group between V and Mg. The carbon atoms of the bridging methyl groups are located slightly closer to the vanadium [V-C_{methyl}: 2.200(7) and 2.227(7)Å, Mg-C_{methyl}: 2.382(7) and 2.408(7)Å] and the V-C_{methyl} distances are longer than those reported for vanadium complexes with terminal alkyl groups [2.04-2.08Å] (Scollard, McConville & Rettig, 1997; Coles & Gibson, 1994; Jordan, Bajgur, Willet & Scott, 1986; Noh, Sendlinger, Janiak & Theopold,

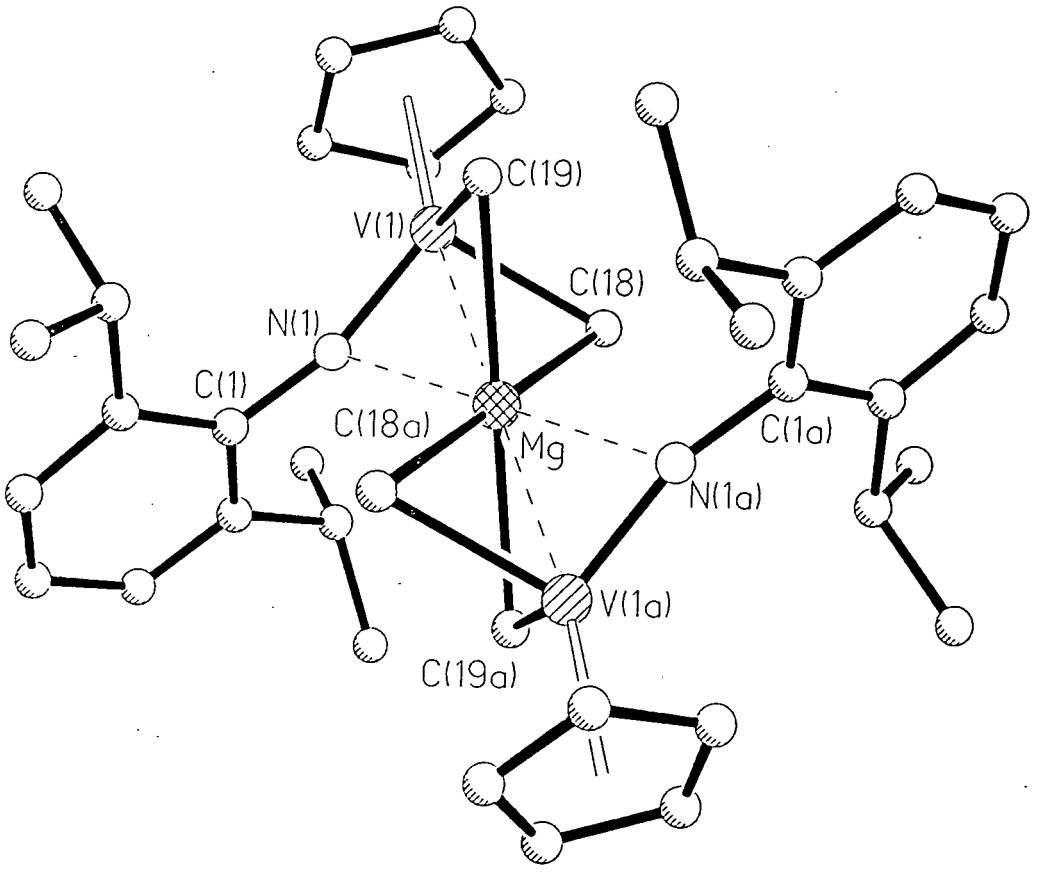

Figure 9.2.1 - The molecular structure of compound 2.

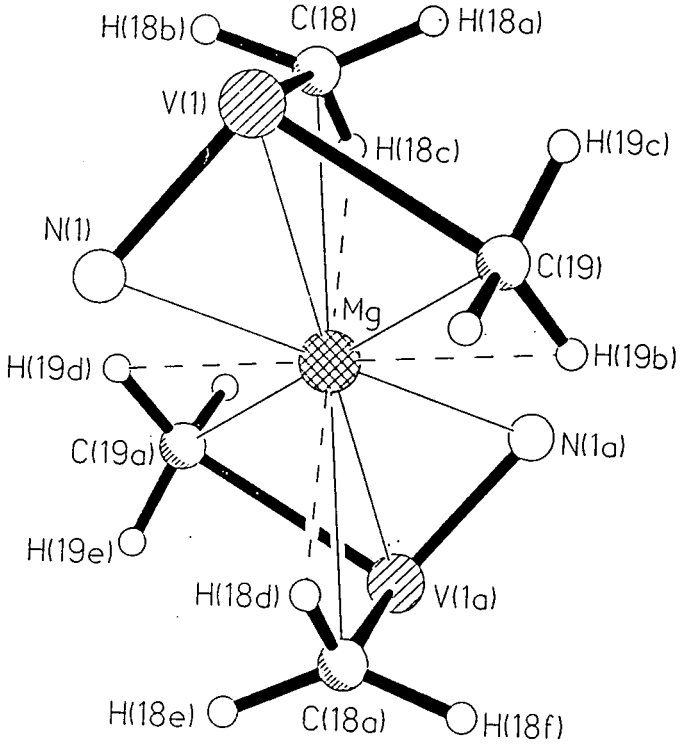

Figure 9.2.2 - A plot of 2 which shows the presence of C-H...Mg agostic interactions.

1989). The two V-C_{methyl}-Mg angles are identical [68.4(2)°] and are typical for methyl groups bridging two metals (Kaschube, Pörschke, Angermund, Kruger & Wilke, 1988; Noh, Sendlinger, Janiak & Theopold, 1989; Noh, Heintz, Sendlinger, Janiak & Theopold, 1990). The two highly distorted V-C-H angles [55° and 77°] and the particularly short Mg-H separations [2.04Å and 2.35Å] for H(18c) and H(19b) respectively, ‡ indicate the presence of C-H...Mg agostic interactions (***Figure 9.2.2***). The presence of the magnesium core with its attendant weak ligand interactions [bonding distances in the range 2.366-2.594Å] appears to lend significant stability to this unusual product.

By contrast, in the presence of diethyl ether and tetrahydrofuran, (**1**) reacts with excess MeMgCl to afford the paramagnetic mono μ-methyl complex (**3**) (***Figure 9.2.3***).

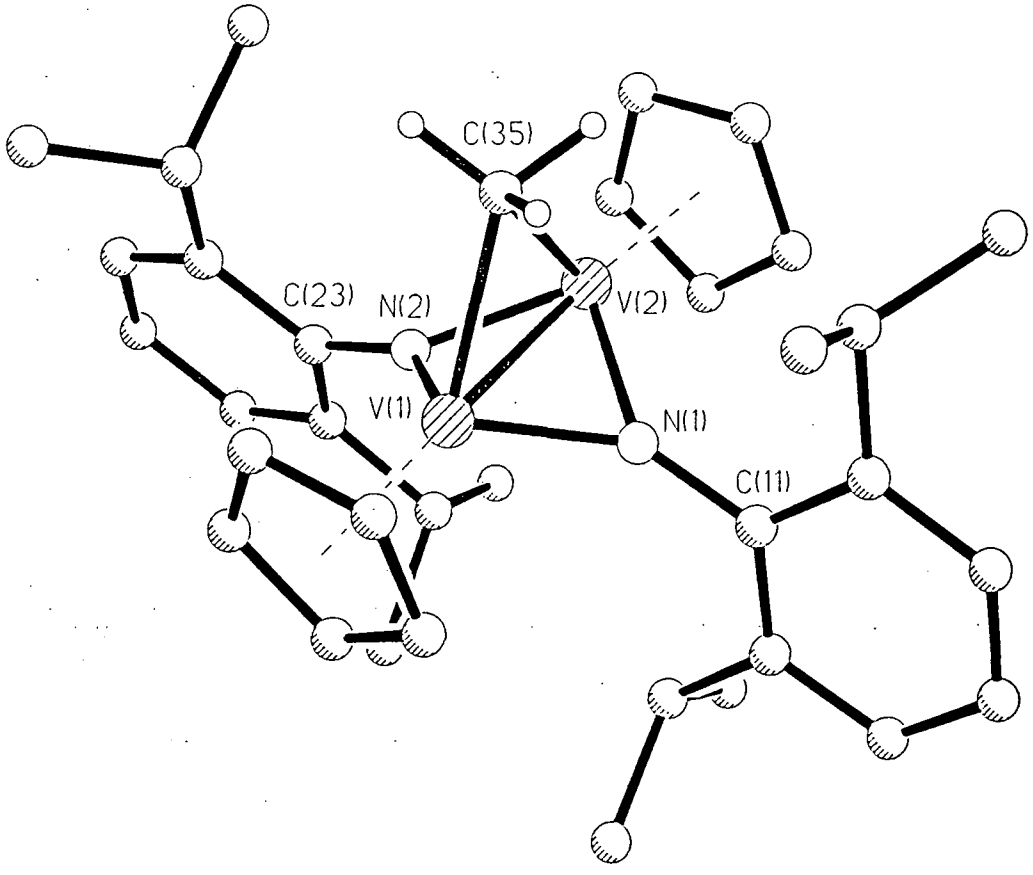

Figure 9.2.3 - The molecular structure of 3.

Table 9.2.3 - Selected bond lengths and angles for compound (3).

Bond	Distance (Å)	Angle	Angle (°)
V(1)-N(1)	1.867(3)	V(1)-N(1)-C(11)	143.8(2)
V(1)-N(2)	1.882(3)	V(2)-N(1)-C(11)	139.9(2)
V(1)-C(35)	2.215(4)	V(1)-N(1)-V(2)	76.3(1)
V(1)-V(2)	2.324(1)	V(1)-N(2)-C(23)	142.4(2)
V(2)-N(1)	1.896(3)	V(2)-N(2)-C(23)	141.6(2)
V(2)-N(2)	1.894(3)	V(1)-N(1)-V(2)	76.3(1)
V(2)-C(35)	2.310(4)	V(1)-N(2)-V(2)	76.0(1)
		V(1)-C(35)-V(2)	61.8(1)

The crystal structure of (**3**) consists of a single methyl and two arylimido groups bridging two [CpV] units. The distances V(1)-C(35) [2.310(4)Å], V(2)-C(35) [2.215(4)Å] and the V(1)-C(35)-V(2) angle [61.8(1)°] are comparable with (**2**). In this case, however, there are no close interactions of the bridging methyl C-H bonds with the adjacent metal centres. The V-N distances [av. 1.885(4)Å] are longer than for (**2**) due to the decreased bond order resulting from the fact that the imido substituents are bridging. The V(1)-V(2) distance of 2.324(1)Å is within the range for a bonding interaction (Cotton & Millar, 1977; Vahrenkamp, 1978) and the Cp(centroid) vectors are almost coaxial with the V-V bond. Finally, the bridging methyl and imides are arranged around the V-V axis such that C(35), N(1) and N(2) are approximately 120° to each other. We note that Teuben and co-workers have reported a related tolylimido complex, [CpV(μ-N*p*-tolyl)Me]$_2$, which contains bridging imido ligands and terminal methyl groups (Buijink, Teuben, Kooijman & Spek, 1994; Buijink, Meetsma, Teuben, Kooijman & Speck, 1995).

Since dialkylation of a dihalide precursor is the prevalent route to a well defined cationic alkyl catalyst species, these observations provide an explanation for the rapid deactivation of [CpV(NR)] procatalysts and are likely to be of general relevance to other rapidly deactivating catalyst systems.

9.3 DICHLORO (η^5-CYCLOPENTADIENYL) (PHENYLIMIDO) VANADIUM(V)

9.3.1 Abstract

The crystal structure of $CpV(NC_6H_5)Cl_2$ (**4**) is reported herein. It contains vanadium in a tetrahedral coordination geometry, with the cyclopentadienyl ligand occupying one of the four sites and showing an allyl-ene distortion. The V-N-C angle is 169.1(4)°. The crystal packing is mediated by C-H...Cl interactions, with H...Cl distances in the range 2.87(5) - 2.89(4)Å.

9.3.2 Introduction

The chemistry of the half-sandwich vanadium imido system has recently been investigated due to the isolobal relationship between the [CpV(NR)] and [Cp_2Ti] fragments (Buijink, Teuben, Kooijman & Spek, 1994; Chan, 1995). As part of this work, the subject complex, **4**, was prepared by the imido ligand exchange reaction between $CpV(N^tBu)Cl_2$ (Becker, Häusler & Preuss, 1987) and aniline, and the X-ray crystal structure was determined.

9.2.3 Experimental

The structure of **4** was determined using the Rigaku AFC6S diffractometer. The crystal was mounted using the oil-drop method (Stalke & Kottke, 1994) and graphite monochromatized Mo-Kα radiation (λ=0.71073Å) was employed. Data collection was carried out at 150K via ω scans with profile analysis (Lehmann & Larsen, 1974). Cell refinement and data collection used MSC/AFC *Diffractometer Control Software* (Molecular Structure Corporation, 1991). TEXSAN (Molecular Structure Corporation, 1989) was used to reduce the data. A semi-empirical absorption correction using φ-scans (North, Phillips & Mathews, 1968) was applied.

The structure was solved using SHELXS-86 (Sheldrick, 1990) by direct methods. Subsequent least-squares refinement used the SHELXL-93 (Sheldrick, 1993) package. Scattering factors were taken from International Tables for Crystallography, Vol. C, 1992.

All positional and anisotropic thermal parameters for non-H atoms were refined. All H isotropic displacement parameters were constrained to the riding model, $U_{iso}(H) = 1.2U_{eq}(C)$.

A summary of the crystal, data collection and refinement parameters for the structure of **4** is given in ***Table 9.3.1***.

Table 9.3.1 - *Crystallographic data for compound **4**.*

Compound	**4**	Compound	**4**
Molecular Formula	$VC_{11}H_{10}NCl_2$	Absorption coefficient (mm^{-1})	1.251
Formula weight	278.04	Crystal Morphology	block
a(Å)	13.641(3)	Crystal Colour	very dark purple
b(Å)	7.034(1)	Crystal Size (mm)	0.30x0.25x0.08
c(Å)	12.403(2)	Total number of reflections	2821
α(°)	90	Unique reflections	2098
β(°)	94.66(3)	Observed Reflections [I>2σ(I)]	1244
γ(°)	90	R_{int}	0.0487
Cell Volume($Å^3$)	1186.1(4)	θ range (°)	3-25
Crystal System	monoclinic	Data / Parameters	2098 / 166
Space Group	$P2_1/c$	R1 [I > 2σ(I)]	0.0545
Z	4	wR2 [I > 2σ(I)]	0.0795
Calculated Density (gcm^{-1})	1.557	Goodness of fit on F^2	0.994
Temperature (K)	150(2)	Weighting Scheme	a = 0.0278; b = 0.0179
Wavelength (Å)	0.71073	$\Delta\rho_{(max, min)}$ ($eÅ^{-3}$)	0.405 / -0.351

9.3.4 Results and discussion

The molecular structure of **4** is given in ***Figure 9.3.1***. Selected bond distances and angles are given in ***Table 9.3.2***. Fractional coordinates and anisotropic displacement parameters are given in ***Appendix A.9.4***and ***A.9.5*** respectively.

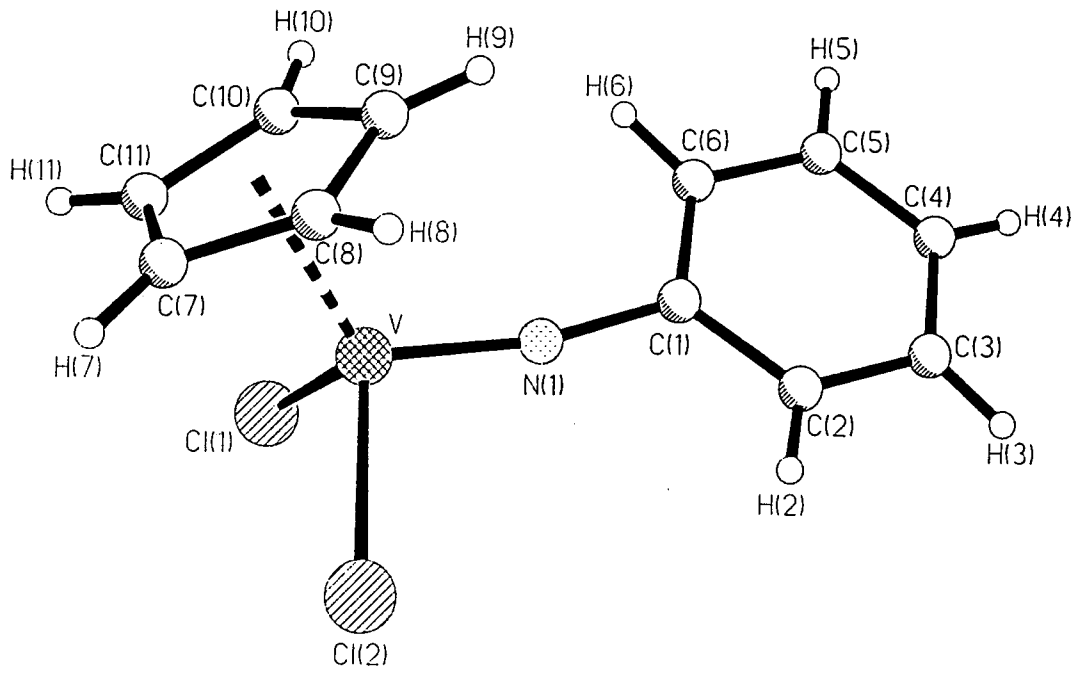

Figure 9.3.1 *- The molecular structure of* ***4****.*

Table 9.3.2 *- Selected bond lengths and angles for compound* ***4****.*

Bond	Distance (Å)	Angle	Angle (°)
V-N(1)	1.653(4)	N(1)-V-Cl(1)	99.7(1)
V-C(9)	2.236(6)	Cl(1)-V-Cl(2)	103.65(6)
V-C(10)	2.246(6)	C(1)-N(1)-V	169.1(4)
V-Cl(1)	2.258(2)	Cl(1)-V-$Cp_{centroid}$	114.1(8)
V-Cl(2)	2.259(2)	Cl(2)-V-$Cp_{centroid}$	113.5(8)
V-C(8)	2.263(6)	N(1)-V-$Cp_{centroid}$	121.2(7)
V-C(7)	2.351(5)		
V-C(11)	2.354(5)		
V-$Cp_{centroid}$	1.968(6)		
Cl(1)-H(8)	2.88(6)		
Cl(2)-H(6)	2.89(4)		
Cl(2)-H(10)	2.87(5)		

The V-N(1) distance of 1.653(4)Å and the small deviation from linearity of the V-N(1)-C(1) angle [169.1(4)°] are typical for vanadium-(terminal imido) complexes (Nugent & Mayer, 1988) which exhibit multiple pπ-dπ interactions between the nitrogen and vanadium atoms. The geometry around the metal centre is approximately tetrahedral due to the bulky nature of the Cp ring. An allyl-ene distortion of this ring is evident (***Table 9.3.2***) with the metal displaced towards C(9) which eclipses the V-N bond. The distance from the centroid of the ring to the vanadium atom is 1.968(6)Å.

The nature of the molecular packing was investigated. ***Figure 9.3.2*** illustrates the anti-parallel herringbone packing arrangement of the molecule with respect to its Cp rings. An alternate double layer appearance of the [$CpVCl_2$] moieties and the twisted stacked phenyl groups is also visible.

The Cl(1)...H(8) [A], Cl(2)...H(6) [B] and Cl(2)...H(10) [C] intermolecular distances [2.88(6)Å, 2.89(4)Å and 2.87(5)Å respectively] are less than the sum of the corresponding van der Waals radii [2.95Å] (Bondi, 1964); these secondary interactions presumably have a significant effect upon the observed packing arrangement.

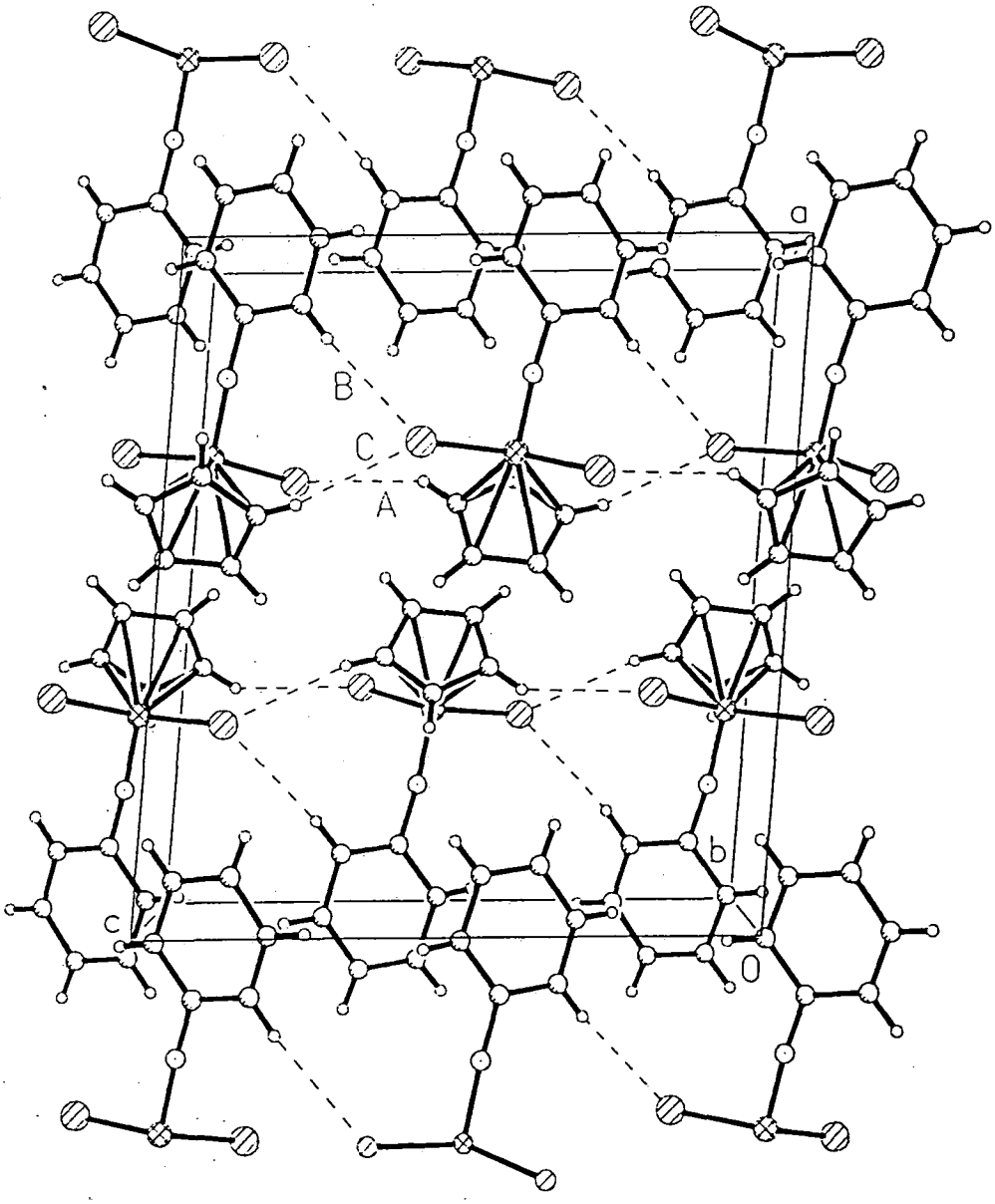

Figure 9.3.2 *- The molecular packing arrangement of* ***4****.*

9.4 A NEW PRECURSOR FOR SYNTHESISING HALF-SANDWICH IMIDO COMPLEXES OF NIOBIUM BEARING ALKYNE LIGANDS - RELATIVES OF THE ZIRCONOCENE FAMILY

9.4.1 Abstract

The crystal structure of the reaction precursor, $(C_5H_5)Nb(N\text{-}2\text{-}t\text{-}BuC_6H_4)Cl_2$ (**5**) for synthesis of a half-sandwich imido alkyne complex, $(C_5H_5)Nb(N\text{-}2\text{-}Bu^tC_6H_4)(\eta^2\text{-}PhC{\equiv}CPh)(PMe_3)$ (**6**) is described. A comparison of **5** with its di-isopropyl analogue and with **6** is made.

9.4.2 Introduction

Zirconocene complexes find widespread application as reagents in organic synthesis (Negishi, 1991; Buchwald & Nielsen, 1988; Negishi & Takahashi, 1994; Broene & Buchwald, 1993), ranging from hydrozirconation (Schwartz & Labinger, 1976) and carbomagnesiation (Takahashi et al, 1991; Knight, Wang, Waymouth & Ziller, 1994) through to C-C coupling reactions involving alkenes (Takahashi et al, 1991; Buchwald, Watson & Huffman, 1986 and 1987; Nugent & Taber, 1989; Kondakov & Negishi, 1996), alkynes (Warner, Davis & Buchwald, 1994; Negishi, Kondakov, Choueiry, Kasai & Takahashi, 1996), benzynes (Tidwell, Senn & Buchwald, 1991; Tidwell & Buchwald, 1992 and 1994) and imines (Buchwald, Watson, Wannamaker & Dewan, 1989; Coles, Whitby & Blagg, 1990; Coles, Harris, Whitby & Blagg, 1994), and as catalysts for the polymerization of, for example, alkenes (Jordan, 1991; Kaminsky, 1994; Brintzinger, Fisher, Mülhaupt, Rieger & Waymouth, 1995; Kaminsky et al, 1988), α,ω-dienes (Resconi & Waymouth, 1990; Coates & Waymouth, 1991) and silanes (Tilley, 1993; Bourg, Corriu, Enders & Moreau, 1995).

Several half-sandwich niobium imido complexes containing benzyne and benzylidene ligands have been studied in Durham (Chan et al, 1997), complexes that find direct analogues in zirconocene chemistry. These studies have provided a useful insight into the viability and extent of the 'isolobal' analogy between [CpM(NR)] (M = Group VA metal) and $[Cp_2M]$ (M = Group IVA metal) fragments. Such studies have helped to delineate some of the more subtle steric and electronic factors contributing to the stability of these metallocene-like molecules. Investigations have concentrated on derivatives containing either C_5H_5 or C_5Me_5 ligands in combination with arylimido ligands, combinations that were envisaged to allow sufficient flexibility for groups of differing steric requirements to be accommodated at the half-sandwich metal imido centres. Aspects of this work have been communicated (Cockcroft et al, 1992; Siemeling & Gibson, 1992).

The work reported here concentrates on the nature of the dichloride precursor for the synthesis of half-sandwich niobium imido complexes containing *alkyne* ligands. The crystal structure of the preferred reaction precursor is described and compared to the precursor used for the synthesis of the benzyl and benzylidene analogues (Williams et al, 1992). A comparison between **5** and the product complex **6** is also made.

9.4.3 Experimental

The air sensitive sample of **5** was mounted on a glass fibre using a perfluoropolyether oil (Stalke and Kottkle, 1993). Crystal data were collected at 150K, using a four-circle Rigaku AFC6S diffractometer. Graphite monochromated Mo Kα radiation (λ = 0.71073Å) was employed. Three standard reflections measured every 150 reflections during the data collection showed no variation in intensity. Cell parameters were determined from 20 reflections located using a systematic zig-zag search through reciprocal space and data were reduced using TEXSAN (Molecular Structure Corporation, 1989). A semi-empirical absorption correction using φ-scans was applied in XPREP (Sheldrick, 1995) [Tmin / Tmax = 0.850 / 1.000].

The structure was solved by Patterson methods using the SHELXS-86 program (Sheldrick, 1990). A semi-empirical absorption correction using φ-scans was applied in XPREP (Sheldrick, 1995) [Tmin / Tmax = 0.850 / 1.000]. Subsequent least-squares refinement used the SHELXL-93 (Sheldrick, 1993) package. Atomic scattering factors were taken from International Tables for Crystallography Volume C (1992).

Positional and anisotropic atomic dispacement parameters were refined for all non-hydrogen atoms. Hydrogen atoms were placed geometrically and positional paramenters were refined using a riding model (including free rotation about C-C bonds for methyl groups). Isotropic atomic displacement parameters were constrained to be 1.2 (1.5 for methyl groups) times $U_{eq}(C)$.

A summary of crystal, data collection and refinement parameters is given in ***Table 9.4.1***.

Table 9.4.1 - Crystallographic data for compound 5.

Compound	5	Compound	5
Molecular Formula	$NbC_{15}H_{18}NCl_2$	Absorption coefficient (mm^{-1})	1.090
Formula weight	376.11	Crystal Morphology	Block
a(Å)	11.897(2)	Crystal Colour	Red
b(Å)	9.400(2)	Crystal Size (mm)	0.75 x 0.55 x 0.40
c(Å)	14.081(3)	Total number of reflections	1975
α(°)	90	Unique reflections	1471
β(°)	90	Observed Reflections [I>2σ(I)]	1471
γ(°)	90	R_{int}	0.0166
Cell Volume($Å^3$)	1574.7(5)	θ range (°)	2.61 - 25.0
Crystal System	orthorhombic	Data / Parameters	1471 /133
Space Group	Pnma	R1 [I > 2σ(I)]	0.0223
Z	4	wR2 [I > 2σ(I)]	0.0615
Calculated Density (gcm^{-1})	1.586	Goodness of fit on F^2	1.299
Temperature (K)	150(2)	Weighting Scheme	a = 0.0127; b = 3.4491
Wavelength (Å)	0.71073	$\Delta\rho_{(max, min)}$ ($eÅ^{-3}$)	0.307 / -0.341

9.4.4 Results and discussion

Alkyne derivatives of niobium have been synthesised from a niobium dichloride via a Nb(III) bis(trimethylphosphine) intermediate, according to the equations given below.

$$CpNb(NAr)Cl_2 \xrightarrow[2PMe3]{Mg} CpNb(NAr)(PMe_3)_2$$

$$CpNb(NAr)(PMe_3)_2 \xrightarrow[-PMe_3]{R^1C{\equiv}CR^2} CpNb(NAr)(R^1C{\equiv}CR^2)(PMe_3)$$

where Ar = 2,6-$Pr^i_2C_6H_3$ or 2-$Bu^tC_6H_4$

We have found previously that the C_5H_5 / N-2,6-$Pr^i_2C_6H_3$ ligand combination affords a bis(phosphine) complex that is exceedingly sensitive, whereas the C_5H_5 / 2-

tertbutylphenylimido derivatives are quite robust. The N-2-Bu^{t}C$_6$H$_4$ system was, therefore, preferred for these studies and in order to gain further insight into the factors influencing the stability of these closely related arylimido derivatives, the structure of the dichloride precursor (**5**) was investigated.

A view of the crystal structure of **5** is shown in ***Figure 9.4.1*** and selected bond distances and angles are given in ***Table 9.4.2***. Fractional coordinates and anisotropic displacement parameters are given in ***Appendix A.9.6*** and ***A.9.7*** respectively.

Table 9.4.2 *- Selected bond lengths and angles for compound* ***5****.*

Bond	Distance (Å)	Angle	Angle (°)
Nb-N(1)	1.782(3)	N(1)-Nb-Cl	101.76(7)
Nb-Cl	2.3455(8)	Cl-Nb-Cl#1	104.58(4)
Nb-C(12)	2.379(3)	Ccentroid-Nb-N(1)	119.7(3)
Nb-C(11)	2.464(3)	Ccentroid-Nb-Cl	113.6(8)
Nb-C(10)	2.523(4)	C(1)-N(1)-Nb	165.1(3)
Nb-Ccentroid	2.128(5)	N(1)-C(1)-C(2)	117.3(4)
N(1)-C(1)	1.394(5)	N(1)-C(1)-C(6)	122.9(4)
C(1)-C(2)	1.397(6)	C(1)-C(6)-C(7)	122.6(4)
C(1)-C(6)	1.423(6)		
C(2)-C(3)	1.375(6)		
C(3)-C(4)	1.374(7)		
C(4)-C(5)	1.385(7)		
C(5)-C(6)	1.397(6)		
C(6)-C(7)	1.531(6)		
C(7)-C(9)	1.540(4)		
C(7)-C(8)	1.541(6)		
C(10)-C(11)	1.404(4)		
C(11)-C(12)	1.409(5)		

Symmetry transformation used to generate equivalent atom: #1 x,-y+1/2,z

The key difference between **5** and the di-isopropyl analogue (Williams et al, 1992) lies in the orientation of the aryl ring which aligns in the plane that bisects the Cl-Nb-Cl angle, thus allowing the t-butyl group to be directed away from the Cp ring and to be accommodated in the plane bisecting the Cl-Nb-Cl angle. By contrast, the 2,6-disubstituted aryl rings of (C$_5$H$_5$)Nb(N-2,6-Pr$^i_2$C$_6$H$_3$)Cl$_2$ are oriented perpendicular to this alignment, in order to avoid unfavourable steric interactions between the Cp ring and one of the ortho substituents.

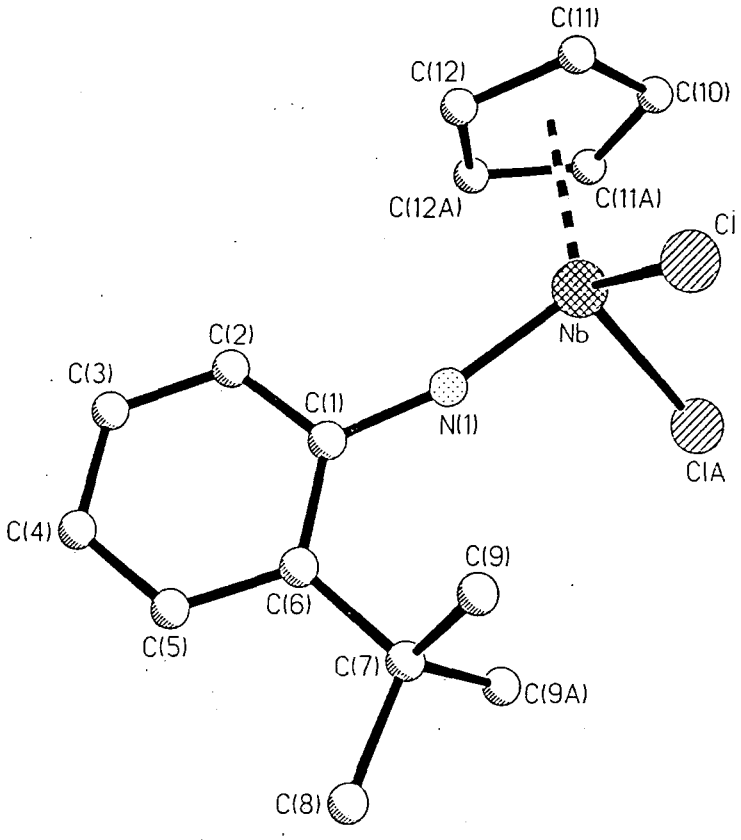

Figure 9.4.1 - The molecular structure of 5.

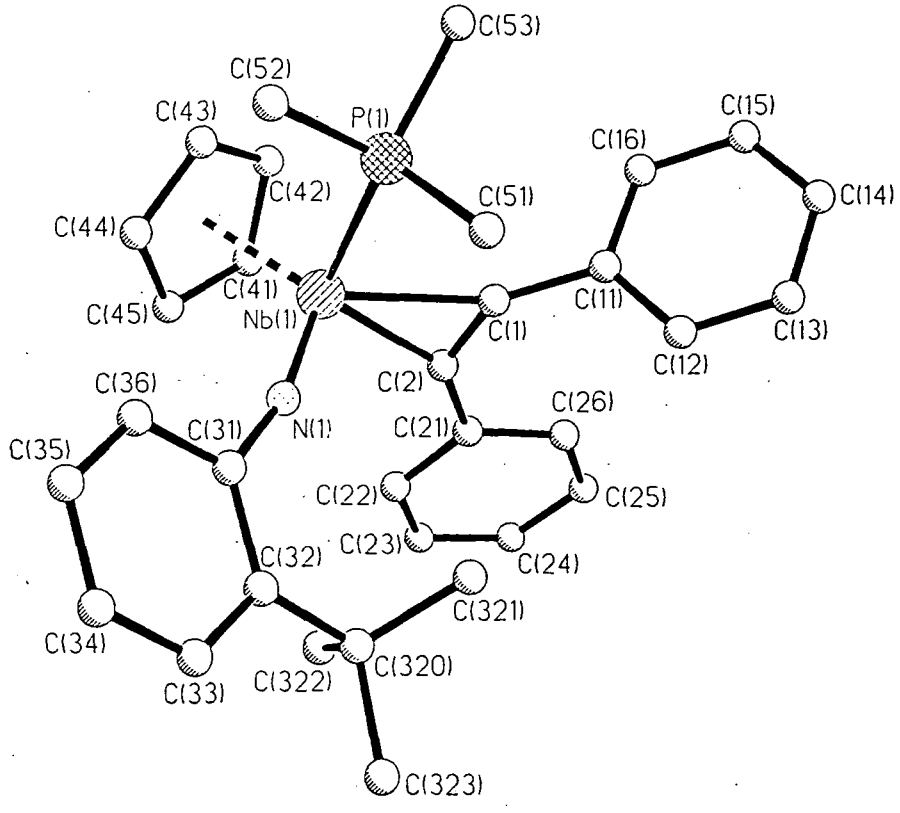

Figure 9.4.2 - The molecular structure of 6.

The crystal structure of the product complex (**6**) resulting from the use of **5** as a precursor is given in ***Figure 9.4.2***. This structure was determined by Dr. Christian Lehmann at Durham but since it is not yet published, selected geometrical parameters are given here (***Table 9.4.3***) for comparative purposes.

Table 9.4.3 *- Selected bond lengths and angles for compound* ***6****.*

Bond	Distance (Å)	Angle	Angle (°)
Nb(1)-N(1)	1.813(3)	N(1)-Nb(1)-C(2)	105.90(12)
Nb(1)-C(2)	2.144(3)	N(1)-Nb(1)-C(1)	109.52(12)
Nb(1)-C(1)	2.200(3)	C(2)-Nb(1)-C(1)	35.05(12)
Nb(1)-P(1)	2.5462(12)	N(1)-Nb(1)-P(1)	88.46(10)
P(1)-Ccentroid	2.154(6)	C(2)-Nb(1)-P(1)	116.11(9)
N(1)-C(31)	1.392(4)	C(1)-Nb(1)-P(1)	81.18(9)
C(1)-C(2)	1.309(5)	Ccentroid-Nb(1)-P(1)	111.5(1)
C(1)-C(11)	1.457(5)	Ccentroid-Nb(1)-N(1)	121.5(2)
C(2)-C(21)	1.469(5)	Ccentroid-Nb(1)-C(1)	127.1(2)
		Ccentroid-Nb(1)-C(2)	111.8(2)
		C(31)-N(1)-Nb(1)	166.3(2)
		C(2)-C(1)-C(11)	137.7(3)
		C(2)-C(1)-Nb(1)	70.1(2)
		C(11)-C(1)-Nb(1)	152.2(2)
		C(1)-C(2)-C(21)	136.0(3)
		C(1)-C(2)-Nb(1)	74.8(2)
		C(21)-C(2)-Nb(1)	149.0(2)
		C(31)-C(32)-C(320)	121.9(3)

The angle at the imido nitrogen [165.1(3)°] is approximately the same as that found in **5** [166.3(2)°], the bending being imposed by the bulky t-butyl substituent. The Nb-N bond distance in **6** is substantially longer than for **5** [1.813(3)Å c.f. 1.782(3)Å] reflecting the lower formal oxidation state of the metal in the alkyne complex. The phenyl ring of the imido substituent is twisted by 51(1)° relative to its position in **5** such that the t-butyl substituent is accommodated in a pocket beneath the alkyne group.The phosphorus atom of the PMe_3 ligand in **6** lies close to the Nb-C(1)-C(2) plane (displacement 0.021Å) consistent once again with the metallocene-like characteristics of the [CpNb(NAr)] fragment. The alkyne C-C bond length in **6** is identical within experimental error to the distance found in the 'isolobal' molybdenum complex, $Mo(NBu^t)(PMe_3)(PhC{\equiv}CPh)$ (Dyer, Gibson, Howard, Whittle & Wilson, 1995), while the Nb-P and Nb-C distances

lie intermediate between those determined for the zirconocene (Takahashi, Swanson & Negishi, 1987) and bis(imido)molybdenum (Poole et al, 1993) analogues.

9.4.5 Conclusions

The use of the described dichloride precursor (**5**) for the synthesis of the half-sandwich niobium imido alkyne complex (**6**) lends support to the isolobal relationship between zirconocene and half-sandwich niobium imido complexes. The use of the bulky t-butyl reaction precursor instead of the di-isopropyl analogue has necessary steric consequences. An investigation of the relative reactivities of these complexes is of future interest.

9.5 EFFECTS OF THE [OC_6F_5] MOIETY UPON STRUCTURAL GEOMETRY: CRYSTAL STRUCTURES OF HALF-SANDWICH TANTALUM(V) ARYLOXIDE COMPLEXES FROM REACTION OF CP*TA(N^TBU)($CH_2R)_2$ WITH PENTAFLUOROPHENOL

9.5.1 Abstract:

Reaction of Cp*Ta(N^tBu)Cl_2 with two molar equivalents of RCH_2MgCl in Et_2O yields Cp*Ta(N^tBu)($CH_2R)_2$ (R=Ph (**7**), CMe_2Ph(**8**), CMe_3(**9**)). Multiple agostic interactions in **9** are indicated by ^1H and ^{13}C NMR data and confirmed by X-ray crystallography. Upon treatment with pentafluorophenol, **7** affords the tantalum(V) dimer [Cp*Ta(CH_2Ph)(OC_6F_5)(μ-O)]$_2$ (**10**) whereas the reaction with **8** yields the related complex [Cp*Ta($OC_6F_5)_2$(μ-O)]$_2$ (**12**) plus monomeric Cp*Ta($OC_6F_5)_4$ (**11**); no reaction is observed with **9**. The crystal structures of **10**, **11** and **12** are determined. The aryloxide and oxo Ta-O distances are comparatively long and the largest of these exceeds any previously reported value. Complex **11** possesses two strong intermolecular interactions: a C-H···O hydrogen bond and more unusually, an F···F contact. Despite the similarities between **10** and **12**, their respective structural geometries exhibit remarkable differences which are ascribed to the influence of the perfluorinated phenyl ring.

9.5.2 Introduction

The attention given to organometallic alkoxide and aryloxide complexes has continued unabated (Chisholm, 1992; Chisholm & Rothwell, 1995) since they have shown the ability to mediate olefin metathesis polymerization processes (Schrock, 1990). Reports on organometallic tantalum compounds bearing oxygen donor ligands have focused on the relationship between structural aspects and reactivity (Lapointe, Wolczanski & Mitchell, 1986; Lubben & Wolczanski, 1985; Lapointe & Wolczanski, 1985; Ballard, Gardner & Wigley, 1989; Bruck, Copenhaver & Wigley, 1987; Rothwell, 1988; Steffey, Fanwick & Rothwell, 1990). Our interest in this class of compounds derives from the diverse chemistry in organometallic imido complexes of Group VA metals that has been observed through previous work at Durham (Williams et al, 1991; Poole, Gibson & Clegg, 1992; Siemeling & Gibson, 1992; Cockcroft et al, 1992; Gibson & Poole, 1995). Herein we describe the crystal structures of Cp*Ta(N^tBu)($CH_2CMe_3)_2$ and the products of the reaction of the dialkyl derivatives Cp*Ta(N^tBu)($CH_2R)_2$ (R=Ph, CMe_2Ph, CMe_3) with pentafluorophenol. The structural results demonstrate the electronic and steric effects of the pentafluorophenoxide ligand in different molecular environments.

9.5.3 Experimental

Crystal structure determinations of **9**, **10** and **11** were carried out using the Siemens P4 diffractometer whilst the structure of **12** was determined using the Siemens SMART-CCD diffractometer. All crystals were mounted using the oil-drop method (Stalke & Kottke, 1994) and graphite monochromatized Mo-Kα radiation (λ=0.71073Å) was used throughout. Data collections were carried out at 150K and no decay was observed during any of the experiments. For **9**, **10** and **11**, cell refinement, data collection and data reduction proceeded via Siemens XSCANS (Siemens Analytical X-ray Instruments, 1994) whereas Siemens SMART software (Siemens Analytical X-ray Instruments, 1995a and 1995b) was used for **12**. All structures were solved using SHELXS-86 (Sheldrick, 1990) by Patterson and difference Fourier methods. An absorption correction was applied to each data set: semi-empirical corrections using φ-scans were applied in XPREP (Sheldrick, 1995) for compounds **9**, **10** and **11** [Tmin / Tmax = 0.267 / 0.365; 0.261 / 1.000; 0.674 / 0.770 respectively] whilst DIFABS (Walker & Stuart, 1983) was used to correct the data for **12** [Tmin / Tmax = 0.343 / 0.447]. Subsequent least-squares refinement used the SHELXL-93 (Sheldrick, 1993) package. Scattering factors were taken from International Tables for Crystallography, Vol. C, 1992. All non-hydrogen positional parameters were refined as were the hydrogen positions of **9** and **11**. Anisotropic displacement parameters were refined for all non-hydrogen atoms except for the carbon atoms [C(14) - C(18A)] of the Cp* ring (**10**) and [C(30) - C(35A)] of the Cp* ring (**6**). Isotropic displacement parameters of all hydrogen atoms were modelled in the riding model [$U_{iso}(H) = 1.2\ U_{eq}(C)$]. A summary of crystal, data collection and refinement parameters for the structural determinations of **9**, **10**, **11** and **12** is given in ***Table 9.5.1***.

Table 9.5.1 *- Crystallographic data for compounds* ***9, 10, 11*** *and* ***12****.*

Complex	**9**	**10**	**11**	**12**
Chemical formula	$C_{19}H_{31}NTa$	$C_{46}H_{44}O_4F_{10}Ta_2$	$C_{34}H_{15}O_4F_{20}Ta$	$C_{44}H_{30}O_4F_{20}Ta_2$ .C_7H_8
Formula weight	529.57	606.36	1048.41	1488.71
Crystal system	monoclinic	triclinic	orthorhombic	monoclinic
a (Å)	9.083(2)	9.239(2)	8.341(2)	12.793(2)
b (Å)	16.216(3)	11.647(2)	26.389(5)	15.242(2)
c (Å)	16.872(3)	11.803(2)	15.145(3)	25.708(3)
α (°)	90	117.25(3)	90	90
β (°)	99.76(3)	96.37(3)	90	100.178(5)
γ (°)	90	106.63(3)	90	90
Volume ($Å^3$)	2449.1(8)	1037.3(3)	3334(1)	4934(1)
Space group	$P2_1/c$	P-1	Pbcm	$P2_1/n$
Z	4	2	4	4
D_c (gcm^{-3})	1.436	1.941	2.089	2.004
F(000)	1080	588	2016	2872
Crystal colour	yellow	yellow	yellow	yellow
Crystal morphology	cuboid	hexagonal	needle	irregular
Crystal dimensions (mm)	0.26 x 0.24 x 0.20	0.80 x 0.64 x 0.44	0.46 x 0.12 x 0.08	0.80 x 0.45 x 0.30
μ(mm^{-1})	4.495	5.360	3.451	4.559
θ range of data collection (°)	2.28-35	2.05-25.00	2.05-25.00	1.56-23.26
No of data measured	13104	3942	3749	17825
Unique data / parmeters	10777 / 373	3310 / 221	3043 / 306	6926 / 619
Observed data [I>2σ(I)]	7822	2985	2150	6101
R_{merg}	0.03	0.1448	0.0542	0.0533
R	0.0378	0.0727	0.0448	0.0764
wR	0.0554	0.1824	0.0879	0.0976
Goodness of fit	1.032	1.022	1.023	2.326
Δρ(max/min) ($eÅ^{-3}$)	1.107 / -0.762	5.300 / -3.767	0.861 / -1.065	1.414 / -0.956

9.5.4 Results and Discussion

Treatment of [Cp*Ta(N^{t}Bu)Cl_2] with two equivalents of the appropriate Grignard reagent RCH_2MgCl in diethyl ether readily affords the dialkyl complexes [Cp*Ta(N^{t}Bu)$(CH_2R)_2$] (R = Ph (**7**), CMe_2Ph (**8**), CMe_3 (**9**)). The low $^1J_{CH}$ coupling constant (106Hz) of the metal-bound methylene groups in **9** is indicative of the presence of weak α-agostic interactions (Poole et al, 1993) and this is supported by an X-ray structural determination (***Figure 9.5.1***). Selected bond distances and angles for **9** are given in ***Table 9.5.2***. Fractional coordinates and anisotropic displacement parameters are given in ***Appendix A.9.8*** and ***A.9.9*** respectively.

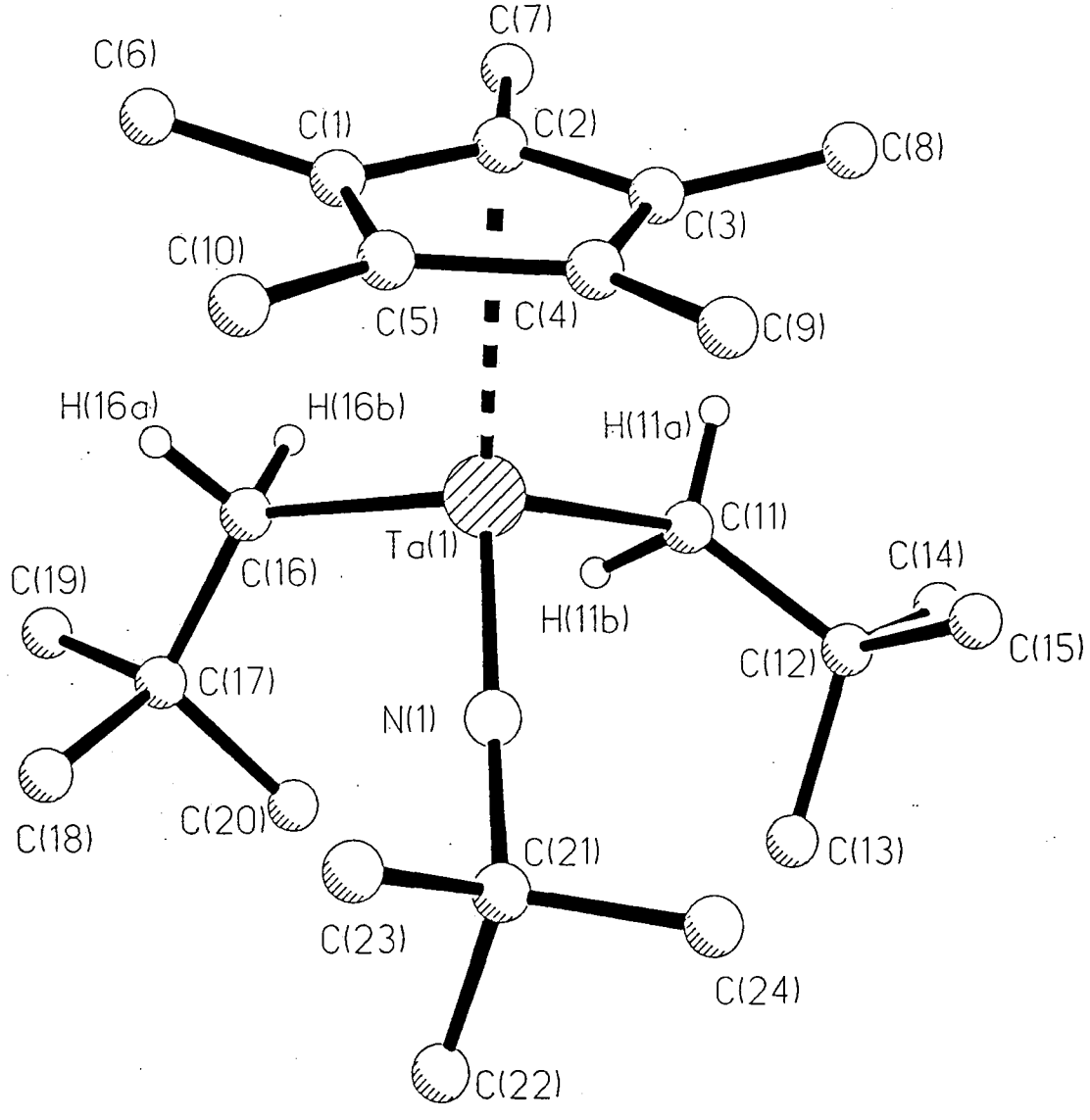

Figure 9.5.1 *- The molecular structure of* ***9****.*

Table 9.5.2 - Selected bond lengths and angles for compound 9.

Bond	Distance (Å)	Angle	Angle (°)
Ta(1)-N(1)	1.788(2)	N(1)-Ta(1)-C(11)	103.6(1)
Ta(1)-C(1)	2.527(3)	N(1)-Ta(1)-C(16)	105.0(1)
Ta(1)-C(2)	2.554(3)	N(1)-Ta(1)-Cpcentroid	126.1(2)
Ta(1)-C(3)	2.503(3)	C(11)-Ta(1)-C(16)	101.8(1)
Ta(1)-C(4)	2.425(3)	C(11)-Ta(1)-Cpcentroid	110.3(2)
Ta(1)-C(5)	2.429(3)	C(16)-Ta(1)-Cpcentroid	107.4(3)
Ta(1)-Cpcentroid	2.175(3)	Ta(1)-N(1)-C(21)	170.7(2)
Ta(1)-C(11)	2.199(3)	Ta(1)-C(11)-C(12)	128.8(2)
Ta(1)-C(16)	2.208(3)	Ta(1)-C(11)-H(11a)	108(2)
C(11)-H(11a)	0.98(4)	Ta(1)-C(11)-H(11b)	88(2)
C(11)-H(11b)	1.00(4)	Ta(1)-C(16)-C(17)	126.7(2)
C(16)-H(16a)	0.91(4)	Ta(1)-C(16)-H(16a)	113(2)
C(16)-H(16b)	1.01(4)	Ta(1)-C(16)-H(16b)	99(2)
Ta(1)···H(11b)	2.390(4)	Ta(1)···H(11b)-C(11)	24.8(6)
Ta(1)···H(16b)	2.575(4)	Ta(1)···H(16b)-C(16)	22.8(6)

The tantalum atom lies in a pseudo-tetrahedral environment. The Ta(1)–N(1) bond length [1.788(2)Å] is within the expected range for a tantalum imido complex (Nugent & Harlow, 1978; Chamberlain, Rothwell & Huffman, 1986) and the imido angle Ta(1)-N(1)-C(21) is close to linearity [170.7(2)°].

Two hydrogens, one on each of the two neopentyl methylene groups, lie in close contact with the metal centre [Ta(1)···H(11b) 2.390(4)Å, Ta(1)···H(16b) 2.575(4)Å] giving rise to highly distorted Ta(1)-C(11)-H(11b) and Ta(1)-C(16)-H(16b) angles of 88(2)° and 99(2)° respectively*. By nature of this bond geometry, the agostic interaction involving H(11b) appears stronger. These parameters compare well with the related complex [CpNb(N-2,6-$^{i}Pr_2C_6H_3$)(CH_2CMe_3)$_2$] [Nb···Hα mean 2.36Å, Nb-Cα-Hα 87° and 89°] (Poole et al, 1993) and the isolobal [Mo(N-2,6-$^{i}Pr_2C_6H_3$)(N^{t}Bu)(CH_2CMe_3)$_2$] [Mo···Hα mean 2.40Å, Mo-Cα-Hα 91° and 98°] (Bell et al, 1994). In addition, the orientation of both neopentyl groups *towards* the imido moiety, which would be sterically disfavoured, implies an electronic preference for this configuration due to the agostic interactions.

* H(11a), H(11b), H(16a) and H(16b) were found in the Fourier difference map and their positions were freely refined.

9.5.4.1 Reaction of Complexes **7-9** with Pentafluorophenol

Treatment of **7** with two molar equivalents of C_6F_5OH in toluene gives a bright red solution from which yellow crystals are obtained. Analysis by ^1H NMR spectroscopy indicates the presence of Cp* and benzyl groups in a 1:1 ratio, while ^{19}F NMR data support the expected ligation of the $[OC_6F_5]$ moiety. Elemental analysis confirms the removal of the *t*-butylimido substituent. The product is shown by X-ray crystallography to be the tantalum(V) dimer $[Cp^*Ta(CH_2Ph)(OC_6F_5)(\mu\text{-}O)]_2$ (**10**). Its formation is likely to proceed *via* the initial protonation and elimination of the imido moiety as *t*-butylamine# to form the bis(aryloxide) intermediate $[Cp^*Ta(CH_2Ph)_2(OC_6F_5)_2]$. The presence of an oxo bridge is unexpected and presumably results from loss of bis(pentafluorophenyl) ether.

The molecular structure of **10** is shown in ***Figure 9.5.2***, and selected bond distances and angles are given in ***Table 9.5.3***. Fractional coordinates and anisotropic displacement parmameters are given in ***Appendix A.9.10*** and ***A.9.11*** respectively.

Table 9.5.3 *- Selected bond lengths and angles for compound **10**.*

Bond	Distance (Å)	Angle	Angle (°)
Ta-O(1)	2.005(8)	O(1)-Ta-O(2)	80.7(3)
Ta-O(2)	1.957(7)	O(1)-Ta-O(2)#1	150.8(4)
Ta-O(2)#1	1.950(8)	O(1)-Ta-C(7)	83.2(4)
Ta-C(7)	2.20(1)	O(1)-Ta-Cpcentroid	102.2(4)
Ta-C(14)	2.56(1)	O(2)-Ta-O(2)#1	76.7(3)
Ta-C(15)	2.53(1)	O(2)-Ta-C(7)	113.4(4)
Ta-C(16)	2.45(1)	O(2)-Ta-Cpcentroid	137.6(4)
Ta-C(17)	2.39(1)	O(2)#1-Ta-C(7)	89.1(4)
Ta-C(18)	2.48(2)	O(2)#1-Ta-Cpcentroid	106.9(4)
Ta-Cpcentroid	2.17(3)	C(7)-Ta-Cpcentroid	108.9(5)
		Ta-O(1)-C(1)	139.8(8)
		Ta-O(2)-Ta#1	103.3(3)
		Ta-C(7)-C(8)	125.2(8)

^1H NMR monitoring of the reaction in C_6D_6 shows the appearance of butylamine before resonances for toluene are observed, hence this suggests that the imido group is protonated before the benzyl ligand.

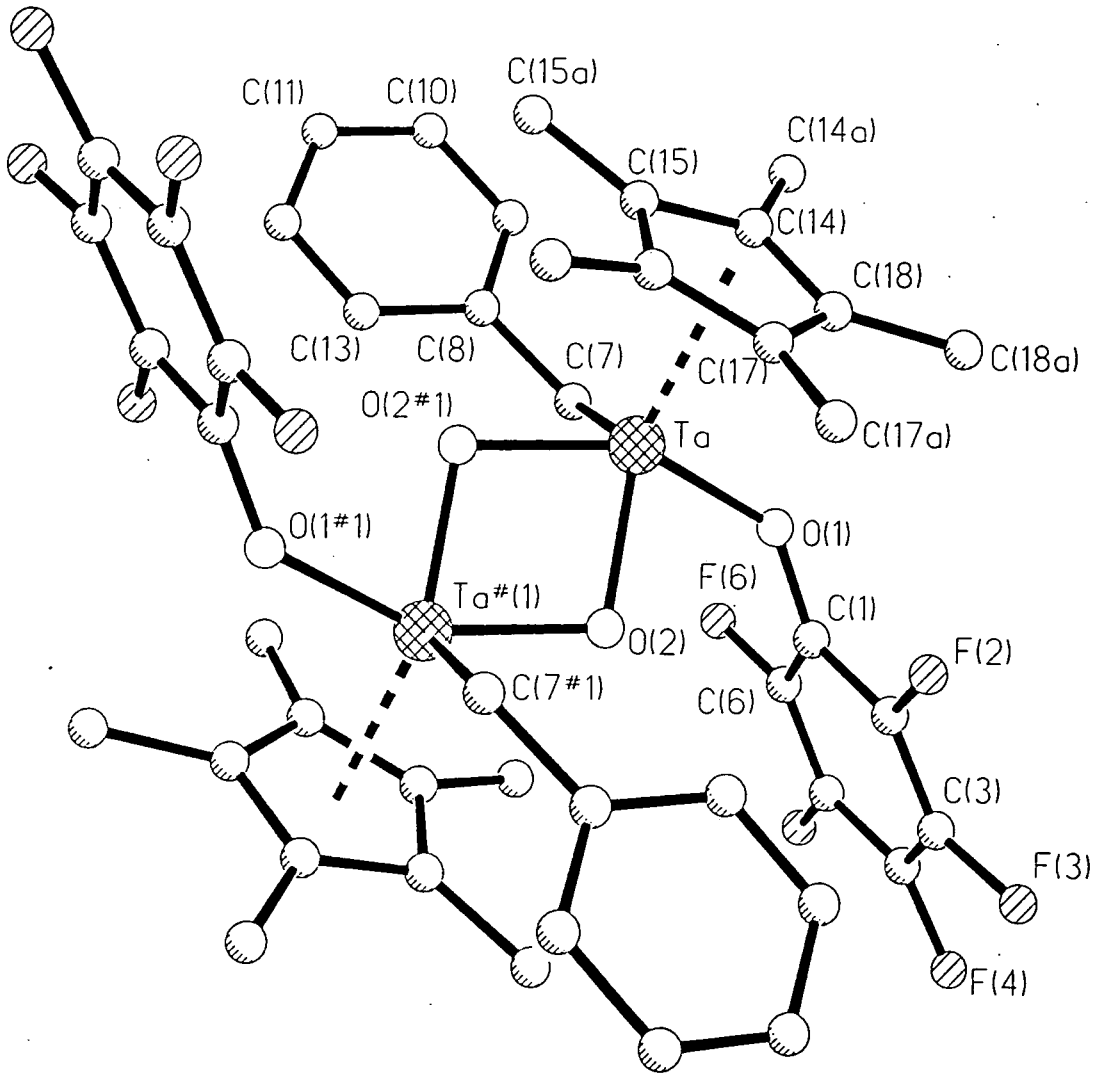

***Figure 9.5.2** - The molecular structure of **10**.*

Complex **10** is a centrosymmetric oxo-bridged dimer with the tantalum atom adopting a distorted square pyramidal configuration. The remarkable aryloxide Ta–O(1) bond length of 2.005(8)Å is greater than any previously reported Ta(V)–$OC_{sp}2$ distance (Steffey, Fanwick & Rothwell, 1990; Allen et al, 1991). The oxo Ta–O(2) bond is also very long [1.957(7)Å]. These elongated contacts can be rationalised by considering the fierce competition for the vacant d_π symmetry orbitals of the electrophilic Ta(V) centre. As well as the Cp* ligand which is an extremely strong π-donor, there are three oxygen atoms per metal attempting to participate in p_π–d_π interactions via donation from their lone pairs. The Ta–Cp* bonding is not distorted and appears to dominate, hence the tantalum–oxygen p_π–d_π interactions are relatively weak and these bonds are intrinsically lengthened. In addition, the filled oxygen p_π orbital of $[OC_6F_5]$ is delocalised into the highly electron-withdrawing pentafluorophenyl ring which further reduces its ability for π-donation to the metal.

The structure of **10** displays severe steric congestion around each tantalum atom, and this appears to be alleviated by the twist angle of 102.9° between the pentafluorophenyl ring [C(1)–C(6)] and the benzyl ring [C(8)–C(13)] (*vide infra*). The molecules pack in a layer-like fashion with the group in orthogonal orientations to the benzyl group and are held together in the three-dimensional lattice by Van der Waals forces.

Reaction of **8** with two equivalents of pentafluorophenol in n-heptane at 60°C results in the precipitation of yellow needle crystals. Their ^{1}H and ^{13}C NMR spectra implies the loss of the *t*-butylimido and neophyl groups while resonances for C_6F_5 units are observed in the ^{19}F NMR spectrum. The nature of the crystals is confirmed to be $Cp^*Ta(OC_6F_5)_4$ (**11**) by an X-ray crystal analysis. The dimeric species $[Cp^*Ta(OC_6F_5)_2(\mu\text{-}O)]_2$ (**12**) is also isolated from the reaction mixture and structurally characterised.

Complex **11** is presumably generated by the reaction of **8** with four molecules of C_6F_5OH with the conconmitant elimination of *t*-butylamine and two molecules of $PhCMe_3$. The mechanism for the formation of the μ-oxo dimer **12** is likely to be related to that for compound **10**.

The crystal structure of **11** is shown in ***Figure 9.5.3***, and selected bond distances and angles are listed in ***Table 9.5.4***. Fractional coordinates and anisotropic displacement parameters are given in ***Appendix A.9.12*** and ***A.9.13*** respectively.

Table 9.5.4 - *Selected bond lengths and angles for compound **11**.*

Bond	Distance (Å)	Angle	Angle (°)
Ta(1)-O(1)	1.985(5)	O(1)-Ta(1)-O(2)	83.5(2)
Ta(1)-O(2)	1.956(8)	O(1)-Ta(1)-O(3)	85.6(2)
Ta(1)-O(3)	1.907(8)	O(1)-Ta(1)-Cpcentroid	104.0(3)
Ta(1)-C(1)	2.43(1)	O(2)-Ta(1)-O(3)	133.3(3)
Ta(1)-C(2)	2.451(8)	O(2)-Ta(1)-Cpcentroid	115.3(3)
Ta(1)-C(3)	2.419(7)	O(3)-Ta(1)-Cpcentroid	111.3(3)
Ta(1)-Cpcentroid	2.111(9)	Ta(1)-O(1)-C(7)	142.7(5)
		Ta(1)-O(2)-C(13)	160.2(7)
O(2)...H(4a')	2.491(7)	Ta(1)-O(3)-C(17)	169.5(7)
F(9)...F(9')	2.875(5)		

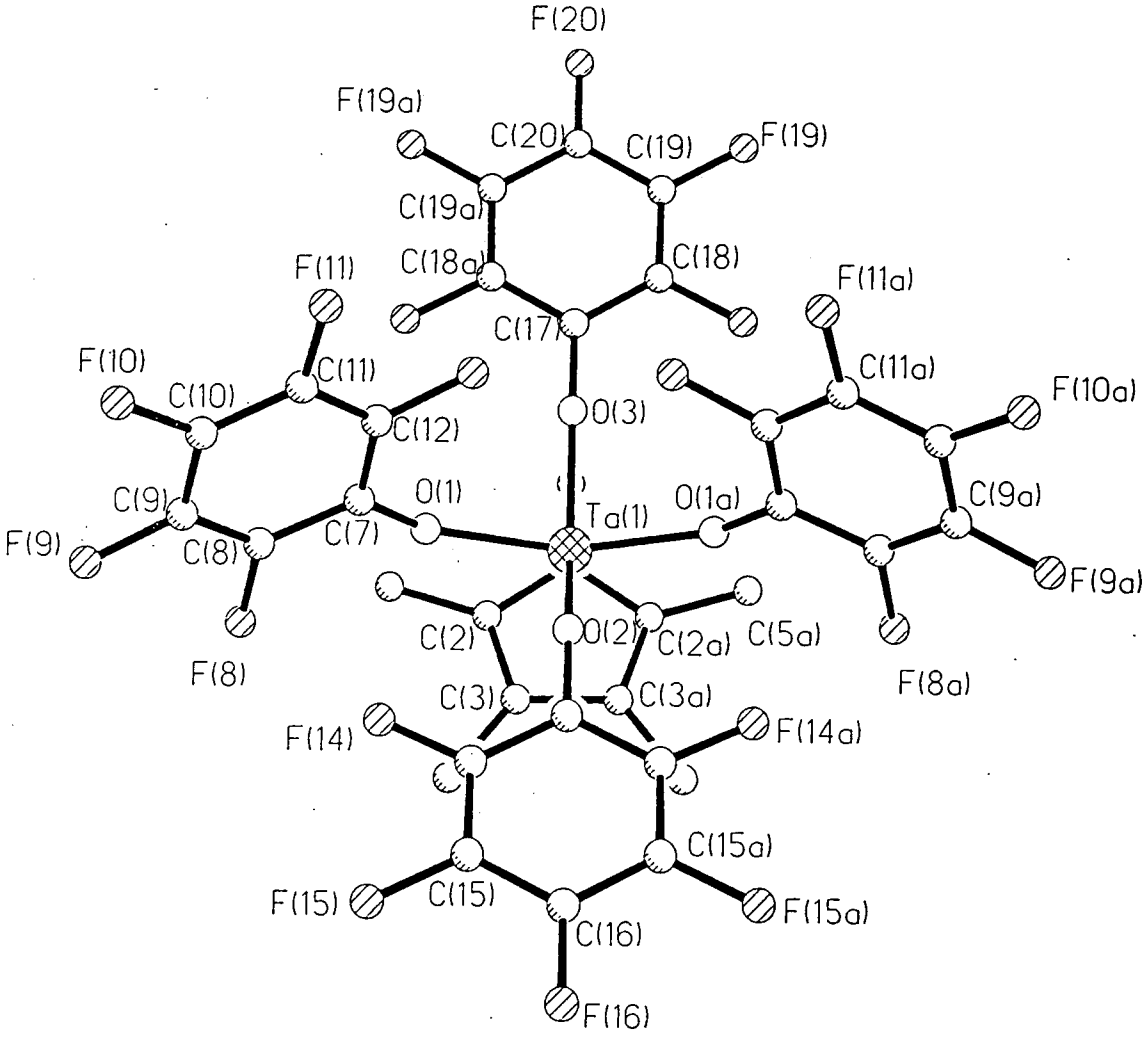

Figure 9.5.3 *- The molecular structure of* ***11****.*

The molecule contains a mirror plane through O(2) and O(3) and the tantalum atom resides in a distorted trigonal bipyramidal geometry. Rationale for the relatively long Ta-O contacts [1.907(8), 1.956(8) and 1.985(5)Å] has already been given [see structure $[Cp^*Ta(CH_2Ph)(OC_6F_5)(\mu\text{-}O)]_2$ (**10**). The pentafluorophenyl rings are approximately orthogonal to each other like the aryl rings in **10** and this evidently minimises the steric and electronic repulsion between the fluorine atoms. Additionally, there are two intermolecular interactions in the crystal lattice, namely C(4')-H(4a')···O(2) and the unusual F(9)···F(9') contact with separations of 2.491(7)Å and 2.875(5)Å respectively.

The crystal structure of **12** is shown in ***Figure 9.5.4***, and selected bond distances and angles are given in ***Tables 9.5.5***. Fractional coordinates and anisotropic displacement parameters are given in ***Appendix A.9.14*** and ***A.9.15***.

Table 9.5.5 *- Selected bond lengths and angles for compound* ***12****.*

Bond	Distance (Å)	Angle	Angle (°)
Ta(1)-O(1)	1.971(6)	O(1)-Ta(1)-O(4)	84.4(3)
Ta(1)-O(4)	1.952(7)	O(1)-Ta(1)-O(10)	83.3(3)
Ta(1)-O(10)	1.969(6)	O(1)-Ta(1)-O(11)	136.2(3)
Ta(1)-O(11)	1.918(6)	O(1)-Ta(1)-Cpcentroid	110.6(5)
Ta(1)-C(1)	2.458(9)	O(4)-Ta(1)-O(10)	140.7(3)
Ta(1)-C(2)	2.482(9)	O(4)-Ta(1)-O(11)	87.2(3)
Ta(1)-C(3)	2.464(9)	O(4)-Ta(1)-Cpcentroid	106.7(4)
Ta(1)-C(4)	2.43(1)	O(10)-Ta(1)-O(11)	76.6(2)
Ta(1)-C(5)	2.42(1)	O(10)-Ta(1)-Cpcentroid	112.6(4)
Ta(1)-Cpcentroid	2.13(1)	O(11)-Ta(1)-Cpcentroid	113.0(4)
Ta(2)-O(2)	1.939(6)	O(2)-Ta(2)-O(3)	85.2(3)
Ta(2)-O(3)	2.014(6)	O(2)-Ta(2)-O(10)	129.2(3)
Ta(2)-O(10)	1.933(6)	O(2)-Ta(2)-O(11)	87.6(3)
Ta(2)-O(11)	1.961(6)	O(2)-Ta(2)-Cpcentroid2	110.3(4)
Ta(2)-C(30)	2.44(1)	O(3)-Ta(2)-O(10)	82.8(2)
Ta(2)-C(31)	2.48(1)	O(3)-Ta(2)-O(11)	146.2(3)
Ta(2)-C(32)	2.47(1)	O(3)-Ta(2)-Cpcentroid2	105.0(4)
Ta(2)-C(33)	2.45(1)	O(10)-Ta(2)-O(11)	76.4(2)
Ta(2)-C(34)	2.39(1)	O(10)-Ta(2)-Cpcentroid2	120.5(4)
Ta(2)-Cpcentroid2	2.14(1)	O(11)-Ta(2)-Cpcentroid2	108.5(4)
		Ta(1)-O(1)-C(6)	145.7(6)
		Ta(2)-O(2)-C(12)	163.0(6)
		Ta(2)-O(3)-C(18)	134.5(6)
		Ta(1)-O(4)-C(24)	168.5(7)
		Ta(1)-O(10)-Ta(2)	103.0(3)
		Ta(1)-O(11)-Ta(2)	103.9(3)

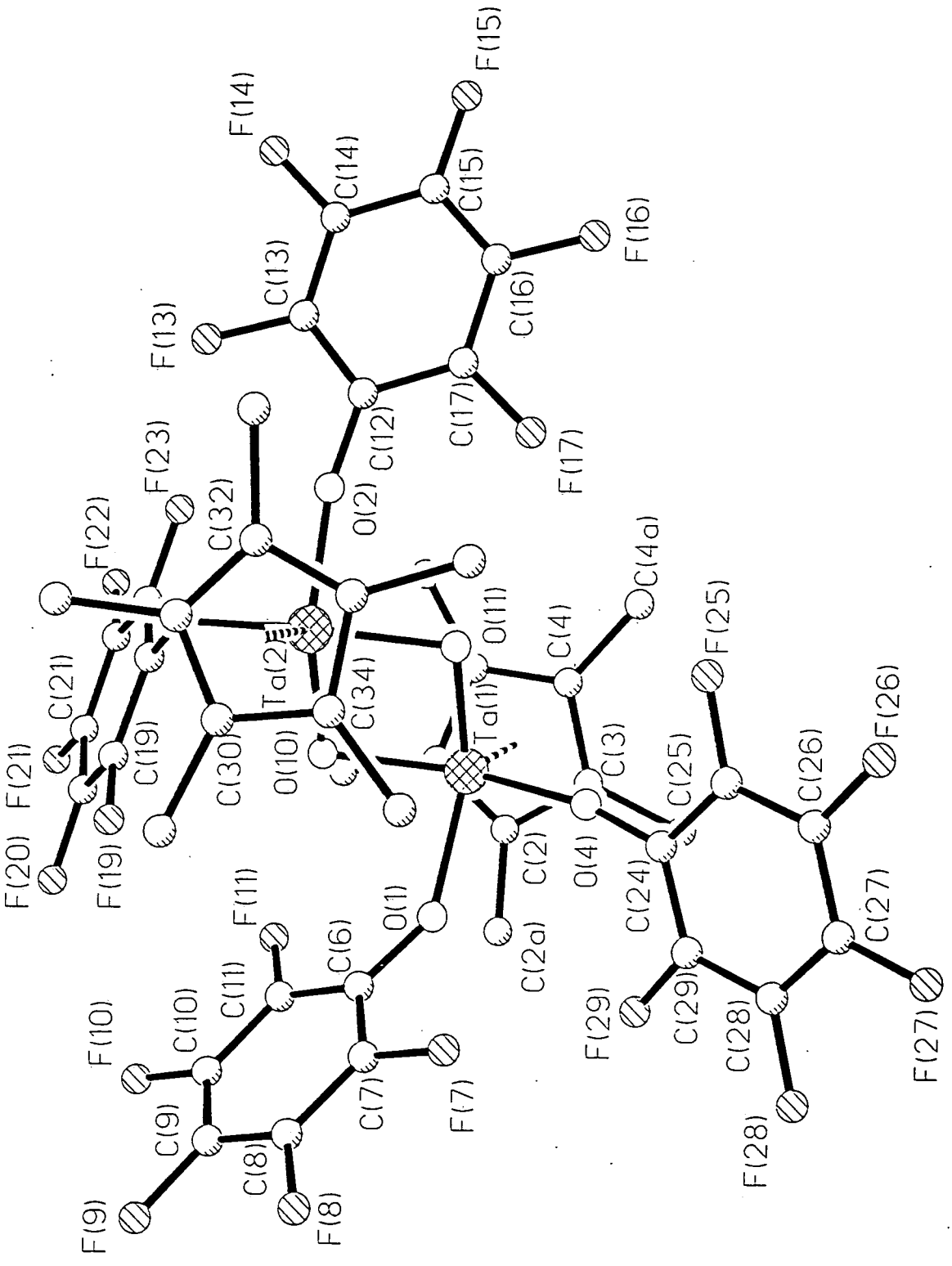

***Figure 9.5.4** - The molecular structure of 12.*

The molecule is a dimer with a highly distorted square pyramidal arrangement around each tantalum atom, but unlike the apparently related structure of **10**, no inversion centre exists in **12**. The largest Ta–O separation [2.014(6)Å] exceeds even that in **10** [2.005(8)Å] and reflects the replacement of a benzyl group in **10** by an [OC_6F_5] group, which intensifies the competition between the π-donating ligands for the empty d_π metal orbitals.

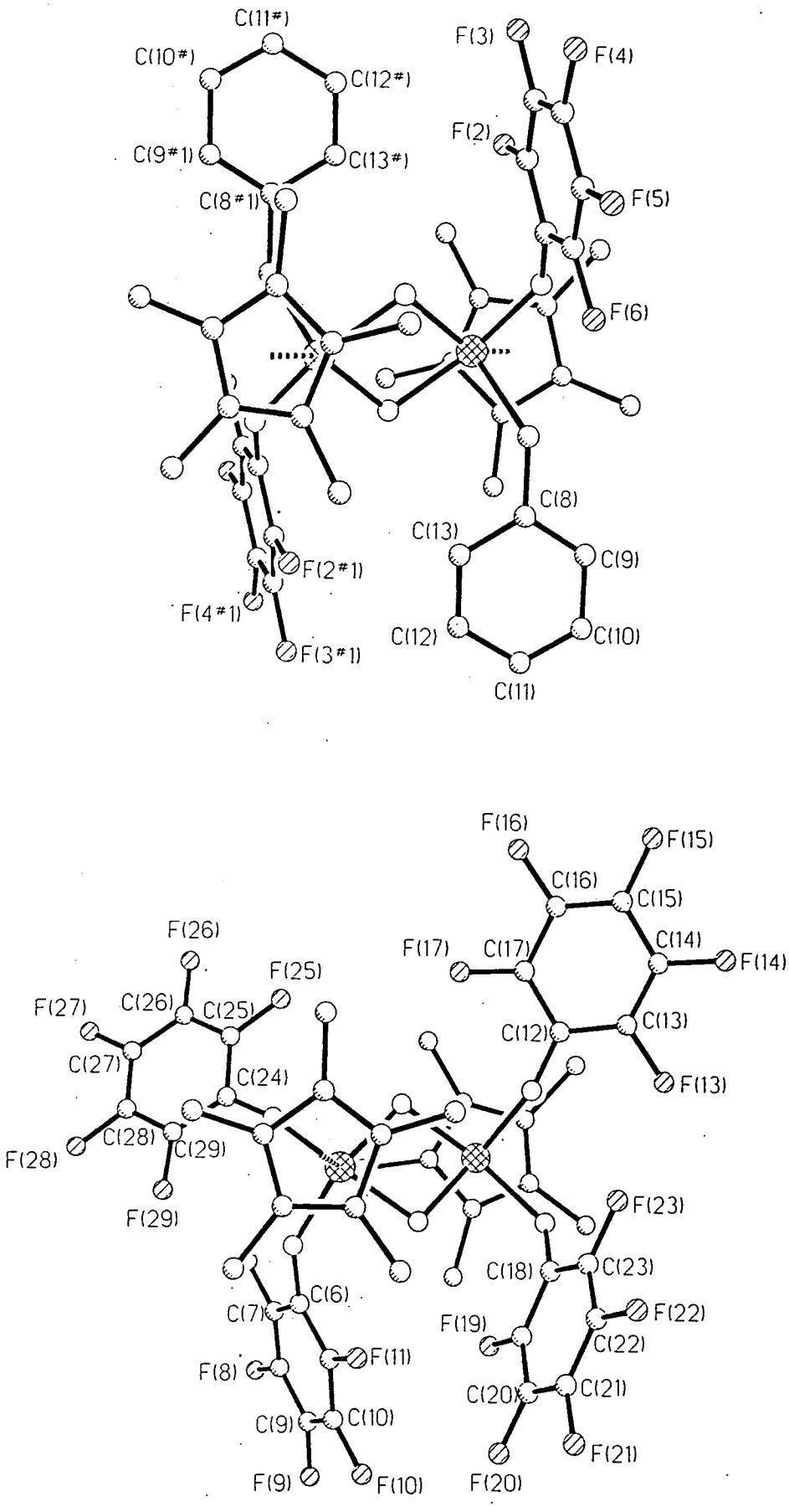

Figure 9.5.5 *- A comparison of the twist angles between the rings in* ***10*** *and* ***12****.*

The Ta(1)–O–Ta(2) angles of 103.0(3)° and 103.9(3)° are almost identical to that in **10** [103.3(3)°] and are comparable with other Ta(V)–O–Ta(V) angles (Allen et al, 1991). The four relatively large aryloxide Ta–O–C_{ipso} angles range from 134.5(6)° to 168.5(7)° and presumably contribute to a reduction in unfavourable repulsive forces between the pentafluorophenyl moieties. Consequently, the twist angles between the rings (range 34.1°–57.3°; mean 42°) are smaller than those in **10** [102.9°] (***Figure 9.5.5***). Compared to $Cp^*Ta(OC_6F_5)_4$ (**11**), which also exhibits large twist angles, the C_6F_5 rings in **12** experience less steric congestion due to the undemanding nature of the oxo bridges.

Even at elevated temperatures in toluene, no reaction is observed between **9** and C_6F_5OH. This stability presumably results from the presence of α-agostic interactions. The stability may also have a steric origin: the Cp* and three bulky *t*-butyl groups form a virtual barrier to the inner coordination sphere of the molecule (***Figure 9.5.1***), thus preventing attack at the metal centre and imido moiety.

9.5.5 Conclusions

This study reveals the presence of α-agostic interactions in several of the compounds described. We believe that these interactions inhibit the chemical reactivity of such compounds, for example, with pentafluorophenol. Examination of the tantalum-aryloxide interactions in this study reveals a correlation between the Ta–O(C_6F_5) distance and Ta–O–C_6F_5 angle. For example, the two longest bonds [Ta(2)–O(3) in **12**: 2.014(6)Å; Ta–O(1) in **10**: 2.005(8)Å] exhibit the smallest angles [134.5(6)° and 139.8(8)° respectively], while the shortest contact [Ta(1)–O(3) in **11**: 1.907(8)Å] corresponds to the largest angle [169.5(7)°]. This relationship arises from the expected widening of the tantalum-aryloxide angle as π-donation from the oxygen lone pair to the metal increases and the Ta–O distance falls. In general, we have illustrated that the nature of the [OC_6F_5] substituent can dramatically transform the geometry of related molecules in the solid state.

9.6 BIS (2-T-BUTYLPHENYLIMIDO) CHLORO (η^5-PENTAMETHYL-CYCLOPENTADIENYL) TANTALUM(V) ANION

9.6.1 Abstract

The bulky 2,6-diisopropylphenyl substituent has been investigated widely in transition metal imido chemistry, and has been shown to stabilize a variety of unusual imido metal species. (Cockcroft et al, 1992; Glueck, Wu, Hollander & Bergman, 1991; Anhaus, Kee, Schofield & Schrock, 1990; Gibson & Poole, 1995). The presence of two bulky ortho isopropyl substituents undoubtedly plays an important role in this stabilization. Imido aryl substituents containing one bulky substituent in the ortho position also offer the possibility for substantial steric protection, not only due to the presence of the large substituent but also as a result of bending at the imido nitrogen. We have thus studied the bis (2-t-butylphenylimido) chloro (η^5-pentamethylcyclopentadienyl) tantalum(V) anion (**13**) with a view to comparing its structure with its previously reported 2,6-diisopropylphenylimido analogue (Baldwin, Huber, Bruck & Wigley, 1993).

9.6.2 Experimental

The structure of **13** was determined using the Siemens SMART-CCD diffractometer. The crystal was mounted using the oil-drop method (Stalke & Kottke, 1994) and graphite monochromatized Mo-Kα radiation (λ=0.71073Å) was employed. Data collection was carried out at 150K. Cell refinement, data collection and data reduction proceeded via Siemens SMART software (Siemens Analytical X-ray Instruments, 1995a and 1995b). The data collection nominally covered over a hemisphere of reciprocal space, by a combination of three sets of exposures; each set had a different ϕ angle for the crystal and each exposure covered 0.3° in ω. The crystal-to-detector distance was 6.117 cm. Coverage of the unique set is over 97% complete to at least 26° in θ. Crystal decay was monitored by repeating the initial frames at the end of data collection and analyzing the duplicate reflections. No decay was observed.

The structure was solved using SHELXS-86 (Sheldrick, 1990) by Patterson and difference Fourier methods. A semi-empirical absorption correction using φ-scans was applied in XPREP (Sheldrick, 1995) [Tmin / Tmax = 0.346 / 0.666]. Subsequent least-squares refinement used the SHELXL-93 (Sheldrick, 1993) package. Scattering factors were taken from International Tables for Crystallography, Vol. C, 1992.

Positional and anisotropic thermal parameters for all non-hydrogen atoms and positional parameters of all hydrogen atoms within the anionic constituent of the molecule were refined. All hydrogen isotropic displacement parameters were constrained to the riding

model, $U_{iso}(H) = 1.2U_{eq}(C)$. Likewise, the lithium atom within the cation was refined anisotropically. Disorder in the oxydiethyl group resulted in only the positional parameters and the occupancy of the oxygen atom being refined with the isotropic temperature factors constrained to 0.070Å^2. It was not possible to model the ethyl groups at all.

A summary of the crystal, data collection and refinement parameters for the experiment is given in ***Table 9.6.1***.

Table 9.6.1 *- Crystallographic data for compound* ***13***.

Compound	**13**	Compound	**13**
Molecular Formula	$TaC_{34}H_{51}N_2ClLiO$	Absorption coefficient (mm^{-1})	3.331
Formula weight	727.11	Crystal Morphology	block
a(Å)	19.537(1)	Crystal Colour	yellow
b(Å)	16.354(1)	Crystal Size (mm)	0.60x0.34x0.16
c(Å)	21.327(1)	Total number of reflections	27230
α(°)	90	Unique reflections	5721
β(°)	90	Observed Reflections [I>2σ(I)]	4883
γ(°)	90	R_{int}	0.0559
Cell Volume(Å^3)	6814.2(7)	θ range (°)	1.88-25.24
Crystal System	orthorhombic	Data / Parameters	5645 / 323
Space Group	Pbca	R1 [I > 2σ(I)]	0.0433
Z	8	wR2 [I > 2σ(I)]	0.1246
Calculated Density (gcm^{-1})	1.418	Goodness of fit on F^2	1.085
Temperature (K)	150(2)	Weighting Scheme	a = 0.0583; b = 64.8027
Wavelength (Å)	0.71073	$\Delta\rho_{(max, min)}$ (eÅ^{-3})	2.776 / -0.769

9.6.3 Results and discussion

The molecular structure of **13** is given in ***Figure 9.6.1***. Selected bond distances and angles are given in ***Table 9.6.2***. Fractional coordinates and anisotropic displacement parameters are given in ***Appendix A.9.16*** and ***A.9.17*** respectively.

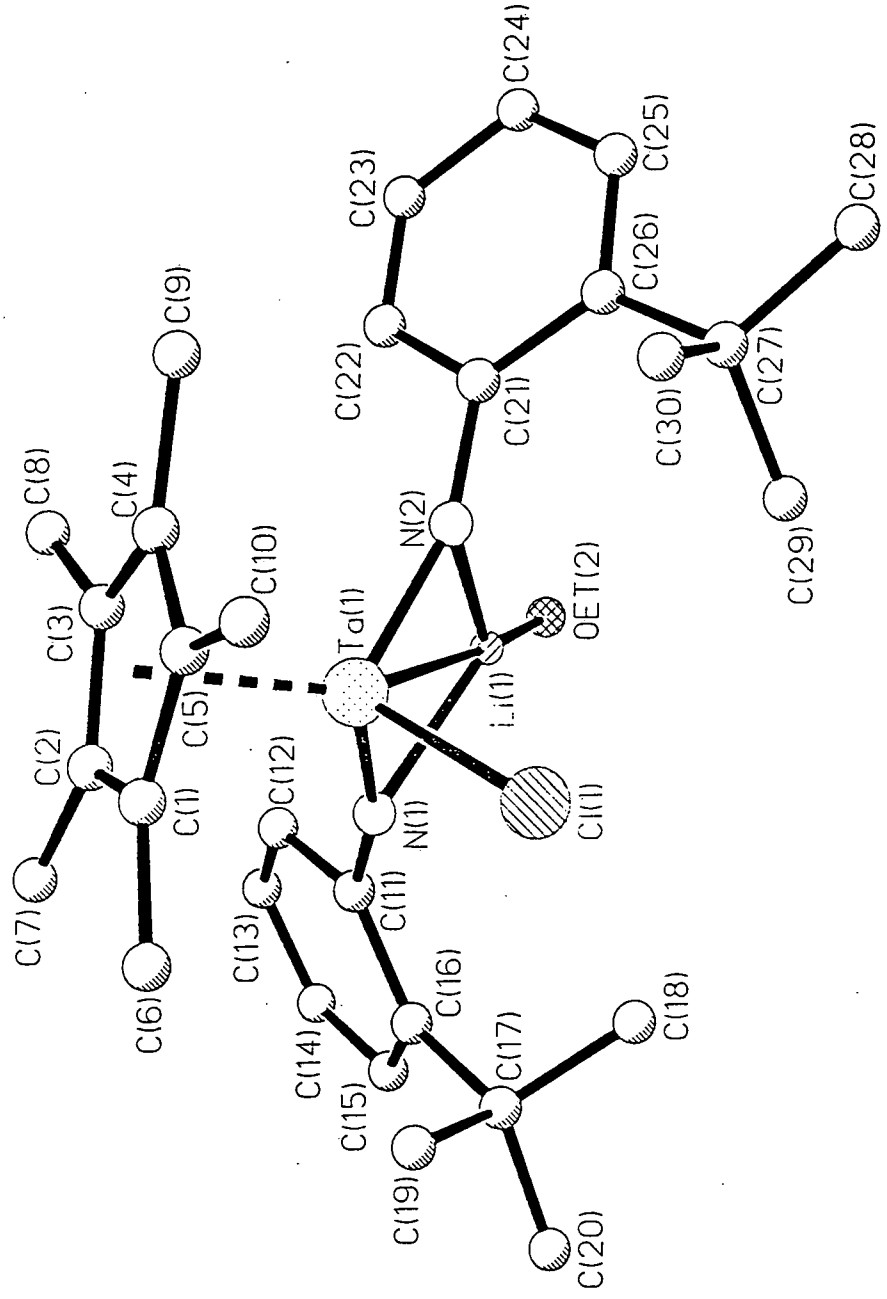

Figure 9.6.1 *- The molecular structure of 13.*

***Table 9.6.2** - Selected bond lengths and angles for compound **13**.*

Bond	Distance (Å)	Angle	Angle (°)
Ta(1)-N(1)	1.844(6)	N(1)-Ta(1)-N(2)	100.5(3)
Ta(1)-N(2)	1.848(6)	N(1)-Ta(1)-Cl(1)	102.6(2)
Ta(1)-Cl(1)	2.396(2)	N(2)-Ta(1)-Cl(1)	103.4(2)
Ta(1)-C(3)	2.408(7)	N(1)-Ta(1)-C(3)	104.9(3)
Ta(1)-C(2)	2.443(7)	N(2)-Ta(1)-C(3)	99.8(3)
Ta(1)-C(4)	2.459(7)	N(1)-Ta(1)-Li(1)	50.3(4)
Ta(1)-C(1)	2.478(7)	N(2)-Ta(1)-Li(1)	50.3(4)
Ta(1)-C(5)	2.493(7)	Cl(1)-Ta(1)-Li(1)	108.8(4)
Ta(1)-Li(1)	2.68(1)	C(11)-N(1)-Ta(1)	165.9(5)
N(1)-C(11)	1.393(9)	C(11)-N(1)-Li(1)	98.3(6)
N(1)-Li(1)	2.06(2)	Ta(1)-N(1)-Li(1)	86.3(5)
N(2)-C(21)	1.41(1)	Ta(1)-N(2)-Li(1)	86.2(5)
N(2)-Li(1)	2.06(2)	O(1')-Li(1)-N(1)	134.8(8)
Li(1)-O(1')	1.92(2)	O(1')-Li(1)-N(2)	137.6(9)
Li(1)-O(1)	2.10(3)	N(1)-Li(1)-N(2)	86.9(6)
		O(1')-Li(1)-O(1)	29.9(7)
H(12)...Cl(1)	2.89(2)	N(1)-Li(1)-O(1)	130(1)
		N(2)-Li(1)-O(1)	134(1)
		O(1')-Li(1)-Ta(1)	172(1)
		N(1)-Li(1)-Ta(1)	43.4(3)
		N(2)-Li(1)-Ta(1)	43.5(3)
		O(1)-Li(1)-Ta(1)	158(1)

The overall bond geometry of the title compound is generally similar to the reference compound. In particular, the Ta(1)-N(1) and Ta(1)-N(2) distances and Ta(1)-N(1)-C(11) and Ta(1)-N(2)-C(21) angles are comparable [1.844(6)Å, 1.848(6)Å, 165.9(5)° and 161.7(5)° repectively].

However, several geometrical differences exist between the two compounds as a result of the presence of a more bulky aryl imido substituent in this case.

In the 2,6-diisopropylphenylimido structure, the planes of the arylimido and Cp* rings are approximately parallel to each other to minimize steric repulsion between the respective isopropyl and methyl groups. The situation for the 2-t-butylphenylimido congener is comparable, except that the single bulky t-butyl substituent on each imido

ligand is now positioned in a less congested orientation away from the $[\mu\text{-Li(OEt2)}]^+$ moiety, such that they point in a similar direction to the Ta-Cl vector.

The Ta(1)-Li(1) distance of 2.68(1)Å is slightly longer than in the Wigley derivative, being the only other reported. We presume that this is also consequent upon the greater steric repulsion from the tertiary butyl groups compared to the isopropyl groups of the phenylimido ligands.

Unlike the Wigley derivative, the OEt_2 fragment is disordered in this compound. The oxygen exists in two sites with an O(1'):O(1) occupancy ratio of approximately 7:3. The Li(1)-O(1') and Li(1)-O(1) distances and C(21)-Li(1)-O(1') and C(11)-Li(1)-O(1) angles are 1.92(2)Å, 2.11(3)Å, 110.0(7)° and 99.3(9)° respectively. The gross disorder in the ethyl moieties precluded a satisfactory refinement model and the contributions from the four carbon atoms were not included in the structure factor calculations. The largest residual electron density consequently lies in the proposed ethyl fragment regions.

The structure contains a weak C-H(12)...Cl(1) interaction [H...Cl = 2.89(2)Å, symmetry code: 1.5-x,-0.5+y,+z; c.f. sum of van der Waals radii of H and Cl = 2.95Å (Bondi, 1964)]. This links adjacent molecules forming chains which are almost parallel to the y-axis. Adjacent chains are arranged anti-parallel to each other thus completing the three-dimensional structure. No intermolecular interactions are reported in the diisopropylphenyl structure.

9.7 REFERENCES

Allen, F. H., Davies, J. E., Galloy, J. J., Johnson, O., Kennard, O., Macrae, C. F., Mitchell, E. M., Mitchell, G. F., Smith, J. M. & Watson, D. G. (1991). J. Chem. Inf. Comput. Sci., **31**, 187-204.

Anhaus, J. T., Kee, T. P., Schofield, M. H. & Schrock, R. R. (1990). J. Am. Chem. Soc., **112**, 1642-1643.

Baldwin, T. C., Huber, S. R., Bruck, M. A. & Wigley, D. E. (1993). Inorg. Chem., **32**, 5682-5686.

Ballard, K. R., Gardner, I. M., Wigley, D. E. (1989). J. Am. Chem. Soc., **111**, 2159.

Becker, H., Häusler, H. J. & Preuss, F. (1987). Z. Naturforsch., **42b**, 881-888.

Bell, A., Clegg, W., Dyer, P. W., Elsegood, M. J., Gibson, V. C. & Marshall, E. L. (1994). J. Chem. Soc., Chem. Commun., 2547.

Bondi, A. (1964). J. Phys. Chem., **68**, 441-451.

Bourg, S., Corriu, R. J. P., Enders, M. & Moreau, J. J. E. (1995). Organometallics, **14**, 564.

Brand, H., Capriotti, J. A. & Arnold, J. (1994). Organometallics, **13**, 4469.Bruck, M. A., Copenhaver, A. S. & Wigley, D. E. (1987). J. Am. Chem. Soc., **109**, 6525.

Brintzinger, H. H., Fisher, D., Mülhaupt, R., Rieger, B. & Waymouth, R. M. (1995). Angew. Chem. Int. Ed. Engl., **34**, 1143.

Broene, R. D. & Buchwald, S. L. (1993). Science, **261**, 1696.

Buchwald, S. L. & Nielsen, R. B. (1988). Chem. Rev., **88**, 1047.

Buchwald, S. L., Watson, B. T. & Huffman, J. C. (1986). J. Am. Chem. Soc., **108**, 7411.

Buchwald, S. L., Watson, B. T. & Huffman, J. C. (1987). J. Am. Chem. Soc., **109**, 2544.

Buchwald, S. L., Watson, B. T., Wannamaker, M. W. & Dewan, J. C. (1989). J. Am. Chem. Soc., **111**, 4486.

Buijink, J. -K. F., Meetsma, A., Teuben, J. H., Kooijman, Spek, A. L. (1995). J. Organomet. Chem., **497**, 161.

Buijink, J. -K. F., Teuben, J. -H., Kooijman, H. & Spek, A. L. (1994). Organometallics, **13**, 2922-2924.

Chamberlain, L. R., Rothwell, I. P. & Huffman, J. C. (1986). J. Chem. Soc. Chem. Commun., 1203.

Chan, M. C. W. (1995). Ph. D. Thesis, University of Durham, U.K.

Chan, M. C. W., Cole, J. M., Gibson, V. C. & Howard, J. A. K. (1997a). J. Chem. Soc., Chem. Commun., (in press).

Chan, M. C. W., Cole, J. M., Gibson, V. C. & Howard, J. A. K. (1997b). Acta Crystallogr., **C53**, 202-204.

Chan, M. C. W., Cole, J. M., Gibson, V. C. & Howard, J. A. K. (1997c). J. Chem. Soc., Dalton Trans., (in preparation).

Chan, M. C. W., Cole, J. M., Gibson, V. C. & Howard, J. A. K. (1997d). Acta Crystallogr., **C**, (submitted).

Chan, M. C. W., Cole, J. M., Gibson, V. C., Howard, J. A. K., Lehmann, C. W., Poole, A. D. & Siemeling, U. (1997). J. Chem. Soc., Dalton Trans., (submitted).

Chien, J. C. W., Tsai, W. M. & Rausch, M. D. (1991). J. Am. Chem. Soc., **113**, 8570.

Chisholm, M. H., (1992). Chemtracts Inorg., **4**, 273.

Chisholm, M. H. & Rothwell, I. P. (Eds), (1995). Polyhedron Symposium-in-Print Number 16, *'Alkoxides and Related O-Donor Ligands in Organometallic Chemistry'*, Polyhedron, **14**, 3175-3366.

Coates, G. W. & Waymouth, R. M. (1991). J. Am. Chem. Soc., **113**, 6270.

Cockcroft, J. K., Gibson, V. C., Howard, J. A. K., Poole, A. D., Siemeling, U. & Wilson, C. (1992). J. Chem. Soc., Chem. Commun., 1668-1670.

Coffindaffer, T. W., Steffey, B. D., Rothwell, I. P., Folting, K., Huffman, J. C. & Streib, W. E. (1989). J. Am. Chem. Soc., **111**, 4742.

Coles, M. P., Dalby, C. I., Gibson, V. C., Clegg, W. & Elsegood, M. R. J. (1995). J. Chem. Soc., Chem. Commun, 1709.

Coles, M. P. & Gibson, V. C. (1994). Polymer Bulletin, **33**, 529.

Coles, N., Whitby, R. J. & Blagg, J. (1990). Synlett., 271.

Coles, N., Harris, M. C. J., Whitby, R. J. & Blagg, J. (1994). Organometallics, **13**, 190.

Cotton, F. A. & Millar, M. J. (1977). J. Am. Chem. Soc., **99**, 7886.

Dyer, P. W., Gibson, V. C., Howard, J. A. K., Whittle, B. & Wilson, C. (1992). J. Chem. Soc. Chem. Commun., 1666.

Ewen, J. A. & Elder, M. J. (1993). Macromol. Chem. Macromol. Symp., **66**, 179.

Gibson, V. C. & Kee, T. P. (1989). J. Chem. Soc., Chem. Commun., 656.

Gibson, V. C. & Poole, A. D. (1995). J. Chem. Soc., Chem. Commun., 2261-2262.

Glueck, D. S., Wu, J. X., Hollander, F. J. & Bergman, R. G. (1991). J. Am. Chem. Soc., **113**, 2041-2054.

Green, M. L. H., Moser, G. A., Packer, I., Petit, F., Forder, R. A. & Prout, K. (1974). J. Chem. Soc., Chem. Commun., 839.

Hlatky, G. C., Turner, H. W. & Eckman, R. R. (1989). J. Am. Chem. Soc., **111**, 2728.

Huber, S. R., Baldwin, T. C. & Wigley, D. E. (1993). Organometallics, **12**, 91-97.

International Tables for Crystallography, Volume C, Mathematical, Physical and Chemical Tables (1992). Ed. Wilson, A. J. C., Dordrecht, Boston, London. Tables 4.2.6.8 & 6.1.1.4. 219-222, 500-503.

Jonas, K. Koepe, G. & Krüger, C. (1986). Angew. Chem. Int. Ed. Engl., **25**, 9.

Jordan, R. F. (1991). Adv. Organomet. Chem., **32**, 325.

Jordan, R. F., Bajgur, C. S., Willet, R. & Scott, B. (1986). J. Am. Chem. Soc., **108**, 7410.

Kaminsky, W. (1994). Catalysts Today, **20**, 257.

Kaminsky, W., Bark, R., Spiehl, R., Moller-Lindenhof, N. & Niedoba, S. (1988). *'Transition Metals and Organometallics as Catalysts for Olefin Polymerisation'*, Eds. Kaminsky, W. & Sinn, H., Springer-Verlag, Berlin.

Kaschube, W., Pörschke, K. R., Angermund, K., Krüger, C. & Wilke, G. (1988). Chem. Ber., **121**, 1921.

Kerschner, J. L., Fanwick, P. E., Rothwell, I. P. & Huffman, J. C. (1989). *Inorg. Chem.*, **28**, 780.

Knight, K. S., Wang, D., Waymouth, R. M. & Ziller, J. (1994). J. Am. Chem. Soc., **116**, 1845.

Kondakov, D. Y. & Negishi, E. (1996). J. Am. Chem. Soc., **118**, 1577.

Lapointe, R. E. & Wolczanski, P. T. (1985). Organometallics, **4**, 1810.

Lapointe, R. E., Wolczanski, P. T. & Mitchell, J. F. (1986). J. Am. Chem. Soc., **108**, 6283.

Lehmann, M. S. & Larsen, F. K. (1974). Acta Crystallogr., **A30**, 580-584.

Lubben, T. V. & Wolczanski, P. T. (1985). J. Am. Chem. Soc., **107**, 701.

Mack, H. & Eisen, M. S. (1996). J. Organomet. Chem., **526**, 81 and references therein.

Miyatake, T., Mizunuma, K. & Kakugo, M. (1993). Makromol. Chem. Macromol. Symp., **66**, 203.

Molecular Structure Corporation (1989). *TEXSAN: Single Crystal Structure Analysis Software*, Version 5.1, MSC, 3200 Research Forest Drive, The Woodlands, TX77381, U.S.A.

Molecular Structure Corporation (1991). *MSC/AFC Diffractometer Control Software.* MSC. 3200 Research Forest Drive, The Woodlands, TX77381, U.S.A..

Negishi, E. (1991) in *'Comprehensive Organic Synthesis'*, Ed. Paquette, L., Pergamon Press, New York, Volume 5, p. 1163.

Negishi, E., Kondakov, D. Y., Choueiry, D., Kasai, K. & Takahashi, T. (1996). J. Am. Chem. Soc., **118**, 9577.

Negishi, E. & Takahashi, T. (1994). Acc. Chem. Res., **27**, 124.

Noh, S. K., Heintz, R. A., Sendlinger, S. C., Janiak, C. & Theopold, K. H. (1990). Angew. Chem. Int. Ed. Engl., **29**, 775.

Noh, S. K., Sendlinger, S. C., Janiak, C. & Theopold, K. H. (1989). J. Am. Chem. Soc., **111**, 9127.

North, A. C. T., Phillips, D. C. & Matthews, F. S. (1968). Acta Crystallogr., **A24**, 351-359.

Nugent, W. A. & Harlow, R. L. (1978). J. Chem. Soc. Chem. Commun., 579.

Nugent, W. A. & Mayer, J. M. (1988). *'Metal-Ligand Multiple Bonds'*, Wiley Interscience, New York.

Nugent, W. A. & Taber, D. F. (1989). J. Am. Chem. Soc., **111**, 6435.

Poole, A. D., Gibson, V. C. & Clegg, W. (1992). J. Chem. Soc, Chem. Commun., 237.

Poole, A. D., Williams, D. N., Kenwright, A. N., Gibson, V. C., Clegg, W., Hockless, D. C. R. & O'Neil, P. A. (1993). Organometallics, **12**, 2549.

Resconi, L. & Waymouth, R. M. (1990). J. Am. Chem. Soc., **112**, 4953.

Rothwell, I. P. (1988). Acc. Chem. Res., **21**, 153.

Schmidt, S. & Sundermeyer, J. (1994). J. Organomet. Chem., **472**, 127.

Schoettel, G., Kress, J. & Osborn, J. A. (1989). J. Chem. Soc., Chem. Commun., 1062.

Schrock, R. R. (1990). Acc. Chem. Res., **23**, 158.

Schwartz, J. & Labinger, J. A. (1976). Angew. Chem. Int. Ed. Engl., **15**, 333 and references therein.

Scollard, J. D., McConville, D. H. & Rettig, S. J. (1997). Organometallics, **16**, 1810.

Sheldrick, G. M. (1990).Acta Crystallogr. **A46**, 467-473.

Sheldrick, G. M. (1993). SHELXL-93. *Program for the Refinement of Crystal Structures using Single Crystal Diffraction Data*, University of Göttingen, Germany.

Sheldrick, G. M. (1995). SHELXTL. Version 5.03/VMS. Siemens Analytical X-ray Instruments, Inc., Madison, Wisconsin, U.S.A.

Sheldrick, G. M. (1995). XPREP in SHELXTL. Version 5.03/VMS. Siemens Analytical X-ray Instruments, Inc., Madison, Wisconsin, U.S.A.

Siemeling, U. & Gibson, V. C. (1992). J. Organomet. Chem., **426**, C25.

Siemens Analytical X-ray Instruments, (1994). XSCANS. *X-ray Single Crystals Analysis System*, Version 2.1, Siemens Analytical X-ray Instruments, Inc., Madison, Wisconsin, U.S.A.

Siemens Analytical X-ray Instruments, (1995a). SMART. Version 4.050. Siemens Analytical X-ray Instruments, Inc., Madison, Wisconsin, U.S.A.

Siemens Analytical X-ray Instruments, (1995b). SAINT. Version 4.050. Siemens Analytical X-ray Instruments, Inc., Madison, Wisconsin, U.S.A.

Solan, G. A., Cozzi, P. G., Floriani, C., Chiesi-Villa, A. & Rizzoli, C. (1994). Organometallics, **13**, 2572.

Stalke, D. S. & Kottke, T. (1993). J. Appl. Cryst., **26**, 615-619.

Steffey, B. D., Fanwick, P. E. & Rothwell, I. P. (1990). Polyhedron, **9**, 963 and references therein.

Takahashi, T., Seki, T., Nitto, Y., Saburi, M., Rousset, C. J. & Negishi, E. (1991). J. Am. Chem. Soc., **113**, 6266.

Tidwell, J. H. & Buchwald, S. L. (1992). J. Org. Chem., **57**, 6380.

Tidwell, J. H. & Buchwald, S. L. (1994). J. Am. Chem. Soc., **116**, 11797.

Tidwell, J. H., Senn, D. R. & Buchwald, S. L. (1991). J. Am. Chem. Soc., **113**, 4685.

Tilley, T. D. (1993). Acc. Chem. Res., **26**, 22 and references therein.

Tjaden, E. B., Swenson, D. C. & Jordan, R. F. (1995). Organometallics, **14**, 371.

Uhrhammer, R., Black, D. G., Gardner, T. G., Olsen, J. D. & Jordan, R. F. (1993). J. Am. Chem. Soc., **115**, 8493.

Vahrenkamp, H. (1978). Chem. Ber., **111**, 3472.

van der Linden, A., Schaverien, C. J., Meijboom, N., Ganter, C. & Orpen, A. G. (1995). J. Am. Chem. Soc., **117**, 3008.

Viebrock, H. & Weiss, E. (1994). J. Org. Chem., **464**, 121.

Walker, N. & Stuart, D. (1983). Acta Crystallogr., **A39**, 158-166.

Warner, B. P., Davis, W. M. & Buchwald, S. L. (1994). J. Am. Chem. Soc., **116**, 5471.

Williams, D. N., Mitchell, J. P., Poole, A. D., Siemeling, U., Clegg, W., Hockless, D. C. R., O'Neil, P. A. & Gibson, V. C. (1992). J. Chem. Soc, Dalton Trans, 739-751.

Yang, X., Stern, C. L. & Marks, T. J. (1991). J. Am. Chem. Soc., **113**, 3623.

Yang, X., Stern, C. L. & Marks, T. J. (1994). J. Am. Chem. Soc., **116**, 10015.

CHAPTER 10

STRUCTURAL STUDIES OF (BIS)IMIDO GROUP VIA TRANSITION METAL COMPLEXES.

10.1 INTRODUCTION

Whilst the previous chapter concentrated on the isolobal relationship between group IVA and group VA transition metals, the work presented here exploits the isolobal relationship between group VA and group VIA transition metals. Various group VIA isolobal analogues of the bent metallocenes have already been reported (Williams, Schofield, Anhaus & Schrock, 1990; Coles, Dalby, Gibson, Clegg & Elsegood, 1995; Sundermeyer & Runge, 1994) and several such complexes have been shown to be very efficient homogeneous ethylene polymerization catalysts (Coles, Dalby, Gibson, Clegg & Elsegood, 1995; Thomas & Theopold, 1988; Thomas, Noh, Schulte, Sendlinger & Theopold, 1991; Bhandari, Kim, McFarland, Rheingold & Theopold, 1995; Theopold, Heintz, Noh & Thomas, 1992).

Whilst Theopold and co-workers (Thomas & Theopold, 1988; Thomas, Noh, Schulte, Sendlinger & Theopold, 1991; Bhandari, Kim, McFarland, Rheingold & Theopold, 1995; Theopold, Heintz, Noh & Thomas, 1992) have concentrated on half-sandwich group VIA systems, Gibson and co-workers at Durham have investigated bis(imido) group VIA species (Coles, Dalby, Gibson, Clegg & Elsegood, 1995).

As part of these investigations at Durham, the two molybdenum (bis)imido compounds reported in this chapter were synthesized and characterized. A neutron diffraction study shows that the structure of one of these compounds contains multiple α-agostic interactions. Such interactions are considered important in this area of research since it is thought that α-agostic interactions are involved in the mechanism of polymerization catalysis (Grubbs & Coates, 1996; Stovneng & Rytter, 1996). The second of these compounds is synthesized from the first by an oxygen insertion reaction. The X-ray derived structure of this compound is described.

10.2 MULTIPLE α-AGOSTIC INTERACTIONS IN A METAL-METHYL COMPLEX: THE NEUTRON STRUCTURE OF [Mo(N-C_6H_3-2,6-Pr^i_2)$_2Me_2$]

10.2.1 Abstract

The neutron structure of [Mo(N-C_6H_3-2,6-Pr^i_2)$_2Me_2$] (**1**) is described. Results show that multiple methyl α-agostic interactions are present.

10.2.2 Introduction

Since the formalization of the three-centre C-H...M 'agostic' interaction by Brookhart and Green in 1983, these interactions have been found to occur in many coordinatively unsaturated alkyl, aryl and poly-hapto hydrocarbon metal complexes (Poole et al, 1993; Bondcella, Cajigal & Abboud, 1996; Grubbs & Coates, 1996; Braga, Grepioni, Biradha & Desiraju, 1996; Etienne, Mathieu, & Donnadieu, 1997; Trakarnpruk, HylaKryspin, Arif, Gleiter & Ernst, 1997). They are relatively readily observed and detected in alkyl derivatives possessing β-hydrogens, either in solution for rapidly averaging agostic hydrogens via the effect of isotropic perturbation on C-H coupling constants and chemical shift positions, or in the solid state by diffraction methods[$] . Agostic interactions in metal-methyl species have proved more difficult to detect because (i) any isotropic perturbation of the resonance effect is diluted over a greater number of hydrogen environments and (ii) in X-ray structure determinations, there are no obvious ligand distortions of the type seen in longer chain alkyls and it is inherently difficult with X-rays to locate the methyl hydrogen atom positions with any accuracy. The only reliable method of establishing the presence of agostic interactions in metal-methyl complexes is via neutron diffraction.

To date, the only metal methyl complex to have been characterized by neutron diffraction that shows clear evidence for an agostic methyl C-H...M interaction is [TiMeCl_3($Me_2PCH_2CH_2PMe_2$)] (Dawoodi et al, 1986). Here, we describe the neutron structure of the coordinatively unsaturated molybdenum dimethyl complex [Mo(N-C_6H_3-2,6-Pr^i_2)$_2Me_2$] (**1**) which was prepared from the reaction of [Mo(N-C_6H_3-2,6-Pr^i_2)$_2Cl_2$(dme)] with two equivalents of methylmagnesium chloride.

[$] It should be noted that the evidence for β-agostic interactions is often derived from other structural parameters such as a low M-C-C bond angle rather than direct location of the agostic hydrogen atom position.

10.2.3 Experimental

The crystal structure of (**1**) was determined using the four circle diffractometer, D9, at the ILL, in a beam of wavelength 0.8405(2)Å, obtained by reflection from a Cu (220) monochromator. The crystal was smeared in silica grease, wrapped in aluminium foil and mounted on a vanadium pin in an argon atmosphere. The pin was then screwed into the cold head of the APD 201 Displex CCR (Archer & Lehmann, 1986) on D9. Data collection was carried out at 150K and no decay was observed during the experiment. Cell refinement and data collection proceeded via MAD (Barthelemy, 1984) software and the resulting data was reduced using RACER (Wilkinson, Khamis, Stansfield & McIntyre, 1988). Cryostat shield and crystal absorption corrections were made using the local program ABSCAN and the DATAP program (Coppens, 1970) respectively (transmission range: 0.6477-0.8045). The structure was refined by full-matrix least-squares refinement using SHELXL-93 (Sheldrick, 1993). Positional and anisotropic displacement parameters were refined for all atoms except for H(13A) and H(13'). For these two atoms, only positional and isotropic displacement parameters were refined since they are disordered in the ratio 2:1. A summary of crystal, data collection and refinement parameters is given in ***Table 10.2.1***.

Table 10.2.1 - *Crystallographic data for compound 1.*

Compound	1	Compound	1
Molecular Formula	$C_{26}H_{40}N_2Mo$	Absorption coefficient (mm^{-1})	0.233
Formula weight	475.94	Crystal Morphology	rectangular block
a(Å)	20.240(4)	Crystal Colour	orangey-red
b(Å)	6.550(1)	Crystal Size (mm)	6.0 x 1.8 x 1.0
c(Å)	19.910(4)	Total number of reflections	2355
α(°)	90	Unique reflections	2110
β(°)	103.99(3)	Observed Reflections [I>2σ(I)]	1450
γ(°)	90	R_{int}	0.0201
Cell Volume($Å^3$)	2561.2(8)	θ range (°)	3.28 - 30.01
Crystal System	monoclinic	Data / Parameters	2100 / 312
Space Group	C2/c	R1 [I > 2σ(I)]	0.0467
Z	4	wR2 [I > 2σ(I)]	0.0462
Calculated Density (gcm^{-1})	1.234	Goodness of fit on F^2	1.431
Temperature (K)	150.0(1)	Weighting Scheme	$1/\sigma^2$
Wavelength (Å)	0.8405(2)	$\Delta\rho_{(max, min)}$ ($fmÅ^{-3}$)	0.671 / -0.766

10.2.4 Results and discussion

A 50% probability thermal ellipsoid plot of structure **1** is shown in ***Figure 10.2.1*** and selected bond distances and angles are given in ***Table 10.2.2***. Fractional coordinates and anisotropic displacement parameters are given in ***Appendix A.10.1*** and ***A.10.2*** respectively.

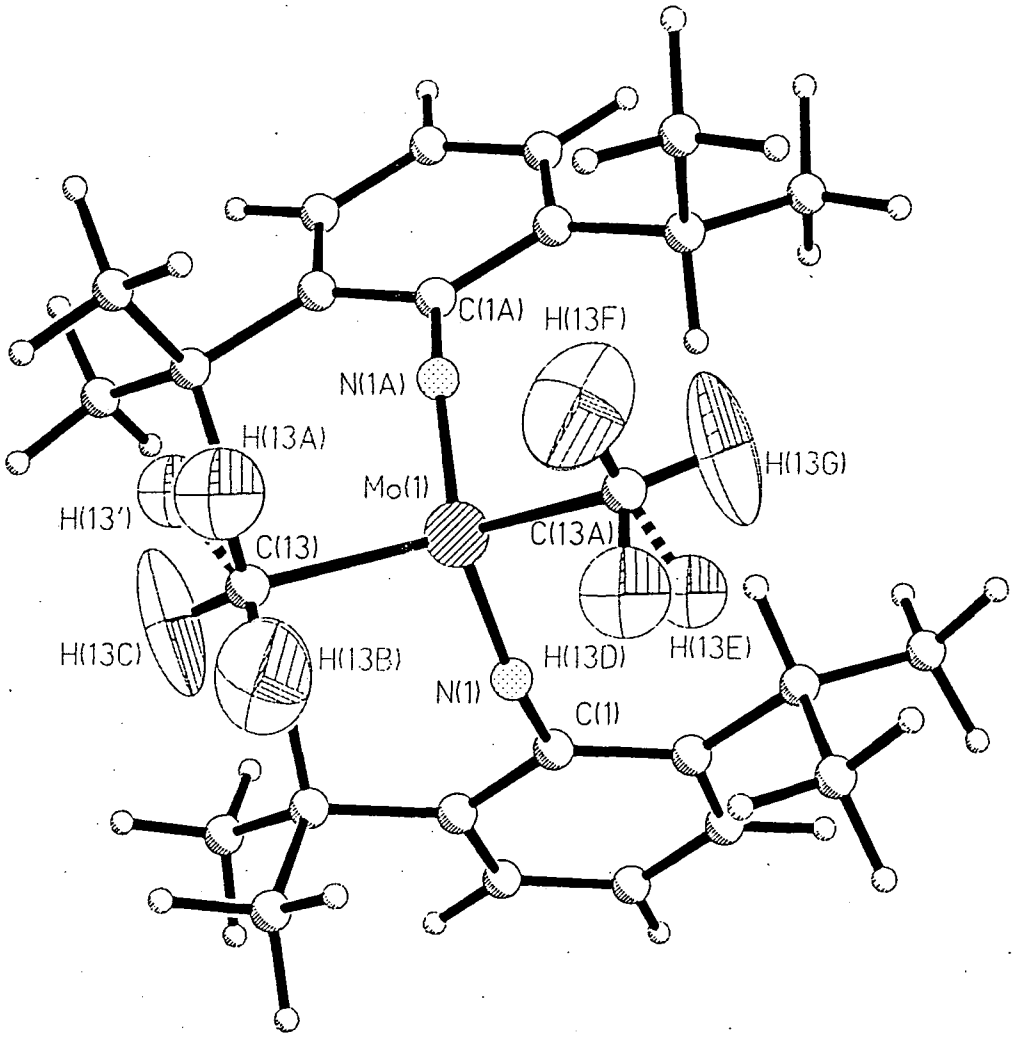

Figure 10.2.1 - The molecular structure of compound 1.

Table 10.2.2 *- Selected bond lengths and angles for compound* ***1****.*

Bond	Distance (Å)	Angle	Angle (°)
Mo(1)-N(1)	1.756(2)	N(1)-Mo(1)-N(1)#1	112.5(1)
Mo(1)-C(13)	2.112(2)	N(1)-Mo(1)-C(13)	107.86(7)
Mo(1)-H(13A)	2.585(8)	N(1)#1-Mo(1)-C(13)	107.29(8)
Mo(1)-H(13B)	2.598(5)	N(1)-Mo(1)-C(13)#1	107.29(8)
Mo(1)-H(13C)	2.755(5)	N(1)#1-Mo(1)-C(13)#1	107.86(7)
Mo(1)-H(13')	2.76(1)	C(13)-Mo(1)-C(13)#1	114.1(2)
N(1)-C(1)	1.382(2)	C(13)-Mo(1)-H(13A)	23.7(2)
C(13)-H(13A)	1.07(1)	C(13)-Mo(1)-H(13B)	23.4(2)
C(13)-H(13')	1.09(2)	C(13)-Mo(1)-H(13C)	19.8(2)
C(13)-H(13B)	1.068(7)	C(13)-Mo(1)-H(13')	21.0(3)
C(13)-H(13C)	1.049(8)	C(1)-N(1)-Mo(1)	159.6(1)
		Mo(1)-C(13)-H(13A)	103.7(4)
		Mo(1)-C(13)-H(13')	115.1(6)
		Mo(1)-C(13)-H(13B)	104.7(3)
		Mo(1)-C(13)-H(13C)	117.2(3)

Symmetry transformations used to generate equivalent atoms: #1 -x,y,-z+1/2

The two methyl groups are crystallographically equivalent so the following discussion concentrates on only one methyl group. A large amount of librational motion exists, thus disguising the exact position of the hydrogen atoms. However, this motion is clearly directed towards the Mo atom (***Figure 10.2.1***) and one can see that the hydrogen atoms, H(13A) and H(13B), lie distinctly closer to the Mo atom than the hydrogen atoms H(13C) and H(13') (the minor disordered part of H(13A) where the occupancy of H(13A):H(13') is 2:1 respectively).

Despite the librational effects, the average geometry gives conclusive results. The coordination of each methyl group is markedly distorted from regular tetrahedral geometry and of special note are the particularly small angles Mo(1)-C(13)-H(13A) [103.7(4)°] and Mo(1)-C(13)-H(13B) [104.7(3)°] which are indicative of agostic interactions where the hydrogen atoms are being 'pulled in' towards the metal atom. Consequently, the angles, C(13)-H(13A)...Mo(1) [52.6(2)°] and C(13)-H(13B)...Mo(1) [51.8(2)°], are noticeably larger than those corresponding to the hydrogen atoms, H(13C) and H(13') [43.0(2)° and 43.9(3)° respectively].

Since the electron density in an agostic interaction is considered to originate from the

centre of a C-H bond (Brookhart and Green, 1983) one would expect to see short Mo...H and C-Mo distances in the presence of such interactions. Indeed, this is apparent: the Mo(1)...H(13A) and Mo(1)...H(13B) distances [2.585(8)Å and 2.598(5)Å respectively] are noticeably shorter than the Mo(1)...H(13C) and Mo(1)...H(13') distances [2.755(5)Å and 2.76(1)Å respectively] and the Mo(1)-C(13) distance [2.112(2)Å] is very short [c.f. literature values (Orpen et al, 1989): Mo-C mean, 2.554Å, lower quartile, 2.189Å]. All C-H distances are identical within experimental error.

Of the two α-agostic hydrogen atoms per methyl group (therefore, four agostic interactions per molecule) both appear strong and of the same strength, judging by their relative geometries.

10.2.5 Conclusions

This neutron diffraction study shows clear evidence for four strong α-agostic methyl C-H...M interactions. The compound is therefore the second reported metal-methyl α-agostic complex and the first one to show *multiple* such interactions.

10.3 BIS(2,6-DIISOPROPYLPHENYL) METHYL (OXYMETHYL) MOLYBDENUM(VI) DIMER

10.3.1 Abstract

The molecular structure of $[MoMe(N\text{-}2,6\text{-}^{i}Pr_2C_6H_3)_2(\mu\text{-}OMe)]_2$ (**2**) is described. The oxo bridge is asymmetric and steric and electronic effects govern the geometry of the imido ligands. Unlike its previously described reaction precursor, $MoMe_2(N\text{-}2,6\text{-}Pr^{i}_2C_6H_3)_2$, (**1**) no agostic interactions are present in **2**.

10.3.2 Introduction

Reactions of alkyl and aryl transition metal compounds with small molecules (e.g. CO_2, NO, RNC) have been well-studied but those with dioxygen have received somewhat less attention. Indeed, only one such compound has been structurally characterized: that of $[(Me_3C)_3CO]Ti(Me_2)(\mu\text{-}OMe)]_2$ (Lublen & Wolczanski, 1987). Other studies have led invariably to oxo species (Koschmieder & Wilkinson, 1991). We therefore wished to develop this field of research and we were particularly interested in the reactivity of arylimido complexes with dioxygen. We therefore tested the reactivity of dioxygen with the previously described arylimido compound, $MoMe_2(N\text{-}2,6\text{-}Pr^{i}_2C_6H_3)_2$. The compound was found to react with dioxygen, yielding the title compound, (**2**). The X-ray structure of **1** was determined and is reported here.

10.3.3 Experimental

The crystal structure determination of **2** was carried out using the Siemens SMART-CCD diffractometer. The crystal was mounted using the oil-drop method (Stalke & Kottke, 1994) and graphite monochromatized Mo-Kα radiation (λ=0.71073Å) was employed. Data collection was carried out at 150K and no decay was observed during the experiment. Cell refinement, data collection and data reduction proceeded via Siemens SMART software (Siemens Analytical X-ray Instruments, 1995a and 1995b) A semi-empirical absorption correction using φ-scans was applied in XPREP (Sheldrick, 1995) [Tmin / Tmax = 0.8162 / 0.9476].

The structure was solved using SHELXS-86 (Sheldrick, 1990) by Patterson and difference Fourier methods. Subsequent least-squares refinement used the SHELXL-93 (Sheldrick, 1993) package. Scattering factors were taken from International Tables for Crystallography, Vol. C, 1992.

Positional and anisotropic displacement parameters were refined for all non-hydrogen

atoms. Hydrogen atoms were placed geometrically, refined using a riding model (including free rotation about C-C bonds for methyl groups) and isotropic displacement parameters for all hydrogen atoms except for those belonging to methyl groups were modelled in the riding model [$U_{iso}(H) = 1.2\ U_{eq}(C)$]. All methyl hydrogen atoms were modelled in the riding model [$U_{iso}(H) = 1.5\ U_{eq}(C)$]. Two deuterated hexane solvent molecules per molecule of **2** were located in the crystal lattice. Its atoms were modelled in the same manner to those in molecule **2**.

A summary of the crystal, data collection and refinement parameters is given in ***Table 10.3.1***.

Table 10.3.1 *- Crystallographic data for compound 2.*

Compound	2	Compound	2
Molecular Formula	$MoC_{26}H_{40}N_2O$ .C_6D_6	Absorption coefficient (mm^{-1})	0.463
Formula weight	570.65	Crystal Morphology	block
a(Å)	10.0757(6)	Crystal Colour	orange
b(Å)	11.3939(7)	Crystal Size (mm)	0.32 x 0.50 x 0.62
c(Å)	14.3761(9)	Total number of reflections	6468
α(°)	93.136(1)	Unique reflections	4795
β(°)	99.548(1)	Observed Reflections [I>2σ(I)]	4542
γ(°)	111.915(1)	R_{int}	0.0206
Cell Volume($Å^3$)	1497.6(2)	θ range (°)	1.45 - 25.39
Crystal System	triclinic	Data / Parameters	4783 / 361
Space Group	P-1	R1 [I > 2σ(I)]	0.0288
Z	2	wR2 [I > 2σ(I)]	0.0777
Calculated Density (gcm^{-1})	1.265	Goodness of fit on F^2	1.105
Temperature (K)	150.0(1)	Weighting Scheme	a = 0.0444; b = 1.3741
Wavelength (Å)	0.71073	$\Delta\rho_{(max, min)}$ ($eÅ^{-3}$)	0.369 / -0.679

10.3.4 Results and discussion

The molecular structure of **2** is shown in ***Figure 10.3.1***. Selected bond distances and angles for **2** are given in ***Table 10.3.2***. Fractional coordinates and anisotropic displacement parameters are given in ***Appendix A.10.3*** and ***A.10.4*** respectively.

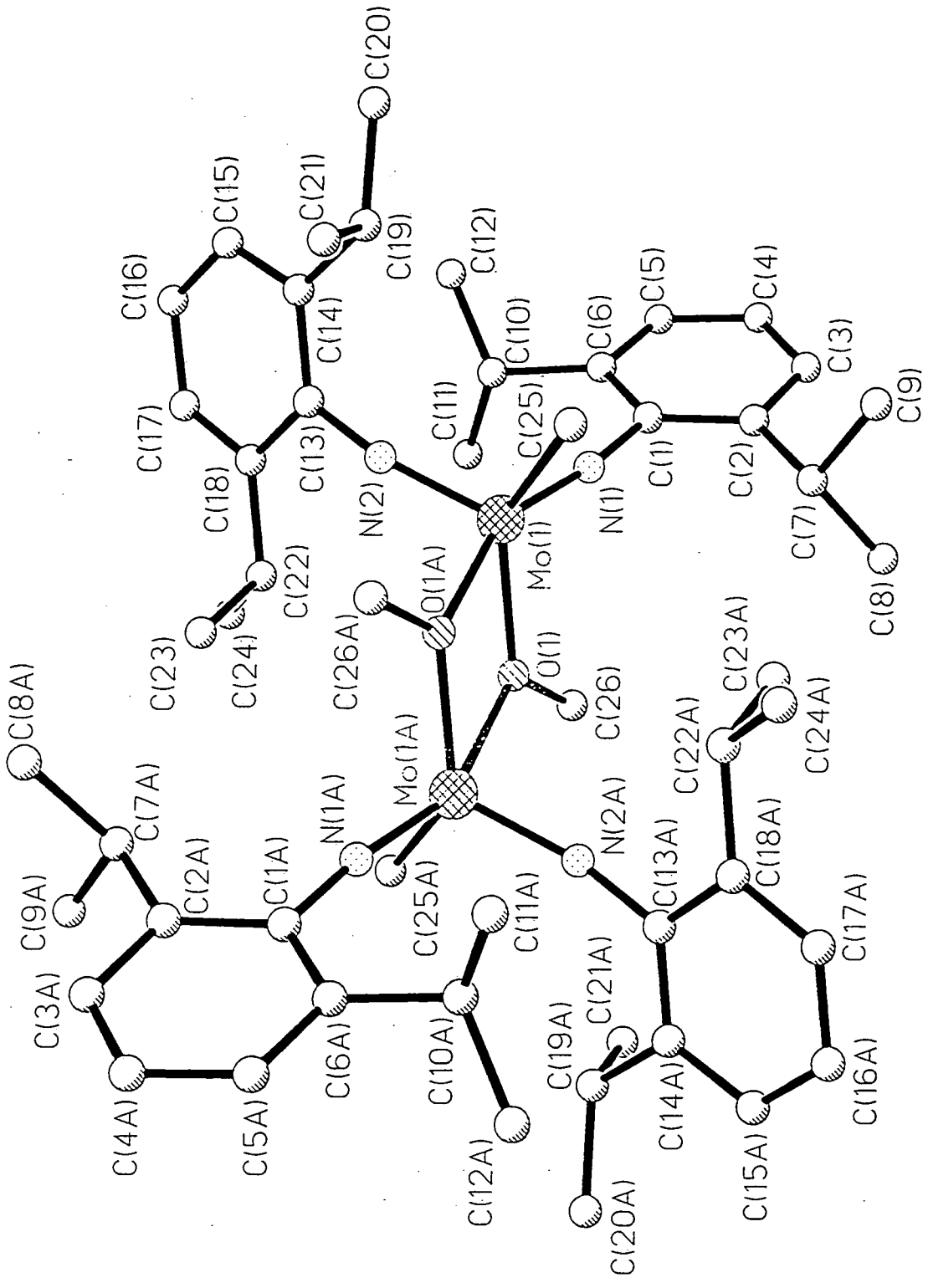

Figure 10.3.1 *- The molecular structure of compound 2.*

Table 10.3.2 *- Selected bond lengths and angles for compound 2.*

Bond	Distance (Å)	Angle	Angle (°)
Mo(1)-N(1)	1.764(2)	N(2)-Mo(1)-N(1)	107.82(9)
Mo(1)-N(2)	1.754(2)	N(1)-Mo(1)-O(1)	97.27(8)
Mo(1)-O(1)	2.048(2)	N(2)-Mo(1)-O(1)	117.65(8)
Mo(1)-O(1)#1	2.207(2)	N(1)-Mo(1)-C(25)	93.6(1)
Mo(1)-C(25)	2.161(3)	N(2)-Mo(1)-C(25)	103.5(1)
O(1)-C(26)	1.430(3)	O(1)-Mo(1)-C(25)	131.34(9)
N(1)-C(1)	1.397(3)	N(1)-Mo(1)-O(1)#1	156.97(8)
N(2)-C(13)	1.401(3)	N(2)-Mo(1)-O(1)#1	94.99(8)
		O(1)-Mo(1)-O(1)#1	68.42(7)
		C(25)-Mo(1)-O(1)#1	83.91(8)
		C(26)-O(1)-Mo(1)	123.6(2)
		C(26)-O(1)-Mo(1)#1	123.2(2)
		Mo(1)-O(1)-Mo(1)#1	111.58(7)
		C(1)-N(1)-Mo(1)	173.2(2)
		C(13)-N(2)-Mo(1)	156.3(2)

The molecule exists as a dimeric species with each Mo metal situated in a highly distorted trigonal bipyramid. The oxo bridge is primarily responsible for this large distortion with a Mo-O-Mo angle of 68.42(7)°. This bridge is fairly asymmetric with Mo(1)-O(1) and Mo(1)-O(1A) distances of 2.048(2)Å and 2.207(2)Å respectively. The shorter of these two distances is typical for Mo-O_{μ}-alkoxy bonds [from literature values (Orpen et al, 1989): mean 2.094Å] whereas the larger value is very long [from literature values (Orpen et al, 1989): upper quartile, 2.154Å]. This asymmetry results because the one oxygen lone pair available for π-donation to the metal is oriented towards the Mo(1) atom.

The two Mo-N bonds are of a typical length [Mo(1)-N(1): 1.765(2)Å; Mo(1)-N(2): 1.754(2)Å] and the angles, Mo(1)-N(1)-C(1) and Mo(1)-N(2)-C(13), are 173.2(2)° and 156.3(2)° respectively. The difference in these angles is reflected in the proton and carbon NMR spectra* . Therefore, we presume that the orientation of π-orbital involved in the N(2)-Mo(1) interaction is slightly less favourable than that of the N(1)-Mo(1) interaction (Williams, Schofield, Anhaus & Schrock, 1990). Given the bulky nature of the imido ligands, steric factors may also play a role in the marked deviation from linearity of the Mo(1)-N(2)-C(13) angle. Indeed, steric factors are thought to be the cause of the large

* ^{1}H NMR(250MHz, C_6D_6, 298K): 7.10-6.90 (m, 12H, *m*- and *p*-C_6H_3-2,6-$^{i}Pr_2$) and ^{13}C NMR(100MHz, C_6D_6, 298K): 152.59 (s, *ipso*- C_6H_3-2,6-$^{i}Pr_2$), 144.23 (s, *o*-C_6H_3-2,6-$^{i}Pr_2$) as determined by Gary L. P. Walker at Durham.

twist angle [109.1(3)°] between the two phenyl rings of each imido ligand (not related by symmetry).

The Mo-C_{Me} distance [2.161(3)Å] is quite short [literature values of Mo-C_{Me} (Orpen et al, 1989): mean: 2.254Å; lower quartile: 2.189Å] but is longer than the equivalent distance in the monomeric reaction precursor [2.112(2)Å - see previous section]. Unlike the reaction precursor, no agostic interactions are thought to be present since very little residual electron density around the Mo atom was observed and ^1H NMR results showed no evidence of any such interactions[#] .

[#] 1H NMR(250MHz, C_6D_6, 298K): 1.45 (s, 6H, CH_3) as determined by Gary L. P. Walker at Durham.

10.4 REFERENCES

Orpen, A. G., Brammer, L., Allen, F. H., Kennard, O., Watson, D. G. & Taylor, R. (1989). J. Chem. Soc., Dalton Trans., S1-S83.

Archer, J. M. & Lehmann, M. S. (1986). J. Appl. Cryst., **19**, 456-458.

Barthelemy, A. (1984). MAD. Institut Laue Langevin Technical Report, 84BA15T.

Bhandari, G., Kim, Y., McFarland, J. M., Rheingold, A. L. & Theopold, K. H. (1995). Organometallics, **14**, 738.

Bondcella, J. M., Cajigal, M. L. & Abboud, K. A. (1996). Organometallics, **15**, 1905-1912.

Braga, D., Grepioni, F., Biradha, K. & Desiraju, G. R. (1996). J. Chem. Soc., Dalton Trans., 3925-3930.

Brookhart, M. & Green, M. L. H. (1983). J. Organomet. Chem., **250**, 395-408.

Coles, M. P., Dalby, C. I., Gibson, V. C., Clegg, W. & Elsegood, M. R. J. (1995). J. Chem. Soc., Chem. Commun., 1709-1711.

Coppens, P. (1970). DATAP. *The Evaluation of Absorption and Extinction in Single-Crystal Structure Analysis* in "Crystallographic Computing", Ed. Ahmed, F. R., (Munksgaard, Copenhagen).

Dawoodi, Z., Green, M. L. H., Mtetwa, V. S. B., Prout, K., Schultz, A. J., Williams, J. M. & Koetzle, T. F. (1986). J. Chem. Soc., Dalton Trans., 1629-1637.

Etienne, M., Mathieu, R. & Donnadieu, B. (1997). J. Am. Chem. Soc., **119**, 3218-3228.

Grubbs, R. H. & Coates, G. W. (1996). Acc. Chem. Res., **29**, 85-93.

International Tables for Crystallography, Volume C, Mathematical, Physical and Chemical Tables (1992). Ed. Wilson, A. J. C., Dordrecht, Boston, London. Tables 4.2.6.8 & 6.1.1.4. 219-222, 500-503.

Koschmieder, S. U. & Wilkinson, G. (1991). Polyhedron, **10**, 135 and references therein.

Lublen, T. V. & Wolczanski, P. T. (1987). J. Am. Chem. Soc., **109**, 424.

Poole, A. D., Williams, D. N., Kenwright, A. M., Gibson, V. C., Clegg, W., Hockless, D. C. R. & O'Neil, P. A. (1993). Organometallics, **12**, 2549-2555.

Sheldrick, G. M. (1990). Acta Crystallogr. **A46**, 467-473.

Sheldrick, G. M. (1993). SHELXL-93. *Program for the Refinement of Crystal Structures using Single Crystal Diffraction Data*, University of Göttingen, Germany.

Sheldrick, G. M. (1995). XPREP in SHELXTL. Version 5.03/VMS. Siemens Analytical X-ray Instruments, Inc., Madison, Wisconsin, U.S.A.

Siemens Analytical X-ray Instruments, (1995a). SMART. Version 4.050. Siemens Analytical X-ray Instruments, Inc., Madison, Wisconsin, U.S.A.

Siemens Analytical X-ray Instruments, (1995b). SAINT. Version 4.050. Siemens

Analytical X-ray Instruments, Inc., Madison, Wisconsin, U.S.A.

Stalke, D. S. & Kottke, T. (1993). J. Appl. Cryst., **26**, 615-619.

Stovneng, J. A. & Rytter, E. (1996). J. Organomet. Chem., **519**, 277-280.

Sundermeyer, J. & Runge, D. (1994). Angew. Chem. Int. Ed. Engl., **33**, 1255-1257.

Theopold, K. H., Heintz, R. A., Noh, S. K. & Thomas, B. J. (1992) in *'Homogeneous Transition Metal Catalysed Reactions'*, Ed. Moser, W. R. & Slocum, D., ACS, Washington, DC, p. 591.

Thomas, B. J. & Theopold, K. H. (1988). J. Am. Chem. Soc., **110**, 5902.

Thomas, B. J., Noh, S. -K., Schulte, G. K., Sendlinger, S. C. & Theopold, K. H. (1991). J. Am. Chem. Soc., **113**, 893.

Trakarnpruk, W., HylaKryspin, I, Arif, A. M., Gleiter, R. & Ernst, R. D. (1997). Inorganica Chimica Acta., **259**, 197-202.

Wilkinson, C., Khamis, H. W., Stansfield, R. F. D. & McIntyre, G. J. (1988). J. Appl. Cryst., **21**, 471-478.

Williams, D. S., Schofield, M. H., Anhaus, J. T. & Schrock, R. R. (1990). J. Am. Chem. Soc., **112**, 6728-6729.

APPENDIX

APPENDIX A

ATOMIC COORDINATES, EQUIVALENT AND ANISOTROPIC DISPLACEMENT PARAMETERS FOR ALL REPORTED STRUCTURAL DETERMINATIONS.

Table A.4.1 *- Atomic coordinates (x 10^4) and equivalent isotropic displacement parameters ($Å^2$ x 10^3) for the 150K X-ray structure of* ***I****.*

Atom	x	y	z	U(eq)
N(1)	5222(2)	12287(1)	-3515(1)	41(1)
N(2)	8684(2)	10467(2)	-3361(1)	43(1)
N(3)	7624(2)	9985(1)	2818(1)	22(1)
N(4)	7848(2)	8346(1)	2123(1)	24(1)
C(1)	6077(2)	11736(2)	-3052(2)	30(1)
C(2)	7953(2)	10754(2)	-2975(2)	31(1)
C(3)	7097(2)	11067(2)	-2448(2)	26(1)
C(4)	7250(2)	10667(2)	-1321(2)	23(1)
C(5)	6415(2)	10952(2)	-765(2)	27(1)
C(6)	6567(2)	10551(2)	303(2)	26(1)
C(7)	7525(2)	9825(1)	850(2)	21(1)
C(8)	8362(2)	9537(2)	312(2)	24(1)
C(9)	8231(2)	9955(2)	-742(2)	25(1)
C(10)	7664(2)	9375(2)	1965(2)	22(1)
C(11)	8019(2)	11094(2)	2897(2)	26(1)
C(12)	9108(2)	11318(2)	4034(2)	33(1)
C(13)	7144(2)	9611(2)	3705(2)	25(1)
C(14)	6099(2)	10323(2)	3777(2)	34(1)
C(15)	8628(2)	7890(2)	3261(2)	27(1)
C(16)	9684(2)	7198(2)	3180(2)	31(1)
C(17)	7286(2)	7604(2)	1155(2)	28(1)
C(18)	6458(2)	6798(2)	1435(2)	32(1)
H(5)	5703(19)	11427(15)	-1163(16)	40(6)
H(6)	5981(17)	10790(13)	671(14)	27(6)
H(8)	9078(17)	9036(13)	709(14)	24(5)
H(9)	8828(17)	9781(13)	-1062(13)	19(5)
H(11A)	8334(18)	11239(15)	2226(15)	37(6)
H(11B)	7175(20)	11529(15)	2763(16)	46(7)
H(12A)	9338(20)	12077(17)	4038(16)	49(7)
H(12B)	8852(19)	11182(16)	4703(17)	51(7)
H(12C)	9899(20)	10891(15)	4114(16)	42(7)
H(13A)	7885(16)	9569(13)	4515(14)	22(5)
H(13B)	6718(17)	8914(14)	3450(14)	24(5)
H(14A)	5688(23)	10010(17)	4260(19)	70(8)
H(14B)	5389(21)	10407(16)	2987(18)	53(7)
H(14C)	6474(18)	11002(15)	4128(15)	34(6)
H(15A)	8035(16)	7482(13)	3565(13)	17(5)
H(15B)	9055(17)	8482(14)	3783(15)	31(6)
H(16A)	9354(18)	6583(15)	2701(15)	36(6)
H(16B)	10244(18)	6935(15)	3974(16)	39(6)
H(16C)	10267(20)	7600(15)	2874(16)	47(7)
H(17A)	8050(18)	7238(14)	968(15)	37(6)
H(17B)	6786(18)	8004(14)	457(15)	31(6)
H(18A)	5788(20)	7090(16)	1670(16)	45(7)
H(18B)	6966(19)	6300(16)	2074(17)	43(6)
H(18C)	5984(19)	6386(16)	722(17)	48(7)

Table A.4.2 *- Anisotropic displacement parameters ($Å^2 \times 10^3$) for the 150K X-ray structure of* ***I****.*

Atom	U11	U22	U33	U23	U13	U12
N(1)	46(1)	39(1)	31(1)	7(1)	6(1)	-3(1)
N(2)	59(1)	43(1)	35(1)	4(1)	28(1)	-2(1)
N(3)	28(1)	18(1)	21(1)	0(1)	11(1)	-2(1)
N(4)	30(1)	22(1)	18(1)	-1(1)	8(1)	-2(1)
C(1)	38(2)	29(1)	20(1)	-1(1)	7(1)	-12(1)
C(2)	43(2)	25(1)	22(1)	5(1)	10(1)	-7(1)
C(3)	32(1)	26(1)	22(1)	2(1)	11(1)	-2(1)
C(4)	27(1)	20(1)	21(1)	-2(1)	7(1)	-5(1)
C(5)	28(1)	26(1)	24(1)	2(1)	6(1)	3(1)
C(6)	26(1)	29(1)	23(1)	-2(1)	10(1)	0(1)
C(7)	22(1)	21(1)	19(1)	2(1)	6(1)	-1(1)
C(8)	24(1)	24(1)	24(1)	0(1)	8(1)	2(1)
C(9)	28(1)	26(1)	25(1)	-3(1)	14(1)	-1(1)
C(10)	19(1)	26(1)	21(1)	0(1)	7(1)	-4(1)
C(11)	34(1)	20(1)	24(1)	-1(1)	11(1)	-5(1)
C(12)	39(2)	32(1)	26(1)	-4(1)	10(1)	-10(1)
C(13)	29(1)	26(1)	24(1)	3(1)	15(1)	0(1)
C(14)	35(2)	34(2)	38(1)	-2(1)	21(1)	-1(1)
C(15)	34(1)	24(1)	20(1)	1(1)	8(1)	2(1)
C(16)	35(2)	24(1)	33(1)	-2(1)	12(1)	2(1)
C(17)	36(1)	26(1)	20(1)	-4(1)	8(1)	-5(1)
C(18)	35(2)	26(1)	35(1)	-2(1)	12(1)	-4(1)

Table A.4.3 *- Atomic coordinates (x 10^4) and equivalent isotropic displacement parameters ($Å^2$ x 10^3) for the 150K X-ray Structure of* ***II****.*

Atom	x	y	z	U(eq)
N(1)	2839(5)	2220(2)	4240(5)	38(1)
N(2)	3554(5)	3441(2)	-842(4)	36(1)
N(3)	2779(5)	-1703(2)	-5357(4)	29(1)
N(4)	3309(4)	-2524(2)	-1035(3)	20(1)
C(1)	2908(5)	2131(2)	2760(5)	26(1)
C(2)	3320(5)	2785(2)	-42(4)	25(1)
C(3)	3044(5)	1983(2)	966(4)	24(1)
C(4)	2883(5)	1061(2)	201(4)	21(1)
C(5)	2506(5)	272(2)	1184(4)	24(1)
C(6)	2450(5)	-617(2)	512(4)	22(1)
C(7)	2820(5)	-789(2)	-1185(4)	20(1)
C(8)	3057(5)	12(2)	-2231(4)	22(1)
C(9)	3099(5)	902(2)	-1558(4)	22(1)
C(10)	2983(5)	-1705(2)	-1889(4)	20(1)
C(11)	2831(5)	-1733(2)	-3843(4)	22(1)
C(12)	4167(5)	-2657(2)	978(4)	24(1)
C(13)	2802(5)	-3285(2)	1687(4)	25(1)
C(14)	2518(6)	-4242(2)	720(4)	27(1)
C(15)	1820(5)	-4101(2)	-1374(4)	27(1)
C(16)	3167(6)	-3434(2)	-2006(4)	24(1)
C(17)	1063(7)	-4859(2)	1341(5)	41(1)
H(5)	2129(64)	359(23)	2319(53)	29
H(6)	2067(60)	-1145(24)	1156(45)	27
H(8)	3203(63)	-48(24)	-3475(52)	26
H(9)	3260(61)	1441(24)	-2243(49)	26
H(12A)	4452(60)	-2043(28)	1636(47)	28
H(12B)	5490(66)	-2956(25)	1193(50)	28
H(13A)	1445(66)	-2969(25)	1473(49)	30
H(13B)	3504(63)	-3385(24)	3021(52)	30
H(14)	3901(68)	-4604(27)	1085(50)	32
H(15A)	375(68)	-3843(28)	-1718(51)	32
H(15B)	1821(68)	-4707(26)	-1988(52)	32
H(16A)	2623(64)	-3305(23)	-3396(53)	28
H(16B)	4599(64)	-3680(26)	-1641(49)	28
H(17A)	-316(86)	-4589(31)	1073(63)	49
H(17B)	957(78)	-5539(30)	721(58)	49
H(17C)	1539(79)	-4970(30)	2720(64)	49

Table A.4.4 *- Anisotropic displacement parameters ($Å^2 \times 10^3$) for the 150K X-ray structure of* ***II****.*

Atom	U11	U22	U33	U23	U13	U12
N(1)	39(2)	42(2)	41(2)	-14(1)	22(1)	-8(1)
N(2)	47(2)	25(2)	32(2)	1(1)	7(1)	0(1)
N(3)	35(2)	28(1)	25(2)	-2(1)	11(1)	-4(1)
N(4)	23(2)	17(1)	20(1)	-4(1)	8(1)	-1(1)
C(1)	21(2)	24(2)	34(2)	-7(1)	10(2)	-3(1)
C(2)	24(2)	24(2)	24(2)	-11(1)	2(1)	3(1)
C(3)	22(2)	23(2)	27(2)	-2(1)	9(2)	3(1)
C(4)	15(1)	25(1)	23(2)	-3(1)	5(1)	1(1)
C(5)	25(2)	29(2)	22(2)	1(1)	12(1)	4(1)
C(6)	23(2)	24(1)	21(2)	1(1)	9(1)	-1(1)
C(7)	19(2)	22(1)	20(1)	1(1)	6(1)	-1(1)
C(8)	23(2)	23(2)	20(1)	-1(1)	7(1)	0(1)
C(9)	21(2)	22(2)	20(2)	3(1)	5(1)	-3(1)
C(10)	16(1)	24(2)	18(2)	-1(1)	4(1)	-2(1)
C(11)	21(2)	19(1)	27(2)	-1(1)	9(1)	-2(1)
C(12)	27(2)	22(2)	19(1)	0(1)	2(1)	1(1)
C(13)	29(2)	24(2)	20(2)	0(1)	6(1)	-2(2)
C(14)	32(2)	18(1)	30(2)	1(1)	7(1)	0(1)
C(15)	31(2)	20(1)	27(2)	-4(1)	5(1)	1(1)
C(16)	34(2)	18(1)	20(2)	-3(1)	9(1)	1(1)
C(17)	53(3)	32(2)	42(2)	-1(2)	21(2)	-9(2)

Table A.4.5 *- Atomic coordinates (x 10^4) and equivalent isotropic displacement parameters ($Å^2$ x 10^3) for* ***III****.*

Atom	x	y	z	U(eq)
N(1)	-6560(3)	4289(3)	7485(1)	45(1)
N(2)	-1275(3)	3526(3)	8803(1)	38(1)
N(3)	4915(3)	1275(3)	3877(1)	36(1)
N(4)	1101(2)	1667(2)	1499(1)	27(1)
C(1)	-4926(3)	3955(3)	7431(1)	31(1)
C(2)	-2012(3)	3548(3)	8147(2)	28(1)
C(3)	-2921(3)	3543(3)	7346(1)	26(1)
C(4)	-1875(3)	3181(3)	6496(1)	23(1)
C(5)	-2802(3)	3169(3)	5700(1)	25(1)
C(6)	-1811(3)	2824(3)	4883(1)	25(1)
C(7)	194(3)	2440(3)	4791(1)	21(1)
C(8)	1122(3)	2434(3)	5588(1)	24(1)
C(9)	133(3)	2803(3)	6404(1)	25(1)
C(10)	1241(3)	2062(3)	3938(1)	23(1)
C(11)	3287(3)	1608(3)	3929(1)	25(1)
C(12)	497(3)	2129(3)	3104(1)	25(1)
C(13)	1641(3)	1600(3)	2328(1)	25(1)
C(14)	-854(3)	2442(3)	1259(2)	32(1)
C(15)	-2162(4)	955(4)	1575(2)	44(1)
C(16)	2486(3)	1031(3)	751(2)	33(1)
C(17)	3151(4)	2689(4)	45(2)	43(1)
H(5)	-4175(31)	3380(30)	5747(14)	31
H(6)	-2513(28)	2830(29)	4354(14)	27
H(8)	2515(30)	2131(29)	5534(14)	26
H(9)	766(29)	2852(29)	6902(15)	27
H(12)	-849(31)	2533(30)	3071(14)	30
H(13)	3022(29)	1046(28)	2394(13)	24
H(14B)	-759(31)	2916(32)	546(16)	42
H(14A)	-1296(30)	3609(33)	1537(15)	35
H(15A)	-2327(34)	572(37)	2262(19)	53
H(15B)	-1633(39)	-329(44)	1313(20)	74
H(15C)	-3428(38)	1552(38)	1324(18)	57
H(16A)	1820(32)	272(33)	446(16)	41
H(16B)	3557(31)	181(32)	1065(15)	33
H(17A)	2046(40)	3544(42)	-293(19)	66
H(17B)	4138(39)	2190(39)	-438(19)	63
H(17C)	3761(33)	3508(36)	342(17)	45

Table A.4.6 *- Anisotropic displacement parameters ($Å^2 \times 10^3$) for the 150K X-ray structure of* ***III****.*

Atom	U11	U22	U33	U23	U13	U12
N(1)	32(1)	67(2)	37(1)	-20(1)	-1(1)	-3(1)
N(2)	40(1)	49(1)	27(1)	-13(1)	-5(1)	-5(1)
N(3)	28(1)	47(1)	34(1)	-8(1)	-5(1)	-6(1)
N(4)	29(1)	30(1)	22(1)	-6(1)	-4(1)	0(1)
C(1)	34(1)	35(1)	23(1)	-7(1)	-2(1)	-3(1)
C(2)	30(1)	27(1)	26(1)	-6(1)	1(1)	-4(1)
C(3)	27(1)	26(1)	24(1)	-5(1)	-3(1)	-4(1)
C(4)	26(1)	17(1)	26(1)	-2(1)	-5(1)	-5(1)
C(5)	21(1)	30(1)	26(1)	-5(1)	-4(1)	-7(1)
C(6)	24(1)	27(1)	26(1)	-3(1)	-7(1)	-6(1)
C(7)	24(1)	18(1)	22(1)	-3(1)	-5(1)	-4(1)
C(8)	22(1)	24(1)	26(1)	-2(1)	-6(1)	-3(1)
C(9)	27(1)	27(1)	23(1)	-5(1)	-9(1)	-5(1)
C(10)	24(1)	20(1)	25(1)	-2(1)	-4(1)	-5(1)
C(11)	31(1)	25(1)	21(1)	-4(1)	-5(1)	-6(1)
C(12)	24(1)	27(1)	24(1)	-4(1)	-5(1)	-3(1)
C(13)	26(1)	22(1)	27(1)	-3(1)	-3(1)	-4(1)
C(14)	34(1)	39(1)	22(1)	-8(1)	-8(1)	6(1)
C(15)	34(1)	59(2)	41(2)	-11(1)	-11(1)	-7(1)
C(16)	36(1)	34(1)	27(1)	-11(1)	0(1)	3(1)
C(17)	46(2)	42(2)	31(1)	-5(1)	8(1)	3(1)

Table A.4.7 *- Atomic coordinates (x 10^4) and equivalent isotropic displacement parameters (Å^2 x 10^3) for the 150K X-ray structure of* ***IV****.*

Atom	x	y	z	U(eq)
N(1)	10145(10)	3833(3)	4356(9)	55(2)
N(2)	4942(9)	3145(2)	1674(10)	55(2)
N(3)	-243(10)	6057(3)	778(10)	52(2)
N(4)	3992(8)	6526(2)	2637(8)	36(2)
C(1)	8631(12)	3901(3)	3663(12)	36(2)
C(2)	5735(12)	3526(3)	2208(11)	40(2)
C(3)	6730(10)	3984(3)	2833(12)	32(2)
C(4)	5902(10)	4496(3)	2693(11)	31(2)
C(5)	6933(10)	4956(3)	3331(11)	31(2)
C(6)	6128(10)	5452(3)	3206(10)	31(2)
C(7)	4221(9)	5541(3)	2402(10)	24(2)
C(8)	3198(10)	5074(3)	1760(12)	35(2)
C(9)	3978(10)	4579(3)	1911(11)	36(2)
C(10)	3323(9)	6040(3)	2222(12)	32(2)
C(11)	1324(12)	6052(3)	1427(12)	36(2)
C(12)	6046(9)	6660(3)	3130(11)	42(2)
C(13)	6150(15)	7270(4)	2724(15)	40(3)
C(13')	5889(53)	7241(14)	3663(51)	74(12)
C(14)	4234(39)	7452(11)	2338(42)	42(9)
C(14')	4163(14)	7447(4)	3437(16)	40(3)
C(15)	2767(9)	7018(2)	2502(11)	46(2)
H(5)	8253(10)	4911(3)	3809(11)	37
H(6)	6865(10)	5748(3)	3703(10)	37
H(8)	1931(10)	5117(3)	1162(12)	43
H(9)	3271(10)	4271(3)	1475(11)	44
H(12A)	6924(9)	6474(3)	2373(11)	50
H(12B)	6359(9)	6576(3)	4379(11)	50
H(13A)	7259(15)	7441(4)	3350(15)	47
H(13B)	6191(15)	7335(4)	1432(15)	47
H(13C)	7095(53)	7419(14)	3370(51)	89
H(13D)	5658(53)	7296(14)	4936(51)	89
H(14A)	3735(39)	7788(11)	2776(42)	50
H(14B)	4610(39)	7498(11)	1097(42)	50
H(14C)	3814(14)	7807(4)	3064(16)	48
H(14D)	4175(14)	7421(4)	4747(16)	48
H(15A)	1613(9)	6982(2)	3184(11)	55
H(15B)	2396(9)	7100(2)	1263(11)	55

Table A.4.8. - *Anisotropic displacement parameters ($Å^2 \times 10^3$) for the 150K X-ray structure of* ***IV****.*

Atom	U11	U22	U33	U23	U13	U12
N(1)	44(5)	60(5)	58(6)	3(4)	-15(4)	8(4)
N(2)	57(4)	38(4)	71(6)	-12(4)	-1(4)	4(4)
N(3)	32(4)	64(5)	59(6)	-2(4)	-6(4)	-1(4)
N(4)	26(4)	29(4)	53(5)	-1(4)	5(4)	-2(3)
C(1)	37(6)	32(5)	40(7)	5(5)	7(5)	0(4)
C(2)	41(5)	49(5)	30(6)	-7(5)	-3(4)	13(5)
C(3)	34(6)	31(5)	31(7)	1(4)	-7(5)	-7(4)
C(4)	28(5)	36(5)	28(6)	6(5)	4(4)	2(5)
C(5)	26(5)	35(5)	32(7)	1(5)	6(4)	-6(4)
C(6)	31(5)	41(5)	21(6)	-10(5)	4(4)	-4(5)
C(7)	15(4)	37(5)	21(6)	4(4)	-1(4)	0(4)
C(8)	26(5)	43(5)	37(7)	-1(5)	0(4)	0(4)
C(9)	33(5)	25(5)	50(7)	5(5)	-2(5)	-8(4)
C(10)	15(5)	44(6)	37(7)	7(5)	-3(4)	0(4)
C(11)	38(6)	38(5)	33(7)	-4(5)	3(5)	-3(5)
C(12)	32(4)	33(4)	61(6)	-5(4)	5(4)	3(4)
C(15)	34(4)	30(4)	75(6)	9(5)	6(4)	9(4)

Table A.4.9 *- Atomic coordinates (x 10^4) and equivalent isotropic displacement parameters ($Å^2$ x 10^3) for the 150K X-ray structure of* ***V****.*

Atom	x	y	z	U(eq)
N(1)	3662(2)	10663(2)	7942(1)	42(1)
N(2)	3785(2)	5993(2)	6333(1)	36(1)
N(3)	2021(2)	-96(2)	10772(1)	31(1)
N(4)	1201(2)	-436(2)	12845(1)	41(1)
N(5)	1535(2)	3788(2)	13475(1)	24(1)
C(1)	3527(2)	9159(2)	7896(1)	29(1)
C(2)	3573(2)	6563(2)	7012(1)	26(1)
C(3)	3320(2)	7286(2)	7854(1)	24(1)
C(4)	2958(2)	6230(2)	8623(1)	22(1)
C(5)	2805(2)	7036(2)	9474(1)	24(1)
C(6)	2512(2)	6061(2)	10231(1)	24(1)
C(7)	2358(2)	4199(2)	10220(1)	21(1)
C(8)	2497(2)	3398(2)	9366(1)	23(1)
C(9)	2773(2)	4359(2)	8600(1)	23(1)
C(10)	2091(2)	3177(2)	11010(1)	21(1)
C(11)	2018(2)	1333(2)	10893(1)	23(1)
C(12)	1979(2)	3885(2)	11876(1)	24(1)
C(13)	1666(2)	2991(2)	12686(1)	22(1)
C(14)	1412(2)	1072(2)	12746(1)	28(1)
C(15)	1718(2)	5711(2)	13556(1)	26(1)
C(16)	3879(3)	7243(2)	13859(1)	36(1)
C(17)	1414(2)	2874(2)	14345(1)	28(1)
C(18)	-742(3)	1658(2)	14507(1)	34(1)
H(5)	2892(24)	8267(24)	9486(11)	31
H(6)	2446(23)	6694(21)	10791(11)	26
H(8)	2418(25)	2156(24)	9337(11)	33
H(9)	2851(25)	3792(24)	8025(12)	35
H(12)	2155(23)	5152(22)	11930(11)	27
H(15A)	868(22)	5692(20)	14009(11)	23
H(15B)	1191(24)	5963(22)	12966(12)	30
H(16A)	3956(27)	8522(27)	13902(13)	44
H(16B)	4733(28)	7241(26)	13420(13)	44
H(16C)	4346(28)	7020(26)	14477(14)	45
H(17A)	2165(25)	3932(24)	14829(12)	35
H(17B)	2119(24)	2111(22)	14329(11)	27
H(18A)	-702(28)	1232(26)	15150(14)	47
H(18B)	-1414(29)	566(27)	14057(14)	45
H(18C)	-1470(26)	2447(25)	14462(12)	39

Table A.4.10 *- Anisotropic displacement parameters ($Å^2$ x 10^3) for the 150K X-ray structure of* ***V****.*

Atom	U11	U22	U33	U23	U13	U12
N(1)	67(1)	37(1)	32(1)	7(1)	12(1)	32(1)
N(2)	45(1)	43(1)	24(1)	1(1)	5(1)	25(1)
N(3)	37(1)	26(1)	32(1)	1(1)	5(1)	16(1)
N(4)	60(1)	30(1)	35(1)	5(1)	6(1)	24(1)
N(5)	33(1)	22(1)	19(1)	3(1)	4(1)	13(1)
C(1)	39(1)	33(1)	19(1)	4(1)	6(1)	20(1)
C(2)	26(1)	28(1)	22(1)	3(1)	1(1)	13(1)
C(3)	26(1)	24(1)	21(1)	1(1)	3(1)	13(1)
C(4)	20(1)	24(1)	21(1)	0(1)	2(1)	10(1)
C(5)	29(1)	22(1)	23(1)	0(1)	5(1)	14(1)
C(6)	28(1)	23(1)	21(1)	-1(1)	4(1)	13(1)
C(7)	20(1)	20(1)	21(1)	0(1)	3(1)	9(1)
C(8)	22(1)	20(1)	25(1)	-2(1)	3(1)	9(1)
C(9)	24(1)	22(1)	21(1)	-2(1)	3(1)	10(1)
C(10)	18(1)	19(1)	24(1)	-1(1)	1(1)	8(1)
C(11)	22(1)	24(1)	21(1)	2(1)	3(1)	9(1)
C(12)	29(1)	21(1)	22(1)	2(1)	4(1)	13(1)
C(13)	24(1)	22(1)	22(1)	1(1)	2(1)	12(1)
C(14)	33(1)	28(1)	23(1)	2(1)	3(1)	15(1)
C(15)	37(1)	24(1)	22(1)	1(1)	6(1)	17(1)
C(16)	41(1)	26(1)	36(1)	4(1)	7(1)	12(1)
C(17)	41(1)	28(1)	18(1)	4(1)	2(1)	18(1)
C(18)	43(1)	36(1)	30(1)	11(1)	12(1)	22(1)

Table A.4.11 *- Atomic coordinates (x 10^4) and equivalent isotropic displacement parameters (Å^2 x 10^3) for the 150K X-ray structure of* ***VI.***

Atom	x	y	z	U(eq)
N(1)	14463(4)	5818(1)	4903(2)	37(1)
N(2)	14946(5)	7227(1)	7035(2)	42(1)
N(3)	4723(4)	5825(1)	8835(2)	40(1)
N(4)	2508(4)	4008(1)	7480(2)	23(1)
C(1)	13865(5)	6032(1)	5526(2)	27(1)
C(2)	14121(5)	6806(1)	6689(2)	28(1)
C(3)	13098(5)	6287(1)	6273(2)	25(1)
C(4)	11304(5)	6050(1)	6558(2)	24(1)
C(5)	10282(4)	5530(1)	6130(2)	24(1)
C(6)	8546(5)	5301(1)	6394(2)	25(1)
C(7)	7706(4)	5568(1)	7119(2)	23(1)
C(8)	8705(5)	6089(1)	7537(2)	26(1)
C(9)	10441(5)	6318(1)	7270(2)	26(1)
C(10)	5968(4)	5311(1)	7445(2)	24(1)
C(11)	5317(5)	5608(1)	8224(2)	27(1)
C(12)	4913(4)	4787(1)	7126(2)	23(1)
C(13)	3504(4)	4523(1)	7629(2)	25(1)
C(14)	2658(5)	3621(1)	6669(2)	25(1)
C(15)	559(5)	3412(1)	6186(2)	32(1)
C(16)	817(5)	3033(2)	5349(2)	37(1)
C(17)	2234(5)	2490(2)	5616(2)	37(1)
C(18)	4320(5)	2697(1)	6115(2)	34(1)
C(19)	4090(5)	3082(1)	6950(2)	29(1)
C(20)	1346(5)	3778(1)	8196(2)	24(1)
C(21)	2773(5)	3657(2)	9093(2)	28(1)
C(22)	1544(5)	3423(1)	9811(2)	30(1)
C(23)	-122(5)	3877(2)	9951(2)	34(1)
C(24)	-1563(5)	3987(2)	9057(2)	36(1)
C(25)	-386(5)	4213(2)	8313(2)	31(1)
H(5A)	10731(4)	5355(1)	5604(2)	29
H(6A)	7959(5)	4931(1)	6129(2)	30
H(8A)	8158(5)	6290(1)	8018(2)	31
H(9A)	11081(5)	6670(1)	7572(2)	31
H(12A)	5135(4)	4603(1)	6565(2)	28
H(13A)	3236(4)	4760(1)	8139(2)	30
H(14A)	3224(5)	3868(1)	6239(2)	30
H(15A)	-293(5)	3758(1)	6008(2)	38
H(15B)	-73(5)	3171(1)	6602(2)	38
H(16A)	1385(5)	3286(2)	4926(2)	44
H(16B)	-491(5)	2890(2)	5051(2)	44
H(17A)	2389(5)	2264(2)	5078(2)	44
H(17B)	1631(5)	2226(2)	6014(2)	44
H(18A)	4988(5)	2926(1)	5698(2)	40
H(18B)	5153(5)	2350(1)	6311(2)	40
H(19A)	3573(5)	2837(1)	7396(2)	35
H(19B)	5411(5)	3231(1)	7222(2)	35
H(20A)	745(5)	3397(1)	7984(2)	29
H(21A)	3499(5)	4020(2)	9302(2)	34
H(21B)	3760(5)	3355(2)	8994(2)	34
H(22A)	2444(5)	3385(1)	10384(2)	36
H(22B)	979(5)	3031(1)	9643(2)	36

H(23A)	465(5)	4255(2)	10188(2)	41
H(23B)	-901(5)	3716(2)	10387(2)	41
H(24A)	-2541(5)	4291(2)	9156(2)	43
H(24B)	-2300(5)	3623(2)	8860(2)	43
H(25A)	-1302(5)	4235(2)	7742(2)	37
H(25B)	145(5)	4612(2)	8459(2)	37

Table A.4.12 *- Anisotropic displacement parameters ($Å^2$ x 10^3) for the 150K X-ray structure of* ***VI****.*

Atom	U11	U22	U33	U23	U13	U12
N(1)	40(2)	39(2)	33(2)	-5(1)	8(1)	-11(1)
N(2)	40(2)	31(2)	56(2)	-6(1)	12(2)	-7(1)
N(3)	40(2)	41(2)	40(2)	-13(1)	11(1)	-10(1)
N(4)	24(1)	23(1)	23(1)	0(1)	6(1)	-1(1)
C(1)	26(2)	24(2)	29(2)	3(1)	3(1)	-5(1)
C(2)	26(2)	23(2)	35(2)	1(1)	7(1)	1(1)
C(3)	27(2)	21(2)	25(2)	0(1)	5(1)	1(1)
C(4)	24(2)	21(2)	24(2)	1(1)	1(1)	0(1)
C(5)	23(2)	28(2)	22(1)	0(1)	4(1)	-3(1)
C(6)	30(2)	21(2)	24(1)	0(1)	5(1)	-4(1)
C(7)	24(2)	21(2)	24(1)	1(1)	3(1)	1(1)
C(8)	26(2)	25(2)	26(2)	-3(1)	6(1)	1(1)
C(9)	27(2)	20(2)	31(2)	-4(1)	5(1)	-4(1)
C(10)	24(2)	22(2)	23(1)	1(1)	0(1)	3(1)
C(11)	27(2)	23(2)	30(2)	-3(1)	5(1)	-4(1)
C(12)	22(2)	23(2)	23(1)	2(1)	4(1)	0(1)
C(13)	24(2)	24(2)	27(2)	1(1)	3(1)	1(1)
C(14)	31(2)	22(2)	24(1)	-2(1)	8(1)	-2(1)
C(15)	30(2)	28(2)	34(2)	-2(1)	-1(1)	4(1)
C(16)	45(2)	30(2)	32(2)	-5(1)	-5(2)	1(2)
C(17)	51(2)	25(2)	34(2)	-6(1)	5(2)	3(2)
C(18)	43(2)	26(2)	33(2)	-2(1)	9(2)	4(1)
C(19)	30(2)	28(2)	28(2)	-1(1)	3(1)	2(1)
C(20)	24(2)	24(2)	24(1)	2(1)	6(1)	-5(1)
C(21)	30(2)	29(2)	25(2)	1(1)	5(1)	0(1)
C(22)	34(2)	32(2)	23(2)	4(1)	3(1)	-4(1)
C(23)	38(2)	33(2)	32(2)	-2(1)	10(2)	-5(2)
C(24)	30(2)	42(2)	38(2)	5(2)	11(2)	1(2)
C(25)	28(2)	33(2)	32(2)	9(1)	8(1)	4(1)

Table A.4.13 *- Atomic coordinates (x 10^4) and equivalent isotropic displacement parameters ($Å^2$ x 10^3) for the 150K X-ray structure of* ***VII****.*

Atom	x	y	z	U(eq)
Cl(1)	-240(1)	2618(4)	3052(2)	93(1)
O(1)	571(2)	9101(7)	4129(5)	62(2)
O(2)	691(2)	11770(7)	4955(5)	62(2)
N(1)	3407(2)	18088(8)	7150(6)	57(2)
N(2)	3783(2)	12850(8)	8149(5)	47(2)
N(3)	2084(2)	8325(7)	5651(5)	38(2)
N(4)	1248(2)	11975(6)	4353(5)	34(2)
C(1)	3360(2)	16620(10)	7223(6)	39(2)
C(2)	3564(2)	13688(10)	7771(6)	40(2)
C(3)	3299(2)	14743(8)	7291(6)	33(2)
C(4)	2998(2)	14028(8)	6918(5)	29(2)
C(5)	2731(2)	15085(8)	6478(6)	31(2)
C(6)	2437(2)	14411(8)	6094(6)	34(2)
C(7)	2383(2)	12540(7)	6135(5)	27(2)
C(8)	2649(2)	11478(8)	6557(5)	31(2)
C(9)	2941(2)	12160(8)	6934(6)	34(2)
C(10)	2082(2)	11763(7)	5719(5)	27(2)
C(11)	2084(2)	9844(8)	5694(6)	31(2)
C(12)	1784(2)	12514(7)	5320(6)	29(2)
C(13)	1721(2)	14493(8)	5323(6)	35(2)
C(14)	1376(2)	14866(8)	5138(6)	43(2)
C(15)	1177(1)	13896(6)	4182(4)	39(2)
C(16)	1525(1)	11410(6)	4857(4)	29(2)
C(17)	991(2)	10719(8)	3885(6)	39(2)
C(18)	817(2)	10232(9)	4650(6)	43(2)
C(19A)	597(5)	7435(26)	4485(17)	80
C(19B)	458(7)	7861(31)	4697(19)	80
C(20)	283(3)	6442(13)	4036(8)	74(3)
C(21A)	685(5)	11659(29)	6063(17)	80
C(21B)	555(7)	11740(36)	5772(20)	80
C(22)	675(3)	13266(15)	6503(9)	93(4)
C(23)	0	1337(15)	2500	87(5)
H(5)	2758(2)	16329(8)	6448(6)	38
H(6)	2266(2)	15182(8)	5797(6)	41
H(8)	2622(2)	10232(8)	6579(5)	37
H(9)	3112(2)	11384(8)	7215(6)	41
H(13A)	1840(2)	15000(8)	6003(6)	42
H(13B)	1796(2)	15072(8)	4771(6)	42
H(14A)	1339(2)	16155(8)	5043(6)	51
H(14B)	1312(2)	14496(8)	5759(6)	51
H(15A)	951(1)	14117(6)	4097(4)	47
H(15B)	1228(1)	14309(6)	3546(4)	47
H(16)	1556(1)	10166(6)	4920(4)	35
H(17A)	1080(2)	9638(8)	3658(6)	46
H(17B)	845(2)	11266(8)	3262(6)	46
H(18)	959(2)	9624(9)	5269(6)	51
H(19A)	653(5)	7439(26)	5257(17)	96
H(19B)	766(5)	6819(26)	4273(17)	96
H(19C)	319(7)	8460(31)	5056(19)	96
H(19D)	636(7)	7340(31)	5237(19)	96
H(20A)	100	6625	4320	111

H(20B)	331	5214	4089	111
H(20C)	210	6777	3306	111
H(20D)	81	7050	4001	111
H(20E)	278	5334	4389	111
H(20F)	286	6224	3337	111
H(21A)	498(5)	10967(29)	6096(17)	96
H(21B)	874(5)	11016(29)	6472(17)	96
H(21C)	606(7)	10608(36)	6157(20)	96
H(21D)	324(7)	11821(36)	5492(20)	96
H(22A)	884	13652	6631	139
H(22B)	615	13171	7132	139
H(22C)	535	14153	6055	139
H(22D)	616	13168	7136	139
H(22E)	533	14149	6058	139
H(22F)	883	13660	6626	139
H(23A)	134	565(15)	3046	105
H(23B)	-134	565(15)	1955	105

Table A.4.14. *- Anisotropic displacement parameters ($Å^2 \times 10^3$) for the 150K X-ray structure of* ***VII****.*

Atom	U11	U22	U33	U23	U13	U12
O(1)	63(5)	44(3)	70(4)	23(3)	4(4)	-27(3)
O(2)	84(6)	47(3)	72(4)	-2(3)	48(4)	2(3)
N(1)	63(6)	32(4)	74(6)	10(4)	17(4)	-14(4)
N(2)	42(6)	36(4)	56(5)	6(4)	0(4)	-11(4)
N(3)	41(5)	20(3)	56(5)	1(3)	18(4)	-2(3)
N(4)	44(5)	11(3)	48(4)	2(3)	15(4)	0(3)
C(1)	41(6)	33(5)	42(5)	5(4)	8(4)	-8(4)
C(2)	55(7)	24(4)	41(5)	4(4)	12(5)	-11(5)
C(3)	36(6)	19(4)	45(5)	0(4)	13(4)	-12(4)
C(4)	42(6)	21(4)	28(4)	-1(3)	14(4)	-5(4)
C(5)	39(6)	9(3)	49(5)	-6(3)	19(4)	-7(4)
C(6)	50(7)	12(3)	46(5)	0(3)	21(4)	4(4)
C(7)	38(6)	8(3)	35(4)	0(3)	11(4)	-4(4)
C(8)	44(6)	10(3)	37(5)	3(3)	9(4)	4(4)
C(9)	49(6)	14(3)	39(5)	-2(3)	12(4)	-3(4)
C(10)	42(6)	7(3)	36(5)	-6(3)	18(4)	-5(4)
C(11)	36(6)	15(4)	47(5)	3(3)	21(4)	8(3)
C(12)	34(6)	8(3)	52(5)	2(3)	23(4)	3(4)
C(13)	47(6)	14(3)	48(5)	0(3)	20(4)	7(3)
C(14)	55(7)	15(3)	66(6)	0(4)	30(5)	8(4)
C(15)	38(6)	17(3)	58(6)	-1(4)	8(4)	7(4)
C(16)	40(6)	12(3)	38(5)	1(3)	15(4)	1(4)
C(17)	45(6)	21(3)	49(5)	0(4)	12(4)	-6(4)
C(18)	38(6)	31(4)	56(6)	10(4)	7(4)	-4(4)
Cl(1)	102(3)	90(2)	94(2)	-28(2)	40(2)	-43(2)
C(23)	86(13)	33(6)	102(12)	0	-40(10)	0

Table A.4.15 *- Atomic coordinates (x 10 ^{4}) and equivalent isotropic displacement parameters (Å^2 x 10^3) for the 20K X-ray structure of compound* ***I****.*

Atom	x	y	z	U(eq)
N(1)	5205(1)	12289(1)	-3536(1)	11(1)
N(2)	8698(1)	10450(1)	-3374(1)	12(1)
N(3)	7622(1)	9986(1)	2825(1)	6(1)
N(4)	7860(1)	8341(1)	2128(1)	6(1)
C(1)	6068(1)	11732(1)	-3070(1)	8(1)
C(2)	7958(1)	10743(1)	-2988(1)	8(1)
C(3)	7102(1)	11063(1)	-2458(1)	7(1)
C(4)	7250(1)	10662(1)	-1335(1)	6(1)
C(5)	6408(1)	10959(1)	-774(1)	8(1)
C(6)	6553(1)	10558(1)	298(1)	7(1)
C(7)	7524(1)	9826(1)	851(1)	6(1)
C(8)	8368(1)	9531(1)	306(1)	7(1)
C(9)	8248(1)	9948(1)	-751(1)	7(1)
C(10)	7673(1)	9373(1)	1973(1)	6(1)
C(11)	8002(1)	11093(1)	2899(1)	7(1)
C(12)	9102(1)	11334(1)	4039(1)	10(1)
C(13)	7146(1)	9605(1)	3714(1)	7(1)
C(14)	6094(1)	10318(1)	3804(1)	10(1)
C(15)	8648(1)	7890(1)	3266(1)	7(1)
C(16)	9711(1)	7190(1)	3178(1)	9(1)
C(17)	7289(1)	7601(1)	1158(1)	8(1)
C(18)	6467(1)	6789(1)	1451(1)	10(1)
H(5)	5690(11)	11442(9)	-1148(10)	14(3)
H(6)	5957(10)	10761(8)	665(9)	8(3)
H(8)	9082(9)	9035(8)	695(9)	5(2)
H(9)	8846(10)	9748(8)	-1097(9)	9(3)
H(11A)	8285(10)	11247(8)	2260(9)	6(2)
H(11B)	7238(10)	11506(8)	2799(9)	5(2)
H(12A)	9347(10)	12072(9)	4048(10)	13(3)
H(12B)	8876(11)	11233(9)	4709(10)	16(3)
H(12C)	9868(11)	10916(9)	4136(10)	14(3)
H(13A)	7883(10)	9557(8)	4473(9)	8(3)
H(13B)	6778(10)	8894(9)	3474(9)	11(3)
H(14A)	6417(11)	10997(9)	4139(10)	16(3)
H(14B)	5703(11)	9982(9)	4320(10)	20(3)
H(14C)	5379(11)	10427(9)	3017(10)	18(3)
H(15A)	9031(10)	8482(8)	3777(9)	7(3)
H(15B)	8090(9)	7511(8)	3574(8)	2(2)
H(16A)	10271(12)	6929(10)	3979(11)	21(3)
H(16B)	9374(11)	6571(9)	2690(10)	16(3)
H(16C)	10266(11)	7594(9)	2861(9)	14(3)
H(17A)	7996(10)	7261(9)	984(9)	11(3)
H(17B)	6757(10)	7998(8)	462(9)	10(3)
H(18A)	5815(11)	7103(9)	1698(10)	15(3)
H(18B)	6993(11)	6309(9)	2061(10)	20(3)
H(18C)	6034(11)	6363(9)	767(10)	18(3)

Table A.4.16 *- Anisotropic displacement parameters ($Å^2 \times 10^3$) for the 20K X-ray structure of compound* ***I****.*

Atom	U11	U22	U33	U23	U13	U12
N(1)	12(1)	12(1)	10(1)	2(1)	2(1)	0(1)
N(2)	15(1)	13(1)	10(1)	1(1)	7(1)	0(1)
N(3)	8(1)	5(1)	5(1)	0(1)	4(1)	0(1)
N(4)	8(1)	6(1)	4(1)	0(1)	2(1)	0(1)
C(1)	10(1)	8(1)	6(1)	0(1)	3(1)	-2(1)
C(2)	11(1)	8(1)	6(1)	1(1)	3(1)	-1(1)
C(3)	9(1)	8(1)	5(1)	1(1)	3(1)	1(1)
C(4)	7(1)	7(1)	5(1)	0(1)	2(1)	-1(1)
C(5)	8(1)	8(1)	7(1)	2(1)	3(1)	2(1)
C(6)	7(1)	9(1)	6(1)	0(1)	3(1)	1(1)
C(7)	7(1)	7(1)	5(1)	0(1)	2(1)	0(1)
C(8)	8(1)	7(1)	6(1)	1(1)	3(1)	1(1)
C(9)	8(1)	8(1)	6(1)	0(1)	3(1)	0(1)
C(10)	6(1)	6(1)	5(1)	0(1)	2(1)	0(1)
C(11)	9(1)	6(1)	7(1)	0(1)	3(1)	-1(1)
C(12)	11(1)	11(1)	7(1)	-2(1)	2(1)	-3(1)
C(13)	9(1)	8(1)	7(1)	1(1)	5(1)	0(1)
C(14)	10(1)	10(1)	11(1)	0(1)	6(1)	1(1)
C(15)	9(1)	7(1)	5(1)	1(1)	2(1)	1(1)
C(16)	9(1)	8(1)	10(1)	0(1)	3(1)	2(1)
C(17)	10(1)	7(1)	6(1)	-1(1)	3(1)	-1(1)
C(18)	11(1)	8(1)	10(1)	0(1)	4(1)	-2(1)

Table A.4.17 *- Atomic coordinates (x 10^4) and equivalent isotropic displacement parameters ($Å^2$ x 10^3) for the 20K neutron structure of* ***I****.*

Atom	x	y	z	U(eq)
N(1)	5204(2)	12287(2)	-3534(2)	14(1)
N(2)	8698(2)	10450(2)	-3376(2)	14(1)
N(3)	7620(2)	9986(2)	2823(2)	8(1)
N(4)	7860(2)	8342(2)	2127(2)	8(1)
C(1)	6066(3)	11729(2)	-3068(2)	8(1)
C(2)	7956(3)	10745(2)	-2983(2)	10(1)
C(3)	7107(3)	11063(2)	-2456(2)	9(1)
C(4)	7248(3)	10665(2)	-1338(2)	7(1)
C(5)	6405(3)	10962(2)	-778(2)	9(1)
C(6)	6549(3)	10562(2)	298(2)	8(1)
C(7)	7527(3)	9822(2)	851(2)	7(1)
C(8)	8369(3)	9527(2)	306(2)	8(1)
C(9)	8251(3)	9947(2)	-754(2)	8(1)
C(10)	7673(3)	9376(2)	1972(2)	7(1)
C(11)	8000(3)	11094(2)	2898(2)	9(1)
C(12)	9099(3)	11336(2)	4042(2)	12(1)
C(13)	7145(3)	9605(2)	3712(2)	9(1)
C(14)	6093(3)	10319(2)	3804(2)	10(1)
C(15)	8650(3)	7892(2)	3265(2)	8(1)
C(16)	9710(3)	7190(2)	3179(2)	10(1)
C(17)	7292(3)	7602(2)	1161(2)	9(1)
C(18)	6462(3)	6789(2)	1449(3)	12(1)
H(5)	5645(7)	11516(6)	-1189(6)	26(1)
H(6)	5887(6)	10801(5)	709(5)	21(1)
H(8)	9141(7)	8981(5)	750(6)	25(1)
H(9)	8937(7)	9726(5)	-1139(5)	23(1)
H(11A)	8298(6)	11252(5)	2181(5)	21(1)
H(11B)	7166(6)	11566(5)	2785(6)	21(1)
H(12A)	9379(8)	12153(5)	4041(6)	30(2)
H(12B)	8838(7)	11205(6)	4778(5)	28(1)
H(12C)	9941(7)	10865(6)	4129(6)	31(2)
H(13A)	7949(6)	9544(6)	4555(5)	23(1)
H(13B)	6736(7)	8836(5)	3449(5)	22(1)
H(14A)	6463(7)	11065(6)	4177(7)	30(2)
H(14B)	5680(7)	9949(6)	4362(6)	31(2)
H(14C)	5320(6)	10449(6)	2957(6)	30(2)
H(15A)	9096(7)	8532(5)	3834(5)	24(1)
H(15B)	8036(6)	7470(5)	3628(5)	22(1)
H(16A)	10318(7)	6921(6)	4047(6)	29(2)
H(16B)	9348(7)	6503(5)	2642(6)	28(2)
H(16C)	10317(7)	7622(5)	2825(7)	30(2)
H(17A)	8056(6)	7240(5)	953(5)	23(1)
H(17B)	6700(6)	8041(5)	407(5)	23(1)
H(18A)	5761(7)	7151(6)	1739(7)	31(2)
H(18B)	7037(7)	6250(6)	2121(6)	30(2)
H(18C)	5959(8)	6341(6)	673(6)	34(2)

Table A.4.18 *- Anisotropic displacement parameters ($Å^2 \times 10^3$) for the 20K neutron structure of* ***I****.*

Atom	U11	U22	U33	U23	U13	U12
N(1)	13(1)	14(1)	12(1)	3(1)	2(1)	2(1)
N(2)	18(1)	14(1)	16(1)	1(1)	12(1)	1(1)
N(3)	11(1)	7(1)	8(1)	0(1)	6(1)	0(1)
N(4)	10(1)	6(1)	6(1)	0(1)	2(1)	1(1)
C(1)	9(1)	7(1)	8(1)	2(1)	2(1)	2(1)
C(2)	13(1)	10(1)	8(1)	0(1)	6(1)	0(1)
C(3)	12(1)	9(1)	6(1)	1(1)	5(1)	0(1)
C(4)	7(1)	7(1)	4(1)	1(1)	1(1)	1(1)
C(5)	9(1)	10(2)	9(1)	2(1)	5(1)	2(1)
C(6)	8(1)	9(1)	8(1)	4(1)	3(1)	3(1)
C(7)	7(1)	7(1)	7(1)	1(1)	5(1)	2(1)
C(8)	10(1)	10(1)	7(1)	2(1)	5(1)	0(1)
C(9)	7(1)	9(1)	9(1)	2(1)	4(1)	3(1)
C(10)	9(1)	7(1)	5(1)	0(1)	3(1)	0(1)
C(11)	11(2)	7(1)	8(1)	1(1)	2(1)	0(1)
C(12)	14(2)	11(2)	10(1)	-2(1)	4(1)	-4(1)
C(13)	7(1)	11(2)	9(1)	-1(1)	5(1)	0(1)
C(14)	8(1)	12(2)	12(1)	1(1)	5(1)	2(1)
C(15)	11(1)	8(1)	7(1)	0(1)	5(1)	3(1)
C(16)	9(1)	10(2)	10(1)	3(1)	2(1)	4(1)
C(17)	11(1)	9(1)	8(1)	-2(1)	4(1)	-5(1)
C(18)	14(2)	9(1)	12(1)	0(1)	5(1)	-3(1)
H(5)	23(3)	33(4)	22(3)	7(3)	7(3)	13(3)
H(6)	22(3)	24(3)	18(3)	5(2)	9(3)	10(3)
H(8)	23(3)	27(3)	25(3)	3(3)	10(3)	10(3)
H(9)	29(3)	24(3)	23(3)	5(2)	19(3)	9(3)
H(11A)	27(3)	24(3)	13(2)	-1(2)	8(2)	-9(3)
H(11B)	17(3)	14(3)	30(3)	-2(2)	6(3)	10(3)
H(12A)	41(4)	15(4)	35(4)	-4(3)	14(3)	-14(3)
H(12B)	30(3)	36(4)	17(3)	2(3)	8(3)	-4(3)
H(12C)	14(3)	41(4)	30(3)	-3(3)	1(3)	7(3)
H(13A)	19(3)	31(3)	15(3)	4(3)	1(3)	3(3)
H(13B)	33(3)	10(3)	27(3)	-1(2)	17(3)	1(3)
H(14A)	29(4)	26(4)	41(4)	-7(3)	19(3)	-2(3)
H(14B)	38(4)	29(4)	40(4)	8(3)	30(3)	4(3)
H(14C)	16(3)	46(4)	21(3)	4(3)	0(3)	11(3)
H(15A)	26(3)	22(3)	20(3)	-7(3)	2(3)	-3(3)
H(15B)	18(3)	28(3)	22(3)	9(2)	11(2)	3(3)
H(16A)	26(3)	34(4)	22(3)	5(3)	6(3)	11(3)
H(16B)	28(3)	20(3)	34(3)	-10(3)	11(3)	0(3)
H(16C)	25(3)	23(3)	51(4)	4(3)	24(3)	2(3)
H(17A)	25(3)	22(3)	28(3)	-4(2)	19(3)	1(3)
H(17B)	25(3)	23(3)	13(3)	1(2)	-1(3)	-2(3)
H(18A)	27(3)	26(3)	47(4)	-2(3)	22(3)	0(3)
H(18B)	26(3)	25(3)	33(4)	10(3)	3(3)	-3(3)
H(18C)	46(4)	28(4)	26(3)	-8(3)	10(3)	-19(3)

Table A.4.19 *- Atomic coordinates and equivalent isotropic displacement parameters for all non-hydrogen atoms in* ***I*** *as derived from the charge density study.*

Atom	x	y	z	U(eq)
N(1)	0.52031(13)	1.22900(10)	-0.35369(10)	0.010
N(2)	0.86993(13)	1.04489(10)	-0.33750(10)	0.012
N(3)	0.76230(9)	0.99858(7)	0.28257(7)	0.005
N(4)	0.78609(9)	0.83403(7)	0.21278(7)	0.005
C(1)	0.60715(11)	1.17302(8)	-0.30693(9)	0.007
C(2)	0.79551(11)	1.07455(8)	-0.29867(8)	0.008
C(3)	0.71014(10)	1.10622(8)	-0.24588(8)	0.007
C(4)	0.72493(10)	1.06629(7)	-0.13366(8)	0.006
C(5)	0.64065(10)	1.09603(8)	-0.07749(8)	0.007
C(6)	0.65513(9)	1.05595(8)	0.02999(8)	0.007
C(7)	0.75245(9)	0.98257(7)	0.08524(8)	0.005
C(8)	0.83700(9)	0.95300(7)	0.03078(8)	0.007
C(9)	0.82493(9)	0.99465(8)	-0.07524(8)	0.007
C(10)	0.76725(9)	0.93723(7)	0.19734(8)	0.005
C(11)	0.80015(10)	1.10920(7)	0.28974(8)	0.007
C(12)	0.91003(10)	1.13345(8)	0.40392(8)	0.009
C(13)	0.71470(10)	0.96045(8)	0.37130(8)	0.007
C(14)	0.60960(10)	1.03173(8)	0.38046(9)	0.010
C(15)	0.86466(10)	0.78911(7)	0.32645(8)	0.007
C(16)	0.97119(10)	0.71900(8)	0.31796(9)	0.009
C(17)	0.72898(10)	0.76029(8)	0.11587(8)	0.007
C(18)	0.64662(11)	0.67883(8)	0.14511(9)	0.009

Table A.4.20 *- Anisotropic displacement parameters for* ***I*** *as derived from the charge density study.*

Atom	U11	U22	U33	U23	U13	U12
N(1)	0.0083(4)	0.0105(4)	0.0098(4)	0.0028(3)	0.0007(3)	0.0019(4)
N(2)	0.0124(5)	0.0130(4)	0.0100(4)	0.0000(3)	0.0078(4)	0.0008(4)
N(3)	0.0076(3)	0.0040(3)	0.0043(3)	-0.0002(2)	0.0032(2)	-0.0005(2)
N(4)	0.0074(3)	0.0043(3)	0.0035(3)	-0.0001(2)	0.0014(2)	0.0002(2)
C(1)	0.0077(4)	0.0070(3)	0.0057(3)	0.0009(3)	0.0014(3)	0.0004(3)
C(2)	0.0091(4)	0.0083(4)	0.0056(3)	0.0003(3)	0.0039(3)	-0.0001(3)
C(3)	0.0078(4)	0.0076(3)	0.0044(3)	0.0015(3)	0.0025(3)	0.0006(3)
C(4)	0.0065(3)	0.0064(3)	0.0041(3)	0.0007(2)	0.0024(3)	0.0004(3)
C(5)	0.0077(4)	0.0078(3)	0.0053(3)	0.0019(3)	0.0029(3)	0.0022(3)
C(6)	0.0063(3)	0.0081(3)	0.0049(3)	0.0011(3)	0.0027(3)	0.0016(3)
C(7)	0.0058(3)	0.0056(3)	0.0045(3)	0.0005(2)	0.0026(3)	0.0006(3)
C(8)	0.0071(3)	0.0068(3)	0.0051(3)	0.0014(3)	0.0032(3)	0.0017(3)
C(9)	0.0071(3)	0.0075(3)	0.0050(3)	0.0010(3)	0.0029(3)	0.0011(3)
C(10)	0.0060(3)	0.0046(3)	0.0037(3)	0.0005(2)	0.0017(3)	0.0005(2)
C(11)	0.0077(3)	0.0053(3)	0.0054(3)	-0.0003(2)	0.0022(3)	-0.0009(3)
C(12)	0.0089(4)	0.0097(4)	0.0060(3)	-0.0017(3)	0.0017(3)	-0.0025(3)
C(13)	0.0078(3)	0.0067(3)	0.0059(3)	0.0003(3)	0.0039(3)	0.0006(3)
C(14)	0.0085(4)	0.0093(4)	0.0103(4)	0.0002(3)	0.0055(3)	0.0014(3)
C(15)	0.0078(3)	0.0062(3)	0.0047(3)	0.0003(3)	0.0021(3)	0.0013(3)
C(16)	0.0080(4)	0.0074(3)	0.0095(4)	-0.0001(3)	0.0028(3)	0.0015(3)
C(17)	0.0089(4)	0.0058(3)	0.0056(3)	-0.0008(3)	0.0026(3)	-0.0010(3)
C(18)	0.0100(4)	0.0071(3)	0.0094(4)	-0.0004(3)	0.0033(3)	-0.0020(3)

Table A.5.1 *- Atomic coordinates (x 10^4) and equivalent isotropic displacement parameters (Å^2 x 10^3) for the 20K X-ray structure of MBANP.*

Atom	x	y	z	U(eq)
O(1)	6478(5)	2991(5)	9696(1)	18(1)
O(2)	3146(5)	3300(5)	8918(1)	18(1)
N(1)	8797(6)	11360(5)	8005(2)	14(1)
N(2)	5700(5)	8778(5)	8023(2)	14(1)
N(3)	5217(5)	3955(5)	9194(2)	15(1)
C(1)	8092(6)	10797(6)	6619(2)	14(1)
C(2)	6276(6)	10835(6)	6014(2)	15(1)
C(3)	6606(7)	9609(6)	5368(2)	17(1)
C(4)	8712(7)	8367(6)	5317(2)	17(1)
C(5)	10543(7)	8334(6)	5918(2)	16(1)
C(6)	10238(6)	9546(6)	6564(2)	16(1)
C(7)	7765(6)	12259(6)	7293(2)	14(1)
C(8)	9060(7)	14378(6)	7161(2)	18(1)
C(9)	7913(6)	9580(6)	8322(2)	14(1)
C(10)	9307(6)	8622(6)	8943(2)	15(1)
C(11)	8455(6)	6760(6)	9238(2)	14(1)
C(12)	6182(7)	5932(6)	8917(2)	14(1)
C(13)	4883(7)	6982(6)	8329(2)	15(1)
H(1N)	9984(84)	11755(88)	8195(25)	17
H(2)	4596(80)	11690(86)	6071(24)	18
H(3)	5202(83)	9651(93)	4964(26)	20
H(4)	9089(78)	7623(92)	4888(25)	20
H(5)	12030(82)	7510(90)	5875(24)	19
H(6)	11533(80)	9553(89)	6992(24)	19
H(7)	5736(78)	12481(87)	7338(23)	17
H(8A)	8868(82)	15294(89)	7581(26)	21
H(8B)	8205(82)	15023(93)	6685(26)	21
H(8C)	10894(82)	14153(88)	7105(24)	21
H(10)	10947(79)	9322(86)	9131(24)	18
H(11)	9549(77)	6060(86)	9668(23)	17
H(13)	3338(80)	6417(85)	8120(24)	18

Table A.5.2 *- Anisotropic displacement parameters ($Å^2 \times 10^3$) for the 20K X-ray structure of MBANP.*

Atom	U11	U22	U33	U23	U13	U12
O(1)	24(1)	15(1)	15(1)	3(1)	-3(1)	2(1)
O(2)	19(1)	14(1)	21(1)	2(1)	-5(1)	-3(1)
N(1)	17(1)	11(1)	15(1)	0(1)	-5(1)	-3(1)
N(2)	16(1)	12(1)	14(1)	0(1)	-2(1)	-1(1)
N(3)	19(1)	12(1)	14(1)	0(1)	-1(1)	-1(1)
C(1)	20(2)	8(1)	14(1)	-1(1)	0(1)	-1(1)
C(2)	18(2)	12(1)	15(1)	1(1)	1(1)	-1(1)
C(3)	19(2)	15(2)	16(1)	1(1)	-4(1)	-1(1)
C(4)	22(2)	13(2)	15(1)	-1(1)	0(1)	-4(1)
C(5)	22(2)	9(1)	17(1)	1(1)	0(1)	1(1)
C(6)	18(2)	12(1)	17(1)	1(1)	-2(1)	-3(1)
C(7)	19(2)	12(2)	12(1)	0(1)	-3(1)	1(1)
C(8)	24(2)	12(2)	16(1)	1(1)	-1(1)	-2(1)
C(9)	16(1)	11(1)	14(1)	-1(1)	0(1)	-3(1)
C(10)	18(1)	13(2)	13(1)	-2(1)	-1(1)	-3(1)
C(11)	16(1)	12(2)	15(1)	1(1)	-1(1)	-1(1)
C(12)	18(1)	11(1)	13(1)	-1(1)	0(1)	-1(1)
C(13)	19(2)	11(1)	14(1)	-1(1)	-1(1)	0(1)

Table A.5.3 *- Atomic coordinates (x 10^4) and equivalent isotropic displacement parameters ($Å^2$ x 10^3) for the 100K X-ray structure of MBANP.*

Atom	x	y	z	U(eq)
O(1)	6418(5)	3012(7)	9688(2)	30(1)
O(2)	3182(5)	3321(7)	8913(2)	36(1)
N(1)	8825(6)	11351(8)	8005(2)	26(1)
N(2)	5722(6)	8783(6)	8019(2)	22(1)
N(3)	5204(6)	3990(7)	9191(2)	23(1)
C(1)	8121(6)	10745(8)	6617(2)	20(1)
C(2)	6293(7)	10834(10)	6016(2)	26(1)
C(3)	6586(7)	9600(9)	5369(2)	24(1)
C(4)	8734(7)	8361(9)	5328(2)	28(1)
C(5)	10552(7)	8326(8)	5924(2)	25(1)
C(6)	10243(7)	9541(9)	6573(2)	24(1)
C(7)	7798(7)	12235(9)	7291(2)	24(1)
C(8)	9086(8)	14346(9)	7161(2)	27(1)
C(9)	7933(6)	9577(8)	8322(2)	19(1)
C(10)	9323(7)	8597(9)	8943(2)	24(1)
C(11)	8435(7)	6795(9)	9237(2)	24(1)
C(12)	6189(7)	5944(9)	8914(2)	22(1)
C(13)	4887(7)	7008(9)	8319(2)	24(1)
H(1N)	10126(6)	12026(8)	8248(2)	31
H(2)	4819(7)	11696(10)	6050(2)	32
H(3)	5332(7)	9636(9)	4956(2)	29
H(4)	8951(7)	7533(9)	4883(2)	33
H(5)	12023(7)	7458(8)	5895(2)	30
H(6)	11511(7)	9540(9)	6982(2)	28
H(7)	6032(7)	12484(9)	7331(2)	29
H(8A)	8873(8)	15252(9)	7587(2)	33
H(8B)	8338(8)	14998(9)	6712(2)	33
H(8C)	10848(8)	14123(9)	7105(2)	33
H(10)	10877(7)	9200(9)	9147(2)	28
H(11)	9332(7)	6116(9)	9657(2)	29
H(13)	3326(7)	6428(9)	8112(2)	29

Table A.5.4 *- Anisotropic displacement parameters ($Å^2 \times 10^3$) for the 100K X-ray structure of MBANP.*

Atom	U11	U22	U33	U23	U13	U12
O(1)	36(2)	23(2)	31(1)	6(2)	3(1)	-1(2)
O(2)	35(2)	34(3)	38(2)	6(2)	-2(1)	-13(2)
N(1)	26(1)	30(3)	22(1)	0(2)	2(1)	-3(2)
N(2)	23(1)	21(2)	23(1)	-1(2)	4(1)	-4(2)
N(3)	26(2)	18(2)	24(1)	-1(2)	3(1)	-3(2)
C(1)	28(2)	6(2)	25(2)	-3(2)	7(1)	-5(2)
C(2)	32(2)	24(3)	25(2)	-2(2)	8(1)	4(2)
C(3)	23(2)	24(3)	26(2)	-4(2)	1(1)	1(2)
C(4)	35(2)	20(3)	28(2)	-1(2)	10(1)	-6(2)
C(5)	28(2)	19(3)	30(2)	-2(2)	12(1)	-2(2)
C(6)	25(2)	19(3)	28(2)	-2(2)	4(1)	-1(2)
C(7)	24(2)	21(3)	26(2)	1(2)	4(1)	2(2)
C(8)	37(2)	18(3)	28(2)	0(2)	6(2)	-4(2)
C(9)	23(2)	15(2)	21(2)	-2(2)	7(1)	-2(2)
C(10)	24(2)	25(3)	23(2)	-2(2)	5(1)	-2(2)
C(11)	27(2)	24(3)	21(2)	-1(2)	5(1)	-1(2)
C(12)	28(2)	13(2)	25(2)	1(2)	9(1)	-5(2)
C(13)	23(2)	26(3)	23(2)	-2(2)	2(1)	1(2)

Table A.5.5 *- Atomic coordinates (x 10^4) and equivalent isotropic displacement parameters ($Å^2$ x 10^3) for the 295K X-ray structure of MBANP.*

Atom	x	y	z	U(eq)
O(1)	6365(7)	1666(8)	4678(2)	74(1)
O(2)	3205(7)	1969(9)	3890(2)	84(1)
N(1)	8862(7)	9822(7)	2995(2)	58(1)
N(2)	5765(6)	7320(7)	3005(2)	50(1)
N(3)	5202(7)	2611(7)	4178(2)	55(1)
C(1)	8163(7)	9242(8)	1622(2)	45(1)
C(2)	6369(8)	9299(11)	1022(2)	59(1)
C(3)	6636(8)	8076(12)	395(2)	65(1)
C(4)	8723(9)	6862(11)	356(3)	67(2)
C(5)	10543(9)	6852(9)	940(3)	59(1)
C(6)	10259(8)	8048(9)	1583(2)	54(1)
C(7)	7857(8)	10694(9)	2290(2)	54(1)
C(8)	9136(12)	12795(9)	2171(3)	69(2)
C(9)	7953(7)	8092(8)	3313(2)	45(1)
C(10)	9287(7)	7149(9)	3934(2)	53(1)
C(11)	8400(7)	5362(9)	4226(2)	52(1)
C(12)	6189(7)	4529(8)	3903(2)	47(1)
C(13)	4924(7)	5573(9)	3307(2)	52(1)
H(1N)	10178(7)	10469(7)	3235(2)	70
H(2)	4933(8)	10177(11)	1047(2)	70
H(3)	5372(8)	8097(12)	-14(2)	78
H(4)	8903(9)	6010(11)	-77(3)	80
H(5)	12018(9)	6029(9)	904(3)	70
H(6)	11515(8)	8024(9)	1994(2)	65
H(7)	6114(8)	10942(9)	2322(2)	64
H(8A)	8937(12)	13688(9)	2592(3)	83
H(8B)	8388(12)	13445(9)	1725(3)	83
H(8C)	10875(12)	12574(9)	2121(3)	83
H(10)	10815(7)	7756(9)	4145(2)	64
H(11)	9257(7)	4705(9)	4654(2)	63
H(13)	3352(7)	5022(9)	3106(2)	62

Table A.5.6 *- Anisotropic displacement parameters ($Å^2 \times 10^3$) for the 295K X-ray structure of MBANP.*

Atom	U11	U22	U33	U23	U13	U12
O(1)	90(2)	64(3)	68(2)	17(2)	4(2)	-11(2)
O(2)	81(2)	75(3)	94(3)	17(3)	-6(2)	-30(3)
N(1)	62(2)	60(3)	52(2)	2(2)	1(1)	-17(2)
N(2)	49(2)	52(2)	49(2)	2(2)	-2(1)	-5(2)
N(3)	60(2)	48(3)	56(2)	1(2)	5(2)	-12(2)
C(1)	52(2)	34(2)	51(2)	-2(2)	10(1)	-8(2)
C(2)	57(2)	60(3)	58(2)	3(2)	9(2)	0(3)
C(3)	64(2)	74(4)	56(2)	-7(3)	-2(2)	-7(3)
C(4)	81(3)	59(4)	60(2)	-5(3)	15(2)	-13(3)
C(5)	64(2)	42(3)	72(2)	-2(2)	21(2)	0(2)
C(6)	56(2)	52(3)	54(2)	2(2)	7(2)	0(2)
C(7)	55(2)	54(3)	52(2)	1(2)	9(2)	-3(2)
C(8)	97(4)	45(3)	69(3)	-3(2)	21(3)	-11(3)
C(9)	51(2)	39(2)	47(2)	-1(2)	10(1)	-10(2)
C(10)	51(2)	64(3)	45(2)	-5(2)	3(1)	-12(2)
C(11)	60(2)	55(3)	42(2)	4(2)	3(2)	-12(2)
C(12)	51(2)	44(3)	46(2)	3(2)	10(1)	-2(2)
C(13)	48(2)	55(3)	52(2)	0(2)	3(1)	-6(2)

Table A.5.7 *- Atomic coordinates (x 10^4) and equivalent isotropic displacement parameters ($Å^2$ x 10^3) for the 100K X-ray structure of MBADNP.*

Atom	x	y	z	U(eq)
O(1)	-1566(3)	9649(4)	7299(3)	31(1)
O(2)	-182(3)	10684(4)	5592(3)	33(1)
O(3)	5153(3)	8907(4)	4943(3)	30(1)
O(4)	6102(3)	6964(4)	6283(3)	30(1)
N(1)	-816(4)	6743(4)	8228(4)	24(1)
N(2)	1773(3)	6038(4)	7886(3)	22(1)
N(3)	-391(4)	9658(4)	6528(3)	25(1)
N(4)	4996(4)	7843(4)	5843(3)	25(1)
C(1)	-2451(4)	5561(5)	10062(4)	22(1)
C(2)	-3860(4)	4728(5)	10004(4)	24(1)
C(3)	-5051(5)	5040(5)	10990(4)	25(1)
C(4)	-4795(5)	6182(5)	12074(4)	27(1)
C(5)	-3371(5)	7024(5)	12167(4)	27(1)
C(6)	-2224(5)	6731(5)	11147(4)	24(1)
C(7)	-1131(5)	5259(5)	8989(4)	23(1)
C(8)	-1526(5)	3981(5)	7838(4)	27(1)
C(9)	574(4)	7090(5)	7635(4)	21(1)
C(10)	824(4)	8462(5)	6760(4)	20(1)
C(11)	2243(4)	8695(5)	6132(4)	21(1)
C(12)	3437(4)	7593(5)	6420(4)	22(1)
C(13)	3165(5)	6315(5)	7310(4)	24(1)
H(1N)	-1506(54)	7390(59)	8077(48)	29
H(2)	-4038(49)	3969(57)	9338(47)	28
H(3)	-6096(49)	4372(53)	10889(43)	30
H(4)	-5689(50)	6433(52)	12831(46)	33
H(5)	-3087(49)	7798(57)	12979(48)	33
H(6)	-1284(51)	7324(54)	11211(45)	29
H(7)	-147(48)	5051(52)	9610(42)	28
H(8A)	-1610(53)	2936(62)	8460(51)	40
H(8B)	-685(55)	3845(60)	7128(49)	40
H(8C)	-2534(56)	4225(59)	7202(49)	40
H(11)	2433(45)	9690(59)	5588(44)	25
H(13)	4075(47)	5478(53)	7521(43)	29

Table A.5.8 *- Anisotropic displacement parameters ($Å^2 \times 10^3$) for the 100K X-ray structure of MBADNP.*

Atom	U11	U22	U33	U23	U13	U12
O(1)	25(1)	26(2)	42(2)	5(1)	11(1)	5(1)
O(2)	32(2)	29(2)	37(2)	10(1)	4(1)	8(1)
O(3)	31(1)	29(2)	29(1)	3(1)	7(1)	0(1)
O(4)	19(1)	29(2)	42(2)	-1(1)	-4(1)	4(1)
N(1)	24(2)	18(2)	31(2)	4(1)	3(1)	1(1)
N(2)	22(2)	19(2)	25(2)	0(1)	0(1)	-1(2)
N(3)	30(2)	20(2)	26(2)	2(2)	0(1)	0(2)
N(4)	27(2)	23(2)	25(2)	-5(2)	3(1)	-5(2)
C(1)	25(2)	22(2)	18(2)	4(2)	-2(1)	2(2)
C(2)	27(2)	19(2)	24(2)	0(2)	-2(2)	-7(2)
C(3)	22(2)	26(3)	27(2)	1(2)	-1(2)	0(2)
C(4)	29(2)	23(2)	30(2)	8(2)	5(2)	5(2)
C(5)	35(2)	25(2)	22(2)	1(2)	2(2)	2(2)
C(6)	25(2)	19(2)	27(2)	1(2)	1(2)	-4(2)
C(7)	22(2)	21(2)	25(2)	2(2)	0(2)	0(2)
C(8)	27(2)	28(3)	26(2)	-1(2)	1(2)	2(2)
C(9)	19(2)	22(2)	22(2)	-1(2)	-2(1)	-2(2)
C(10)	20(2)	17(2)	22(2)	-1(1)	-1(1)	3(2)
C(11)	23(2)	18(2)	21(2)	-2(2)	-2(1)	-1(2)
C(12)	19(2)	20(2)	25(2)	-5(2)	-1(1)	0(2)
C(13)	24(2)	23(2)	26(2)	-2(2)	0(2)	1(2)

Table A.5.9 *- Atomic coordinates (x 10^4) and equivalent isotropic displacement parameters ($Å^2$ x 10^3) for the 20K neutron structure of MBANP.*

Atom	x	y	z	U(eq)
O(1)	6458(6)	1528(5)	4698(2)	10(1)
O(2)	3175(6)	1837(5)	3915(2)	11(1)
N(1)	8817(3)	9896(3)	3004(1)	8(1)
N(2)	5712(3)	7316(3)	3026(1)	8(1)
N(3)	5221(3)	2486(3)	4197(1)	7(1)
C(1)	8083(4)	9335(4)	1617(2)	7(1)
C(2)	6266(4)	9362(4)	1012(2)	8(1)
C(3)	6576(5)	8155(4)	366(2)	9(1)
C(4)	8723(5)	6900(4)	317(2)	9(1)
C(5)	10539(4)	6858(4)	915(2)	8(1)
C(6)	10243(4)	8075(4)	1567(2)	8(1)
C(7)	7761(4)	10788(4)	2293(2)	7(1)
C(8)	9068(5)	12913(4)	2160(2)	10(1)
C(9)	7922(4)	8116(4)	3324(2)	7(1)
C(10)	9319(4)	7158(4)	3944(2)	8(1)
C(11)	8457(4)	5305(4)	4240(2)	7(1)
C(12)	6180(4)	4461(4)	3917(2)	7(1)
C(13)	4876(4)	5519(4)	3326(2)	7(1)
H(1N)	10504(10)	10463(11)	3223(4)	22(1)
H(2)	4594(11)	10339(11)	1057(5)	25(1)
H(3)	5144(13)	8191(12)	-89(4)	24(1)
H(4)	8973(13)	5943(12)	-180(4)	24(1)
H(5)	12218(11)	5898(12)	879(4)	24(1)
H(6)	11690(11)	8058(12)	2031(4)	22(1)
H(7)	5722(9)	11041(10)	2343(4)	18(1)
H(8A)	8927(15)	13966(11)	2642(5)	28(1)
H(8B)	8215(14)	13687(13)	1664(5)	30(2)
H(8C)	11034(13)	12654(12)	2071(5)	29(2)
H(10)	11051(11)	7868(11)	4161(4)	23(1)
H(11)	9485(12)	4492(12)	4702(4)	24(1)
H(13)	3098(11)	4870(12)	3092(4)	22(1)

Table A.5.10 *- Anisotropic displacement parameters ($Å^2 \times 10^3$) for the 20K neutron structure of MBANP.*

Atom	U11	U22	U33	U23	U13	U12
O(1)	9(1)	7(1)	15(2)	3(1)	-2(1)	-3(1)
O(2)	12(1)	9(1)	13(2)	2(1)	-1(1)	-5(1)
N(1)	7(1)	6(1)	11(1)	1(1)	-1(1)	-2(1)
H(1N)	13(2)	24(3)	28(4)	4(2)	-9(2)	-14(2)
N(2)	7(1)	6(1)	11(1)	1(1)	-1(1)	0(1)
N(3)	6(1)	6(1)	10(1)	0(1)	-1(1)	-1(1)
C(1)	8(1)	5(1)	7(1)	-1(1)	0(1)	-1(1)
C(2)	6(1)	8(1)	11(1)	-1(1)	0(1)	0(1)
H(2)	13(2)	25(3)	36(4)	-3(3)	-2(2)	10(2)
C(3)	11(1)	8(1)	9(1)	-2(1)	-2(1)	2(1)
H(3)	24(2)	26(3)	21(3)	-7(3)	-3(2)	4(2)
C(4)	10(1)	7(1)	9(1)	-1(1)	0(1)	1(1)
H(4)	29(3)	26(3)	17(3)	-9(2)	-1(2)	6(2)
C(5)	6(1)	7(1)	11(1)	-2(1)	0(1)	2(1)
H(5)	17(2)	26(3)	29(4)	-6(3)	-3(2)	10(2)
C(6)	7(1)	6(1)	11(1)	0(1)	-1(1)	0(1)
H(6)	16(2)	26(3)	21(3)	-2(2)	-10(2)	7(2)
C(7)	8(1)	6(1)	6(1)	1(1)	1(1)	0(1)
H(7)	7(2)	21(2)	24(3)	1(2)	0(2)	3(2)
C(8)	12(1)	5(1)	13(1)	-1(1)	2(1)	-2(1)
H(8A)	36(3)	19(3)	30(4)	-5(3)	1(3)	-3(2)
H(8B)	26(3)	26(3)	36(4)	11(3)	-6(3)	-6(2)
H(8C)	22(3)	22(3)	42(4)	-1(3)	8(3)	-2(2)
C(9)	6(1)	6(1)	10(1)	-1(1)	-1(1)	1(1)
C(10)	5(1)	6(1)	12(1)	0(1)	-1(1)	-2(1)
H(10)	19(2)	22(3)	26(3)	0(2)	-4(2)	-6(2)
C(11)	6(1)	6(1)	10(1)	1(1)	-1(1)	-2(1)
H(11)	22(2)	26(3)	22(3)	10(2)	-5(2)	2(2)
C(12)	5(1)	5(1)	11(1)	0(1)	0(1)	-1(1)
C(13)	6(1)	6(1)	10(1)	0(1)	-1(1)	-1(1)
H(13)	17(2)	23(3)	25(3)	3(2)	-4(2)	-9(2)

Table A.5.11 *- Atomic coordinates (x 10^4) and equivalent isotropic displacement parameters ($Å^2$ x 10^3) for the 20K neutron structure of MBADNP.*

Atom	x	y	z	U(eq)
O(1)	11559(1)	345(1)	2679(1)	8(1)
O(2)	10195(1)	-683(1)	4407(1)	8(1)
O(3)	4842(1)	1081(1)	5064(1)	7(1)
O(4)	3883(1)	3033(1)	3730(1)	7(1)
N(1)	10810(1)	3253(1)	1756(1)	5(1)
N(2)	8213(1)	3964(1)	2126(1)	5(1)
N(3)	10393(1)	324(1)	3466(1)	4(1)
N(4)	4989(1)	2157(1)	4171(1)	4(1)
C(1)	12440(1)	4442(1)	-64(1)	4(1)
C(2)	13868(1)	5296(1)	-1(1)	6(1)
C(3)	15054(1)	4971(1)	-994(1)	6(1)
C(4)	14808(1)	3814(1)	-2087(1)	6(1)
C(5)	13371(1)	2967(1)	-2170(1)	6(1)
C(6)	12209(1)	3270(1)	-1157(1)	5(1)
C(7)	11129(1)	4740(1)	1003(1)	4(1)
C(8)	11526(1)	6020(1)	2169(1)	6(1)
C(9)	9429(1)	2918(1)	2361(1)	4(1)
C(10)	9186(1)	1539(1)	3233(1)	4(1)
C(11)	7746(1)	1294(1)	3872(1)	4(1)
C(12)	6548(1)	2399(1)	3596(1)	4(1)
C(13)	6823(1)	3700(1)	2703(1)	5(1)
H(1N)	11746(3)	2523(3)	2002(3)	20(1)
H(2)	14081(3)	6228(3)	819(3)	20(1)
H(3)	16170(3)	5630(3)	-907(3)	22(1)
H(4)	15733(3)	3589(3)	-2864(3)	21(1)
H(5)	13150(3)	2087(3)	-3034(3)	22(1)
H(6)	11108(3)	2590(3)	-1218(3)	22(1)
H(7)	10012(2)	5055(3)	343(2)	16(1)
H(8A)	11687(3)	7146(3)	1620(3)	24(1)
H(8B)	10542(3)	6134(3)	2919(3)	24(1)
H(8C)	12630(3)	5746(3)	2847(3)	22(1)
H(11)	7553(3)	257(3)	4533(3)	18(1)
H(13)	5868(3)	4550(3)	2467(3)	20(1)

Table A.5.12 *- Anisotropic displacement parameters ($Å^2 \times 10^3$) for the 20K neutron structure of MBADNP.*

Atom	U11	U22	U33	U23	U13	U12
O(1)	6(1)	6(1)	11(1)	2(1)	4(1)	2(1)
O(2)	9(1)	8(1)	9(1)	5(1)	3(1)	3(1)
O(3)	7(1)	7(1)	8(1)	3(1)	3(1)	1(1)
O(4)	5(1)	7(1)	9(1)	1(1)	1(1)	1(1)
N(1)	5(1)	4(1)	7(1)	2(1)	2(1)	1(1)
H(1N)	14(1)	18(1)	30(1)	10(1)	6(1)	7(1)
N(2)	4(1)	4(1)	7(1)	2(1)	1(1)	1(1)
N(3)	4(1)	4(1)	5(1)	1(1)	0(1)	1(1)
N(4)	4(1)	4(1)	5(1)	0(1)	1(1)	0(1)
C(1)	5(1)	4(1)	4(1)	0(1)	0(1)	-1(1)
C(2)	5(1)	6(1)	6(1)	-1(1)	1(1)	-2(1)
H(2)	20(1)	20(1)	20(1)	-9(1)	3(1)	-6(1)
C(3)	5(1)	7(1)	7(1)	0(1)	2(1)	-1(1)
H(3)	14(1)	27(1)	26(1)	-4(1)	5(1)	-9(1)
C(4)	6(1)	6(1)	6(1)	1(1)	2(1)	1(1)
H(4)	17(1)	26(1)	21(1)	-4(1)	10(1)	0(1)
C(5)	7(1)	6(1)	5(1)	-1(1)	2(1)	0(1)
H(5)	26(1)	19(1)	21(1)	-11(1)	4(1)	-3(1)
C(6)	6(1)	5(1)	5(1)	-2(1)	1(1)	-1(1)
H(6)	16(1)	25(1)	26(1)	-7(1)	5(1)	-11(1)
C(7)	4(1)	3(1)	5(1)	1(1)	0(1)	0(1)
H(7)	12(1)	16(1)	18(1)	3(1)	-3(1)	2(1)
C(8)	7(1)	5(1)	6(1)	-2(1)	1(1)	-1(1)
H(8A)	31(1)	12(1)	28(1)	2(1)	3(1)	-3(1)
H(8B)	23(1)	28(1)	22(1)	-7(1)	11(1)	-1(1)
H(8C)	18(1)	27(1)	20(1)	-4(1)	-7(1)	4(1)
C(9)	4(1)	3(1)	4(1)	1(1)	1(1)	0(1)
C(10)	4(1)	3(1)	5(1)	1(1)	1(1)	0(1)
C(11)	4(1)	3(1)	5(1)	1(1)	1(1)	1(1)
H(11)	18(1)	14(1)	21(1)	8(1)	4(1)	0(1)
C(12)	3(1)	4(1)	6(1)	1(1)	1(1)	0(1)
C(13)	4(1)	4(1)	6(1)	2(1)	1(1)	0(1)
H(13)	12(1)	18(1)	31(1)	7(1)	3(1)	7(1)

Table A.5.13 *- Atomic coordinates (x 10^4) and equivalent isotropic displacement parameters ($Å^2$ x 10^3) for the 20K X-ray structure of MBADNP.*

Atom	x	y	z	U(eq)
O(1)	11566(1)	346(1)	2681(1)	12(1)
O(2)	10194(1)	-688(1)	4412(1)	13(1)
O(3)	4840(1)	1079(1)	5066(1)	12(1)
O(4)	3882(1)	3037(1)	3730(1)	12(1)
N(1)	10811(1)	3250(1)	1756(1)	9(1)
N(2)	8216(1)	3966(1)	2122(1)	9(1)
N(3)	10390(1)	329(1)	3464(1)	9(1)
N(4)	4992(1)	2157(1)	4169(1)	9(1)
C(1)	12445(1)	4446(1)	-67(1)	8(1)
C(2)	13865(1)	5292(1)	-3(1)	10(1)
C(3)	15053(1)	4971(1)	-995(1)	11(1)
C(4)	14805(1)	3814(1)	-2085(1)	10(1)
C(5)	13374(1)	2972(1)	-2168(1)	11(1)
C(6)	12214(1)	3268(1)	-1157(1)	10(1)
C(7)	11127(1)	4740(1)	1008(1)	8(1)
C(8)	11526(1)	6017(1)	2168(1)	11(1)
C(9)	9426(1)	2918(1)	2361(1)	8(1)
C(10)	9182(1)	1537(1)	3232(1)	8(1)
C(11)	7744(1)	1299(1)	3869(1)	8(1)
C(12)	6552(1)	2396(1)	3594(1)	8(1)
C(13)	6816(1)	3700(1)	2700(1)	9(1)
H(1N)	11589(14)	2589(15)	1966(13)	18(3)
H(2)	14088(14)	6074(15)	749(13)	21(3)
H(3)	16034(13)	5557(13)	-882(11)	11(3)
H(4)	15657(11)	3629(12)	-2784(10)	4(2)
H(5)	13214(12)	2169(13)	-2974(11)	6(3)
H(6)	11257(13)	2703(13)	-1211(11)	10(3)
H(7)	10161(12)	4984(12)	412(9)	5(2)
H(8A)	11708(12)	7013(13)	1633(11)	8(3)
H(8B)	10625(14)	6122(15)	2790(12)	21(3)
H(8C)	12559(14)	5757(15)	2733(12)	22(3)
H(11)	7524(12)	403(14)	4428(11)	14(3)
H(13)	5944(11)	4423(13)	2481(10)	3(2)

Table A.5.14 *- Anisotropic displacement parameters ($Å^2$ x 10^3) for the 20K X-ray structure of MBADNP.*

Atom	U11	U22	U33	U23	U13	U12
O(1)	11(1)	11(1)	15(1)	1(1)	5(1)	2(1)
O(2)	15(1)	10(1)	13(1)	5(1)	3(1)	2(1)
O(3)	14(1)	10(1)	11(1)	3(1)	4(1)	0(1)
O(4)	10(1)	11(1)	15(1)	1(1)	0(1)	2(1)
N(1)	10(1)	7(1)	11(1)	2(1)	2(1)	1(1)
N(2)	10(1)	8(1)	10(1)	1(1)	1(1)	0(1)
N(3)	11(1)	8(1)	9(1)	0(1)	1(1)	0(1)
N(4)	10(1)	8(1)	9(1)	-2(1)	1(1)	0(1)
C(1)	9(1)	8(1)	8(1)	1(1)	1(1)	1(1)
C(2)	11(1)	10(1)	9(1)	0(1)	0(1)	-1(1)
C(3)	10(1)	11(1)	11(1)	1(1)	1(1)	-1(1)
C(4)	11(1)	10(1)	10(1)	1(1)	2(1)	2(1)
C(5)	14(1)	8(1)	10(1)	0(1)	1(1)	1(1)
C(6)	10(1)	9(1)	11(1)	0(1)	1(1)	-1(1)
C(7)	9(1)	7(1)	9(1)	1(1)	1(1)	0(1)
C(8)	11(1)	10(1)	11(1)	-2(1)	2(1)	0(1)
C(9)	10(1)	8(1)	7(1)	-1(1)	1(1)	0(1)
C(10)	9(1)	7(1)	9(1)	0(1)	0(1)	1(1)
C(11)	10(1)	7(1)	8(1)	0(1)	1(1)	0(1)
C(12)	8(1)	8(1)	9(1)	-1(1)	2(1)	-1(1)
C(13)	9(1)	9(1)	10(1)	0(1)	0(1)	0(1)

Table A.5.15 *- Atomic coordinates for the non-hydrogen atoms of MBADNP as derived from the charge density study.*

Atom	x	y	z
O(1)	1.1561	0.0346	0.2681
O(2)	1.0194	-0.0685	0.4409
O(3)	0.4839	0.1078	0.5066
O(4)	0.3883	0.3038	0.3731
N(1)	1.0810	0.3256	0.1756
N(2)	0.8213	0.3967	0.2125
N(3)	1.0394	0.0328	0.3467
N(4)	0.4989	0.2158	0.4171
C(1)	1.2440	0.4443	-0.0066
C(2)	1.3869	0.5299	-0.0002
C(3)	1.5053	0.4973	-0.0993
C(4)	1.4806	0.3817	-0.2085
C(5)	1.3368	0.2970	-0.2172
C(6)	1.2208	0.3272	-0.1159
C(7)	1.1128	0.4742	0.1006
C(8)	1.1523	0.6022	0.2169
C(9)	0.9429	0.2920	0.2362
C(10)	0.9186	0.1540	0.3232
C(11)	0.7746	0.1298	0.3870
C(12)	0.6546	0.2399	0.3596
C(13)	0.6822	0.3705	0.2703

Table A.5.16 *- Anisotropic displacement parameters ($Å^2$) for the non-hydrogen atoms of MBADNP as derived from the charge density study.*

Atom	U11	U22	U33	U23	U13	U12
O(1)	0.009932	0.009724	0.015577	0.002230	0.004577	0.002079
O(2)	0.012226	0.010668	0.013153	0.004350	0.002961	0.002906
O(3)	0.010783	0.010903	0.011290	0.002777	0.003518	0.000074
O(4)	0.007962	0.010476	0.014447	0.001567	0.001293	0.000910
N(1)	0.008461	0.007278	0.010874	0.002180	0.002428	0.000446
N(2)	0.008794	0.007501	0.010428	0.001849	0.001759	0.000713
N(3)	0.008619	0.007259	0.009406	0.000596	0.001359	0.000912
N(4)	0.007580	0.008070	0.009231	-0.000301	0.001347	0.000339
C(1)	0.008789	0.008053	0.008176	-0.000486	0.001432	-0.000885
C(2)	0.009614	0.009752	0.009633	-0.001553	0.001709	-0.001864
C(3)	0.009178	0.011292	0.010741	-0.000611	0.002170	-0.001385
C(4)	0.010457	0.010025	0.010123	-0.000121	0.002775	0.000360
C(5)	0.011712	0.009212	0.010044	-0.001308	0.002310	-0.000120
C(6)	0.009891	0.008965	0.009756	-0.001963	0.001618	-0.001386
C(7)	0.008923	0.007541	0.008183	0.000114	0.001449	0.000020
C(8)	0.011382	0.009913	0.010448	-0.001582	0.001734	-0.000447
C(9)	0.008210	0.007236	0.008343	0.000878	0.001474	0.000173
C(10)	0.008477	0.007065	0.008666	0.001017	0.001583	0.000573
C(11)	0.008111	0.007406	0.008794	0.001169	0.001588	0.000638
C(12)	0.007903	0.007646	0.008987	0.000302	0.001519	0.000072
C(13)	0.008217	0.008248	0.010798	0.001787	0.001692	0.000385

Table A.5.17 *- Atomic coordinates (x 10^4) and equivalent isotropic displacement parameters ($Å^2$ x 10^3) for the 20K neutron structure of NMBA.*

Atom	x	y	z	U(eq)
O(1)	11583(4)	9665(2)	6238(3)	11(1)
O(2)	12740(4)	8444(2)	4654(3)	12(1)
N(1)	3211(2)	7049(1)	-1104(2)	9(1)
N(2)	11386(2)	8953(1)	4911(2)	9(1)
C(1)	6025(3)	9190(2)	2429(2)	9(1)
C(2)	5666(3)	8224(2)	1178(2)	8(1)
C(3)	7216(3)	7515(2)	1144(2)	9(1)
C(4)	9103(3)	7756(2)	2343(2)	10(1)
C(5)	9411(3)	8711(2)	3590(2)	8(1)
C(6)	7914(3)	9435(2)	3662(2)	9(1)
C(7)	3647(3)	7962(2)	-35(2)	10(1)
C(8)	1248(3)	6796(2)	-2231(2)	8(1)
C(9)	-368(3)	7430(2)	-2187(2)	9(1)
C(10)	-2240(3)	7103(2)	-3347(2)	9(1)
C(11)	-2561(3)	6131(2)	-4583(2)	8(1)
C(12)	-932(3)	5502(2)	-4630(2)	9(1)
C(13)	939(3)	5823(2)	-3474(2)	9(1)
C(14)	-4582(4)	5789(2)	-5840(2)	11(1)
H(1)	4839(10)	9739(5)	2458(7)	25(1)
H(3)	6917(9)	6769(4)	175(6)	24(1)
H(4)	10315(9)	7204(5)	2348(7)	23(1)
H(6)	8204(10)	10171(5)	4679(7)	24(1)
H(7)	2563(8)	8591(5)	66(7)	32(1)
H(9)	-191(10)	8193(5)	-1247(7)	26(1)
H(10)	-3498(9)	7602(5)	-3301(7)	24(1)
H(12)	-1130(9)	4759(5)	-5613(7)	24(1)
H(13)	2202(9)	5336(5)	-3523(7)	26(1)
H(14A)	-4956(11)	4918(5)	-5537(8)	39(1)
H(14B)	-4754(12)	5801(7)	-7399(6)	41(2)
H(14C)	-5674(11)	6380(7)	-5675(9)	41(2)

Table A.5.18 *- Anisotropic displacement parameters ($Å^2 \times 10^3$) for the 20K neutron structure of NMBA.*

Atom	U11	U22	U33	U23	U13	U12
O(1)	12(1)	7(1)	13(1)	-3(1)	4(1)	-1(1)
O(2)	9(1)	12(1)	14(1)	-1(1)	4(1)	0(1)
N(1)	9(1)	7(1)	11(1)	-2(1)	3(1)	0(1)
N(2)	10(1)	6(1)	11(1)	0(1)	5(1)	-1(1)
C(1)	10(1)	5(1)	13(1)	-2(1)	4(1)	1(1)
H(1)	19(3)	22(2)	33(2)	-7(2)	7(2)	8(2)
C(2)	9(1)	5(1)	10(1)	-1(1)	3(1)	-1(1)
C(3)	9(1)	5(1)	12(1)	-2(1)	4(1)	0(1)
H(3)	25(3)	18(2)	26(2)	-9(1)	5(2)	1(2)
C(4)	11(1)	8(1)	11(1)	-1(1)	5(1)	0(1)
H(4)	18(3)	21(2)	31(2)	-5(1)	8(2)	3(2)
C(5)	8(1)	5(1)	11(1)	0(1)	4(1)	-1(1)
C(6)	9(1)	6(1)	12(1)	-1(1)	4(1)	1(1)
H(6)	25(3)	16(2)	32(2)	-9(1)	10(2)	-1(2)
C(7)	9(1)	5(1)	12(1)	-2(1)	2(1)	-1(1)
H(7)	14(3)	27(3)	49(2)	-15(2)	3(2)	4(2)
C(8)	9(1)	6(1)	10(1)	0(1)	3(1)	0(1)
C(9)	8(1)	7(1)	12(1)	-1(1)	4(1)	1(1)
H(9)	24(3)	23(2)	31(2)	-10(2)	8(2)	2(2)
C(10)	9(1)	5(1)	12(1)	0(1)	3(1)	0(1)
H(10)	22(3)	17(2)	34(2)	-5(1)	10(2)	4(2)
C(11)	8(1)	6(1)	10(1)	0(1)	3(1)	0(1)
C(12)	9(1)	6(1)	11(1)	-2(1)	3(1)	0(1)
H(12)	23(3)	18(2)	28(2)	-12(1)	5(2)	-2(2)
C(13)	10(1)	7(1)	11(1)	-1(1)	3(1)	0(1)
H(13)	23(3)	23(2)	33(2)	-7(2)	11(2)	4(2)
C(14)	10(1)	8(1)	12(1)	0(1)	2(1)	-2(1)
H(14A)	28(4)	25(3)	51(2)	12(2)	-2(2)	-13(3)
H(14B)	43(4)	62(4)	19(2)	-1(2)	9(2)	-15(3)
H(14C)	15(3)	39(4)	59(3)	-22(2)	1(2)	9(3)

Table A.6.1 *- Atomic coordinates (x 10^4) and equivalent isotropic displacement parameters ($Å^2$ x 10^3) for the 100K neutron structure of DCNP.*

Atom	x	y	z	U(eq)
N(1)	5701(2)	603(2)	13336(3)	27(1)
N(2)	5030(2)	3998(2)	12333(3)	28(1)
N(3)	3479(2)	1902(2)	7115(3)	16(1)
N(4)	3112(2)	2653(2)	6018(3)	20(1)
C(1)	5311(3)	1229(2)	12386(4)	18(1)
C(2)	4949(3)	3122(2)	11807(4)	19(1)
C(3)	4857(2)	2022(2)	11260(4)	13(1)
C(4)	4371(3)	1696(2)	9743(4)	15(1)
C(5)	3919(3)	2377(2)	8453(4)	14(1)
C(6)	3396(3)	3781(2)	6549(4)	19(1)
C(7)	3840(3)	3610(2)	8368(4)	18(1)
C(8)	2627(2)	2349(3)	4469(4)	19(1)
C(9)	2549(3)	1256(3)	4005(4)	21(1)
C(10)	2051(3)	958(3)	2467(4)	30(1)
C(11)	1625(3)	1759(4)	1371(4)	35(1)
C(12)	1704(3)	2854(3)	1843(5)	33(1)
C(13)	2216(3)	3162(3)	3365(4)	24(1)
H(4)	4364(6)	851(5)	9431(8)	34(2)
H(6A)	4044(6)	4106(6)	5676(9)	43(2)
H(6B)	2617(6)	4293(5)	6496(9)	37(2)
H(7A)	4669(6)	3991(5)	8556(9)	42(2)
H(7B)	3234(7)	3909(5)	9306(8)	42(2)
H(9)	2865(6)	644(5)	4845(9)	37(2)
H(10)	1971(8)	118(7)	2116(9)	57(2)
H(11)	1231(7)	1564(10)	156(11)	66(3)
H(12)	1383(8)	3469(9)	972(10)	57(2)
H(13)	2263(7)	3981(6)	3674(10)	47(2)

Table A.6.2 *- Anisotropic displacement parameters ($Å^2 \times 10^3$) for the 100K neutron structure of DCNP.*

Atom	U11	U22	U33	U23	U13	U12
N(1)	34(1)	21(1)	27(1)	3(1)	-12(1)	4(1)
N(2)	32(1)	19(1)	33(1)	-9(1)	-4(1)	-3(1)
N(3)	24(1)	12(1)	14(1)	-2(1)	-2(1)	0(1)
N(4)	27(1)	16(1)	16(1)	-1(1)	0(1)	0(1)
C(1)	18(1)	17(1)	18(2)	0(1)	-3(1)	1(1)
C(2)	17(2)	15(2)	25(2)	-4(1)	-1(1)	-6(1)
C(3)	13(1)	12(1)	15(1)	-2(1)	-1(1)	-1(1)
C(4)	17(1)	11(1)	16(1)	-2(1)	1(1)	3(1)
C(5)	15(1)	9(1)	17(1)	-1(1)	0(1)	-1(1)
C(6)	23(2)	15(1)	19(2)	1(1)	3(1)	-1(1)
C(7)	23(2)	15(1)	16(1)	1(1)	2(1)	-1(1)
C(8)	14(2)	23(2)	19(2)	-2(1)	1(1)	0(1)
C(9)	20(2)	28(2)	16(1)	-1(1)	2(1)	-9(1)
C(10)	25(2)	47(2)	19(2)	-9(2)	4(1)	-19(2)
C(11)	15(2)	71(3)	18(2)	1(2)	-3(1)	-10(2)
C(12)	14(2)	64(3)	21(2)	9(2)	2(1)	2(2)
C(13)	15(2)	38(2)	18(2)	10(2)	1(1)	5(1)
H(4)	51(4)	17(3)	34(3)	-10(3)	-8(3)	6(3)
H(6A)	44(4)	44(4)	42(4)	13(3)	7(3)	-20(3)
H(6B)	37(3)	30(3)	43(4)	-9(3)	0(3)	13(3)
H(7A)	41(4)	33(3)	52(4)	6(3)	-15(3)	-17(3)
H(7B)	55(4)	43(4)	27(3)	-1(3)	21(3)	18(3)
H(9)	47(4)	27(3)	36(4)	3(3)	4(3)	-6(3)
H(10)	67(5)	67(5)	37(4)	-19(4)	9(4)	-29(4)
H(11)	37(5)	123(9)	38(4)	-7(5)	-15(4)	-22(4)
H(12)	44(5)	89(6)	38(5)	21(5)	1(4)	15(4)
H(13)	55(5)	37(4)	48(5)	6(4)	-4(4)	20(4)

Table A.6.3 *- Atomic coordinates (x 10^4) and equivalent isotropic displacement parameters ($Å^2$ x 10^3) for the 100K X-ray structure of DCNP.*

Atom	x	y	z	U(eq)
N(1)	5703(1)	601(1)	13340(1)	31(1)
N(2)	5038(1)	4000(1)	12337(1)	31(1)
N(3)	3481(1)	1898(1)	7109(1)	23(1)
N(4)	3111(1)	2646(1)	6016(1)	24(1)
C(1)	5310(1)	1224(1)	12406(1)	24(1)
C(2)	4951(1)	3126(1)	11821(1)	21(1)
C(3)	4853(1)	2017(1)	11255(1)	20(1)
C(4)	4370(1)	1698(1)	9750(1)	21(1)
C(5)	3918(1)	2378(1)	8457(1)	20(1)
C(6)	3392(1)	3784(1)	6550(1)	23(1)
C(7)	3846(1)	3611(1)	8367(1)	23(1)
C(8)	2631(1)	2343(1)	4458(1)	22(1)
C(9)	2549(1)	1249(1)	4003(1)	28(1)
C(10)	2049(1)	962(1)	2470(1)	34(1)
C(11)	1622(1)	1764(1)	1367(1)	39(1)
C(12)	1705(1)	2846(1)	1831(1)	37(1)
C(13)	2209(1)	3153(1)	3361(1)	29(1)
H(4)	4365(7)	961(6)	9541(11)	22(2)
H(6A)	3936(7)	4080(6)	5786(11)	23(2)
H(6B)	2679(8)	4214(7)	6519(12)	32(2)
H(7A)	3290(8)	3890(7)	9196(13)	35(2)
H(7B)	4611(8)	3925(7)	8514(12)	28(2)
H(9)	2802(8)	735(7)	4733(12)	26(2)
H(10)	2019(8)	209(8)	2108(13)	37(3)
H(11)	1286(10)	1539(9)	316(16)	48(3)
H(12)	1457(9)	3352(9)	1149(15)	45(3)
H(13)	2223(9)	3929(7)	3704(13)	31(2)

Table A.6.4 *- Anisotropic displacement parameters ($Å^2 \times 10^3$) for the 100K X-ray structure of DCNP.*

Atom	U11	U22	U33	U23	U13	U12
N(1)	36(1)	26(1)	32(1)	0(1)	-10(1)	0(1)
N(2)	36(1)	27(1)	31(1)	-4(1)	-6(1)	-3(1)
N(3)	29(1)	20(1)	22(1)	1(1)	0(1)	0(1)
N(4)	33(1)	20(1)	21(1)	-1(1)	-2(1)	0(1)
C(1)	25(1)	22(1)	26(1)	-3(1)	-2(1)	-2(1)
C(2)	21(1)	21(1)	22(1)	1(1)	-1(1)	-1(1)
C(3)	19(1)	19(1)	22(1)	0(1)	0(1)	-1(1)
C(4)	24(1)	15(1)	24(1)	-1(1)	1(1)	-1(1)
C(5)	22(1)	16(1)	21(1)	-1(1)	3(1)	-1(1)
C(6)	31(1)	16(1)	24(1)	3(1)	2(1)	1(1)
C(7)	32(1)	16(1)	22(1)	1(1)	2(1)	0(1)
C(8)	19(1)	29(1)	18(1)	0(1)	1(1)	0(1)
C(9)	27(1)	33(1)	23(1)	-2(1)	3(1)	-6(1)
C(10)	28(1)	49(1)	24(1)	-10(1)	3(1)	-16(1)
C(11)	23(1)	73(1)	22(1)	-6(1)	-1(1)	-12(1)
C(12)	23(1)	61(1)	27(1)	9(1)	0(1)	5(1)
C(13)	24(1)	38(1)	24(1)	8(1)	1(1)	6(1)

Table A.6.5 *- Atomic coordinates (x 10^4) and equivalent isotropic displacement parameters ($Å^2$ x 10^3) for the 90K X-ray structure of DCNP.*

Atom	x	y	z	Ueq
N(1)	5704(2)	601(1)	13341(2)	31(1)
N(2)	5034(2)	4000(1)	12328(2)	31(1)
N(3)	3481(2)	1899(1)	7110(2)	25(1)
N(4)	3111(2)	2648(1)	6017(2)	25(1)
C(1)	5311(2)	1224(2)	12408(3)	25(1)
C(2)	4949(2)	3130(2)	11826(3)	22(1)
C(3)	4853(2)	2017(2)	11248(3)	21(1)
C(4)	4370(2)	1699(2)	9753(3)	23(1)
C(5)	3920(2)	2378(2)	8457(2)	21(1)
C(6)	3391(2)	3784(2)	6549(3)	25(1)
C(7)	3845(2)	3613(2)	8367(3)	25(1)
C(8)	2632(2)	2344(2)	4455(2)	24(1)
C(9)	2550(2)	1249(2)	4005(3)	29(1)
C(10)	2048(2)	964(2)	2467(3)	34(1)
C(11)	1622(2)	1762(2)	1370(3)	39(1)
C(12)	1701(2)	2850(2)	1814(3)	36(1)
C(13)	2208(2)	3159(2)	3362(3)	29(1)
H(4)	4372(18)	916(16)	9521(30)	23(6)
H(6A)	2676(20)	4237(18)	6534(31)	31(6)
H(6B)	3947(18)	4085(16)	5823(29)	23(5)
H(7A)	4579(22)	3947(19)	8541(33)	34(6)
H(7B)	3299(21)	3863(18)	9233(32)	31(6)
H(9)	2833(22)	716(19)	4837(35)	35(7)
H(10)	1974(24)	180(22)	2147(37)	48(8)
H(11)	1279(25)	1566(25)	301(42)	49(8)
H(12)	1435(21)	3457(23)	1098(36)	38(8)
H(13)	2235(22)	3965(20)	3713(34)	33(7)

Table A.6.6 *- Anisotropic displacement parameters ($Å^2 \times 10^3$) for the 90K X-ray structure of DCNP.*

Atom	U11	U22	U33	U23	U13	U12
N(1)	35(1)	26(1)	32(1)	0(1)	-9(1)	-1(1)
N(2)	35(1)	27(1)	32(1)	-3(1)	-8(1)	-2(1)
N(3)	27(1)	23(1)	24(1)	0(1)	-1(1)	1(1)
N(4)	33(1)	22(1)	21(1)	-1(1)	-3(1)	0(1)
C(1)	25(1)	22(1)	28(1)	-2(1)	-2(1)	-2(1)
C(2)	21(1)	22(1)	24(1)	1(1)	0(1)	0(1)
C(3)	21(1)	20(1)	23(1)	-2(1)	0(1)	-3(1)
C(4)	24(1)	18(1)	27(1)	-1(1)	0(1)	0(1)
C(5)	22(1)	21(1)	21(1)	0(1)	1(1)	-1(1)
C(6)	30(1)	19(1)	25(1)	3(1)	1(1)	1(1)
C(7)	32(1)	19(1)	23(1)	1(1)	1(1)	-1(1)
C(8)	19(1)	32(1)	21(1)	1(1)	0(1)	-1(1)
C(9)	28(1)	36(1)	24(1)	-1(1)	1(1)	-7(1)
C(10)	29(1)	50(1)	24(1)	-8(1)	1(1)	-15(1)
C(11)	24(1)	69(2)	24(1)	-6(1)	-2(1)	-12(1)
C(12)	21(1)	61(2)	27(1)	8(1)	-2(1)	6(1)
C(13)	23(1)	39(1)	25(1)	8(1)	0(1)	6(1)

Table A.6.7 *- Atomic coordinates (x 10^4) and equivalent isotropic displacement parameters ($Å^2$ x 10^3) for the 200K X-ray structure of DCNP.*

Atom	x	y	z	U(eq)
N(1)	5690(2)	609(2)	13323(2)	63(1)
N(2)	5044(2)	3990(2)	12326(2)	61(1)
N(3)	3482(2)	1907(1)	7113(2)	44(1)
N(4)	3113(1)	2651(1)	6017(2)	46(1)
C(1)	5302(2)	1232(2)	12395(3)	47(1)
C(2)	4958(2)	3120(2)	11825(3)	42(1)
C(3)	4852(2)	2022(2)	11240(3)	39(1)
C(4)	4373(2)	1713(2)	9748(3)	41(1)
C(5)	3924(2)	2385(1)	8456(2)	38(1)
C(6)	3385(2)	3781(2)	6557(3)	47(1)
C(7)	3847(2)	3605(2)	8357(3)	45(1)
C(8)	2631(2)	2350(2)	4462(2)	42(1)
C(9)	2550(2)	1261(2)	4016(3)	52(1)
C(10)	2040(2)	991(3)	2481(3)	64(1)
C(11)	1623(2)	1777(3)	1383(4)	71(1)
C(12)	1706(2)	2847(3)	1832(3)	66(1)
C(13)	2209(2)	3155(2)	3367(3)	54(1)
H(4)	4352(16)	918(14)	9503(26)	50(6)
H(6A)	2659(17)	4214(15)	6502(24)	56(6)
H(6B)	3964(17)	4057(15)	5845(28)	60(6)
H(7A)	4619(18)	3950(16)	8550(25)	56(6)
H(7B)	3339(17)	3836(14)	9238(27)	58(6)
H(9)	2856(19)	702(17)	4856(31)	70(7)
H(10)	2004(19)	258(19)	2186(28)	63(7)
H(11)	1227(20)	1579(22)	278(36)	79(8)
H(12)	1432(20)	3487(23)	1082(34)	80(9)
H(13)	2243(20)	3918(18)	3661(32)	59(7)

Table A.6.8 *- Anisotropic displacement parameters ($Å^2 \times 10^3$) for the 200K X-ray structure of DCNP.*

Atom	U11	U22	U33	U23	U13	U12
N(1)	75(1)	50(1)	63(1)	3(1)	-20(1)	2(1)
N(2)	72(1)	49(1)	61(1)	-10(1)	-12(1)	-4(1)
N(3)	55(1)	34(1)	41(1)	1(1)	-1(1)	0(1)
N(4)	62(1)	36(1)	41(1)	0(1)	-2(1)	0(1)
C(1)	48(1)	40(1)	52(1)	-6(1)	-5(1)	-1(1)
C(2)	42(1)	40(1)	43(1)	1(1)	-1(1)	-2(1)
C(3)	41(1)	37(1)	40(1)	0(1)	3(1)	-1(1)
C(4)	45(1)	32(1)	47(1)	-1(1)	2(1)	-1(1)
C(5)	44(1)	32(1)	39(1)	-2(1)	4(1)	0(1)
C(6)	57(1)	36(1)	48(1)	3(1)	2(1)	1(1)
C(7)	57(1)	34(1)	46(1)	-1(1)	4(1)	-4(1)
C(8)	38(1)	53(1)	36(1)	-1(1)	3(1)	1(1)
C(9)	52(1)	59(2)	44(1)	-5(1)	6(1)	-9(1)
C(10)	59(2)	83(2)	50(1)	-19(1)	5(1)	-28(1)
C(11)	45(2)	126(3)	41(2)	-5(2)	-2(1)	-19(1)
C(12)	45(2)	106(2)	46(2)	12(2)	-3(1)	2(1)
C(13)	49(1)	68(2)	46(1)	11(1)	4(1)	8(1)

Table A.6.9 *- Atomic coordinates (x 10^4) and equivalent isotropic displacement parameters ($Å^2$ x 10^3) for the 290K X-ray structure of DCNP.*

Atom	x	y	z	Ueq
N(1)	5680(3)	617(2)	13306(4)	91(1)
N(2)	5043(3)	3978(3)	12314(5)	89(1)
N(3)	3487(3)	1913(2)	7106(4)	62(1)
N(4)	3117(3)	2651(2)	6021(3)	68(1)
C(1)	5296(3)	1237(3)	12380(5)	68(1)
C(2)	4955(3)	3117(3)	11817(5)	63(1)
C(3)	4852(3)	2029(3)	11231(4)	58(1)
C(4)	4376(3)	1725(3)	9743(5)	59(1)
C(5)	3924(3)	2390(2)	8453(4)	55(1)
C(6)	3377(4)	3779(3)	6567(5)	67(1)
C(7)	3852(4)	3605(3)	8359(5)	64(1)
C(8)	2632(3)	2358(3)	4468(4)	61(1)
C(9)	2547(3)	1276(3)	4016(5)	74(1)
C(10)	2039(4)	1005(5)	2489(6)	92(2)
C(11)	1624(4)	1796(7)	1407(7)	104(2)
C(12)	1710(4)	2852(5)	1856(6)	93(2)
C(13)	2215(3)	3157(4)	3378(6)	78(1)
H(4)	4352(23)	973(21)	9496(39)	55(9)
H(6A)	2600(33)	4194(27)	6514(48)	99(12)
H(6B)	3906(27)	4054(24)	5871(45)	72(10)
H(7A)	4615(34)	3911(29)	8614(52)	97(12)
H(7B)	3306(27)	3833(23)	9147(43)	69(9)
H(9)	2848(30)	726(27)	4873(51)	82(12)
H(10)	1971(31)	297(30)	2237(50)	81(12)
H(11)	1293(37)	1616(39)	278(67)	107(16)
H(12)	1394(34)	3521(38)	1140(56)	99(15)
H(13)	2241(34)	3927(32)	3654(57)	87(12)

Table A.6.10 *- Anisotropic displacement parameters ($Å^2$ x 10^3) for the 290K X-ray structure of DCNP.*

Atom	U11	U22	U33	U23	U13	U12
N(1)	108(2)	72(2)	91(3)	4(2)	-27(2)	4(2)
N(2)	105(3)	69(2)	92(3)	-12(2)	-16(2)	-3(2)
N(3)	76(2)	51(1)	59(2)	1(1)	-4(2)	1(1)
N(4)	90(2)	53(2)	61(2)	1(2)	-1(2)	-2(2)
C(1)	73(2)	61(2)	71(3)	0(2)	-10(2)	-1(2)
C(2)	64(2)	58(2)	66(2)	-1(2)	0(2)	-4(2)
C(3)	57(2)	51(2)	65(2)	-1(2)	3(2)	-5(1)
C(4)	67(2)	43(2)	66(2)	-2(2)	2(2)	-3(2)
C(5)	63(2)	46(2)	56(2)	0(2)	6(2)	-3(2)
C(6)	84(3)	50(2)	69(3)	4(2)	5(2)	-3(2)
C(7)	81(3)	46(2)	65(2)	1(2)	6(2)	0(2)
C(8)	58(2)	71(2)	54(2)	2(2)	4(2)	2(2)
C(9)	75(3)	82(3)	64(2)	-4(2)	5(2)	-13(2)
C(10)	87(3)	120(4)	69(3)	-23(3)	6(2)	-39(3)
C(11)	71(3)	179(6)	61(3)	-7(4)	-3(2)	-27(3)
C(12)	69(3)	142(4)	67(3)	15(3)	-8(3)	6(3)
C(13)	70(3)	93(3)	71(3)	13(3)	3(2)	8(2)

Table A.6.11 *- THMA11 Corrected Anisotropic Displacement Parameters for the 90K X-ray Refinement.*

Atom	U11	U22	U33	U23	U13	U12
N(1)	0.0340	0.0260	0.0290	0.0017	-0.0081	0.0005
N(2)	0.0343	0.0228	0.0271	-0.0039	-0.0030	-0.0016
N(3)	0.0222	0.0216	0.0238	-0.0001	-0.0014	-0.0016
N(4)	0.0225	0.0241	0.0234	0.0008	-0.0003	-0.0001
C(1)	0.0265	0.0232	0.0261	0.0006	-0.0045	-0.0010
C(2)	0.0248	0.0218	0.0244	-0.0020	-0.0010	-0.0017
C(3)	0.0220	0.0208	0.0241	-0.0004	-0.0016	-0.0016
C(4)	0.0232	0.0195	0.0244	-0.0002	-0.0023	-0.0016
C(5)	0.0219	0.0198	0.0235	-0.0001	-0.0008	-0.0011
C(6)	0.0323	0.0225	0.0260	0.0018	-0.0022	0.0012
C(7)	0.0300	0.0200	0.0255	0.0000	-0.0018	0.0006
C(8)	0.0216	0.0292	0.0231	0.0009	-0.0003	-0.0005
C(9)	0.0293	0.0323	0.0241	-0.0038	0.0007	-0.0057
C(10)	0.0328	0.0500	0.0251	-0.0075	0.0017	-0.0133
C(11)	0.0224	0.0695	0.0225	-0.0021	0.0008	-0.0089
C(12)	0.0230	0.0628	0.0239	0.0074	0.0006	0.0034
C(13)	0.0259	0.0402	0.0257	0.0066	0.0006	0.0043

Table A.6.12 *- THMA11 corrected Anisotropic Displacement Parameters of the 100K X-ray refinement.*

Atom	U11	U22	U33	U23	U13	U12
N(1)	0.0344	0.0263	0.0287	0.0025	-0.0079	0.0015
N(2)	0.0347	0.0217	0.0262	-0.0051	-0.0017	-0.0022
N(3)	0.0221	0.0183	0.0220	-0.0002	-0.0001	-0.0014
N(4)	0.0229	0.0210	0.0215	0.0008	0.0011	0.0003
C(1)	0.0265	0.0223	0.0253	0.0009	-0.0040	-0.0005
C(2)	0.0247	0.0203	0.0233	-0.0027	0.0000	-0.0019
C(3)	0.0218	0.0189	0.0229	-0.0006	-0.0009	-0.0015
C(4)	0.0229	0.0167	0.0231	-0.0002	-0.0014	-0.0014
C(5)	0.0219	0.0166	0.0220	-0.0003	0.0004	-0.0008
C(6)	0.0336	0.0192	0.0246	0.0017	-0.0007	0.0018
C(7)	0.0307	0.0168	0.0241	-0.0003	-0.0004	0.0009
C(8)	0.0219	0.0268	0.0210	0.0009	0.0013	-0.0003
C(9)	0.0288	0.0300	0.0234	-0.0041	0.0026	-0.0059
C(10)	0.0316	0.0497	0.0255	-0.0098	0.0034	-0.0130
C(11)	0.0226	0.0720	0.0206	-0.0035	0.0027	-0.0086
C(12)	0.0237	0.0637	0.0220	0.0087	0.0021	0.0027
C(13)	0.0260	0.0385	0.0247	0.0076	0.0016	0.0040

Table A.6.13 *- THMA11 Corrected Anisotropic Displacement Parameters for the 200K X-ray refinement.*

Atom	U11	U22	U33	U23	U13	U12
N(1)	0.0710	0.0501	0.0566	0.0044	-0.0165	0.0029
N(2)	0.0679	0.0422	0.0514	-0.0096	-0.0055	-0.0031
N(3)	0.0435	0.0351	0.0425	-0.0011	0.0006	-0.0020
N(4)	0.0440	0.0396	0.0416	0.0009	0.0024	-0.0002
C(1)	0.0543	0.0432	0.0494	0.0013	-0.0079	-0.0003
C(2)	0.0487	0.0396	0.0452	-0.0051	-0.0005	-0.0029
C(3)	0.0437	0.0371	0.0442	-0.0014	-0.0013	-0.0020
C(4)	0.0456	0.0330	0.0446	-0.0010	-0.0020	-0.0017
C(5)	0.0425	0.0325	0.0423	-0.0011	0.0014	-0.0013
C(6)	0.0636	0.0368	0.0481	0.0029	-0.0026	0.0012
C(7)	0.0583	0.0327	0.0470	-0.0010	-0.0016	0.0007
C(8)	0.0431	0.0493	0.0408	0.0010	0.0028	-0.0011
C(9)	0.0572	0.0545	0.0464	-0.0080	0.0040	-0.0085
C(10)	0.0651	0.0865	0.0489	-0.0169	0.0056	-0.0216
C(11)	0.0474	0.1226	0.0404	-0.0060	0.0046	-0.0172
C(12)	0.0475	0.1093	0.0426	0.0134	0.0030	0.0022
C(13)	0.0519	0.0681	0.0460	0.0116	0.0028	0.0053

Table A.6.14 *- THMA11 Corrected Anisotropic Displacement Parameters for the 290K X-ray Refinement.*

Atom	U11	U22	U33	U23	U13	U12
N(1)	0.1023	0.0731	0.0822	0.0075	-0.0239	0.0043
N(2)	0.0970	0.0615	0.0748	-0.0137	-0.0074	-0.0041
N(3)	0.0637	0.0494	0.0622	-0.0003	0.0003	-0.0035
N(4)	0.0651	0.0556	0.0607	0.0024	0.0032	-0.0006
C(1)	0.0789	0.0627	0.0720	0.0030	-0.0119	-0.0005
C(2)	0.0710	0.0575	0.0660	-0.0069	-0.0009	-0.0042
C(3)	0.0640	0.0536	0.0647	-0.0010	-0.0022	-0.0032
C(4)	0.0663	0.0471	0.0651	-0.0001	-0.0032	-0.0032
C(5)	0.0623	0.0461	0.0618	-0.0004	0.0017	-0.0026
C(6)	0.0923	0.0517	0.0695	0.0051	-0.0029	0.0016
C(7)	0.0844	0.0463	0.0681	-0.0005	-0.0017	0.0003
C(8)	0.0644	0.0693	0.0598	0.0024	0.0033	-0.0012
C(9)	0.0843	0.0767	0.0660	-0.0097	0.0047	-0.0117
C(10)	0.0955	0.1199	0.0700	-0.0211	0.0058	-0.0292
C(11)	0.0722	0.1675	0.0592	-0.0060	0.0046	-0.0226
C(12)	0.0716	0.1495	0.0626	0.0198	0.0028	0.0024
C(13)	0.0759	0.0947	0.0676	0.0172	0.0026	0.0067

Table A.6.15 *- THMA11 corrected anisotropic displacement parameters for the 100K neutron refinement.*

Atom	U11	U22	U33	U23	U13	U12
N(1)	0.0346	0.0245	0.0256	0.0022	-0.0093	0.0042
N(2)	0.0326	0.0167	0.0258	-0.0085	-0.0025	-0.0048
N(3)	0.0169	0.0135	0.0174	-0.0017	0.0001	-0.0014
N(4)	0.0163	0.0186	0.0179	0.0008	0.0011	0.0002
C(1)	0.0223	0.0180	0.0211	-0.0005	-0.0042	0.0009
C(2)	0.0178	0.0146	0.0203	-0.0052	0.0004	-0.0033
C(3)	0.0147	0.0128	0.0184	-0.0026	-0.0004	-0.0012
C(4)	0.0178	0.0097	0.0185	-0.0023	-0.0013	-0.0006
C(5)	0.0151	0.0101	0.0178	-0.0018	0.0007	-0.0004
C(6)	0.0303	0.0154	0.0243	0.0030	-0.0023	0.0022
C(7)	0.0265	0.0104	0.0230	-0.0010	-0.0014	0.0013
C(8)	0.0156	0.0289	0.0168	0.0014	0.0016	-0.0017
C(9)	0.0264	0.0320	0.0177	-0.0031	0.0011	-0.0073
C(10)	0.0312	0.0502	0.0195	-0.0070	0.0009	-0.0144
C(11)	0.0176	0.0703	0.0156	-0.0009	0.0025	-0.0102
C(12)	0.0175	0.0629	0.0180	0.0095	0.0025	0.0009
C(13)	0.0204	0.0400	0.0211	0.0080	0.0014	0.0022
H(4)	0.0310	0.0096	0.0221	-0.0025	-0.0060	0.0004
H(6A)	0.0378	0.0207	0.0271	0.0080	-0.0042	-0.0073
H(6B)	0.0427	0.0222	0.0292	0.0023	-0.0056	0.0133
H(7A)	0.0344	0.0121	0.0259	0.0007	-0.0031	-0.0070
H(7B)	0.0322	0.0159	0.0254	-0.0049	-0.0030	0.0099
H(9)	0.0365	0.0252	0.0211	-0.0060	-0.0053	-0.0070
H(10)	0.0509	0.0511	0.0232	-0.0105	-0.0077	-0.0167
H(11)	0.0189	0.0788	0.0148	0.0006	0.0025	-0.0133
H(12)	0.0240	0.0686	0.0212	0.0138	0.0001	0.0033
H(13)	0.0347	0.0369	0.0260	0.0101	-0.0034	0.0070

Table A.7.1 *- Atomic coordinates (x 10^4) and equivalent isotropic displacement parameters ($Å^2$ x 10^3) for the 100K neutron structure of N-methylurea.*

Atom	x	y	z	U(eq)
O(1)	1971(1)	8754(2)	4464(2)	11(1)
N(1)	4054(1)	8358(1)	6501(1)	14(1)
N(2)	4069(1)	6990(1)	3426(1)	14(1)
C(1)	3302(1)	8067(2)	4781(2)	8(1)
C(2)	3339(2)	6463(2)	1584(2)	21(1)
H(1)	5145(3)	7842(5)	6662(4)	27(1)
H(2)	3595(3)	9308(4)	7474(4)	26(1)
H(3)	5136(3)	6478(5)	3781(4)	27(1)
H(4)	4166(5)	5843(8)	620(7)	66(1)
H(5)	2449(7)	5392(8)	1785(8)	68(1)
H(6)	2807(5)	7689(6)	887(5)	52(1)

Table A.7.2 *- Anisotropic displacement parameters ($Å^2$ x 10^3) for the 100K neutron structure of N-methylurea.*

Atom	U11	U22	U33	U23	U13	U12
O(1)	8(1)	12(1)	14(1)	0(1)	0(1)	2(1)
N(1)	12(1)	18(1)	13(1)	-3(1)	-2(1)	3(1)
N(2)	13(1)	17(1)	13(1)	-4(1)	0(1)	4(1)
C(1)	6(1)	7(1)	11(1)	1(1)	1(1)	-1(1)
C(2)	28(1)	18(1)	16(1)	-7(1)	-5(1)	5(1)
H(1)	20(1)	34(1)	28(1)	-3(1)	-5(1)	9(1)
H(2)	26(1)	27(1)	24(1)	-5(1)	-3(1)	1(1)
H(3)	22(1)	31(1)	29(1)	-3(1)	1(1)	9(1)
H(4)	66(2)	90(4)	41(2)	-36(2)	-13(2)	40(3)
H(5)	84(3)	62(3)	57(3)	-6(2)	-20(3)	-35(3)
H(6)	75(3)	41(2)	39(2)	-6(2)	-20(2)	19(2)

Table A.7.3 *- Atomic coordinates (x 10^4) and equivalent isotropic displacement parameters ($Å^2$ x 10^3) for the 250K neutron structure of N-methylurea.*

Atom	x	y	z	U(eq)
C(1)	3289(4)	8047(6)	4747(5)	23(1)
O(1)	1995(4)	8779(8)	4353(7)	32(1)
N(1)	3994(4)	8313(6)	6472(6)	38(1)
N(2)	4094(4)	6968(5)	3448(5)	36(1)
C(2)	3459(8)	6508(8)	1589(7)	52(2)
H(1)	5069(9)	7759(15)	6684(12)	53(3)
H(2)	3535(12)	9222(15)	7359(15)	48(2)
H(3)	5129(10)	6447(14)	3848(14)	48(2)
H(4)	4426(26)	6350(45)	538(39)	74(5)
H(4')	3971(29)	5518(41)	867(39)	74(5)
H(5)	2206(31)	5796(43)	1876(44)	88(6)
H(5')	2828(36)	5222(51)	1581(47)	88(6)
H(6)	2577(27)	7548(37)	1072(33)	65(4)
H(6')	3211(25)	7777(34)	719(33)	65(4)

Table A.7.4 *- Anisotropic displacement parameters ($Å^2$ x 10^3) for the 250K neutron structure of N-methylurea.*

Atom	U11	U22	U33	U23	U13	U12
C(1)	17(2)	25(2)	28(2)	2(2)	0(2)	-1(2)
O(1)	27(2)	35(3)	34(3)	1(2)	-1(2)	1(2)
N(1)	32(2)	46(2)	36(2)	-1(2)	-1(2)	7(2)
H(1)	40(5)	71(7)	48(6)	-8(5)	-12(4)	22(5)
H(2)	48(5)	53(6)	44(5)	0(5)	2(5)	-2(5)
N(2)	35(2)	38(2)	35(2)	-6(2)	3(2)	8(2)
C(2)	69(3)	51(3)	35(3)	-13(3)	-13(3)	8(3)
H(3)	45(4)	45(5)	54(6)	-3(4)	5(4)	18(5)

Table A.8.1 *- Atomic coordinates (x 10^4) and equivalent isotropic displacement parameters ($Å^2$ x 10^3) for the 100K neutron structure of ZTS as determined using D9.*

Atom	x	y	z	U(eq)
Zn(1)	9317(1)	6560(1)	8513(1)	7(1)
S(1)	8714(2)	8425(3)	10224(1)	6(1)
S(2)	10157(2)	8317(3)	7458(1)	10(1)
S(3)	7921(2)	4900(3)	7756(1)	9(1)
S(4)	10799(2)	4974(3)	9211(1)	8(1)
O(1)	8412(1)	8128(2)	9287(1)	11(1)
O(2)	8358(1)	6897(2)	10721(1)	12(1)
O(3)	8017(1)	9952(2)	10498(1)	10(1)
O(4)	10017(1)	8759(2)	10295(1)	11(1)
N(1)	11482(1)	9598(1)	8759(1)	14(1)
N(2)	12208(1)	10005(1)	7395(1)	15(1)
N(3)	9994(1)	3572(1)	7132(1)	14(1)
N(4)	8370(1)	3591(1)	6223(1)	15(1)
N(5)	8934(1)	2862(1)	9602(1)	15(1)
N(6)	10683(1)	2525(1)	10375(1)	13(1)
C(1)	11366(1)	9382(1)	7920(1)	9(1)
C(2)	8850(1)	3966(1)	6980(1)	9(1)
C(3)	10062(1)	3338(1)	9770(1)	9(1)
H(1A)	10836(2)	9215(3)	9182(2)	25(1)
H(1B)	12176(2)	10333(4)	8991(2)	27(1)
H(2A)	12967(2)	10546(4)	7624(2)	34(1)
H(2B)	12128(2)	9864(4)	6745(2)	26(1)
H(3A)	10360(2)	3830(4)	7711(2)	31(1)
H(3B)	10573(2)	3256(4)	6642(2)	28(1)
H(4A)	8852(2)	2921(4)	5774(2)	30(1)
H(4B)	7538(3)	4028(4)	6085(2)	38(1)
H(5A)	8493(2)	3388(4)	9094(2)	31(1)
H(5B)	8549(2)	1857(3)	9929(2)	26(1)
H(6A)	10371(2)	1396(3)	10619(2)	32(1)
H(6B)	11540(2)	2911(3)	10501(2)	26(1)

Table A.8.2 *- Anisotropic displacement parameters ($Å^2 \times 10^3$) for the 100K neutron structure of ZTS as determined using D9.*

Atom	U11	U22	U33	U23	U13	U12
Zn(1)	7(1)	6(1)	8(1)	0(1)	-1(1)	0(1)
S(1)	8(1)	4(1)	5(1)	0(1)	-2(1)	1(1)
S(2)	10(1)	10(1)	9(1)	1(1)	-1(1)	-3(1)
S(3)	7(1)	13(1)	8(1)	-3(1)	2(1)	0(1)
S(4)	7(1)	9(1)	9(1)	1(1)	2(1)	1(1)
O(1)	13(1)	12(1)	8(1)	-2(1)	-2(1)	4(1)
O(2)	11(1)	10(1)	13(1)	4(1)	-2(1)	-2(1)
O(3)	11(1)	9(1)	9(1)	-1(1)	1(1)	0(1)
O(4)	7(1)	12(1)	13(1)	1(1)	-1(1)	-1(1)
N(1)	15(1)	19(1)	9(1)	-1(1)	0(1)	-7(1)
H(1A)	26(1)	31(1)	19(1)	-1(1)	4(1)	-9(1)
H(1B)	26(1)	34(1)	23(1)	-4(1)	-5(1)	-12(1)
N(2)	13(1)	21(1)	10(1)	1(1)	1(1)	-8(1)
H(2A)	27(1)	46(2)	30(1)	-1(1)	0(1)	-21(1)
H(2B)	30(1)	34(1)	15(1)	-2(1)	3(1)	-7(1)
N(3)	10(1)	19(1)	14(1)	-7(1)	1(1)	2(1)
H(3A)	23(1)	44(2)	26(1)	-13(1)	-7(1)	8(1)
H(3B)	18(1)	35(1)	30(1)	-12(1)	4(1)	4(1)
N(4)	13(1)	22(1)	10(1)	-6(1)	-1(1)	1(1)
H(4A)	30(1)	39(1)	23(1)	-16(1)	4(1)	3(1)
H(4B)	23(1)	61(2)	29(1)	-15(1)	-9(1)	12(1)
N(5)	10(1)	14(1)	20(1)	7(1)	-2(1)	-3(1)
H(5A)	25(1)	31(1)	37(1)	16(1)	-9(1)	-3(1)
H(5B)	20(1)	24(1)	34(1)	9(1)	0(1)	-6(1)
N(6)	13(1)	12(1)	13(1)	5(1)	-1(1)	1(1)
H(6A)	31(1)	29(1)	36(1)	16(1)	-5(1)	-6(1)
H(6B)	21(1)	28(1)	28(1)	5(1)	-4(1)	0(1)
C(1)	9(1)	11(1)	8(1)	0(1)	0(1)	-3(1)
C(2)	8(1)	10(1)	10(1)	-3(1)	1(1)	-1(1)
C(3)	9(1)	9(1)	10(1)	2(1)	1(1)	0(1)

Table A.8.5 *- Atomic coordinates (x 10^4) and equivalent isotropic displacement parameters ($Å^2$ x 10^3) for the 100K neutron structure of ZTS as determined using LADI.*

Atom	x	y	z	U(eq)
Zn(1)	9318(3)	6563(4)	8515(2)	6(1)
S(1)	8717(6)	8440(8)	10225(5)	4(1)
S(2)	10158(7)	8317(11)	7455(6)	12(2)
S(3)	7925(8)	4912(9)	7750(6)	11(2)
S(4)	10803(6)	4977(8)	9204(5)	6(2)
O(1)	8414(3)	8128(5)	9285(3)	9(1)
O(2)	8359(3)	6895(5)	10722(3)	10(1)
O(3)	8016(3)	9957(4)	10496(3)	8(1)
O(4)	10020(3)	8757(5)	10293(3)	11(1)
N(1)	11483(2)	9600(3)	8759(2)	14(1)
N(2)	12216(3)	10000(3)	7396(2)	13(1)
N(3)	9993(2)	3578(4)	7136(2)	14(1)
N(4)	8368(2)	3586(3)	6222(2)	15(1)
N(5)	8939(2)	2869(3)	9602(2)	14(1)
N(6)	10686(2)	2525(3)	10373(2)	12(1)
C(1)	11369(3)	9389(4)	7918(2)	8(1)
C(2)	8854(3)	3958(4)	6979(2)	8(1)
C(3)	10063(3)	3345(4)	9773(2)	8(1)
H(1A)	10857(7)	9215(10)	9188(5)	26(2)
H(1B)	12162(7)	10335(10)	9009(5)	23(2)
H(2A)	12956(8)	10575(12)	7642(5)	32(2)
H(2B)	12135(8)	9864(9)	6743(7)	24(2)
H(3A)	10357(7)	3855(11)	7698(7)	30(2)
H(3B)	10570(6)	3246(11)	6639(5)	27(2)
H(4A)	8858(7)	2906(11)	5784(6)	28(2)
H(4B)	7543(8)	4047(13)	6072(7)	38(2)
H(5A)	8502(6)	3398(11)	9098(6)	28(2)
H(5B)	8552(6)	1858(10)	9934(5)	24(2)
H(6A)	10357(8)	1412(10)	10620(6)	30(2)
H(6B)	11535(7)	2887(10)	10510(6)	26(2)

Table A.8.6 *- Anisotropic displacement parameters ($Å^2 \times 10^3$) for the 100K neutron structure of ZTS as determined using LADI.*

Atom	U11	U22	U33	U23	U13	U12
Zn(1)	5(1)	3(2)	9(2)	1(1)	-1(1)	-2(1)
S(1)	2(3)	1(3)	8(4)	3(3)	-1(3)	0(2)
S(2)	11(3)	14(4)	11(5)	-1(3)	-6(3)	-5(3)
S(3)	10(4)	11(4)	13(6)	-7(3)	-3(3)	-1(3)
S(4)	8(3)	5(3)	6(5)	0(2)	-4(3)	3(2)
O(1)	12(2)	9(2)	7(2)	-3(1)	1(1)	5(1)
O(2)	11(2)	8(2)	11(2)	8(2)	1(1)	-3(1)
O(3)	9(2)	5(2)	9(2)	-1(1)	2(1)	2(1)
O(4)	3(2)	13(2)	16(3)	4(2)	1(1)	-2(1)
N(1)	16(1)	18(1)	7(2)	-1(1)	-2(1)	-7(1)
H(1A)	24(4)	33(4)	22(4)	-1(3)	1(3)	-5(3)
H(1B)	25(3)	34(4)	11(4)	-6(3)	2(3)	-7(3)
N(2)	14(1)	17(1)	10(2)	2(1)	1(1)	-10(1)
H(2A)	30(4)	40(5)	26(5)	-6(4)	-5(3)	-20(4)
H(2B)	32(4)	27(4)	13(6)	-1(3)	1(3)	-8(3)
N(3)	6(1)	20(1)	17(2)	-5(1)	2(1)	2(1)
H(3A)	24(3)	43(5)	23(5)	-12(4)	-7(4)	6(3)
H(3B)	15(3)	42(4)	24(5)	-23(3)	11(3)	4(3)
N(4)	13(1)	22(1)	9(2)	-6(1)	2(1)	-3(1)
H(4A)	28(4)	38(4)	19(5)	-9(3)	3(3)	2(4)
H(4B)	31(4)	51(5)	31(5)	-19(4)	-11(3)	11(4)
N(5)	8(1)	13(1)	22(2)	7(1)	-3(1)	-4(1)
H(5A)	18(3)	30(4)	35(5)	14(3)	-9(3)	-5(3)
H(5B)	18(3)	21(3)	32(5)	7(3)	2(3)	-3(3)
N(6)	10(1)	9(1)	16(2)	5(1)	-1(1)	-1(1)
H(6A)	32(4)	21(4)	36(5)	20(3)	-9(3)	-6(3)
H(6B)	17(4)	26(3)	34(5)	3(4)	-10(3)	2(3)
C(1)	8(1)	8(2)	8(2)	1(1)	2(1)	-5(1)
C(2)	7(1)	9(1)	8(2)	-3(1)	5(1)	-4(1)
C(3)	7(2)	7(2)	12(2)	2(1)	1(1)	3(1)

Table A.9.1 *- Atomic coordinates (x 10^4) and equivalent isotropic displacement parameters ($Å^2$ x 10^3) for the 150K X-ray structure of* $Mg0.5VC_{19}H_{28}N$.

Atom	x	y	z	U(eq)
V(1)	267(2)	1483(1)	1175(1)	31(1)
Mg	0	0	0	31(1)
N(1)	1717(7)	1100(5)	907(3)	25(2)
C(1)	3062(8)	1077(6)	891(4)	24(2)
C(2)	3582(9)	2068(7)	494(4)	33(2)
C(3)	4904(9)	1951(8)	476(4)	50(3)
C(4)	5725(10)	961(8)	841(4)	61(3)
C(5)	5241(10)	15(7)	1270(4)	46(2)
C(6)	3912(8)	54(7)	1293(4)	31(2)
C(7)	2682(8)	3219(7)	118(3)	38(2)
C(8)	2988(9)	4454(8)	634(4)	60(3)
C(9)	2903(8)	3604(8)	-656(4)	62(3)
C(10)	3438(9)	-935(7)	1780(4)	36(2)
C(11)	3952(9)	-541(7)	2603(4)	58(3)
C(12)	3878(9)	-2364(7)	1700(4)	58(3)
C(13)	-859(9)	3050(7)	1744(4)	48(3)
C(14)	416(9)	3565(8)	1728(4)	40(2)
C(15)	1430(9)	2741(7)	2168(4)	46(3)
C(16)	755(8)	1699(7)	2441(4)	40(2)
C(17)	-618(8)	1897(7)	2197(4)	39(2)
C(18)	-673(8)	-525(7)	1114(4)	37(2)
C(19)	-1136(8)	2065(7)	95(4)	36(2)
H(3A)	5249(9)	2581(8)	180(4)	60
H(4A)	6653(10)	923(8)	820(4)	73
H(5A)	5836(10)	-662(7)	1544(4)	55
H(7A)	1753(8)	2960(7)	51(3)	46
H(8A)	2836(9)	4245(8)	1109(4)	72
H(8B)	3920(9)	4694(8)	696(4)	72
H(8C)	2420(9)	5196(8)	416(4)	72
H(9A)	2703(8)	2858(8)	-995(4)	74
H(9B)	2337(8)	4356(8)	-859(4)	74
H(9C)	3837(8)	3855(8)	-579(4)	74
H(10A)	2467(9)	-916(7)	1659(4)	44
H(11A)	3664(9)	355(7)	2687(4)	70
H(11B)	3632(9)	-1167(7)	2912(4)	70
H(11C)	4923(9)	-570(7)	2722(4)	70
H(12A)	3531(9)	-2634(7)	1193(4)	69
H(12B)	4850(9)	-2379(7)	1827(4)	69
H(12C)	3559(9)	-2976(7)	2017(4)	69
H(13A)	-1728(9)	3443(7)	1522(4)	58
H(14A)	557(9)	4401(8)	1499(4)	48
H(15A)	2385(9)	2920(7)	2299(4)	55
H(16A)	1191(8)	1022(7)	2789(4)	48
H(17A)	-1301(8)	1359(7)	2329(4)	47
H(18A)	-1671	-181	1026	50
H(18B)	61	-976	1540	50
H(18C)	-872	-985	719	50
H(19A)	-505	3000	23	50
H(19C)	-1797	2211	366	50
H(19B)	-1526	1787	-409	50

Table A.9.2 *- Atomic coordinates (x 10^4) and equivalent isotropic displacement parameters ($Å^2$ x 10^3) for the 150K X-ray structure of $V_2C_{35}H_{47}N_2$.*

Atom	x	y	z	U(eq)
V(1)	2957(1)	7762(1)	6373(1)	28(1)
V(2)	1721(1)	8381(1)	5358(1)	27(1)
N(1)	3193(3)	8604(1)	6190(2)	29(1)
N(2)	2394(3)	7572(1)	5242(2)	30(1)
C(1)	3946(5)	6817(2)	6716(3)	45(1)
C(2)	3101(4)	6951(2)	7307(3)	42(1)
C(3)	3618(4)	7478(2)	7746(2)	43(1)
C(4)	4784(4)	7673(2)	7430(3)	44(1)
C(5)	4986(4)	7265(2)	6790(3)	44(1)
C(6)	893(4)	8540(2)	3970(2)	35(1)
C(7)	-181(4)	8636(2)	4423(2)	35(1)
C(8)	142(4)	9146(2)	4958(2)	37(1)
C(9)	1426(4)	9362(2)	4836(2)	37(1)
C(10)	1896(4)	8987(2)	4228(2)	37(1)
C(11)	3960(4)	9127(2)	6484(2)	32(1)
C(12)	3404(4)	9572(2)	6979(2)	38(1)
C(13)	4210(5)	10078(2)	7271(3)	50(1)
C(14)	5500(5)	10157(2)	7086(3)	55(1)
C(15)	6024(5)	9730(2)	6595(3)	46(1)
C(16)	5281(4)	9214(2)	6281(2)	37(1)
C(17)	1996(5)	9489(2)	7217(3)	44(1)
C(18)	2113(5)	9197(2)	8082(3)	57(1)
C(19)	1153(6)	10085(2)	7181(3)	69(2)
C(20)	5891(4)	8777(2)	5706(2)	39(1)
C(21)	7252(4)	8509(2)	6108(3)	52(1)
C(22)	6031(5)	9106(2)	4882(3)	50(1)
C(23)	2398(4)	7095(2)	4652(2)	33(1)
C(24)	3269(4)	7130(2)	4040(2)	36(1)
C(25)	3234(5)	6650(2)	3459(3)	49(1)
C(26)	2368(5)	6154(2)	3469(3)	55(1)
C(27)	1527(5)	6122(2)	4069(3)	52(1)
C(28)	1524(4)	6576(2)	4675(2)	39(1)
C(29)	4270(4)	7654(2)	4009(3)	42(1)
C(30)	4112(5)	7962(2)	3151(3)	58(1)
C(31)	5732(5)	7416(2)	4272(3)	60(1)
C(32)	579(4)	6531(2)	5319(3)	44(1)
C(33)	-812(4)	6826(2)	5009(3)	52(1)
C(34)	378(6)	5870(2)	5613(4)	70(2)
C(35)	811(4)	7986(2)	6476(3)	44(1)
C(36)	-99(12)	10136(6)	9651(7)	71(3)
C(37)	-1291(12)	10575(6)	9486(8)	73(3)
C(38)	-1558(14)	10736(6)	8840(9)	88(4)
H(1A)	3889(5)	6457(2)	6367(3)	54
H(2A)	2354(4)	6704(2)	7430(3)	50
H(3A)	3274(4)	7653(2)	8216(2)	52
H(4A)	5392(4)	7998(2)	7652(3)	53
H(5A)	5751(4)	7264(2)	6492(3)	53
H(6A)	905(4)	8249(2)	3525(2)	42
H(7A)	-1032(4)	8416(2)	4348(2)	42
H(8A)	-445(4)	9336(2)	5303(2)	44
H(9A)	1872(4)	9726(2)	5079(2)	44

H(10A)	2710(4)	9055(2)	3988(2)	44
H(13A)	3841(5)	10379(2)	7609(3)	60
H(14A)	6035(5)	10507(2)	7303(3)	65
H(15A)	6928(5)	9788(2)	6466(3)	55
H(17A)	1504(5)	9202(2)	6832(3)	53
H(18A)	2639(5)	8824(2)	8104(3)	68
H(18B)	2557(5)	9486(2)	8482(3)	68
H(18C)	1220(5)	9106(2)	8209(3)	68
H(19A)	1066(6)	10266(2)	6636(3)	83
H(19B)	265(6)	9990(2)	7312(3)	83
H(19C)	1602(6)	10370(2)	7585(3)	83
H(20A)	5269(4)	8439(2)	5577(2)	47
H(21A)	7136(4)	8306(2)	6618(3)	63
H(21B)	7576(4)	8217(2)	5738(3)	63
H(21C)	7901(4)	8838(2)	6225(3)	63
H(22A)	5164(5)	9269(2)	4633(3)	60
H(22B)	6675(5)	9438(2)	4994(3)	60
H(22C)	6350(5)	8817(2)	4507(3)	60
H(25A)	3825(5)	6667(2)	3043(3)	59
H(26A)	2364(5)	5826(2)	3070(3)	66
H(27A)	906(5)	5781(2)	4061(3)	62
H(29A)	4096(4)	7960(2)	4408(3)	50
H(30A)	3192(5)	8107(2)	3004(3)	70
H(30B)	4729(5)	8305(2)	3167(3)	70
H(30C)	4313(5)	7668(2)	2744(3)	70
H(31A)	5811(5)	7225(2)	4811(3)	72
H(31B)	5942(5)	7119(2)	3872(3)	72
H(31C)	6358(5)	7756(2)	4294(3)	72
H(32A)	994(4)	6758(2)	5799(3)	53
H(33A)	-678(4)	7243(2)	4836(3)	62
H(33B)	-1280(4)	6595(2)	4547(3)	62
H(33C)	-1348(4)	6828(2)	5454(3)	62
H(34A)	1255(6)	5690(2)	5800(4)	84
H(34B)	-153(6)	5867(2)	6061(4)	84
H(34C)	-84(6)	5634(2)	5154(4)	84
H(35A)	984	8139	7123	52
H(35B)	183	7602	6438	52
H(35C)	184	8381	6367	52

Table A.9.3 *- Anisotropic displacement parameters ($Å^2$ x 10^3) for the 150K X-ray structure of $V_2C_{35}H_{47}N_2$.*

Atom	U11	U22	U33	U23	U13	U12
V(1)	30(1)	24(1)	30(1)	2(1)	4(1)	1(1)
V(2)	27(1)	24(1)	30(1)	2(1)	4(1)	1(1)
N(1)	29(2)	28(2)	29(2)	-1(1)	4(1)	0(1)
N(2)	28(2)	27(2)	34(2)	1(1)	2(1)	0(1)
C(1)	61(3)	26(2)	47(3)	5(2)	1(2)	12(2)
C(2)	43(2)	35(2)	46(2)	17(2)	1(2)	-2(2)
C(3)	56(3)	47(3)	26(2)	9(2)	1(2)	8(2)
C(4)	43(2)	39(2)	45(2)	9(2)	-13(2)	0(2)
C(5)	36(2)	46(3)	50(3)	13(2)	6(2)	13(2)
C(6)	43(2)	31(2)	29(2)	2(2)	1(2)	2(2)
C(7)	28(2)	33(2)	42(2)	7(2)	-2(2)	0(2)
C(8)	35(2)	34(2)	40(2)	6(2)	6(2)	11(2)
C(9)	45(2)	23(2)	40(2)	9(2)	-2(2)	0(2)
C(10)	37(2)	39(2)	36(2)	12(2)	9(2)	2(2)
C(11)	41(2)	26(2)	26(2)	4(2)	-2(2)	-1(2)
C(12)	54(3)	27(2)	28(2)	1(2)	-4(2)	2(2)
C(13)	78(3)	33(2)	34(2)	-6(2)	-3(2)	-2(2)
C(14)	72(3)	35(3)	49(3)	4(2)	-14(2)	-18(2)
C(15)	48(3)	39(2)	47(2)	10(2)	-8(2)	-14(2)
C(16)	39(2)	32(2)	37(2)	7(2)	-3(2)	-6(2)
C(17)	61(3)	35(2)	36(2)	-5(2)	8(2)	10(2)
C(18)	71(3)	48(3)	53(3)	4(2)	15(2)	6(2)
C(19)	88(4)	56(3)	66(3)	3(3)	19(3)	31(3)
C(20)	31(2)	45(2)	41(2)	5(2)	4(2)	-8(2)
C(21)	35(2)	66(3)	55(3)	10(2)	6(2)	6(2)
C(22)	51(3)	55(3)	44(2)	9(2)	6(2)	-10(2)
C(23)	40(2)	25(2)	32(2)	-3(2)	-5(2)	6(2)
C(24)	39(2)	32(2)	35(2)	-2(2)	0(2)	11(2)
C(25)	58(3)	47(3)	39(2)	-13(2)	-1(2)	13(2)
C(26)	74(3)	38(3)	48(3)	-17(2)	-7(2)	9(2)
C(27)	65(3)	31(2)	53(3)	-2(2)	-14(2)	-4(2)
C(28)	47(2)	28(2)	38(2)	1(2)	-8(2)	0(2)
C(29)	46(2)	40(2)	41(2)	-5(2)	14(2)	6(2)
C(30)	72(3)	54(3)	53(3)	0(2)	24(2)	9(3)
C(31)	44(3)	60(3)	77(3)	-5(3)	13(2)	6(2)
C(32)	50(3)	37(2)	41(2)	8(2)	-8(2)	-11(2)
C(33)	50(3)	52(3)	50(3)	8(2)	-2(2)	-5(2)
C(34)	82(4)	51(3)	76(4)	21(3)	6(3)	-12(3)
C(35)	36(2)	47(3)	51(3)	-5(2)	18(2)	-7(2)

Table A.9.4 *- Atomic coordinates (x 10^4) and equivalent isotropic displacement parameters ($Å^2$ x 10^3) for the 150K X-ray structure of $VC_{11}H_{10}NCl_2$.*

Atom	x	y	z	U(eq)
V	6924(1)	1498(1)	4469(1)	26(1)
Cl(1)	6605(1)	-671(2)	3144(1)	42(1)
Cl(2)	7055(1)	-266(2)	5995(1)	36(1)
N(1)	8086(3)	1976(6)	4288(3)	30(1)
C(1)	8995(3)	2704(7)	4060(4)	24(1)
C(2)	9811(4)	2368(7)	4774(4)	30(1)
C(3)	10734(3)	2949(8)	4507(5)	36(1)
C(4)	10828(4)	3909(8)	3543(5)	42(2)
C(5)	10006(4)	4311(8)	2869(4)	39(1)
C(6)	9090(3)	3704(7)	3099(4)	30(1)
C(7)	5451(4)	2710(10)	5054(6)	55(2)
C(8)	6229(5)	3874(11)	5373(5)	60(2)
C(9)	6611(4)	4618(9)	4454(7)	58(2)
C(10)	6058(5)	3810(10)	3578(5)	50(2)
C(11)	5334(4)	2668(9)	3972(6)	50(2)
H(2)	9732(31)	1729(67)	5357(36)	36
H(3)	11247(32)	2553(69)	4975(37)	43
H(4)	11415(33)	4206(73)	3343(38)	50
H(5)	10062(32)	4992(72)	2252(39)	46
H(6)	8564(30)	4127(66)	2639(34)	36
H(7)	5083(36)	2100(78)	5553(42)	66
H(8)	6576(39)	4299(87)	5956(46)	71
H(9)	7117(37)	5399(81)	4450(44)	70
H(10)	6192(36)	4203(82)	2941(41)	61
H(11)	4852(34)	2030(78)	3468(39)	60

Table A.9.5 *- Anisotropic displacement parameters ($Å^2$ x 10^3) for the 150K X-ray structure of $VC_{11}H_{10}NCl_2$.*

Atom	U11	U22	U33	U23	U13	U12
V	23(1)	28(1)	28(1)	-1(1)	4(1)	0(1)
Cl(1)	56(1)	37(1)	34(1)	-8(1)	4(1)	-4(1)
Cl(2)	34(1)	44(1)	31(1)	8(1)	2(1)	4(1)
N(1)	28(2)	31(3)	31(2)	3(2)	6(2)	5(2)
C(1)	27(3)	15(3)	32(3)	-2(2)	6(2)	0(2)
C(2)	34(3)	26(3)	30(3)	4(3)	4(2)	6(3)
C(3)	25(3)	34(4)	48(4)	-15(3)	-2(3)	2(3)
C(4)	31(3)	40(4)	59(4)	-12(3)	23(3)	-11(3)
C(5)	51(4)	33(3)	33(3)	4(3)	14(3)	-3(3)
C(6)	35(3)	23(3)	30(3)	-2(3)	-2(2)	3(3)
C(7)	42(4)	55(5)	72(5)	24(4)	33(4)	26(4)
C(8)	73(5)	55(5)	47(4)	-22(4)	-18(4)	37(4)
C(9)	27(3)	23(4)	124(7)	2(4)	8(4)	-1(3)
C(10)	62(4)	51(5)	40(4)	21(4)	18(3)	23(4)
C(11)	34(3)	44(4)	68(4)	-9(4)	-19(3)	15(3)

Table A.9.6 *- Atomic coordinates (x 10^4) and equivalent isotropic displacement parameters ($Å^2$ x 10^3) for the 150K X-ray structure of $NbC_{15}H_{18}NCl_2$.*

Atom	x	y	z	U(eq)
Nb	4984(1)	2500	3802(1)	16(1)
Cl	4436(1)	526(1)	2894(1)	26(1)
N(1)	3953(3)	2500	4720(2)	18(1)
C(1)	3392(4)	2500	5590(3)	17(1)
C(2)	4051(4)	2500	6411(3)	21(1)
C(3)	3581(4)	2500	7303(3)	26(1)
C(4)	2431(4)	2500	7391(4)	29(1)
C(5)	1762(4)	2500	6586(3)	26(1)
C(6)	2199(4)	2500	5666(3)	20(1)
C(7)	1426(4)	2500	4797(3)	24(1)
C(8)	177(4)	2500	5084(4)	38(1)
C(9)	1633(3)	1149(4)	4204(2)	29(1)
C(10)	7038(4)	2500	3356(3)	24(1)
C(11)	6817(3)	1291(4)	3912(2)	25(1)
C(12)	6466(3)	1745(4)	4818(2)	26(1)
H(2)	4795(44)	2500	6346(34)	26
H(3)	4011(44)	2500	7845(37)	32
H(4)	2122(46)	2500	7962(38)	35
H(5)	990(45)	2500	6655(35)	32
H(8A)	21(34)	1589(42)	5454(27)	46
H(8B)	-242(50)	2500	4549(44)	46
H(9A)	2360(32)	1031(40)	3969(24)	34
H(9B)	1500(30)	287(41)	4589(24)	34
H(9C)	1104(30)	1044(39)	3695(25)	34
H(10)	7240(43)	2500	2723(36)	29
H(11)	6878(28)	338(40)	3718(24)	30
H(12)	6260(29)	1122(39)	5335(24)	32

Table A.9.7 *- Anisotropic displacement parameters ($Å^2$ x 10^3) for the 150K X-ray structure of $NbC_{15}H_{18}NCl_2$.*

Atom	U11	U22	U33	U23	U13	U12
Nb	15(1)	17(1)	16(1)	0	1(1)	0
Cl	27(1)	24(1)	27(1)	-7(1)	1(1)	-2(1)
N(1)	17(2)	18(2)	21(2)	0	0(2)	0
C(1)	19(2)	15(2)	16(2)	0	3(2)	0
C(2)	19(2)	22(2)	23(2)	0	2(2)	0
C(3)	29(3)	30(2)	21(2)	0	-5(2)	0
C(4)	32(3)	37(3)	19(2)	0	7(2)	0
C(5)	17(2)	35(3)	27(2)	0	5(2)	0
C(6)	18(2)	18(2)	23(2)	0	0(2)	0
C(7)	16(2)	32(3)	24(2)	0	-3(2)	0
C(8)	16(3)	59(4)	39(3)	0	-3(2)	0
C(9)	24(2)	32(2)	30(2)	-6(2)	-6(2)	-7(2)
C(10)	17(2)	32(3)	25(2)	0	3(2)	0
C(11)	18(2)	21(2)	37(2)	-4(2)	-2(1)	5(1)
C(12)	17(2)	36(2)	26(2)	13(2)	-3(1)	1(1)

Table A.9.8 *- Atomic coordinates (x 10^4) and equivalent isotropic displacement parameters ($Å^2$ x 10^3) for the 150K X-ray structure of* $TaC_{19}H_{31}N$.

Atom	x	y	z	U(eq)
Ta(1)	1464(1)	2412(1)	4292(1)	15(1)
N(1)	3194(3)	2444(2)	4979(1)	18(1)
C(11)	1720(4)	3380(2)	3413(2)	22(1)
C(16)	1582(4)	1281(2)	3577(2)	23(1)
C(1)	-1037(4)	1767(2)	4379(2)	22(1)
C(2)	-1378(3)	2489(2)	3919(2)	22(1)
C(3)	-883(4)	3176(2)	4410(2)	21(1)
C(4)	-204(4)	2881(2)	5179(2)	19(1)
C(5)	-289(4)	2003(2)	5159(2)	21(1)
C(6)	-1570(5)	910(2)	4152(3)	31(1)
C(7)	-2175(4)	2524(3)	3064(2)	32(1)
C(8)	-1256(5)	4055(2)	4199(3)	29(1)
C(9)	315(5)	3396(2)	5904(2)	29(1)
C(10)	122(5)	1427(2)	5862(2)	29(1)
C(12)	2767(4)	4143(2)	3516(2)	22(1)
C(13)	4395(4)	3875(2)	3630(3)	29(1)
C(14)	2440(6)	4677(2)	2753(3)	35(1)
C(15)	2505(5)	4661(2)	4235(2)	31(1)
C(17)	3002(4)	847(2)	3417(2)	21(1)
C(18)	3709(5)	386(2)	4172(2)	33(1)
C(19)	2598(5)	219(2)	2732(3)	33(1)
C(20)	4116(5)	1461(2)	3174(3)	31(1)
C(21)	4452(3)	2475(2)	5639(2)	23(1)
C(22)	5897(4)	2211(3)	5343(2)	32(1)
C(23)	4173(4)	1882(2)	6303(2)	30(1)
C(24)	4657(5)	3350(2)	5970(2)	32(1)
H(11A)	721(45)	3524(22)	3122(23)	26
H(11B)	2102(43)	2946(23)	3074(22)	26
H(16A)	979(45)	871(23)	3709(23)	28
H(16B)	939(45)	1459(22)	3056(25)	28
H(6A)	-2512(52)	857(25)	4295(26)	37
H(6B)	-1643(49)	797(25)	3639(29)	37
H(6C)	-969(51)	509(26)	4446(27)	37
H(7A)	-1738(49)	2932(27)	2816(26)	39
H(7B)	-2137(49)	2045(27)	2829(25)	39
H(7C)	-3233(49)	2651(25)	3044(25)	39
H(8A)	-2205(51)	4204(25)	4250(26)	35
H(8B)	-601(48)	4425(24)	4558(26)	35
H(8C)	-1142(48)	4188(25)	3699(28)	35
H(9A)	1096(49)	3137(25)	6302(26)	35
H(9B)	813(50)	3867(25)	5785(26)	35
H(9C)	-552(49)	3565(24)	6173(26)	35
H(10A)	-827(49)	1181(24)	6053(25)	34
H(10B)	529(49)	1715(25)	6302(26)	34
H(10C)	725(51)	1054(25)	5777(26)	34
H(13A)	4591(50)	3608(25)	3200(27)	35
H(13B)	4702(49)	3554(25)	4010(27)	35
H(13C)	5039(48)	4312(26)	3721(25)	35
H(14A)	2491(51)	4381(26)	2247(28)	42
H(14B)	1362(51)	4920(26)	2684(26)	42
H(14C)	3059(53)	5126(28)	2870(27)	42

H(15A)	2687(47)	4314(25)	4711(26)	37
H(15B)	3215(50)	5135(25)	4329(26)	37
H(15C)	1636(52)	4882(25)	4173(26)	37
H(18A)	4583(53)	93(26)	4159(27)	40
H(18B)	3037(51)	-47(26)	4316(27)	40
H(18C)	3876(49)	746(26)	4664(27)	40
H(19A)	1865(51)	-193(26)	2869(26)	40
H(19B)	2206(51)	481(26)	2236(28)	40
H(19C)	3445(51)	-61(26)	2626(28)	40
H(20A)	3751(48)	1789(25)	2690(26)	38
H(20B)	4436(51)	1789(26)	3552(27)	38
H(20C)	4997(50)	1208(25)	3102(26)	38
H(22A)	5848(48)	1648(27)	5148(25)	39
H(22B)	6050(44)	2566(24)	4854(24)	39
H(22C)	6690(48)	2256(25)	5746(25)	39
H(23A)	4033(49)	1324(25)	6090(26)	36
H(23B)	5084(48)	1825(24)	6738(24)	36
H(23C)	3309(48)	2028(25)	6541(24)	36
H(24A)	4866(48)	3730(25)	5585(26)	38
H(24B)	3770(51)	3556(25)	6204(26)	38
H(24C)	5384(52)	3422(25)	6416(27)	38

Table A.9.9 *- Anisotropic displacement parameters ($Å^2$ x 10^3) for the 150K X-ray structure of* $TaC_{19}H_{31}N$.

Atom	U11	U22	U33	U23	U13	U12
Ta(1)	14(1)	15(1)	16(1)	-1(1)	2(1)	1(1)
N(1)	17(1)	19(1)	19(1)	0(1)	4(1)	0(1)
C(11)	22(2)	21(1)	22(2)	-1(1)	3(1)	-1(1)
C(16)	20(2)	21(1)	29(2)	-6(1)	3(1)	1(1)
C(1)	18(2)	20(1)	27(2)	-4(1)	5(1)	-1(1)
C(2)	14(1)	27(2)	24(1)	-2(1)	1(1)	0(1)
C(3)	14(1)	20(1)	28(2)	1(1)	5(1)	4(1)
C(4)	17(1)	20(1)	20(1)	-1(1)	3(1)	3(1)
C(5)	19(2)	18(1)	26(2)	4(1)	6(1)	1(1)
C(6)	27(2)	23(2)	44(2)	-10(2)	9(2)	-6(1)
C(7)	23(1)	47(2)	25(1)	1(2)	-3(1)	-3(2)
C(8)	26(2)	22(2)	39(2)	4(1)	6(2)	6(1)
C(9)	30(2)	30(2)	29(2)	-9(1)	7(2)	4(1)
C(10)	28(2)	29(2)	29(2)	10(1)	6(2)	0(1)
C(12)	23(2)	22(1)	22(2)	3(1)	6(1)	-1(1)
C(13)	24(2)	32(2)	32(2)	3(1)	6(2)	-1(1)
C(14)	40(2)	29(2)	38(2)	11(2)	8(2)	-3(2)
C(15)	33(2)	27(2)	34(2)	-4(1)	9(2)	-5(2)
C(17)	25(2)	19(1)	21(2)	-1(1)	6(1)	3(1)
C(18)	42(2)	26(2)	30(2)	5(1)	2(2)	9(2)
C(19)	40(2)	29(2)	30(2)	-10(1)	4(2)	5(2)
C(20)	33(2)	31(2)	33(2)	-3(1)	13(2)	-1(2)
C(21)	20(1)	31(2)	17(1)	-1(1)	2(1)	-3(1)
C(22)	19(2)	46(2)	29(2)	3(2)	0(1)	5(1)
C(23)	28(2)	38(2)	23(2)	5(1)	-1(1)	-1(2)
C(24)	30(2)	35(2)	27(2)	-4(1)	-3(2)	-9(2)

Table A.9.10 *- Atomic coordinates (x 10^4) and equivalent isotropic displacement parameters ($Å^2$ x 10^3) for the 150K X-ray structure of* $Ta_2C_{46}H_{44}O_4F_{10}$

Atom	x	y	z	U(eq)
Ta	733(1)	1467(1)	212(1)	23(1)
F(2)	398(9)	3517(9)	3795(7)	43(2)
F(3)	1504(11)	4073(10)	6275(8)	53(2)
F(4)	4415(11)	4098(9)	7073(7)	51(2)
F(5)	6121(9)	3448(9)	5299(8)	47(2)
F(6)	5032(8)	2935(8)	2836(7)	37(2)
O(1)	2143(10)	2989(9)	2031(8)	31(2)
O(2)	221(9)	498(8)	1188(7)	26(2)
C(1)	2678(15)	3175(12)	3217(10)	29(3)
C(2)	1807(15)	3467(15)	4138(14)	39(3)
C(3)	2366(17)	3758(15)	5418(13)	44(4)
C(4)	3809(18)	3750(16)	5798(12)	43(4)
C(5)	4719(16)	3455(14)	4918(12)	36(3)
C(6)	4124(14)	3173(13)	3641(11)	29(3)
C(7)	2984(14)	1553(14)	-272(11)	32(3)
C(8)	3170(14)	951(13)	-1647(11)	29(3)
C(9)	4144(15)	1776(14)	-2021(12)	32(3)
C(10)	4270(16)	1223(18)	-3333(14)	47(4)
C(11)	3455(16)	-128(17)	-4242(12)	43(3)
C(12)	2506(15)	-997(16)	-3875(12)	39(3)
C(13)	2365(14)	-487(14)	-2611(12)	34(3)
C(14)	1002(15)	3316(15)	-438(12)	36(1)
C(15)	-41(15)	1989(15)	-1569(12)	36(1)
C(16)	-1400(15)	1532(15)	-1155(12)	36(1)
C(17)	-1136(15)	2512(14)	187(12)	36(1)
C(18)	309(15)	3613(15)	610(12)	36(1)
C(14A)	2501(14)	4282(14)	-396(12)	36(1)
C(15A)	125(15)	1263(15)	-2925(12)	36(1)
C(16A)	-2844(15)	233(15)	-2066(12)	36(1)
C(17A)	-2362(15)	2485(15)	926(12)	36(1)
C(18A)	1005(15)	4993(14)	1920(12)	36(1)
H(7A)	3681	2554	214	39
H(7B)	3445	1119	144	39
H(9A)	4747(15)	2744(14)	-1376(12)	39
H(10A)	4942(16)	1819(18)	-3574(14)	56
H(11A)	3518(16)	-497(17)	-5140(12)	51
H(12A)	1947(15)	-1971(16)	-4522(12)	46
H(13A)	1720(14)	-1104(14)	-2377(12)	40
H(14A)	2266(14)	4868(14)	-693(12)	43
H(14B)	3182(14)	4852(14)	497(12)	43
H(14C)	3015(14)	3750(14)	-968(12)	43
H(15A)	-240(15)	1627(15)	-3432(12)	43
H(15B)	1212(15)	1407(15)	-2872(12)	43
H(15C)	-491(15)	281(15)	-3350(12)	43
H(16A)	-3553(15)	450(15)	-2521(12)	43
H(16B)	-2544(15)	-467(15)	-2704(12)	43
H(16C)	-3356(15)	-111(15)	-1557(12)	43
H(17A)	-2988(15)	2964(15)	784(12)	43
H(17B)	-3029(15)	1535(15)	606(12)	43
H(17C)	-1852(15)	2943(15)	1858(12)	43
H(18A)	674(15)	5666(14)	1834(12)	43

H(18B)	650(15)	4869(14)	2605(12)	43
H(18C)	2133(15)	5318(14)	2147(12)	43

Table A.9.11 *- Anisotropic displacement parameters ($Å^2$ x 10^3) for the 150K X-ray structure of* $Ta_2C_{46}H_{44}O_4F_{10}$.

Atom	U11	U22	U33	U23	U13	U12
Ta	25(1)	18(1)	24(1)	12(1)	3(1)	7(1)
F(2)	38(4)	43(5)	48(4)	24(4)	12(3)	15(4)
F(3)	66(5)	55(6)	42(4)	22(4)	29(4)	26(4)
F(4)	71(6)	42(5)	33(4)	23(4)	2(4)	11(4)
F(5)	44(4)	42(5)	50(4)	24(4)	-3(4)	16(4)
F(6)	36(4)	33(4)	34(4)	15(3)	8(3)	11(3)
O(1)	35(4)	21(4)	32(4)	13(4)	0(3)	6(4)
O(2)	33(4)	20(4)	27(4)	17(3)	4(3)	7(3)
C(1)	48(7)	9(6)	25(5)	9(5)	2(5)	3(5)
C(2)	35(7)	24(7)	43(7)	10(6)	7(5)	5(5)
C(3)	56(8)	32(8)	36(7)	20(6)	11(6)	3(6)
C(4)	59(9)	35(8)	26(6)	20(6)	-1(6)	3(7)
C(5)	39(6)	29(7)	38(6)	20(6)	3(5)	8(5)
C(6)	39(6)	17(6)	26(5)	12(5)	1(5)	4(5)
C(7)	33(6)	34(7)	30(6)	20(5)	4(4)	10(5)
C(8)	33(6)	23(6)	29(5)	12(5)	5(4)	13(5)
C(9)	40(6)	25(7)	40(6)	22(6)	14(5)	13(5)
C(10)	38(7)	69(11)	51(8)	43(8)	16(6)	22(7)
C(11)	40(7)	61(10)	33(6)	24(7)	12(5)	27(7)
C(12)	34(6)	42(8)	38(6)	18(6)	12(5)	16(6)
C(13)	33(6)	36(8)	38(6)	22(6)	9(5)	15(6)

Table A.9.12 *- Atomic coordinates (x 10^4) and equivalent isotropic displacement parameters ($Å^2$ x 10^3) for the 150K X-ray structure of* $TaC_{34}H_{30}O_4F_{20}$.

Atom	x	y	z	U(eq)
Ta(1)	1838(1)	1332(1)	2500	15(1)
C(1)	-1057(13)	1426(4)	2500	23(3)
C(2)	-498(9)	1689(3)	1742(5)	22(2)
C(3)	490(9)	2097(3)	2028(5)	17(2)
C(4)	-2238(14)	1003(5)	2500	28(3)
C(5)	-925(13)	1551(5)	813(6)	34(2)
C(6)	1282(11)	2475(4)	1439(6)	31(2)
O(1)	2321(7)	1232(2)	1228(3)	28(1)
C(7)	3464(9)	1091(3)	681(5)	20(2)
C(8)	3589(9)	1303(3)	-165(5)	23(2)
F(8)	2576(6)	1686(2)	-372(3)	35(1)
C(9)	4755(11)	1159(3)	-750(5)	30(2)
F(9)	4794(6)	1386(2)	-1551(3)	48(1)
C(10)	5846(11)	786(4)	-527(6)	37(2)
F(10)	6963(7)	656(3)	-1124(4)	60(2)
C(11)	5745(10)	568(3)	281(6)	28(2)
F(11)	6823(7)	210(2)	511(4)	51(2)
C(12)	4575(11)	716(3)	860(5)	27(2)
F(12)	4527(6)	480(2)	1658(3)	38(1)
O(2)	3892(9)	1689(3)	2500	30(2)
C(13)	4959(14)	2073(4)	2500	24(3)
C(14)	5538(10)	2275(3)	1719(5)	23(2)
F(14)	5028(6)	2099(2)	942(3)	38(1)
C(15)	6669(10)	2657(3)	1725(5)	29(2)
F(15)	7197(7)	2850(2)	944(3)	44(2)
C(16)	7245(13)	2857(5)	2500	25(3)
F(16)	8301(9)	3233(3)	2500	42(2)
O(3)	1266(9)	632(3)	2500	27(2)
C(17)	592(13)	176(4)	2500	21(2)
C(18)	239(10)	-70(3)	3273(6)	29(2)
F(18)	549(7)	160(2)	4043(3)	45(1)
C(19)	-440(11)	-543(3)	3292(7)	41(3)
F(19)	-751(8)	-778(2)	4059(4)	69(2)
C(20)	-770(16)	-792(5)	2500	43(4)
F(20)	-1423(10)	-1249(3)	2500	83(4)
H(4A)	-3644(145)	1157(44)	2500	33
H(4B)	-2123(99)	839(33)	1973(51)	33
H(5A)	-2120(112)	1695(34)	582(59)	41
H(5B)	-579(131)	1694(38)	472(64)	41
H(5C)	-913(122)	1192(38)	703(60)	41
H(6A)	521(113)	2673(33)	1128(57)	37
H(6B)	2130(106)	2608(35)	1752(59)	37
H(6C)	1682(110)	2246(33)	802(56)	37

Table A.9.13 *- Anisotropic displacement parameters ($Å^2$ x 10^3) for the 150K X-ray structure of $TaC_{34}H_{15}O_4F_{20}$.*

Atom	U11	U22	U33	U23	U13	U12
Ta(1)	13(1)	16(1)	18(1)	0	0	1(1)
C(1)	5(5)	17(7)	47(7)	0	0	1(5)
C(2)	10(4)	27(4)	29(4)	3(4)	-4(4)	0(3)
C(3)	11(4)	18(4)	23(4)	6(3)	2(4)	6(3)
C(4)	14(7)	24(7)	46(8)	0	0	-2(5)
C(5)	31(6)	52(6)	18(5)	-2(4)	-12(4)	6(5)
C(6)	24(5)	32(5)	36(5)	18(4)	-1(4)	3(4)
O(1)	27(3)	38(4)	20(3)	-3(3)	5(2)	11(3)
C(7)	18(5)	28(4)	14(3)	0(3)	3(3)	0(4)
C(8)	25(4)	20(4)	25(4)	7(4)	-8(3)	-4(4)
F(8)	39(3)	39(3)	28(3)	6(2)	-4(2)	1(3)
C(9)	37(6)	37(5)	15(4)	-3(4)	13(4)	-16(4)
F(9)	46(3)	78(4)	19(2)	8(3)	7(2)	-17(3)
C(10)	31(5)	47(6)	33(5)	-16(5)	8(5)	-3(5)
F(10)	40(3)	90(5)	50(3)	-22(3)	23(3)	9(4)
C(11)	14(4)	26(5)	45(5)	-7(4)	4(4)	7(4)
F(11)	34(3)	58(4)	61(4)	-12(3)	4(3)	14(3)
C(12)	28(5)	26(5)	28(5)	-3(4)	-7(4)	5(4)
F(12)	30(3)	50(3)	32(3)	16(2)	3(3)	7(3)
O(2)	14(4)	31(5)	45(5)	0	0	-3(4)
C(13)	15(6)	17(6)	40(7)	0	0	10(5)
C(14)	15(4)	24(4)	32(5)	-7(4)	-3(4)	1(4)
F(14)	36(3)	44(3)	33(3)	-10(2)	3(2)	-10(3)
C(15)	24(5)	25(4)	37(5)	5(4)	17(4)	-3(4)
F(15)	43(4)	53(3)	35(3)	2(3)	12(3)	-15(3)
C(16)	13(7)	32(7)	29(6)	0	0	0(5)
F(16)	34(4)	37(4)	55(5)	0	0	-17(4)
O(3)	18(4)	19(4)	44(5)	0	0	-11(4)
C(17)	6(5)	23(6)	34(6)	0	0	-1(5)
C(18)	22(4)	24(4)	39(5)	-5(4)	10(4)	5(4)
F(18)	54(4)	49(3)	32(3)	9(3)	10(3)	0(3)
C(19)	19(4)	30(5)	75(7)	27(5)	6(5)	-1(4)
F(19)	62(4)	58(4)	87(5)	44(4)	20(4)	-3(3)
C(20)	21(7)	11(6)	99(13)	0	0	-1(6)
F(20)	41(5)	21(5)	187(11)	0	0	-20(4)

Table A.9.14 *- Atomic coordinates (x 10^4) and equivalent isotropic displacement parameters (Å^2 x 10^3) for the 150K X-ray structure of* $Ta_2C_{44}H_{30}O_4F_{20}.C_7H_8$.

Atom	x	y	z	U(eq)
Ta(1)	2737(1)	2098(1)	840(1)	27(1)
Ta(2)	1955(1)	1223(1)	1769(1)	27(1)
O(10)	3209(5)	1325(4)	1449(2)	27(2)
O(11)	1482(5)	1954(4)	1144(2)	29(2)
C(1)	3258(8)	883(6)	311(4)	29(2)
C(1A)	3965(8)	133(7)	539(4)	43(3)
C(2)	3553(8)	1646(7)	74(4)	32(3)
C(2A)	4649(7)	1916(7)	15(4)	41(3)
C(3)	2602(8)	2125(6)	-128(4)	33(3)
C(3A)	2561(9)	2940(7)	-438(4)	52(3)
C(4)	1715(8)	1647(7)	-4(4)	33(3)
C(4A)	569(8)	1910(8)	-158(5)	54(3)
C(5)	2109(7)	881(6)	266(4)	29(2)
C(5A)	1477(7)	136(6)	427(4)	36(3)
O(1)	4150(5)	2631(4)	1058(3)	37(2)
C(6)	5039(7)	2649(6)	1430(4)	29(2)
C(7)	5339(8)	3402(6)	1706(4)	36(3)
F(7)	4696(4)	4117(4)	1633(2)	42(2)
C(8)	6256(9)	3450(6)	2090(4)	33(3)
F(8)	6511(5)	4215(4)	2351(2)	47(2)
C(9)	6922(8)	2728(7)	2178(4)	44(3)
F(9)	7833(5)	2785(4)	2528(3)	59(2)
C(10)	6660(8)	1969(7)	1896(4)	40(3)
F(10)	7298(5)	1285(4)	1979(3)	59(2)
C(11)	5716(8)	1931(6)	1531(4)	32(3)
F(11)	5502(5)	1178(3)	1265(2)	42(2)
O(2)	694(5)	517(4)	1550(3)	35(2)
C(12)	-298(8)	267(6)	1394(4)	31(2)
C(13)	-676(8)	-537(7)	1531(4)	35(3)
F(13)	8(5)	-1058(4)	1864(3)	50(2)
C(14)	-1699(9)	-814(7)	1384(5)	44(3)
F(14)	-2000(5)	-1603(4)	1535(3)	57(2)
C(15)	-2440(9)	-296(8)	1054(4)	41(3)
F(15)	-3440(5)	-559(4)	900(2)	57(2)
C(16)	-2113(9)	487(8)	904(4)	47(3)
F(16)	-2788(5)	1022(5)	596(3)	63(2)
C(17)	-1057(9)	776(7)	1064(4)	39(3)
F(17)	-780(5)	1562(4)	897(3)	57(2)
O(3)	2645(5)	89(4)	2046(3)	35(2)
C(18)	3345(8)	-448(7)	1891(4)	30(2)
C(19)	4455(8)	-277(6)	2011(4)	30(2)
F(19)	4796(4)	451(4)	2281(2)	42(2)
C(20)	5199(9)	-844(7)	1863(4)	37(3)
F(20)	6223(5)	-632(4)	1983(2)	50(2)
C(21)	4870(8)	-1608(7)	1599(4)	35(3)
F(21)	5580(5)	-2161(4)	1457(2)	51(2)
C(22)	3793(9)	-1798(6)	1481(4)	36(3)
F(22)	3480(5)	-2544(4)	1232(3)	55(2)
C(23)	3061(8)	-1234(6)	1624(4)	36(3)
F(23)	2022(5)	-1433(3)	1500(2)	47(2)

O(4)	2273(6)	3302(4)	676(3)	46(2)
C(24)	2158(9)	4149(7)	609(4)	36(3)
C(25)	1169(8)	4558(7)	616(4)	37(3)
F(25)	340(5)	4063(4)	691(3)	54(2)
C(26)	1013(9)	5449(8)	543(4)	45(3)
F(26)	72(5)	5809(4)	559(3)	67(2)
C(27)	1838(10)	5971(7)	453(4)	39(3)
F(27)	1698(6)	6845(3)	392(3)	66(2)
C(28)	2803(9)	5600(6)	455(4)	36(3)
F(28)	3644(5)	6107(4)	381(3)	64(2)
C(29)	2959(9)	4703(6)	524(4)	40(3)
F(29)	3904(5)	4359(4)	480(3)	53(2)
C(30)	2749(9)	1958(8)	2588(5)	50(3)
C(30A)	3979(18)	2209(16)	2650(10)	17(6)
C(30B)	3944(19)	1861(16)	2879(10)	82(8)
C(31)	2054(9)	1368(7)	2736(5)	51(3)
C(31A)	2775(20)	689(15)	3123(9)	18(6)
C(31B)	2143(18)	580(15)	3130(9)	73(7)
C(32)	1042(9)	1590(8)	2510(5)	53(3)
C(32A)	-283(28)	1411(23)	2490(14)	60(10)
C(32B)	120(14)	976(12)	2652(7)	42(5)
C(33)	1065(9)	2350(7)	2207(5)	50(3)
C(33A)	515(24)	3166(19)	1846(12)	42(8)
C(33B)	-49(15)	2701(12)	1897(8)	53(5)
C(34)	2158(9)	2578(7)	2241(5)	48(3)
C(34A)	2935(20)	3314(16)	2123(10)	21(6)
C(34B)	2321(18)	3448(14)	1955(9)	69(7)
C(35)	7530	4319	1102	86
C(36)	6535	4700	952	86
C(37)	6311	5500	1168	86
C(38)	7081	5919	1532	86
C(39)	8076	5538	1682	86
C(40)	8301	4738	1467	86
C(41)	7659	3476	862	86
H(1AA)	4082(8)	-270(7)	268(4)	52
H(1AB)	4635(8)	357(7)	717(4)	52
H(1AC)	3614(8)	-166(7)	789(4)	52
H(2AA)	4818(7)	1683(7)	-307(4)	49
H(2AB)	4690(7)	2545(7)	9(4)	49
H(2AC)	5145(7)	1694(7)	310(4)	49
H(3AA)	2503(9)	2803(7)	-807(4)	63
H(3AB)	1960(9)	3285(7)	-386(4)	63
H(3AC)	3202(9)	3266(7)	-322(4)	63
H(4AA)	310(8)	1675(8)	-503(5)	64
H(4AB)	170(8)	1666(8)	91(5)	64
H(4AC)	492(8)	2536(8)	-166(5)	64
H(5AA)	1316(7)	-270(6)	139(4)	43
H(5AB)	1875(7)	-158(6)	729(4)	43
H(5AC)	829(7)	360(6)	514(4)	43
H(36A)	6003	4411	700	103
H(37A)	5624	5763	1064	103
H(38A)	6926	6472	1681	103
H(39A)	8608	5828	1934	103
H(40A)	8988	4475	1570	103
H(41A)	7017	3327	624	103

H(41B)	8237	3505	670	103
H(41C)	7806	3036	1133	103

Table A.9.15 *- Anisotropic displacement parameters ($Å^2$ x 10^3) for the 150K X-ray structure of* $Ta_2C_{44}H_{30}O_4F_{20}.C_7H_8$.

Atom	U11	U22	U33	U23	U13	U12
Ta(1)	32(1)	23(1)	27(1)	3(1)	7(1)	3(1)
Ta(2)	30(1)	23(1)	28(1)	2(1)	9(1)	3(1)
O(10)	33(4)	27(4)	23(4)	8(3)	11(3)	11(3)
O(11)	34(4)	24(4)	31(4)	4(3)	9(3)	3(3)
C(1)	52(7)	19(5)	14(5)	-4(4)	0(5)	14(5)
C(1A)	49(7)	45(7)	32(7)	-8(5)	-1(6)	7(6)
C(2)	40(7)	43(6)	20(6)	-9(5)	20(5)	-5(5)
C(2A)	37(7)	55(7)	33(7)	7(6)	10(5)	-1(6)
C(3)	60(8)	29(6)	12(5)	1(5)	5(5)	1(6)
C(3A)	73(9)	51(7)	35(7)	15(6)	15(6)	9(7)
C(4)	34(6)	37(6)	27(6)	5(5)	0(5)	-1(5)
C(4A)	35(7)	64(8)	58(9)	9(7)	-1(6)	8(6)
C(5)	20(6)	38(6)	28(6)	1(5)	1(4)	-4(5)
C(5A)	34(6)	39(6)	33(7)	-7(5)	4(5)	7(5)
O(1)	37(4)	35(4)	38(5)	6(3)	1(4)	-12(3)
C(6)	25(6)	36(6)	28(6)	5(5)	8(5)	-10(5)
C(7)	43(7)	26(6)	41(7)	-9(5)	17(6)	-6(5)
F(7)	45(4)	37(3)	47(4)	0(3)	12(3)	-1(3)
C(8)	49(7)	31(6)	21(6)	-4(5)	16(5)	-8(5)
F(8)	55(4)	42(4)	43(4)	-17(3)	3(3)	-14(3)
C(9)	36(7)	53(8)	42(7)	-18(6)	1(6)	-1(6)
F(9)	45(4)	69(5)	58(5)	-22(4)	-4(3)	-4(4)
C(10)	30(6)	50(7)	39(7)	-14(6)	4(5)	-5(6)
F(10)	47(4)	63(4)	61(5)	-21(4)	-6(3)	17(4)
C(11)	29(6)	32(6)	39(7)	-15(5)	15(5)	-11(5)
F(11)	53(4)	33(3)	39(4)	-12(3)	8(3)	0(3)
O(2)	24(4)	36(4)	44(5)	-3(4)	4(3)	-4(3)
C(12)	37(7)	26(6)	32(6)	1(5)	15(5)	-5(5)
C(13)	24(6)	40(7)	41(7)	6(5)	8(5)	7(5)
F(13)	43(4)	38(4)	72(5)	10(3)	14(3)	-2(3)
C(14)	44(8)	39(7)	52(8)	-18(6)	13(6)	-13(6)
F(14)	49(4)	45(4)	81(5)	-6(4)	20(4)	-19(3)
C(15)	37(7)	53(8)	36(7)	-23(6)	12(6)	-14(6)
F(15)	32(4)	90(5)	48(4)	-25(4)	4(3)	-16(4)
C(16)	45(8)	67(9)	27(7)	-4(6)	2(6)	18(7)
F(16)	44(4)	97(6)	45(4)	20(4)	-2(3)	12(4)
C(17)	49(8)	32(6)	41(7)	5(5)	21(6)	3(6)
F(17)	49(4)	53(4)	70(5)	22(4)	12(4)	11(3)
O(3)	36(4)	31(4)	40(5)	3(3)	18(4)	4(3)
C(18)	34(6)	32(6)	25(6)	18(5)	4(5)	8(5)
C(19)	51(7)	22(6)	13(5)	8(4)	1(5)	2(5)
F(19)	44(4)	38(4)	39(4)	-11(3)	-5(3)	2(3)
C(20)	37(7)	43(7)	32(7)	2(6)	7(5)	16(6)
F(20)	32(4)	62(4)	54(4)	2(3)	1(3)	12(3)
C(21)	36(7)	48(7)	20(6)	-1(5)	3(5)	20(6)
F(21)	55(4)	46(4)	53(4)	-5(3)	14(3)	23(3)

C(22)	58(8)	20(6)	30(6)	2(5)	8(6)	11(5)
F(22)	71(5)	35(4)	56(5)	-12(3)	6(4)	-1(3)
C(23)	41(7)	28(6)	39(7)	7(5)	10(5)	-3(5)
F(23)	37(4)	40(4)	64(4)	7(3)	12(3)	-8(3)
O(4)	50(5)	22(4)	69(6)	15(4)	15(4)	4(4)
C(24)	46(7)	32(6)	29(6)	1(5)	3(5)	1(5)
C(25)	37(7)	53(7)	23(6)	0(6)	6(5)	-7(6)
F(25)	47(4)	52(4)	65(5)	11(4)	14(3)	4(3)
C(26)	51(8)	43(7)	40(7)	-1(6)	1(6)	22(6)
F(26)	66(5)	56(4)	77(6)	-3(4)	5(4)	27(4)
C(27)	56(8)	28(6)	28(7)	-1(5)	-7(6)	3(6)
F(27)	94(6)	17(3)	81(5)	2(3)	-1(4)	11(3)
C(28)	43(7)	25(6)	33(7)	9(5)	-10(5)	-7(5)
F(28)	78(5)	41(4)	69(5)	16(4)	5(4)	-19(4)
C(29)	60(8)	23(6)	37(7)	6(5)	7(6)	11(6)
F(29)	46(4)	49(4)	67(5)	11(4)	18(3)	5(3)

Table A.9.16 *- Atomic coordinates (x 10^4) and equivalent isotropic displacement parameters ($Å^2$ x 10^3) for the 150K X-ray structure of* $TaC_{34}H_{51}N_2ClLiO$.

Atom	x	y	z	U(eq)
Ta(1)	7707(1)	5949(1)	-1314(1)	23(1)
Cl(1)	7692(1)	4536(1)	-1019(1)	37(1)
C(1)	8798(4)	5660(5)	-1863(4)	33(2)
C(2)	8750(4)	6525(5)	-1766(3)	32(2)
C(3)	8178(4)	6821(5)	-2116(3)	33(2)
C(4)	7884(4)	6154(5)	-2445(4)	33(2)
C(5)	8265(4)	5429(5)	-2287(3)	31(2)
C(6)	9331(4)	5114(5)	-1601(4)	44(2)
C(7)	9228(5)	7034(6)	-1372(4)	49(2)
C(8)	7993(5)	7702(5)	-2195(4)	43(2)
C(9)	7303(4)	6191(6)	-2898(4)	40(2)
C(10)	8145(4)	4597(5)	-2545(4)	38(2)
N(1)	7910(3)	6467(4)	-569(3)	31(1)
C(11)	8148(4)	6991(4)	-103(3)	27(2)
C(12)	8094(4)	7836(5)	-222(4)	36(2)
C(13)	8283(5)	8415(5)	224(4)	42(2)
C(14)	8516(5)	8166(5)	788(4)	47(2)
C(15)	8587(4)	7336(5)	915(4)	43(2)
C(16)	8419(4)	6725(5)	486(4)	32(2)
C(17)	8506(4)	5823(5)	645(4)	39(2)
C(18)	7817(5)	5368(6)	631(4)	49(2)
C(19)	8992(5)	5421(6)	175(4)	51(2)
C(20)	8817(6)	5687(7)	1303(4)	57(3)
N(2)	6790(3)	6206(4)	-1394(3)	29(1)
C(21)	6171(4)	6522(5)	-1628(3)	30(2)
C(22)	6146(4)	7354(5)	-1804(4)	36(2)
C(23)	5568(4)	7703(5)	-2032(4)	44(2)
C(24)	4969(4)	7251(5)	-2089(4)	41(2)
C(25)	4978(4)	6437(5)	-1910(4)	40(2)
C(26)	5561(4)	6047(5)	-1671(3)	30(2)
C(27)	5531(4)	5141(5)	-1473(4)	38(2)
C(28)	4806(5)	4795(6)	-1537(5)	57(3)

C(29)	5755(5)	5033(5)	-785(4)	45(2)
C(30)	5990(5)	4645(5)	-1916(5)	50(2)
Li(1)	6888(7)	6785(11)	-538(7)	51(4)
O(1)	6415(14)	7811(18)	-129(12)	70
O(1')	6297(6)	7250(7)	86(5)	70
H(6A)	9632(4)	5428(5)	-1323(4)	53
H(6B)	9601(4)	4878(5)	-1943(4)	53
H(6C)	9113(4)	4674(5)	-1362(4)	53
H(7A)	9576(5)	6679(6)	-1183(4)	59
H(7B)	8967(5)	7308(6)	-1041(4)	59
H(7C)	9451(5)	7444(6)	-1637(4)	59
H(8A)	8272(5)	8036(5)	-1912(4)	51
H(8B)	7507(5)	7779(5)	-2095(4)	51
H(8C)	8078(5)	7868(5)	-2629(4)	51
H(9A)	7204(4)	5640(6)	-3055(4)	48
H(9B)	7425(4)	6548(6)	-3249(4)	48
H(9C)	6896(4)	6409(6)	-2686(4)	48
H(10A)	7746(4)	4608(5)	-2823(4)	46
H(10B)	8061(4)	4215(5)	-2200(4)	46
H(10C)	8549(4)	4420(5)	-2781(4)	46
H(12A)	7925(4)	8015(5)	-617(4)	43
H(13A)	8248(5)	8982(5)	132(4)	50
H(14A)	8633(5)	8559(5)	1099(4)	57
H(15A)	8758(4)	7177(5)	1314(4)	51
H(18A)	7890(5)	4791(6)	735(4)	59
H(18B)	7616(5)	5410(6)	211(4)	59
H(18C)	7504(5)	5613(6)	937(4)	59
H(19A)	9047(5)	4841(6)	279(4)	62
H(19B)	9439(5)	5693(6)	192(4)	62
H(19C)	8803(5)	5472(6)	-249(4)	62
H(20A)	8862(6)	5099(7)	1382(4)	68
H(20B)	8517(6)	5930(7)	1620(4)	68
H(20C)	9269(6)	5945(7)	1323(4)	68
H(22A)	6546(4)	7679(5)	-1761(4)	43
H(23A)	5572(4)	8262(5)	-2154(4)	53
H(24A)	4563(4)	7494(5)	-2247(4)	49
H(25A)	4569(4)	6128(5)	-1950(4)	48
H(28A)	4495(5)	5097(6)	-1260(5)	69
H(28B)	4807(5)	4216(6)	-1420(5)	69
H(28C)	4652(5)	4852(6)	-1972(5)	69
H(29A)	6218(5)	5250(5)	-731(4)	54
H(29B)	5749(5)	4451(5)	-676(4)	54
H(29C)	5438(5)	5330(5)	-511(4)	54
H(30A)	6461(5)	4848(5)	-1889(5)	60
H(30B)	5824(5)	4702(5)	-2347(5)	60
H(30C)	5978(5)	4067(5)	-1794(5)	60

Table A.9.17 *- Anisotropic displacement parameters ($Å^2$ x 10^3) for the 150K X-ray structure of $TaC_{34}H_{51}N_2ClLiO$.*

Atom	U11	U22	U33	U23	U13	U12
Ta(1)	23(1)	22(1)	25(1)	2(1)	-1(1)	-2(1)
Cl(1)	43(1)	24(1)	44(1)	6(1)	1(1)	-3(1)
C(1)	29(4)	39(4)	33(4)	-4(3)	6(3)	-5(3)
C(2)	29(4)	41(4)	27(4)	-1(3)	6(3)	-11(3)
C(3)	39(4)	32(4)	28(4)	-1(3)	10(3)	-12(3)
C(4)	42(4)	31(4)	27(4)	1(3)	4(3)	-4(4)
C(5)	34(4)	29(4)	30(4)	-3(3)	5(3)	-4(3)
C(6)	35(5)	47(5)	50(5)	-9(4)	0(4)	8(4)
C(7)	45(5)	51(6)	50(5)	-13(4)	7(4)	-23(4)
C(8)	59(6)	25(4)	44(5)	3(3)	9(4)	-5(4)
C(9)	48(5)	43(5)	30(4)	1(4)	-8(3)	3(4)
C(10)	42(5)	28(4)	44(5)	-12(3)	3(4)	-1(4)
N(1)	27(3)	32(3)	34(3)	4(3)	1(3)	-1(3)
C(11)	24(4)	34(4)	23(3)	-2(3)	2(3)	-1(3)
C(12)	42(5)	34(4)	32(4)	0(3)	-2(3)	2(4)
C(13)	53(5)	26(4)	47(5)	-4(3)	6(4)	4(4)
C(14)	52(5)	44(5)	46(5)	-14(4)	-12(4)	-3(4)
C(15)	43(5)	53(5)	33(4)	-3(4)	-11(4)	1(4)
C(16)	27(4)	34(4)	36(4)	0(3)	-2(3)	4(3)
C(17)	41(5)	43(5)	33(4)	7(3)	-8(4)	10(4)
C(18)	64(6)	44(5)	40(5)	15(4)	1(4)	-5(4)
C(19)	54(6)	51(6)	49(5)	0(4)	-9(4)	25(5)
C(20)	72(7)	56(6)	42(5)	8(4)	-14(5)	22(6)
N(2)	26(3)	31(3)	30(3)	-1(3)	2(3)	-7(3)
C(21)	23(4)	42(4)	24(4)	-4(3)	1(3)	-3(3)
C(22)	32(4)	32(4)	44(4)	4(3)	-6(3)	3(3)
C(23)	44(5)	37(5)	50(5)	3(4)	-4(4)	9(4)
C(24)	36(4)	46(5)	41(5)	-2(4)	-7(4)	9(4)
C(25)	29(4)	49(5)	41(5)	-15(4)	-3(3)	-2(4)
C(26)	27(4)	36(4)	27(4)	-4(3)	-1(3)	1(3)
C(27)	37(5)	30(4)	47(5)	-1(4)	1(4)	-6(3)
C(28)	44(5)	47(6)	81(7)	2(5)	-2(5)	-15(4)
C(29)	49(5)	39(5)	48(5)	13(4)	6(4)	-13(4)
C(30)	49(5)	34(5)	67(6)	-12(4)	-3(5)	-1(4)
Li(1)	35(8)	81(11)	38(8)	-16(8)	-2(6)	21(8)

Table A.10.1 *- Atomic coordinates (x 10^4) and equivalent isotropic displacement parameters ($Å^2$ x 10^3) for the 150K neutron structure of [Mo(N-C_6H_3-2,6-Pr^i_2)$_2$$Me_2$].*

Atom	x	y	z	U(eq)
Mo(1)	0	1237(3)	2500	22(1)
N(1)	-722(1)	-251(2)	2498(1)	21(1)
C(1)	-1119(1)	-1959(2)	2514(1)	19(1)
C(2)	-1477(1)	-2867(2)	1883(1)	21(1)
C(3)	-1882(1)	-4553(3)	1918(1)	29(1)
C(4)	-1943(1)	-5340(3)	2551(1)	33(1)
C(5)	-1589(1)	-4433(3)	3165(1)	30(1)
C(6)	-1172(1)	-2744(2)	3161(1)	23(1)
C(7)	-1418(1)	-1948(3)	1198(1)	25(1)
C(8)	-1616(1)	-3425(3)	586(1)	41(1)
C(9)	-1841(1)	3(3)	1042(1)	33(1)
C(10)	-793(1)	-1706(3)	3827(1)	26(1)
C(11)	-655(2)	-3073(4)	4460(1)	54(1)
C(12)	-1170(1)	217(3)	3954(1)	41(1)
C(13)	-210(1)	2991(3)	1583(1)	35(1)
H(3)	-2157(2)	-5289(6)	1447(2)	50(1)
H(4)	-2262(3)	-6660(6)	2561(2)	60(1)
H(5)	-1630(2)	-5070(6)	3654(2)	54(1)
H(7)	-887(2)	-1545(6)	1257(2)	44(1)
H(8A)	-1529(3)	-2726(8)	129(2)	65(1)
H(8B)	-2156(3)	-3794(7)	474(2)	61(1)
H(8C)	-1336(3)	-4839(8)	682(2)	69(1)
H(9A)	-1711(3)	1082(6)	1473(2)	60(1)
H(9B)	-2391(2)	-352(7)	950(2)	61(1)
H(9C)	-1758(3)	746(7)	582(2)	65(1)
H(10)	-297(2)	-1216(7)	3751(2)	50(1)
H(11A)	-334(3)	-2281(8)	4900(3)	78(2)
H(11B)	-401(4)	-4489(9)	4382(2)	97(2)
H(11C)	-1118(4)	-3481(9)	4601(3)	87(2)
H(12A)	-874(3)	1046(7)	4401(3)	71(1)
H(12B)	-1664(3)	-169(9)	4055(3)	79(2)
H(12C)	-1273(3)	1209(7)	3509(3)	68(1)
H(13A)	224(4)	3969(13)	1645(4)	67(2)
H(13')	231(7)	3343(20)	1380(7)	43(3)
H(13B)	-591(4)	4054(9)	1645(3)	101(2)
H(13C)	-390(4)	2209(10)	1114(3)	111(3)

Table A.10.2 *- Anisotropic displacement parameters ($Å^2$ x 10^3) for the 150K neutron structure of [Mo(N-C_6H_3-2,6-Pr^i_2)$_2$$Me_2$].*

Atom	U11	U22	U33	U23	U13	U12
Mo(1)	19(1)	23(1)	23(1)	0	5(1)	0
N(1)	21(1)	23(1)	19(1)	0(1)	4(1)	-3(1)
C(1)	18(1)	22(1)	17(1)	0(1)	3(1)	0(1)
C(2)	21(1)	22(1)	20(1)	-3(1)	2(1)	-1(1)
C(3)	26(1)	25(1)	33(1)	-6(1)	4(1)	-5(1)
H(3)	47(2)	49(2)	47(2)	-19(2)	-2(2)	-9(2)
C(4)	29(1)	24(1)	46(1)	0(1)	11(1)	-8(1)
H(4)	65(3)	45(2)	73(3)	3(2)	21(2)	-28(2)
C(5)	31(1)	27(1)	35(1)	8(1)	12(1)	-1(1)
H(5)	67(3)	51(2)	48(2)	17(2)	24(2)	-4(2)
C(6)	24(1)	25(1)	21(1)	4(1)	7(1)	2(1)
C(7)	25(1)	31(1)	17(1)	-3(1)	2(1)	3(1)
H(7)	38(3)	61(3)	33(2)	4(2)	8(2)	-3(2)
C(8)	51(2)	41(1)	24(1)	-10(1)	-3(1)	9(1)
H(8A)	87(4)	79(3)	27(2)	-4(2)	8(2)	12(3)
H(8B)	53(3)	68(3)	49(3)	-12(2)	-11(2)	-7(2)
H(8C)	95(4)	63(3)	41(2)	-16(2)	2(2)	30(3)
C(9)	37(2)	34(1)	26(1)	0(1)	2(1)	7(1)
H(9A)	84(3)	44(2)	46(3)	-13(2)	7(2)	11(2)
H(9B)	33(3)	72(3)	72(3)	2(2)	0(2)	17(2)
H(9C)	93(4)	63(3)	39(3)	20(2)	17(2)	20(2)
C(10)	28(1)	34(1)	17(1)	2(1)	5(1)	5(1)
H(10)	34(3)	78(3)	39(2)	-8(2)	7(2)	-7(2)
C(11)	93(2)	45(2)	20(1)	12(1)	7(1)	14(2)
H(11A)	109(4)	89(4)	29(3)	5(2)	0(3)	11(3)
H(11B)	156(6)	70(4)	50(3)	10(3)	-4(3)	57(4)
H(11C)	134(6)	84(4)	55(3)	12(3)	44(4)	-13(4)
C(12)	40(2)	42(1)	38(1)	-12(1)	6(1)	7(1)
H(12A)	73(3)	74(3)	59(3)	-30(3)	4(3)	7(3)
H(12B)	48(3)	102(4)	92(4)	-33(3)	28(3)	9(3)
H(12C)	90(4)	53(3)	56(3)	1(2)	9(3)	18(2)
C(13)	33(1)	37(1)	37(1)	17(1)	10(1)	7(1)
H(13B)	123(5)	87(4)	103(4)	45(3)	49(4)	68(4)
H(13C)	193(8)	95(4)	28(3)	12(3)	-4(3)	-4(4)

Table A.10.3 *- Atomic coordinates (x 10^4) and equivalent isotropic displacement parameters ($Å^2$ x 10^3) for the 150K X-ray structure of [MoMe(N-2,6-^{i}Pr$_2$C$_6$H$_3$)$_2$(μ-OMe)]$_2$.*

Atom	x	y	z	U(eq)
Mo(1)	6494(1)	5752(1)	5952(1)	18(1)
O(1)	4386(2)	5518(2)	5410(1)	23(1)
N(1)	6964(2)	7151(2)	6740(1)	22(1)
N(2)	6764(2)	4590(2)	6622(1)	22(1)
C(1)	7419(2)	8195(2)	7442(2)	21(1)
C(2)	7794(3)	9442(2)	7174(2)	26(1)
C(3)	8335(3)	10471(3)	7889(2)	31(1)
C(4)	8484(3)	10297(3)	8839(2)	32(1)
C(5)	8066(3)	9076(3)	9097(2)	29(1)
C(6)	7526(3)	8009(2)	8417(2)	24(1)
C(7)	7639(3)	9681(3)	6143(2)	35(1)
C(8)	6681(4)	10443(4)	5913(3)	60(1)
C(9)	9112(4)	10382(4)	5892(2)	53(1)
C(10)	7006(3)	6684(3)	8713(2)	30(1)
C(11)	5470(4)	6293(3)	8895(3)	60(1)
C(12)	8039(4)	6553(3)	9570(2)	46(1)
C(13)	6935(3)	4010(2)	7443(2)	22(1)
C(14)	8353(3)	4206(2)	7933(2)	24(1)
C(15)	8464(3)	3615(2)	8752(2)	31(1)
C(16)	7241(3)	2873(3)	9078(2)	34(1)
C(17)	5858(3)	2694(3)	8590(2)	31(1)
C(18)	5668(3)	3249(2)	7764(2)	25(1)
C(19)	9677(3)	5029(3)	7569(2)	30(1)
C(20)	11099(3)	5523(3)	8315(2)	45(1)
C(21)	9853(3)	4322(3)	6685(2)	41(1)
C(22)	4160(3)	3027(3)	7203(2)	30(1)
C(23)	3767(3)	2038(3)	6335(2)	40(1)
C(24)	2961(3)	2634(3)	7786(2)	43(1)
C(25)	8458(3)	6507(3)	5382(2)	29(1)
C(26)	3700(3)	6307(3)	5745(2)	35(1)
C(27)	13109(4)	9375(3)	8938(2)	44(1)
C(28)	14125(4)	9226(3)	8467(3)	48(1)
C(29)	13740(4)	8777(3)	7514(3)	48(1)
C(30)	12330(4)	8469(3)	7032(2)	47(1)
C(31)	11317(4)	8618(3)	7508(2)	43(1)
C(32)	11711(4)	9073(3)	8458(2)	42(1)
H(3)	8609(10)	11317(29)	7721(6)	37
H(4)	8874(14)	11014(25)	9314(17)	39
H(5)	8150(4)	8967(5)	9756(22)	35
H(7)	7213(17)	8927(29)	5779(14)	42
H(8A)	5771(25)	10018(17)	6071(18)	89
H(8B)	6552(25)	10523(22)	5263(17)	89
H(8C)	7135(18)	11255(22)	6265(17)	89
H(9A)	8982(5)	10483(23)	5250(16)	80
H(9B)	9691(18)	9915(17)	6017(18)	80
H(9C)	9564(17)	11179(21)	6254(16)	80
H(10)	6972(3)	6131(20)	8212(18)	36
H(11A)	5131(15)	5430(23)	9041(20)	90
H(11B)	4835(17)	6351(26)	8337(15)	90
H(11C)	5470(7)	6850(22)	9421(18)	90

H(12A)	9012(21)	6826(22)	9443(7)	69
H(12B)	7713(17)	5674(19)	9686(11)	69
H(12C)	8044(20)	7075(21)	10122(12)	69
H(15)	9368(33)	3720(5)	9080(12)	37
H(16)	7351(5)	2473(14)	9656(20)	41
H(17)	5017(29)	2178(18)	8824(8)	37
H(19)	9505(7)	5757(25)	7374(7)	36
H(20A)	11873(18)	6153(21)	8061(8)	68
H(20B)	11379(15)	4810(15)	8470(13)	68
H(20C)	10955(8)	5923(22)	8890(14)	68
H(21A)	10613(23)	4909(13)	6404(11)	62
H(21B)	8935(20)	3992(20)	6223(12)	62
H(21C)	10122(25)	3619(19)	6868(5)	62
H(22)	4205(3)	3799(27)	6980(8)	36
H(23A)	2863(22)	1926(16)	5984(12)	60
H(23B)	3738(25)	1272(17)	6532(4)	60
H(23C)	4462(20)	2318(12)	5963(12)	60
H(24A)	2040(20)	2605(21)	7399(9)	64
H(24B)	3251(13)	3261(17)	8361(14)	64
H(24C)	2818(18)	1781(20)	7977(14)	64
H(25A)	8476(11)	7157(17)	5118(14)	44
H(25B)	8470(11)	5946(13)	4977(13)	44
H(25C)	9197(15)	6715(18)	5828(9)	44
H(26A)	3456(21)	6084(14)	6339(13)	52
H(26B)	2839(21)	6186(15)	5298(11)	52
H(26C)	4351(15)	7176(17)	5821(14)	52
D(27)	13381(11)	9692(13)	9607(26)	53
D(28)	14992(40)	9412(9)	8765(14)	58
D(29)	14427(29)	8681(5)	7197(14)	58
D(30)	12095(12)	8196(14)	6460(28)	57
D(31)	10430(39)	8424(9)	7208(13)	52
D(32)	11032(28)	9176(5)	8775(13)	51

Table A.10.4 *- Anisotropic displacement parameters ($Å^2$ x 10^3) for the 150K X-ray structure of [MoMe(N-2,6-^{i}Pr$_2$C$_6$H$_3$)$_2$(μ-OMe)]$_2$.*

Atom	U11	U22	U33	U23	U13	U12
Mo(1)	20(1)	17(1)	14(1)	0(1)	1(1)	5(1)
O(1)	23(1)	24(1)	19(1)	-4(1)	1(1)	9(1)
N(1)	22(1)	22(1)	19(1)	2(1)	3(1)	5(1)
N(2)	22(1)	20(1)	22(1)	0(1)	4(1)	7(1)
C(1)	17(1)	21(1)	22(1)	-2(1)	1(1)	6(1)
C(2)	26(1)	23(1)	25(1)	1(1)	4(1)	7(1)
C(3)	35(2)	21(1)	33(2)	1(1)	7(1)	7(1)
C(4)	37(2)	26(1)	30(1)	-9(1)	2(1)	11(1)
C(5)	37(2)	31(1)	21(1)	-2(1)	3(1)	19(1)
C(6)	25(1)	25(1)	23(1)	0(1)	3(1)	12(1)
C(7)	48(2)	21(1)	27(1)	2(1)	3(1)	4(1)
C(8)	45(2)	88(3)	49(2)	34(2)	6(2)	28(2)
C(9)	61(2)	74(2)	45(2)	28(2)	28(2)	39(2)
C(10)	48(2)	26(1)	18(1)	0(1)	3(1)	17(1)
C(11)	46(2)	46(2)	79(3)	23(2)	13(2)	7(2)
C(12)	64(2)	41(2)	34(2)	10(1)	1(2)	25(2)
C(13)	29(1)	17(1)	19(1)	0(1)	2(1)	10(1)
C(14)	29(1)	20(1)	23(1)	-1(1)	1(1)	11(1)
C(15)	35(2)	29(1)	27(1)	2(1)	-4(1)	14(1)
C(16)	48(2)	29(1)	25(1)	7(1)	3(1)	16(1)
C(17)	39(2)	25(1)	28(1)	7(1)	10(1)	11(1)
C(18)	30(1)	19(1)	25(1)	2(1)	6(1)	9(1)
C(19)	27(1)	29(1)	33(2)	4(1)	1(1)	11(1)
C(20)	30(2)	48(2)	47(2)	9(2)	-7(1)	8(1)
C(21)	34(2)	48(2)	45(2)	5(1)	14(1)	18(1)
C(22)	29(1)	26(1)	35(2)	9(1)	8(1)	9(1)
C(23)	32(2)	42(2)	36(2)	-1(1)	-2(1)	7(1)
C(24)	33(2)	47(2)	48(2)	11(1)	13(1)	13(1)
C(25)	27(1)	30(1)	26(1)	1(1)	7(1)	5(1)
C(26)	31(2)	37(2)	37(2)	-12(1)	3(1)	16(1)
C(27)	54(2)	38(2)	35(2)	0(1)	5(1)	13(2)
C(28)	30(2)	39(2)	66(2)	-4(2)	-5(2)	10(1)
C(29)	42(2)	36(2)	69(2)	-2(2)	30(2)	11(1)
C(30)	59(2)	42(2)	34(2)	-3(1)	7(2)	14(2)
C(31)	34(2)	40(2)	54(2)	5(1)	0(1)	16(1)
C(32)	43(2)	33(2)	54(2)	4(1)	22(2)	14(1)

APPENDIX B

CONFERENCES, COURSES, WORKSHOPS AND LECTURES ATTENDED, PERIODS SPENT WORKING AWAY FROM HOST INSTITUTION AND PUBLICATION LIST.

B.1 - CONFERENCES, COURSES AND WORKSHOPS ATTENDED AND OTHER PERIODS SPENT WORKING AWAY FROM HOST INSTITUTION.

(i) During academic year 1 when based at Durham, U.K.

16/11/94 : BCA Chemical Crystallography Group Autumn Meeting (Edinburgh, U. K.).

5/12/94-9/12/94 : ISIS neutron practical training course (Didcot, U.K.).

16/12/94 : Fifth Meeting of the U.K. Charge Density Group (Glasgow, U.K.).

17/1/95-24/1/95: ISIS single crystal neutron diffraction experiment with V.J.Hoy on SXD (2-amino-phenol).

27/3/95-31/3/95 : BCA Spring Meeting (Cardiff, U.K.) - poster presented, entitled *'Structural Studies of Non-linear Optical Materials'.*

2/4/95-7/4/95 : BCA Aston Intensive Course in Single Crystal Structure Analysis (Aston, U.K.).

13/4/95-30/4/95: Two ILL single-crystal neutron diffraction experiments on D9: the first one (14-23rd) was carried out to determine the structure of I described in chapter 4; the second one (24-30th) was carried out with Dr. A. S. Batsanov (potassium hydrogen maleate). During this time, I also oversaw one of my co-supervisor's magnetic experiments on the instrument D3B ($Na_2Ni(CN)_4.3H_2O$) and I conversed with my co-supervisor on progress so far and plans for future work.

18/5/95-25/5/95 : The International School and Workshop in Charge Density Analysis (La Plata, Argentina) - poster presented, entitled *'Structural Studies of Non-linear Optical Materials'.*

23/8/95-28/8/95: Neutron experiment on D9 at the ILL (the structure of [Mo(N-C_6H_3-2,6-Pr^i_2)$_2Me_2$] as described in chapter 10).

12/9/95-21/9/95 : Fourth Oxford Summer School in Neutron Scattering (Oxford, U.K.) - poster presented, entitled '*Structural Studies of Non-Linear Optical Materials*'.

(i) During academic years 2 and 3 when based at the ILL, Grenoble, France.

13/11/95-23/11/95: Durham University to test neutron crystals via X-rays (13-14th); ISIS experiment on SXD carried out in order to determine the neutron structure of DCNP described in chapter 6 (15-23rd); BCA Chemical Crystallography Group Autumnal Meeting, Manchester, U.K. (17th)

14/12/95-20/12/95: The First International meeting in Charge Density Analysis (Durham, U.K.) - invited talk given entitled *'Non-linear Optical Phenomena of Organic Molecules: Theory and Applications to Charge Density Studies'* (14-16th); One X-ray experiment (17-20th).

8/1/96-21/2/96: Durham University for the charge density X-ray experiment (at 20K) described in chapter 4; six conventional X-ray experiments; synthesis of more crystals for neutron work.

25/2/96-4/4/96: HERCULES (Higher European Research Course for Users of Large Experimental Systems), (Grenoble / Paris, France) - poster presented, entitled '*Structure / Property Relationships in Organic Non-Linear Optical Materials*'.

1/7/96 - 20/7/96: Charge density X-ray data set collected on the Siemens SMART at 100K in Durham (as described in chapter 6), followed by an experiment on SXD at ISIS, U.K. (N-methylurea - see chapter 7).

8/8/96-17/8/96: The International Union of Crystallography 17th Congress and General Assembly (Seattle, U.S.A.) - poster presented, entitled *'Charge Density Studies of Organic Non-Linear Optical Materials'*.

19/9/96-20/9/96: Neutron and Muon Beam Users Meeting (Didcot, U.K.) - invited talk entitled '*The Use of Neutrons in the Non-Linear Optical Phenomenon*'.

8/10/96-11/10/96: The First European Conference in Neutron Scattering (Interlaken, Switzerland) - poster presented entitled *'The Use of Neutrons in the Analysis of the Non-Linear-Optical Phenomenon'.*

4/3/97-6/3/97: The International Seminar on Structure and Properties of Crystalline Materials (Dubna, Russia) - invited talk entitled *'Structure / Property Relationships in Organic Non-linear Optical Materials'.*

9/3/97-25/5/97: Performing a charge density X-ray experiment at 20K (Durham, U.K.) and attending the BCA Spring Meeting, Leeds, U.K. (14-18th April) - poster presented entitled *'Agostic: to be or not to be?'.*

B.2 - LECTURES AND DEPARTMENTAL COURSES ATTENDED

(i) During academic year 1 when based at Durham, U.K.

26/10/94-30/11/94:	Six lecture course in polymer systems given by Dr. R. W. Richards (examination date: 12/12/94).
11/1/95-15/2/95:	Six lecture course in diffraction theory given by Professor J. A. K. Howard (examination date: 22/2/95).
5/10/94:	Professor N.L.Owen (Utah, U.S.A.) - Determining molecular structures the INADEQUATE NMR way.
13/10/94:	Prof. N. Bartlett (California, U.S.A.) - Rare gas halides.
2/11/94:	Dr. P.G.Edwards (Cardiff, U.K.) - The manipulation of electronic and structural diversity in metal complexes.
3/11/94:	Prof. B.F.G.Johnson (Edinburgh, U.K.) - Metal arene clusters.
1/2/95:	Dr. T.Cosgrove (Bristol, U.K.) - Polymers do it at interfaces.
8/2/95:	Dr D. O'Hare (Oxford, U.K.) - Synthesis and solid state properties of poly-,oligo- and multidecker metallocenes.
1/3/95:	Dr. M.Rosseinsky (Oxford, U.K.) - Fullerene intercalation chemistry.
11/5/95:	Prof. T Klapötke (Glasgow, U.K.) - Molecules made up of non-metals.
7/6/95:	Third year graduate seminars - in particular, 'New Vistas in Metal-Imido Chemistry' given by M.C.W.Chan.

(i) During academic years 2 and 3 when based at the ILL, Grenoble, France.

3/10/95:	Dr. G. Swallow (Loughborough, U.K.) - Applications of neutrons to stress and strain.

31/10/95:	Dr. V. N. Shvetsov (JINR, Dubna, Russia) - New UCN-source at a pulsed reactor.
6/12/95:	Dr. M. Johnson (ILL, Grenoble, France) - Half a problem: tunnelling spectroscopy of molecular crystals of unknown structures.
2/5/96:	Thesis student seminars: (1) W. Henggeler (ILL and ETHZ/PSI, Villegen, Switzerland) - Spin wave excitations in Nd in Nd_2CuO_4. (2) M. Weber (ILL and Innsbruck, Austria) - The interferometer of very cold neutrons: measurement of the gravitational phase shift.
17/6/96:	Professor R. Rinaldi (Perugia, Italy) - Neutrons in the earth sciences: recent perspectives and applications to mantle minerals.
22/10/96:	P. Guinneau (Bordeaux, France) - X-ray diffraction at low temperature and high pressure of organic conducting salts.
15/1/97:	Dr. B. O'Connor (Perth, Australia) - Time resolved studies of kinetic behaviour in alumina-matrix ceramic processing.
16/1/97:	A. R. George (Harlow, U.K.) - A whistle stop tour of computational chemistry.
29/1/97:	Dr. M. G. Davidson (Durham, U.K.) - The interaction of ylidic molecules with s-block metals and organic acids.
20/2/97:	Dr. V. J. Hoy (Durham, U.K.) - Experimental characterization of weak non-covalent interactions.

B.3 - PUBLICATION LIST

1. M. Szablewski, P. R. Thomas, A. Thornton, D. Bloor, G. H. Cross, J. M. Cole, J. A. K. Howard, M. Malagoli, F. Meyers, J. -L. Brédas, W. Wenseleers, E. Goovaerts, 'Highly Dipolar, Optically Non-Linear Adducts of TCNQ:- Synthesis, Physical Characterization and Theoretical Aspects', *J. Am. Chem. Soc.*, **119** (1997) 3144-3154..

2. M. C. W. Chan, J. M. Cole, V. C. Gibson, J. A. K. Howard, '(η^5-Cyclopentadienyl)dichloro(phenylimido)vanadium(V)' *Acta Crystallogr.* **C53** (1997) 202-204.

3. J. M. Cole, J. A. K. Howard, G. J. McIntyre, R. C. B. Copley, A. E. Goeta, M. Szablewski, G. H. Cross, 'Charge Density Studies of Organic Non-Linear Optical Materials', Acta Crystallogr. A52 (1996) Supplement **C-349**.

4. J. C. Cole, J. M. Cole, G. H. Cross, M. Farsari, J. A. K. Howard, M. Szablewski, 'Structural Studies of Non-Linear Optical Materials', *Acta. Crystallogr. B,* (in press).

5. J. M. Cole, B. Dorner, J. A. K. Howard, G. J. McIntyre, 'The Use of Neutrons in the Analysis of the Non-Linear-Optical Phenomenon', *Physica B*, **234-236** (1997) 922-924.

6. J. M. Cole, J. A. H. MacBride, J. A. K. Howard, '3,5-Dinitro-2-[(R(-)-1-phenylethyl)amino]pyridine', *Acta Crystallogr. C* (in press).

7. M. C. W. Chan, J. M. Cole, V. C. Gibson, J. A. K. Howard, 'Novel μ-Methyl Complexes of Vanadium and their Relevance to Bimolecular Deactivation of Homogeneous Imidovanadium Polymerisation Catalysts', *J. Chem Soc., Chem. Commun.,* (in press).

8. M. C. W. Chan, J. M. Cole, V. C. Gibson, J. A. K. Howard, 'Bis(2-t-Butylphenylimido)chloro(η^5-pentamethylcyclopentadienyl)tantalum(V) Anion', *Acta Crystallogr. C*, (submitted).

9. M. C. W. Chan, J. M. Cole, V. C. Gibson, J. A. K. Howard, C. W. Lehmann, A. D. Poole, Siemeling, U., 'Half-sandwich Imido Complexes of Niobium Bearing Alkyne, Benzyne and Benzylidene Ligands: - Relatives of the Zirconocene Family', *J. Chem. Soc., Dalton Trans.*, (submitted).

10. M. C. W. Chan, J. M. Cole, V. C. Gibson, J. A. K. Howard, 'Effects of the $[OC_6F_5]$ moiety upon structural geometry: synthesis and crystal structures of half-sandwich tantalum (V) aryloxide complexes from reaction of $Cp^*Ta(N^tBu)(CH_2R)_2$ with pentafluorophenol', *J. Chem. Soc., Dalton Trans.,* (in preparation).

11. J. M. Cole, J. A. K. Howard, G. J. McIntyre, 'The Role of Hydrogen-Bonding in the Structure/Property relationship of Non-Linear Optical Materials', *J. Chem. Soc., Chem. Commun.*, (in preparation).

12. J. M. Cole, V. C. Gibson, J. A. K. Howard, G. J. McIntyre, G. L. P. Walker, 'Multiple α-Agostic Interactions in a Metal-methyl Complex: The Neutron Structure of $[Mo(N\text{-}C_6H_3\text{-}2,6\text{-}Pr^i_2)_2Me_2]$', *J. Chem. Soc., Chem. Commun.*, (in preparation).